

AD-A148 634

PROCEEDINGS OF THE INTERNATIONAL CONFERENCE ON THE
PERFORMANCE OF OFF-ROAD (U) INTERNATIONAL SOCIETY FOR
TERRAIN-VEHICLE SYSTEMS W J DWYER AUG 84

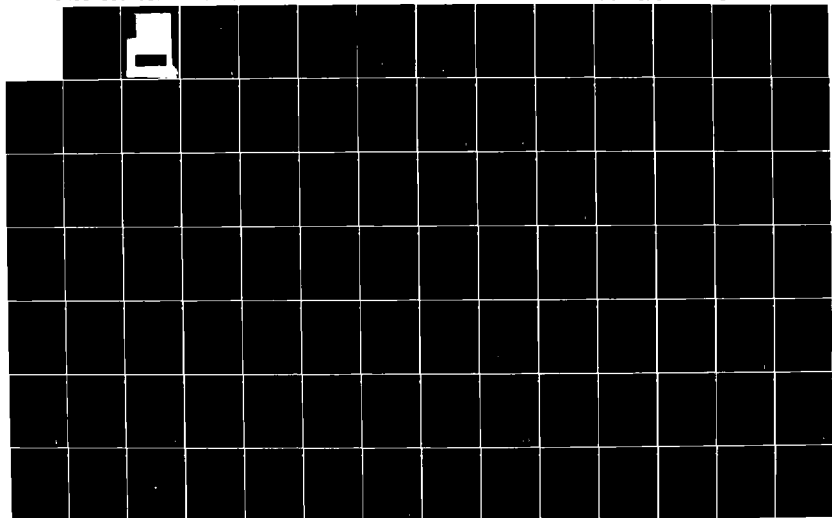
1/6

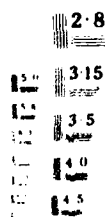
UNCLASSIFIED

DAJA45-84-M-0251

F/G 13/8

NL





AD-A148 634

APPROVED FOR PUBLIC RELEASE: DISTRIBUTION
UNLIMITED

DTIC
ELECT

COMPONENT PART NOTICE

THIS PAPER IS A COMPONENT PART OF THE FOLLOWING COMPILATION REPORT:

(TITLE): Proceedings of the International Conference on the Performance of
Off-Road Vehicles and Machines (8th) - Volume I - Bell at Cambridge
Cambridge August 2-11, 1984

(SOURCE): International Society for Terrain-Vehicle Systems

DTIC
SELECTED
S
DEC 27 1984

TO ORDER THE COMPLETE COMPILATION REPORT USE AD-154 043

A

THE COMPONENT PART IS PROVIDED HERE TO ALLOW USERS ACCESS TO INDIVIDUALLY AUTHORED SECTIONS OF PROCEEDINGS, ANNALS, SYMPOSIA, ETC. HOWEVER, THE COMPONENT SHOULD BE CONSIDERED WITHIN THE CONTEXT OF THE OVERALL COMPILATION REPORT AND NOT AS A STAND-ALONE TECHNICAL REPORT.

THE FOLLOWING COMPONENT PART NUMBERS COMPRISE THE COMPILATION REPORT:

AD#:

TITLE:

- | | |
|-------------|---|
| AD-P004 259 | Modélisation des Paramètres Reales et du Sol en Vue de l'Amélioration de la Traction (Modelling of Off-Road Tyres and Soil to Improve Traction) |
| AD-P004 260 | Development of a Dual-Wheel Interaction Model |
| AD-P004 261 | Soil Compliance Influence on Tyre Performance |
| AD-P004 261 | The Rolling Resistance and Sinkage of Towed Dual Wheel Combinations in Soil |
| AD-P004 262 | Performance Prediction of Pneumatic Tyres on Sand |
| AD-P004 263 | Effects of Slip on Energy Distribution between Tyre and Soil |
| AD-P004 264 | Traction Forces of Drive Tyre on the Compacted Soil |
| AD-P004 265 | Prediction of In-Sand Tire and Wheeled Vehicle Drawbar Performance |
| AD-P004 266 | Dynami Simulation of Track Laying Vehicles |
| AD-P004 267 | Designing Off-Road Vehicles with Good Ride Behaviour |
| AD-P004 268 | Theoretische Untersuchung Einer Aktiv-Federung fuer Rad-Schlepper (A Theoretical Investigation of an Active Suspension System for Wheeled Tractors) |

This document has been approved
for public release and sale; its
distribution is unlimited.

Copy available to DTIC does not
permit fully legible reproduction

COMPONENT PART NOTICE (CON'T)

AD#:

TITLE:

- AD-P004 270 Leistung^Ssteigerung und Verbesserung des Fahrkomforts bei Selbstfahrenden Rammschienen Durch Reduzierung Einsatzbedingter Nick- und Hubschwingungen (Increase in Performance and Improvement of Ride Comfort of Self-Propelled Construction Machinery by Reducing Pitch and Vertical Vibration)
- AD-P004 271 Stresses and Strain Generated by Bulldozers
- AD-P004 271 Finite Element Analysis of Ground Deformation Beneath Moving Track Loads
- AD-P004 271 A Rig for Testing the Soft Soil Performance of Track Systems
- AD-P004 271 Die Abhängigkeit der Bodentragfähigkeit und der Zugkraft von der Abstandsgroesse der Bodenplatten (The Dependence of Soil Bearing Capacity and Drawbar Pull on the Spacing between Track Plates)
- AD-P004 274 The Dynamic Interaction between Track and Soil
- AD-P004 275 Analysis of Ground Pressure Distribution Beneath Tracked Model with Respect to External Loading
- AD-P004 276 A Comparison between a Conventional Method and an Improved Method for Predicting Tracked Vehicle Performance
- AD-P004 277 Effect of Hitch Positions on the Performance of Track/Grouser Systems
- AD-P004 278 Grouser Effect Studies
- AD-P004 279 Ride Comfort of Off-Road Vehicles
- AD-P004 280 Further Development in Ride Quality Assessment
- AD-P004 281 Comparison of Measured and Simulated Ride Comfort for an Agricultural Tractor and Influence of Travel Speed and Tyre-Inflation Pressure on Dynamic Response
- AD-P004 282 Characteristics of Fram Field Profiles as Sources of Tractor Vibration

Distribution/		
Availability Codes		
Avail and/or		
Dist	Special	
A-1		

INTERNATIONAL SOCIETY FOR TERRAIN VEHICLE SYSTEMS

USACRREL, 72 Lyme Road, Hanover, New Hampshire,
03755, USA

SFM/FOA 2, Box 27322, S-102 54, Stockholm, Sweden

8th International Conference

The Performance of Off-Road Vehicles
and Machines

August 5-11, 1984

Churchill College, Cambridge University, England

Proceedings
Volume I of III

ACKNOWLEDGEMENT

The assistance of the following organisations is gratefully acknowledged.

James A. Cuthbertson Ltd., Biggar, Scotland

Military Vehicles and Engineering Establishment, Chertsey,
England

National Institute of Agricultural Engineering, Silsoe,
England

Silsoe College, Silsoe, England

United States Army Research Development and Standardization
Group - UK, London, England



PREVIOUS PAGE
IS BLANK

Accession For	
DSIR	<input checked="" type="checkbox"/>
DSIR	<input type="checkbox"/>
DSIR	<input type="checkbox"/>
DSIR	<input type="checkbox"/>
DSIR	<input type="checkbox"/>
DSIR	<input type="checkbox"/>
DSIR	<input type="checkbox"/>
DSIR	<input type="checkbox"/>
DSIR	<input type="checkbox"/>
DSIR	<input type="checkbox"/>
Dist	<input type="checkbox"/>
A-1	

CONTENTS

VOLUME I

	Page
TOPIC 1 TYRE-SOIL INTERACTION	1
Chairman: R.D. Wismer, Deere and Company, USA	
Rapporteur: Prof. J.Y. Wong, Carleton University, Canada	
Modelisation des pneus hors routes et du sol en vue de l'amélioration de la traction (Modelling of off-road tyres and soil for improved traction) (including English translation)	
Prof. P.F.J. Abeels, Louvain University, Belgium	3
Development of a soil-wheel interaction model	
Dr. G.Y. Baladi and B. Rohani, US Army Engineer Waterways Experiment Station	33
Soil compliance influence on tyre performance	
P. Boonsinsuk and Prof. R.N. Yong, McGill University, Canada	61
The rolling resistance and sinkage of towed dual wheel combinations in sand	
J.G. Hetherington and I. Littleton, Royal Military College of Science, England	81
Performance prediction of pneumatic tyres on sand	
Lt. Col. Tej Paul, Vehicles Research and Development Establishment, India	87
Effects of slip on energy distribution between tyre and soil	
Dr. M. Ronai, Institute for Mechanization, Yugoslavia	97
Traction forces of drive tyre on the compacted soil	
Dr. Ing. J. Swiech, Institute for Buildings, Mechanization and Electrification in Agriculture, Poland	109
Prediction of in-sand tire and wheeled vehicle drawbar performance	
G.W. Turnage, US Army Engineer Waterways Experiment Station	121

	Page
TOPIC 2 THEORETICAL ASPECTS OF RIDE DYNAMICS	151
Chairman: Dr. H. Schwanghart, Munich University, Germany	
Rapporteur: Dr. D.A. Crolla, Leeds University, England	
 Dynamic simulation of track laying vehicles	
M.D. Bennett and P.G.H. Penny, Royal Military College of Science, England	153
 Designing off-road vehicles with good ride behaviour	
D.N.L. Horton and Dr. D.A. Crolla, University of Leeds, England	171
 Theoretische Untersuchung einer Aktiv-Federung für Rad-Schlepper (Theoretical study of an active suspension for wheel tractors) (including English translation)	
Dipl.-Ing. H. Junker and Dipl.-Ing. A. Seewald, Institut für Kraftfahrwesen, Germany	185
 Leistungssteigerung und verbesserung des fahrkomforts bei selbstfahrenden baumaschinen durch reduzierung einsatzbedingter nick- und hubschwingungen (Increase in performance and improvement of ride comfort of self-propelled construction machinery by reducing pitch and vertical vibration) (including English translation)	
Prof. Dr.-Ing. W. Poppy and Dr.-Ing. A. Ulrich, Berlin Technical University, Germany	215

TOPIC 3	TRACK-SOIL INTERACTION	Page
		257
Chairman:	Dr. G. Rigamonti, CNR-Cemoter, Italy	
Rapporteur:	Prof. R.N. Yong, McGill University, Canada	
Stresses in situ generated by bulldozers		
	H. Fueni and T. Watanabe, Okayama University, Japan; T. Sawada, Kyoto University, Japan	259
Finite element analysis of ground deformation beneath moving track loads		
	Dr. M.H. Karafiath, Grumman Aerospace Corporation, USA	277
Land for testing the soft soil performance of track systems		
	Col. MacLaurin, Military Vehicles and Engineering Establishment, England	291
Die Abhängigkeit der Bodentransföhrigkeit und der Zugkraft von der AbstandsgröÖsse der Bodenplatten (The dependence of soil bearing capacity and drawbar pull on the spacing between track plates) (including English translation)		
	Dr.-Ing. A. Mierzwicki, Warsaw Technical University, Poland	313
The dynamic interaction between track and soil		
	Dr. Dipl.-Ing. F. Parrinier, IAG-Ottobrunn, Germany	329
Analysis of ground pressure distribution beneath tracked model with respect to external loading		
	M.M. Pencylus, Warsaw Technical University, Poland	349
A comparison between a conventional method and an improved method for predicting tracked vehicle performance		
	Prof. J.Y. Wong and J. Preston-Thomas, Carleton University, Canada	361
Effect of hitch positions on the performance of track/ crawler systems		
	Prof. R.N. Yong, H. Elmaglouk and N. Skiadak, McGill University, Canada	381
Crawler effect studies		
	Zhang Fei-jian, North Vehicle Research Institute, China	399

TOPIC 4	PRACTICAL ASPECTS OF RIDE DYNAMICS	Page
		411
Chairman:	E. Myhrman, Skogsrådet, Sweden	
Rapporteur:	E.B. MacLaurin, Military Vehicles and Engineering Establishment, England	
	Ride comfort of off-road vehicles	
	G.B. Kobi, Ministry of Defence, Austria	413
	Further development in ride quality assessment	
	N.R. Murphy, Jr., US Army Engineer Waterways Experiment Station	433
	Comparison of measured and simulated ride comfort for an agricultural tractor and influence of travel speed and tyre-inflation pressure on dynamic response	
	Dipl-Ing. C. Strauss and W. Christ, Battelle Institut e.V., Germany	451
	Characteristics of farm field profiles as sources of tractor vibration	
	K. Ohnura and K. Matsui, Hokkaido University, Japan	473

VOLUME II

	Page
REPORT: OPERATION IN PADDY FIELDS	493
Chairman: Dr. A.R. Reese, Soil Machine Dynamics Ltd., England	
Supporters: Prof. T. Tanaka, Kyoto University, Japan	
The research of the driving wheel with movable lugs of the paddy field floating tractor	
Prof. Xiao Junde and Zhao Yu Fan, Jilin University of Technology, China	495
Measurement of the driving wheel thrust of paddy field tractor	
Prof. Zhang Hong and Yeai Shucheng, Luoyang Tractor Research Institute, China	507
Stability of the small combine (track type) on soft ground - Relationship between the position of the center of gravity and the stability	
Prof. H. Isaki, Tsukuba University, Japan	521
The stress-strain-time graph of rheological soils and its application	
Prof. Han Jun Zheng, Jiangsu Institute of Technology, China	539
Behaviour of soil under a lugged wheel	
Prof. Shi, J.H. Shi and Prof. J.Y. Wong, Carleton University, Canada	545
Prediction accuracy of the torques for rotary tillage by an unlisted tool	
Minoru Yamazaki and Prof. Takashi Tanaka, Kyoto University, Japan	561
Analysis on the dynamic performance of a single lug	
Zhang T.H. and Prof. J.Y. Shao, South China Agricultural College	575

(x)

TOPIC 6	OPERATION ON STEEP SLOPES	Page 593
Chairman:	Dr. E. Haarlaa, Helsinki University, Finland	
Rapporteur:	Dr. A. Grecenko, Agricultural Machinery Research Institute, Czechoslovakia	
Study of the motion of agricultural vehicles on steep snow- covered slopes		
Dr. A. Grecenko, Agrozet-Research Institute of Agricultural Machinery, Czechoslovakia		595
Some stability and control problems with trailed farm tractors on slopes		
A.G.M. Hunter, Scottish Institute of Agricultural Engineering		615
Control of tractors on sloping ground		
H.B. Spencer, Scottish Institute of Agricultural Engineering, and Dr. D.A. Crolla, Leeds University, England		635
Stability indicators for front end loaders		
G. Wray and J. Nazalewicz, Stevens Institute of Technology, USA, and A.J. Kwitowski, US Bureau of Mines		655

TOPIC 7	SOIL COMPACTION	Page
Chairman:	Prof. W. Soehne, Munich University, Germany	673
Supporter:	Dr. J.H. Taylor, National Tillage Machinery Laboratory, USA	
Pressure tests in soil below tires of agricultural vehicles		
Engl.-Ing. L. Bolling, München Technische Universität, Germany		675
Quality control in soil compaction by behaviour of exciter		
Dr. Hata and K. Tateyama, Kyoto University, Japan		691
Another terrain machine		
A. Marklund, Swedish University of Agricultural Sciences		707
Excitation of sand using ordinary off-road vehicles		
Col. Dr. H. Shaban, Military Technical College, Egypt		725
A simple prediction model for soil compaction under various wheel loads and geometries as an aid to vehicle design		
Dr. J. Smith, Scottish Institute of Agricultural Engineering		737
Rotation of tires and subsurface compaction		
Dr. J.H. Taylor and Dr. E.C. Burt, National Tillage Machinery Laboratory, USA		751
Tractor power selection with compaction constraints		
Dr. E.A. Whitney, E.R. Elbanna, and F. Eradat Oskoun, North of Agricultural College of Agriculture		761

TOPIC 8	STEERING	Page 775
Chairman:	Prof. A.J. Soltynski, Warsaw University, Poland	
Rapporteur:	Dr. P. Dudzinski, Wroclaw University, Poland	
The guidelines to design the lever turning gears in articulated vehicles		
Dr. P. Dudzinski and Prof. Dr. H. Hawrylak, Technical University of Wroclaw, Poland		777
Study on controllability and stability of high speed tracked vehicles		
F. Eiyo and Prof. M. Kitano, The National Defence Academy, Japan		789
Forces on undriven, angled wheels		
M. McAllister, National Institute of Agricultural Engineering, England		803
Turning behaviour of articulated frame steering tractor		
Dr. A. Oida, Kyoto University, Japan		821
A tracked vehicle test plant for the simulation of dynamic operation		
Prof. Dr.-Ing. I. Schmid, University of German Armed Forces		835
Profileinfluss auf Widerstands- und lenkkräfte frei rollender reifen (The influence of the tyre tread on the rolling resistance and steering forces on undriven wheels) (including English translation)		
Dr. H. Schwanghart and K. Rott, Technische Universität München, Germany		855
Basic study on the turning resistance of track		
Dr. N. Sugiyama and H. Kondo, Tokai University, Japan		889
Study on steerability of articulated tracked vehicles		
F. Watanabe and Prof. M. Kitano, The National Defence Academy, Japan		901

VOLUME III

	Page
PREFACE COMPUTER MODELING	917
Chairman: Dr. E.-M. Melzer, Battelle Institute, Germany	
Reporteur: W. Köppel, Battelle Institute, Germany	
Energy for field operations in developing countries	
Ch. Chensley, Silsoe College, England	919
Computer models to predict the performance of agricultural tractors on heavy draft operations	
Dr. M. J. Dwyer, National Institute of Agricultural Engineering, Silsoe, England	933
Differential equations of the vehicle's linear motions: Mathematical solution and experimental approaches	
Dr. G. Lorenz, Italian Army	953
Tractor-soil-implements - Functional interactions and models	
Dr. G. Jahn and Dr. H. Steinkampf, Federal Research Center of Agriculture, Germany	969
Aerial evaluation of vehicle mobility	
W. Köppel and Dipl.-Ing. G. Strauss, Battelle-Institut e.V., Germany	985
Predicting the performance of fast cross country vehicles	
Major G. L. Lammie, England	1005

TOPIC 10	VEHICLE COMPONENT DESIGN	Page
Chairman:	Dr. R.I. Ehrlich, Stevens Institute of Technology, USA	1
Microprocessor based speed governing of diesel engines used in mobile applications for best all round performance	B.S. Chittawadgi, H.C. Dhariwal, R.S. Bhatkeshwar, Indian Institute of Technology	1027
Electronic-commutator AC/DC motor-driven tracked all-terrain vehicles with extremely high mobility	Dr. B.T. Fijalkowski, Cracow Polytechnic, Poland	1045
Rotary hydraulic suspension damper for high mobility off-road vehicles	T.J. Holman, Horstman Defence Systems Ltd., England	1065
Quick connect intervehicle coupling system	I.C. Kamm, G. Wray and J. Nazalewicz, Stevens Institute of Technology, USA	1077
Estimation of wear life of heavy dump truck tyre	Prof. T. Muro, Ehime University, Japan, Prof. S. Hata and F. Fukagawa, Kyoto University, Japan	1089
RUD introduces a chain device type "Terra" - The new combination of polyurethan and alloy steel for snow, sand and off-the-road terrain	Dr.-Ing. H. Rieger, RUD - Kettenfabrik Rieger and Dietz GmbH u. Co., Germany	1105
Use of microcomputer technology to improve the performance of tractor implement combinations	J.M. Wilkes, S.W. Burrage and M.J. Varley, Wye College, England	1123

	Page
TOPIC 11 MEASUREMENT OF SOIL AND SNOW PROPERTIES AND SOIL BIN FACILITIES	1133
Chairman: Dr. R.A. Liston, US Army Cold Regions Research Laboratory	
Measurement of soil properties in dryland and wetland conditions	
Dr. D. Gee-Clough and M.A. Sargara, Asian Institute of Technology, Thailand	1135
The measurement of snow properties for mobility applications: The unfrozen water content	
Dr. W.L. Harrison, Dr. G.G. Gimmetstad and Dr. S.M. Lee, Michigan Technological University, USA	1149
The modification of soil strength characteristics due to the presence of vegetation	
I. Littleton and J.G. Hetherington, Royal Military College of Science, England	1157
Microwave sensor for the trafficability studies of snow	
M. Saarimäki, University of Dar es Salaam, Tanzania	1165
A lubricated cone penetrometer for quantifying the soil physical condition	
Prof. E.W. Tollner, University of Georgia, USA	1171
A consideration of elasto-plastic model for the composite soil	
M. Ueno, University of Ryukyus, Japan	1189
Soil bin facilities: characteristics and utilization	
P.D. Wismer, Deere & Company, USA	1201
Properties of desert silty soil in relation to vehicle mobility	
A.-F.A. Youssef, King Saud University, Saudi Arabia	1217

TOPIC 12	VEHICLE DESIGN	Page
Chairman:	Brig. Gen. S.A.K. Areskoug, Sweden	1235
Cuthbertson tracks		
J.A. Cuthbertson, James A. Cuthbertson Ltd., Scotland		1237
An all terrain vehicle equipped with central tire inflation system		
Prof. A.E. Hassan, North Carolina State University, USA		1241
Central tire inflation systems (CTIS) - A means to enhance vehicle mobility		
R.W. Kaczmarek, US Army Tank-Automotive Command		1255
Rubber tracks for machinery and vehicles in forestry and agriculture		
P.I. Mickelson, Skega AB, Sweden		1273
Improvements in crawler tractor traction		
K. Ogaki and Y. Tamura, Komatsu Ltd., Japan		1281
Noise reduction in the terrain-vehicle T 11		
Dr.-Ing. V. Tandara, Germany		1291

TOPIC 1

TYRE-SOIL INTERACTION

MODELISATION DES PNEUS HORS ROUTES ET DU SOL EN VUE DE L'AMELIORATION DE LA TRACTION

Prof. Dr. ir. P.F.J. ABEELS
U.C.L., Génie Rural
Louvain-la-Neuve, Belgium

RESUME

De très nombreuses réactions à l'introduction de moyens mécaniques sur les terres agricoles et en forêts se font jour en raison notamment des compactages induits. D'autre part, l'évolution hors route doit envisager de plus en plus de véhicules sur pneus à diverses finalités. Il est donc important d'aborder les questions liées aux propriétés des enveloppes déformables pour voir de quelle manière il peut être possible d'en approprier la conception en fonction des sols non aménagés sur lesquels ils doivent évoluer.

Les caractéristiques nécessaires à la promotion de nouveaux concepts doivent mettre en évidence la déformabilité des enveloppes et dégager les propriétés de chacune des parties principales du pneu dans la transmission des charges sur le support. C'est pourquoi, taux d'aplatissement, taux d'écrasement, distribution des épaisseurs de matière sur la section du pneu, propriétés de l'épaulement, fléchissement de la bande de roulement, raideur du tore, caractéristique d'amortissement de l'enveloppe sont à déterminer. La relation pneu-sol ressort des effets de compression, de rotation et de pivotement du pneu sur le sol.

La modélisation qui résulte de la connaissance de ces caractéristiques permet d'introduire des concepts et des méthodes de calcul d'enveloppes. La réalisation de prototypes confirme expérimentalement les possibilités ainsi développées.

AVANT-PROPOS

Lorsque les altérations et dégâts aux sols prennent une importance exagérée en agriculture et en sylviculture, un certain nombre de réactions se font jour à l'encontre de la mécanisation sous la forme par exemple d'interdits souvent subjectifs ou de mesures compensatoires fréquemment onéreuses. En effet, si une part des causes de dégradations peut être attribuée aux véhicules et machines elles-mêmes, c'est bien plus généralement les opérateurs qui sont en cause pour ne pas avoir adapté leurs conditions de travail.

Dès lors, les notions de compactage des sols par les effets des pneumatiques doivent être précisées pour être enseignées et vulgarisées. Cette vulgarisation permettra aussi, d'une part de mieux orienter les choix parmi les manufactures et, d'autre part de suggérer de nouvelles solutions pour améliorer la propulsion hors route et réduire les impacts des pneus sur les sols. Des économies directes et indirectes d'énergie sont dès lors possibles en garantissant mieux l'environnement.

LA MODELISATION DU PNEU HORS ROUTES

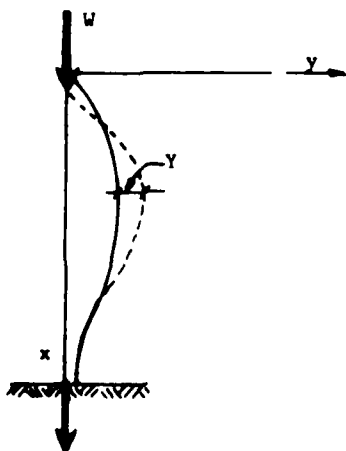
Propos

Le pneumatique reçoit les charges reprises par le moyeu de l'essieu d'un véhicule et qui lui sont transmises par le voile et la jante sur laquelle il est monté pour former la roue. L'analyse des effets de cette transmission porte sur la déformabilité de l'enveloppe et sur les effets enregistrés au sein d'un substrat donné comme support.

La déformabilité de l'enveloppe torique ou pneu

La déformabilité d'enveloppe est renseignée par les taux d'aplatissement et d'écrasement qui ressortent de la géométrie externe de l'enveloppe. Il est connu que ces taux augmentent avec la charge appliquée et diminuent avec l'élévation de la pression de gonflage ou du nombre de plis. Il est aussi noté que les variations de ces taux respectifs permettent de ranger certaines manufactures en des catégories différentes de la notion de ply rating. Les valeurs des variations de hauteur de tore pneumatique étant supérieures à celles de largeur, les taux renseignés expriment la déformabilité générale du tore d'une part et celle des flancs d'autre part. Il reste encore à souligner que la coupe transversale d'un pneu révèle une distribution variable des épaisseurs de matière tout au long des parois et qu'une pression de gonflage donnée se distribuant équirépartie dans toutes les directions n'engendrera pas les mêmes effets quant à la déformabilité. Celle-ci est particulièrement importante aux basses pressions de gonflage recommandables en locomotion hors routes et plus particulièrement sur milieu granuleux.

La variation de la pression de gonflage contribue principalement à une modification de la raideur du flanc de l'enveloppe et influence peu la bande de roulement.



L'application d'une contrainte sur la bande de roulement engendre des sollicitations dans la section du flanc du type effort normal, effort tranchant et moment fléchissant. Une équation de flexion du flanc soumis à une charge et soutenu par une pression de gonflage peut s'établir.

L'expression générale est :

$$Y = - \frac{M}{EI} = - \frac{W \cdot y(x)}{EI}$$

En retirant une portion unitaire de flanc formée d'une section de 1 cm de largeur, il vient :

$$Y = - \frac{W + y(x)}{E_r \cdot e / 12}$$

et

$$e = \left(- \frac{12 W + y(x)}{E_r \cdot Y} \right)^{1/3}$$

où : e = épaisseur de paroi du flanc

W = charge

y = flèche de la déformation

E_r = module de rigidité

Ainsi, l'épaisseur d'enveloppe en chaque point dépend du module de rigidité, du centre de flanc, de la charge appliquée et de la flèche tolérée. La déformation étant donnée qu'elle est liée à la pression de gonflage, la programmation à l'ordinateur permet une résolution définissant toutes les caractéristiques, les autres étant fixées.

Le contact entre le flanc s'associe à des effets dans la bande de roulement en raison de l'existence d'une continuité à l'endroit de l'épaulement.

En effet, on y localise des efforts normaux, tranchants et certains moments flexionnants. Ceux-ci établissent alors certaines propriétés de la bande de roulement lorsqu'elle s'applique sur un support.

On peut alors statiquement en des lieux de la bande de roulement permettre d'apprécier les déplacements verticaux ainsi causés. Le pneu étant soumis à des déformations verticales nettement moins importantes qu'en général. Ici aussi la pression de gonflage agit comme raidissement des déplacements à considérer. Le premier invoque la relation entre bande de roulement à l'intervention de l'épaulement. Le second élément concerne l'influence de la longueur et du nombre de barrettes. Plus les barrettes et plus longues sont ces barrettes, moins grande est l'influence de la pression de gonflage. Les déformations relevées dans le sens transversal à l'équateur révèlent l'importance particulièrement grande des déplacements transversaux. Ceux-ci apparaissent comme des lieux de poinçonnement de l'armature du pneu lorsque seules les faces supérieures des barrettes partent sur un support et il est noté que la déformation verticale transversale est d'autant plus grande que les barrettes ne couvrent pas l'équateur.

La bande de roulement se conçoit bien évidemment comme l'élément du pneumatique en contact avec le support. Assimilé pour les besoins de son étude à une poutre de section unitaire rectangulaire, il est possible d'y utiliser les expressions connues. Les flèches mesurées en divers endroits de la bande de roulement infléchie par des charges permettent d'utiliser les équations de référence. Ainsi, la flèche ou f à la distance x des supports pour a et b , les distances du lieu d'application de la charge par rapport aux mêmes appuis, vaut :

$$\frac{W}{6EI} (1^2 - b^2 - x^2) \quad \text{si } x < a$$

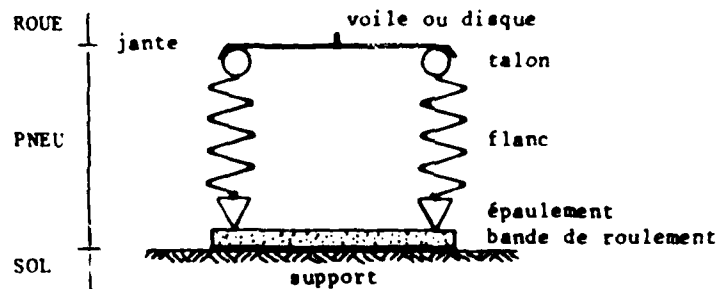
et

$$\frac{Wa(1-x)}{61EI} (2x1 - a^2 - x^2) \quad \text{si } a < x < 1$$

où W = charge appliquée, M ou F
 l = longueur de la poutre, L
 E = module d'élasticité, FL⁻²
 I = moment d'inertie = $\frac{bh^3}{12}$, L⁴

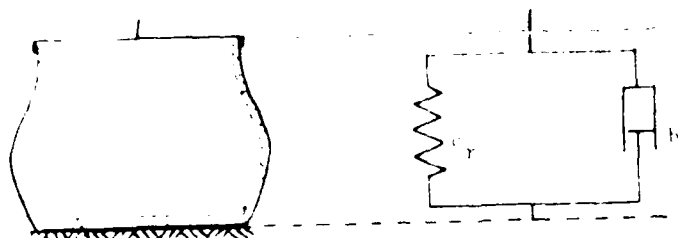
Ainsi qu'on peut le voir, la flèche prise par la bande de roulement suite à action ou réaction localisée en sa surface est essentiellement dépendante de E si celui-ci peut prendre des valeurs élevées par rapport à l'échelle de variation possible des autres cotes dans la réalisation d'une enveloppe de pneumatique.

Le pneumatique hors route ou tore déformable distingue les parties flancs, épaulements et bande de roulement. A celles-ci il convient d'ajouter les talons qui assurent la liaison avec l'élément rigide jante associé à la masse du véhicule, par construction. Le schéma du pneu agraire, forestier et hors route en général est donc :



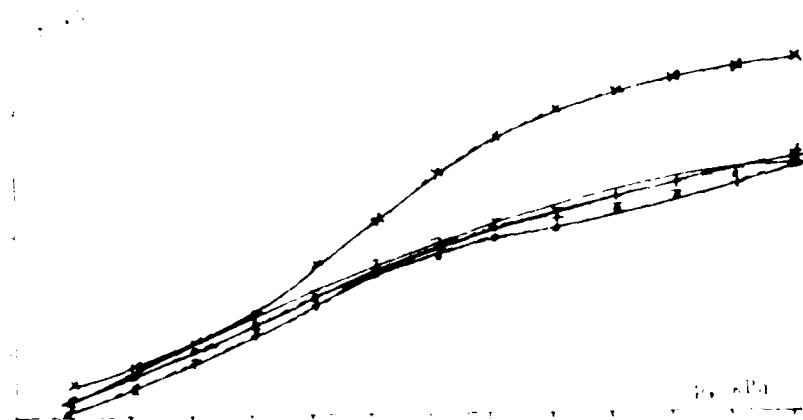
Les conditions du comportement dynamique du pneu sont approchées en vue de préciser le mode d'action des charges supportées sur le sol. Un banc spécial d'essais en statique a été réalisé pour ce faire. Essentiellement, il s'agit de voir comment l'enveloppe produit un certain "martelage" du sol du fait de la constitution élastique du pneu. Le pneu est assimilé pour ce faire à un système composé d'un ressort et d'un amortisseur disposés en parallèle.

Le schéma simplifié est alors le suivant :



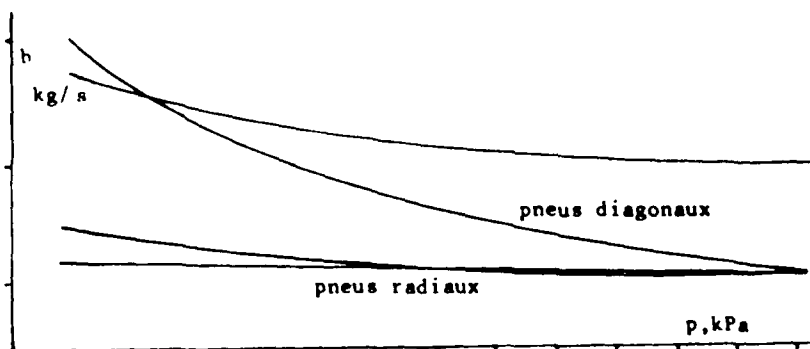
a) coefficient de raideur
b) caractéristique d'amortissement

Le coefficient de raideur c_r est une fonction de la pression et cela sera pris en compte dans les calculs et sera noté $c_r(p)$ au lieu de c_r car c_r n'est pas une constante mais une fonction de la pression.



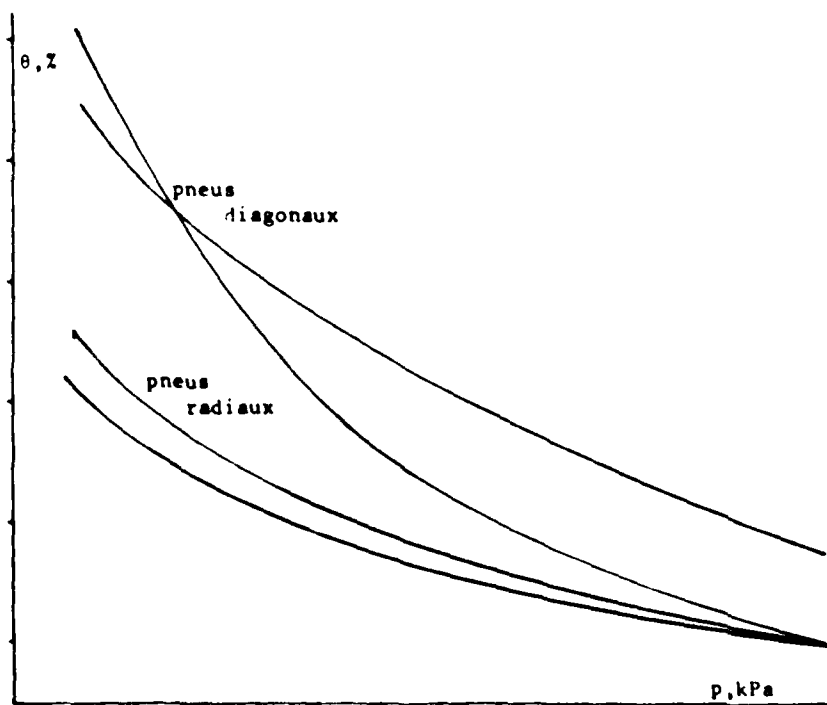
Evolution du coefficient de raideur en fonction de la pression

La caractéristique de l'amortissement créé par l'enveloppe du pneu évolue différemment pour les pneus radiaux et diagonaux. Les dimensions du pneu influencent cette caractéristique. L'élévation de la pression de gonflage diminue la valeur de la caractéristique d'amortissement et cela d'autant plus nettement pour les pneus diagonaux.



b : caractéristique d'amortissement, kg/s

Quant au degré d'amortissement réalisé par les enveloppes, il apparaît nettement influencé par la pression de gonflage et cela plus pour les carcasses diagonales que pour les radiales.



θ : degré d'amortissement

la relation pneu-sol

la relation pneu-sol permet d'enregistrer les effets au sein d'un substrat donné comme support. Ces effets sont causés par trois modes d'action du pneu sur un sol, à savoir :

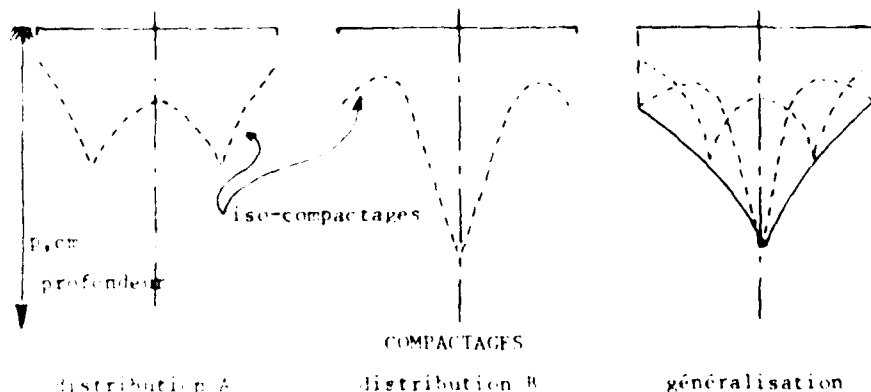
- la compression qui se traduit par l'enfoncement et s'accompagne de tassements et de compactages pour laisser soit une empreinte locale soit une trace, c'est-à-dire l'ornière;
- la traction qui se traduit par du frottement et de l'accrochage avec le sol entraînant le détachement de portions de sol;
- le mouvement de pivot qui entraîne le raclage en surface du sol.

le sol en place constitue un massif hétérogène où coexistent des particules, des grumeaux et des mottes avec des vides plus ou moins distribués dans les réseaux.

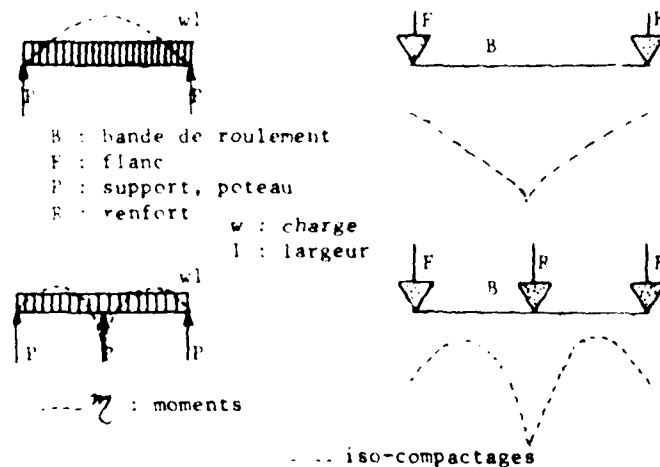
le passage de la roue sur le sol peut entraîner un tassement structural sans affecter les assemblages élémentaires entre les particules, causer certaines coalescences des mottes et grumeaux ou provoquer un compactage textural atteignant les assemblages élémentaires. Dès lors, compression, traction et pivotement du pneu auront des conséquences plus ou moins réversibles quant à l'état du sol et plus exactement de la partie supérieure de la couche arable.

les poinçonnements exercés par un pneumatique dans un sol se traduisent par des compressions localisées dont la distribution, suivant un profil transversal à l'équateur de la trace du pneu, est mesurée pour restituer l'action de la bande de roulement sur le massif granuleux.

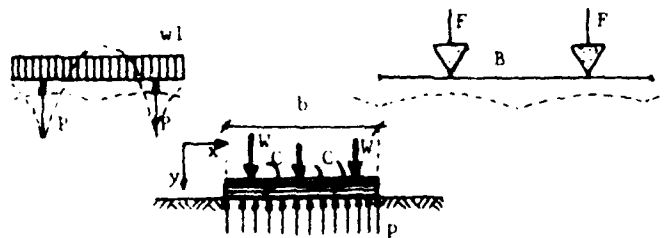
considérant ces profils donnant la distribution des compactages suivant la section transversale, il est possible de constater que les effets apparaissent répartis comme si les moments fléchissants créés par le mode de transfert des charges dans la bande de roulement à l'endroit des épaulements pouvaient s'exprimer dans la masse granuleuse du support sol. les représentations suivantes rappellent ces enregistrements relatifs à la profondeur où se placent de mêmes compactages (iso-compactages)



Les modèles d'effets des charges sur appuis repris de la théorie de la résistance des matériaux donnent ce qui est représenté aux figures suivantes



L'élaboration d'un profil de pneu hors route n'entraînant qu'un compactage réduit doit tenir compte des modèles donnant la distribution des effets la mieux appropriée pour atteindre ce but. Un tel modèle entend disposer les appuis de la bande de roulement à l'intérieur de celle-ci et non plus à l'emplacement des épaulements.



C'est ainsi que la bande de roulement fait considérer une poutre de section rectangulaire chargée ponctuellement par W_1, W_2, W_3, \dots et soumise aux couples localisés C_1, C_2, C_3, \dots posée sur le sol. La distribution des réactions de contact p_1, p_2, p_3, \dots n'est pas connue à priori, mais elle doit être uniforme transversalement et longitudinalement, elle est proportionnelle à la flèche prise. Dès lors, il est possible de trouver un coefficient de raideur. En effet, si q est la réaction uniformément répartie sous la bande de roulement, alors

$$q = pb$$

où p = réaction localisée

b = largeur

En posant que $t = -kx$, la relation entre q et y étant fixée par :

$$\frac{d^4 y}{dx^4} + \frac{k}{EI} y = 0 \quad \text{il vient :} \quad \frac{d^4 y}{dx^4} + \frac{khy}{EI} = 0$$

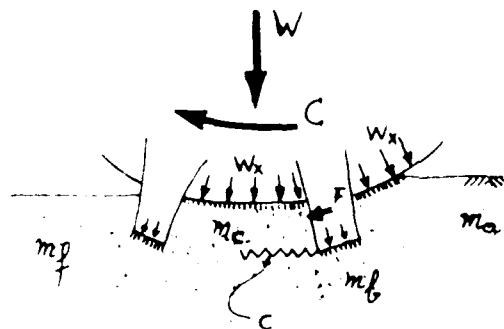
Le facteur k est un coefficient de raideur. Les dimensions en cause sont :

$$k = \frac{F}{\delta} \quad \text{ou} \quad k = \frac{q}{\delta} \quad \text{ou} \quad k = \frac{F}{\delta} \quad \text{ou} \quad k = \frac{q}{\delta} \quad \text{ou} \quad k = \frac{F}{\delta} \quad \text{ou} \quad k = \frac{q}{\delta}$$

La dimension de k , un nombre de cm d'enfoncement pour une charge appliquée de 1 kg/cm².

Le produit se donne une dimension kg/cm² et équivalent au module d'élasticité du terrain pour le sol. La valeur de k est ainsi liée à la déformabilité du terrain et à l'enfoncement admissible.

La roue en roulement en contact et en prise avec le sol invoque du frottement et de l'adhérence pour entraîner la propulsion, c'est-à-dire la réaction et l'application du couple moteur. La bande de roulement doit donc satisfaire les conditions nécessaires à l'obtention de ces frottements et adhérences d'accrochage. C'est ainsi que le schéma interne de la roue peut être proposé.



- W : charge
- C : couple moteur
- W_x : charges distribuées
- F : effort appliqué
- f : zones de frottements
- c : zone sollicitée en cisaillement
- m_a : milieu initial
- m_b : milieu sous les barrettes
- m_c : milieu conditionné par l'entre-barrette
- m_f : milieu après passage de la roue

Le déplacement longitudinal du pneu crée l'ornièrre et implante les parties saillantes de la bande de roulement dans le support. Ainsi se créent différentes zones de contact au sein de l'aire d'empreinte qui se définit à chaque instant. Les faces tangentielles au plan du sol distribuent les charges sur le massif sous-jacent et leur contact procède du frottement lors de l'application d'efforts tangentiels issus du couple moteur. Les faces orthogonales au plan du sol, implantées dans le massif granuleux à concurrence de la possibilité de pénétration vont solliciter le milieu en cisaillement.

Il apparaît ainsi que barrettes et entre-barrettes jouent des rôles mécaniques pour la constitution d'un massif cohésif, résistant au cisaillement et offrant les meilleures qualités de frottement tant interne qu'externe. Dès lors intervient également la nature et les propriétés des matières en contact pour ce qui relève de l'adhésion entre elles. Ainsi, s'évoque le déburrage des portions entre-barrettes et le maintien des barrettes au lieu d'implantation sur la bande de roulement. Ces considérations influencent les cotes géométriques des barrettes, des entre-barrettes et des congés de raccordement des parties saillantes sur la bande de roulement.

L'APPLICATION DE LA MODELISATION ET SES RESULTATS

La réalisation

Le principe de base à l'élaboration d'un pneu hors route comporte la nécessité de réaliser une bande de roulement en encorbellement sur ses appuis. Dès lors, pour une largeur de pneu donnée ou imposée en raison des exigences de travail, comme en labour par exemple, les flancs sont placés à l'intérieur de la largeur. La localisation en est calculable. Le recours à un moule classique permet un déplacement d'une portion des flancs de manière à répondre à la condition première. Ce type de pneu hors route est dénommé Camel Shoe et symbolisé par CS.

Les premières applications du principe sont obtenues en rechappage de carcasses appropriées.

L'expérimentation et les résultats

Comme pour les pneus de manufactures classiques, les versions CS sont soumises aux essais de déformation, d'empreinte et de transmission de couple en procédant aux bancs statiques. Les conditions de réponse dynamique et les performances sont analysées sur pistes d'essais et en travail sur le terrain.

D'une manière générale la déformation du flanc d'un CS est plus grande que celle d'un pneu classique mais ses variations sont plus faibles car le profil déformé devient moins dépendant de la pression de gonflage comme aussi de la charge.

Dès lors, la surface de contact effective de la bande de roulement augmente. Comme il a été constaté des profondeurs d'enfoncement moins grandes que pour un profil classique à mêmes pressions de gonflage et charges, il faut noter que ces dernières se répercutent plus et mieux sur la matière des flancs. Ainsi, la souplesse donnée aux flancs engendre-t-elle un meilleur confort et provoque-t-elle un meilleur transfert des charges vers

la bande de roulement sans induire des moments de flexion trop importants aux épaulements.

Les valeurs de module de rigidité spécifiques aux parties du flanc sont données ci-après pour deux types de pneus :

Partie	Pneu classique	Pneu CS
	Module de rigidité, daN/cm ²	
Épaulement	22000	47000
Milieu du flanc	34000	35500
Talon	25000	42500
Flanc en totalité (module moyen)	34000	41000

Les pneus présentent peu de différences en moyenne, toutefois les répartitions des valeurs sont inverses quant à leur grandeur pour chaque partie. Les lors, pour une même distribution des épaisseurs de matière il faut s'attendre à des déformations semblables au talon et à l'épaulement alors que la cambrure du flanc proprement dit est plus importante dans le cas du CS.

Les performances de traction obtenues avec différents pneus sont évaluées en tenant compte de la consommation de fuel, du régime moteur, de la vitesse d'avancement, du glissement relatif, du travail effectué. Ce dernier concerne des travaux agricoles de labour, de hersage et de traction, conditions moyennes similaires intégrant les variations rencontrées sur un même terrain dans les mêmes circonstances.

L'évolution des valeurs mesurées des surfaces comprises entre barrettes consécutives de mêmes profils de bande de roulement en deux conceptions de manufacture - classique et CS - permet d'apprécier l'incidence de la pression de gonflage pour une même charge.

Pneu	Evolution de la pression de gonflage, kPa		
	120 à 160	160 à 200	200 à 240
	Réduction de la surface de contact, %		
CS	1 à 2	6 à 11	8 à 13
Classique	6	24	31

Il est évident que le type CS vérifie l'indépendance plus grande vis-à-vis de la pression de gonflage et cela pour toutes les charges admissibles.

Les performances de traction sont liées directement à la surface effective de contact des barrettes de la bande de roulement. Des valeurs expérimentales sont données ci-après.

Operation	Labour 1		Labour 2		Hersage	
	CS	ORD	CS	ORD	CS	ORD
Pneu						
Superficie travail- lee, ha/h	0,22	0,19	0,22	0,20	0,64	0,61
Volume travaillé, m ³ /h	792	513	660	450	1280	1220
Consommation à l'unité de volume, ml/m ³	6,2	8,4	7,1	9,0	3,8	4,1

Labour 1 = sans blocage de différentiel et sans 4 x 4

Labour 2 = avec blocage et 4 x 4

D'autres essais confirment ces valeurs. Elles se traduisent lors d'expériences pratiques à la ferme par une possibilité de recourir à un tracteur de moindre puissance motrice pour effectuer un même travail en des conditions semblables. Il faut noter que le CS permet de travailler plus efficacement à basses pressions de gonflage et qu'une première comparaison entre des profils différents de bande de roulement n'a pas démontré d'avantages. En tout état de cause, les glissements enregistrés se révèlent toujours plus faibles avec les manufactures CS.

CONCLUSIONS

L'expérimentation en statique et en dynamique sur pneus agricoles et forestiers permet de quantifier des caractéristiques physiques propres aux enveloppes manufacturées. Parallèlement, l'observation des effets dans les milieux granuleux autorise l'élaboration de modèles interprétatifs. L'utilisation de ceux-ci dans la conception de nouveaux profils transversaux d'assaut permet alors le calcul raisonné de la composition ou de la présentation des enveloppes.

La réalisation expérimentale de pneus suivant les informations calculées permet de procéder à des essais qui confirment les modèles élaborés. La standardisation des méthodes de test des pneus manufacturés, telle que déjà suggérée dans une communication précédente, est donc bien de nature à mieux renseigner les utilisateurs quant aux conditions d'utilisation et une évolution des techniques de manufacture peut également être envisagée à partir de connaissances que la recherche a permis d'initier.

LITTÉRATURE

- ABEELS P., 1975 : Deformation des pneumatiques et propriétés au contact avec le sol. 5th International Conference ISTVS, Détroit-Houghton, Michigan, USA.
- ABEELS P., 1976 : Tire deflection and contact studies. Journal of Terra-mechanics, vol. 13, n° 3, pp. 183-196, 14 fig.
- ABEELS P. et D. DECLERCO, 1976 : La locomotion tout terrain. La compaction du sol. Revue de l'Agriculture, n° 1, pp. 131-150.
- ABEELS P., 1978 : Classical and Camel Shoe tyres in agriculture. Communication au Congrès ISIV, 1 p.

- ABEELS P., 1979 : Recherche en matière de locomotion hors-route, pneus agricoles et forestiers, conception et effets induits. Publication du Département de Génie Rural, 37 p.
- ABEELS P. et J.M. BAUDEWYNS, 1980 : Essais sur pneus. Développement du type "Camel Shoe". Groupe de Mécanisation Rurale et Forestière, 24p.
- ABEELS P., 1981 : Agricultural and forestry tyres choice in the context of energy savings. Proceedings of the 7th International Conference of ISTVS, Calgary, Alberta, Canada, vol. 1, pp. 1-10.
- ABEELS P., 1981 : Studies of agricultural and forestry tyres on testing stands, basis for datas standardization. Proceedings of the 7th International Conference of ISTVS, Calgary, Alberta, Canada, vol. 2, pp.419-454.
- ABEELS P., 1981 : Interactions between tyre and soils, relations for the design of flexible toric casings. Proceedings of the 7th International Conference of ISTVS, Calgary, Alberta, Canada, vol. 2, pp. 455-470.
- ABEELS P., 1981 : Performances comparées de manufactures de pneumatiques agraires et forestiers. Proceedings of the 7th International Conference of ISTVS, Calgary, Alberta, Canada, vol. 2, pp. 472-486.
- ABEELS P., 1982 : Le pneu agricole et forestier. Tracteurs et Machines Agricoles, n° 799, pp. 29-32.
- ABEELS P., 1982 : Performances of agricultural tractors and tyre improvements. ASAE Meetings, Palmer House, Chicago, Illinois, Paper 82-1570, 19 p.
- ABEELS P., 1983 : Überlegungen zur Herstellung von Reifen für forstwirtschaftliche Fahrzeuge. Forstwissenschaftliches Centralblatt, H.2, S.80-86.
- ABEELS P., 1983 : Advance in matters of agricultural tyres. Journal of Agricultural Engineering Research. A paraître.

MODELLING OF OFF-ROAD TYRES AND SOIL FOR IMPROVED TRACTION

PROF. DR. IR. P.F.J. ABEELS

UNIVERSITE CATHOLIQUE DE LOUVAIN, GENIE RURAL, LOUVAIN-LA-NEUVE, BELGIUM

TRANSLATED BY S. HECAPT, NIAE, SILSCE, ENGLAND

Abstract

Many effects have been observed as a consequence of introducing machinery to agricultural land and forestry. In the main these effects are due to induced compaction. Moreover, off-road development must look to more and more vehicles with different types of tyres for different purposes. Thus it is important to deal with the problems of flexible tyres in order to see how it may be possible to adapt their design to the unprepared soils on which they must run.

The characteristics necessary for developing new concepts must include firstly the flexibility of the tyre identifying the properties of each of the principal parts of the tyre in transmitting loads to the supporting surface. That is why the following parameters must be determined: load-deflection relationship, variation of thickness of material over the tyre's section, properties of the shoulder, deflection of the tyre tread, stiffness of the torus, and the damping properties of the tyre. The tyre-soil relationship is related to the effects of compression, rotation and turning of the tyre on the soil.

The modelling which results from the knowledge of these parameters has enabled introduction of concepts and methods for designing tyres. The production of prototypes has confirmed experimentally the potential thus developed.

Foreword

When deformation and damage to soil take on exaggerated importance in agriculture and silviculture, a certain number of effects appear as a result of mechanization in the form, for example, of often restricted operations or frequently onerous remedial measures. Indeed if part of the cause of the damage may be ascribed to the vehicles and machines it is more generally the case that their operators are at fault for not having adapted them to their working conditions.

The ideas of soil compaction due to tyres must be specified in order to be understood. This will also enable a better choice for manufacturers on the one hand, and proposals of new solutions for improving off-road locomotion and reducing the effects of tyres on soil on the other. Direct and indirect savings in energy are thus possible through better protection of the environment.

MODELLING OFF-ROAD TYRES

Introduction

The tyre is loaded through the axle of a vehicle; loads are transmitted through the wheel disc and wheel rim on which the tyre is mounted to form the wheel. The effects of this transmission on tyre deflection and on the effects recorded in a supporting medium are analysed.

Deformability of the toric casing or tyre

Tyre deformability is measured by the load-deflection relationship and the external geometry of the casing. It is known that the values of these parameters increase with applied load and decrease with increasing inflation pressure or ply rating. It has also been observed that variations in these respective parameters enable certain makes of tyre to be put into ply rating categories. Variations in torus height being greater than variations in width, the measured parameters express the general deformability of the torus on the one hand, and of the sidewalls on the other. It should still be stressed that the cross-section of a tyre reveals a variable distribution in thickness along the walls and that an omnidirectional equipotential inflation pressure will not give rise to the same deformation effects. This is particularly important at the low inflation pressures as recommended for off-road operation and more especially on a granular medium.

The variation in inflation pressure contributes mainly to a modification in the stiffness of the sidewall and has little bearing on the tyre tread.

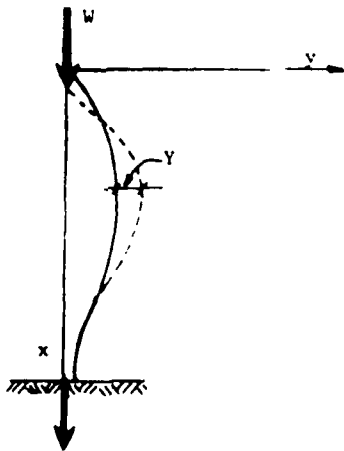


Fig. 1

The application of force to the tread gives rise to normal and shearing forces and a bending moment in the section of the sidewall. An equation for the deflection of the sidewall subjected to a load sustained by an inflation pressure may be established. The general expression is:

$$Y = \frac{M}{EI} = - \frac{W \cdot y(x)}{EI}$$

By retaining a unit of sidewall formed by a section 1 cm wide we have:

$$Y = - \frac{W \cdot y(x)}{E_r \cdot e^3/12}$$

and

$$e = \left(\frac{-12W \cdot y(x)}{E_r \cdot Y} \right)^{1/3}$$

where e = thickness of the sidewall
 W = load
 Y = bending deflection
 E_r = Young's modulus of elasticity

Thus, the casing thickness at each point depends on the value of E_r given to the sidewall, the applied load and the tolerated bending of the sidewall for the deformation, given that deformation is a function of inflation pressure. One of the parameters may be calculated using computer programming whilst the others remain constant.

The deformation of the sidewall is determined by effects in the tread because of the existence of continuity at the shoulder point. In fact normal, shear effects and certain moments are localised at the shoulder and they then establish certain tread properties when the tread is applied to a supporting surface.

The loads exerted statically on the tread can help us to understand the vertical displacements thus caused. The crossply tyre exhibits vertical deformations which are clearly less than in the radial. In this case the inflation pressure also acts as stiffener, but two factors should be taken into account, firstly the sidewall-tread relation at the shoulder and secondly the length and number of lugs. The more numerous and the longer the lugs, the smaller the effect of inflation pressure. The deformations observed in the transverse direction on the centreline show the particularly great importance of the lug fillet radii. These appear to be places of indentation in the carcass of the tyre when only the tips of the tread bars support the load and it is observed that the vertical deflection in the transverse section is so great that the lugs do not cover the centreline.

The tread of the tyre is clearly designed as the part of the tyre in contact with the ground. Simulated for the needs of the study to a beam of rectangular unit section, it is possible to apply known relations. The deflections measured at different locations of a tread inflected by loads enable use of reference equations. Thus the deflection (f) at distance x from the supports for a and b , the distances from the point of application of the load with respect to the same supports, is given by:

$$\frac{W}{6EI} \frac{bx}{EI} (l^2 - b^2 - x^2) \quad \text{if } x < a$$

$$\text{and} \quad \frac{Wa}{6EI} \frac{(1-x)}{EI} (2 \times 1 - a^2 - x^2) \quad \text{if } a < x < l$$

where W = applied load

l = length of the beam

E = modulus of elasticity

I = moment of inertia = $\frac{bh^3}{12}$

Thus as may be seen, the deflection in the tread following localised action or reaction on its surface is essentially dependent on E if it can take values which are great compared with the possible scale of variation of the other values in the design of a tyre.

The off-road tyre or deformable torus distinguishes between the sidewall, shoulders and tread. To these we should add the beads which ensure contact with the rigid rim, part of the vehicle mass by virtue of its construction. The figure below is a general diagrammatic representation of the field, forestry and off-road tyre:

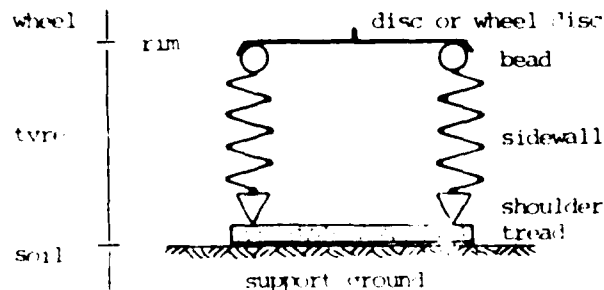


Fig. 2

The conditions of the dynamic behaviour of the tyre are approached with a view to specifying the mode of action of the loads supported on the soil. A special static test rig has been designed to this end. Basically it is a matter of seeing how the tyre produces a certain indentation in the soil due to its elastic nature. The tyre is simulated so that this may be studied on a system comprising a spring and a damper in parallel as illustrated in the diagram below.

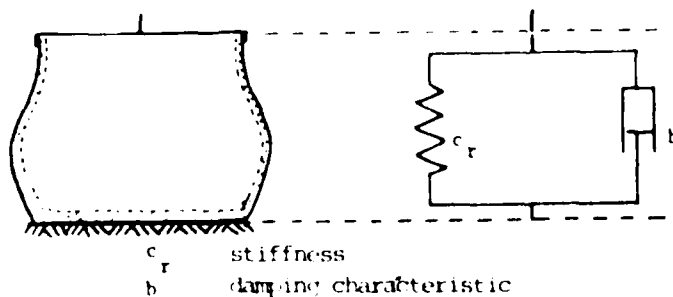
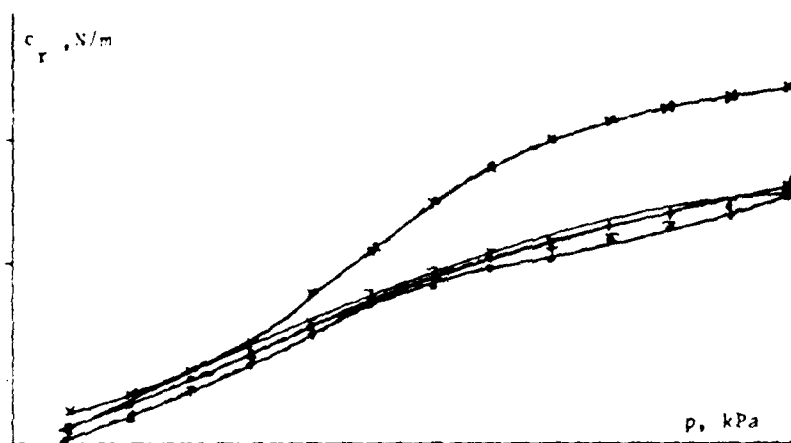


Fig. 3

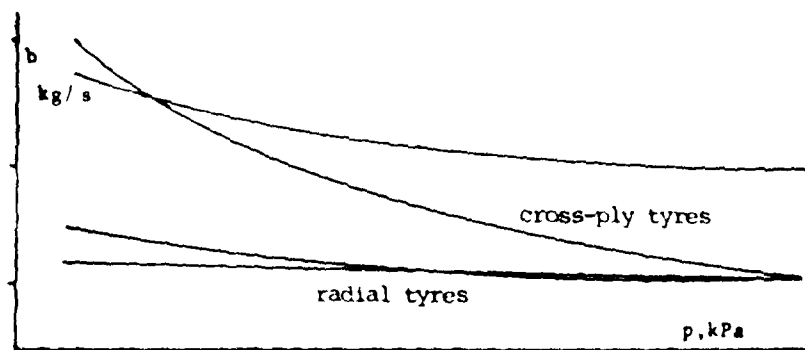
The stiffness of a tyre increases with inflation pressure, for both radial and diagonal tyres. No effect has been found due to ply rating.



Variation in stiffness as a function of inflation pressure

Fig. 4

Radial and cross-ply tyres have different damping characteristics which are also influenced by their dimensions. Increased inflation pressure reduces the damping, particularly with cross-ply tyres.



b : damping factor, kg/s

Fig. 5

Damping is clearly influenced by inflation pressure even more with cross-ply tyres than with radials.

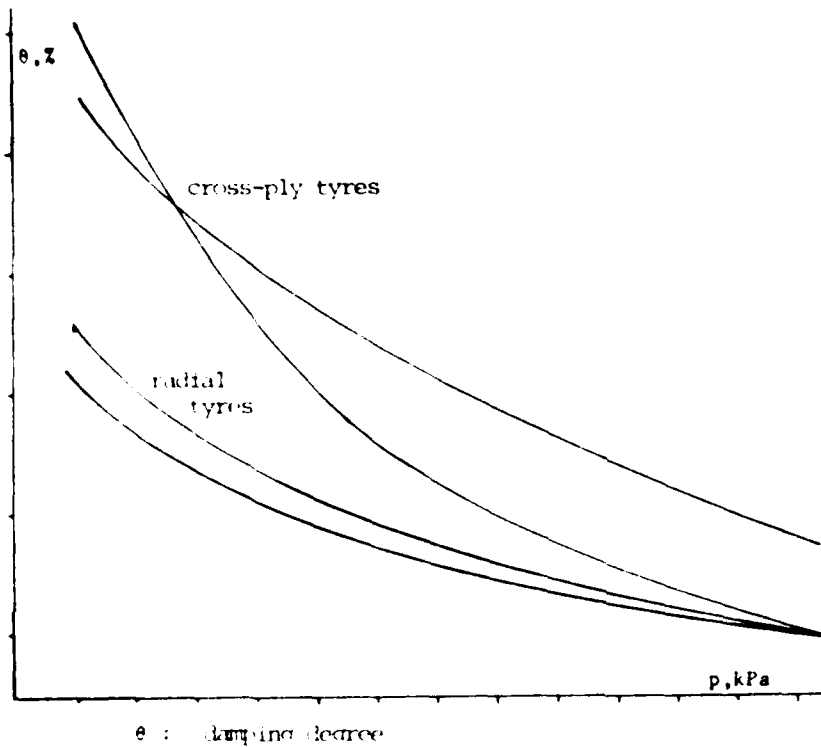


Fig. 6

Tyre-soil relation

The tyre-soil relation allows the effects within the supporting medium to be understood. These effects are caused in three ways by the action of the tyre on a soil:

1. compression which is shown by sinkage and which is accompanied by compaction and packing leaving either a local print or a track i.e. the rut;
2. rotation which is shown by friction, grip, smearing or breaking away of blocks of soil;
3. pivoting movement which includes scraping the soil surface.

The soil constitutes a heterogeneous or coexistent mass of particles, lumps and clods more or less evenly distributed or in networks with voids.

The passing of the tyre over the soil can lead to structural compaction without affecting the basic inter-particulate structure, cause some coalescence of lumps and clods or lead to textural packing affecting the basic structure. Hence compression, rotation and pivoting of the tyre will have consequences which are more or less reversible as far as the state of the soil is concerned and which will affect the top arable soil layers.

Indentations by a tyre are shown by localised compression, the distribution of which is measured from a transverse profile at the centricline of the wheel mark, in order to reconstruct the action of the tread on the granular mass.

If, considering these profiles around the compaction distribution according to the transverse section we may state that the effects seem to be distributed as if the bending moments created by the mode of transfer of the load in the tread at the shoulders could be expressed in the granular mass of the supporting soil. The following diagrams serve to illustrate this information as a function of depth where similar compaction occurs (iso-compaction).

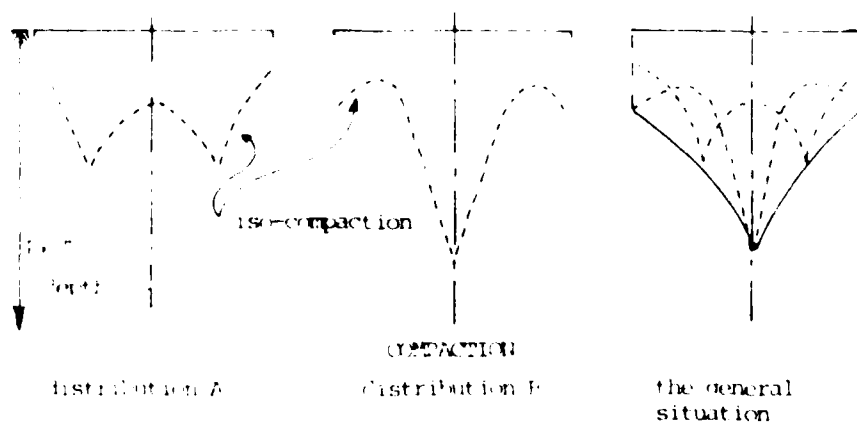


Fig. 7

The models of load effects on supports taken from the theory of the strength of materials give what is shown in the figures below.

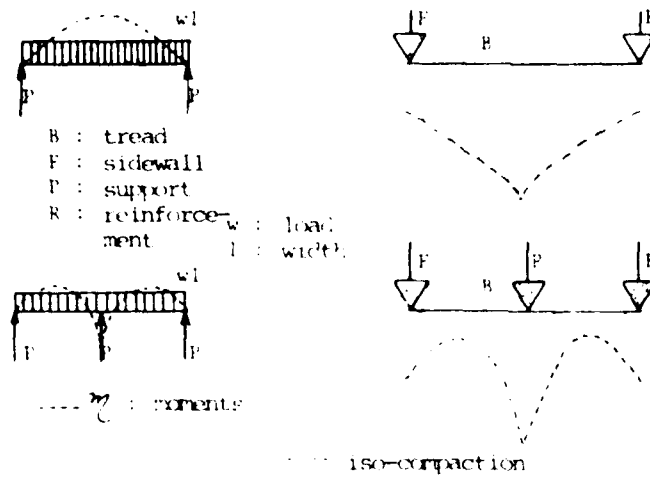


Fig. 8

The building-up of an off-road tyre profile which only involves reduced compaction must take into account models which best give the distribution of effects to attain this goal. Such a model requires the tread supports to be moved from the shoulder region inwards towards the centre of the tread.

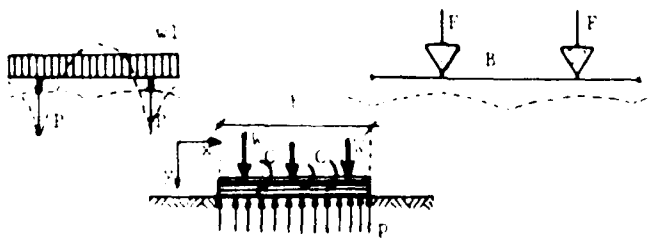


Fig. 9

Thus it is that the tread leads us to consider a beam of rectangular section loaded at intervals by W_1, W_2, W_3, \dots and subjected to localised couples C_1, C_2, C_3, \dots on the soil. The distribution of contact reactions P_1, P_2, P_3, \dots is not known a priori, but must be transversely and longitudinally uniform; it is proportional to the bending. It is thus possible to find a stiffness. In fact if q is the uniformly distributed reaction under the tread, then

$$q = pl$$

where p = localised reaction
 l = width

By substitution of $p = -ky$, the relation between q and y being given by

$$\frac{d^4 y}{dx^4} = \frac{q}{EI}$$

we get $\frac{d^4 y}{dx^4} + \frac{kby}{EI} = 0$

where k is stiffness.

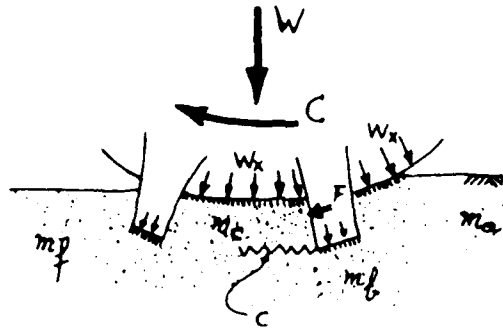
The units concerned are:

$$y, \text{ cm}; \quad b, \text{ cm}; \quad q, \text{ kg/cm} \text{ and } k, \text{ kg/cm}^3$$

with k being defined as sinkage depth under a pressure of 1 kg/cm^2 .

The product kb gives units of kg/cm^2 and is equivalent to the modulus of elasticity to be found for the soil. Thus the value of k is related to deformability of the ground and acceptable sinkage.

Rotation of the tyre in contact with the soil leads to friction and grip to provide propulsion, i.e. the reaction to the application of the engine torque. The tread must possess or create the conditions necessary for obtaining this friction and grip. The following interpretive diagram may be proposed.



- W : load
- C : engine torque
- w_x : distributed loads
- F : effort applied
- f : frictional zones
- c : shearing zone
- m_a : initial soil conditions
- m_b : soil conditions under the lugs
- m_c : inter-lug soil conditions
- m_f : soil after passage of the wheel

Fig. 10

The forward movement of the tyre creates the rut and implants the lugs in the support medium. Thus different contact areas are created with the imprint area which is continuously defined. The tangential faces at soil level distribute the loads on the underlying soil and their contact gives way to friction when tangential forces are applied from the engine torque. The orthogonal faces at soil level, implanted in the granular mass up to the limit of the possibility of penetration are going to shear the medium.

It thus appears that lugs and inter-lugs play mechanical roles in making a cohesive mass, providing resistance to shearing and increasing friction both internally and externally. The nature and properties of the materials in contact with the soil also have a role to play in so far as there is adhesion between the tyre and the soil. This is relevant to the cleaning of inter-lug areas and the strength of the attachment of the lugs on the tread. These factors affect the geometrical positioning of the lugs, inter-lugs, and fillet radii of the lugs on the tread.

APPLICATION OF THE MODEL AND RESULTS

Development of the model

The underlying principle in the development of an off-road tyre is the need to produce a tread of corbelled construction on its supports. Hence for a tyre of given width, or for a width determined by a particular application such as ploughing, the beads are placed inside the width. The position may be calculated. Use of a conventional mould allows displacement of a part of the sidewalls in such a way as to satisfy the first condition. This type of off-road tyre is called the Camel Shoe and denoted by CS.

The first applications of the principle are obtained by remoulding of the appropriate casings.

Experiments and results

As in the case of conventionally manufactured tyres, the CS versions are subjected to static tests for deflection, sinkage and torque transmission. The dynamic response characteristics and performance are analysed on test tracks and in work in the field.

Generally the sidewall deflection of a CS is greater than in a conventional tyre but its variations are less since the deflected profile becomes less dependent on inflation pressure and load.

Hence the effective contact area of the tread increases. As stated for sinkage depths smaller than for conventional profile at similar inflation pressures and loads, it should be noted that the pressures and loads affect the materials of the sidewalls to a better and greater extent. Thus the suppleness given to the sidewalls provides better comfort and better load transfer to the tread without inducing bending moments which are too great at the shoulders.

The values of the modulus of stiffness specific to the parts of the sidewall are given below for two types of tyre:

Tyre part	Modulus of stiffness, daN/cm ²	
	Conventional tyre	CS tyre
Shoulder	22 000	47 000
Middle of sidewall	54 000	35 500
Bead	24 000	42 500
Complete sidewall (mean modulus)	34 000	41 000

On average there are few differences between the tyres, yet the distribution of the values is inversely related to their size for each part. Hence for a given distribution of material thicknesses we should expect to find similar deformations at the bead and shoulder although the camber of the sidewall is, strictly speaking, greater in the CS.

Traction performances obtained with different tyres are evaluated by taking the following factors into consideration: fuel consumption, engine speed, forward speed, slip and work done. The latter concerns tasks such as ploughing, harrowing and traction, similar mean conditions which integrate the variations encountered on given terrain under similar circumstances.

The development of values measured from areas between consecutive lugs of the same tread profiles in 2 manufactured designs - conventional and CS - enables appreciation of the effect of inflation pressure for an identical load.

Tyre	Tyre inflation pressure kPa		
	120-160	160-200	120-200
CS Conventional tyre	Decrease in contact patch area, %		
	1-2	6-13	8-13
	6	24	31

It is obvious that the CS verifies the greater independence with respect to inflation pressure, and this applies to all acceptable loads.

Traction performance is related directly to the effective contact area of the lugs on the tread. Experimental values are given below:

Operation	Ploughing 1		Ploughing 2		Harrowing	
Tyre	CS	CON	CS	CON	CS	CON
Area worked, ha/h	0.22	0.19	0.22	0.20	0.64	0.61
Volume worked, m ³ /h	792	513	660	450	1280	1220
Fuel consumption per unit volume, ml/m ³	6.2	8.4	7.1	9.0	3.8	4.1

Ploughing 1 : without differential locking or four-wheel drive

Ploughing 2 : with locking and four-wheel drive

CS : Camel Shoe CON : conventional tyre

Other tests confirm these values. They may be translated into practical farming terms by the possibility of using a tractor of less power to do the same work in the same conditions. It should be noted that the CS enables more effective work at low inflation pressures and that a first comparison between different tread profiles has not shown any advantages. In any case recorded slippage is always less with the CS.

CONCLUSIONS


Static and dynamic experiments on agricultural and forestry tyres enable quantification of the physical characteristics of manufactured tyres. At the same time, observation of the effects in the granular mass helps in the development of explanatory models. Their use in the design of new cross-sections thus enables reasoned calculation of the construction of tyres.

After experimental production of tyres from the calculated data, tests may be carried out to justify the developed models. Standardisation of test methods for manufactured tyres, such as those considered in the course of a previous paper, is thus desirable to inform users as to the conditions

of use; manufacturing techniques can also be developed by using the knowledge gleaned from this research as a starting point.

BIBLIOGRAPHY

1. ABEELS, P. Déformation des pneumatiques et propriétés au contact avec le sol (Deflection and properties of tyres when in contact with the soil). Proc. 5th int. Conf. ISTVS, Detroit-Houghton, MI, USA, 2-6 June 1975
2. ABEELS, P. Tire deflection and contact studies J. Terramechanics, 1976 13 (3) 183-196
3. ABEELS, P.; DECLEROQ, D. La locomotion tout terrain. La compaction du sol (All terrain locomotion and soil compaction). Revue de l'Agriculture, 1976 No. 1, 131-150
4. ABEELS, P. Classical and Camel Shoe tyres in agriculture Proc 6th int. Conf. ISTVS, Vienna, Austria, 22-25 August 1978, Vol. 2, 501-512
5. ABEELS, P. Recherche en matière de locomotion hors-route, pneus agricoles et forestiers, conception et effets induits (Research on off-road locomotion, design and induced effects of agricultural and forestry tyres). Publication Département de Génie Rural, Université Catholique de Louvain, Belgium, 1979, 37 pp
6. ABEELS, P.; BAUDEWYNS, J.M. Essais sur pneus. Développement du type "Camel Shoe" (Tests on tyres and the development of the "Camel Shoe"). Groupe de Mécanisation Rurale et Forestière, Belgium, 1980, 24 pp
7. ABEELS, P. Agricultural and forestry tyres choice in the context of energy savings Proc. 7th int. Conf. ISTVS, Calgary, Alberta, Canada, 16-20 August 1981, Vol. 1, 1-10.
8. ABEELS, P. Studies of agricultural and forestry tyres on testing stand, basis for data standardisation Proc. 7th int. Conf. ISTVS, Calgary, Alberta, Canada, 16-20 August 1981, Vol. 2, 439-454
9. ABEELS, P. Interactions between tyre and soils, relations for the design of flexible toric casings Proc. 7th int. Conf. ISTVS, Calgary, Alberta, Canada, 16-20 August 1981, Vol. 2, 455-470

10. ABEELS, P. Performances comparées de manufactures de pneumatiques agraires et forestiers (Comparing the performance of the manufacture of agricultural and forestry tyres). Proc. 7th int. Conf. ISTVS, Calgary, Alberta, Canada, 16-20 August 1981, Vol. 2, 472-486
 11. ABEELS, P. Le pneu agricole et forestier (The agricultural and forestry tyre) Tracteurs et Machines Agricoles, 1982 No. 799, 29-32
 12. ABEELS, P. Performances of agricultural tractors and tyre improvements. ASAE Meetings, Palmer House, Chicago, IL, USA, 1982, Paper 82-1570, 19 pp
 13. ABEELS, P. Überlegungen zur Herstellung von Reifen für forstwirtschaftliche Fahrzeuge (Considerations regarding the manufacture of tyres for forestry vehicles). Forstwissenschaftliches Centralblatt, 1983 No. 2, 80-86
 14. ABEELS, P. Developments in agricultural tyres J. agric. Engng Res., (in press)
- 

DEVELOPMENT OF A SOIL-WHEEL INTERACTION MODEL

George Y. Baladi (Member, ISTVS) and Behzad Rohani

U.S. Army Engineer Waterways Experiment Station, Vicksburg, Mississippi

ABSTRACT

The development of a mathematical model for calculating the motion resistance, sinkage, drawbar pull, torque, and side force for a flexible wheel traversing a yielding (or deformable) surface is described. In order to make the problem tractable, the deformed boundary of the wheel is assumed to be an arc of a larger circular wheel. The entire soil-wheel interaction process is treated as two springs in series, one describing the flexibility of the tire and one describing the elastic-plastic deformation of the soil. Mathematical expressions are derived for the two spring constants in terms of the load deflection characteristics of the tire, the undeflected configuration of the wheel, and the mechanical properties of the soil (both shearing response and compressibility characteristics).

The system of equations describing the performance of the wheel is solved numerically via a computer program called TIRE. Using this program, a series of parametric calculations is conducted to demonstrate the application of the methodology and to study the performance of flexible wheels on different types of soil under various kinematic conditions. A partial validation of the proposed interaction model is established by comparing the results of a large number of laboratory single wheel tests on both clay and sand with the corresponding model predictions.

INTRODUCTION

The determination of the response of a single flexible wheel traversing a yielding (or deformable) surface is essential for the analysis of the steering performance of wheeled vehicles. Specifically, the sinkage, motion resistance, drawbar pull, torque, and side forces acting on a powered flexible wheel moving on a yielding soil must be accurately determined. Due to the overwhelming complexity of this problem, previous research in this area has been directed, by and large, towards extensive experimentation and the development of empirical equations relating the various parameters of the problem, (Reference 1). Unfortunately, these empirical equations are not generic and apply only within the range of the experimental data on which they are based. On the other hand, most of the analytical investigations conducted in this area are based on the assumption of a rigid wheel (Reference 2). That is, the effect of the flexibility (elasticity) of the tire on the kinematics of the wheel is neglected. Even in the case of the rigid wheel, there is no general equation that can predict accurately the sinkage as a function of applied load, configuration of the wheel, and the engineering properties of soil (Reference 3). In a recent article, Fujimoto (Reference 4) introduced the flexibility of the tire in his analysis of the performance of elastic wheels on cohesive soils. He introduced an empirical relation between the central angle of the wheel, the internal pressure of the tire, and the radial stress acting on the periphery of the tire. The radial stress was assumed to be constant over the periphery of the tire. Fujimoto concluded that the determination of the radial stress is the most difficult problem in the analysis of soil-wheel interaction and recommended an empirical relation between the mobility cone index (CI) and the radial stress.

The objective of the present investigation is to develop a rational soil-wheel interaction model that is free from excessive empiricism and is

general enough to treat a wide range of problems. The core of the model is a method for predicting the sinkage as a function of applied load, deflection of the tire, slip, undeformed geometry of the wheel, and the fundamental engineering properties of the soil (such as cohesion, angle of internal friction, density, compressibility, etc.). Accordingly, the model can be used to predict sinkage in sand, clay, or soils exhibiting both cohesive and frictional properties. The equilibrium conditions and the sinkage of the wheel are then combined to calculate motion resistance, drawbar pull, torque, etc.

To demonstrate the application of the proposed model, a series of parametric calculations is conducted to determine the performance of flexible wheels on different types of soil under various kinematic conditions. Also, a partial validation of the model is established by comparing the results of a large number of laboratory single wheel tests on both clay and sand with corresponding model predictions.

DERIVATION OF THE SOIL-WHEEL INTERACTION MODEL

General Procedure

The most essential part of the soil-wheel interaction model is a procedure for determining the sinkage of a flexible wheel. The basic parameters that must be included in such a procedure are the applied load, configuration of the wheel, flexibility or elasticity of the tire, slip, and the fundamental engineering properties of the soil (such as shear strength and compressibility). The development of the physical soil-wheel interaction model is presented in detail in the subsequent sections and is based on the assumption that the entire interaction process can be simulated by two springs in series, with one spring defining the elasticity of the tire and the other describing the elastic-plastic deformation of the soil. These two springs are then combined into a single equivalent spring describing the interaction of the soil-wheel system.

The simulation of the resistance of the soil by a spring constant leads to a nonuniform distribution of normal stresses at the soil-wheel interface. The shear stresses at the soil-wheel interface are calculated from a rheological model which describes the shearing stress-strain characteristics of the soil. The final step of the analyses is to

determine the motion resistance, drawbar pull, torque, efficiency, and side force for a flexible wheel traversing a yielding surface. These parameters are calculated based on the assumption that the deformed boundary of the tire is an arc of a larger circular wheel.

Spring Constant for a Flexible Tire

A typical load-deflection curve for a flexible tire on a rigid surface is shown in Figure 1 where Δ denotes the deflection of the tire at point A. In practice, Δ is usually expressed as a percentage of the unloaded section height of the tire (Figure 2). The radial deflection of a generic point B along the periphery of the tire at an angle α is specified by Δ_1 (Figure 1). If the deformed section of the tire is characterized by a continuous spring with constant k_t , then the vertical differential force dF applied at point B can be expressed as

$$dF = k_t \Delta_1 \cos \alpha \, d\alpha \quad \dots \dots \dots (1)$$

From Figure 1, Δ_1 can be expressed in terms of Δ , α , and the undeformed radius of the wheel R

$$\Delta_1 = R - \frac{R - \Delta}{\cos \alpha} = \frac{R}{\cos \alpha} \left[\cos \alpha - \left(1 - \frac{\Delta}{R} \right) \right] \quad \dots \dots \dots (2)$$

Substitution of Equation 2 into Equation 1 leads to

$$dF = Rk_t \left[\cos \alpha - \left(1 - \frac{\Delta}{R} \right) \right] d\alpha \quad \dots \dots \dots (3)$$

Also, from Figure 1,

$$\cos \frac{\theta_t}{2} = 1 - \frac{\Delta}{R} \quad \dots \dots \dots (4)$$

In view of Equations 3 and 4 and static equilibrium, the applied load W can be expressed as

$$W = 2 \int_0^{\frac{\theta_t}{2}} dF = 2Rk_t \int_0^{\frac{\theta_t}{2}} \left(\cos \alpha - \cos \frac{\theta_t}{2} \right) d\alpha \quad \dots \dots \dots (5)$$

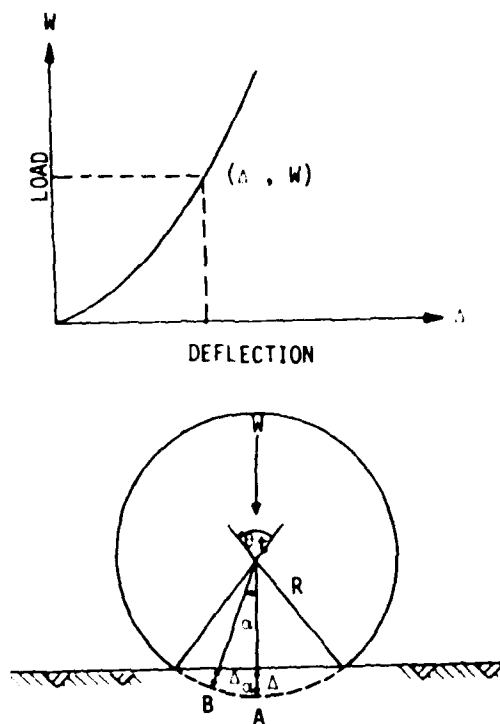


Figure 1. Load-deflection curve for a flexible tire on a rigid surface

1. UNLOADED SECTION WIDTH (D)
2. UNLOADED RADIUS (R)
3. UNLOADED SECTION HEIGHT (h)
4. DEFLECTION AT GIVEN LOAD = Δ/h

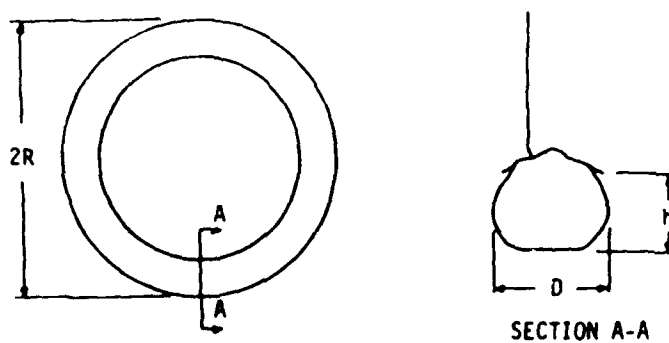


Figure 2. Tire geometry

Integration of Equation 5 leads to the following relation for the spring constant k_t

$$k_t = \frac{W}{2R \left(\sin \frac{t}{2} - \frac{t}{2} \cos \frac{t}{2} \right)} \dots \dots \dots (6)$$

The spring constant k_t can also be expressed in terms of Δ by combining Equations 4 and 6:

$$k_t = \frac{W}{2\Delta \left[\sqrt{\frac{2R}{\Delta}} - 1 - \left(\frac{R}{\Delta} - 1 \right) \cos^{-1} \left(1 - \frac{\Delta}{R} \right) \right]} \dots \dots \dots (7)$$

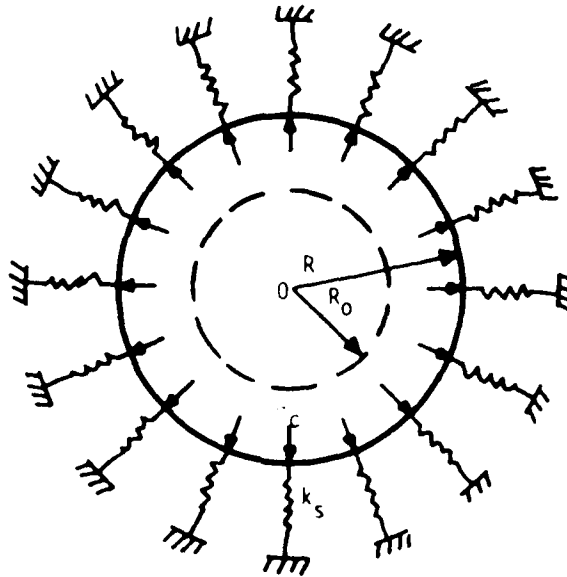
Equation 7 is portrayed in the top of Figure 1.

Spring Constant for Soil

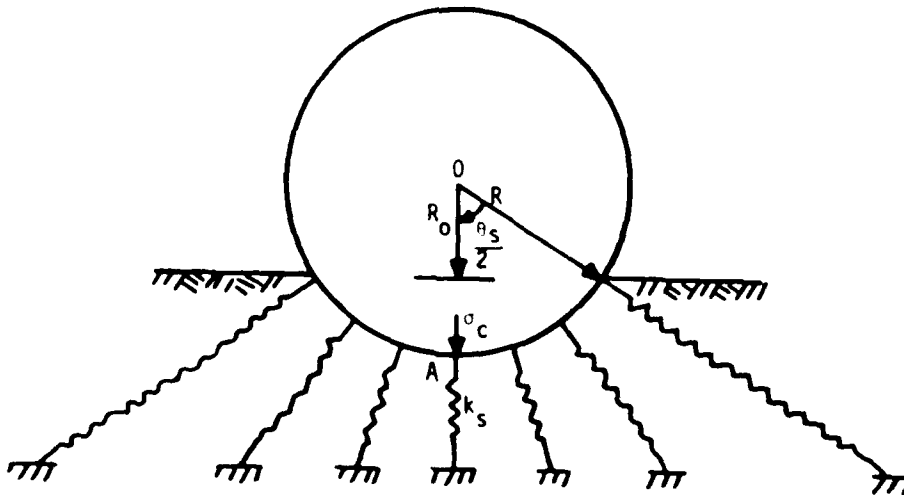
Let σ_c be the radial stress necessary to maintain a slow expansion of a spherical cavity in an elastic-plastic medium from radius R_o to R (Figure 3a). The radial stress σ_c is expressed analytically in terms of the shear strength parameters and the volume change characteristics of soil (Reference 5). The resistance of the soil to expansion of the spherical cavity can be simulated by a continuous spring characterized by spring constant k_s . From Figure 3a, the spring constant k_s can be expressed as

$$k_s = \frac{\pi(R^2 - R_o^2) \sigma_c}{R - R_o} = \pi(R + R_o) \sigma_c \dots \dots \dots (8)$$

where $R - R_o$ corresponds to spring deflection. Now consider a wheel of radius R embedded in soil to a depth $R - R_o$ (Figure 3b). The normal stress at point A resisting the embedment of the wheel is assumed to be equal to the radial stress σ_c inside the expanding cavity. Similar to expansion of the spherical cavity (Figure 3a), the resistance of the soil to the embedment of the wheel can also be simulated by a continuous spring with constant k_s given by



a. EXPANSION OF SPHERICAL CAVITY



b. ANALOGY BETWEEN A WHEEL EMBEDDED IN SOIL AND CAVITY EXPANSION PROBLEM

Figure 3. Proposed model for computing the spring constant for soil

$$k_s = \frac{RD}{R - R_o} \cdot c \quad (9)$$

where D is the unloaded section width of the wheel (Figure 2). Combining Equations 8 and 9 we obtain

$$\frac{\pi(R + R_o)(R - R_o)}{RD} = 1 \quad (10)$$

where, from Figure 3b

$$R + R_o = R \left(1 + \cos \frac{\theta_s}{2} \right) \quad (11)$$

$$R - R_o = R \left(1 - \cos \frac{\theta_s}{2} \right) \quad (12)$$

Substituting Equations 11 and 12 into Equation 10 and solving for $\cos \theta_s/2$ and θ_s , we obtain

$$\cos \frac{\theta_s}{2} = \sqrt{1 - \frac{D}{\pi R}} \quad (13)$$

$$\theta_s = 2 \cos^{-1} \sqrt{1 - \frac{D}{\pi R}} \quad (14)$$

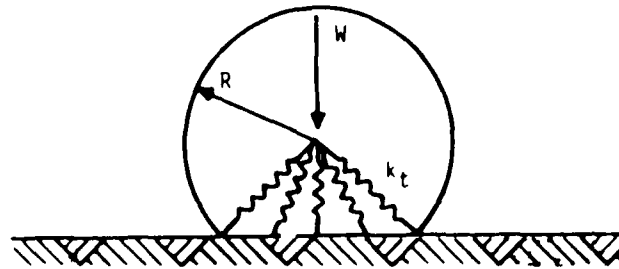
Substitution of Equations 11 and 13 into Equation 8 leads to the following expression for the spring constant k_s :

$$k_s = \pi R \left(1 + \sqrt{1 - \frac{D}{\pi R}} \right) \cdot c \quad (15)$$

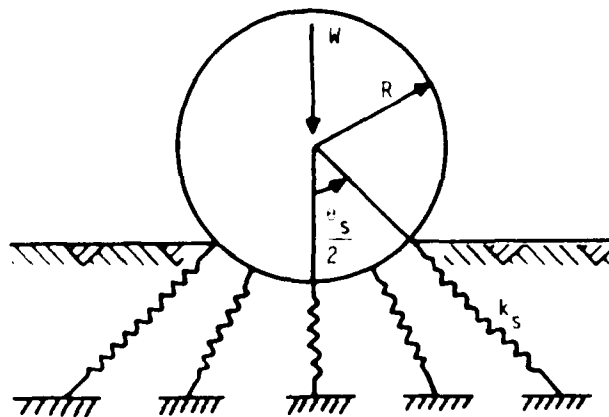
It is clear from Equation 15 that the apparent spring constant of the soil is a function of the engineering properties of soil through c and the geometry of the tire.

Equivalent Spring Constant for the Soil-Tire System

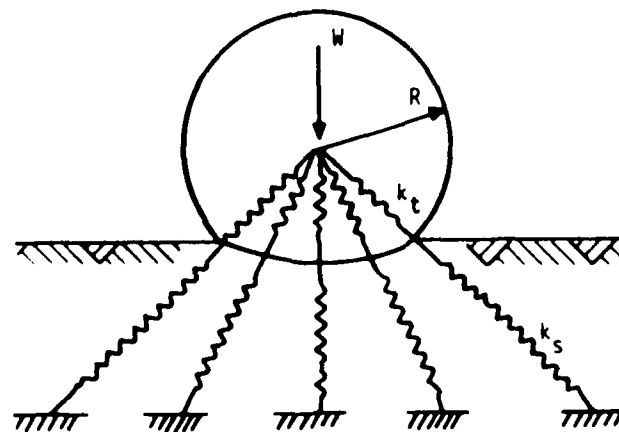
The model of the soil-tire system in terms of the spring constants k_t and k_s is portrayed in Figure 4. The equivalent spring constant k_e for



a. SPRING CONSTANT FOR FLEXIBLE TIRE (k_t)



b. SPRING CONSTANT FOR SOIL (k_s)



c. SPRING CONSTANT FOR SOIL-TIRE SYSTEM $\frac{k_s k_t}{k_s + k_t}$

Figure 4. Equivalent spring constant for soil-tire system

the soil-tire system can be determined from static equilibrium and is given as

$$k_e = \frac{k_t k_s}{k_s + k_t} \dots \dots \dots (16)$$

Normal and Shear Stress Distributions at the Soil-Tire Interface

Based on the concept of the spring analogy advanced in the previous sections, the expression for differential vertical force at a generic point at the soil-tire interface can be expressed as (Figure 5)

$$dF = DR \sigma_N \cos\left(\alpha + \frac{\alpha}{2}\right) d\alpha = \frac{k_s R \left(\cos \alpha - \cos \frac{\alpha}{2}\right) \cos\left(\alpha + \frac{\alpha}{2}\right) d\alpha}{\cos \alpha} \dots \dots \dots (17)$$

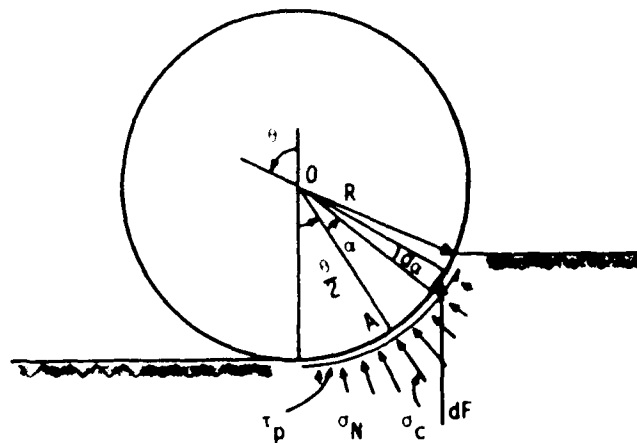


Figure 5. Normal stress distribution along the soil-tire interface

Solving Equation 17 for σ_N , we obtain

$$\sigma_N = \frac{k_s \left(\cos \alpha - \cos \frac{\alpha}{2}\right)}{D \cos \alpha} \dots \dots \dots (18)$$

In view of Equations 9 and 12, Equation 18 becomes

$$S = \frac{(\cos \alpha - \cos \frac{\pi}{2})}{(1 - \cos \frac{\pi}{2})} \cos \alpha \quad (19)$$

Equation 19 describes the distribution of normal stress τ_N at the soil-tire interface. Note that at point A (Figure 5) where $\alpha = 0$, Equation 19 indicates that $\tau_N = \tau_c$, which is consistent with the assumption made in the previous sections. On the other hand, at the free surface where $\alpha = \pi/2$ (Figure 5) Equation 19 indicates that $\tau_N = 0$ at these points.

Consider now a tire with turn angle θ with respect to the direction of motion. The plan view of the tire is shown in Figure 6a. If slip in the plane of the wheel is defined by the slip ratio S , then slip in the direction of the motion can be expressed as

$$S_m = \frac{S}{\cos \theta} \quad (20)$$

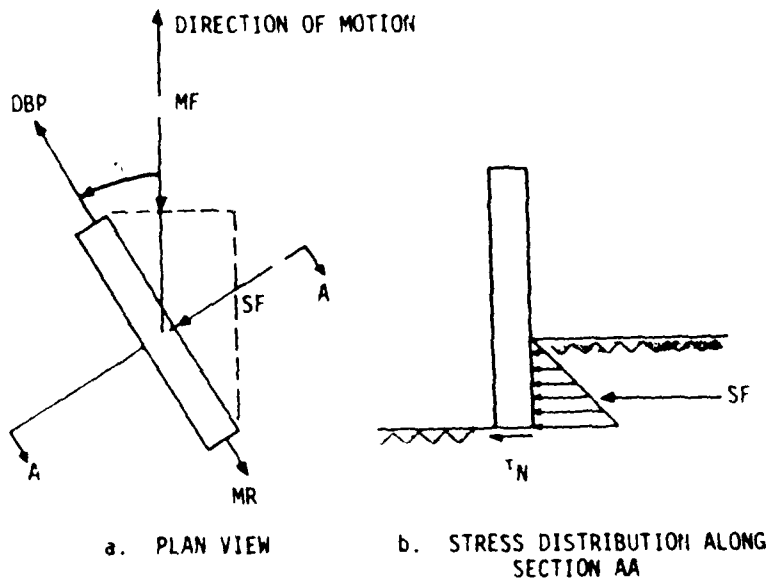


Figure 6. Geometry of the tire with turn angle θ

The components of shear stress parallel and perpendicular to the plane of the wheel τ_p and τ_N , respectively, can be obtained from the rheological soil model presented in Reference 5.

Combining Equation 20 with the rheological soil model results in the following expressions for τ_p and τ_N

$$\tau_p = \frac{G(C + \sigma_N \tan \phi)S}{\left| \frac{GS}{\cos \eta} \right| + C + \sigma_N \tan \phi} \dots \dots \dots (21)$$

$$\tau_N = \frac{G(C + \sigma_N \tan \phi)S \tan \eta}{\left| \frac{GS}{\cos \eta} \right| + C + \sigma_N \tan \phi} \dots \dots \dots (22)$$

where σ_N is given by Equation 19. In Equations 21 and 22, G , C , and ϕ correspond, respectively, to shear modulus, cohesion, and angle of internal friction of the material.

Deflection and Sinkage of a Flexible Tire

If the deflection of a flexible tire on a rigid surface under a given load W is denoted by Δ (Figure 1), then the corresponding deflection on a yielding soil Δ_t (Figure 7b) can be determined from the concept of the equivalent spring constant

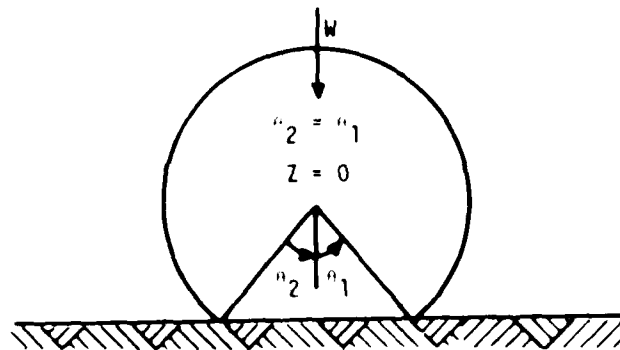
$$\Delta_t = \frac{k_s}{k_s + k_t} \Delta \dots \dots \dots (23)$$

Similarly, if Z_r is the sinkage of a rigid wheel under a given load W (Figure 7c), then the corresponding sinkage Z of a flexible wheel (Figure 7b) is

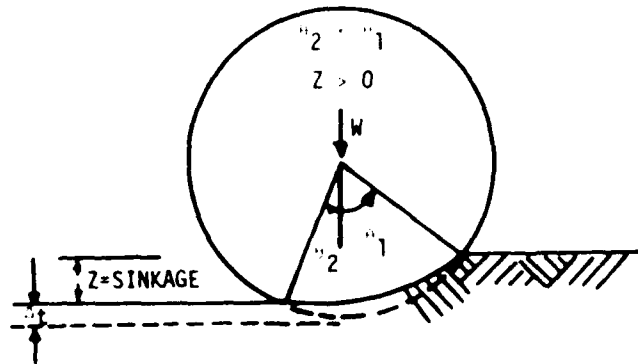
$$Z = \left(\frac{k_t}{k_s + k_t} \right) Z_r \dots \dots \dots (24)$$

The sinkage Z_r can be calculated from the balance of forces in the vertical direction (Figure 8a)

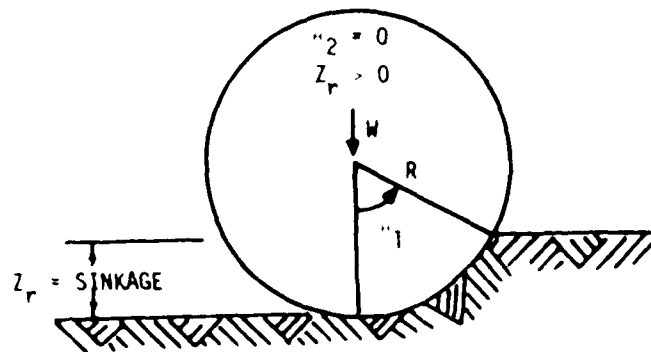
$$W = DR \int_{-\frac{1}{2}}^{\frac{1}{2}} \left[\tau_N \cos \left(\alpha + \frac{\eta}{2} \right) + \tau \sin \left(\alpha + \frac{\eta}{2} \right) \right] du \dots \dots \dots (25)$$



a. RIGID SURFACE-FLEXIBLE TIRE

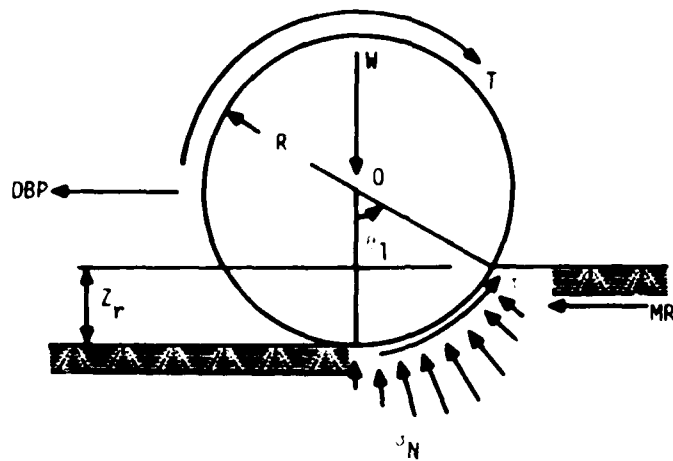


b. SOFT GROUND-FLEXIBLE TIRE

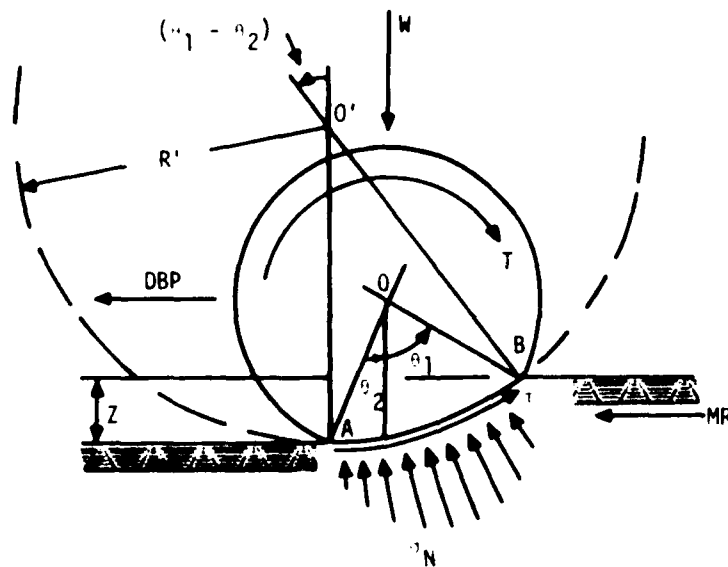


c. RIGID TIRE-SOFT GROUND

Figure 7. Variation of the central angles α_1 and α_2 and sinkage Z with relative rigidity of the tire and soil



a. SINKAGE OF A RIGID WHEEL



b. SINKAGE OF A FLEXIBLE WHEEL

Figure 8. Geometry of the problem

where J_N is given by (see Equation 19)

$$J_N = \frac{\left(\cos \theta_1 - \cos \frac{\theta_1}{2} \right) c}{\left(1 - \cos \frac{\theta_1}{2} \right) \cos \theta_1} \dots \dots \dots (26)$$

The shear stress τ in Equation 25 can be obtained from the rheological soil model described in Reference 5 and has the following form

$$\tau = \frac{c(C + \gamma_N \tan \phi)}{GS_0 + C + \gamma_N \tan \phi} \quad (27)$$

where γ_N is given by Equation 26. The solution of Equation 25 leads to an expression for α_1 . The actual sinkage Z_r can then be calculated from (Figure 7c)

$$Z_r = R(1 - \cos \alpha_1) \quad (28)$$

Relationships Governing Single Wheel Performance

Geometry of the problem

Consider the geometry and boundary conditions for a flexible wheel-soil system shown in Figure 8b. The contact surface between the wheel and the soil is assumed to be an arc of a circle with a radius equal to or larger than the undeflected radius of the wheel (only in the case of the rigid wheel is the radius equal to the undeflected radius). The center of this circle O' is located at the intersection of the vertical line through point A and the bisector of the angle AOB . According to Figure 7b, the relationship between the angle α_1 , the sinkage Z , and the deflection of the tire Δ_t is

$$\alpha_1 = \cos^{-1} \left(1 - \frac{Z}{R} - \frac{\Delta_t}{R} \right) \quad (29)$$

Also, from the geometry of Figure 7b

$$\alpha_2 = \cos^{-1} \left(1 - \frac{\Delta_t}{R} \right) \quad (30)$$

From the geometry of Figure 8b

$$R' = \frac{Z}{1 - \cos(\alpha_1 - \alpha_2)} \quad (31)$$

Using Equations 29 and 30 to eliminate Z from Equation 31, we obtain the following relation for R' in terms of R and the central angles α_1 and α_2

$$R' = R \frac{\sin \frac{\alpha_1 + \alpha_2}{2}}{\sin \frac{\alpha_1 - \alpha_2}{2}} \quad \dots \dots \dots (32)$$

Equations 29 through 32 completely define the shape of the contact surface between the soil and the tire.

Tire internal motion resistance

The internal motion resistance (IMR) of the tire is expressed in terms of the deflection of the tire on a rigid surface. Data from a number of experiments where IMR has been measured are portrayed in Figure 9 (Reference 6), which shows that IMR increases rapidly with deflection. The dashed curves in Figure 9 are approximate upper and lower bounds to the

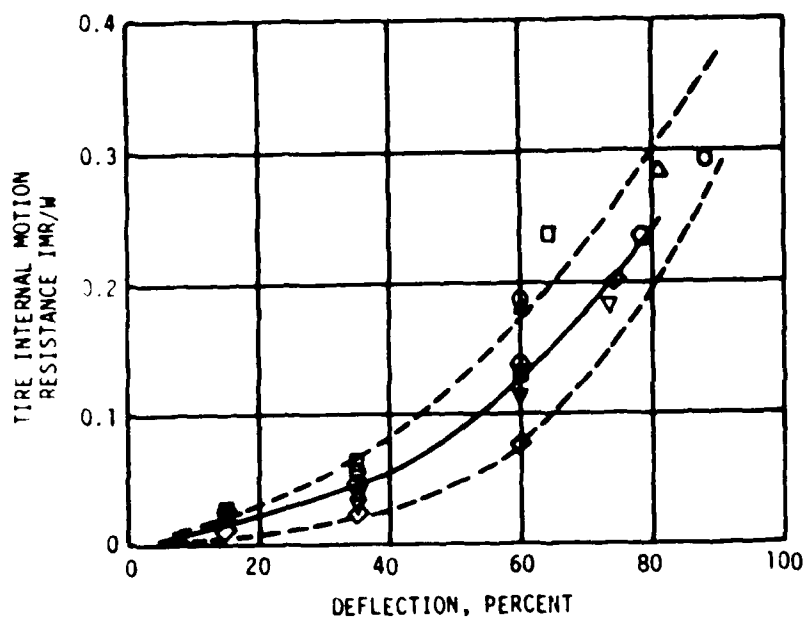


Figure 9. Tire internal motion resistance-deflection relation (Reference 6)

test data. The solid curve in Figure 9 may be viewed as the average response and is fitted with the following mathematical expression for calculations of internal motion resistance:

$$IMR = \left[4 \left(\frac{\dot{\theta}}{h} \right)^2 + 0.2 \left(\frac{\dot{\theta}}{h} \right) \right] \frac{W}{10} \dots \dots \dots (33)$$

Motion resistance, drawbar pull, torque, efficiency and side force

We can now proceed to develop appropriate equations for motion resistance (MR), drawbar pull (DBP), torque (T), and efficiency (E). From Figures 6 and 8:

$$MR = R'D \int_{-\frac{(\sin^{-1} 2)}{2}}^{\frac{(\sin^{-1} 2)}{2}} \tau_N \sin \left(\alpha + \frac{(\sin^{-1} 2)}{2} \right) d\alpha + IMR + MF \cos \alpha \dots \dots \dots (34)$$

$$DBP = R'D \int_{-\frac{(\sin^{-1} 2)}{2}}^{\frac{(\sin^{-1} 2)}{2}} \tau_p \cos \left(\alpha + \frac{(\sin^{-1} 2)}{2} \right) d\alpha - MR \dots \dots \dots (35)$$

$$T = R'D \int_{-\frac{(\sin^{-1} 2)}{2}}^{\frac{(\sin^{-1} 2)}{2}} \tau_p \left(R' - \frac{R \sin^2 \alpha}{\sin \frac{(\sin^{-1} 2)}{2}} \cos \alpha \right) d\alpha \dots \dots \dots (36)$$

$$E = \frac{DBP}{T} (1 - S) (R - \Delta_t) \dots \dots \dots (37)$$

where τ_N and τ_p are given by Equations 19 and 21, respectively, with α_1 replaced by $\alpha_1 - \alpha_2$, and $MF = R^2 \left(\alpha_1 - \frac{\sin 2\alpha_1}{2} \right) \tau_c \sin \alpha_1$. Similarly, from Figures 6 and 8 the side force (SF) is

$$SF = R'D \int_{\frac{(1-\alpha)^2}{2}}^{\frac{(1+\alpha)^2}{2}} \tau_N d\alpha + MR \tan \phi \quad \dots \dots \dots (38)$$

where τ_N is given by Equation 22. The above system of equations provides a complete solution to the performance of a flexible tire traversing a yielding soil. A computer program called TIRE has been developed which numerically solves the above system of equations.

PARAMETRIC STUDIES OF THE PERFORMANCE OF A FLEXIBLE WHEEL ON A YIELDING SOIL

In this part, the performance of a flexible wheel on both clay soil and sand is parametrically investigated (for $\phi = 0$). In addition, the effects of the unloaded section width, the deflection of the tire, and the slip ratio on the performance of the wheel are also analyzed. The radius of the flexible wheel used for the central case is 14.1 in., its width is 8.28 in., and its carcass section height is 6.35 in. All calculations were conducted for an applied wheel load of 1000 lbs. The results of the parameter study are presented in the following sections.

Sinkage

The results of the calculations for assessing the effect of soil type, slip ratio, and tire deflection on sinkage are presented in Figures 10 through 13. Figures 10 and 12 indicate that for both clay soil and sand sinkage increases with increasing slip ratio. The effect of tire deflection on sinkage is portrayed in Figures 11 and 13 for clay and sand, respectively. As indicated in these figures, the sinkage decreases rapidly with increasing tire deflections from zero (rigid wheel) up to approximately 40 percent deflection. Beyond 40 percent deflection, the rate of decrease in sinkage is small.

Motion Resistance

The effects of soil type, slip ratio, and tire deflection on motion resistance are shown in Figures 14 through 17. Figures 14 and 16 indicate that

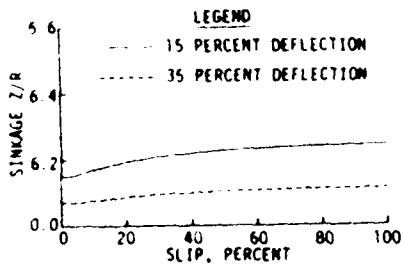


Figure 10. Relationship between sinkage and slip ratio for clay

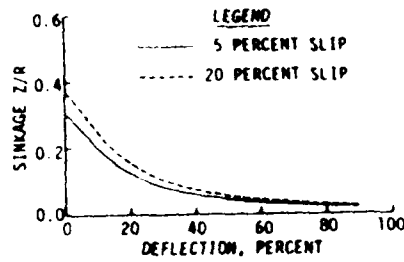


Figure 11. Relationship between sinkage and tire deflection for clay

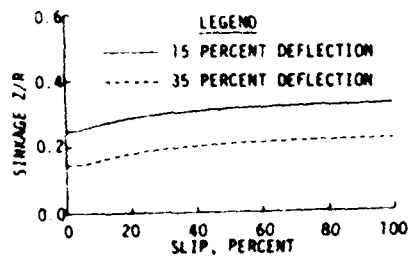


Figure 12. Relationship between sinkage and slip ratio for sand

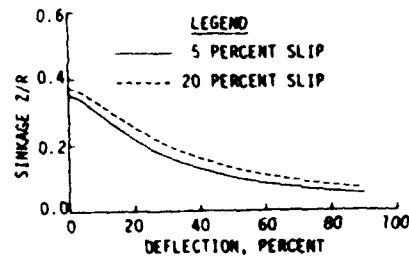


Figure 13. Relationship between sinkage and tire deflection for sand

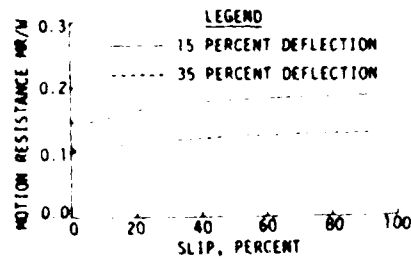


Figure 14. Relationship between motion resistance and slip ratio for clay

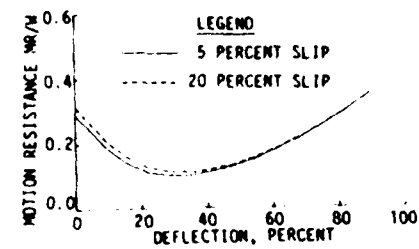


Figure 15. Relationship between motion resistance and tire deflection for clay

motion resistance initially decreases with increasing slip ratio up to a slip ratio of approximately 4 percent and increases thereafter. This initial decrease in motion resistance has been observed experimentally and is attributed to the plowing action of the tire. The increase in motion resistance at higher slip ratios is due to an increase in sinkage (see Figures 10 and 12). Relationships between motion resistance and tire deflection for each soil type studied are shown in Figures 15 and 17. The motion resistance initially decreases with increasing tire deflection and reaches a minimum value at about 30 percent deflection. At tire deflections higher than 30 percent, the motion resistance increases again. The initial decrease in motion resistance can be attributed to the initial rapid decrease in sinkage (see Figures 11 and 13). The increase in motion resistance at deflections larger than 40 percent is due to a rapid increase in the internal motion resistance of the tire (see Figure 9).

Drawbar Pull

Figures 18 through 21 portray the effects of soil type, slip ratio, and tire deflection on drawbar pull. Figure 18 indicates that for clay soil the drawbar pull increases rapidly for slip ratios between zero and about 10 percent. For higher slip ratios, the increase in drawbar pull is relatively small. For sand, on the other hand, the drawbar pull increases rapidly and reaches a peak value at about 20 percent slip ratio (Figure 20). The drawbar pull then drops for slip ratios in the range of about 20 to 50 percent. Beyond 50 percent slip ratio, the drawbar pull increases very slowly. This type of behavior also has been observed experimentally. Relationships between drawbar pull and tire deflection for each type of soil studied are presented in Figures 19 and 21. As indicated in Figures 19 and 21, the drawbar pull initially increases with deflection up to a deflection of approximately 50 percent. Beyond this deflection, the drawbar pull decreases because of a rapid increase in the internal motion resistance of the tire (see Figure 9).

Effect of Section Width on Tire Performance

Figures 22 through 25 present the effect of the unloaded section width on sinkage, motion resistance, drawbar pull, and torque, respectively, for clay soil at 15 percent tire deflection. Figure 22 shows that sinkage decreases rapidly as tire width increases from approximately $D/R = 0.2$ to

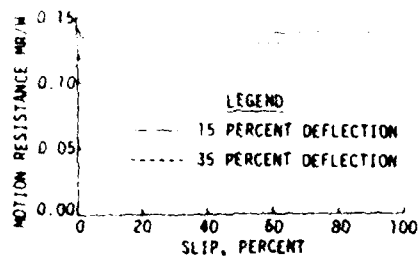


Figure 16. Relationship between motion resistance and slip ratio for sand

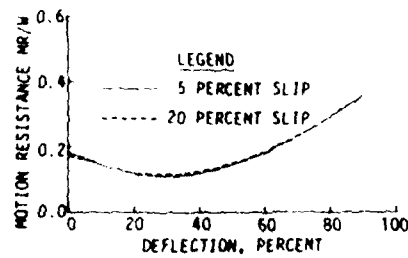


Figure 17. Relationship between motion resistance and tire deflection for sand

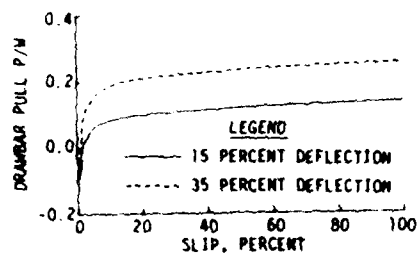


Figure 18. Relationship between drawbar pull and slip ratio for clay

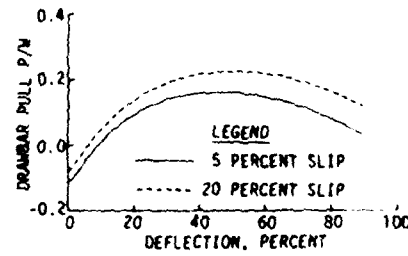


Figure 19. Relationship between drawbar pull and tire deflection for clay

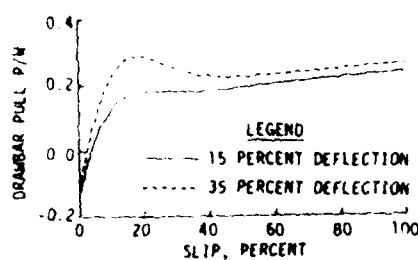


Figure 20. Relationship between drawbar pull and slip ratio for sand

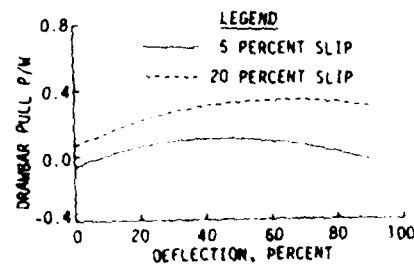


Figure 21. Relationship between drawbar pull and tire deflection for sand

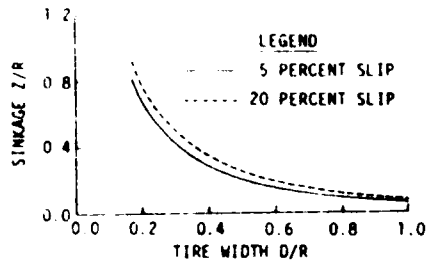


Figure 22. Relationship between sinkage and tire width for clay; 15 percent tire deflection

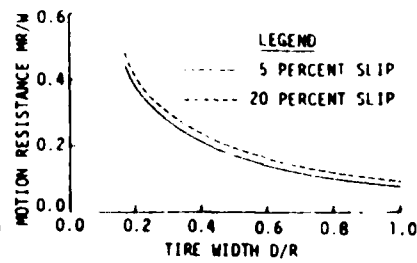


Figure 23. Relationship between motion resistance and tire width for clay; 15 percent tire deflection

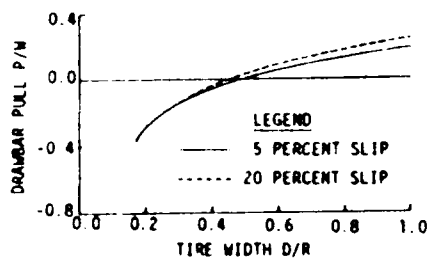


Figure 24. Relationship between drawbar pull and tire width for clay; 15 percent tire deflection

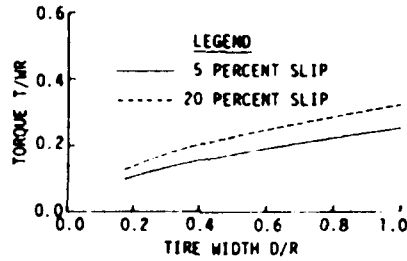


Figure 25. Relationship between torque and tire width for clay; 15 percent tire deflection

$D/R = 0.5$. For larger tire widths the decrease in sinkage is relatively small. Figure 23 shows that the motion resistance decreases as the width of the tire increases. This is expected because as the width of the tire increases, the sinkage decreases (see Figure 22). It should be pointed out that in Figure 23 the internal motion resistance of the tire was assumed to be independent of the width of the tire. If the effect of width on the internal motion resistance of the tire were taken into consideration, the result in Figure 23 would have been different.

Figure 24 indicates that the drawbar pull increases as the tire width increases. Most of the increase in the drawbar pull takes place for the tire widths less than 50 percent of the radius. For larger tire widths, the rate of increase in drawbar pull is relatively small. This behavior is also related to sinkage (Figure 22), where it is observed that most of the decrease in sinkage takes place for tire widths less than 50 percent of the radius. The relationship between torque and tire width is shown in Figure 25. The trend in Figure 25 is similar to Figure 24.

CORRELATION OF TEST DATA WITH MODEL PREDICTIONS

Background

The results of the extensive parameter studies presented in the previous section indicated that the model predictions are qualitatively in agreement with the observed performance of flexible wheels on a yielding soil. A detailed quantitative validation of the proposed model requires controlled laboratory tests and the measurement of the appropriate soil properties discussed in Reference 5. A partial validation of the model, however, can be accomplished by using test data already documented in the literature. The main drawback in using existing data from the literature is the lack of information on the mechanical properties of the soil used in the experiment. Usually the soil is characterized in terms of simple indices such as the mobility cone index (CI). These indices must be translated to the appropriate soil properties required by the proposed model. This is not an easy task and requires a separate analysis (divorced from the soil-wheel interaction model) to make such a translation. Usually one is forced to determine the numerical values of several material constants from an index such as the CI. This inherently introduces uncertainties

(or a bias) in the numerical values of the constants which, of course, will affect the degree of correlation between the model predictions and the test data. In spite of such uncertainties, a partial validation of the proposed soil-wheel interaction model is attempted for the zero turn angle.

Test Parameters

Test data for 13 different tires and 2 soil types (clay and sand) were selected from the literature for correlation with model predictions (Reference 1). The D/R of the tires ranged from 0.122 (bicycle tire) to 1.737. A total of 165 data points was selected (65 test data for clay and 100 for sand) for different wheel loads and tire deflections. The tests, however, were all conducted at 20 percent slip. Soil data for all the tests were given in terms of the mobility cone index (CI). Using a methodology developed in Reference 7, the appropriate soil properties required by the model were estimated from the CI data. A summary of all the test data and the companion soil properties are given in Reference 5 and for the sake of brevity are not included in this paper.

Model Predictions

The results of model predictions are plotted against the corresponding test data in Figures 26 through 31 for sinkage, drawbar pull, and torque. Each figure contains a 45-degree line (line of perfect correlation), a line of least square fit, and the standard deviation σ which signifies the deviation between the experimental data and the corresponding model predictions. It is a measure of the deviation of the data points in the figures from the line of perfect correlation. Comparisons between the least square lines and the 45-degree lines indicate that the overall correlation of the model predictions with the test data is very reasonable in spite of two possible sources of error--that is, the general scatter in the test data and the uncertainty in estimating several soil properties from a single cone index. The sinkage, which is one of the most difficult parameters to predict, has the lowest standard deviation. The degree of correlation exhibited between the test results and model predictions indicates that the physical basis of the proposed soil-wheel interaction model is sound for both cohesive soils and granular materials. Therefore, it may be concluded that the proposed model is capable of simulating the interaction

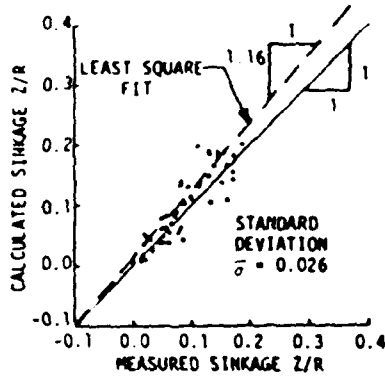


Figure 26. Predicted versus measured sinkage for clay

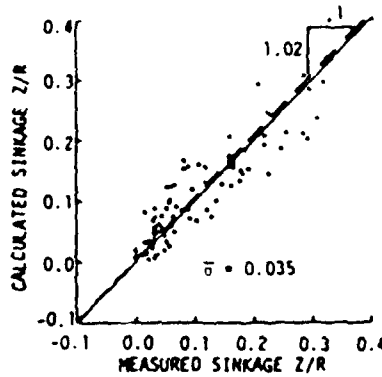


Figure 27. Predicted versus measured sinkage for sand

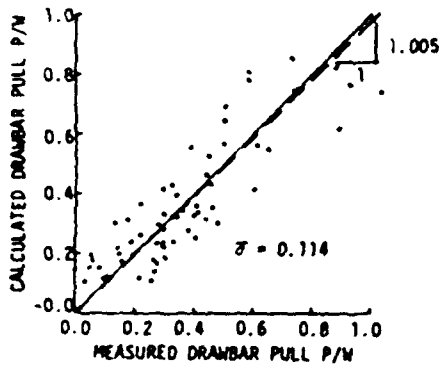


Figure 28. Predicted versus measured drawbar pull for clay

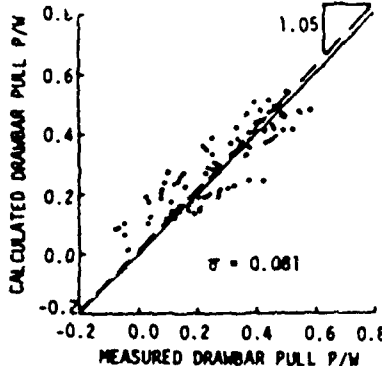


Figure 29. Predicted versus measured drawbar pull for sand

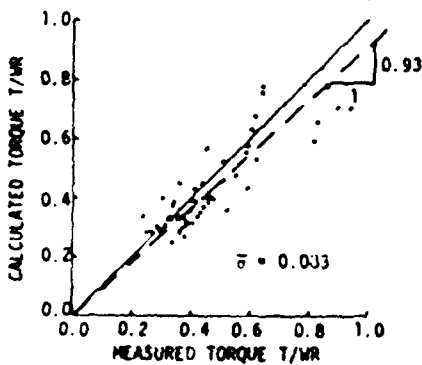


Figure 30. Predicted versus measured torque for sand

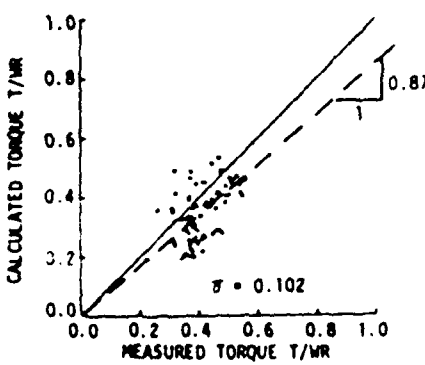


Figure 31. Predicted versus measured torque for sand

between a flexible tire and a soil exhibiting both cohesive and frictional properties.

SUMMARY AND CONCLUSIONS

A mathematical model for calculating the motion resistance, sinkage, drawbar pull, torque, and side force of a flexible wheel traversing a yielding soil has been developed and computerized for numerical application. The entire soil-wheel interaction process was treated as two springs in series, one describing the flexibility of the tire and the other describing the strength of the soil. Mathematical expressions were derived for the two spring constants in terms of the load-deflection characteristics of the tire, the undeflected configuration of the wheel, and the mechanical properties of the soil. The motion resistance, drawbar pull, torque, efficiency, and side force for the flexible wheel were obtained from the equilibrium equations by assuming that the deformed boundary of the tire is an arc of a circle with a radius equal to or greater than the undeflected radius of the wheel. The model is partially validated by comparing the results of a large number of laboratory test data for single tires on both clay and sand with the corresponding model predictions. Efforts are presently underway at WES to couple the soil-wheel interaction model with the dynamic equilibrium equations of multi-axle wheeled vehicles for analysis of the steering performance of such vehicles.

ACKNOWLEDGEMENT

The work reported herein was conducted at the U. S. Army Engineer Waterways Experiment Station under the sponsorship of the Office, Chief of Engineers, Department of the Army, as part of Project 4A161102AT22, "Dynamic Soil-Track Interactions Governing High-Speed Combat Vehicle Performance."

The authors are grateful to Mr. Clifford J. Nuttall, Jr., for providing valuable insight during the course of this study. The efforts of Mr. Donald E. Barnes in assisting in the numerical calculations and Ms. Bobbie B. Morrow in typing the paper are appreciated.

REFERENCES

1. Turnage, G. W. 1972. "Performance of Soils Under Tire Loads; Report 8; Application of Test Results to Tire Selection for Off-Road Vehicles," Technical Report 3-666, U. S. Army Engineer Waterways Experiment Station, CE, Vicksburg, Miss.
2. Wong, L. and Reece, A. R. 1967. "Prediction of Rigid Wheel Performance Based on the Analysis of Soil-Wheel Stresses," Journal of Terramechanics, Vol 4, No. 1.
3. Hvorslev, M. L. 1970. "The Basic Sinkage Equations and Bearing Capacity Theories," Technical Report M-70-1, U. S. Army Engineer Waterways Experiment Station, CE, Vicksburg, Miss.
4. Furimote, Y. 1977. "Performance of Elastic Wheels on Yielding Cohesive Soils," Journal of Terramechanics, Vol 14, No. 4.
5. Baladi, G. Y., Rohani, B., and Barnes, D. E. 1984. "Steerability Analysis of Multi-Axle Wheeled Vehicles; Report 1; Development of a Soil-Wheel Interaction Model" Technical Report GL-84-1, U. S. Army Engineer Waterways Experiment Station, CE, Vicksburg, Miss.
6. Turnage, G. W. 1976. "In-Soil Tractive Performance of Selected Radial and Bias-Ply Tires," Paper 76-1520, The 1976 Annual Meeting of the American Society of Agricultural Engineers, Chicago, Ill.
7. Rohani, B. and Baladi, G. Y. 1981. "Correlation of Mobility Cone Index with Fundamental Engineering Properties of Soil," Miscellaneous Paper SL-81-4, U. S. Army Engineer Waterways Experiment Station, CE, Vicksburg, Miss.

NOTATION

C	Cohesion
D	Unloaded section width of the tire
DBP	Drawbar pull applied on the tire
dF	Vertical differential force
E	Efficiency of the tire
G	Shear modulus
h	Unloaded section height
IMR	Internal motion resistance of the tire
k_e	Equivalent spring constant for soil-tire system
k_s	Spring constant of the soil
k_t	Spring constant of the tire
MF	Motion resistance in the direction of motion
MR	Motion resistance in the plane of the tire
R	Radius of the tire

R_0	Initial radius of an expanded cavity
R'	Radius of a circle containing the deflected portion of the wheel
S	Slip of the wheel in the plane of the wheel
SF	Side force Applied on the tire
S_m	Slip of the wheel in the direction of motion
T	Torque applied on the tire
W	Tire load
Z	Sinkage of a flexible wheel
Z_r	Sinkage of a rigid wheel
α	Generic angle
Δ	Maximum deflection of the tire on a hard surface
Δ_t	Maximum deflection of the tire on a yielding soil
Δ_1	Deflection of the tire at the generic point
θ	Angle between the direction of motion and the plane of the wheel
α_t	$2\cos^{-1}\left(1 - \frac{\Delta}{R}\right)$
α_B	$2\cos^{-1}\left(\frac{R_0}{R}\right) = 2\cos^{-1}\sqrt{1 - \frac{D}{\pi R}}$
α_1	$\cos^{-1}\left(1 - \frac{Z + \Delta_t}{R}\right)$
α_2	$\cos^{-1}\left(1 - \frac{\Delta_t}{R}\right)$
σ	Radial stress inside a cavity
σ_N	Normal stress at the soil-tire interface
τ	Shear stress at the soil-tire interface
τ_N	Shear stress perpendicular to the plane of the wheel
τ_p	Shear stress in the plane of the wheel
ϕ	Angle of internal friction

AD-P004 260

SOIL COMPLIANCE INFLUENCE ON TYRE PERFORMANCE

P. BOONSINSUK AND RAYMOND N. YONG

GEOTECHNICAL RESEARCH CENTRE, MCGILL UNIVERSITY, MONTREAL, CANADA

ABSTRACT

It is not uncommon in off-road mobility for vehicles to operate over varying types of terrain. In situations where inorganic clay soils constitute the primary substrate material, considerable differences in soil stability and compliance characteristics can occur because of local variations in soil type, density and water content.

This study takes into account the above constraints in the methodology developed for evaluation and prediction of efficient tyre performance. This requirement for capability in development of efficient tyre traction on soil for mobility purposes is critical if off-road operations are performed in remote regions where minimum fuel expenditure is particularly important. The developed analytical procedure utilizes the experience gained from experimental tow-bin tests which studied tyre-soil interaction under varying tyre and soil conditions.

Because of the interdependent relationships formed between the forcing function (tyre loading) and the response function (soil response), variations in the properties and characteristics of one partner will affect the other. In view of the interdependencies, both tyre sinkage and contact patch will also vary - dependent on tyre and soil properties. Thus, tyre performance which will be characterized by the mechanics of energy transfer at the interface must account for contact patch and normal and tangential load distributions over the patch. Soil compliance under load must also be included in the accounting since this will dictate bearing stability, sinkage and tractive slip.

INTRODUCTION

In the performance of wheeled-vehicles under off-road circumstances the specific requirement scrutinized for evaluation of vehicle performance relates to capability of the machine to produce maximum work. In the present concern for minimization of fuel expenditure, the production of maximum tractive effort, i.e. work done, becomes most important. This requirement is especially critical in situations where vehicles operate in remote and poorly accessible regions. Under such circumstances, climatic and local environmental conditions such as operational terrain characteristics become significant considerations in the production of useful work.

With a given vehicle, the ability to provide adequate mobility will finally depend upon interactions established between the wheels and the supporting terrain material. For this particular examination, tyres are considered as the tractive elements producing the transfer of energy between the vehicle and the terrain surface. If consideration of the

proper utility of input energy is to be made in regard to efficient performance of tyres under bearing loads relative to the nature of the supporting terrain, losses in energy arising from energy-dissipating characteristics of the tyres must be minimized. The efficiency of energy transfer from the tyre to the ground will then be maximized.

The contact patch established between the tyre and the ground surface and the manner in which the sets of forces are distributed and transferred across the tyre contact patch are the controlling parameters which will establish the efficiency or productivity of the tyre in mobility/tractive performance. In this study the relevance between inorganic soil support materials and the tyre is studied in relation to the development of efficient tractive effort. The analytical model developed accounts for the compliance of both the tyre and the soil system and the analysis for prediction of drawbar pull-slip relationships utilizes the interactions between tyre and soil. The load and unload sequence of the supporting soil material in response to input from the moving tyre is an important consideration in the analysis.

LABORATORY TEST PROGRAM

Because the size of the soil tow bin was limited, model-sized tyres were used in the study. This was considered acceptable in the context of development of the basic structure of the evaluation and prediction tool. It by no means pretends to fully model life-sized tyres in interaction with the ground. Since the compliance of the soil can be adjusted in the laboratory study to provide some form of "scale-appreciation" - i.e. the soil was deliberately made much softer than most real-life conditions - it was hoped that the test results obtained could provide the basis for the necessary analytic formulations and test validations. At a later time, expansion to full field-scale testing would be useful.

Three model tyres were investigated in this study, namely, Tyre 3.00-8.00 2 PR (buffed), Tyre 3.00-4.00 4 PR (buffed) and Tyre 4.10/3.50-4.00 2 PR (originally-treaded) as shown in figure 1(a-c). Once the last tyre underwent all required tests, it was buffed, thereby resulting in another model tyre for testing [called Tyre 4.10/3.50-4.00 2 PR (buffed) in Fig. 1d] which was later treaded with the directional tread pattern as shown in Fig. 1e [called Tyre 4.10/3.50-4.00 2 PR (re-treaded)]. In effect, a total of five model tyres were studied, each of which was subjected to similar test requirements. Hence, it was possible to investigate the influences of various tyre characteristics, i.e. carcass construction, dimension, surface condition, etc. with respect to the tyre-soil mobility performances.

Two main series of experimentation were performed in this study as follows:

1. Static loading of the model tyres onto soils with different stiffness to measure the corresponding tyre deformations and contact areas.
2. Wheel tow-bin tests in which each model tyre was powered to move through different soils compacted in a soil bin, being slightly wider than the tyre width, in order to measure the torques required and the drawbar pulls developed. The details of such a test procedure have already been presented (e.g. Yong and Webb, 1969).

Three types of supporting ground were used namely,

1. rigid wooden floor to create "unyielding" surface,
2. kaolinite clay to resemble "soft" ground, and
3. clayey sand to simulate "stiff" ground.

The kaolinite clay was prepared at 95% saturation while the clayey sand was a mixture of fine silica sand passing sieve number 30 and kaolinite proportioned at 30% of the sand dry weight. The clayey sand was compacted in the soil bin at a dry density of 1.88 t/m^3 and a moisture content of 13%.

Soil specimens prepared under the same conditions as those used in the preparation of soil for the soil bin were tested under plane-strain conditions using the triaxial test. The resultant stress-strain curves of both the clayey sand and the kaolinite clay are shown in Fig. 2. It is obvious that the clayey sand is much stiffer than the kaolinite clay, i.e. the compliance of the clayey sand is lower than that of the clay.

LOAD-DEFORMATION CHARACTERISTICS

By loading each model tyre statically through its rim at various inflation pressures, the relationships between the static wheel load and tyre carcass deformation on a rigid unyielding surface can be established as illustrated in Fig. 3. All the model tyres exhibited a linear relationship between the applied wheel load and the tyre deformation. Amongst the tyres tested, tyre 4.10/3.50-4.00 2 PR (originally treaded) (Fig. 1c), with heavy sidewall stiffening of the treads, is the stiffest. However, when the tread is removed completely (by buffing) resulting in a smooth surface, the tyre stiffness is reduced significantly as demonstrated in Fig. 3c. Furthermore, the influence of retreading with the directional tread pattern [wide-spaced tread bars without sidewall stiffening, i.e. tyre 4.10 3.50-4.00 2 PR (re-treaded), Fig. 1e] on the tyre stiffness is negligible, as can be seen in the comparison curves shown in Fig. 3d. A comparison of the curves shown in Fig. 3c for the buffed tyre with the results in Fig. 3d indicates no significant difference between the load deformation characteristics of the two types of tyres.

TYRE CONTACT AREA CHARACTERISTICS

The contact area between a tyre carrying a given wheel load and the supporting ground is the key factor which controls its mobility performance through its characteristic ability to transfer the interfacial forces developed. The nature (geometry and area) of the contact patch is a direct reflection on the relative compliance of both the tyre and the soil support system. Of particular interest is the case of a moving tyre as it indicates the actual service condition. Because of the actual physical distortions of the contact patch and particularly because the micro-compliance of tyre and soil are not uniform, the distribution of both normal and tangential stress (or pressures) developed and transmitted through the contact patch area become exceedingly sensitive to slip.

Whilst the contact patch area of a tyre under motion can be measured by taking photographs beneath the tyre when it travels over a rigid transparent plate at various slip rates, as illustrated schematically in Fig. 4, it is well understood that the patch geometry and area will differ in respect to the compliance of the supporting medium. In addition, the slip-generated effects created by the rigid plate need not be similar to

that produced by the actual compliant soil interface interaction. Recognizing the preceding, it is nevertheless essential that a base value be established - for later comparisons with predicted patch influence. Thus in the rigid plate tests used for measurement of the contact patch established, the translational velocity of the test model tyre was kept constant at 15.2 cm/sec while the rotational velocity was varied to obtain approximately 0-80% slip rates.

The measured contact areas of the five model tyres using the procedures described are shown in Figs. 5 and 6. It is noticeable that the majority of the measured contact areas are not sensitive to the changes in the slip rates. Two interesting points are noted:

- 1 At low inflation pressures, or in the situation where the load is sufficiently high with respect to the inflation pressure, the contact patch area shows a marked sensitivity to slip. This is evident in the top curves shown in Figs. 5a and 5b.
- 2 At higher inflation pressures, the dependence of patch area on slip is considerably reduced.

In general, it is noted that the stationary contact areas are slightly higher than those developed while the tyres are in motion. This corresponds to the normal phenomenon that the overall diameter of a moving tyre is increased from the stationary one due to the centrifugal force effect on the tyre casing (Turley, 1970-71). It is expected that for larger tyres, the changes in contact areas at various slip rates should be more detectable.

The influence of side-wall stiffening of the tyre carcass in tyre 4.10/5.50-4.00 2 PR (originally treaded) is clearly observable in Fig. 5c, indicating that this is the main mechanism controlling patch area and that this is not significantly altered with inflation pressure.

The results shown in Fig. 6 indicate that buffing and subsequent retreading will provide significant changes in the patch area characterization with inflation pressure. Furthermore, the contact area of the buffed tyre can be less than that of the originally-treaded one as can be noticed in the case of 13.6 kg wheel load and 0.41 kg/cm² inflation pressure. In other cases, the contact area of the buffed tyre is always higher, implying the effect of tyre wear.

While it is very difficult, if not impossible, to measure the exact contact area of a tyre moving through a soft ground, the test results presented above demonstrate that changes in contact area during motion should be anticipated. As noted previously, the degree of such change will depend on the relative stiffness of the tyre-soil system, i.e. the compliance of the tyre and supporting soil, and the slip-interface relationships.

In order to compare the tyre-soil interaction the average computed values of interfacial stresses can be used, i.e. the computed values of tangential stress and normal stress developed at the interface. The tangential stresses developed by the model tyres were calculated by dividing the measured torques with the product of the rolling radius and the stationary tyre-soil contact (patch) area, whilst the normal stress was obtained by dividing the applied load with the stationary patch area. The tangential stresses obtained are related to the corresponding normal stresses as

illustrated in Fig. 7. For all model tyres, either the peak values or the asymptotic values of the measured torques were used in calculating the tangential stresses. The soil-soil shear stresses measured in a direct shear soil test are also presented for direct comparison.

The test results indicate that the nature of the tangential stresses between the tyre-soil interfaces are governed by both soil compliance and surface characteristics of the tyre and terrain. In the situation where the bearing soil is less compliant - i.e. the clayey-sand as shown in Fig. 7a, the influence of surface properties of both tyre and terrain can be seen in the different curves produced for the different tyres. However, for a more compliant soil where tyre sinkage apparently becomes more significant, the influence of surface properties of the tyre or terrain becomes considerably reduced - to the point of insignificance at higher normal stresses. As indicated in Fig. 7b, the various tyres appear to produce a common average tangential (shear) stress for the same normal stress at higher normal stresses - in contrast to the results shown in Fig. 7a.

MOBILITY PERFORMANCE

The influence of soil compliance on the tyre-soil interaction problem is demonstrated in terms of alteration of the patch characteristics and significance of surface characteristics on development of tangential stresses - as seen in the preceding section. In constructing an analytical model to predict mobility performance, it is noted that this item plays an important role in the structure of the analysis - since the forces transmitted from the tyre to the ground must act through the contact patch. This is not unusual since the problem is a boundary value problem. The analytical model designed to incorporate the effects of tyre flexibility and soil compliance in regard to mobility performance has been previously developed. A detailed description of the analytical model and its application can be found in Yong et al. (1978a,b), (1980a,b).

The finite element method (FEM) solution technique solves the equilibrium equations for the supporting soil with output information given in terms of strain rate field, velocity field, and stress field. Input and other necessary information requirements for solution using the FEM are load boundary condition, and load-unload stress-strain relations for the soil.

For specification of the load boundary condition, it is necessary to establish: (a) footprint (patch) length, (b) distribution of normal stress, (c) distribution of tangential stress and (d) variation of distribution profiles for normal and tangential stresses. For simplicity in solution, the problem is treated as a two-dimensional problem. Figure 8 shows the finite element mesh scheme used and the contact patch length used as a fundamental sizing unit for determination of mesh size. Note that simulation of tyre motion is achieved by considering successive stationary positions for the tyre.

Considering the tyre as an elastic system and the soil as a piecewise linear elastic material, the length of the contact patch footprint can be determined as: Poritsky, 1950

$$\frac{1}{R_1} + \frac{1}{R_2} = \frac{4P}{\pi a^2} \left[\frac{1-\nu_1^2}{E_1} + \frac{1-\nu_2^2}{E_2} \right] \quad (1)$$

$$= \frac{4P}{\pi a} [C_1(1-\nu_1^2) + C_2(1-\nu_2^2)] \quad (2)$$

where R_1 = undeformed radius of tyre

$R_2 = r$, since soil terrain surface is considered horizontal

P = applied wheel load

$2a$ = length of contact patch

E_1, E_2 = elastic moduli of tyre and soil respectively

C_1, C_2 = compliance of tyre and soil = $1/E_1, 1/E_2$

ν_1, ν_2 = Poisson's ratio for tyre and soil respectively

= 0.5 for both tyre and soil as first approximation

Using the actual compliance values measured for tyres and soil, the contact patch lengths for the tyres on the soils used can be calculated and compared in terms of equivalent patch area with the patch area values actually measured from patch points in the soil in stationary tyre-soil tests. The actual soil patch areas are compared to the predicted (computed) values in Fig. 9 and 10. For further comparisons, the test results from the stationary tyre tests on the rigid transparent plate for the same tyres at the same inflation pressure are also shown. The differences between the rigid plate measured values, the actual soil patch values and the computed (predicted) values for the patch areas taking into account the compliance of the soil can be noted in the figures. Two specific points can be noted:

- a. The patch area developed on the rigid transparent plate is, in general, less than that in the soil since tyre sinkage into the soil occurs. This is particularly obvious in the case of the kaolinite clay where the tyre sinkage is high. In effect, the patch area reflects the influence of tyre sinkage into the soil, tyre deflection in the soil, tyre carcass stiffness and tyre configuration. It should be noted that the contact area in soil as reported herein is the horizontally-projected area, not the actual curved surface area.
- b. The computed (predicted) results closely match the actual patch footprints measured in the tyre-soil load deformation studies - indicating that the analytical model used is valid.

The applications arising from the information given in Figs. 9 and 10 are quite obvious. Because of the soil compliance, modification of the patch area occurs. Since the compliance of the soil will always be higher than the rigid reference test base, the actual patch area will be lesser. In an off-road situation, the presence of a varying support terrain system is recognized - leading thereby to the realization that the patch area developed by the contact tyre will always be a variable area, most often considerably more than that measured on a hard unyielding support.

The motion resistance R_t is used to provide a means for determining the geometry assumed by the patch at the interface - i.e. the curvature assumed by the patch. Since the contact pressure at the tyre-soil interface is not really known, an iterative procedure is needed to reconcile pressure distribution with contact area and soil properties. Taking R_t as:

$$R_t = \frac{\sum_{i=1}^n P_i \Delta x_i}{\sum_{i=1}^n [R_i \Delta x_i]} \quad (3)$$

where R_i = tyre width

P_i = nodal force at node i - see Fig. 11

Δx_i = tyre deformation at node i

α = contained angle at hub defined by contact area as shown in Fig. 11

R_0 = undeformed tyre radius

n = number of nodal points at patch length

Δx = tyre deformation at wheel centre

Implementation of the FEM solution technique can begin with an initially assumed pressure distribution at each nodal point on a profile, also assumed as shown in Fig. 11. By an iterative procedure, the actual dynamic shape profile shown in Fig. 11 - as the profile surface B predicted by the FEM - can be obtained. If, for example, an improper distribution of pressure is assumed, the analysis will produce a solution which indicates a negative tyre deformation at the respective nodal points - which is obviously untenable in the context of the problem.

Using the motion resistance R_t from equation (3), the energy consumed in deforming the tyre can be computed as a rate term as follows:

$$\dot{E}_t = R_t \dot{x} \quad (4)$$

where \dot{x} is the translational velocity of the tyre.

The tyre-soil mobility performance can best be viewed in terms of an energy budget, i.e., energy input and output of the system. Using equation (4), the energy lost in deforming the tyre casing during its motion through the supporting ground can be predicted and incorporated in the evaluation of overall mobility performance. The governing equation is:

$$\dot{E} = D^* + P_0 + \dot{E}_t + \dot{E}_l \quad (5)$$

where \dot{E} = input energy = torque at hub multiplied by angular velocity

D^* = soil deformation energy obtained from output information provided by the FEM analysis

P_0 = overall output energy

E_f = interfacial energy obtained by determination of shearing stresses at interface and slip rate, and

E_t = tyre deformation energy obtained as output information from the FEM analysis [equation (4)].

A typical energy balance is shown schematically in fig. 12 in which all participating energy components are demonstrated. By assessing the input energy and all energy losses, the output energy can be predicted leading to the drawbar pull produced by the tyre-soil system, if so required.

The influence of assumptions made concerning the nature of normal pressure distribution across the patch length in the load-unload sequence as a tyre moves over the ground can be evaluated. This is demonstrated by considering two cases - a uniform and a parabolic pressure distribution. The two cases are considered in the analytical model in the evaluation of the amount of tyre deformation energy and tyre deflection in fig. 13. The tyre deformation energy of a model tyre moving through soils of different stiffness has been predicted and compared to the situation of the same tyre moving on a rigid unyielding surface. It is expected that the correct trend will be attained when the flexibility of the tyre in the supporting soil is sufficiently high. It is noticed that when the modulus of elasticity of the soil (E_{soil}) is less than that of the tyre (E_{tyre}), i.e. $E_{\text{soil}}/E_{\text{tyre}} < 1$, the tyre is stiffer than the underlying soil, thereby resulting in no appreciable flexibility. Thus when $E_{\text{soil}}/E_{\text{tyre}}$ is less than one, a rigid wheel model (i.e. $E_t = 0$) can be used in the analysis. In other words, if the ratio of the soil compliance C_{soil} to the tyre compliance is greater than unity, a rigid model analysis could be used.

CONCLUDING REMARKS

From the preceding discussion, it is apparent that the soil compliance controls the tyre performance, depending on the degree of tyre flexibility on the given soil and the interface characteristics. In the general evaluation of mobility performance, the selection of a suitable vehicle-tyre-soil system is primarily dependent on the drawbar pull developed by the system. The parameters which affect the output of the vehicle-tyre-soil system are compiled in fig. 14 according to the observed performances of the small model tyres tested herein. It is obvious that the tyre-soil contact area plays a very important role and some parameters such as the inflation pressure can influence others as well. In essence, the soil compliance cannot be excluded from the analysis of the off-the-road vehicular performance.

Owing to the inter-relationships of these parameters and the complexity of the vehicle-tyre-soil system, a simple mathematical expression for the overall behaviour cannot be established at this stage. Hence, the extent of change in any parameter cannot be expressed quantitatively without a complete analysis. Nevertheless, the relative importance of each parameter can be compared to others qualitatively as very important (V), less important (L) and more study needed (M) in table 1. In addition, each parameter is recommended to be increased (I) or decreased (D), if such a change is feasible, in order to increase the drawbar pull.

REFERENCES

- Forlev, L.A. (1970-71): Engineering Aspects of Tyre Testing, Proc. Inst. Mech. Engrs., Automobile Div., Vol. 185, pp. 1003-1014.
- Yong, R.N., Boonsinsuk, P. and Fattah, E.A. (1980a): Tyre Flexibility and Mobility on Soft Soils, *Journal of Terramechanics*, Vol. 17, No. 1, pp. 43-58.
- Yong, R.N., Boonsinsuk, P. and Fattah, E.A. (1980b): Tyre Load Capacity and Energy Loss with Respect to Varying Soil Support Stiffness, *Journal of Terramechanics*, Vol. 17, No. 2, pp. 131-147.
- Yong, R.N., Fattah, E.A. and Boonsinsuk, P. (1978a): Analysis and Prediction of Tyre-Soil Interaction and Performances Using Finite Elements, *Journal of Terramechanics*, Vol. 15, No. 1, pp. 43-63.
- Yong, R.N., Boonsinsuk, P. and Fattah, E.A. (1978b): Prediction of Tyre performance on Soft Soils Relative to Carcass Stiffness and Contact Area, *Proc. 6th Int. Conf. on Int. Soil. for Terrain-Vehicle System* (ISTVS), Vienna, Vol. II, pp. 643-675.
- Foritsky, R. (1950): Stresses and Deflection of Cylindrical Bodies in Contact with Application to Contact of Gears, and of Locomotive wheels, *J. Applied Mech.*, Vol. 17, pp. 191-201.

TABLE 1 RELATIVE IMPORTANCE OF PARAMETERS

Parameters		To Increase Drawbar Pull			
		Soft Cohesive Soil		STIFF Cohesionless Soil	
		Relative Importance	How to Change?	Relative Importance	How to Change?
Parameters Used in the Analysis by the Finite Element Method	Normal pressure intensity (Wheel load)	V	D	V	D
	Tangential pressure intensity	V	I	V	I
	Contact area	V	I	V	D
	Soil stress-strain relationship (stiffness)	V	I	V	I
	Soil Poisson's ratio	L	-	L	-
	Pressure distribution pattern	L	-	L	-
	Slip rate (positive)	V	I	L	D
	Tyre rolling radius	L	I	L	I
	Others e.g. translational velocity, acceleration, soil topography, soil layer, etc	S	S	S	S
	Others	Inflation pressure	V	D	V
Tyre surface conditioning (treaded or buffed)		V	Treaded	L	-
Tread pattern		V	-	L	-
Tyre carcass stiffness		L	-	L	-
Tyre carcass construction (radial or cross-bias)		S	S	S	S
Others e.g. lug depth, lug spacing, etc		S	S	S	S

V - Very Important,

L - Less Important,

I - Increase,

D - Decrease,

S - More Study Needed

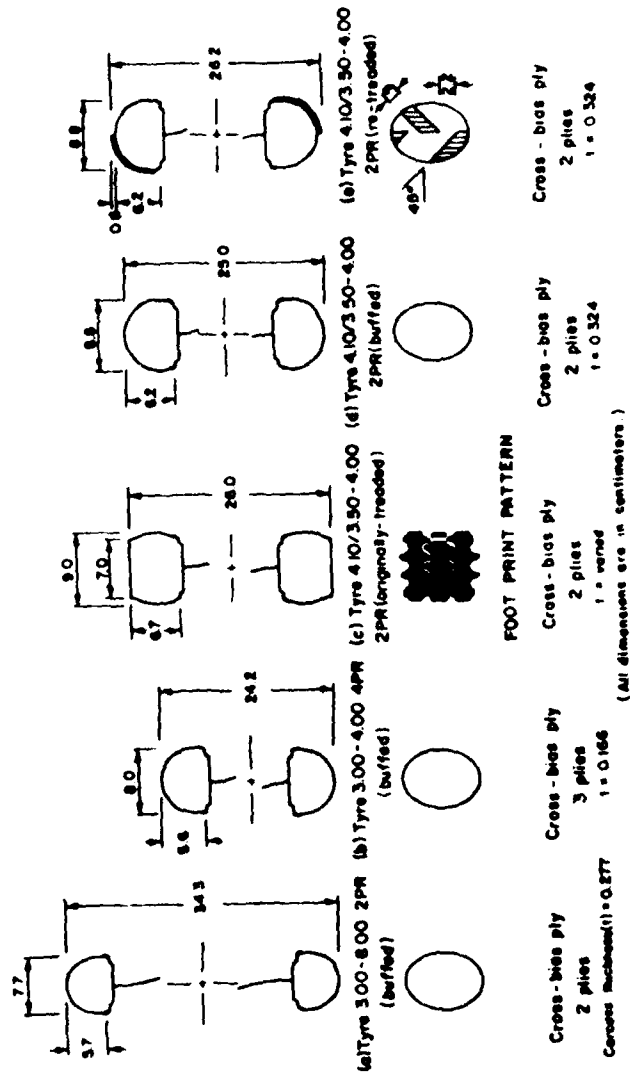


Fig. 1 Undeformed tyre sections used in the study

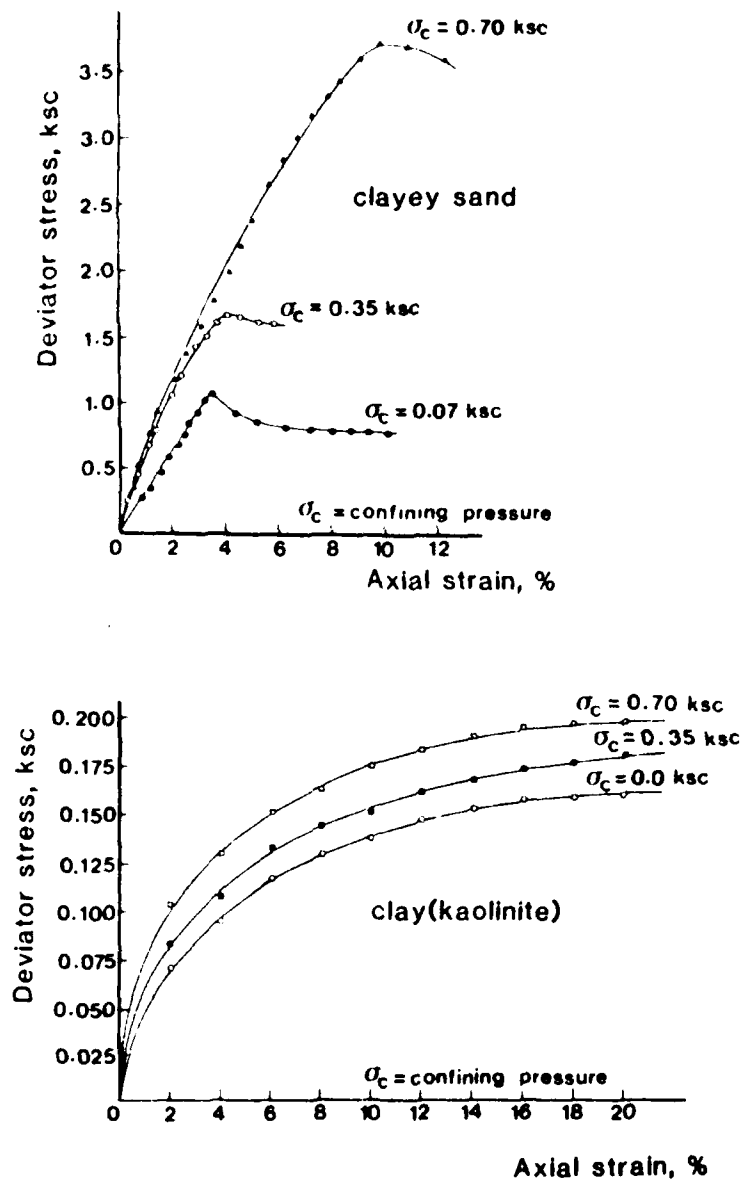


Fig. 2 Stress-strain relationships of clayey sand and clay (kaolinite)

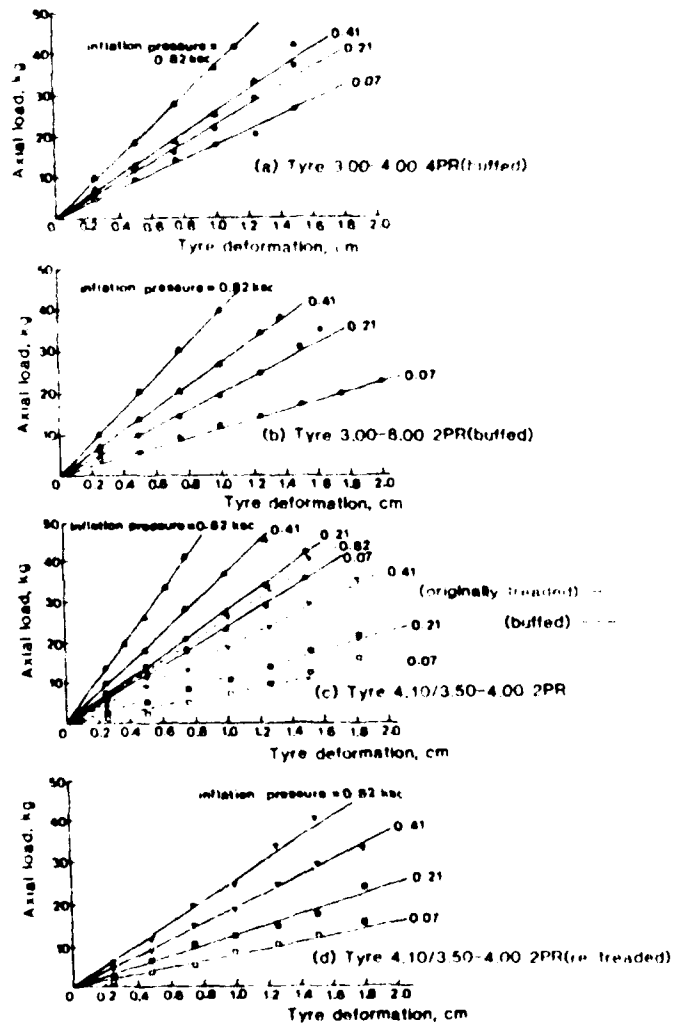


Fig. 3 Wheel load - tyre deformation relationships

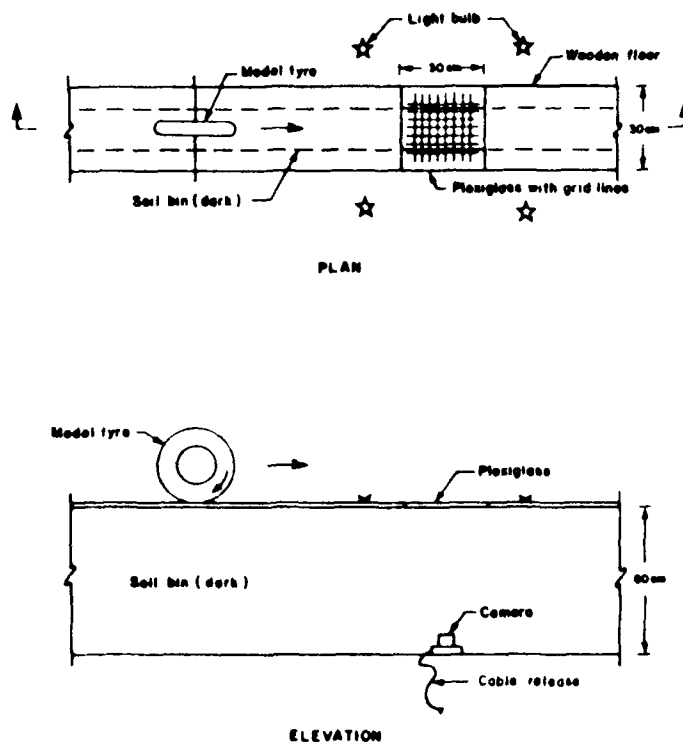


Fig. 4 Technique used for measurement of moving tyre-rigid unyielding surface contact area

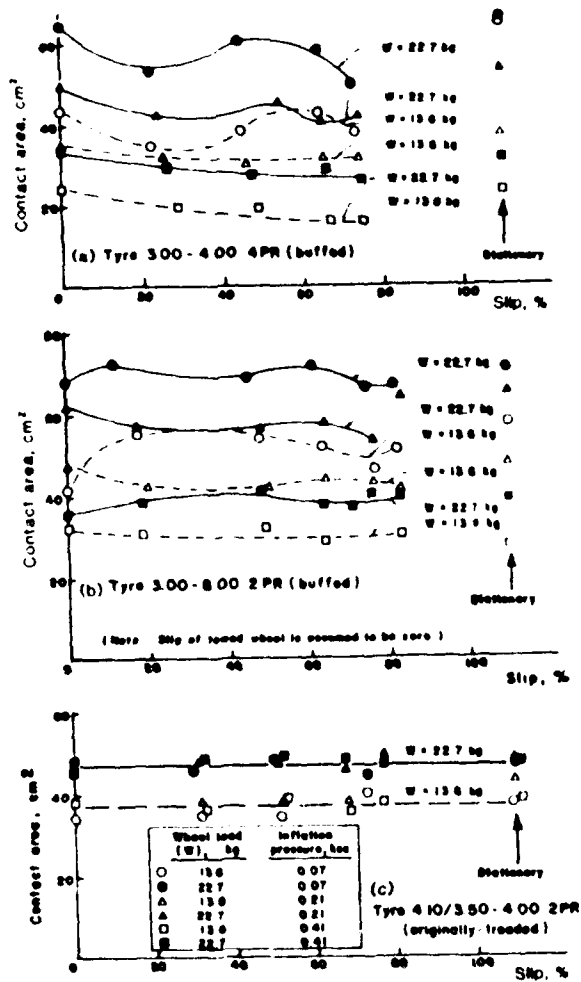


Fig. 5 Contact area - slip rate relationship (3 original model tyres)

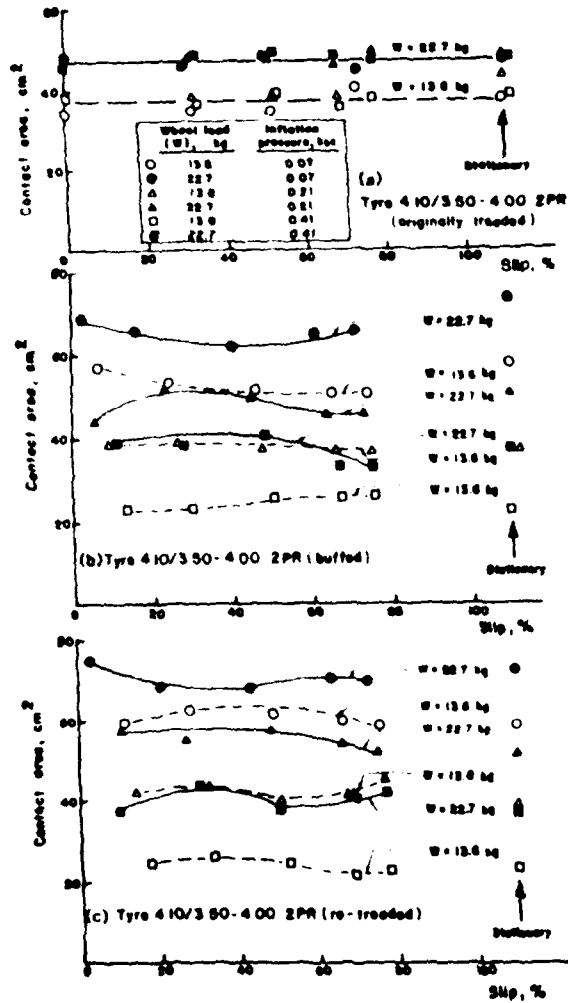


Fig. 6 Contact area - slip rate relationship (3 types of tyre 4.10/3.50-4.00)

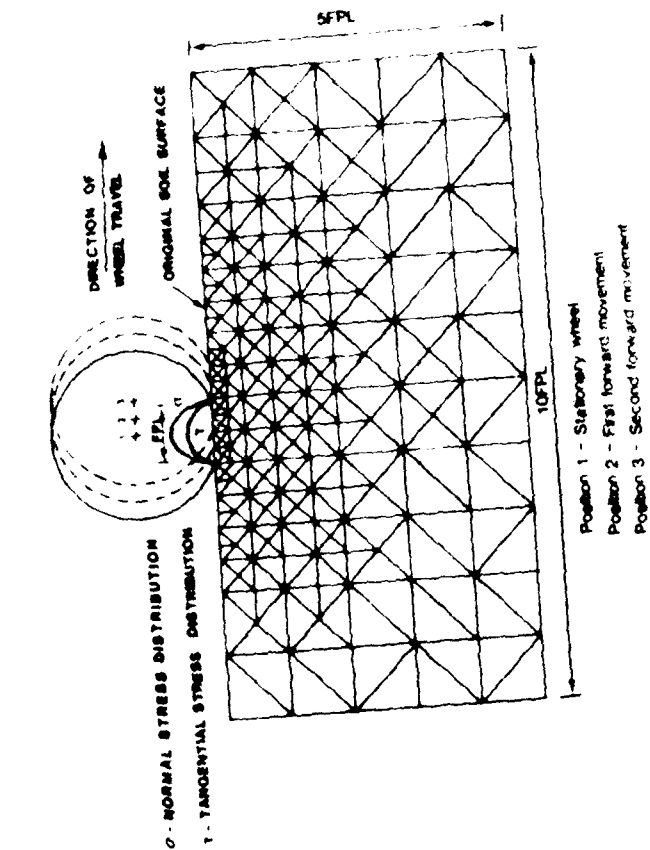


Fig. 8 Idealization of tyre-soil system using the finite element method

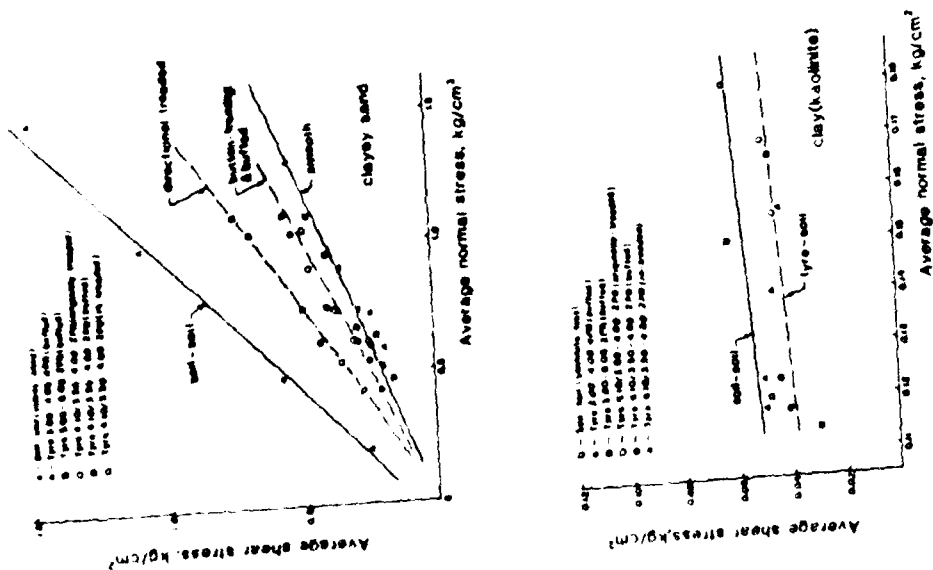


Fig. 7 Shear stress - normal stress relationships

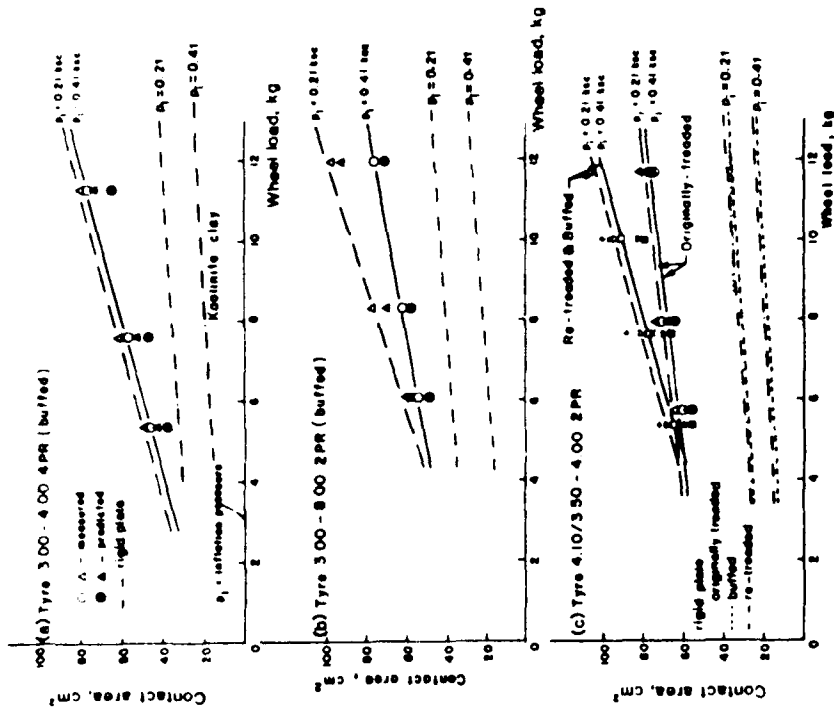


Fig. 10 Prediction of tyre-soil contact area on kaolinite clay

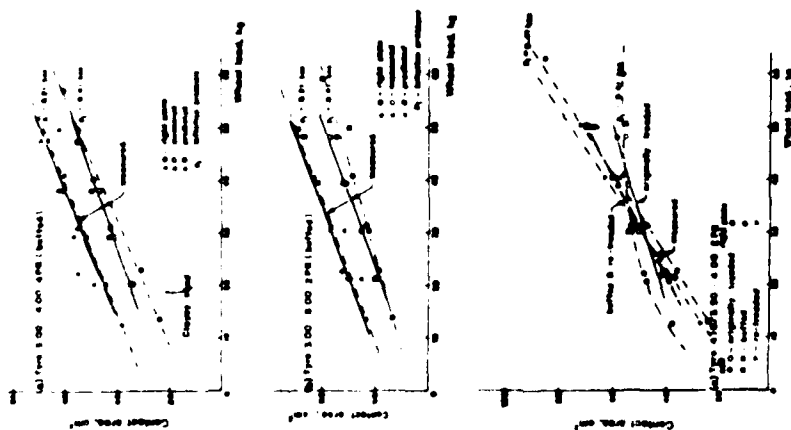


Fig. 9 Prediction of tyre - soil contact area on clayey sand

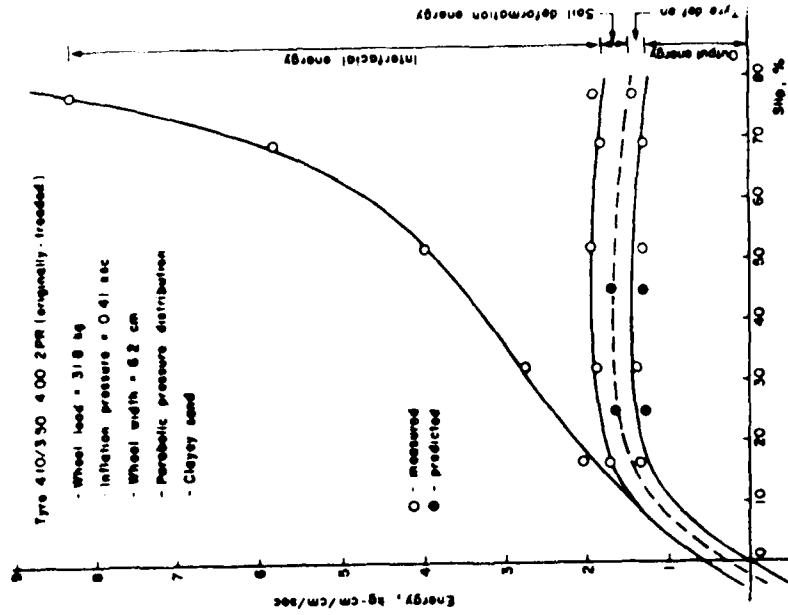


Fig. 12 Energy balance - slip relationship

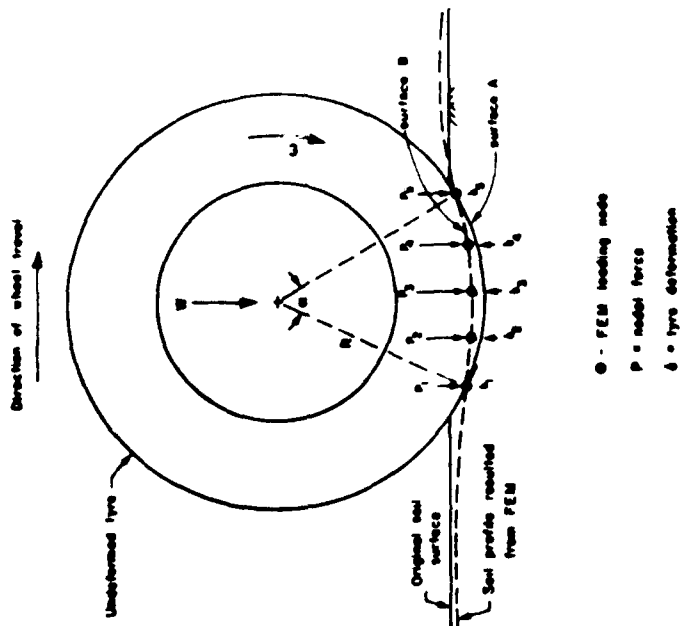


Fig. 11 Schematic diagram of tyre loading for determination of tyre deformation.

Note that FEM = finite element method

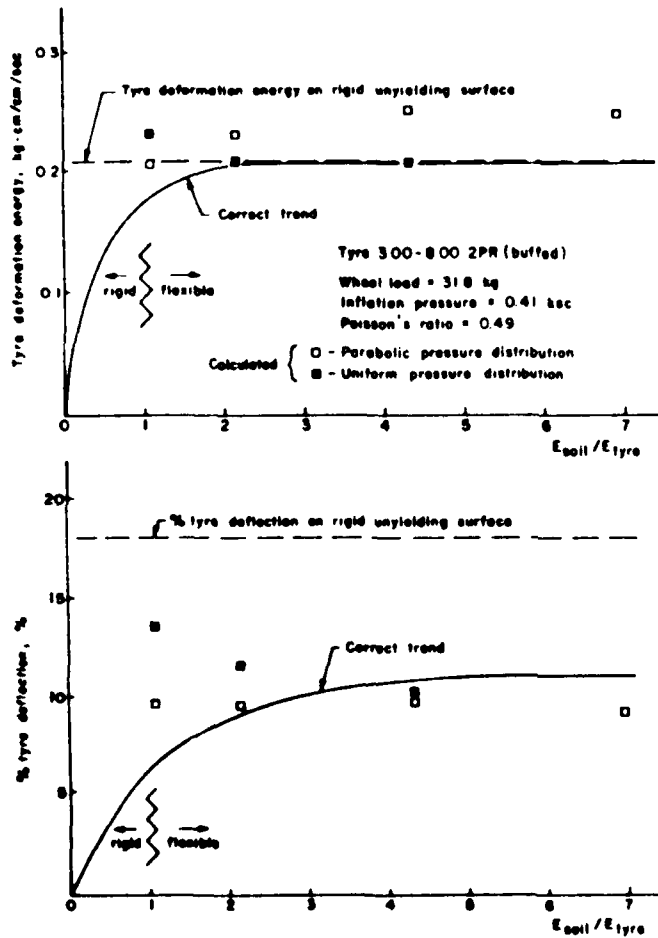


Fig. 13 Verification of pressure distribution pattern (inflation pressure 0.41 kg/cm²).
Note that when E_{soil}/E_{tyre} is less than one, the rigid wheel model should be used in the computations.

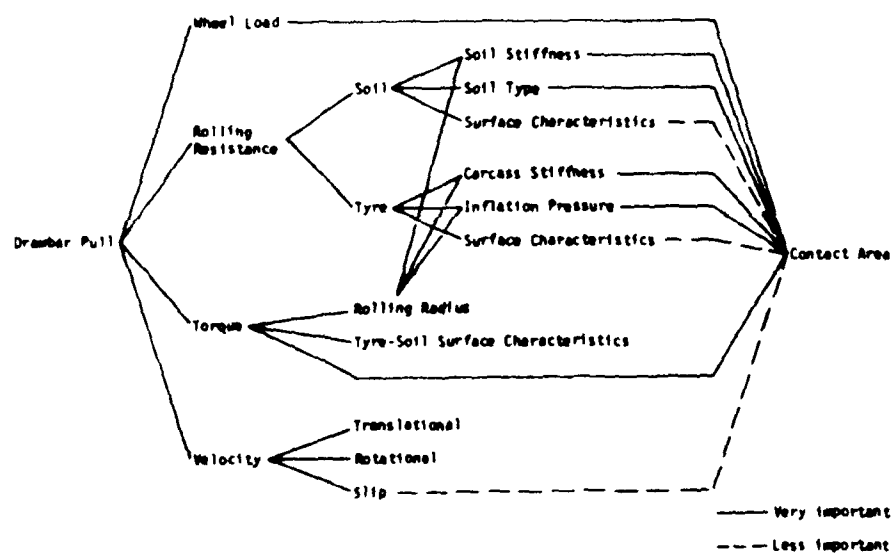


Fig. 14 Parameters affecting drawbar pull

THE ROLLING RESISTANCE AND SINKAGE OF TOWED DUAL WHEEL COMBINATIONS IN SAND

Lieut. BETHERINGTON and L. LITTLETON

ROYAL MILITARY COLLEGE OF SCIENCE, SHRIVENHAM, SWINDON, WILTS. SN6 8LA

INTRODUCTION

The ability to predict the performance of wheeled vehicles across country is of paramount importance in both the design of military vehicles and assessing their effectiveness within a specified theatre of operation. In a previous paper by the authors (1) a predictive formula was developed which effected the prediction of the rolling resistance and sinkage of towed wheels on sand. The advantage of the form of the equation was that, where other workers had employed the cone index gradient as a measure of sand strength for mobility studies, this prediction used only the soil bulk unit weight and the angle of friction of the soil. The predictive equation was shown to correlate well with experiments on a wide range of wheel geometries, loads and granular soils.

It has been shown, Rowland (2), that the typical peak pressures beneath an armoured, wheeled vehicle are generally very high, and certainly much higher than their tracked counterpart. In general it is assumed that high pressure equates to poor performance. This is certainly so on fine grained soils, where increased pressure produces no benefit in traction, but incurs the penalty of extra sinkage and rolling resistance. For this reason the draw-bar pull reduces and the mobility suffers. However, on coarse grained soils, increased pressure both increases traction and resistance, with the result that draw-bar pull can actually increase with increased vehicle weight. For vehicle designers attempting to improve mobility, it has commonly been a tempting solution to consider dualling the wheels on a particular axle. The effect of this action has proved difficult to understand and often disappointing in outcome. Melzer and Knight in their paper on this subject (3) quote examples of field tests on both agricultural and military vehicles in which the single wheeled version out-performed the dual wheeled on certain soil conditions.

Tests performed by Rouch, Liljedahl and Clark (4, 5) on a cohesive soil showed that, whilst dual-wheels consistently out-performed single wheels, the magnitude of the improvement decreased with soil strength. Melzer and Knight (3) performed a comprehensive series of tests on driven dual wheel combinations and presented their results within the system of mobility numerics developed by Freitag (6). They found that the draw bar pull mobilised with a dual wheel system, with zero separation between wheels, coincided with that which would be obtained from a single wheel of the same overall dimensions. The total draw bar pull from the pair of wheels decreased with increased separation and they confirmed the findings of references 4 and 5 that the benefit of dual wheels was greatest on weak soils. Gee Clough (7) has observed that the reduction in rolling resistance with separation found by Melzer and Knight, and confirmed himself experimentally, contradicted the prediction from mobility numeric analysis.

Whilst the work of Gee Clough examined wheel separation ratios (a/b Figure 1) in the range of 0 to 0.33, Melzer examined ratios of 0 and 1 to

AD-A148 634

PROCEEDINGS OF THE INTERNATIONAL CONFERENCE ON THE
PERFORMANCE OF OFF-ROAD (U) INTERNATIONAL SOCIETY FOR
TERRAIN-VEHICLE SYSTEMS M J DWYER AUG 84

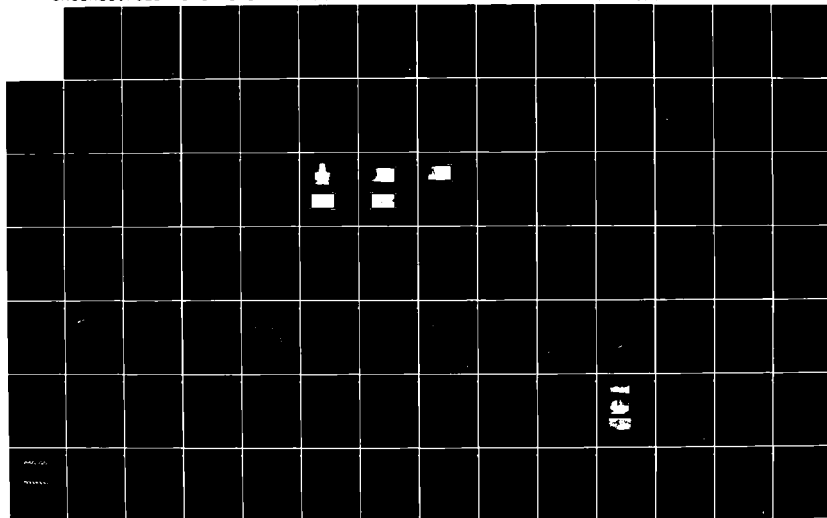
246

UNCLASSIFIED

DAJA45-84-M-0251

F/G 13/6

NL





1.0

2.8



2.5

3.15



2.2

3.5



2.0



1.1

4.0

4.5



1.8



1.25



1.4



1.6

where z_s is the sinkage of single wheel

and z_d is the sinkage of dual wheel system carrying the same load.

Thus these parameters are simply the percentage improvement derived from doubling up the wheels.

By considering a dual combination with zero spacing ($a/b = 0$) values of F_R and F_S can be obtained from equations (1):

$$\text{For } a/b = 0, F_R = \frac{\left(\frac{2W^4}{bd^2\gamma N_q}\right)^{1/3} - \left(\frac{2W^4}{2bd^2\gamma N_q}\right)^{1/3}}{\left(\frac{2W^4}{bd^2\gamma N_q}\right)^{1/3}} \times 100 = 20.6\%$$

$$\text{and } F_S = \frac{d\left(\frac{2W}{b\gamma N_q d^2}\right)^{2/3} - d\left(\frac{2W}{2b\gamma N_q d^2}\right)^{2/3}}{d\left(\frac{2W}{b\gamma N_q d^2}\right)^{2/3}} \times 100 = 37\%$$

For small separations, the soil will be unable to perceive the wheels as discrete and therefore the performance of a pair of wheels, each of width b , separated by an amount ' a ', can be represented by a single wheel of breadth $(2b+a)$. Thus

$$\begin{aligned} F_R &= \frac{\left(\frac{2W^4}{b\gamma N_q d^2}\right)^{1/3} - \left(\frac{2W^4}{(2b+a)\gamma N_q d^2}\right)^{1/3}}{\left(\frac{2W^4}{b\gamma N_q d^2}\right)^{1/3}} \times 100\% \\ &= 100 \left\{ 1 - \left(\frac{b}{2b+a}\right)^{1/3} \right\} = 100 \left\{ 1 - \left(\frac{1}{2}\right)^{1/3} (1 + a/2b)^{-1/3} \right\} \\ &= 100 \left\{ 1 - 0.794 \left(1 - \frac{a}{6b} + \dots\right) \right\} \\ &= 20.6\% + 13.2 a/b\% \end{aligned}$$

Similarly $F_S = 37\% + 21 a/b\%$.

These expressions predict that, for small values of a/b , the improvement derived from dualling will increase linearly with wheel separation.

EXPERIMENTAL WORK

A programme of tests was carried out on model scale, rigid wheels in single and dual configurations. The wheels were towed at a slow, constant speed on a uniform bed of dry Calne sand, the details of which are contained in reference 7. The wheels used were 0.047 m wide, with diameters of 0.25 m and 0.3 m, and 0.072 m wide with a diameter of 0.3 m. For each wheel combination, both axle load and wheel spacing were varied, and the rolling resistance and sinkage of the combination recorded. The results of the experimental tests are presented in Figures 2 and 3.

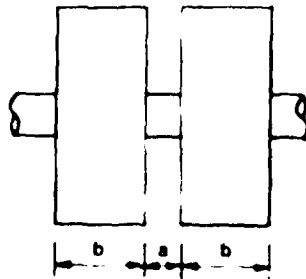


Figure 1

8. Thus the findings and anomalies could be attributable to the different ranges examined. Clearly there is a complex interaction between traction and rolling resistance in the case of driven wheels as investigated by Melzer and Knight. The aim of this work is to isolate the parameters of sinkage and rolling resistance by studying the towed case. By taking experimental results for a range of ratios between 0 and 5, and comparing these with the predictions from the formula of reference 1, this paper seeks to quantify and explain the reductions in sinkage and rolling resistance which accrue from dualling towed wheels.

THEORY

Reference (1) gives the following expressions for the rolling resistance and sinkage of a towed rigid wheel in sand:

$$\begin{aligned} R &= \left(\frac{2W^2}{bd^2\gamma N_q} \right)^{1/3} \\ z &= d \left(\frac{2W}{b\gamma N_q d^2} \right)^{2/3} \end{aligned} \quad (1)$$

where R is rolling resistance
 W is vertical axle load on wheel
 b is wheel breadth
 d is wheel diameter
 γ is soil bulk unit weight
 N_q is a Terzaghi bearing capacity factor

These expressions were shown to predict, within tolerable limits of accuracy, performance parameters for a wide range of wheels on several sands of widely differing properties. The advantages of these equations over other systems lies in their ease of use, and in their dependence only on soil bulk unit weight and angle of friction in defining soil properties. An informative method of describing the performance of dual wheel systems is to examine the benefit which accrues from replacing a single wheel with a double wheel unit. In this paper this benefit will be characterised by a "resistance improvement factor" (F_R) and a sinkage improvement factor (F_S) defined as follows:

$$F_R = \frac{R_s - R_d}{R_s} \cdot 100\%$$

where R_s is the resistance of single wheel
 and R_d is the resistance of dual wheel system carrying the same load

$$F_S = \frac{z_s - z_d}{z_s} \cdot 100\%$$

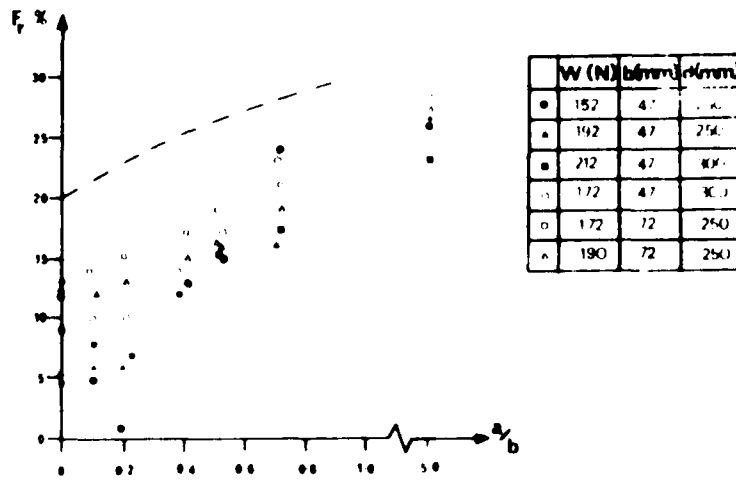


Figure 2

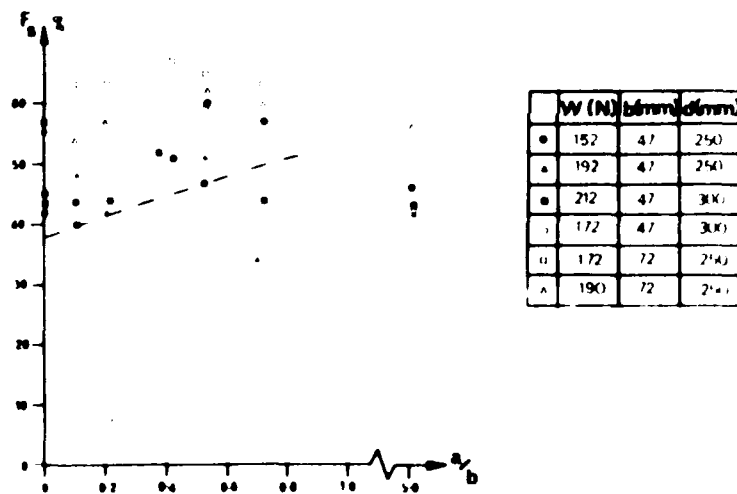


Figure 3

DISCUSSION

One advantage of assessing dual wheel performance by comparison with a single wheel carrying the same load is that the major source of error, which comes from soil property measurement, is eliminated. The only significant sources of error in this work were in the measurement of rolling resistance and sinkage. It is estimated that the determination of both sinkage and rolling resistance could be subject to errors of up to $\pm 10\%$.

Since both single and dual wheel measurements are subject to errors, their

Experiment will be subject to errors of up to 20%. The experimental results indicate the following characteristics of behaviour:

- 1) Replacing a single wheel with a dual wheel combination will reduce both sinkage and rolling resistance.
- 2) The improvement derived from dualling wheels increases with wheel spacing, until the wheels act as separate entities.
- 3) As a rule of thumb, the percentage improvement derived varies from 10 to 25% for resistance and about 50% for sinkage.

The dotted lines added to the figures represent the theoretical predictions. In the case of rolling resistance, the predicted benefit is considerably more than that actually observed, although the variation with separation is comparable. In the case of sinkage, both the levels of benefit derived and their dependence on a/b show some correlation.

It is interesting to observe that the presentation of Figures 2 and 3 apparently removes the distinction between different families of tests. Differences in axle load, wheel breadth and wheel diameter do not manifest themselves in data grouping when the results are analysed in this way. Thus both the sinkage and the rolling resistance improvement factors appear to be independent of mobility numeric. This is consistent with the findings of previous workers who observed that the magnitude of the benefit derived diminished with increased numeric value since, for towed wheels, both sinkage and resistance also diminish with increased numeric value.

Finally, it is worth making an observation on the case of driven dual wheel systems. In both sands and clays reductions will be observed in sinkage and rolling resistance through dualling wheels. The increased contact area will improve traction significantly in cohesive soils but not in frictional soils. It is probable therefore that there will be more to be gained from dualling wheels for applications on clays than there will be in sands. There is clearly a need for more information on the performance of driven dual wheel combinations on clay soils.

CONCLUSIONS

- 1) A programme of tests on towed, rigid wheels on sand has shown that replacing a single wheel with a dual wheel unit will reduce both sinkage and rolling resistance.
- 2) The improvement derived from dualling wheels increases with spacing, until the wheels act as separate entities.
- 3) As a rule of thumb, a 50% reduction in sinkage and between 10 and 25% reduction in rolling resistance derives from dualling wheels.
- 4) By modelling the dual wheel unit with a single wheel of the same external dimensions, some trends of behaviour can be predicted.

REFERENCES

1. Hetherington, J.G. and Littleton, I., "The Rolling Resistance of Towed Rigid Wheels in Sand", *Journal of Terramechanics*, Vol 15, No 2, 1978.
2. Rowland, D., "Tracked Vehicle Ground Pressure", Report No 72043. MVEE Chertsey, U.K., September 1972.

3. Melzer, K.-J., "Dual Wheel Performance in Sand", A.S.A.E. Paper No 71-132 presented at 1971 Annual Meeting of A.S.A.E., June 1971, Washington State University.
4. Rouch, K.E. and Liljedahl, J.B., "The Effect of Dual Tire Spacing on Tractive Performance in Soil", Paper presented at 1967 Annual Meeting of A.S.A.E., Saskatoon, Saskatchewan, Canada, June 1967.
5. Clark, S.J. and Liljedahl, J.B., "Model Studies of Single, Dual and Tandem Wheels", Transactions of the A.S.A.E. Vol 12, No 2, 1969.
6. Freitag, D.R., "A Dimensional Analysis of the Performance of Pneumatic Tires on Soft Soils", Technical Report No 3-688, Aug 1965, U.S. Army Engineer Waterways Experimental Station, Vicksburg, Mass.
7. Gee-Clough, D., "The Effect of Separation on the Rolling Resistance of Dual Rigid Wheels in Sand", Departmental Note DN T/935/01002 January 1979 (Internal report of NIAE, Silsoe, Beds, UK).
8. Littleton, I., "Some Observations on the Mechanical Properties of Frictional Soils used at RMCS". Technical Note MAT/14 RMCS, Shrivenham, Swindon, UK.

PERFORMANCE PREDICTION OF PNEUMATIC TYRES ON SAND

TES PAUL

V.R.D.E. AMBEDNAGAR, INDIA

ABSTRACT

In this paper the applicability of laboratory test results on the scaled models of pneumatic tyres in the dry sand test bins to predict mobility of vehicles in actual desert conditions in Western Rajasthan has been studied by a field test programme. The tests conducted at two test sites 150 km apart show that the mobility equations derived by laboratory tests could to a fair degree of accuracy predict the trafficability over sand in actual field conditions of varying soil strength.

For the purpose of vehicular mobility, soils are broadly classified as fine grained soils like clay and frictional soils like sand. The mode of generation of thrust as well as motion resistance is different in both these types of soils. Thrust is provided in case of the fine grained soils basically by cohesion between soil particles and weight of the vehicle contributes little to it. On the contrary in the case of frictional soils the thrust generated is a function of vehicle weight.

Off the road vehicular mobility is of paramount importance to military operations, mechanised farming, successful forest and other engineering operations of public utility. Efforts have been made by various researchers to co-relate the vehicle and soil parameters to predict the trafficability of vehicle in off the road condition, to determine the availability of draw bar pull under such condition and to draw purposeful conclusions in design of the running gears of an off the road vehicle. Most of the research has been confined to the areas of fine grained soils due to strategic and economic importance of such areas in the past, like North West Europe, South East Asia, Korea. Not much attention was paid to frictional soils and the areas where such soils exist have recently attained great military and economic importance e.g. West Asia, Western Rajasthan.

With a view to obtain more useful correlation between vehicle parameters and soil parameters in the frictional soils the present study of performance prediction of pneumatic Tyres on Sand was taken up.

SOIL - VEHICLE INTERACTION APPROACHES

Primary object of a soil - vehicle interaction approach is to determine the rolling resistance, bearing capacity and traction in terms of the vehicle and soil parameters. From these relationships, trafficability of a vehicle i.e. whether it would be able to cross a particular terrain or not could be predicted. A number of relationships correlating these, some theoretical and some empirical has been drawn up, over the years and these relationships predict results to a fair degree of accuracy (Approx $\pm 20\%$) in the case of fine grained soils. Similar relationships for frictional soils derived at the US Army Engineers Waterways Experimental Station^{1,2} are

Dimensionless Mobility Numeric

For wheeled vehicle for operation on freely drained dry sand (N_s)

$$N_s = \frac{G_s (b.d)^{3/2}}{W} \times \frac{\delta}{h} \quad (1)$$

Where G_s = Soil penetration resistance gradient MN/m³

b = Tyre width m

d = Outer diameter of a pneumatic tyre m

W = Weight of wheel MN

$\frac{\delta}{h}$ = Ratio of tyre deflection to section height, dependent upon tyre stiffness, inflation pressure and ground condition.

Most commonly used value - 15 to 17%

Vehicle Performance Parameters

$$\text{Specific Rolling resistance} \quad \frac{R}{W} = 0.025 + \frac{0.0385 N_s + 0.481}{N_s - 2.58} \quad (2)$$

$$\text{Specific drawbar pull} \quad \frac{D_{20}}{W} = \frac{0.521 N_s - 2.66}{N_s + 19.4} \quad (3)$$

Where R = Towed Rolling resistance of a wheel

D_{20} = Drawbar pull at 20% wheel slip

SOIL PENETRATION RESISTANCE GRADIENT (G)

This is an important soil parameter of frictional soils and is the average slope of the curve, cone penetration resistance Vs depth of penetration in sand. Mathematically

$$G = \frac{CI_z - CI_0}{z/2} \quad \text{MN/m}^3 \quad (4)$$

CI_z = Average Cone Index, 0-z depth - m

CI_0 = Cone Index at surface

z = Depth of penetration of the cone base

When a 30 degree right circular cone of 3.23 cm^2 base area is forced through the soil normal to the soil surface at a rate of 3 cm/s, soil penetration resistance is recorded as Cone Index (force/unit area)

FIELD TEST PROGRAMME

The mobility numeric described above has been derived from laboratory tests on scaled model of wheels under controlled conditions of environments and on soil test beds of uniform soil parameters. It is, therefore, necessary to ascertain the applicability of these relationships to actual ground conditions and on full size tyres. The field test programme was taken up as :

- (a) Trafficability test on a car size pneumatic tyre at Test Site I near the city of BARMER in South west Rajasthan.

- (1) Trafficability test on a heavy truck size pneumatic tyre at Test Site II near the city of JAISALMER in western Rajasthan. (Separated from Test Site I by over 150 kms distance).

The two test sites separated over 150 km apart and the two tyre sizes of wide range were selected for the tests to assess the universal applicability of the soil wheel interaction relationships at equations (1) to (3) in the desert conditions.

TRAFFICABILITY TESTS AT SITE I

An all wheel drive light vehicle with 9.00 x 13 tyres was selected as test vehicle as the load distribution on its four wheels was found to be fairly equal. Weight on each tyre was determined as 5.4 kN. The soil parameter 'G' was computed from the field measurement of Cone Index Values taken with Penetrometer Soil Hand Operated, commonly in use in UK. The field tests were carried out on 31 May 1981 and 01 June 1981 on sandy areas both on plain sandy patches and on sandy dunes. Sufficient soil parameter measurements to forecast the soil strength[†] were taken and are given at Table 1. Drawbar pull was calculated using equations (1) and (3) and from this the trafficability of the vehicle was predicted. The test vehicle was then moved over this site to ascertain its trafficability. The results are shown at the Table 1.

It can be seen from the values at the table that the model equations can be applied to field conditions and predict results to a reasonable accuracy.

TRAFFICABILITY TESTS AT SITE II

Soil parameter measurements on a sandy area termed as Test Site II about 150 km north of the first test site were taken on 23 and 24 June 1981.

The soil value measurements and computation of soil parameter are given at Table 2.

A six wheel drive heavy vehicle with each wheel sharing a weight of 21.6 kN, with tyres of 12.00 x 20 inflated to the required pressure was now taken up as test vehicle. Its performance on the test site was predicted using the mobility equations (1) and (3). Mobility test on the vehicle was carried out to confirm the predicted performance. The results of the test are shown at Table 3.

DISCUSSION ON THE TEST RESULTS

The predicted pneumatic tyre performance in the actual ground conditions appears to differ slightly than those obtained under laboratory conditions. The drawbar pull predicted by the equation (3), is less compared to what actually achieved on the ground. However, it is rare that one would come across a purely cohesive soil or a purely frictional soil under actual ground conditions. Also keeping in mind that the soil parameters vary from place to place and from time to time i.e. weather dependent, and the complexity of the process by which the soil generates thrust by interaction with wheels, which is dependent on vehicle speed, spacing of tyres etc., it can be concluded that the laboratory test results on models i.e. equations (1) to (4) can be applied to actual ground conditions and for interaction with full scale wheels on frictional soils with a reasonable accuracy.

REFERENCES

1. FREITAG DR Dimensionless Analysis of
Performance of Pneumatic
tyres on Sand. ASAE Vol II
No.5.
2. TURNAGE GW Performance of soils under
tyre loads. Report No.8.
Sep 1972. US Army Engineers
Waterways Experimental
Station.
3. Users Handbook for
Penetrometer, Soil Hand
operated 60285
MVEE(c) July 1968.
4. GARINER G M Forecasting Soil
Strength Measurements
from a random sample.
Journal of Terramechanics
Vol 10 No. 1, 1973.

TABLE - 1
SOIL PARAMETER MEASUREMENTS AT SITE I AND TRAFFICABILITY PREDICTION

Cone Index (psi) at depth in inches	G	Ns	Specific Drawbar pull	Ground slope	Predicted Trafficability	Mobility Test Result	Remarks
0 3 6 CIZ MN/m ³							
Test Site I (a)							
0 5 40 15		Tyre		Level	Availability	Vehicle	
0 10 60 23		Size		sand	of drawbar	crossed	
0 10 25 12		9.00 x		patch	pull indi-	with	
0 20 70 30		13			cates that	ease	
0 50 75 41		Wheel			vehicle		
0 10 50 20		Load			should		
0 20 60 27		5.4			cross		
0 25 80 35		kN					
0 45 90 45							
0 5 250 65*							* Data ignored
Average CIZ	26	2.39	5.74	0.01			
Test Site I (b)							
0 10 60 23		Tyre		15 to	Drawbar	Vehicle	
0 50 250 100*		Size		20	pull not	could not	
0 10 80 30		9.00 x		sand	enough to	climb upto	
0 10 75 28		13		dune	cross this	full	
0 5 70 25		Wheel			gradient.	length of	
0 10 90 33		Load				slope.	
		5.4 kN				Bogged	
Average CIZ	28	2.53	6.08	0.01		down.	* Data ignored

Cone Index (psi) at depth in inches			G	Ns	Specific Drawbar pull	Ground Slope	Predicted Stiffness	Mobility Test Result	Remarks
0	3	6	CIz	KN/m ³	$\frac{D_{50}}{N}$				
<u>Test Site I (c)</u>									
0	50	250	100	Tyre Size 9.00 x 13 Wheel Load 5.4 kN		8° to 15° sand dune	The available drawbar pull is enough to move on 11° sand gradient only.	Crossed the sand dune with initial momentum	
0	120	250	123						
0	60	160	73						
0	100	250	116						
0	50	180	76						
0	20	150	56						
Average CIz			91	6.23	19.76	0.19			

TABLE - 2
SOIL PARAMETER MEASUREMENTS AT TEST SITE II

Cone Index (psi) at depth (inches)			G	Ground Slope	Weather Conditions
0	3	6	9	140/m ³	
<u>Test Site II (a)</u>					
0	50	175	210 ⁺	109	Hot and dry (23 June 1981)
0	30	60	75 ⁺	41	
0	50	160	200 ⁺	102	
0	145	170	280 ⁺	149	
0	100	160	280 ⁺	135	
0	30	130	180 ⁺	85	+ Values by interpolation
0	25	75	90	47	
Average CIz			95	5.76	
<u>Test Site II (b)</u>					
0	20	80	130	58	Sagd dune of 12 th average slope Hot and Dry (24 June 1981)
0	20	90	100	52	
0	35	130	170	84	
0	15	80	170	66	
0	20	60	100	45	
0	20	70	90	45 [*]	* Data ignored
0	5	20	25	12.5 [*]	
Average CIz			58	3.52	

Cone Index (psi) at depth (inches)				CIz	G MN/m ³	Ground Slope	Weather Conditions
0	3	6	9				
<u>Test Site II (c)</u>							
0	10	80	120	52		Sand dune of 18° average slope	Hot and dry (24 June 1981)
0	35	80	105	55			
0	40	90	110	60			
Average CIz				56	3.38		

TABLE - 3

VEHICLE MOBILITY PREDICTION AND RESULTS OF MOBILITY
TESTS AT TEST SITE II

Test Site	Soil Parameter G	Mobility Numeric Ns	Ground Slope	Predicted Specific Drawbar pull $\frac{D2Q}{W}$	Predicted Trafficability	Mobility Test Results
II a	5.76	8.99	Level	.064	Vehicle would cross this sand patch	Crossed with ease
II b	3.52	5.49	12°	0	The vehicle can move on level sand patches but cannot cross gradient	Crossed with initial momentum. The length of gradient was only 9 m.
II c	3.38	5.27	18°	-.004	Drawbar pull -ve. the vehicle cannot cross this gradient.	Bogged down after running for 6.5 m

EFFECTS OF SLIP ON ENERGY DISTRIBUTION BETWEEN TYRE AND SOIL

D. M. RONAI

INSTITUTE FOR MECHANIZATION, NOVI SAD, YUGOSLAVIA

Introduction

Any calculation of the drawbar pull of a agricultural tractor moving over agricultural land requires a detailed study of power losses thereby occurring, which may, in principle, be defined as follows:

- losses depending on pneumatic tyres and
- losses in connection with the soil, including interface phenomena occurring between tyres and soil, i.e.

$$\Delta P = \Delta P_S + \Delta P_C \quad \dots (1)$$

wherein ΔP means the total power loss, ΔP_S power loss caused by compaction of the soil, the bulldozing and dragging effects, ΔP_C power losses caused mainly by hysteresis of pneumatic tyre on the hard surfaces.

Equation (1) makes it possible to conclude, that locomotion in a field has to include, besides of the power losses caused by deformation of the soil, the total power losses as occurring on hard surfaces, similar to when moving over concrete cement runway, at an unchanged regime of movement. This equation would simply mean that movement over a field has to overcome power losses as occurring when tyres move over a solid surfaces at an unchanged regime of movement. This assumption, however, is only approximately right, for it is known that the deformation of the tyres moving over solid ground is not the same as in soft soil [1], under the same regime of movement which circumstance influences the total power loss value at the soft soil surfaces.

Also, the phenomenon of slip, which occurs when there is a drawbar pull, and complex characteristics of the soil, including the soil thrust characteristics, make this assum, e.g. the value of above formula doubtful. It is only possible to notice, because of certain absolute amount of power loss which is unquestionable generated, that slip and other phenomena which existed under such conditions, effect power loss distribution between tyre and soil.

Equation (1) will be taken as a base for discussion and the power losses generated by tyres moving over a concrete cement surface, on one side, and on the soil bin, on the other, will be analysed separately as a first and relatively as a second for varied values of slip and tyres dynamic load.

Test conditions

For the purpose of this analysis tests with four different tyres, i.e. 16.1-4 6PR, 16.4R-4 6PR, 16.4-42 10PR and 16.4R-42 10 PR are performed. Tests were made on two types of ground surfaces:

- concrete cement surface and

- sandy loam soil surface of the following characteristics given on table 1.

Table 1: Some characteristics of sandy loam soil

PARTICLE SIZE DISTRIBUTION			ORGANIC MATER %	LOWER LIQU. LIMIT %	LOWER PLAST. LIMIT %	PLASTICITY INDEX	SPECIFIC GRAVITY gr/cm ³
SAND %	SILT %	CLAY %					
71,6	17,4	11,0	0	20,5	17,6	2,9	2,65

The tests were made at NTML, Auburn, Alabama with single wheel agricultural tester /2/. During tests the following motion parameters were continually registered: dynamic load, torque, transversal velocity, tyre revolution

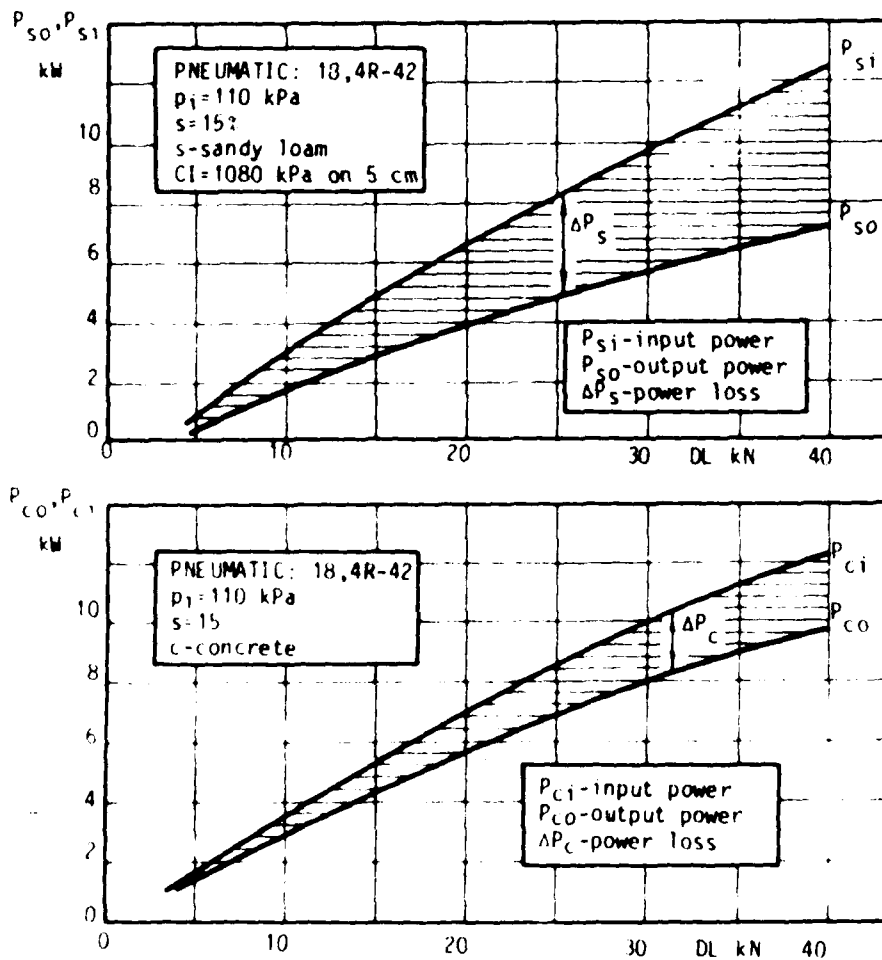


Figure 1. Relation between input and output power on concrete cement and sandy loam surfaces for the given tyre and motion conditions

inflation pressure and net traction. The following values were calculated from tests data: slip, input power, output power, pull ratio and tractive efficiency.

The inflation pressure during the tests was constant at 110 kPa for all of tested tyres, while the slip varied within 0 and 30% and dynamic load amounted continually from 0 to approximately 50 kN.

Soil moisture content was in average about 9% and soil bulk density after preliminary compaction 1.79 gr/cm³ in average. The average value of penetrometer reading on 5 cm depth was approximately 2315 kPa.

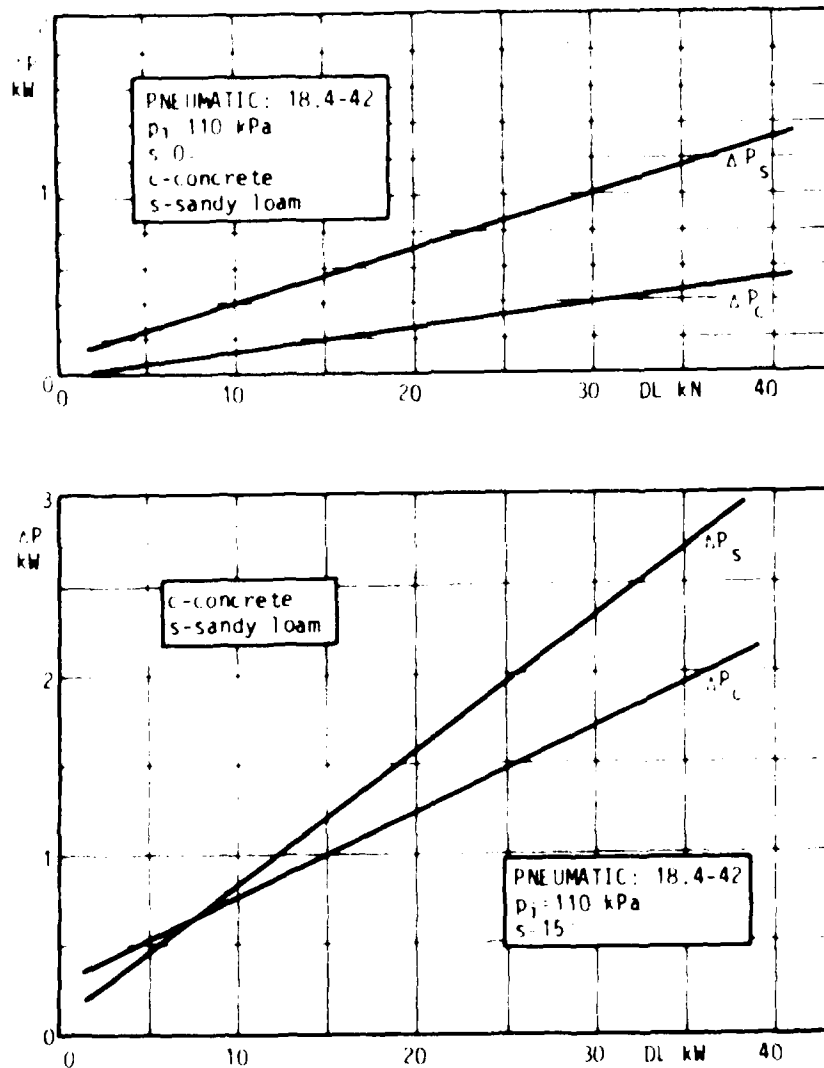


Figure 2. Total power loss as a function of dynamic load for given tests conditions

From these data it results that the soil in the soil bin was relatively dry and the preliminary compaction quite effective.

The testing itself was performed so that for a constant slip and tyre inflation pressure the dynamic load was continually increased within the limits stated above.

Results

The total loss of power occurring when pneumatic wheels run over the concrete cement runway as well as over the selected soil surface were calculated from the difference of the input power exerted on the tyre (P_{si}, P_{ci}) respectively, and the output efficient power (P_{so}, P_{co}), as it was shown in figure 1.

From diagrams shown in figure 1. can be seen that power losses for both tested surfaces (ΔP_s and ΔP_c) increase with increased dynamic load at constant slip value and inflation pressure in the tyre.

Figure 2. shows calculated values of total power losses for the movement of tyres on concrete cement and selected type of the soil with particular selected slip values, constant inflation pressure and varying dynamic load. It is characteristic that the lines showing power losses could be very efficiently analytically approximated by straight line equation of the type of:

$$\Delta P_{c,s} = a + bDL \quad \dots (2)$$

whereby the lowest coefficient of regresion (r) amounted to 0.929.

Similarly it can be found that losses of power increase with increased slip, as formerly found, and dynamic load. Besides, from figure 2. it is possible to conclude that a progressive trend of power losses on concrete cement surface increase at a higher rate relative to increase of power losses on soft soil surface with increased slip and constant dynamic load values. So, for instance, with a load of 20 kN and 110 kPa inflation pressure, an increase of slip from 0 to 15% the absolute level of losses on concrete cement surface increased approximately 5.46 fold, whilst when moving in the soil bin the loss of power increased 2.15 fold only.

This circumstance indicates the extraordinary influence of slip on power losses and leads to the conclusion that the study of losses on a solid ground as against the losses on soft ground could resulted in certain useful experiance.

From the diagrym in figure 3. and from other data established until now, it becomes clearly evident that power losses owing to slip increase in case of movement over hard surface at a higher rate than in case of movement in soft soil conditions. For example, the slope of power loss lines for concret cement runway increase approximately 3.4 fold at the increasin slip from 0 to 15%, whils, under the same regime of movement, the rise of slope of power loss lines for the sandy loam soil surface in the bin is approximately 2.4 fold, as it evident from fig.3.

That means that at a certain amount of slip power losses on hard surface could exceed the loss occurring in case of soft soil surface, at otherwise equal conditions. It could be possible to see some disagreement of this statement and statement which was given as an explanation of equation (1),

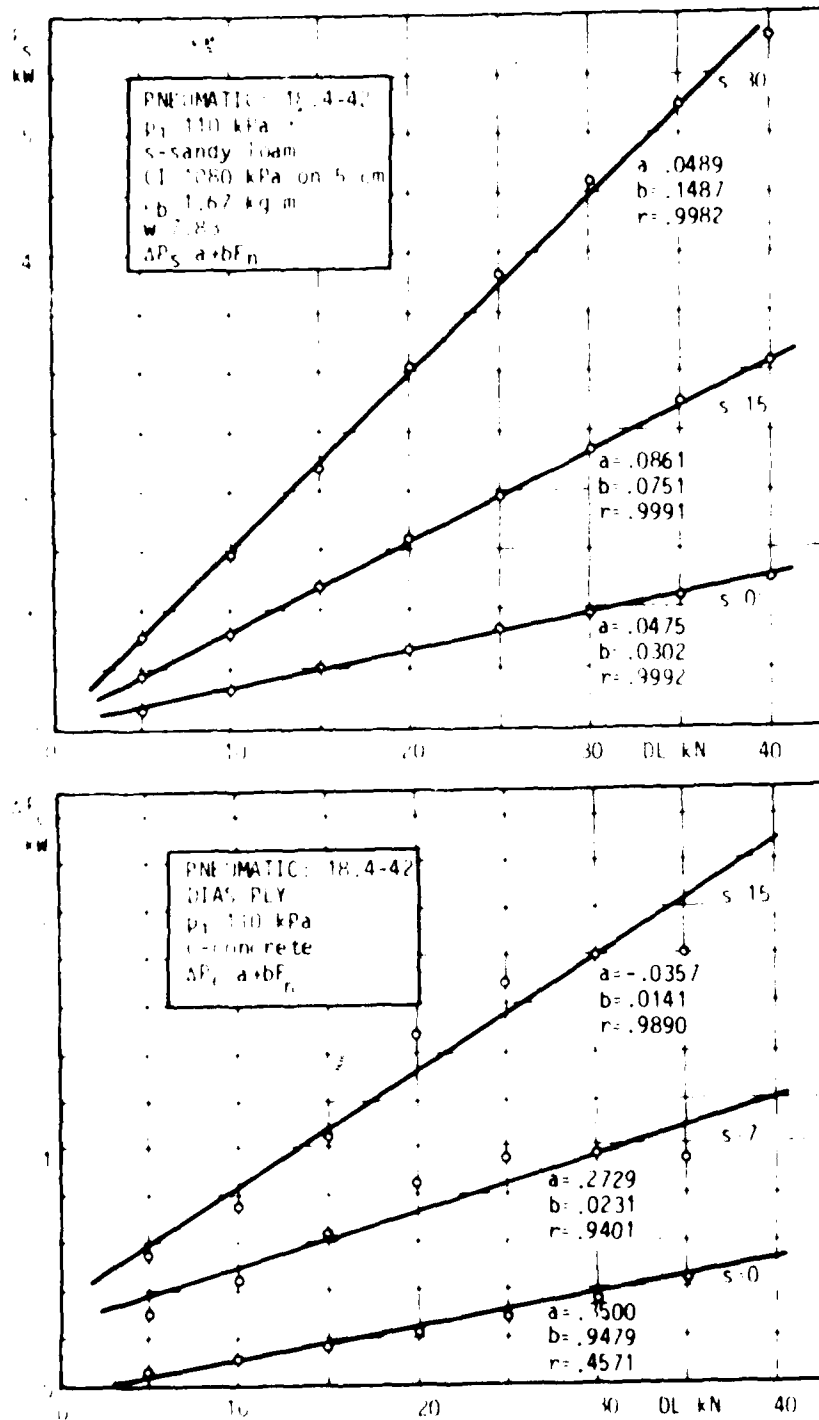


Figure 5. Parallel data of power losses with tyre moving over soil bin and over concrete cement runway, for two slip values

For as it was seen from measured data, the total amount of power loss on the soft soil surface has not to overcome total power loss on the hard surface for the same tyre, dynamic load, slip level and tyre inflation pressure.

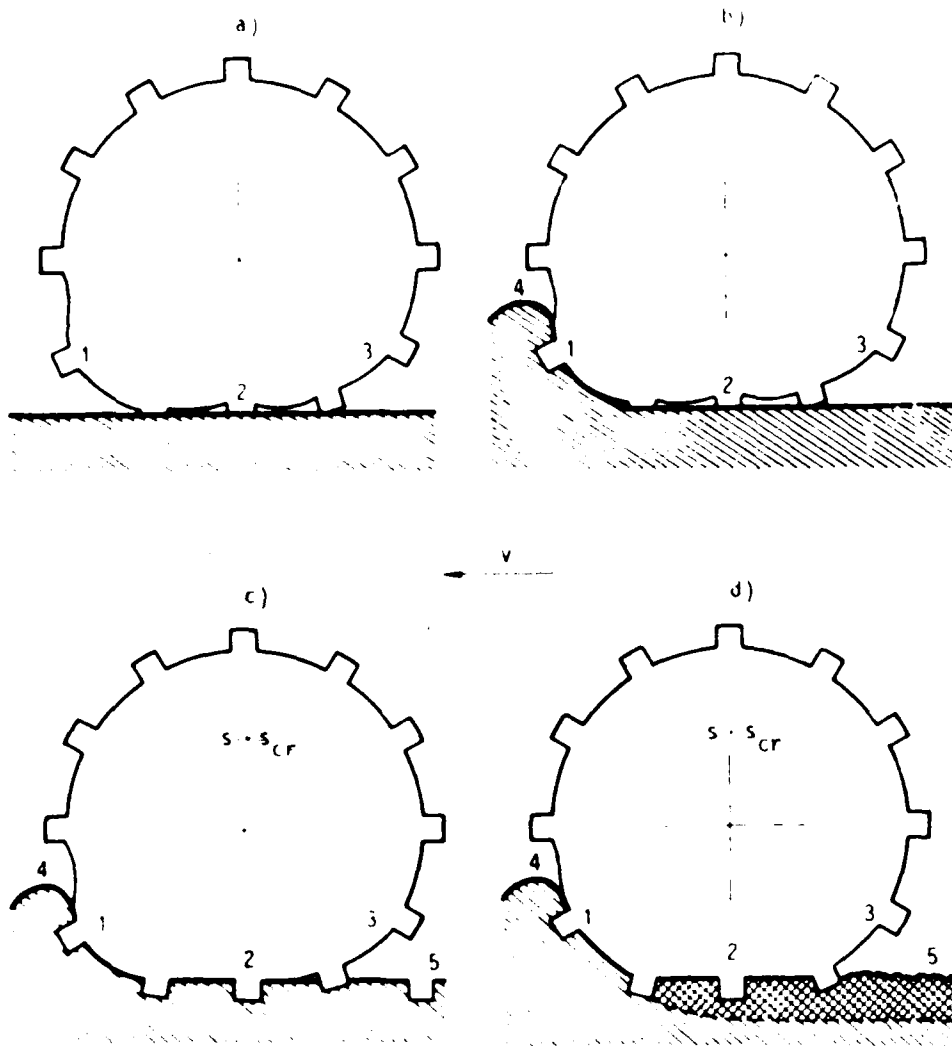


Figure 4. Schematic picture of idealised and real tyre deformations

Schematic picture of idealized statement in accordance with equation (1) is given in pictures 4a and 4b. Picture 4a shows the reason of power loss when moving over hard surface. In this case the tyre is subject to deformations by alternate pressure in front of (zone 1, and in the zone of direct contact with the ground (zone 2) and stretching behind of the zone of direct contact (zone 3). According to data contained in literature [3], and also to equation (1), the pneumatic wheel moving in the field first meets resistance of the soil and some energy is consumed in compacting the soil and when it has come to a quasi-equilibrium between active forces and the resistance of the soil, the tyre now gets deformed on the same

way as when moving on solid ground (picture 4b). The total energy consumed in the case of the picture 4a would be higher for the amount of energy spent for soil deformation in the case 4b.

Actually, however, the pneumatic tyres behave otherwise. First of all the intensity of tyre deformations in case of movement under the soft soil conditions are somewhat minor. 1. because there is not enough time for complete consolidation of the soil for such dynamic process as moving tyre is, 2. enough time for quasi equilibrium state between active and reactive forces in the soil. Besides, the deformation of tyre ribs is in most cases at a minimum, for the tyre ribs are generally much stiffer than the soil in the field, as shown in picture 4c.

Well, irrespective of this circumstances the total loss of power should be higher in soft soil and, actually it is so until the slip reaches a certain level (critical slip value s_{cr}). As is shown by figure 3, the difference between amount of energy consumed by the deformation of the tyre on hard surface and the total power consumption by deformation of the tyre and the soil on soft surface diminishes gradually, which trend is in favour of the fact that with increased slip deformations of pneumatic wheel on concrete cement runway are more evident, which leads to a permanent increase of power losses, whilst with the same conditions of movement, but this time in sandy loam soil bin, this increase of total power losses is essentially less.

Observed behavior of power losses makes the difference between hard-soft losses less and less with increased slip so, in one moment lines for power loss on concrete cement surface and natural soil surface should have point of intersection, as it was shown in picture 3. Slip level relative to point of equal losses could be called "critical slip value" for given conditions.

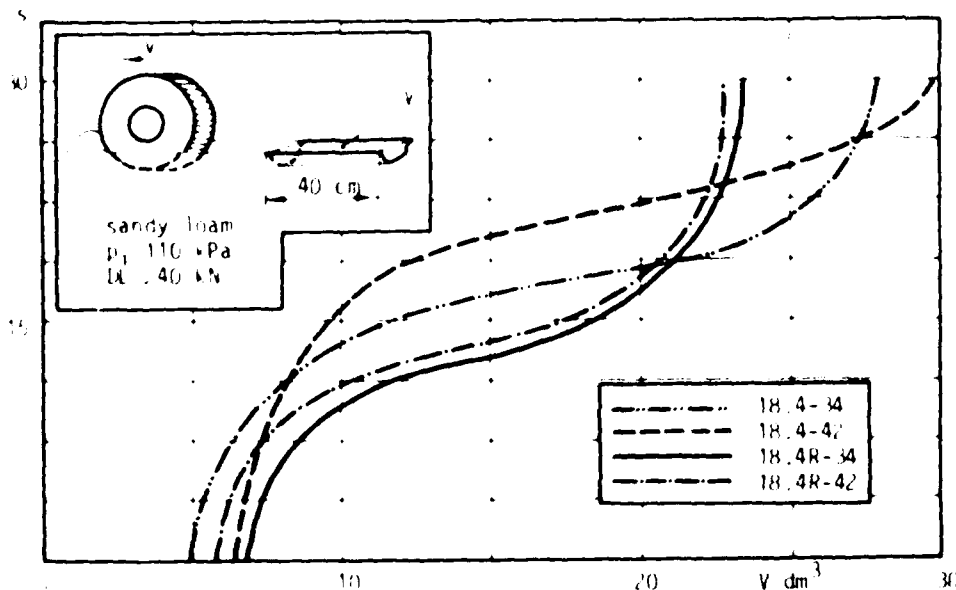


Figure 5. Volumetric relation between compressed and sheared particles of the soil on 40cm of track length with various tyre and slip values

since there is a deformation of the soil occurring in every case the explanation for diminishing loss of power on soil surface has to be accepted as a consequence of diminishing deformation of tyres. The reasons for diminishing of tyre deformations could be connected to:

- decreasing of dynamic load on,
- decreasing of soil resistance.

Since the dynamic load of pneumatics during the test is constant for certain parallel observation (hard-soft surfaces) and the level of slipping rises, therefore the general level of power losses does not diminish. There can not be the question that possible explanation could be found by complete analysis of tyre-soil system. The sole possible explanation is the occurrence of an intensive redistribution of power losses between pneumatic wheel and the soil. In such case occur the phenomenon of returning of certain amount of energy to the system, i.e. of that part of energy that has been accumulated by the deformed tyres.

This would mean that with the movement of tyres over the soft surface under the growing slip condition, the intensity of deformation of pneumatic tyres gradually decreases in zone 1 and 3 (figure 4), whilst the intensity of the soil deformation gradually increases.

The moment when a certain slip level is reached, which is mainly function of the dynamic load and mechanical characteristics of the soil, and of the observed pneumatic tyre and it comes to the maximum possible reduction of deformation of the tyre on the circumference and to maximum deformation of the soil. The hypothesis prevails that in that moment the level of active forces is equal to the value of the supporting capacity of the soil (soil thrust value), or, that it comes to the destruction of soil structure under the contact zone between the tyre and the soil.

A possible explanation may be obtained by the application of Coulomb's criterion of soil failure, or

$$H = Ac + DL \operatorname{tg} \phi \quad \dots (3)$$

wherein H is soil thrust value, A loaded contact area, c soil cohesion, DL dynamic load and ϕ angle of internal friction of the soil.

In case of movement under the zero slip conditions upper layer of the soil is destroyed and the tyre penetrates to a certain depth z as could be determined by equation

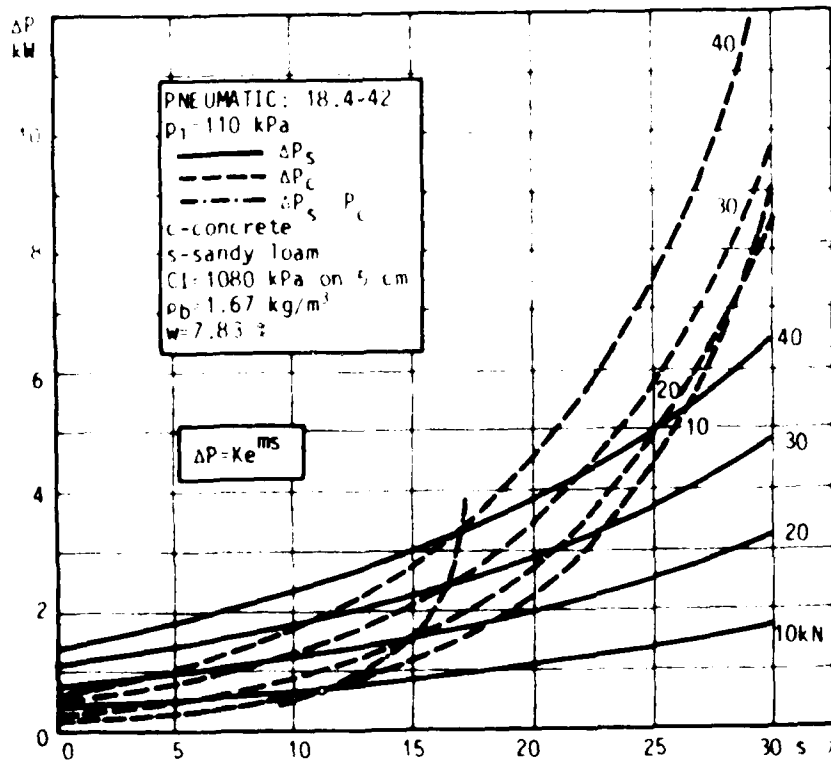
$$p = k z^n \quad \dots (4)$$

wherein k and n are parameters (mechanical) of the soil and p the active pressure on the soil.

In such event the horizontal load on the soil is at the minimum, as there is no pull and, except compacting, there is no deformations of the soil. With increasing slip, and the appearance and increase of pull it comes to a horizontal loading of the soil. Knowing the characteristics of the distribution of the pressure in the soil, i.e. their variability (directly under the tyre rib the intensity of pressure is much higher) it results that the microdistribution of horizontal stresses in the soil varied from point to point and that is presumed that local overload occurs. It follows that in the overloaded zones of the contact local destruction of the soil occurs and, in connection with a reduction of the total cohesion in the soil that increases its deformation, in the same time forming a space

for restoring pneumatic wheel of deformation.

With additional increase of slip and the force of pull a further increase in horizontal stresses of the soil occurs until the total destruction of cohesive ties between soil particles. The certain volume of the soil slides in that moment in known epicycloid surfaces and a further increase



F_n kN	ΔP_s kW		ΔP_c kW	
	K	m	K	m
10	0.3762	0.0491	0.1347	0.1394
20	0.7001	0.0510	0.2828	0.1132
30	1.0242	0.0516	0.4264	0.1039
40	1.3470	0.0520	0.5685	0.0990

Figure 6. Relation between power loss as a function of slip with variable values of dynamic load for the movement of the tyre on concrete cement runway and in the sandy loam soil bin.

of the drawbar pull is generated by the characteristics of internal friction of the soil. In that moment an essential reduction of deformations in the tyre occurs in the zones in front of and behind of the soil-tyre contact area (zones 1 and 3, picture 4d) and the reduction of level of energy losses on the tyre itself, on the account of the energy increase spent for deformation of the soil. Some amount of energy which was

accumulated on deformed tyre would be taken back to the system at that moment, making process of excessive soil deformation more successful. Thereby it comes to a rapid increase of the squeezed volume of soil particle in the zone of the track (zone 5, picture 4d).

A look at the picture 5, indicates a quick rise of the sheared (squeezed) volume of the soil in the zone between 10 and 20% of slip, i.e. around critical slip values for all of investigated tyres. This statement could be used as a prove for given hypothesis.

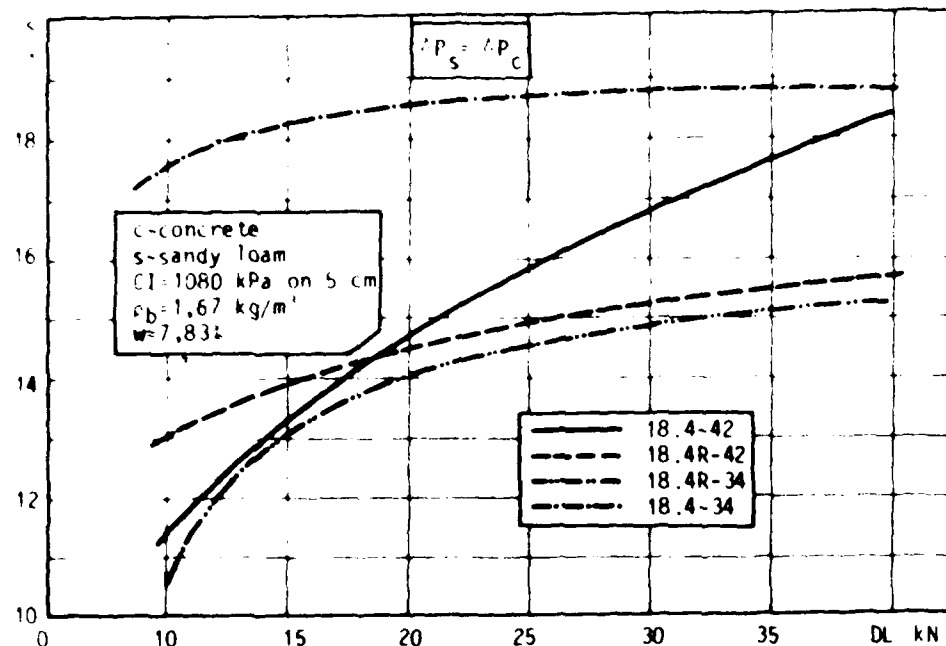


Figure 7. Lines of critical slip as a function of dynamic load for all of tested tyres

Curves of power loss as a function of slip with constant dynamic load and inflation pressure, with high correlativity be represented by an exponential function, i.e.

$$\Delta P = k e^{ms} \quad \dots(5)$$

wherein k and m are analitical factors.

By utilizing formula (5) the extrapolation of curves was done and the result whereof are given in figure 6.

As an interesting feature it can be pointed out that for all other examined tyres, the curves obtained were practically identical.

From figure 6, the characteristical cross reference points can be noticed where the power losses occuring in movement of a hard surface are identical with losses occuring with movement on a soft surface, assuming an unchanged regime of movement, in conformance with hypothesis given, points when the cohesion characteristics of the soil are coming to be destroyed.

From Figure 2 it can also be noticed that the value of critical slip increases with increasing of dynamic load, what is more clearly visible from Figure 3. This could be expected to happen, for with the increase of dynamic load soil compaction is getting increased, which on its side increases the bearing capacity of the soil, which again requires an increased load for further destruction.

If now the curves covering the points with computed critical slip values for all examined tyres will be drawn, as shown in Figure 7, it could be noticed that for examined dynamic load and tyres inflation pressure the values of critical slip are between 12 and 19, i.e. that for examined conditions of movement the destruction of soil structure characteristics of the soil is reached at reported values of slip.

Values of utilization of soil strength show that an optimum pull is reached at 12-19% of slip, which very indicatively is in conformance with results obtained by such typical comparisons of the relative distribution of power losses occurring on agricultural lands, namely, that with critical slip the destruction of the soil structure occurs, that means directly decreasing of soil strength, before the maximum utilization of the bearing capacity of the soil is reached. It is clear that under such circumstances the peak efficiency or maximum degree of pull utilization is reached.

Conclusion

The analysis of the results of experiments unquestionably prove that the loss of energy on deformation of pneumatic tyre with movement on soft soil surface in principle are lower than losses occurring in movement of tyres over a hard surface, at equal conditions of movement.

With an increase of slip the losses get reduced on account of increased losses on the destruction of soil structure and compaction, so that when the critical bearing capacity of the soil is reached with the critical slip even partial disburdening of the tyre structure happens, and deformation diminish.

The value of the critical slip laying between 12 and 19 for all of tested tyres and variable conditions of movement, represent in principle, optimum slip values, when the optimum degree of pull utilization occurs. This means a possibility of useful application of presented methodology in this domain.

Literature

1. S.J. Knight A.J.Green Deflection of Moving Tire on Firm to Soft Surfaces, Transaction of the ASAE 1962.
2. E.C.Burt A Machine for testing tractor tires in soil bins, NTML, Auburn, Alabama.
3. M.G.Bekker Introduction to terrain vehicle system. The University of Michigan Press, Ann Arbor, 1969.
4. E.C.Burt C.A. Bailey M.R. Patterson R.J. Taylor Combined effect of dynamic load and travel reduction on tire performance Transaction of the ASAE, vol 22, 1979.

TRACTION FORCES OF DRIVE TYRE ON THE COMPACTED SOIL

J. SWIECH

IBMER, WARSAW, POLAND

INTRODUCTION

Kind of soil and its condition exerts an important influence on the size of traction forces achieved by driving systems. The kind of soil determined by its mechanical composition may be assumed as unaltered even for a long period of time. The condition of soil determined by its physical and mechanical properties is dependant on the kind of cultivation, vegetation humidity and compaction. As a result the value of traction forces depends on the temporary condition of soil. In order to find out the value of traction forces as influenced by the compaction of soil traction tests of tractor drive tyre were effected at the institute for Buildings, Mechanization and Electrification in Agriculture in Warsaw. Tests dealt with in this report were made under humidity of soil and operation parameters of the tyre (vertical load and inflation pressure) kept fixed while changing the compaction of soil.

TEST PROCEDURE

Measurements were made under laboratory conditions in a soil bin filled with natural soil of the following mechanical composition:

- sand (1-0.1 mm) - 42 per cent
- silt (0.1-0.02 mm) - 36 per cent
- clay (<0.02 mm) - 22 per cent.

The humidity of soil during the testing was $m = 11 \pm 0.5$ per cent. Before measurement of traction the soil was tilled 0.25 m deep, levelled and stripped. In order to obtain various compaction of soil it was rolled with a smooth roller

$$d_w = 0.41 \text{ m}$$

$$G_w = 415 \text{ kg}$$

The measurements were made for 4 different conditions of soil

- 1 - tilled and levelled soil
- 2 - soil rolled 2 times
- 3 - soil rolled 4 times
- 4 - soil rolled 6 times.

Traction parameters of soil were established by way of compaction test [1] as represented in Table 1. Measurements

AD-P004 264

of drawbar pull force - F_p , torque - T and depth of tyre rut z_k were made for a tyre 14.9/13-28 8 PR AN-10 (lug angle $\alpha = 0.4$ rad). Fig. 1 by using a device Trak [2]. During the measurements a vertical load $W = 8.0$ kN inflation pressure $p_0 = 90.0$ kPa. Trace of tyre left in the soil prepared for testing each of the conditions is shown in Fig. 2-5.

RESULTS AND DISCUSSION

Results of measurements are displayed in Fig. 6-9 as diagrams of mean values F_p , T and z_k in the function of slip - s . Curves of mean values were plotted through the middle of dispersion field for measurement values on diagrams recorded with X-Y recorder. Fig. 6-9 show also curves of tractive efficiency η_t computed by way of the formula

$$\eta_t = \frac{F_p}{T} r_r (1 - s)$$

where r_r - rolling radius.

Under given test conditions the maximum positive slip of the tyre $s = 50$ per cent was achieved regardless of the soil compaction. The curves of drawbar pull force were increasing. The maximum force of drawbar pull achieved under compaction corresponding to rolling the soil 6 times amounted to $F_p = 5.93$ kN. Following measurements of tyre rut it was found that it depends on the level of compaction. As soon as after the second rolling the depth of tyre rut decreases by 0.045-0.05 m as compared to the soil not compacted. Further compacting of the soil (up to 4 and 6 times) brings about not so large decrease in the depth of tyre rut. Differences in depth after successive rollings are no higher than 0.01 m.

The difference in depth of tyre rut between the non compacted soil and the 6 times rolled one is depending on the slip 0.06-0.07 m. Rolling resistance forces computed by the author $F_p = 0$ have shown that value of the force on the not compacted soil was maximum $F_r = 1.44$ kN. With growing compaction the value of rolling resistance force was decreasing, after 6-th roll $F_r = 1.05$ kN that is by about 27 per cent lower than on the soil not compacted. With increasing compaction of soil there grows tractive efficiency to reach, at the slip $s = 15$ per cent, the maximum value regardless of the level of soil compaction. After 6 times of rolling the soil $\eta_{t \max} = 67.7$ per cent and is by about 15 per cent higher than on the soil not compacted.

In order to compare actual values of drawbar pull forces, tractive efficiency and depth of tyre rut there are put together in Table 2, results of measurements and compaction of the values for the slip $s = 10, 15$ and 20 per cent.

Following results available in the above table it is possible to establish that under maximum tractive efficiency corresponding to the slip $s = 15$ per cent, the difference between the value of drawbar pull force in the soil not compacted and that rolled 6 times amounts to about 18 per cent. The depth of tyre rut decreases with growing compaction of soil. In the soil rolled 6 times it is about 56 per cent lower than in the soil not compacted.

CONCLUSION

The research on the influence of soil compaction on the value of traction forces was made in an average silt soil having the humidity of 11 ± 0.5 per cent. Measurements were made in a tilled and levelled soil as well as one compacted with a roll 2, 4 and 6 times. There was measured value of traction forces achieved by a tyre 14.9/13-28 8 PR AN-10 Stomil under vertical loading $W = 8.0$ kN and inflation pressure $p_0 = 90.0$ kPa. The tests have shown that under given soil conditions and growing compaction of soil:

- drawbar pull force is increasing and under slip corresponding to maximum tractive efficiency in the soil rolled 6 times, it is about 18 per cent higher than on the soil not compacted,
- rolling resistance force for $F_p = 0$ is decreasing to fall in the soil rolled 6 times, by about 27 per cent as compared to the not compacted one,
- the depth of tyre rut decrease and in the soil rolled 6 times it is about 56 per cent ($z_k = 0.047$ m) smaller than in the soil not compacted.

KEY TO SYMBOLS

1)	d_w	- dimension of roller	m
2)	F_p	- drawbar pull	kN
3)	F_r	- rolling resistance	kN
4)	G_w	- weight of roller	kg
5)	k_m	- modulus of unitary deformation of soil	kG/cm ²
6)	m	- humidity	%
7)	n	- exponent of soil deformation	-
8)	p_0	- inflation pressure	kPa
9)	r_r	- rolling radius	m
10)	T	- torque	kNm
11)	W	- vertical load	kN
12)	x	- scale - forces exponent	-
13)	z_k	- deep of tyre rut	m

- 14) α - lug angle rad
 15) η_t - tractive efficiency %

REFERENCES

1. Sołtyński, A., Traction parameters of soil. Proceedings of International Conference. Perspectives of agricultural tractor development. Sept.17-22, 1973 Warszawa
2. Sołtyński, A., Świech, J., The dynamometric carriage for traction elements investigation. Proceedings of International Conference. Perspectives of agricultural tractor development. Sept.17-22, 1973 Warszawa

Table 1.

TRACTION PARAMETERS OF SOIL

Soil conditions	k_m kg/cm ²	x -	n -
Tilled and levelled	0.73	3.121	1.226
2 times rolled	2.671	2.526	0.817
4 times rolled	3.591	2.081	0.598
6 times rolled	3.796	2.193	0.61

RESULTS OF MEASUREMENTS AND CALCULATIONS

Test conditions	Drawbar pull P_p / kgf		Tractive efficiency η_t / %		Slip of top run s_{top} / %	
	slip s / %	10	15	20	25	30
Roller and levelled	2.01	3.25	3.77	4.2	4.6	4.9
3 times rolled	1.87	3.6	4.2	4.6	4.9	5.2
4 times rolled	1.8	3.6	4.2	4.6	4.9	5.2
5 times rolled	1.8	3.6	4.2	4.6	4.9	5.2



Fig. 1. Tyre 14.9/13-28 RIR AN-10 STOMIL



Fig. 2. Tyre trace - filled and levelled soil



Fig. 3. Tyre trace - soil rolled 2 times



Fig. 4. Tyre trace - soil rolled 4 times



Fig. 1. Tyre trace - soil rolled 6 times

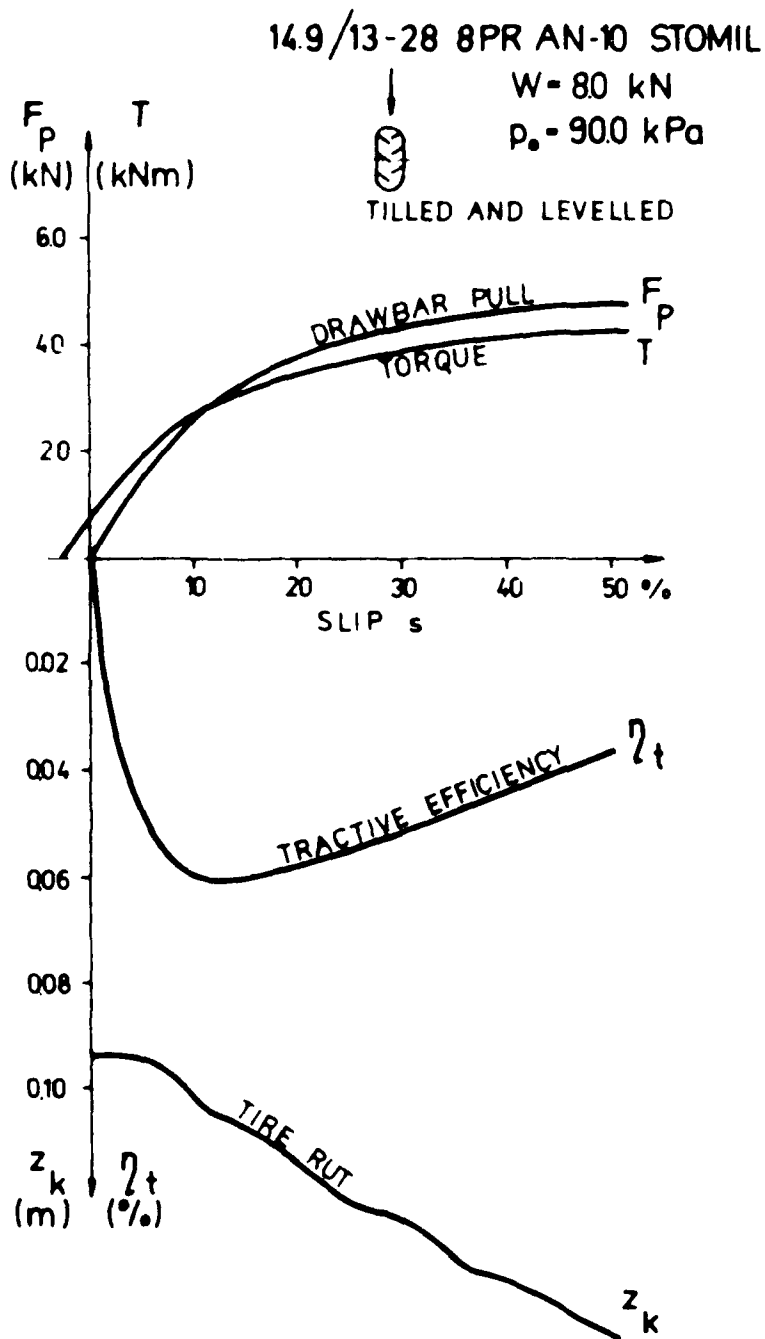


Fig.6 Drawbar pull - F_p , torque - T ,
Tire rut - z_k and tractive efficiency vs.
slip - s (mean values.)

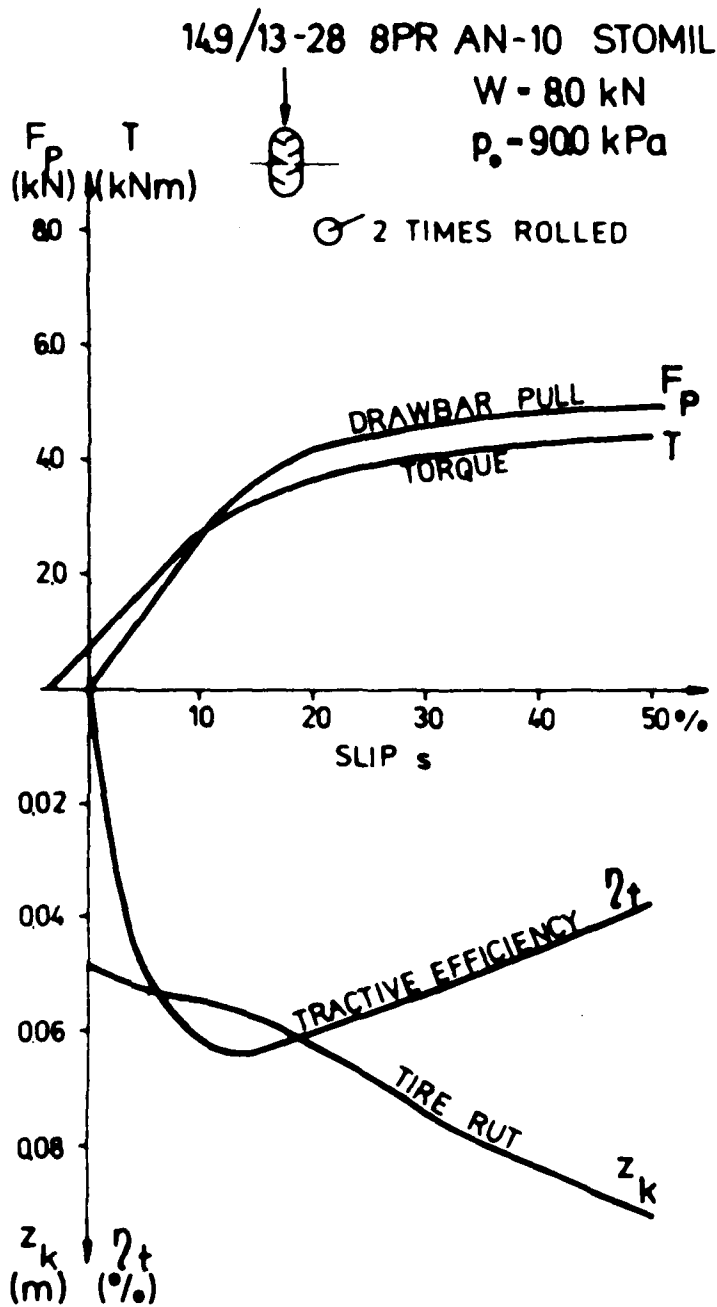


Fig. 7 Drawbar pull - F_p , torque - T , tire rut - z_k and tractive efficiency vs. slip - s (mean values.)

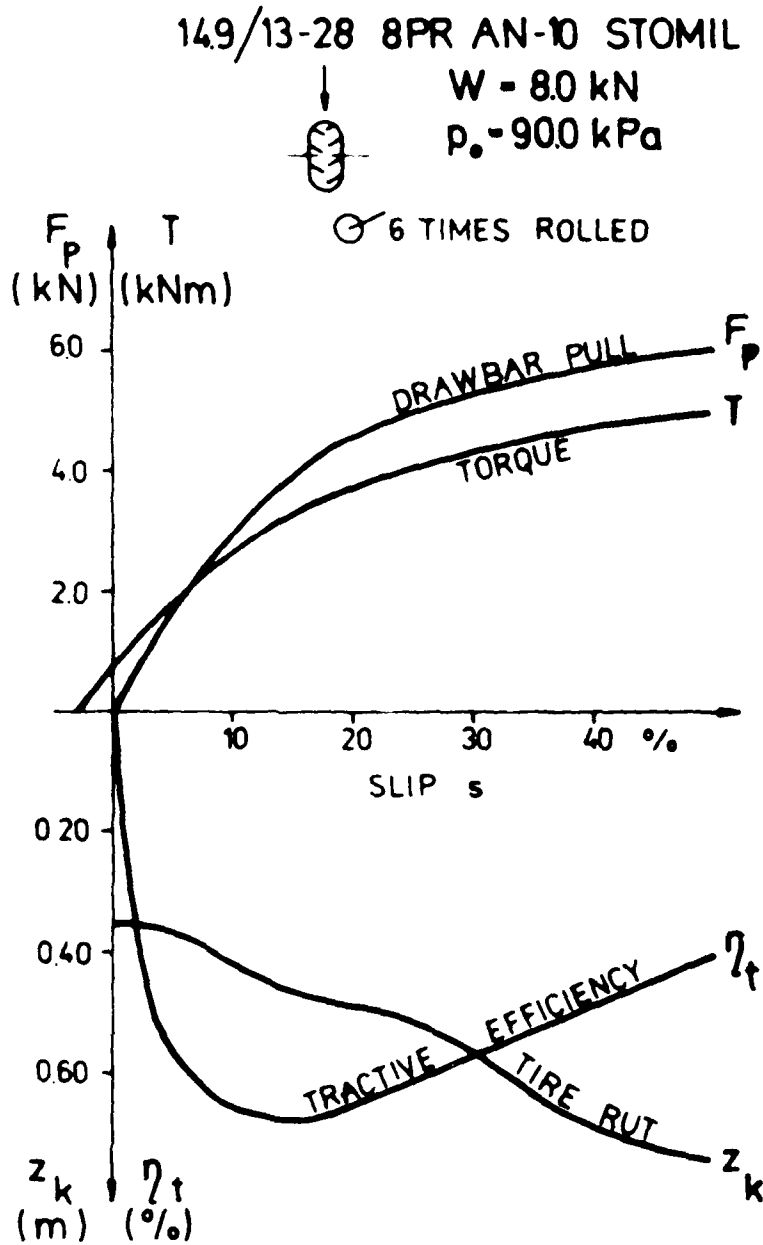


Fig.9 Drawbar pull - F_p , torque - T ,
tire rut - z_k and tractive efficiency vs.
slip - s (mean values.)

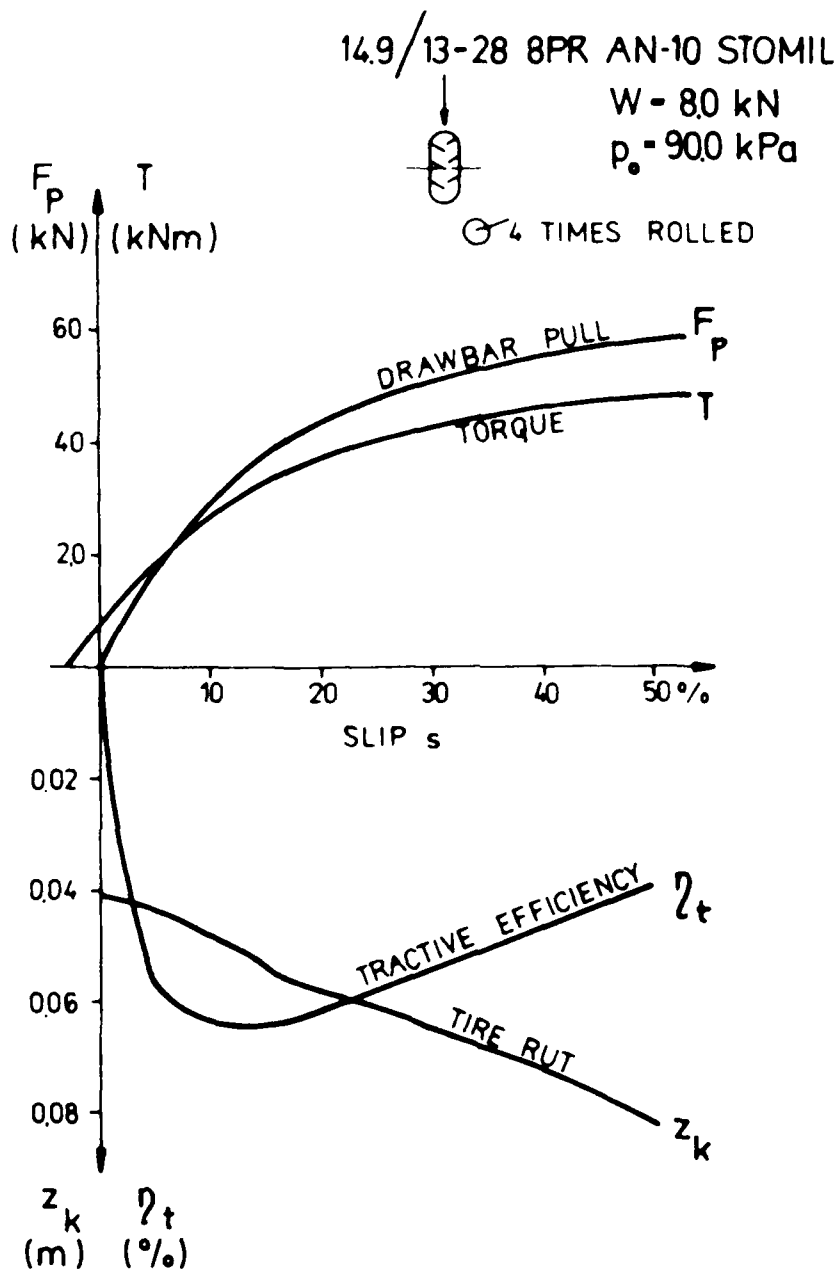


Fig.8 Drawbar pull - F_P , torque - T
 tire rut - z_k and tractive efficiency vs
 slip - s (mean values)

DEFINITION OF IN-SAND TIRE AND WHEELED VEHICLE DRAWBAR PERFORMANCE

WILLIAM L. REECE, Member, ISTVS

U. S. Army Engineer Waterways Experiment Station, Vicksburg, Mississippi

ABSTRACT

In an appendix of the ISTVS 6th International Conference Paper, "A Synopsis of Tire Design and Operational Considerations Aimed at Increasing In-Soil Tire Drawbar Performance," the author developed a procedure for defining G_p , effective sand penetration resistance (pascal). G_p was devised to approximate the value of G that predominated during a given tire pass, normalized to one type of frictional soil (selected as Yuma sand). G_p subsequently served as the soil strength term in sand-tire numeric N_{ge} , which aimed at providing a normalized description of tire drawbar performance in different types of sands. Because the range of sand types included in the development of G_p and N_{ge} was necessarily quite limited, the author suggested in the "Synopsis" paper that other investigators test the universality of relations involving N_{ge} and tire drawbar performance by using tire test results obtained in a variety of sands.

In their ISTVS 6th International Conference paper, "An Assessment of the Value of the Cone Penetrometer in Mobility Prediction," A. R. Reece and J. O. Peca applied the N_{ge} methodology for a quite different sand and obtained N_{ge} versus tire drawbar performance results that were not described well by those in the "Synopsis" paper. This prompted a reexamination by the author of information in the "Synopsis" paper, an analysis of data presented in Reece and Peca's "Assessment" paper, and a reanalysis of a sizeable body of U. S. Army Engineer Waterways Experiment Station (WES) field data on wheeled vehicle performance tests in a variety of sands (all supplemented by new laboratory sand test data). The primary result of this work is definition of a new N_{gey} methodology that accurately predicts tire and wheeled vehicle drawbar performance in a very broad range of sand types and conditions, including those of the "Assessment" paper.

AD-P004 265

INTRODUCTION

To obtain best wheeled vehicle performance in sandy soils requires implementation of a rational methodology for selecting the most appropriate tires and then using those tires to best advantage. In turn, such a methodology requires an ability to predict accurately in-sand tire and wheeled vehicle performance. Using laboratory and field test results, this paper describes a useful methodology for predicting the drawbar performance of tires and wheeled vehicles operating in a broad range of sand types and conditions.

BACKGROUND

Drawbar pull and drawbar efficiency were selected to describe in-sand tire performance herein because (a) the amount of pull a powered wheel can develop is often of major concern in vehicle in-sand operations, and (b) the efficiency with which a given amount of pull is developed determines the input energy required, a major concern in today's energy-conscious world.

It has proved useful to describe in-sand tire performance by relating dimensionless tire performance terms to a dimensionless sand-tire prediction term, or numeric. Tire drawbar performance is described herein by the following two terms:

$$\text{Drawbar coefficient } (\mu) = DP/W \quad (1)$$

where

DP = drawbar pull, the "force available for external work in a direction parallel to the horizontal surface over which the (tire) is moving"^{1*}

W = weight (load) on the tire

and

$$\text{Drawbar efficiency } (\eta) = \frac{DP \cdot v}{T \cdot \omega} \quad (2)$$

where

DP = drawbar pull

v = forward velocity of the wheel axle

T = torque input to the wheel

ω = rotation velocity of the torque input shaft

* Each raised number in the main text refers to a reference of the same number at the end of the text.

The sand-tire numeric N_s is defined as:

$$N_s = \frac{c(bd)^{3/2}}{W} \cdot \frac{\delta}{h} \quad (3)$$

where

- c = sand penetration resistance gradient (described in the next paragraph)
- b = unloaded tire section width
- d = unloaded tire outside diameter
- h = unloaded tire section height
- δ = tire deflection (the difference between unloaded tire section height h and loaded tire section height, with each height measured as the tire rests on a flat, level, unyielding surface)

c is the average slope of the curve of soil penetration resistance C versus cone penetration depth, with C and cone depth measured within a specified soil layer (ordinarily the 0- to 15-cm layer). C is the force per unit cone base area required to penetrate a soil normal to its surface at 3.0 cm/sec with a right circular 30-deg-apex-angle cone of 4.23-sq-cm base area. (The equivalent of C in English units is cone index, C.I.) Figure 1 shows sample recordings of C versus cone penetration depth for a laboratory-prepared sand test bed. Note that zero cone penetration depth is defined as occurring when the base of the 4.23-sq-cm cone is flush with the initial sand surface.

For simplification, drawbar performance is analyzed herein only at 20 percent slip--i.e., only γ_{20} and γ_{20} data are considered. Use of this nominal slip value is meaningful because, as illustrated in Figure 2 (taken from Reference 2), 20 percent slip provides a reasonable balance of good in-sand tire γ_{20} and γ_{20} performance (with somewhat greater weight given to γ_{20}) for a broad range of values of N_s .

EVOLUTION OF DRAWBAR PERFORMANCE PREDICTIONS

BY N_s AND N_{s2}

Early Development of N_s

N_s was first defined by Freitag almost 20 years ago¹ by means of dimensional analysis of the results of laboratory dynamometer tests of single tires in air-dry Yuma sand (a desert sand taken from active dunes near Yuma, Arizona). Using data from Reference 4 for 10 tires tested in this sand, Figure 3 illustrates that N_s effectively consolidates γ_{20} test data to one well-defined relation (Figure 3a) and γ_{20} data to another (Figure 3b) for very broad ranges of values of c , b , d , W , and δ/h . Thus, Figure 3 strongly supports the conclusion that N_s describes in-sand tire γ_{20} and γ_{20} performance quite well--at least for air-dry Yuma sand.

In Reference 4, the relation of drawbar pull data to N_s was also examined for tests "conducted on coarse-grained soils in various parts of the world with a variety of military vehicles." In these field tests, sand "usually was moist or even wet; drawbar-pull tests usually were not run at a controlled slip but were made at several levels of pull with only the data relevant to the maximum pull recorded for each test; and no

special provisions were made to control differential wheel slip, dynamic weight transfer, or steering forces." Figure 4 illustrates, as would be expected, (a) that the μ_{20} versus N_s relation defined by these field test data shows much smaller values of μ_{20} at corresponding values of N_s than does the single-tire laboratory relation of Figure 3a, and (b) that the field relation exhibits substantially more data scatter than does the laboratory relation.* (Data from tests at sand moisture contents only up to about 7 percent are shown in Figure 4.) The field relation in Figure 4 was considered sufficiently well defined, however, to "offer the basis for a tentative performance prediction system . . . for vehicles operating in dry-to-moist sands."

For a number of years this "tentative performance prediction system" was accepted as workable, although it was recognized that the system had potential for further refinement. Such refinements were made piecemeal and in an evolutionary manner, primarily because of the lack of data for defining in detail a range of physical properties of the sands for which tire and wheeled vehicle drawbar performance data were available. Events of the past few years have caused a renewed interest, however, in refining and improving the drawbar performance versus sand-tire numeric methodology for wheeled vehicles. The remainder of this paper describes development of such a methodology, first taking into account some insights gained in earlier studies of the influence of sand type on single-tire drawbar performance.

First Considerations of Two Sand Types

In addition to single-tire tests in air-dry Yuma sand, WES also conducted a smaller, but significant, number of laboratory tests in air-dry mortar sand (a coarser-grained riverbed sand). Figure 5a uses data from tests of five tires in mortar sand, together with the μ_{20} versus N_s curve from Figure 3a for Yuma sand, to demonstrate that these tires developed consistently smaller values of μ_{20} in mortar than in Yuma sand at corresponding values of N_s .

In 1972, Reference 5 attempted to account for this difference by using the relations of G to relative density (D_r) for the two sands, defined from Reference 6. For air-dry mortar sand:

$$D_r = 75.0 \log G + 39.3 \quad (4)$$

and for air-dry Yuma sand:

$$D_r = 71.1 \log G + 51.6 \quad (5)$$

where

$$D_r = \frac{e_{\max} - e}{e_{\max} - e_{\min}} \cdot 100, \text{ percent} \quad (6)$$

* For simplicity, all drawbar coefficient data considered herein are designated μ_{20} data, although μ in the wheeled vehicle field tests was sampled at the near-maximum-pull level, not necessarily 20 percent slip. Also, for brevity, tire drawbar performance in several subsequent figures is defined only in terms of μ_{20} . Performance is described in terms of both μ_{20} and μ in appropriate concluding figures.

e_{\max} and e_{\min} are void ratios for the loosest and densest sand states, respectively, and e is void ratio for the before-tire-pass sand condition. A given value of mortar sand G (G_M in Figure 5) was converted to Yuma sand G (G_Y) by first determining the mortar sand D_r value in Equation 4 and then using that same D_r value to solve for Yuma sand G in Equation 5. This use of D_r as the intermediate soil parameter in translating G values between different sands appeared to produce the desired result, as evidenced in Figure 5b by the shift of the mortar sand tire test data to locations clustered about the μ_{20} versus N'_g curve for Yuma sand. Reference 5 recognized, however, that use of D_r as described above must be considered tentative, and recommended "that tests be conducted in several additional sands so that the relative density approach . . . can be further verified."

In 1976, Reference 7 reported drawbar performance results from a later series of tests in air-dry mortar sand, these conducted with four 9.00R20 radial ply tires (each different in terms of tread design and other construction features), plus two 9.00-20 bias-ply tires (one with nondirectional cross-country tread, the other with tread buffed smooth). Tests for each tire were conducted over a range of wheel loads and tire deflections, and at two levels of G , approximately 2.2 and 5.5 MPa/m. For tire deflections of 15 and 35 percent, Figure 6a shows that the relation of μ_{20} to N'_g separated as a function of G . Further, Figure 6b shows that the relation of μ_{20} to $(N'_g)_Y$ for these test data also separated by G_Y (where G_Y values in $(N'_g)_Y$ were obtained by Equations 4 and 5 and the process described in the previous paragraph). In attempting to account for this separation, Reference 7 noted that "Ideally, the G value to use in describing tire performance for a given (tire) pass is the value that predominated during that pass. For first pass, this value lies between the 0- and 1-pass values"--i.e., between the before- and after-first-pass values. Examination of mortar sand tire test data showed "that G changes with tire traffic in a funnel-shaped pattern" like that shown in Figure 6c, and "indicated that the best G value for describing first-pass, 20-percent-slip tire performance is G at "pass number" 0.75 (hereafter termed $G_{0.75}$). That is, G should be weighted 3:1 toward its after-first-pass value." Figure 6d shows the well-defined

relation obtained for μ_{20} versus N'_g , where $N'_g = \frac{G_{0.75}(bd)^{3/2}}{W} \cdot \frac{\delta}{h}$. While the μ_{20} versus N'_g relation collapsed the mortar sand test data for the six 9.00x20 tires quite well, the central curve in Figure 6d is notably different from the one in Figure 3a for Yuma sand. The thrust of the analysis in Reference 7 was not directed at accounting for the influence of sand type on tire drawbar performance. However, Reference 7 recognized that "Clearly, more work is needed to develop techniques for describing sand soil strength that changes significantly with tire traffic."

A First-Cut, More General N'_g Methodology

In 1978, Reference 8 attempted to define a methodology to satisfy the two needs demonstrated in Figures 5 and 6--i.e., to define a means (a) for translating G values between different sand types, and (b) for describing the effective (predominant) during-tire-pass value of G . This methodology was applied by means of the nomogram shown in Figure 7.

The aim of the nomogram was to define G_e , "effective sand penetration gradient, the value of G that predominated during a given tire pass, normalized to one type of frictional soil (selected as Yuma sand)."

Use of the nomogram required known before-tire-pass values of G and of D_r (G_b and D_{rb} , respectively), and involved the following steps (identified by circled numbers in Figure 7):

Step 1: For the sand of interest (taken as mortar sand in Figure 7a), determine for G_b the corresponding value of D_{rb} .

Steps 2 and 3: For the tire b/d value of concern (0.29 in Figure 7b, for example), translate the D_{rb} value of step 1 from Figure 7a to 7b (shown as a dot in the example). In Figure 7b, use the family of curves that relate D_{rb} to D_{re} (effective relative density) as a function of tire b/d to estimate D_{re} .

Steps 4 and 5: Translate D_{re} of step 3 for the sand of interest to D_{re} for Yuma sand (step 4), and then to G_e for Yuma sand (step 5).

G_e from step 5 was then used as the soil strength term in

$$N_{se} = \frac{G_e (bd)^{3/2}}{W} \cdot \frac{1}{h}, \text{ and } N_{se} \text{ was related to tire drawbar performance}$$

terms $\mu_{20} \tan \phi_{70}$ and $\eta_{20} \tan \phi_{70}$. The rationale for using $\tan \phi_{70}$ (tangent of sand internal friction angle from a direct shear test at 70 percent relative density) as a multiplier of μ_{20} and η_{20} was that (a) D_{rb} tends toward a D_{re} value of about 70 percent for common tire shapes (b/d values from about 0.2 to 0.3), particularly with repeated transformations of D_{rb} to D_{re} to correspond to multiple tire passes, and (b) the products $\mu_{20} \tan \phi_{70}$ and $\eta_{20} \tan \phi_{70}$ appeared, in conjunction with N_{se} , to provide a normalized description of tire drawbar performance for the three frictional soils considered in Reference 8 (Yuma and mortar sands, plus a finely crushed basalt used as lunar soil simulant, LSS, described in Reference 9).

Figure 8 shows the relations (a) of μ_{20} to N_s and (b) of $\mu_{20} \tan \phi_{70}$ to N_{se} based on test results in Yuma sand for the same 10 tires as in Figure 3a, in mortar sand for the same 11 tires as in Figures 5 and 6, and in LSS for one tire-like wheel. (This wire-mesh wheel was evaluated for use on the lunar rover vehicle by testing the wheel in the rather exotic LSS. The two asterisks of Figure 7a define coordinates of D_r and G for the two LSS test conditions.) For the test data considered, the relation of $\mu_{20} \tan \phi_{70}$ to N_{se} in Figure 8b is considerably better defined than is that of μ_{20} to N_s in Figure 8a. While the Figure 8b relation appeared promising, Reference 8 "recognized that the range of frictional soil types considered . . . is limited; thus it is hoped that other investigators will test the universality of the $\mu_{20} \tan \phi_{70}$ and $\eta_{20} \tan \phi_{70}$ versus N_{se} relations using tire test results obtained in a variety of frictional soils."

In 1981, References 10 and 11 applied the methodology described in Figures 7 and 8 to drawbar performance data obtained with a 6.00-16, 2-PR treadless (smooth) tire in air-dry Cresswell sand. For this tire-sand combination, Figure 9 shows that the $\mu_{20} \tan \phi_{70}$ versus N_{se} relation obtained was very different from that obtained in Figure 8b. Clearly, the $\mu_{20} \tan \phi_{70}$ and $\eta_{20} \tan \phi_{70}$ versus N_{se} methodology was shown not to successfully treat all sand tire situations, and the need was established for analyzing a broad range of sand types and conditions in one study. A description of that analysis follows.

New Analysis Methodology for a Broad Range of Sand Types and Conditions

The Test Sands. Two major limitations in the WES analyses described to this point are that (a) only two ordinary test sands were considered (Yuma and mortar sand--the exotic LSS is hereafter not considered), and (b) these sands were each used only air-dry in single-tire testing. The new analysis considers 10 sands--the Yuma, mortar, and Cresswell sands, plus seven other sands for which vehicle field drawbar test data were available (six sands from References 4 and 12, one from Reference 10). A separate value of sand moisture content was reported in References 12 and 13 for each wheeled vehicle test; tests at moistures from 1 to 7 percent are considered herein.

A necessary first step in the analysis was to obtain samples of approximately 100 kg each for the 10 test sands. In this regard, particular thanks are extended to Dr. A. R. Reece for supplying the needed sample of Cresswell sand (the sand used in References 10 and 11), and to Dr. L. L. A. C. Grosjean, Etablissement Technique d'Angers, for supplying sand samples from beaches at La Turballe and at Suscinio, France (two of the test sites in References 4 and 12). Samples of the Yuma and mortar sands were obtained from large stockpiles at WES, and samples of the remaining five sands were obtained in re-visits to wheeled vehicle test sites in the United States.

A major concern in the new analysis was how closely the 10 sand samples matched the sands actually used in the tests of single tires or wheeled vehicles reported in References 4, 10, 11, 12, and 13. One means of evaluating this was to compare the original grain-size distribution curves shown in these references with the corresponding curves shown in Figure 10 for the sand samples that were used in 1983 WES soils laboratory testing. Results of this comparison are shown in Table 1 for grain-size diameters at the 10, 30, 50, 70, and 90 percent finer by weight levels. As expected, the original and the 1983 curves matched very closely for the Yuma and mortar sands (WES laboratory test sands). For Paw Paw Island sand, the original and 1983 curves are one and the same. For Cresswell sand, there is a noticeable difference between the original and 1983 curves.

The remaining six sands were tested in the field during 1958-1961, as reported in Reference 12 (1963). It was anticipated that the passage of some 20-25 years time, plus inability to locate precisely some of the original test sites, could cause substantial differences between the original and 1983 distribution curves, at least for some of the six Reference 12 sands. As it turned out, the original and the 1983 curves showed almost perfect agreement for the Padre Island site, very close agreement for the Mississippi River Bridge site, somewhat less agreement for the La Turballe and the two National Seashore Headquarters sites, and least agreement (by a considerable margin) for the Suscinio site. Implications of comparisons between the original and the 1983 sand grain diameters as described in Table 1 are discussed later in the analysis.

Relations Among C_r , D_r , and Sand Moisture Content. In analyzing data for the 10 sand samples, it was recognized, first, that D_r appeared not to be suitable for use as an intermediate soil parameter in translating between sand types. (Recall from Figures 6a and 6b that operation of D_{20} data for the Yuma and mortar sands was not alleviated

by the use of D_r in a translation role.) However, D_r did appear promising for use in a standardized description of the change in sand strength that occurs during a given tire pass. (Note that Figure 7b uses D_r in this role to describe the same process somewhat more crudely described in Figure 6c.) Further, D_r has the advantageous characteristics (a) of increasing in value as G increases, decreasing as G decreases, and (b) of taking values within the same range (0 to 100 percent) for all sands.

To develop the desired standardized description, the relation between G and D_r was determined for each of the 10 sand samples at sand moisture conditions at least from air-dry to 7 percent moisture. Additionally, measurements of G and D_r were obtained for the Yuma and Cresswell sands at a fully saturated condition and for Cresswell sand at 0.1 percent moisture content.

Figure 11 shows relations among G , D_r , and sand moisture content representative of those obtained for the 10 sand samples. For Yuma sand, this figure illustrates that the G versus D_r relation is described by

$$D_r = a_1 \log G + a_2 \quad (7)$$

where a_1 is a constant for a given sand, and a_2 changes value as a function of sand moisture content. Note in Figure 11 that a_2 decreases as sand moisture content increases from air-dry to about 7 percent (this same pattern was obtained for all the test sands), but a_2 increases markedly as moisture increases from about 7 percent to the fully saturated condition (this pattern was also obtained for Cresswell sand).

Figure 12 illustrates the relations (a) of a_2 to sand moisture content, and (b) of G (at $D_r = 70$ percent) to sand moisture content that were obtained for the Yuma and Cresswell sands. For each of the 10 sand samples, the pattern of change in a_2 with change in moisture from air-dry to 7 percent was similar to that shown by the dashed curves in Figure 12--i.e., for each sand, a_2 decreased semilogarithmically as moisture increased from air-dry to about 2 percent, and then continued to decrease, but at a fast-diminishing rate until a minimum a_2 value was obtained at about 7 percent moisture. For the Yuma and Cresswell sands, a_2 increased rapidly as sand moisture increased beyond about 7 percent.

The influence on G caused by this pattern of change in a_2 with sand moisture content is seen by rearranging Equation 7 to

$$G = \text{antilog} \frac{D_r - a_2}{a_1} \quad (8)$$

Thus, for each of the 10 sand samples (constant a_1) and any constant level of D_r , G attained a maximum value at minimum a_2 --i.e., at about 7 percent moisture content. Further, based on data for two of the test sands (Yuma and Cresswell), it appears that, for a given sand and constant D_r , G decreases rapidly as sand moisture content increases beyond about 7 percent.

Table 2 summarizes in columns 1-9 for each of the 10 sand samples the relation of D_r to G obtained in 1983 WES laboratory testing at sand moisture contents from air-dry to 7 percent. (Values in other columns of Table 2 will be discussed subsequently.) Note in column 2 that each listed value of air-dry sand moisture content was obtained

in the WES soils laboratory after a given sand sample remained undisturbed for at least seven days. These at-WES air-dry moisture contents do not necessarily correspond to air-dry moisture contents at other sites.

Prediction of During-Tire-Pass G_e . To predict G_e for the 10 test sands required implementation of both (a) the relations among G , D_r , and sand moisture content (summarized in columns 1-9 of Table 2), and (b) the relations among G_b , tire shape factor b/d , and G_e shown in Figure 13. A three-step process is involved:

- (1) Use Equation 8 to estimate D_{rb} (from known values of G_b , a_1 , and a_2).
- (2) Obtain D_{re} from Figure 13 (using D_{rb} from step 1 and known b/d).
- (3) Compute $G_e = \text{antilog } \frac{D_{re} - a_2}{a_1}^2$ (using the same values of a_1 and a_2 as in step 1).

Before applying the above process, it is useful to examine the relation in Figure 13. The shape of each curve in Figure 13a is the same as in Figure 7b for b/d values of about 0.2 and larger. For smaller b/d values, the curves in Figure 13a reflect recent analysis of single-tire drawbar test data in Yuma sand using the 1.75-26 bicycle and 4.00-20, 2-PR tires (b/d values of 0.068 and 0.150, respectively) not considered in Reference 8.*

In agreement with Reference 7 and with Figure 6c herein, D_{re} in Figure 13a reflects the condition obtained at tire pass number 0.75--i.e., first-pass D_{re} is considered weighted 3:1 toward the after-first-pass condition. For two powered-wheel tire passes, the appropriate D_{re} value is for tire pass 1.75; for three tire passes, 2.75; and for four tire passes, 3.75. The relation in Figure 13a was successively applied to obtain D_{re} values for tire pass multiples of 0.75; D_{re} values for tire passes 2, 3, and 4 were then obtained by interpolation as needed.

Detailed application of the D_{rb} , b/d , D_{re} relation for a given all-axes-powered wheeled vehicle would require that a separate value of G_e be determined for each axle, and that these G_e values then be averaged to determine G_e for the overall vehicle. Figures 13b, 13c, and 13d avoid this cumbersome process by reflecting averaged values of D_{re} for tire passes 1 and 2, passes 1 through 3, and passes 1 through 4, respectively. For a given 4x4, 6x6, or 8x8 vehicle, then, use of the

* In Reference 8, μ_{20} (and μ_{20}) values for all the tires considered reflected a mechanical/electrical correction to negate dynamometer carriage acceleration forces developed in the single-tire, programmed-increasing-slip tests. No such correction had been in use during tests of the 1.75-26 bicycle and 4.00-20, 2-PR tires reported in Reference 4. However, for a number of single tires tested over a broad range of N_s values, acceleration-corrected μ_{20} from Reference 4 has been determined to be smaller than uncorrected μ_{20} by a near-constant 0.045. For both the 1.75-26 and the 4.00-20 tires, the acceleration-corrected μ_{20} values used herein were obtained by subtracting 0.045 from μ_{20} values previously uncorrected for carriage acceleration.

single appropriate relation in Figure 13b, 13c, or 13d produces a single D_{re} value and a subsequent value of G_e very close to that obtained by treating each axle singly.

Use of G_e in N_{se} . The intended application of G_e , as defined by the three-step process described earlier, was to serve as the

soil strength term in sand-tire numeric $N_{se} = \frac{G_e (bd)^{3/2}}{W} \cdot \frac{\delta}{h}$, such that N_{se} would collapse both single-tire and wheeled-vehicle drawbar data for a broad range of sand conditions to a single relation for a given sand type. The success of G_e in this role is illustrated, first, in Figures 14a and 14b which show for 10 single tires and for three 4x4 vehicles, all tested in air-dry Yuma sand, that all the test data cluster closely about the same central μ_{20} versus N_{se} relation.

N_{se} was also determined to be more effective than N_s in consolidating μ_{20} data for each of the nine other test sands, in each case producing (as expected) a separate μ_{20} versus N_{se} relation. Figure 15 shows representative results, using data (a) from tests of a single 6.00-16, 2-PR tire in air-dry Cresswell sand and (b) from tests of four wheeled vehicles in moist sand at the Padre Island site.

Normalization of G_e to G_{ey} . Having developed a means to predict G_e , it remained to develop a means for normalizing G_e to one sand type, selected as Yuma sand. Analyses were made involving a number of parameters descriptive of physical properties of the 10 sand samples, with best results obtained by application of the relations shown in Figure 16.

In Figure 16, three sand parameters are involved--penetration resistance gradient (G), sand compactibility (D'), and sand grain median diameter (d_{50}). Compactibility is defined as

$$D' = \frac{e_{\max} - e_{\min}}{e_{\min}} \times 100, \text{ percent} \quad (9)$$

and d_{50} (sand grain diameter for which 50 percent of the sand sample is finer by weight) is read directly from a sand's grain-size distribution curve. In Figure 16, subscript x denotes sand x, and subscript y denotes Yuma sand. For a given sand x, known values of D'_x/D'_y and $(d_{50})_x/(d_{50})_y$ are used in Figure 16 to determine corresponding values of $(G_{ex}/G_{ey})_{D'}$ and $(G_{ex}/G_{ey})_{d_{50}}$, respectively. A given value of G_e for sand x (G_{ex}) is then normalized to the corresponding value for Yuma sand (G_{ey}) by the relation

$$G_{ey} = G_{ex} + (G_{ex}/G_{ey}) \quad (10)$$

where

$$G_{ex}/G_{ey} = (G_{ex}/G_{ey})_{D'} \times (G_{ex}/G_{ey})_{d_{50}} \quad (11)$$

For use in normalizing G_{ex} to G_{ey} , the curves in Figure 16 exhibit expected trends. A given sand of high compactibility requires less force for its displacement than does one of low compactibility at the same relative density. Thus, for $D'_x/D'_y > 1$ (all other conditions constant), G_{ex} must be increased for normalization to G_{ey} . This is accomplished by taking the appropriate value of $(G_{ex}/G_{ey})D'_x < 1$ from Figure 16, applying this value in Equation 11, and then using Equation 10. (For $D'_x/D'_y < 1$, $(G_{ex}/G_{ey})D'_x > 1$ and G_{ex} is decreased in normalization to G_{ey} .)

Note, also, that the penetration resistance of a sand with large-diameter grains is greater than that of one with smaller grains (all other conditions constant). Thus, for $(d_{50})_x/(d_{50})_y > 1$, $(G_{ex}/G_{ey})d_{50} > 1$ and G_{ex} is decreased in normalization to G_{ey} . (For $(d_{50})_x/(d_{50})_y < 1$, G_{ex} is increased in normalization to G_{ey} .)

Use of G_{ey} in N_{sey} . Having determined the value of G_{ey} for a particular sand x, the next step is to use G_{ey} in $N_{sey} = \frac{G_{ey}(bd)^{3/2}}{W} \cdot \frac{\delta}{h}$ to predict in-sand μ_{20} and η_{20} tire and wheeled vehicle performance. The success of G_{ey} in this role is illustrated in the following comparisons.

In Figure 17a, data for all of the single-tire tests considered herein for the Yuma, mortar, and Cresswell sands cluster about the same μ_{20} versus N_{sey} curve obtained earlier for Yuma sand in Figures 14a and 14b. (Note that $N_{sey} = N_{se}$ for Yuma sand only.) In Figure 17b, single-tire test data for these three sands all cluster about the same η_{20} versus N_{sey} relation. Note further that, based on results from the same laboratory single-tire tests, data collapse about the two relations involving N_{sey} in Figure 17 is considerably better than that about corresponding relations in Figure 18 involving N_s .

In Figure 19, the wheeled-vehicle test data for six sandy field test sites show much less data scatter about the central μ_{20} versus N_{sey} curve (the same curve as in Figures 14 and 17a) than do corresponding data for the same test sites in Figure 4 about the central curve of μ_{20} versus N_s .*

Based on Figures 17 and 19, N_{sey} is demonstrated to be very effective in consolidating single-tire and wheeled-vehicle μ_{20} data to one relation, η_{20} data to another. Remarks modifying this general conclusion need to be made, however, relative primarily to one of the laboratory test sands in Figure 17 (Cresswell sand) and to the one field test sand not shown in Figure 19 (Suscinio sand).

Some Strengths and Limitations of the N_{sey} Methodology. First, regarding the Cresswell sand, determination of its G_{ey} values in Figure 17 was made using as input data one set of G values gleaned from References 10 and 11, plus values of a_1 , a_2 , D' , and d_{50} from the 1983 WES laboratory tests of the Cresswell sand sample (using

* No η_{20} versus N_{sey} relation is shown in Figure 19 because measurements of η_{20} were not obtained in any of the wheeled vehicle tests considered herein.

a_2 at the WES air-dry condition). There was interest in determining how these predicted values of G_{ey} (and of N_{sey}) compared with those obtained by using the same set of G values, together with input values of a_1 , a_2 , D' , and d_{50} , obtained from References 10, 11, and 14. Table 3 summarizes this comparison.

For the 11 air-dry Cresswell sand test conditions considered, the major conclusion from Table 3 is that, although two quite different sets of input values of a_1 , a_2 , D' , and d_{50} were used (see the two footnotes of Table 3), nearly identical values of G_{ey} and of N_{sey} were predicted (compare results in columns 9 and 10 with those in columns 14 and 15). This close agreement reflects that the overall process for translating values of G to G_{ey} (summarized in the first footnote of Table 3) is reasonably robust. That is, based on the comparison in Table 3, the G -to- G_{ey} prediction process appears not to be unduly influenced by even fairly sizeable variations in values of its required input parameters.

This tentative conclusion is supported by the wheeled vehicle field relations shown in Figures 4 and 19. For the first five sands in the legends of these two figures, the sand samples used in defining values of a_1 , a_2 , D' , and d_{50} by 1983 WES laboratory testing were like the sands used in actual 1958 to 1961 field testing only to varying degrees--see Table 1. (For the sixth sand, from the Paw Paw Island site, the 1983 sand sample was taken from the precise location of field testing.) For the first five sands, taking this discontinuity between sample and test sands into account, the improvement in the relation of μ_{20} versus N_{sey} in Figure 19 versus the μ_{20} versus N_s relation in Figure 4 is rather remarkable, even with one significant caveat: the μ_{20} versus N_{sey} relation obtained for Suscinio sand (not shown in Figure 19) is considerably different from that shown in Figure 19 for the six other field test sands (it is displaced far to the left).

There are two principal possibilities for explaining what at first seems to be the atypical μ_{20} versus N_{sey} behavior of the Suscinio data. First, it is possible that one or more sand parameters needed in the process for translating G to G_{ey} have been omitted. The process described herein is the one that was determined to make the G -to- G_{ey} translation best for the test data examined, based on analysis not only of the sand parameters now included in the process, but also of several other parameters initially considered potentially important (coefficient of uniformity $C_u = d_{60}/d_{10}$, angle of internal friction, etc.). Still, modifications might substantially improve the G -to- G_{ey} translation process, and such modifications are welcomed.

The second, and much more likely, reason for the μ_{20} versus N_{sey} behavior of the Suscinio sand relates to the fact that, of the 10 sand samples used in 1983 WES laboratory testing, Suscinio's grain diameter distribution showed least agreement with its corresponding original distribution, by a large margin--see Table 1. Thus, it was not surprising, when the $D_r = 141.0 \log G + a_2$ laboratory relation for Suscinio sand was applied to Suscinio field values of G , that values of D_r considerably larger than 100 percent were obtained in some cases. (This did not occur with the nine other sands.) Note, also, from Table 1 that the Suscinio field sand was considerably less coarse than the 1983 Suscinio sample sand (which included almost as much gravel as sand--see Figure 10). In fact, from Table 1, the Suscinio field sand's overall distribution of d values is approximated just as well by the 1983 La Turballe laboratory sample (from the low side) as it is by the Suscinio laboratory sample (from the high side). (Prediction of Suscinio G_{ey} values by using for input

Suscinto field G values and La Turballe laboratory a_1 , a_2 , D' , and d_{50} values produced a Suscinto μ_{20} versus N_{sey} relation very closely approximated by the relation in Figure 17.) Finally, note that the good fit of the Suscinto data in the μ_{20} versus N_s relation of Figure 4 further indicates that characteristics of the Suscinto sand, as encountered on-site and measured at least by G , were not foreign to those of the six other sands in Figure 4.

The above observations suggest that, for the Suscinto beach site, the discontinuity between 1983 sample sand and 1959 field sand was simply too large to overcome in using a_1 , a_2 , D' , and d_{50} values from the sample sand to describe drawbar performance in the field sand. These observations also lead to the caveat that it remains to be determined how coarse a sand must be for the N_{sey} relations not to apply. (Sands at least as coarse as the La Turballe sand are successfully treated by N_{sey} .) A second caveat is that a substantial amount of laboratory testing is necessary to define the input values of a_1 , a_2 , D' , and d_{50} required by the process for translating G to G_{ey} for use in N_{sey} (particularly to define a_1 and a_2 for the range of values of D_r and sand moisture content of possible concern). If the user is not restricted by these two caveats, the N_{sey} relations of Figures 17 and 19 are useful now in predicting drawbar performance with better accuracy than do the N_s relations of Figures 18 and 4. If the above caveats negate use of the N_{sey} relations, the μ_{20} versus N_s relation of Figure 4 is still judged sufficiently well defined to offer the basis for a useful wheeled vehicle drawbar performance system.

SUMMARY AND CONCLUSIONS

To summarize, a five-step process was developed for predicting tire and wheeled vehicle μ_{20} and η_{20} performance for a given sand and sand moisture content, described as follows:

- (1) Use Equation 7 to estimate D_{rb} (from known values of G_b , a_1 , and a_2).
- (2) Obtain D_{re} from Figure 13.
- (3) Compute $G_e = \text{antilog } \frac{D_{re} - a_2}{a_1}$. For sand x , this is G_{ex} .
- (4) Convert G_{ex} to G_{ey} by use of Figure 16 and Equations 11 and 10.
- (5) Use G_{ey} in N_{sey} and the relations in Figure 17 to predict μ_{20} and η_{20} .

Relations of μ_{20} and η_{20} to N_{sey} now offer better prediction accuracy than do those of μ_{20} and η_{20} to N_s for a broad range of sand types and strengths, and for sand moisture contents up to about 7 percent. Implementation of the N_{sey} relations is limited, however, by two caveats: (a) the exact range of sand types for which the N_{sey} relations are applicable remains to be determined (sands from at least as fine as the Yuma sand to at least as coarse as the La Turballe sand considered herein are successfully treated by N_{sey}), and (b) substantial laboratory testing is necessary to define values of a_1 , a_2 , D' , and d_{50} , which are required as input by the process for defining G_{ey} for use in N_{sey} . Further work is needed to minimize or eliminate the influence of these two caveats. For now, with proper account taken of their

limitations, either the N_{sey} or the N_g methodology can be employed to predict in-sand tire and wheeled vehicle drawbar performance with useful accuracy.

REFERENCES

1. Meyer, M. P. et al., "International Society for Terrain-Vehicle Systems Standards," Journal of Terramechanics, Vol 14, No. 3, 1977, pp 153-182.
2. Melzer, K.-J., "Power Requirements for Wheels Operating in Sand," Proceedings of the International Conference of CIGR on the Perspectives of the Development of Agricultural Tractor Design, Vol 1, p 197, Warsaw, Poland.
3. Freitag, D. R., "A Dimensional Analysis of the Performance of Pneumatic Tires on Soft Soils," Technical Report No. 3-688, August 1965, U. S. Army Engineer Waterways Experiment Station, CE, Vicksburg, Miss.
4. Turnage, G. W., "Performance of Soils Under Tire Loads; Application of Test Results to Tire Selection for Off-Road Vehicles," Technical Report No. 3-666, Report 8, September 1972, U. S. Army Engineer Waterways Experiment Station, CE, Vicksburg, Miss.
5. Patin, T. R., "Performance of Soils Under Tire Loads; Extension of Mobility Prediction Procedures to Rectangular Cross-Section Tires in Coarse-Grained Soil," Technical Report No. 3-666, Report 7, April 1972, U. S. Army Engineer Waterways Experiment Station, CE, Vicksburg, Miss.
6. Melzer, K.-J., "Measuring Soil Properties in Vehicle Mobility Research; Relative Density and Cone Penetration Resistance," Technical Report 3-652, Report 4, July 1971, U. S. Army Engineer Waterways Experiment Station, CE, Vicksburg, Miss.
7. Turnage, G. W., "In-Soil Tractive Performance of Selected Radial- and Bias-Ply Tires," Paper No. 76-1520, December 1976, American Society of Agricultural Engineers, St. Joseph, Mich.
8. Turnage, G. W., "A Synopsis of Tire Design and Operational Considerations Aimed at Increasing In-Soil Tire Drawbar Performance," Proceedings, 6th International Conference, International Society for Terrain-Vehicle Systems, Vol II, pp 757-810.
9. Melzer, K.-J., "Performance of the Boeing LRV Wheels in a Lunar Soil Simulant; Effects of Speed, Wheel Load, and Soil," Technical Report M-71-10, Report 2, December 1971, U. S. Army Engineer Waterways Experiment Station, CE, Vicksburg, Miss.
10. Peca, J. O. and Reece, A. R., "Tyre Performance on Submerged Sand," Proceedings, 7th International Conference, International Society for Terrain-Vehicle Systems, Vol II, pp 755-796.
11. Reece, A. R. and Peca, J. O., "An Assessment of the Value of the Cone Penetrometer in Mobility Prediction," Proceedings, 7th International Conference, International Society for Terrain-Vehicle Systems, Vol III, pp A1-A33.

12. Rush, E. S., "Trafficability of Soils; Tests on Coarse-Grained Soils with Self-Propelled and Towed Vehicles 1958-1961," Technical Memorandum No. 3-240, Seventeenth Supplement, May 1963, U. S. Army Engineer Waterways Experiment Station, CE, Vicksburg, Miss.
13. Schreiner, B. G., Moore, D. W., and Grimes, K., "Mobility Assessment of the Heavy Expanded Mobility Tactical Truck - Initial Production Vehicles," Technical Report (in preparation), U. S. Army Engineer Waterways Experiment Station.
14. Peca, J. O., "Traction on Sand," unpublished Ph.D. Thesis, August 1983, Department of Agricultural Engineering, University of Newcastle upon Tyne.

NOTATION

a_1, a_2	Constant and variable, respectively, in the equation $D_r = a_1 \log G + a_2$ for a given sand over a range of sand moisture contents
b	Unloaded tire section width
C	Soil penetration resistance
C_u	Coefficient of uniformity
CI	Cone index
d	Unloaded tire outside diameter
$d_{50}, (d_{50})_x, (d_{50})_y$	Median diameter of sand grains, d_{50} of sand x , d_{50} of Yuma sand
D', D'_x, D'_y	Compactibility, compactibility of sand x , compactibility of Yuma sand
D_r, D_{rb}, D_{re}	Relative density, before-tire-pass relative density, effective (predominant during-tire-pass) relative density
DP, DP_{20}	Drawbar pull, drawbar pull at 20 percent slip
e, e_{max}, e_{min}	Before-tire-pass sand void ratio, maximum sand void ratio, minimum sand void ratio
$G, G_b, G_e, G_{ex}, G_{ey}$	Sand penetration resistance gradient, before-tire-pass G , effective (predominant during-tire-pass) G , G_e for sand x , G_e for Yuma sand
h	Unloaded tire section height
i	Slip
N_s, N_{se}, N_{sey}	Sand-tire numerics $N_s = \frac{G(bd)^{3/2}}{W} \cdot \frac{\delta}{h}$, $N_{se} = \frac{G_e(bd)^{3/2}}{W} \cdot \frac{\delta}{h}$, and $N_{sey} = \frac{G_{ey}(bd)^{3/2}}{W} \cdot \frac{\delta}{h}$

T	Torque input to wheel
v	Forward velocity of wheel axle
W	Load on a single tire
δ	Tire deflection (under load)
μ_{20}	Drawbar coefficient, drawbar coefficient at 20 percent slip
η_{20}	Drawbar efficiency, drawbar efficiency at 20 percent slip
ω	Rotation velocity of the torque input shaft

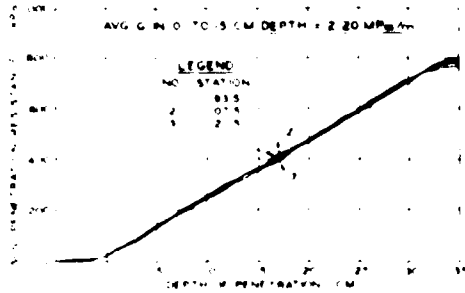


Figure 1. Sample recordings of cone penetration tests in a sand test bed

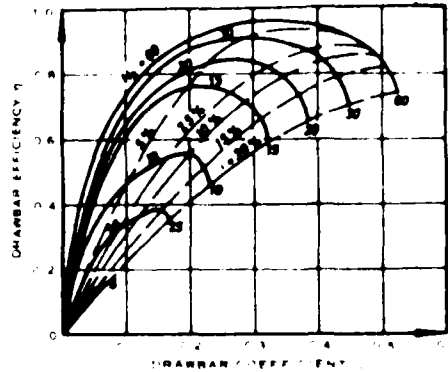


Figure 2. Relations of μ and ϕ to N_g and slip (i) for pneumatic tires operating in a frictional sand (adapted from Reference 2)

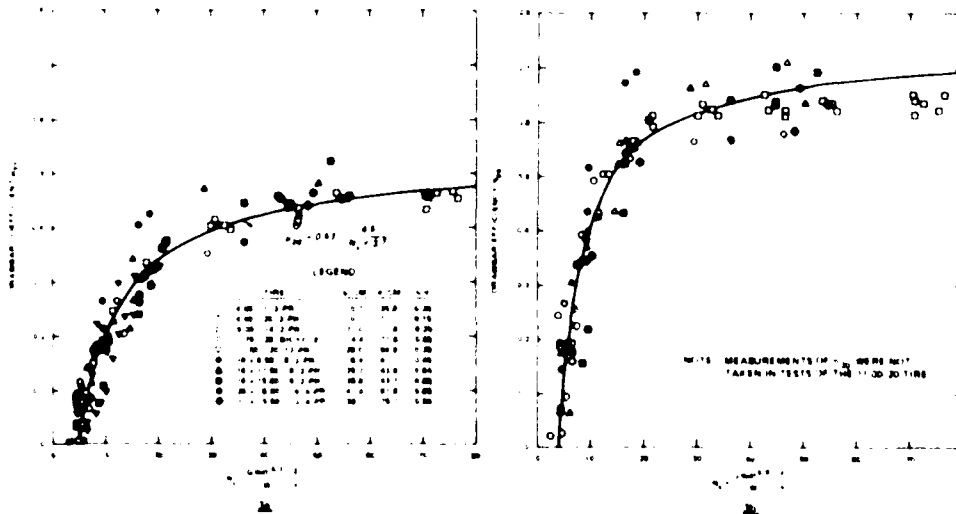


Figure 3. Relations of μ_{20} and ϕ_{20} to N_g for ten single pneumatic tires tested in air-dry Yuma sand (values of G from 0.62 to 7.52 MPa/m, W from 0.41 to 20.02 kN, and i/h from 0.15 to 0.35)

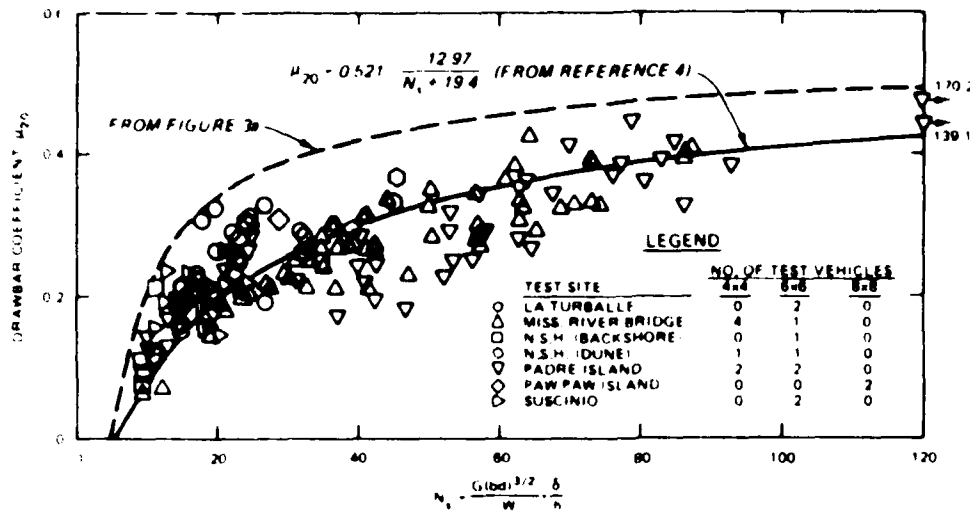


Figure 4. Relation of μ_{20} to N_s for tests with a variety of wheeled vehicles at seven sandy field sites

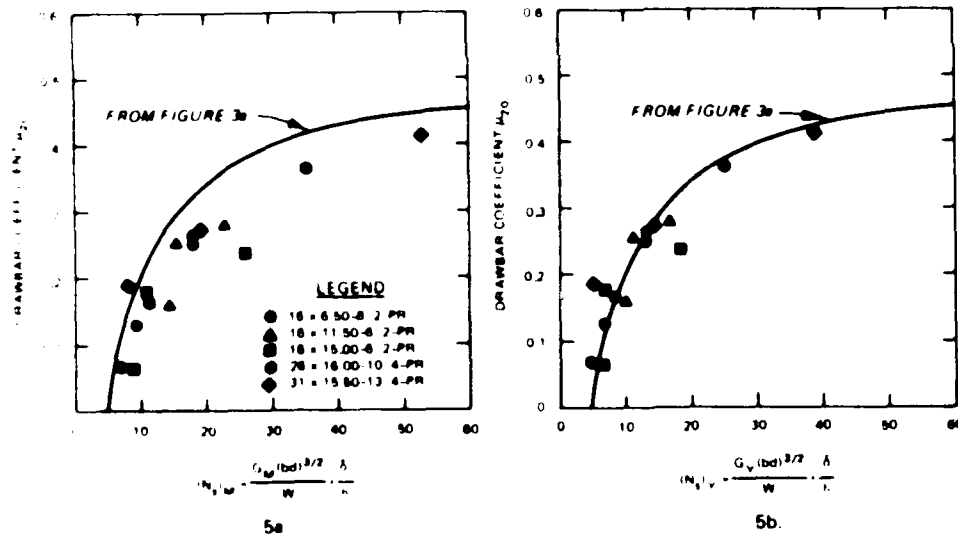


Figure 5. Effect of converting G_M to G_Y in the relation of μ_{20} to N_s for tires operating at 20 percent slip in mortar sand

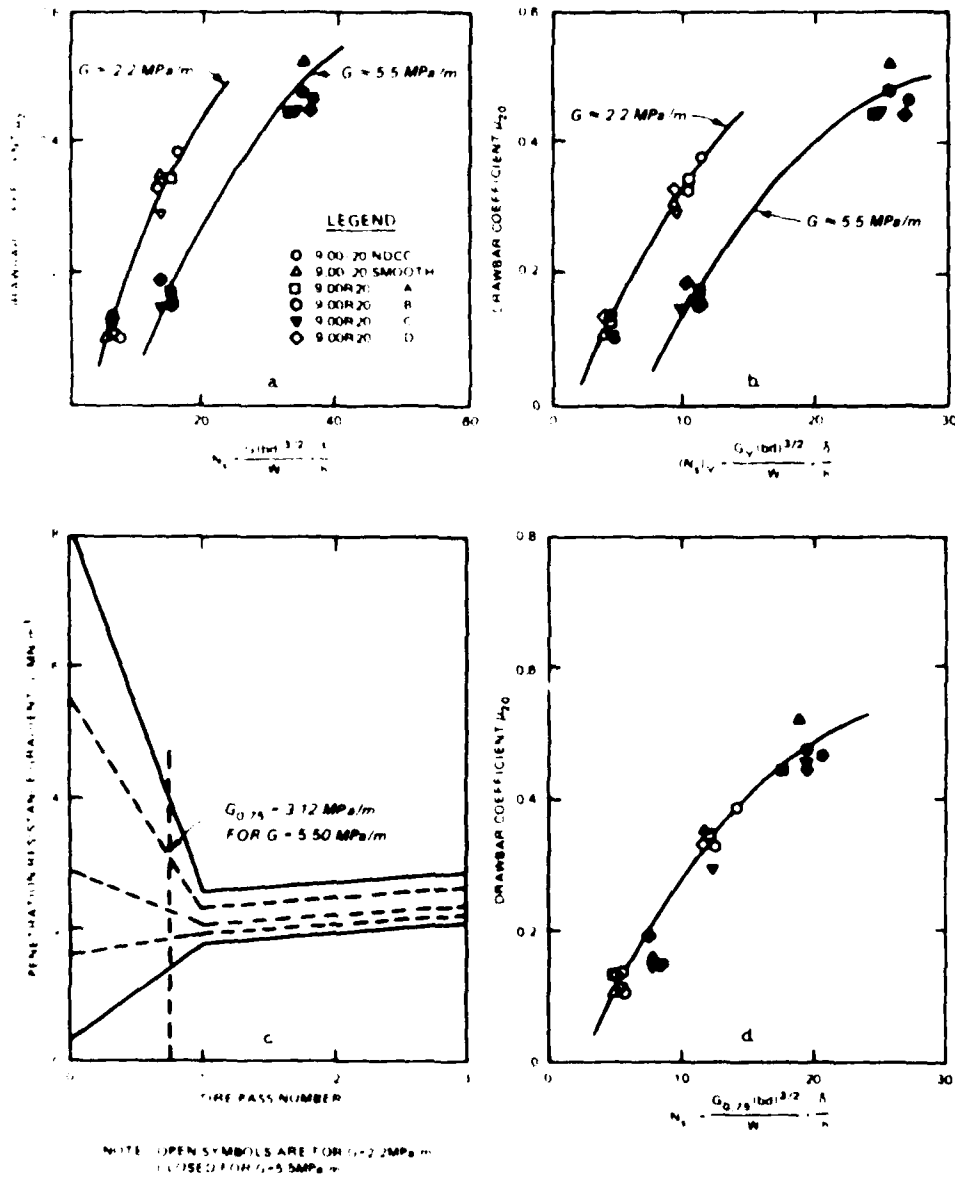


Figure 6. Relations of (a) μ_{20} to N_s , (b) μ_{20} to $(N_s)_v$, (c) G to tire pass number, and (d) μ_{20} to N_s' for tests of six 9.00x20 tires in mortar sand

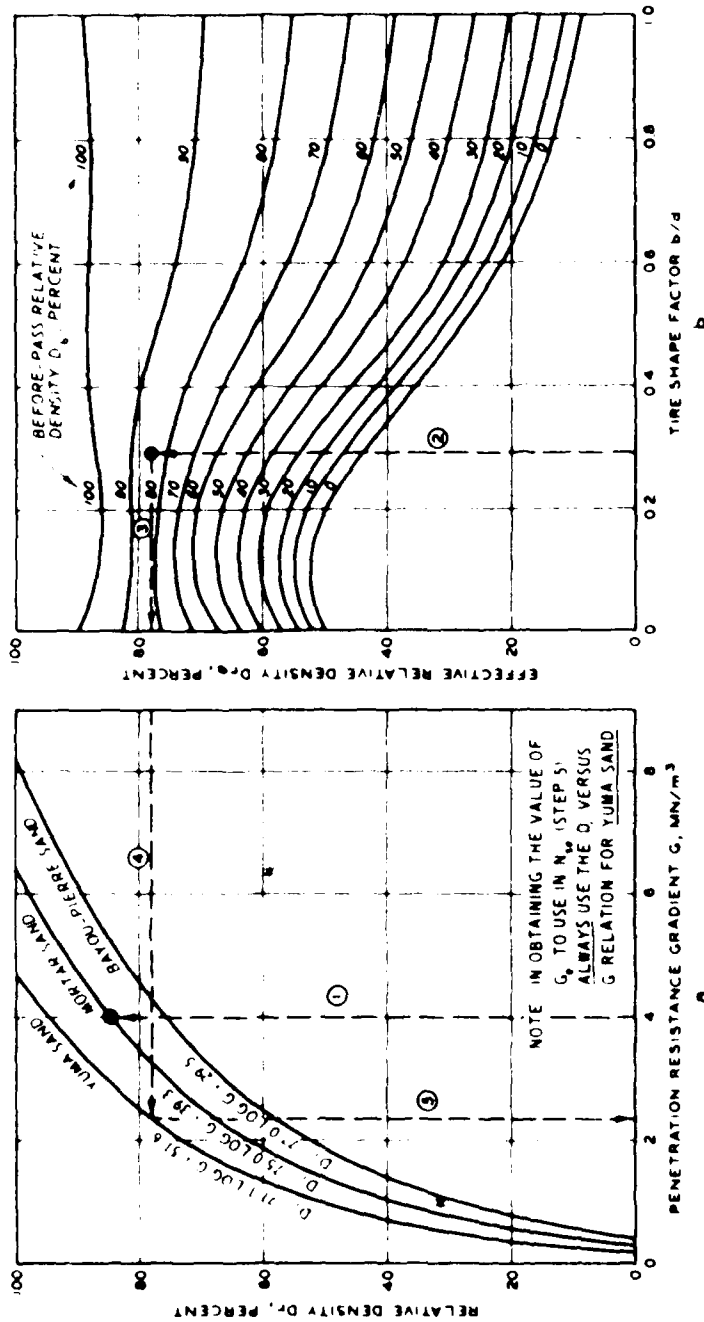


Figure 7. (a) Relations of D_r to G for three sands, and (b) from Reference 8, tentative relations among b/d , D_{rb} , and D_{re} for sands in general (subsequently replaced by relations developed herein

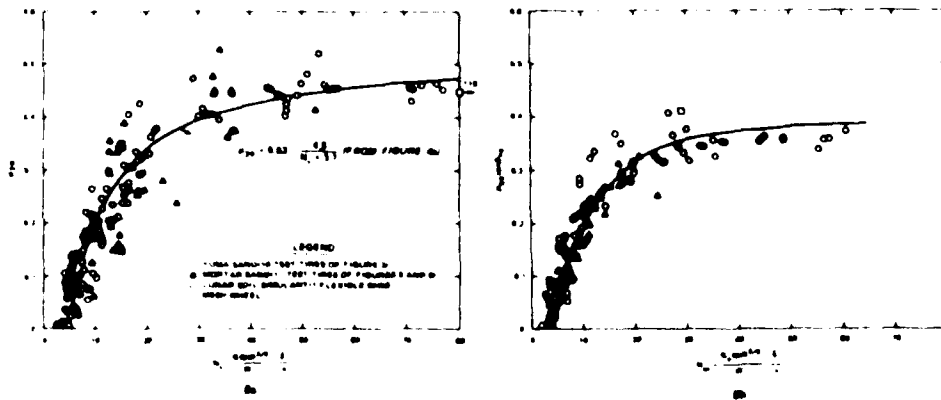


Figure 8. Relations of (a) u_{20} to N and (b) $u_{20} \tan \phi_{70}$ to N_{se} for the three frictional test soils considered in Reference 8

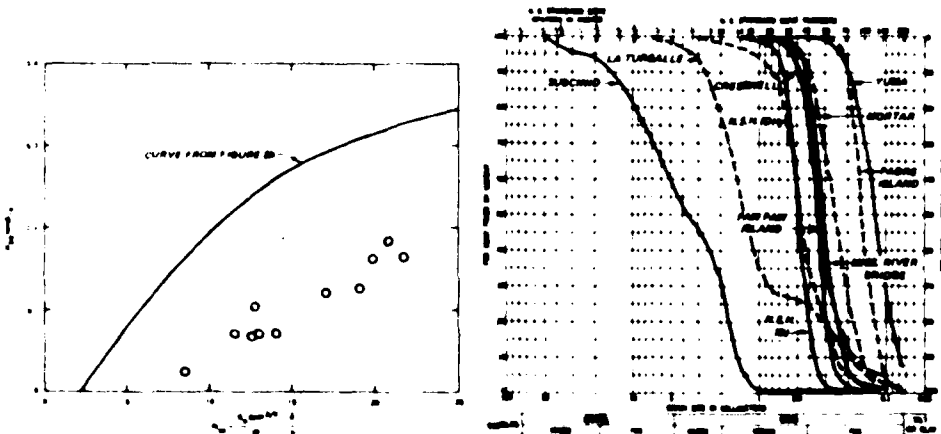


Figure 9. Relation of $u_{20} \tan \phi_{70}$ to N_{se} for 6.00-16, 2-PR tire tested in air-dry Cresswell sand (adapted from Reference 11)

Figure 10. Grain size distributions of ten sand samples analyzed at WES in 1983

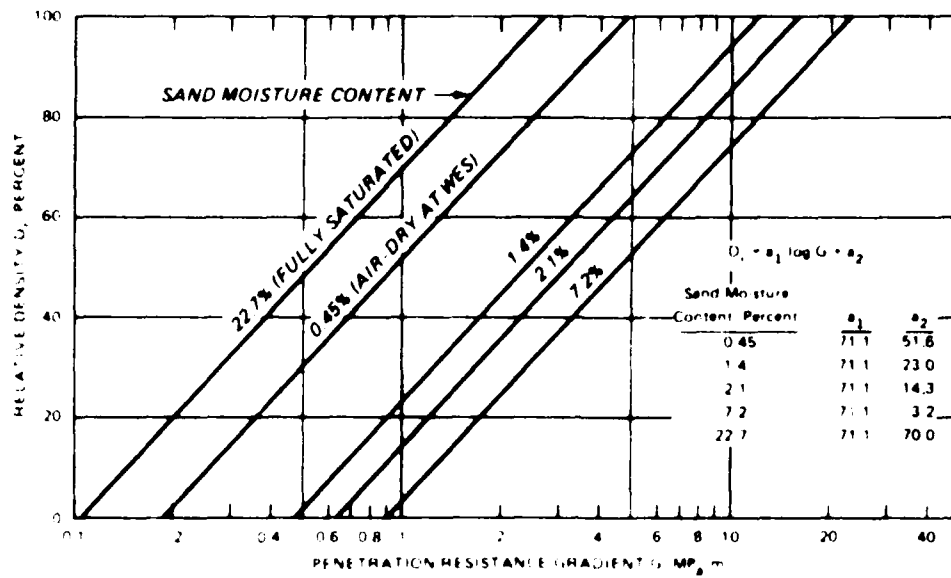


Figure 11. Relations among G , D_r , and sand moisture content for Yuma sand

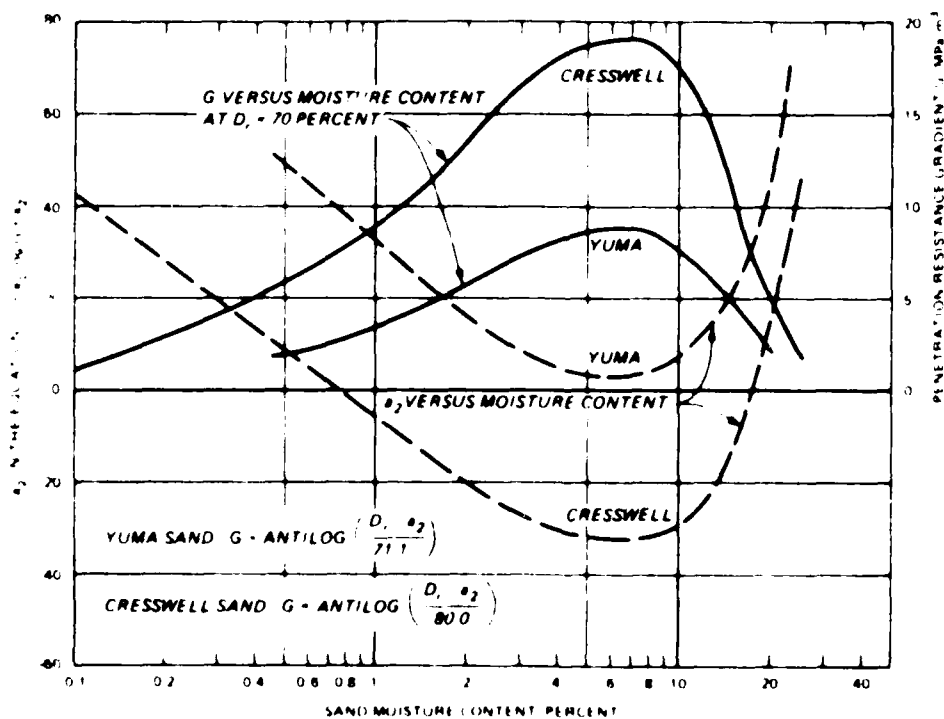


Figure 12. Relations of (a) a_2 to sand moisture content and (b) G at $D_r = 70$ percent to sand moisture content for Yuma and Cresswell sands

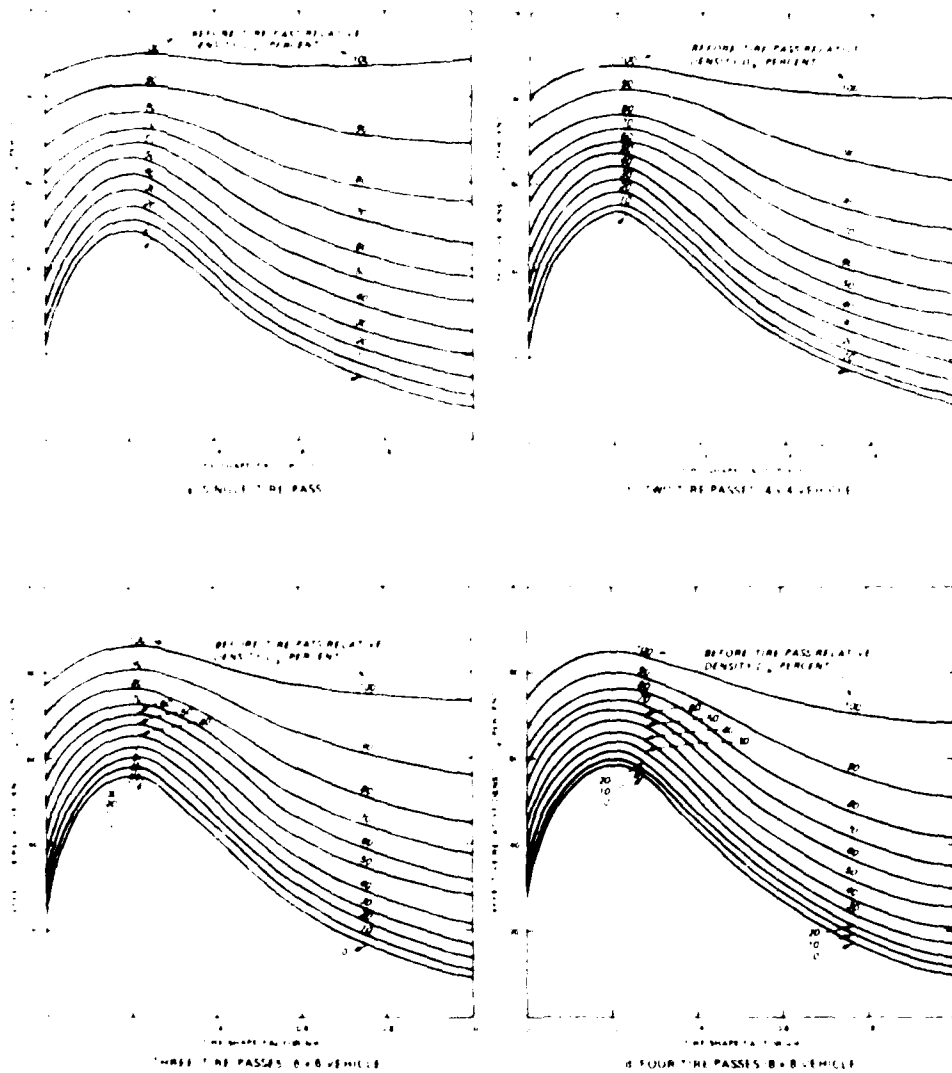


Figure 13. Relations among D_{rb} , b/d , and D_{re} for one, two, three, and four tire passes in sand (at 20 percent slip with tire deflection in the 15 to 35 percent range)

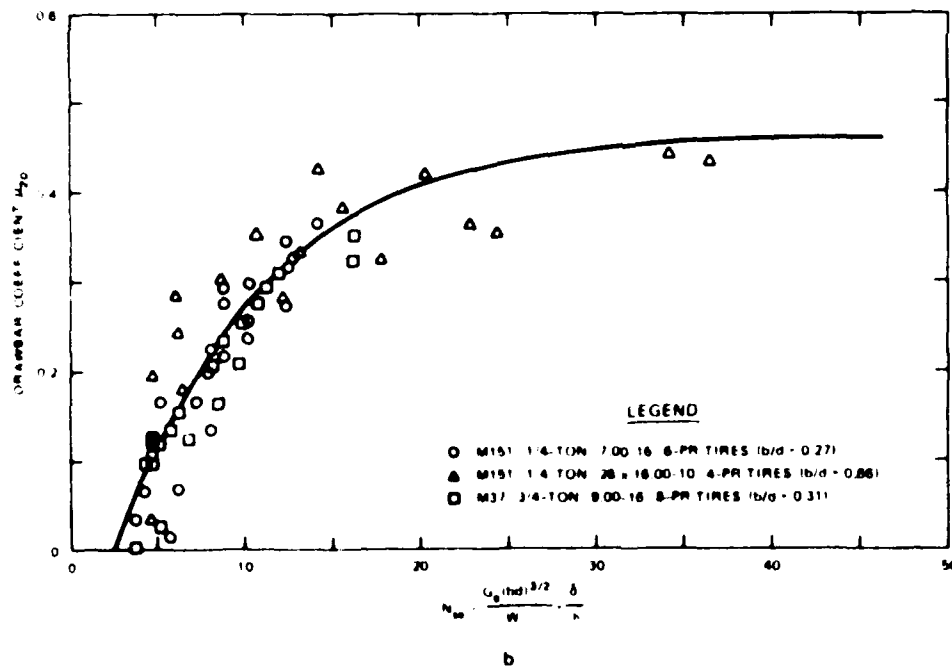
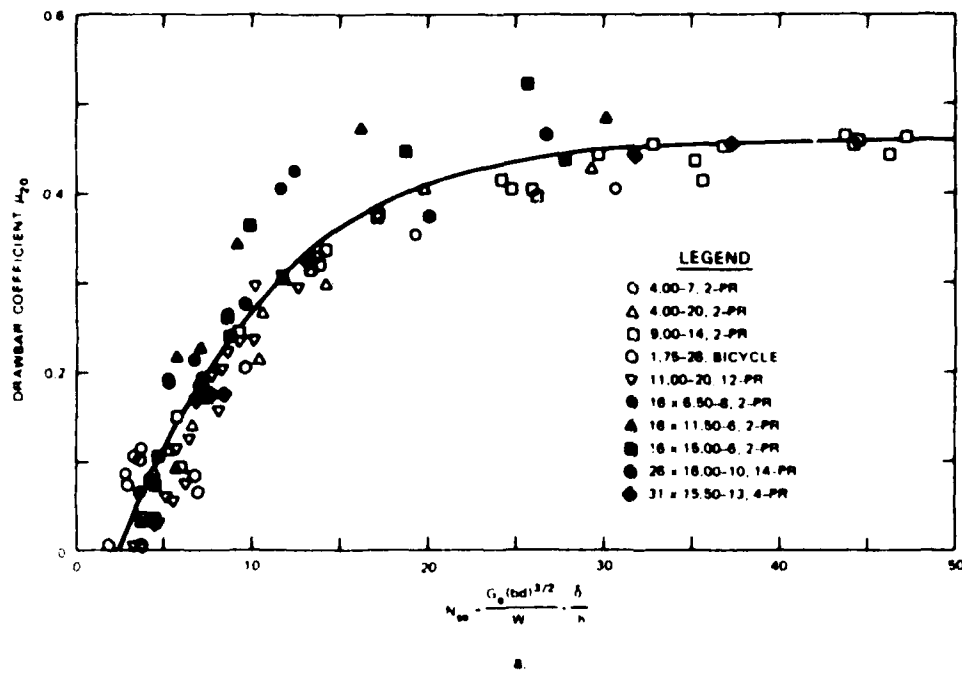


Figure 14. Single relation of μ_D to N_{se} (a) for ten single tires and (b) for three 4x4 vehicles, each tested in air-dry Yuma sand

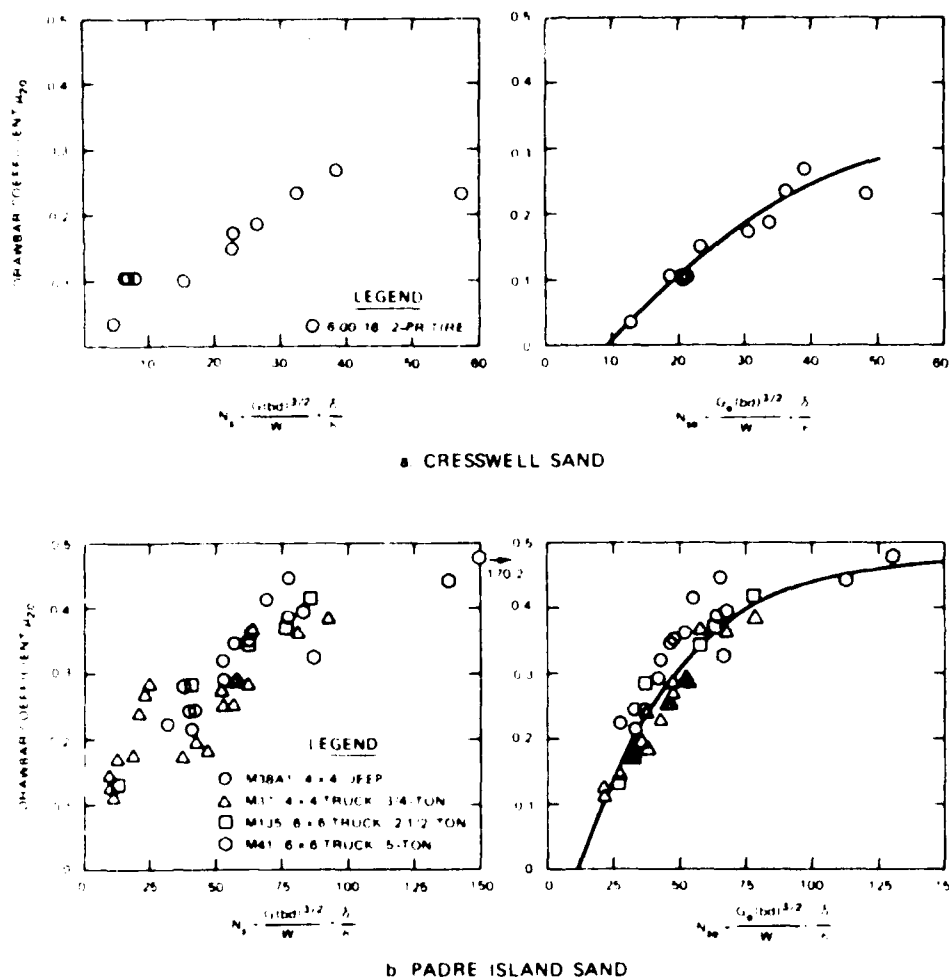


Figure 15. Relations of u_{20} to N_q and u_{20} to N_{sq} (a) for the 6.00-16, 2-PR tire in air-dry Cresswell sand, and (b) for four wheeled vehicles in moist Padre Island sand

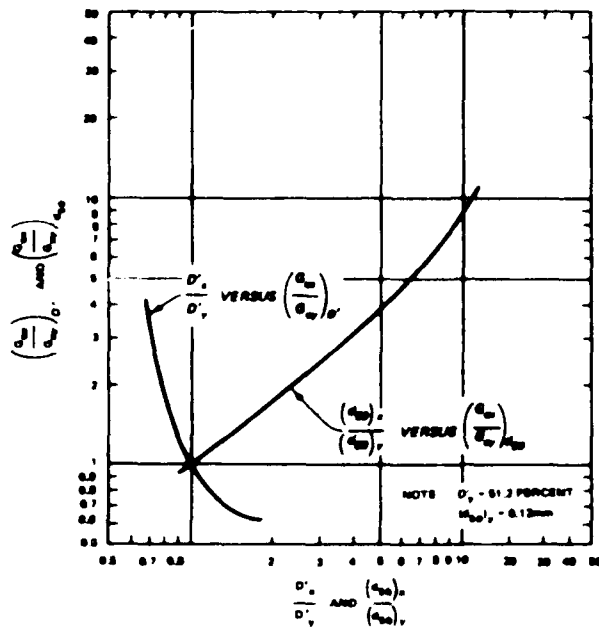


Figure 16. Relations of $\frac{D'_x}{D'_y}$ to $\left(\frac{G_{ex}}{G_{ey}}\right)_{D'}$ and

$$\frac{(d_{50})_x}{(d_{50})_y} \text{ to } \left(\frac{G_{ex}}{G_{ey}}\right)_{d_{50}}$$

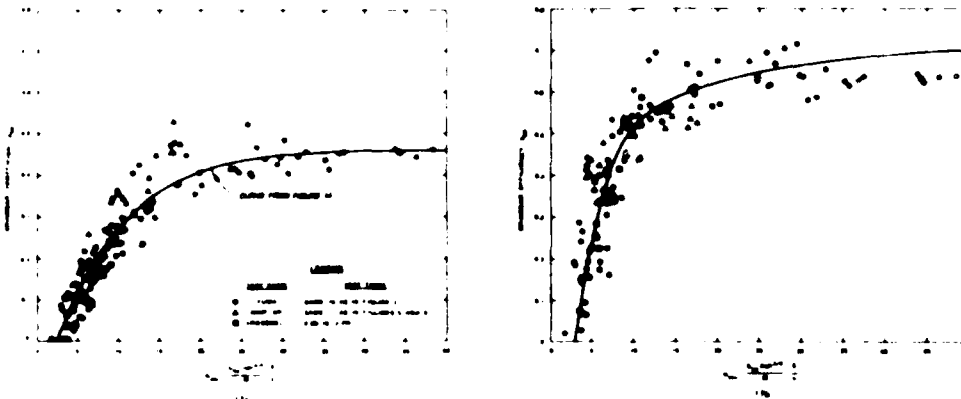


Figure 17. Relations of (a) v_{20} to N_{ey} and (b) n_{20} to N_{ey} for single-tire tests in air-dry Yuma, mortar, and Cresswell sands

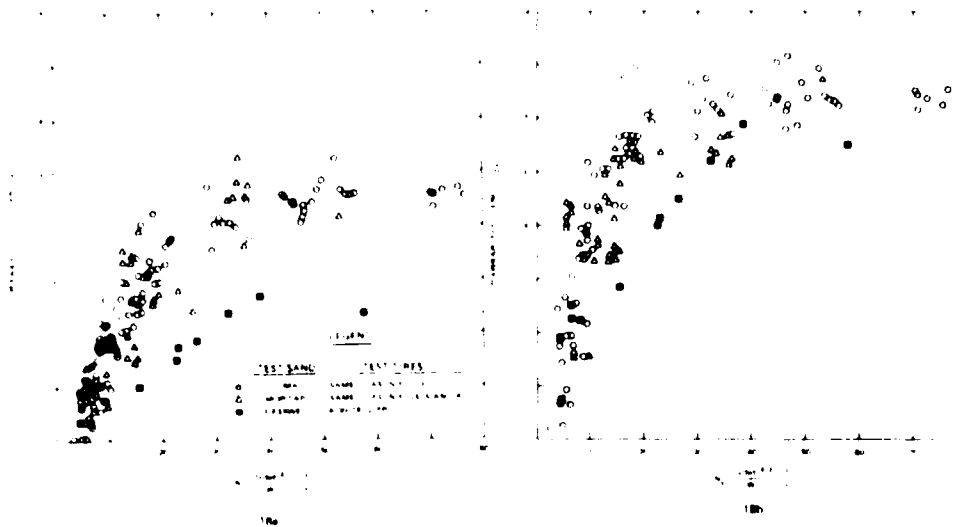


Figure 18. Relations of (a) μ_{20} to N_8 and (b) μ_{20} to N_8 for single-tire tests in air-dry Yuma, mortar, and Cresswell sands

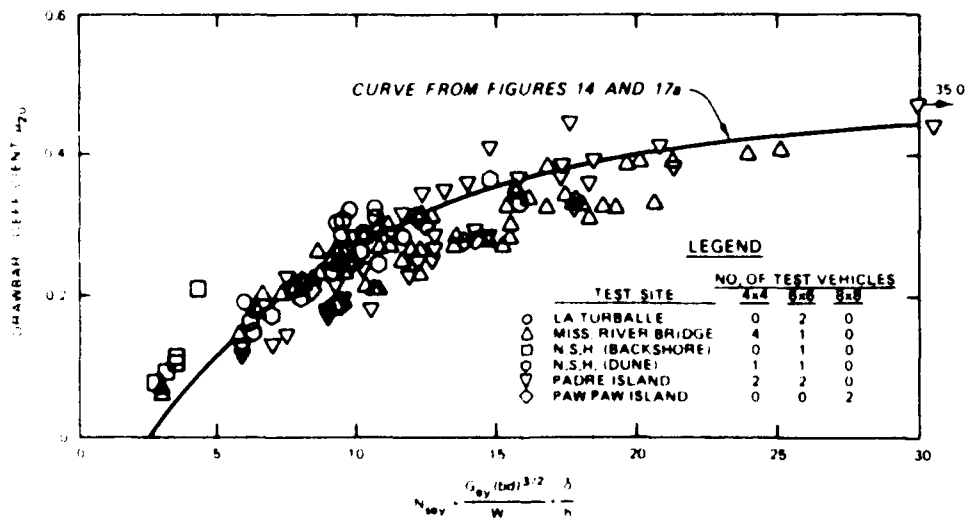


Figure 19. Relation of μ_{20} to N_{sev} for tests with a variety of wheeled vehicles at six sandy field sites

Table 1
Comparison of Grain Diameters of 10 Sands from Original Test
Reports and from 1983 WES Laboratory Tests

Sand	(d ₁₀) orig.	(d ₃₀) orig.	(d ₅₀) orig.	(d ₇₀) orig.	(d ₉₀) orig.	Reference No. of Original Test Report
	(d ₁₀) 1983	(d ₃₀) 1983	(d ₅₀) 1983	(d ₇₀) 1983	(d ₉₀) 1983	
Cresswell	0.32/0.26	0.40/0.31	0.45/0.34	0.59/0.39	0.90/0.50	11
La Turballe**	0.48/0.24	0.97/0.86	1.45/1.30	1.75/1.80	2.80/2.70	12
Mississippi River Bridge	0.16/0.21	0.22/0.27	0.26/0.31	0.30/0.36	0.37/0.41	12
Mortar	0.17/0.17	0.22/0.20	0.25/0.25	0.30/0.30	0.35/0.39	4,6
N.S.H.* (backshore area)	0.39/0.36	0.50/0.42	0.57/0.49	0.65/0.54	0.81/0.64	12
N.S.H. (dune area)	0.17/0.20	0.31/0.37	0.56/0.47	0.96/0.56	4.00/0.79	12
Padre Island	0.11/0.11	0.15/0.14	0.16/0.15	0.18/0.18	0.21/0.20	12
Paw Paw Island	0.19/0.19	0.27/0.27	0.32/0.32	0.38/0.38	0.49/0.49	13
Suscunio**	0.56/1.50	1.45/2.00	2.45/3.50	4.40/7.00	9.60/16.00	12
Yuma	0.08/0.08	0.10/0.10	0.12/0.12	0.14/0.16	0.19/0.20	4,6

* All d values are in mm, and were obtained from plots such as those in Figure 10.

** For the La Turballe and the Suscunio test sites, each d value listed above from the original test report is the average of d values from similar grain-size distributions for two test areas at that site--a foreshore test area and a backshore test area.

N.S.H. is National Seashore Headquarters, the agency in Massachusetts that presently occupies the test area occupied by Camp Wellfleet when the wheeled vehicle tests of Reference 12 were conducted.

Table 2
VES Measurements of Some Key Sand Parameters Related to In-Sand Drawbar Performance

(1)	(2)	(3)	(4)	(5)	(6)	(7)	(8)	(9)	(10)	(11)	(12)	(13)	(14)	(15)
	At-WPS Air-Dry Moisture Content, %	Constant a_1	In $D_r = a_1 \log G + a_2$ Air-Dry a_2 at Moisture Content of	0.5 %	1 %	2 %	3 %	7 %	Maximum Void Ratio e_{max}	Minimum Void Ratio e_{min}	Compara- tibility D_r , %	Grain Diameter d_{50} , mm	D_r $\frac{D_r}{D_r}$	$(\frac{D_r}{D_r})_{50}$
Sand														
Creswell	0.22	80.0	+26.0	+8.0	-6.0	-20.5	-27.0	-30.5	0.782	0.548	42.7	0.34	0.43	2.43
La Turballe	0.20	60.0	+35.5	+16.5	+2.7	-11.0	-15.5	-18.0	0.630	0.345	82.6	1.30	1.61	10.80
Mississippi River Bridge	0.20	115.8	+25.3	-12.7	-41.0	-69.0	-82.0	-90.0	0.732	0.532	37.6	0.31	0.73	2.58
Meritar	0.08	75.0	+39.3	+29.0	-1.0	-13.0	-19.5	-25.0	0.908	0.572	58.7	0.25	1.15	2.08
N.S.H. (backshore area)	0.16	134.5	+47.0	+6.0	-18.5	-43.3	-55.5	-67.5	0.778	0.557	39.7	0.49	0.78	4.08
N.S.H. (dune area)	0.12	116.7	+27.0	-12.5	-31.5	-50.5	-56.0	-58.5	0.685	0.466	47.0	0.47	0.92	3.92
Padre Island	0.13	132.6	+40.7	-24.5	-54.5	-84.0	-94.0	-103.0	0.813	0.596	36.4	0.15	0.71	1.25
Paw Paw Island	0.32	65.0	+39.0	+33.0	+26.5	+18.0	+14.5	+11.5	0.839	0.518	62.0	0.32	1.40	2.67
Suscinto	0.12	141.0	+27.0	-1.0	-14.5	-26.5	-30.0	-33.0	0.528	0.380	38.9	3.50	0.76	29.20
Yuma	0.45	71.1	+51.6	+49.5	+31.5	+15.2	+9.2	+3.5	0.919	0.608	51.2	0.12	1.00	1.00

* a_2 values for the air-dry moisture contents of column 2 were obtained in tests at the particular moisture content values indicated. a_2 values for moisture contents of 0.5, 1, 2, 3, and 7 percent were obtained from curves similar to those in Figure 12.

Table 3
Comparison of G_{ey} Values Obtained for Air-Dry Crosswell Sand from Two Sets
of Input Values of a_1 , a_2 , D' , and d_{50}

(1)	(2)	(3)	(4)	(5)	(6)	(7)	(8)	(9)	(10)	(11)	(12)	(13)	(14)	(15)
Test No.	γ_{20}	γ_{20}	N_a	G_e MPa m	D_{rb}^* z	D_{re} z	G_{ex}^* MPa m	G_{ey}^* MPa m	N_{sey}	D_{rb}^{**} z	D_{re}^* z	G_{ex}^* MPa m	G_{ey}^* MPa m	N_{sey}
1	0.035	0.074	4.7	0.78	39.4	61	2.06	0.60	3.6	17.4	53	2.18	0.58	3.5
2	0.102	0.250	6.4	0.65	35.3	60	1.97	0.57	5.6	11.0	52	2.11	0.56	5.5
3	0.102	0.225	6.7	0.78	39.4	61	2.06	0.60	5.2	17.4	53	2.18	0.58	5.0
4	0.102	0.220	8.1	0.82	40.5	62	2.15	0.62	6.1	19.1	54	2.24	0.59	5.8
5	0.100	0.282	15.6	2.58	66.0	71	3.23	0.94	5.7	48.9	69	3.45	0.91	5.5
6	0.150	0.400	22.7	3.76	74.4	74	3.69	1.07	6.5	72.0	74	3.98	1.05	6.3
7	0.174	0.413	23.0	2.59	66.1	71	3.23	0.94	8.3	59.1	69	3.45	0.91	8.1
8	0.185	0.450	26.5	2.68	66.9	71	3.23	0.94	9.3	60.3	69	3.45	0.91	9.0
9	0.236	0.520	32.5	3.29	71.4	74	2.53	1.02	10.1	67.4	71	3.65	0.97	9.6
10	0.268	0.588	38.4	3.89	75.2	75	3.86	1.12	11.1	73.2	74	3.98	1.05	10.4
11	0.234	0.550	57.9	6.53	86.7	80	4.83	1.40	12.4	91.2	85	5.46	1.44	12.8

* Note that $D_{rb} = a_1 \log G + a_2$; D_{re} is obtained from Figure 13; $G_{ex} = \text{antilog } \frac{D_{re} - a_2}{a_1}$; and $G_{ey} = G_{ex} + \frac{G_{ex}}{G_{ey}}$. For columns 6-10, the following input data values were used: $a_1 = 51.3$, $a_2 = 4.9$, $d_{50} = 0.45$ mm (from References 10 and 11), and $D' = 47.6$ percent (from Reference 14). (These D' and d_{50} values produced a $\frac{G_{ex}}{G_{ey}}$ value from Figure 16 of 3.45.)

** For columns 11-15, the following input data values were used from 1983 WES soils laboratory testing: $a_1 = 80.0$, $a_2 = 26.0$, $D' = 42.7$ percent, and $d_{50} = 0.34$ mm. (These D' and d_{50} values produced a $\frac{G_{ex}}{G_{ey}}$ value of 3.45.)

TOPIC 2

THEORETICAL ASPECTS OF RIDE DYNAMICS

✓
DYNAMIC SIMULATION OF TRACK LAYING VEHICLES

M. J. BENNETT AND P. H. G. PENNY

ARMY RESEARCH ESTABLISHMENT, WINDSOR, WINDSOR, WINDSOR

ABSTRACT

A computer model to simulate the dynamic response of a track laying vehicle traversing defined terrain is described. Results used for validation tests are given together with a selection of typical applications. The model has proved to be flexible with applicability to a wide range of problems.

1. INTRODUCTION

Track laying vehicles generally have distinct advantages over wheeled vehicles in cross country terrain, primarily because the track results in a lower ground pressure, leading to reduced sinkage and a better distribution of tractive effort. Against this the steering system, which is usually integrated with the transmission, is more complex.

Most all road wheeled vehicles have independently mounted wheels and prediction of the dynamic behaviour of such a vehicle travelling over a defined terrain is relatively straight forward. However, when the road wheels are connected by a track, their motion is not independent, and this, together with the motion of the track itself, makes prediction much more difficult. Bearing in mind the complexity and high cost of such vehicles, this difficulty is a serious handicap for the designer. This is particularly true of military tracked vehicles which additionally usually have quite sophisticated suspension systems.

The aim of the work described in this paper was:

- a. To develop a computer model that would simulate the behaviour of a track laying vehicle.
- b. To validate this model against field measurements on real vehicles.

The development and proving of such a computer model would result in an extremely useful design aid and allow competing designs to be compared before the expensive process of prototype production begins. A computer model would also allow the vehicle parameters to be changed very easily and the design optimised for given criteria. The main areas of interest for the model in question are vehicle ride, loading and motion of the suspension components, and the track tension which not only has an important bearing on track wear, but also has a considerable influence on the vehicle response in general.

Previous work on tracks is mostly confined to the classic kinematic analysis of a roller chain passing around fixed sprockets (1), and more recently to the consequences of this "polygonal action" in terms of such problems as noise and vibration (2). More recently still (3) this work has been extended to a study of the dynamics of the top run of a tank track, but the track is held above the ground and passes over fixed axis sprockets.

By contrast the motion of the track or "chain" of a real tracked vehicle is very different and much more complex because:

- a. Torque is applied through a sprocket which moves with the vehicle.
- b. The load is distributed in an indeterminate manner along a finite length of essentially stationary track in contact with the ground.
- c. The track inertia is a significant fraction of the system inertia, and its motion is very non-linear.
- d. There is significant coulomb friction between adjacent track links.

It is clear, then, that whilst the previous work has produced useful results, the analysis has not yet reached the stage where it is directly applicable to a tracked vehicle computer model. The model described in Section 2 therefore makes some simplifying assumptions, and a parallel programme of more detailed work is in progress to investigate real track dynamics (4).

2. COMPUTER SIMULATION

The computer simulation comprises a main program which solves the differential equations of motion describing the vehicle response, a data file describing the vehicle, a terrain file which describes the ground over which the vehicle is to be run, and a number of sub-programs which can be selected according to the output required.

2.1 Main Program for the Model.

The vehicle is modelled in side elevation only, giving 3 degrees of freedom for the hull (one each for pitch, bounce and longitudinal motion), and one for each road wheel (typically 5, 6 or 7). The hull and parallel suspension links are assumed to be rigid. The suspension compliances include the main spring element (most commonly torsion bar or hydro-pneumatic), bump and rebound stops, and road wheel tyre stiffness. Friction is included at all wheel stations, and damping is included at those wheel stations where damper units are fitted (commonly front and rear only).

As noted in Section 1 the vehicle track is an area of uncertainty and difficulty. For the model described the track is considered as a light string with an exponential elastic characteristic (measured from an initial fitted tension) due to catenary effects. A portion of the actual track mass is added to the model sprung mass. During operation the track

tension is assumed to be constant from the tight side of the drive sprocket (which may be at the front or rear of the vehicle) to a point immediately in front of the rear road wheel which is in contact with the ground. Then, tension is assumed to decrease in equal steps, one for each wheel in ground contact, to the value of the tension at the slack side of the sprocket. The vehicle model may be "driven" with a constant sprocket torque against a speed-dependent rolling resistance, or at a sensibly constant speed. Work is in hand to enable sprocket torque or speed profiles to be used to drive the model.

When a real vehicle traverses cross country terrain such that the pitch frequency is excited, it is not uncommon to find that the front lower leading edge of the hull strikes the ground. This occurrence is monitored in the program for the model and may be displayed as part of the output, but since the hull is assumed to be rigid, grounding forces cannot be calculated and hence are not included in the equations of motion.

The program solves the differential equations of motion simultaneously using a fourth-order Runge-Kutta technique. Because of the "stiff" nature of the equations instabilities can arise with the higher derivatives relating to the smaller masses. If displacement only is of interest this instability is less important since the double integration gives a significant filtering effect. However, for accelerations, and to a lesser extent for velocities, the instability may lead to unacceptable errors. Decreasing the integration step length ultimately solves the problem but can lead to very long computer run times, and so a variable step length has been introduced into the Runge-Kutta routine. This generally takes coarse steps where the rates of change of the higher derivatives are slow and finer steps where the rates of change are high, thus giving good accuracy with reasonable computer run times. Experience has also taught us those areas of the system which are sensitive to these errors and what local error formulation is best suited to the problem.

The program is written in modular form thus allowing easy modification to suit particular real cases. The results discussed in Section 4 are derived from a number of variants of the basic program.

4.1. Vehicle Data File.

A considerable amount of detailed data is needed to describe the vehicle used for the model. This data comprises:

- a. Sprung and unsprung masses, and a factor to allow for rotating masses dependent on the gear in use.
- b. Moments of inertia.
- c. Complete vehicle dimensions, geometry and initial conditions.
- d. Suspension compliances, friction and damping characteristics.
- e. Rolling resistance characteristic.
- f. Track characteristic.

Depending on the nature of the vehicle the data may be constants, or algebraic or tabulated functions which are evaluated or interpolated as necessary. A sub-program allows easy display and modifications of the current data file.

2.3 Terrain Data File.

The terrain is recorded as a series of vertical co-ordinates at uniform horizontal intervals. The program joins these points by straight line segments. Experience has shown that there is little to be gained by using a horizontal interval of less than one third road wheel radius. The effect of the finite wheel size - ground profile geometry is taken fully into account, but the ground is assumed to be rigid.

A library of terrain profiles is available including flat ground used to check equilibrium and steady state positions, simple obstacles such as ramps and steps which are easy to make and use for real vehicle testing and which form useful standards for comparative purposes, synthetic random courses, and representations of real "random" course which have been surveyed.

2.4 Output Sub-Programs.

The program is capable of giving as output any of the calculated forces or moments, any of the displacements (or first or second derivatives) of any motion corresponding to each of the degrees of freedom, algebraic functions of these such as various relative motions, and indicators corresponding to hull grounding, bump stop action, and so on. Any of these variables can be plotted as a function of any other, or as a function of time. For terrain crossing it has been found convenient to use horizontal displacement of the hull mass centre as the independent variable.

3. EXPERIMENTAL MEASUREMENTS

It is most important that all computer models are validated against field measurements as thoroughly as possible. To this end the model described in Section 2 has been used to predict various aspects of the responses of three particular real vehicles. The vehicles used were:

- a. A Chieftain Mk VP Main Battle Tank over flat ground and ramps.
- b. A Suspension Research Vehicle running over flat ground, ramps, sinewaves and a 200m random course.
- c. A model tracked vehicle of approximately one-eighth full scale.

These three vehicles are shown in Fig 1.

Further details of the vehicles and the instrumentation used to record the various motions is described more fully in Sections 3.1, 3.2 and 3.5. Some of the results of the trials are shown and discussed in Section 4.

Some further validation of the model has been possible from work done by RMCS for Herstman Defence Systems of Bath on their rotary damper units. Some results from this work are also shown in Section 4.

4.1 Suspension Research Vehicle Trials.

This vehicle was made available specifically for this work, and has been fitted with a range of transducers. These include:

- a. Sprocket hub units to give sprocket speed and torque.
- b. Hull and suspension accelerometers.
- c. Torsion bar strain gauges.
- d. Damper pressure gauges.

A considerable amount of data has been collected for this vehicle.

4.2 Shettain Trials.

This vehicle was not under the authors' control and hence only instrumentation which could be fitted easily and removed without modification to the vehicle was possible. This was primarily accelerometers fitted to the front and rear of the hull. The weighted sum and difference of these signals then gave mass centre bounce and pitch accelerations respectively. Cine film taken at 64 frames/second was found to be extremely useful for qualitative analysis and for suggesting reasons for otherwise unexplained features on the accelerometer recordings. The film included a calibrated clock, but attempts to measure displacements by examination of consecutive frames was only partially successful. Runs were completed at three different speeds and at two different values of initial track tension (5).

More recently a spare track link has been reduced in section and strain gauged so that track tension could be measured around the track circuit (6). The connections to the strain gauges are by flying leads and hence to date, only slow speed, straight line, flat ground runs have been possible. The results obtained show that measurement of track tension by this method is perfectly feasible, and the work is continuing. A telemetry system is being developed and will be incorporated in the body of the track link, and will transmit to an aerial attached to the hull.

4.3 The Eighth Scale Model

Because of the obvious difficulty in handling and modifying any full scale tracked vehicle, a model was designed, built and tested (7). It does not represent any particular full scale vehicle, but can be modified easily to represent a wide range of possible vehicles. The scale model is driven by an integral electric motor having an umbilical lead to a sophisticated control system allowing either speed or torque control. As yet it has no steering mechanism.

Accelerometers are fitted to the hull, and potentiometers are fitted to the wheel arm axes. A selected link has been modified to allow measurement of track tension. Appropriate pick up points in the motor control unit allow signals to be recorded which can be calibrated against sprocket speed and torque. At present only preliminary results are available, but the system shows every indication of being an extremely useful validating tool. In particular it will allow the computer model to be validated for operating conditions beyond those currently experienced by the full scale vehicles.

4. TYPICAL RESULTS

This section shows some typical results from work done over a period of several years. During this period the computer model underwent continuous development to suit the various requirements.

Section 4.1 compares some computer model and field trials results to illustrate the degree to which the model agrees with the real vehicle it represents.

Section 4.2 shows some results from computer models used to compare different suspensions and changes to the vehicle layout.

Section 4.3 shows the results of work done to support assessment of the performance of a rotary damper unit.

4.1 Computer Model Validation

The earliest work in this connection used the Suspension Research Vehicle, Fig 1 (a), running over test ramps. The vehicle has four road wheels on trailing arms with torsion bars and tubes. Figs 2 and 3 show the front wheel arm angle relative to the hull, and the hull pitch angle respectively. The computed and measured results show generally good agreement, although it is noted that the real vehicle appears to have a lower pitch frequency than the computer model vehicle. It is believed that this may be due to the fitted track tension tending to lift the end road wheel stations, thus reducing the contribution which their torsion bars make to the pitch stiffness. The computer model should take account of this if the track characteristics are correctly assessed, and this is still being investigated. A further difficulty is that the vehicle pitch moment of inertia and mass centre position are seldom known accurately.

Fig 4 shows SRV3 traversing part of a random course. The real vehicle speed of 2.4 m/s was the fastest that could be sustained over what is a very severe course. Again the agreement in terms of hull pitch angle is seen to be good in respect of both amplitude and frequency.

Fig 5 shows some results for a Chieftain Main Battle Tank, Fig 1 (b). This vehicle has six road wheels, interconnected in pairs with wheels mounted alternatively on leading and trailing arms. A nest of coil springs is fitted between wheel pairs. The computed and measured acceleration levels for vertical motion of the mass centre agree well. Fig 6 shows the displacement of all six wheels together with the mass

entre vertical displacement and pitch angle. The wheel displacement traces also show where the rebound stop was active. Photographic recording of the field trial gave extremely good qualitative agreement, especially where the road wheels are clear of the ground and are supported either by the rebound stop or by the track.

Figs 7 and 8 show some preliminary results from the scale model vehicle, Fig 10c. This vehicle has six road wheels mounted on trailing arms, with coil springs between the wheel arms and the hull. The measured acceleration signals shown in Fig 7 have been filtered at approximately 1 Hz to remove structural vibration responses. The model speed of 1.2 m/s scales to a full size vehicle speed of approximately 6 m/s, and the repeated ramps scale to 0.4 m, thus representing a very severe condition. The general shapes of the measured and computed accelerations and wheel arm angles are in good agreement, although the results from the front wheel station suggest that the computer model includes too much damping or friction. Further studies with the scale model are in progress.

4.1 Computer Predictions

A wide range of predictions have been made. Fig 9 shows one such example (courtesy of Vickers Defence Systems) for a light tracked vehicle, which compares two different suspension systems. The vehicle is traversing a series of 2 m sinewaves at 1.5 m/s, and hull acceleration and front wheel displacement are used as the comparison criterion. The improvement offered by the particular Hydrogas system over the torsion bar system is clearly evident, but it should be noted that the systems represent two very different build standards; in particular the wheel travel and damping are not the same for each system. The comparison is not intended to imply that Hydrogas suspensions in general are better than torsion bar suspensions. It is not possible to state how accurate the predicted levels are, but the previous validation of the computer model allows the two systems to be ranked with confidence.

As stated earlier the track plays an important role in determining the vehicle response to terrain disturbance. This is particularly true in heavy going. Fig 10 shows the effect of front and rear drive sprocket on pitch response. When the drive is at the rear, the vehicle assumes a steady response on flat ground of about 2 degrees, nose up, and subsequent pitch response to the disturbance is increased. When the drive is at the front this effect is negligible.

4.2 Rotary Damper Performance

To achieve the required level of damping on tracked vehicles results in high damper loads and a high rate of heat generation. The concept of a rotary damper bolted to the hull at the wheel arm pivot is an attractive compact solution. Fig 11 shows some predictions for wheel arm angle, wheel arm angular velocity and damper torque for a rotary damper fitted to a light tracked vehicle, (courtesy of Hortsman Defence Systems). At the lower speed of 1.2 m/s the action of the "blow-off" valves in the two directions to limit the damper torques is clearly evident.

At the higher speed of 3.4 m/s the wheel arm angular velocity, and hence

the damper fluid flow rate, are such that the damper is operating on the blow-off valve characteristic and very large torques can now be generated. It should be noted, however, that the obstacle is rather abrupt and that high angular velocities are to be expected. Even so the predicted velocities are somewhat higher than those reported by Hortsman Defence Systems, and this difference is being investigated. Measured pressures on the real damper show lags at the blow-off pressure and in the transition from positive to negative velocity; this opens up the possibility of frequency dependent damping. These lags are not shown in this particular prediction.

5. CONCLUSIONS

The validation work described and the results obtained show clearly that computer modelling of tracked vehicles can be quite accurate, and an extremely useful design tool for investigating competing designs and the effects of design modifications.

The particular model developed is flexible and easy to use. The modular structure of the program allows easy modifications to accept different vehicle configurations, and to output a wide range of predicted responses.

The model also allows further development and adaption to new problems, in particular investigation of the vehicle response to firing its guns (8,9).

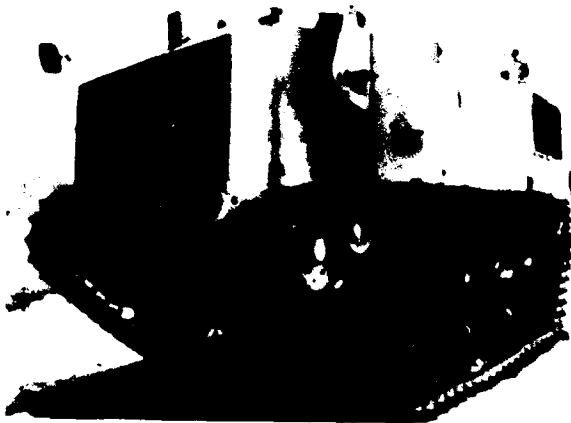
The model described in this report and a transmission simulation model (10) are being combined to give a more realistic vehicle model which can respond to engine throttle and gear change demands as well as to ground profiles.

REFERENCES

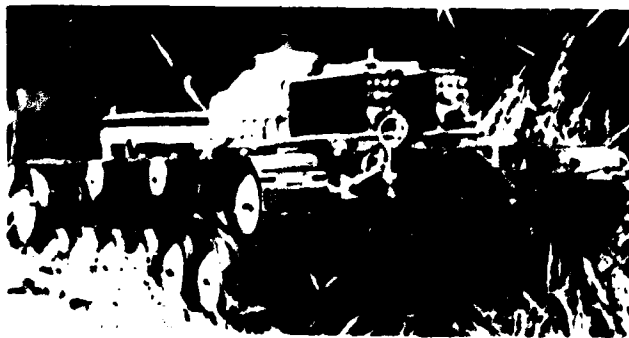
1. MORRISON R A Polygonal Action in Chain Drives. *Machine Design*, Sept 1952.
2. FAWCETT J N and NICOL S W. The Influence of Lubrication on Tooth-Roller Impacts in Chain Drives. *Proc Inst Mech Engrs*, 191, (21), 1977, 271-5.
3. FAWCETT J N and ROBERTSON B. Dynamic Behaviour of Tank Tracks. Final Report under MOD contract 2043/057, MVEE, Chertsey, Surrey, June 1981.
4. FARMILLO R. Vehicle Track Dynamics: The Prediction of Track Link Kinematics by Computer Simulation. Royal Military College of Science, Shrivenham, Swindon, Wilts, Tech Note MD/TM 25.
5. FARMILLO R. Unpublished work.
6. WALKER A.A. Measurement of Tracked Vehicle Track Tension. Res Project Report 26, June 83. Royal Military College of Science, Shrivenham, Swindon, Wilts.
7. MARKS P. The Construction and Testing of a Model for Track and Suspension Analysis. MSc Project Report 11 MVT/2, Sept 1983, Royal Military College of Science, Shrivenham, Swindon, Wilts.
8. BENNETT M D and PENNY P H G P. Computer Simulation of Vehicle Gun Stability. Royal Military College of Science, Shrivenham, Swindon, Wilts. Tech Note MD/14, March 1983.
9. BENNETT M D and PENNY P H G P. Computer Simulation of Vehicle-Gun Stability. A Comparison between two Light Vehicles. Royal Military College of Science, Shrivenham, Swindon, Wilts. Tech Note MD/20, July 1983.
10. PENNY P H G P and BENNETT M D. Tracked Vehicle Performance Using a Simple Computer Simulation Model. Royal Military College of Science, Shrivenham, Swindon, Wilts. Tech Note MD/15, June 1983.



a. Chieftain Main Battle Tank.



b. Suspension Research Vehicle (SRV 3).



c. Model Tracked Vehicle.

Fig.1 VEHICLES USED FOR EXPERIMENTAL WORK.

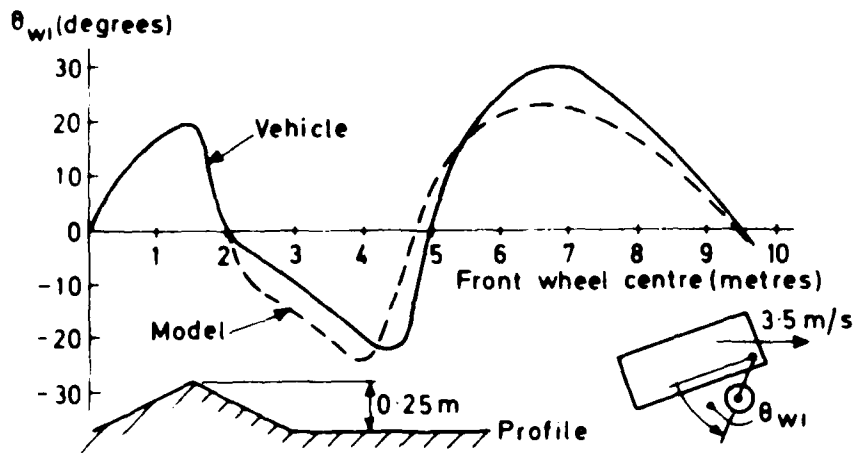


**Fig. 2 FRONT WHEEL ARM ANGLE - DISPLACEMENT
RELATIVE TO HULL (SRV 3)**

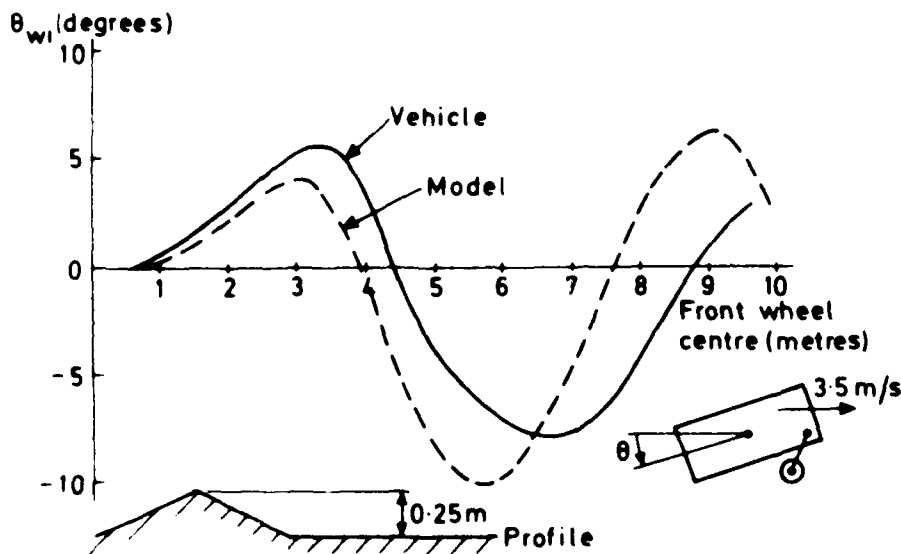


Fig 3 HULL PITCH ANGLE (SRV 3)

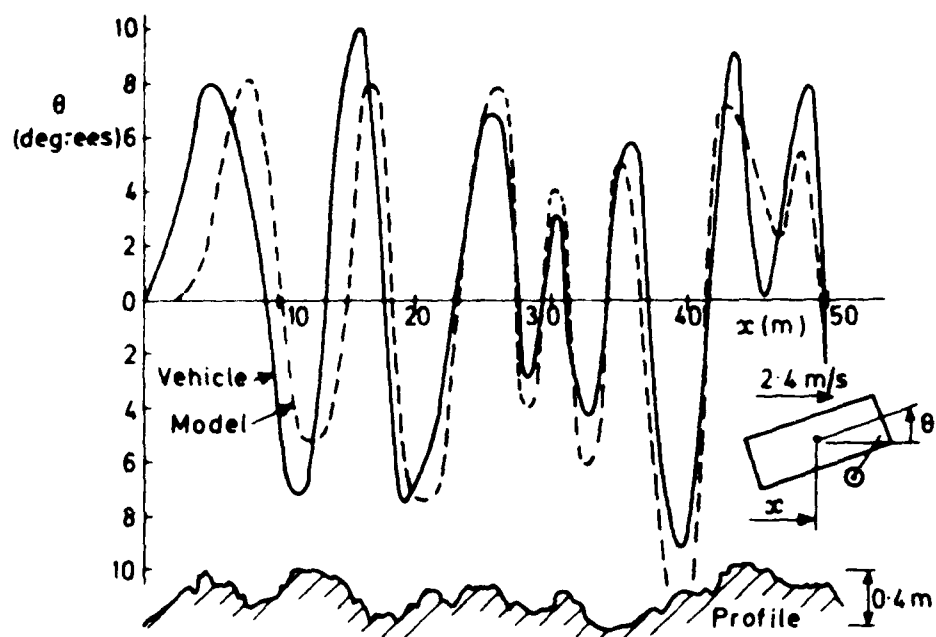


Fig. 4 HULL PITCH ANGLE (SRV3)

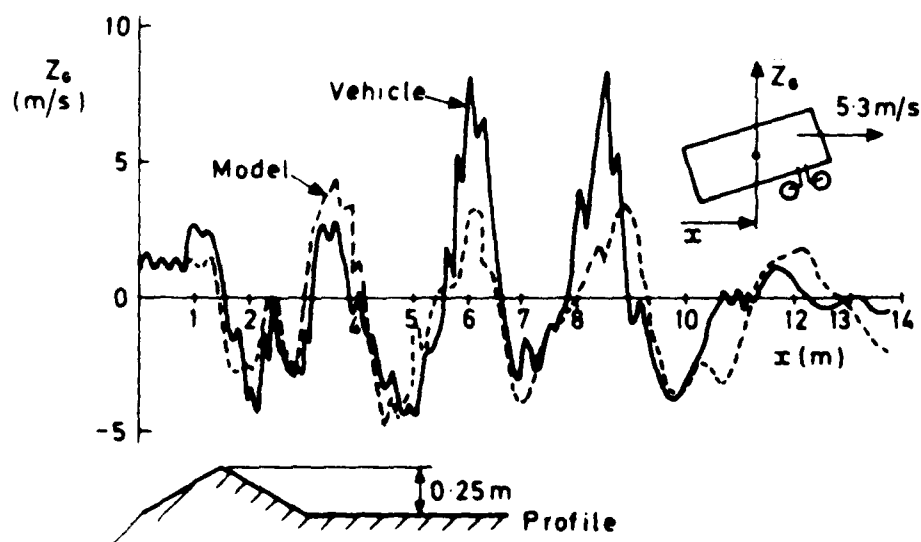


Fig. 5 MASS CENTRE - VERTICAL ACCELERATION (CHIEFTAIN)

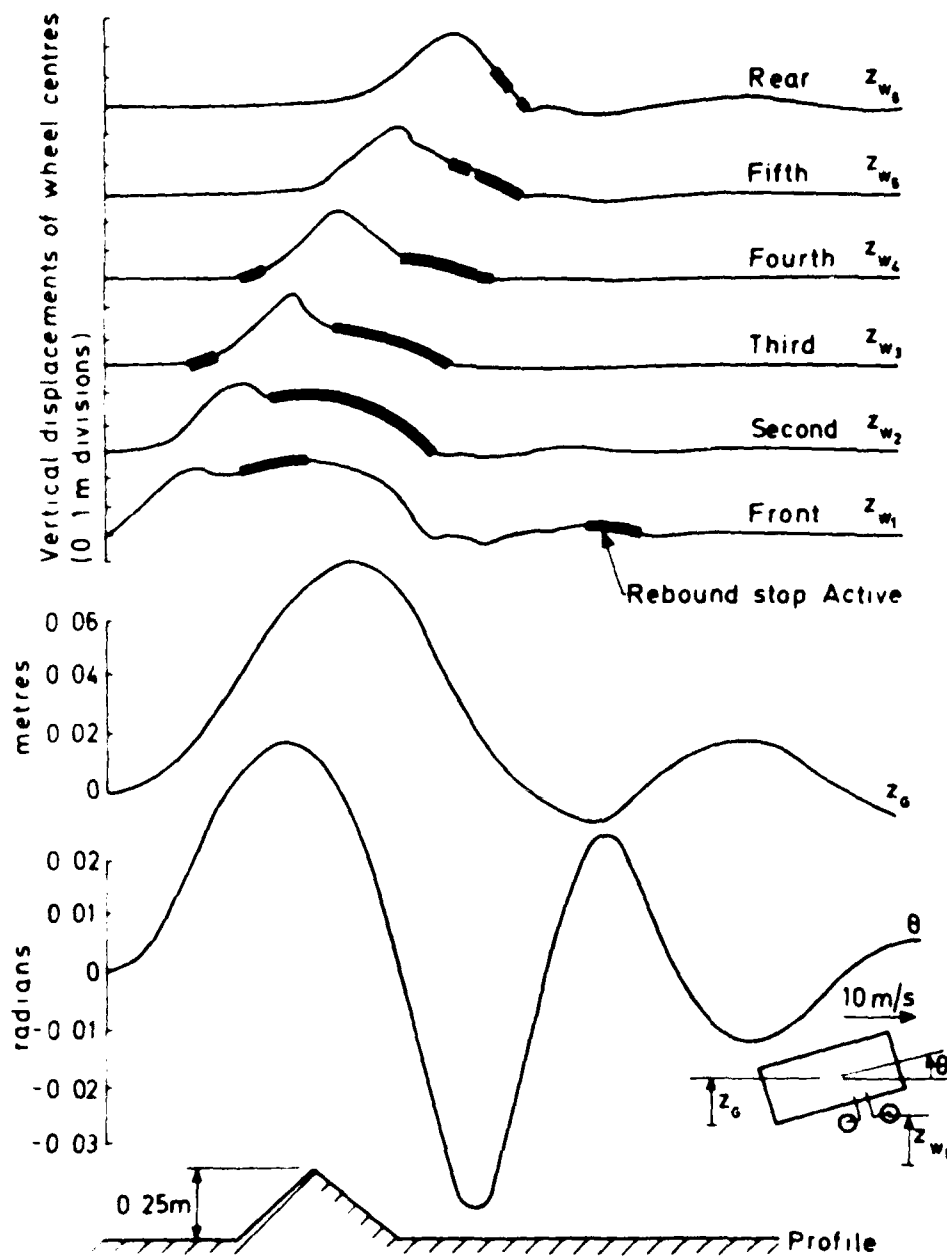


Fig 6 HULL AND WHEEL DISPLACEMENT-COMPUTER
MODEL PREDICTIONS (CHIEFTAIN)

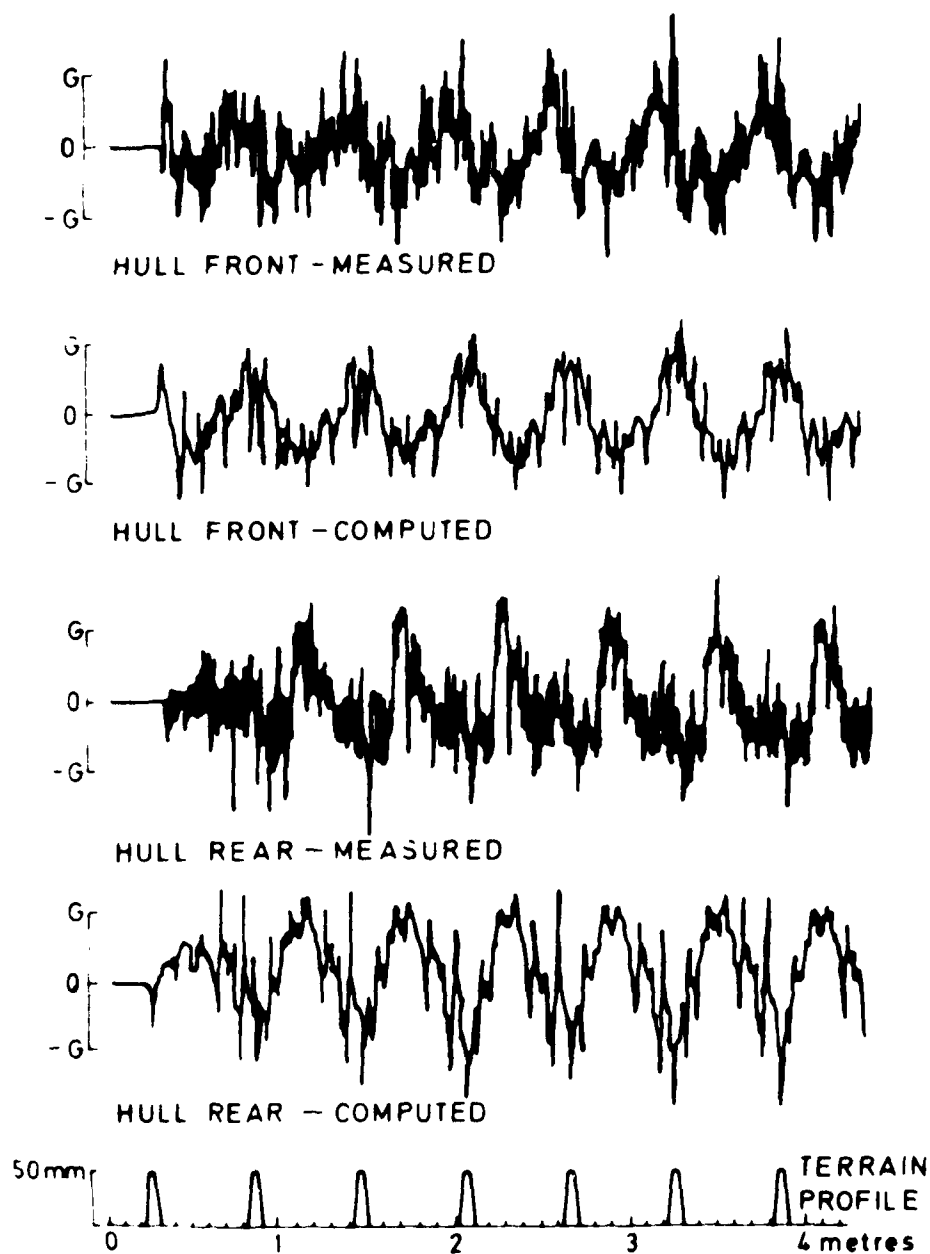


Fig 7 COMPARISON BETWEEN MEASURED AND COMPUTED
HULL ACCELERATION AT MODEL SPEED OF 1.9 m/s

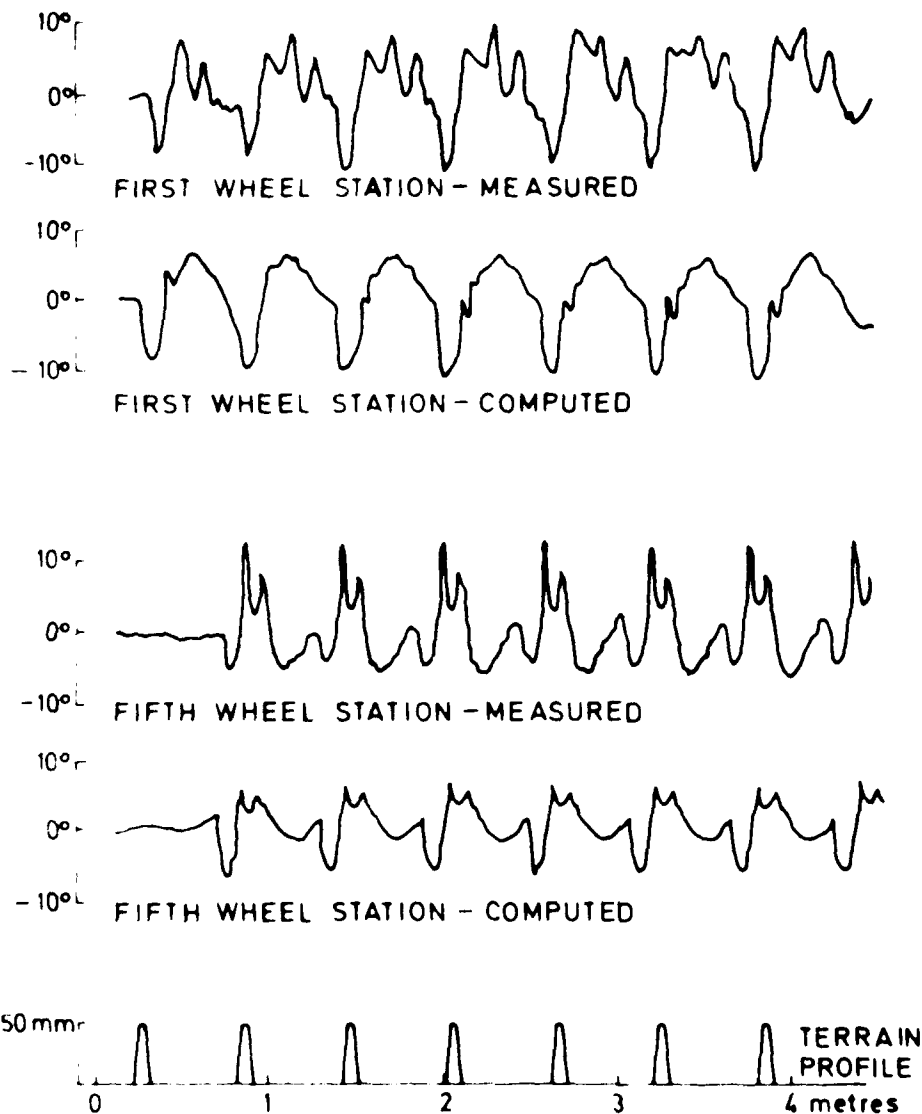
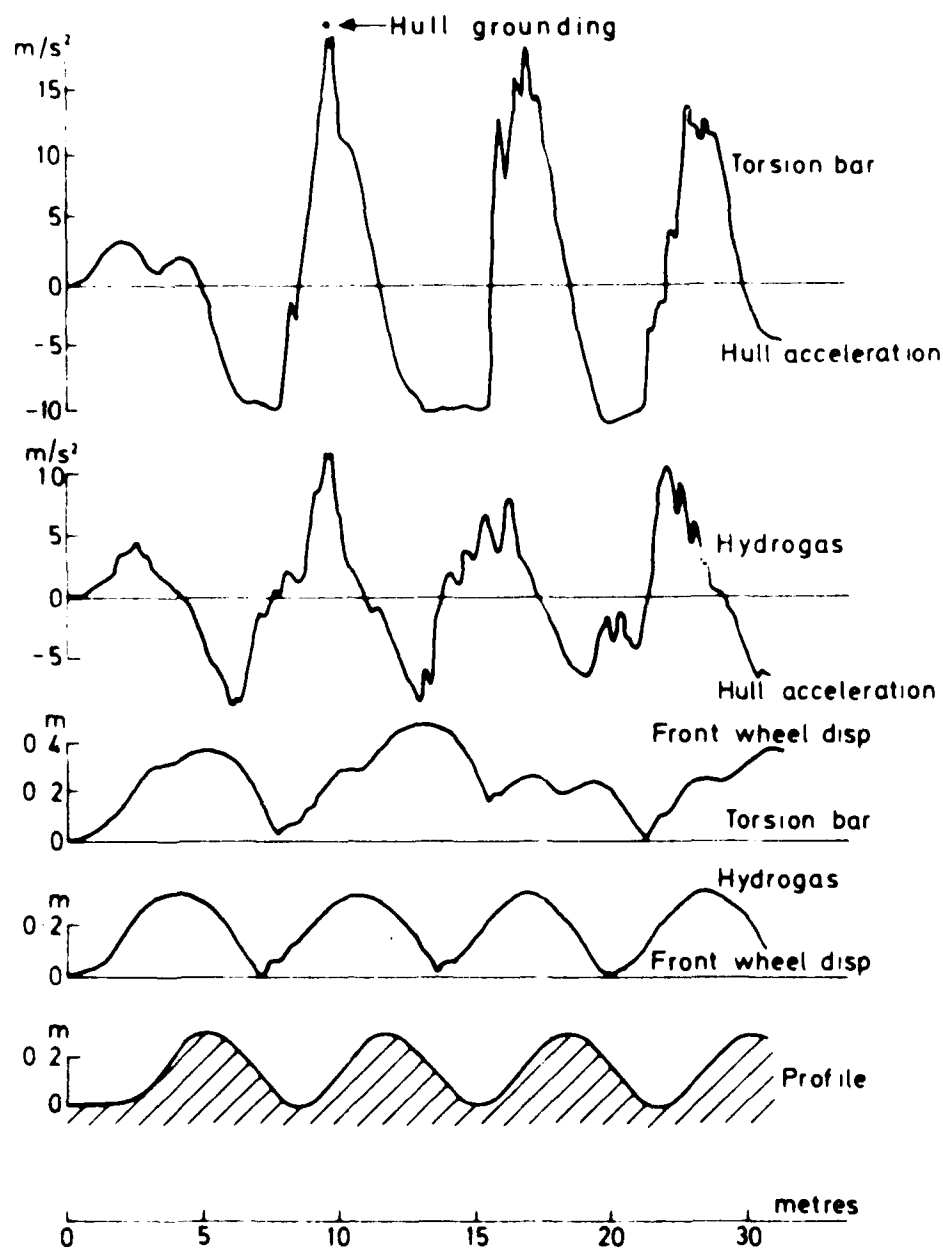
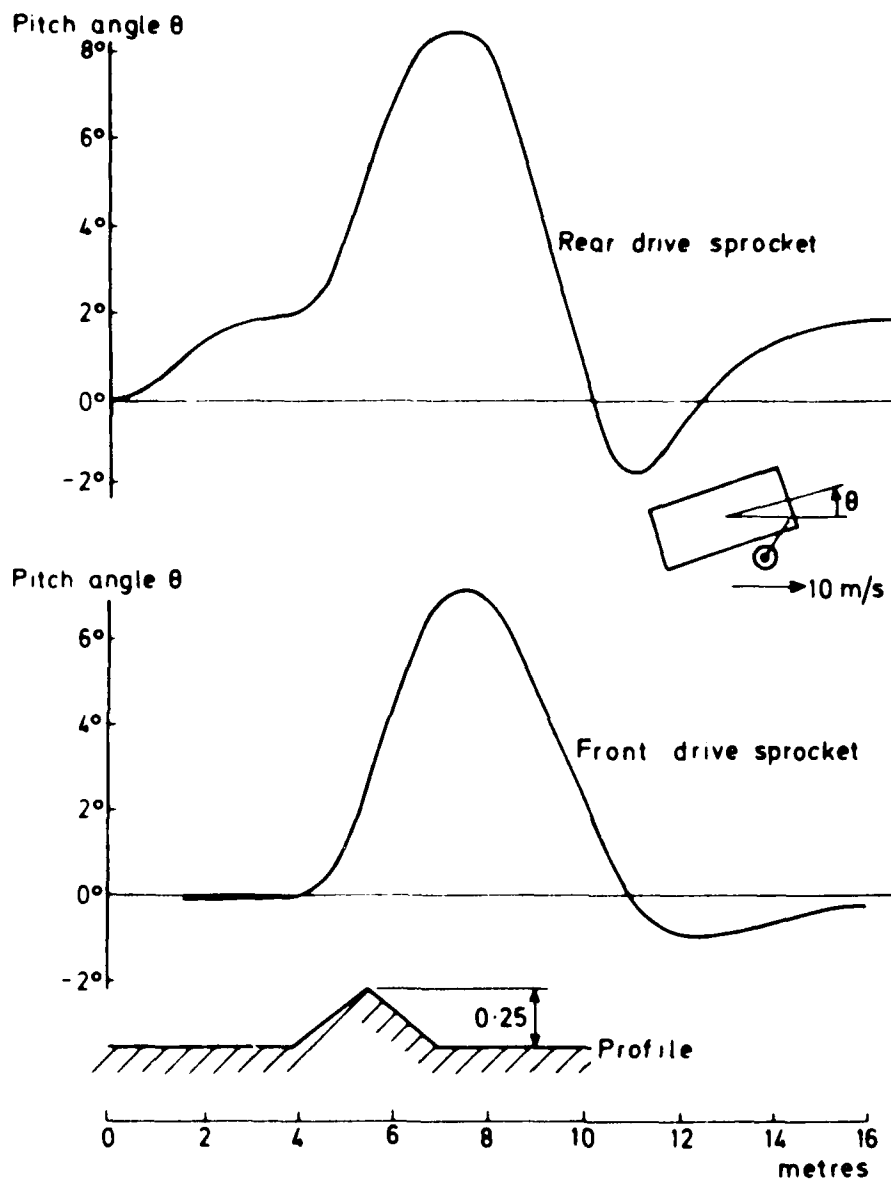


Fig. 8 COMPARISON BETWEEN MEASURED AND COMPUTED
WHEEL ARM ANGLES AT MODEL SPEED OF 1.9 m/s
(ANGLES ARE SHOWN RELATIVE TO ARM EQUILIBRIUM
POSITION)



**Fig 9 COMPUTER COMPARISON BETWEEN TORSION
BAR AND HYDROGAS TRAILING ARM SUSPENSIONS
ON 16 TONNE TRACKED VEHICLE TRAVERSING
7m SINEWAVES AT 10 m/s**



**Fig. 10 EFFECT OF FRONT OR REAR DRIVE SPROCKET
ON PITCH ANGLE ON 16 TONNE TRACKED
VEHICLE AGAINST HIGH ROLLING RESISTANCE**

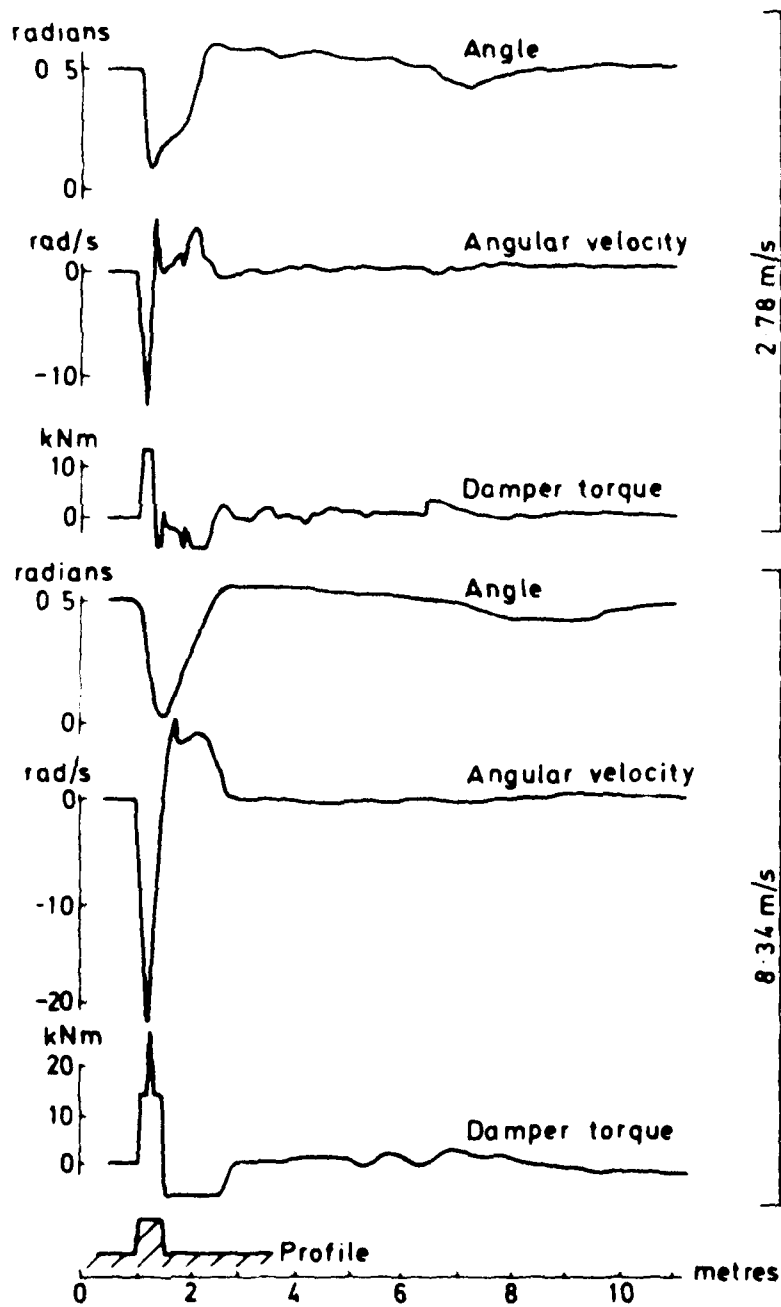


**Fig. 11 COMPUTER PREDICTIONS FOR ROTARY
DAMPER PERFORMANCE ON A LIGHT
TRACKED VEHICLE**

DESIGNING OFF-ROAD VEHICLES WITH GOOD RIDE BEHAVIOUR

D.N.L. HORTON, D.A. CROLLA

Department of Mechanical Engineering, University of Leeds, Leeds, U.K.

ABSTRACT

The results from simple ride vibration models of off-road vehicles are examined in terms of natural frequencies, mode shapes, frequency response and response to realistic ground inputs.

Despite the limitations of such models inherent in the assumptions, it is concluded that they provide designers with useful information about the dominant features of vehicle ride response.

1. INTRODUCTION

The background to the off-road vehicle ride problem is well documented and understood. Reviews of relevant work on the topic appear at intervals and re-emphasise the effects of poor ride behaviour, e.g. operator discomfort, spinal injuries, limiting of operating speed, premature fatigue failures, etc. Agricultural tractors often lead the list of vehicles which transmit high acceleration levels to the operator (or other cargo), but there are plenty of other examples in the earth-moving, forestry and military industries.

In general, there are only three methods of isolating the operator: by suspending his seat, the cabin or the whole vehicle. Again, the merits and disadvantages of each of these systems has been thoroughly discussed. In practice, the major factor in selecting one of these systems is cost, so that agricultural tractors are universally equipped with a seat suspension, whereas military vehicles have axle suspensions, often of a sophisticated design.

A designer ought to know something about the ride behaviour of his vehicle at the design stage. Consequently, much effort has been invested in developing mathematical models to predict ride behaviour. However, there appears to be a gap between the sometimes very sophisticated models that have been developed and their transformation into useful design information. Certainly, such models have limitations, in particular, because the precise nature of the tyre/ground interaction and the resulting vibrational response is not understood. But despite this, even simple vehicle models do indicate the primary features of the ride response.

The object of this paper is to try and exploit the results obtained from simple vehicle models and examine whether they lead to design guidelines. Three vehicles are studied:

- (1) a 5t agricultural tractor
- (2) a 5t off-road transport vehicle, unladen
- (3) a 5t off-road transport vehicle with a 5t payload.

The model restricts motion to the symmetry plane of the vehicle giving three degrees of freedom, namely vertical (z), pitch (θ), and longitudinal (x) (see Fig. 2). This restriction simplifies the equations of motion and the inputs are reduced from four wheels to two, front and rear, but it has the disadvantage of neglecting lateral and roll motion. These directions are obviously important in practical terms, but they usually rank as secondary aspects of behaviour compared with the bounce, pitch and longitudinal directions.

2. NOTATION

c	damping coefficient, kNsec/m
C	matrix of damping terms ($n \times n$)
f	frequency, Hz
G	ground roughness coefficient
$H(\omega)$	frequency response function
k	stiffness coefficient kN/m
K	matrix of stiffness terms ($n \times n$)
l	vehicle wheelbase, m
m	number of inputs
M	matrix of masses and inertias ($n \times n$)
n	number of degrees of freedom
$S_x(\Omega)$	displacement spectral density of variable x , $m^2/(\text{cycle}/m)$
$S_x(f)$	displacement spectral density of variable x , m^2/Hz
$S_x(f)$	acceleration spectral density of variable x , $(m/\text{sec}^2)^2/\text{Hz}$
u	input vector, dimension m
U_1, U_2	matrices relating input displacement and rate of change of displacement to vehicle motion ($n \times m$)
V	vehicle speed, m/sec
x	state vector, dimension n
X	forward distance from vehicle centre of mass
z	downward direction
Z	downward distance from vehicle centre of mass
θ	pitch coordinate
σ	root mean square
ω	frequency, rad/sec
Ω	wave number, cycles/m

Suffices:	F	front axle
	R	rear axle
	S	seat (when applied to X, Z)
		suspension (when applied to k, C)
	x	input variable
	y	output variable

3. TYRE/GROUND INTERACTION

Little work has been done on the vibrational characteristics of off-road tyres, either on or off road, but a review of current knowledge appears in [1]. The particular problems relating to this field are:

- diversity of off-road tyres
- non-linear tyre characteristics
- the need to consider longitudinal as well as vertical tyre/ground forces
- the deformable nature of off-road surfaces.

Of the many tyre models which have been proposed the simplest is the point contact model (Fig. 1a) which has been used extensively in on-road vehicle dynamics. Its use, however, needs careful consideration since it over-emphasises the effect of any high frequency components in the surface over which it travels. For off-road surfaces containing sharp irregularities the point contact model is inadequate but may be modified to filter out higher frequencies; examples are the fixed footprint and rigid treadband models (Figs. 1b, c). Output from these models is equivalent to that from a point contact model traversing an appropriately smoothed surface. Off-road surfaces also give rise to significant longitudinal forces at the tyre, for which the above models are inadequate. The radial spring model (Fig. 1d), of which there are various forms, goes some way towards predicting these forces, and if tangential components are included it has the potential to model interaction between a tyre and a deformable surface.

In the frequency domain idealised surfaces decrease in displacement amplitude and increase in acceleration amplitude as frequency increases. The filtering effect of tyres on high frequencies can be formulated in a tyre enveloping function (Fig. 1e) applied to the ground input spectrum, although the exact form of such a function is open to question. However, the frequency response of the vehicle itself, which decreases rapidly with increasing frequency, acts as an effective filter when considering vehicle acceleration levels, and for this reason the point contact model may not be as inadequate as is commonly imagined.

4. THEORETICAL BACKGROUND

4.1 Linearisation of Models

When predicting vehicle natural frequencies and modes of vibration the tyres are treated as linear damped springs in both the vertical and longitudinal directions. However, longitudinal components of ground input will be neglected. These have only a secondary effect and difficulties still exist in describing their relationship with the vertical components.

For motion restricted to small excursions from steady state values, and for tyres and suspensions treated as linear spring/damper combinations, the equations of motion of the vehicle assume a linear form

$$M\ddot{\underline{x}} + C\dot{\underline{x}} + K\underline{x} = U_1 \underline{u} + U_2 \dot{\underline{u}} \quad (1)$$

where \underline{x} is the state vector of dimension equal to the number of degrees of freedom, n ; and \underline{u} is the input vector of dimension equal to the number of inputs, m . M , C and K denote respectively the mass, damping and stiffness matrices; U_1 and U_2 are matrices relating input displacement and rate of change of displacement to the vehicle motion.

Equation (1) may be transformed into a first order system of dimension $2n$ in the form

$$A\dot{\underline{y}} + B\underline{y} = C\underline{u} + D\dot{\underline{u}} \quad (2)$$

4.2 Natural Frequencies and Modes of Vibration

The n natural frequencies of the vehicle may be obtained from the eigenvalues of the matrix $A^{-1}B$, with A and B defined in equation (2). The corresponding eigenvalues define n modes of vibration, each associated with a natural frequency. Each mode may be visualised as oscillation about a point in the x - z plane. Such a point situated in or very near

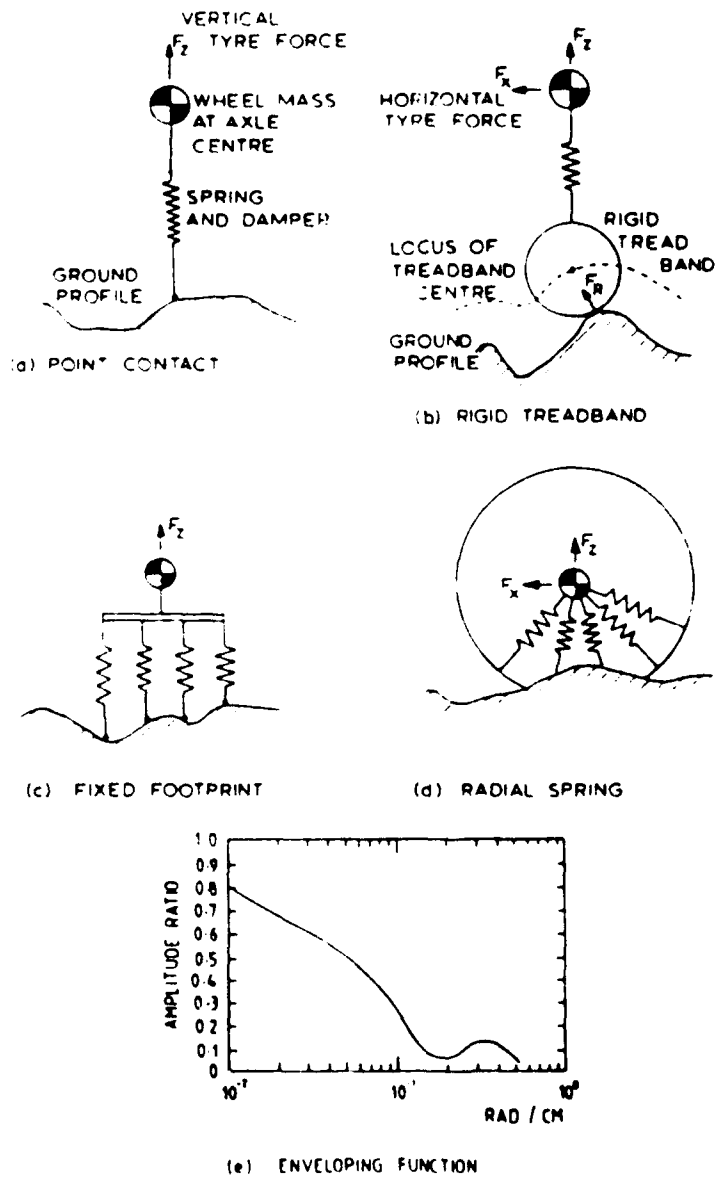


Fig. 1 Tyre Models

the vehicle denotes predominantly pitch motion; a point forward or behind the vehicle denotes vertical motion; and a point above or below denotes longitudinal motion. For centres of oscillation well away from the vehicle the actual distance is unimportant; the direction from the vehicle then indicates the amount of coupling between vertical and longitudinal modes.

4.3 Frequency Response

Response of the vehicle to a unit displacement input over a range of frequencies may be obtained by Laplace transforming equation (1) to give

$$(Ms^2 + Cs + K)X(s) = (U1 + U2s) \underline{U}(s) \quad (3)$$

and then substituting $s = e^{i\omega t}$ to give

$$\underline{X}(i\omega) = \frac{-M\omega^2 + C1\omega + K}{(U1 + U2i\omega)}^{-1} \underline{U}(i\omega) \quad (4)$$

$$\text{or } \underline{X}(i\omega) = H(\omega) \underline{U}(i\omega) \quad (5)$$

The frequency response function $H(\omega)$ may then be calculated over a range of frequencies, ω .

4.4 Response to Ground Inputs in the Frequency Domain

The statistical properties of many surface irregularities may be formulated in a displacement spectral density function of the form, [2],

$$S_x(\Omega) = G \Omega^{-p} \quad (6)$$

where Ω = wave number, cycles/m

$S_x(\Omega)$ = displacement spectral density, $m^2/(\text{cycle}/m)$

G = ground roughness coefficient

Agricultural surfaces have been measured and found to be representable in this form with G in the region 10^{-4} to 10^{-5} [3], and the exponent, p , typically around 2.

In terms of frequency, f , the displacement and acceleration spectral densities become

$$S_x(f) = V G f^{-2} \quad (7)$$

$$S_{\ddot{x}}(f) = (2\pi f)^4 S_x(f) = 16\pi^4 V G f^2 \quad (8)$$

where V = vehicle speed, m/sec

and $f = V\Omega$, Hz

Output spectral densities S_y are related to S_x through the frequency response H and its complex conjugate H^* , in the form

$$S_y(\omega) = H(\omega) S_x(\omega) H^*(\omega) \quad (9)$$

where $\omega = 2\pi f$

$$\text{and } S_y(f) = 2\pi S_y(\omega) \quad (10)$$

Root mean square displacement, σ_y , of an output variable y is given by

$$\sigma_y^2 = \int_0^{\omega_{\max}} S_y(\omega) d\omega \quad (11)$$

with ω_{\max} chosen so that higher frequencies have negligible effect.

A similar expression holds for $\sigma_{\ddot{y}}$ in terms of $S_{\ddot{y}}$.

The spectral density function is also used to measure amplitude of vibration associated with given frequencies. Within a specified bandwidth either side of the frequency of interest the area under the spectral density curve gives mean square displacement (or acceleration) over this bandwidth.

When using a vehicle model in which rear wheel input is equal to front wheel input delayed by l/V seconds, where l is the wheelbase, then the resulting output spectral density curves exhibit a rippled effect. A component in the ground spectrum of wavelength l/n metres ($n = 1, 2, \dots$) will result in the front and rear wheels bouncing in phase with frequency nV/l Hz, with no contribution in pitch. Components with wavelength $l/(n + \frac{1}{2})$ metres have the opposite effect, enhancing pitch at frequencies $(n + \frac{1}{2})V/l$ Hz. The effect on the output spectrum is seen as a superimposed periodic component of wavelength V/l Hz.

4.5 Response to Ground Input in the Time Domain

The equations of motion (1) may be integrated to give a time history $x(t)$ for a given speed and ground profile, such as a surface feature or a random profile generated from a spectral density function. Time histories may be compared for different parameter values but for the ride estimation they are of limited use, showing only dominant frequencies and maximum excursions from initial conditions. A better idea of frequency content is obtained by transforming the time history to the frequency domain using Fourier analysis, to give spectral densities. One advantage of this method is that non-linear vehicle equations may be used to generate the time history, whereas the methods of the previous section require linear equations.

5. ANALYSIS OF THE UNSPRUNG VEHICLES

The three vehicles chosen for analysis are:-

- (1) A typical large (5t, 90 kW) four wheel drive agricultural tractor.
- (2) A possible configuration for an off-road transport vehicle of 5t unladen weight, with a front-mounted cab.
- (3) Vehicle (2) with a 1t payload which alters the position of its centre of mass.

The coordinate system and parameter necessary to describe the vehicle model are shown in Fig. 2, with values for the three vehicles given in Table 1. Unladen weights and tyre characteristics are deliberately set equal to facilitate later comparison of axle suspensions.

Natural frequencies are given in Table 2 and indicate a dependence more on weight than on configuration. Corresponding centres of oscillation are shown in Fig. 3. In each case, the three modes are only weakly coupled; each can be identified as a predominantly vertical, pitch or longitudinal mode. The mode shapes for all three vehicles are noticeably similar despite the apparent geometrical differences.

Since ride information is required at the operator's seat position, frequency response and spectral density are referred to this point. The vertical and longitudinal seat motions z_s and x_s are related to the vehicle coordinates z, θ, x (see Fig. 2) by

$$z_s = z - x_s \theta \quad (12)$$

$$x_s = x - z_s \theta \quad (13)$$

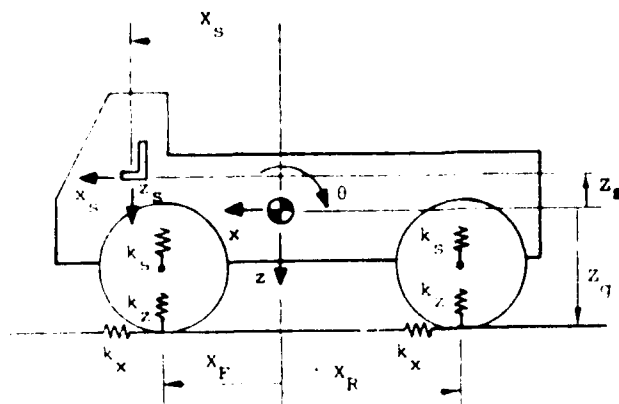


Fig. 2. Vehicle coordinate system and parameters

Table 1. Vehicle parameter values (see Fig. 2 for symbols)

Vehicle	1	2	3
Body mass (kg)	4000	4000	9000
Body inertia ($\text{kg}\cdot\text{m}^2$)	5000	8000	18000
Front axle mass (kg)	250	500	500
Rear axle mass (kg)	750	500	500
Total mass (kg)	5000	5000	10000
Wheelbase (m)	2.4	3.6	3.6
x_F (m)	1.0	1.6	1.9
x_R (m)	-1.4	-2.0	-1.7
x_S (m)	-0.6	1.4	1.7
z_s (m)	0.9	0.9	1.5
z_g (m)	-0.5	-0.5	0.1
k_x (kN/m) per axle	900	900	900
k_z (kN/m) per axle	900	900	900
c_x (kNsec/m) per axle	5.0	5.0	5.0
c_z (kNsec/m) per axle	5.0	5.0	5.0

Frequency response of vertical seat motion resulting from a unit vertical input at the front wheel is shown for the three vehicles in Fig. 4. Again there is an overall similarity between the three vehicles. In each case the dominant responses arise from the two lower frequencies associated with vertical and longitudinal motion, with relatively little contribution from the pitch mode. The difference in amplitude of the 4 to 5 Hz peak between the tractor (1) and unladen transport vehicle (2) reflects the position of the associated pitch centre with respect to the seat. Since the centre is further horizontally from the seat in vehicle 2, the contribution to seat vertical motion, for a given pitch amplitude, will be greater. The effect of loading the transport vehicle is to lower the natural frequencies and also to sharpen the peaks of the frequency response, indicating a reduction in effective damping arising from the increased mass.

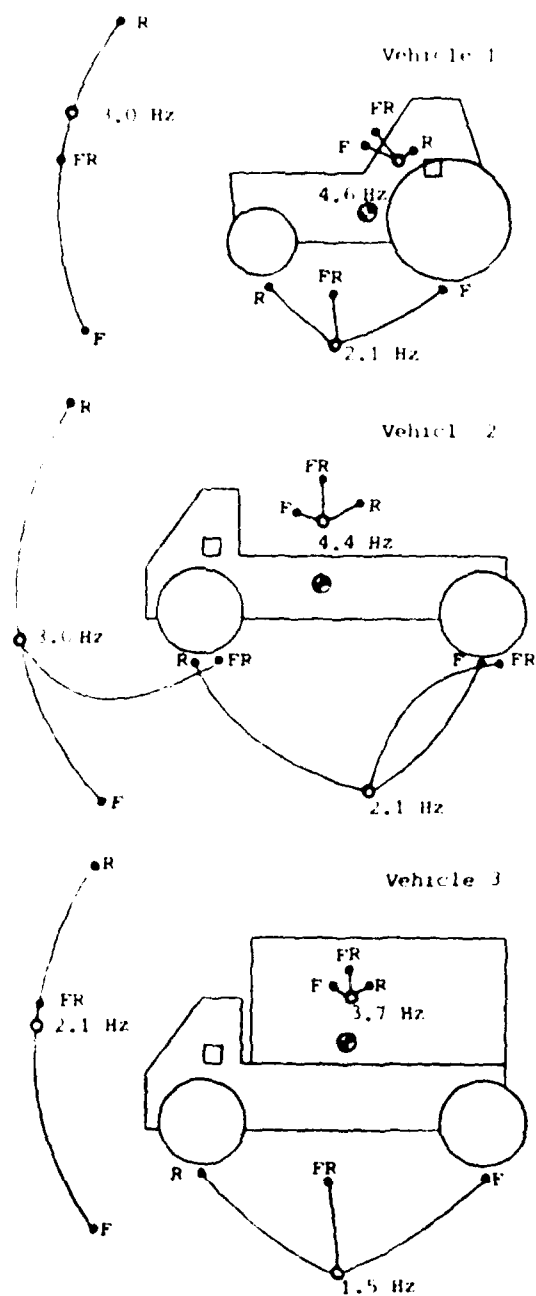


Fig. 3 Centres of rotation with natural frequencies for the three vehicles, lines indicate change in position of the centres as suspension is added, up to a value of $k_s = 100 \text{ kN/m/axle}$, $c_s = 10 \text{ kN sec/m/axle}$. F = front, R = rear, FR = full suspension

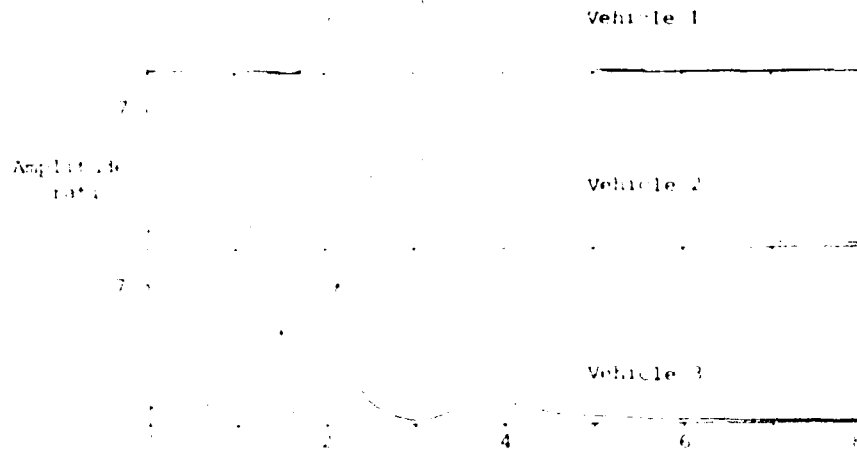


Fig. 4 Frequency response of vertical seat motion for a unit vertical input at the front wheel, Vehicles 1, 2 and 3.

Vehicle	1			2			3		
Natural frequencies	2.1	3.0	4.6	2.5	3.0	4.4	1.9	2.1	3.7
Full suspension:									
$k_s = 40, c_s = 40$	1.7	2.4	4.4	2.1	2.4	4.2	1.2	1.6	3.5
$k_s = 40, c_s = 20$	1.4	1.9	4.1	1.7	1.9	4.0	1.0	1.2	3.4
$k_s = 40, c_s = 10$	1.8	1.1	4.1	1.1	1.0	3.8	0.6	0.7	3.3

Table 1. Natural frequencies (Hz) for the three degrees of freedom of the vehicle body. Values of suspension stiffness, k_s , are in kN/m/axle; values of suspension damping, c_s , are in kN sec/m/axle.

Frequency response analysis provides a useful tool for estimating the effects of changing vehicle parameters. New parameter values are inserted in equation (1) and fast, efficient computer routines exist to generate natural frequencies, mode shapes and frequency response curves. This enables the vehicle designer to quickly build up a simple picture of the vehicle vibrational characteristics.

Frequency response to single inputs, however, cannot predict the relative amplitudes of vibration associated with each mode under practical operating conditions. A fuller description of these requires a ground input with a prescribed amplitude distribution against frequency, applied to both front and rear wheels. Figure 5 shows the seat vertical acceleration spectral densities resulting from equation (3) applied to an input acceleration profile of the form of equation (8), with speed $V = 7$ m/sec and roughness $Q = 10^{-5}$. The corresponding root mean square and seat

AD-A148 634

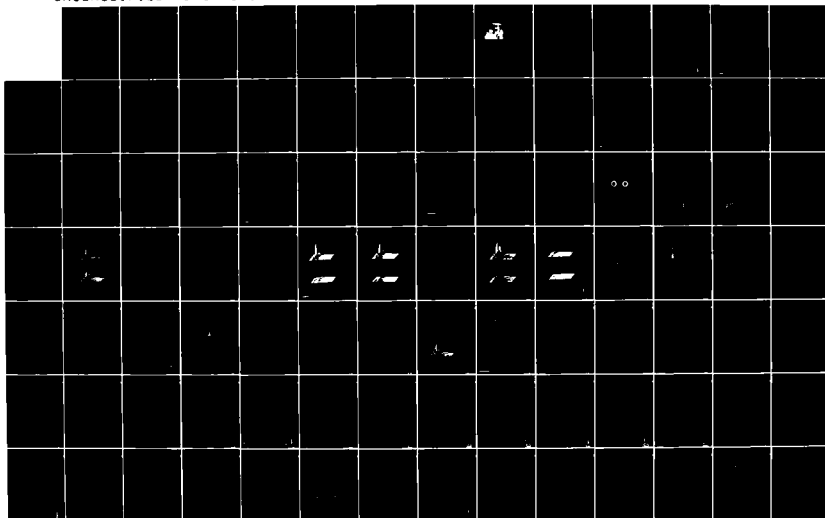
PROCEEDINGS OF THE INTERNATIONAL CONFERENCE ON THE
PERFORMANCE OF OFF-ROAD (U) INTERNATIONAL SOCIETY FOR
TERRAIN-VEHICLE SYSTEMS W J DWYER AUG 84
DAJA45-84-M-0251

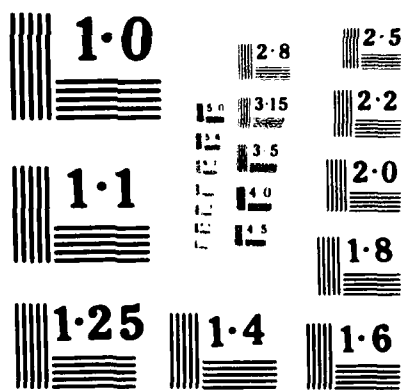
3/6

UNCLASSIFIED

F/G 13/8

NL





vertical acceleration spectral densities are presented in Table 5.

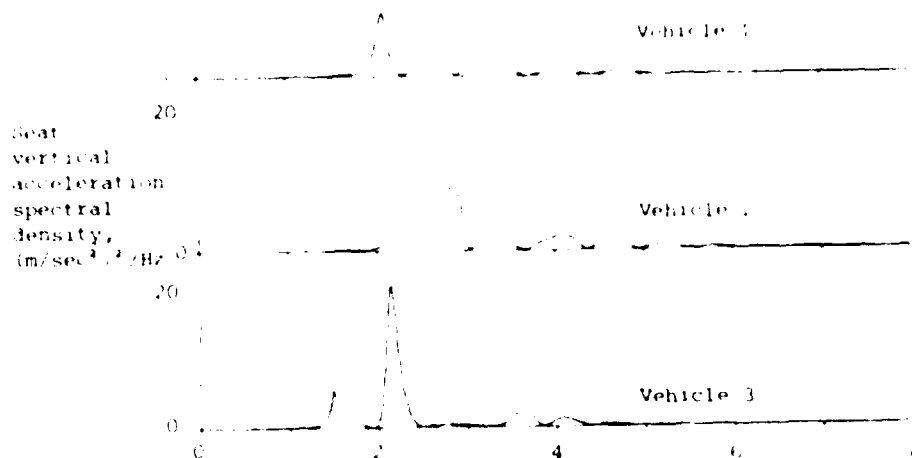


Fig. 5. Vertical seat acceleration spectral densities for an input of roughness $G = 10^{-5}$ at speed $V = 2$ m/sec, Vehicles 1, 2 and 3.

Vehicle	Vertical			Longitudinal		
	1	2	3	1	2	3
Suspension:						
None	2.4	2.8	2.3	2.8	2.1	1.5
Front	2.0	1.7	1.3	1.0	1.4	0.8
Rear	1.5	2.4	2.3	1.2	1.4	1.5
Full	1.0	1.2	0.8	0.8	0.8	0.4

Table 5. Unweighted root mean square vertical and longitudinal seat accelerations (m/sec^2) for vehicles with suspension parameters $k_s = 400$ kN/m, $c_s = 20$ kN sec/m travelling at speed $V = 2$ m/sec over a surface of roughness $G = 10^{-5}$.

The figure indicates the distribution of this acceleration over frequency in such a way that the area under the curve in a given bandwidth represents the mean square seat vertical acceleration over that bandwidth.

The tractor exhibits high acceleration levels around 2.1 Hz, corresponding to the mode of that frequency; and at 3 to 3.5 Hz, which results from a combination of the 3.0 Hz mode and a component from the wheelbase effect (mode 4.4) at 3.3 Hz. It is this effect also which gives rise to the intermediate peak at about 2.5 Hz, and the smaller peaks above 4 Hz. The proximity of the 4.6 Hz pitch centre to the seat results in a negligible contribution to seat acceleration from this mode.

For the unladen transport vehicle the spread of acceleration over frequency is more noticeable, with a significant contribution between 4 and 5 Hz, since the pitch centre is now well behind the seat. The effect of loading is to reduce rms acceleration and concentrate the accelerations into the three natural frequencies, especially the vertical mode at 2.1 Hz, which is enhanced at this speed by a peak at 2.2 Hz due to the wheelbase effect.

If speed is varied from 2 m/sec the peaks produced by the wheelbase effect move along the frequency axis relative to the stationary peaks due to natural frequencies. This will lead to differing patterns of acceleration as these peaks interfere with each other.

6. SUSPENSION DESIGN

To investigate the effects of axle suspension on seat acceleration, the vehicle model was modified to include the suspension elements shown in Fig. 2, with the option of front, rear or full suspension. Table 2 shows the effect of the full suspension on natural frequencies for three values of stiffness and damping, namely:

- (i) $k_s = 900 \text{ kN/m/axle}$, $c_s = 30 \text{ kN sec/m/axle}$
- (ii) $k_s = 400 \text{ kN/m/axle}$, $c_s = 20 \text{ kN sec/m/axle}$
- (iii) $k_s = 100 \text{ kN/m/axle}$, $c_s = 10 \text{ kN sec/m/axle}$

For the soft suspension (iii) compared with the unsuspended vehicles the longitudinal, vertical and pitch frequencies are reduced by factors of about 2.5, 2.0 and 1.1 respectively, independent of the vehicle type. This results in an approximate doubling in the separation of the three frequencies.

Figure 3 shows the effect on the modes of vibration caused by the three suspension options. The patterns for a single axle suspension are similar for all three vehicles. The pitch mode is affected only slightly, the vertical mode moves to include more longitudinal component, and the longitudinal mode moves up to include more pitch. For a suspension on the front axle this last centre moves to a point near the rear axle, and vice versa.

The vehicles behave differently, however, when fully suspended. For vehicles 1 and 3 the patterns are again similar with little change in pitch or vertical modes and the longitudinal mode moving up to a mid-wheelbase position. In contrast, for vehicle 2 the vertical and longitudinal modes each move to a point near the front and rear wheels, respectively.

As a general rule, movement of a mode centre towards the seat will reduce its effect on the vertical and longitudinal motion of the seat. However, the movement of one mode is accompanied by movement of all the others, not necessarily in favourable directions. Here again, the response to real ground inputs provides further insight for the designer.

The effect on rms values is shown in Table 3 for the middle value of suspension stiffness at front, rear and both axles. The table confirms that for suspension to be effective at reducing vertical seat acceleration it needs to be mounted at least on the axle nearest the seat. A front suspension on the tractor or a rear suspension on the transport vehicle have little effect. In contrast, a suspension on either axle will signifi-

cantly reduce longitudinal seat acceleration. These results are highlighted in Fig. 6 which compares the four suspension options for the unladen transport vehicle. A rear suspension reduces higher frequency components while retaining the 2.5 and 3 Hz bounce peak. A front suspension reduces this also and is seen to be almost as good as a full suspension from the operator's point of view.

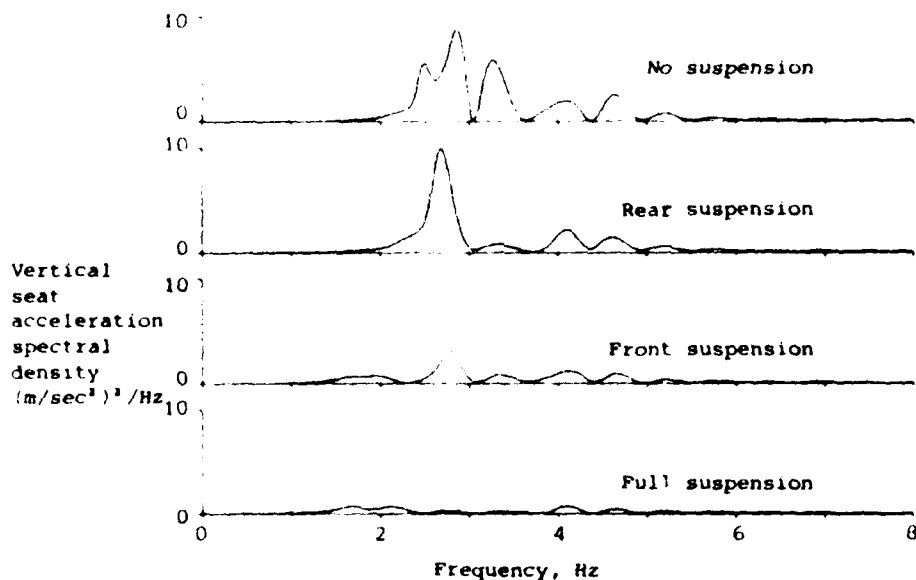


Fig. 6 Vertical seat acceleration spectral density for Vehicle 2, with input as in Fig. 5, for each suspension option. Suspension parameters are $k_s = 400 \text{ kN/m/axle}$, $c_s = 20 \text{ kN sec/m/axle}$.

The disadvantages of a soft suspension is the increased static deflection which it causes. The largest suspension stiffness is set equal to that of the tyres and gives a static deflection of about 25 mm for vehicles 1 and 2, and about 50 mm for vehicle 3. The softest value gives respectively 250 and 500 mm. These may be prohibitively large, especially for the laden transport vehicle, but the value is included here for illustrative purposes. By simulating vehicle behaviour for different values of stiffness and damping, the designer will obtain the necessary information to provide a compromise value.

As an example of a solution in the time domain, Fig. 7 shows a 5 second time history of vertical seat displacement for the unladen transport vehicle crossing a square cut furrow 200 mm deep by 400 mm across, at a speed of 2 m/sec. Since the point contact model was used, the shape of the furrow was modified by application of a rigid treadband to give a smoothed profile (Fig. 7, inset). The solid trace is for the unsuspended vehicle and the dotted trace shows the effect of mounting a full suspension of stiffness $k_s = 400 \text{ kN/m/axle}$. Rms vertical seat displacement is reduced from 17 to 10 mm and acceleration is reduced from 5.6 to 2.1 m/sec². Corresponding values for the unsprung vehicle with an unmodified furrow profile are 74 mm and 19 m/sec², which are clearly unrealistic, as one would expect. This confirms that it is necessary for any ground inputs with significant high frequency components, to either

identify the point contact tyre model, or modify the effective input by, for example, the rigid treadband approximation

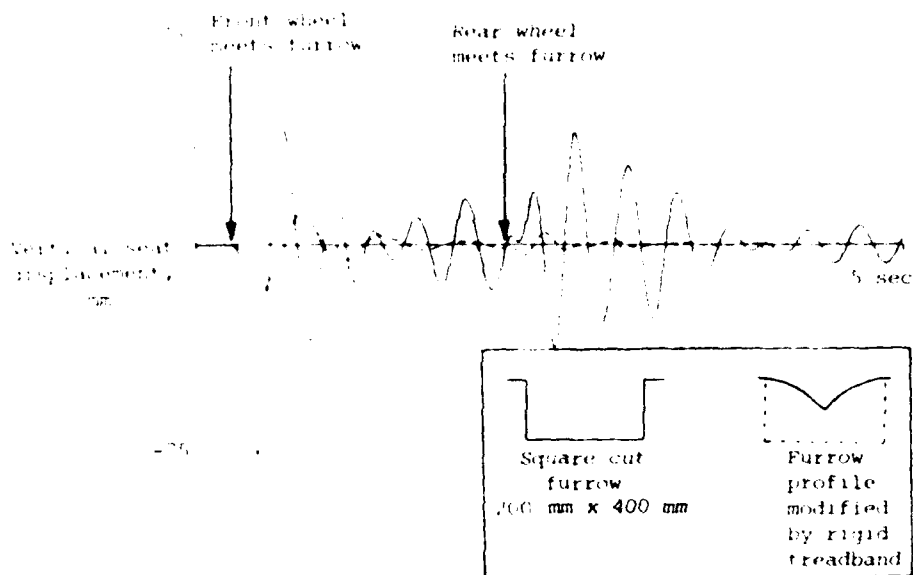


Fig. 2 Time history of vertical seat displacement for Vehicle 2 crossing a 200 x 400 mm furrow, modified by a rigid treadband input, at a speed of 2 m/sec. The solid line is for no suspension; the dashed line is for full suspension with $k_s = 400$ kN/m/axle, $c_s = 20$ kN sec/m/axle.

7. CONCLUSIONS

1. Although the simple vehicle models described contain many limiting assumptions, they are nevertheless useful in providing designers with some 'feel' for ride vibration behaviour.
2. Another justification for keeping the vehicle models simple is that a more accurate representation is limited by the tyre model. Until a more accurate description of off-road tyre vibration is available, sophisticated vehicle models are inappropriate.
3. In predicting the dominant aspects of ride behaviour, simple models enable off-road vehicle designers to understand the effect of, for example, seat position and vehicle geometry on the operator acceleration levels. Furthermore, fast interactive computing methods mean that extensive parameter optimisation studies can be done quickly.
4. In the agricultural industry, the addition of axle suspension to currently unsuspended vehicles is a subject of great interest at present. The model shows that full axle suspension is significantly better than a single axle suspension. If a single axle only is suspended then the one nearest the driver's seat offers the greatest reduction in vertical acceleration level. However, the axle furthest from his seat offers some reduction in pitch, and hence longitudinal accelerations.

REFERENCES

1. Lines, J.A. Vibration characteristics of tractor tyres - a literature survey. Div. Note IN/1104, Natn. Inst. Agric. Engrs. Silsoe, February 1982 (unpubl.).
2. Sayles, R.S., Thomas, T.R. Surface topography as a non-stationary random process. Nature, vol.271, 2 Feb. 1978.
3. Matthews, J. Ride comfort for tractor operators IV. Assessment of the ride quality of seats. J. Agric. Eng. Res., 11, 1966.

Theoretische Untersuchung einer Aktiv-Federung für Rad-Schlepper

H. Junker; A. Seewald

Inst. f. Kraftfahrwesen, TH Aachen, BR Deutschland

EINFÜHRUNG

Durch die Einsatzbedingungen auf unebenen Feldwegen und im unbefestigten Gelände werden Rad-Schlepper in der Regel zu starken vertikalen Schwingungen angeregt. Da außerdem aufgrund von Zielkonflikten mit der praxisgerechten Erfüllung wichtiger Arbeitsaufgaben bewußt auf eine separate Federung des Schlepperrumpfes verzichtet wird, ist der Fahrzeugführer hohen Schwingungsbelastungen ausgesetzt, die im Extremfall zu vermindertem Leistungsvermögen und sogar zu Gesundheitsschäden führen können.

In der Vergangenheit konnten durch eine verbesserte Abstimmung und Auslegung der Sitzfederung und -dämpfung deutliche Verbesserungen des Schwingungskomforts bei Rad-Schleppern erzielt werden. Dennoch sind in vielen Einsatzfällen mit hohen Belastungen die heute verwendeten konventionellen, passiven Sitzfederungen als einziges System zur Schwingungsisolierung überfordert /10, 12/. Den vielen Vorteilen der einfachen passiven Federungssysteme stehen als Nachteile ihre bekannten physikalischen Grenzen gegenüber /7, 13/.

Daher wurden im Rahmen einer von der Deutschen Forschungsgemeinschaft geförderten Arbeit /8/ die Verbesserungsmöglichkeiten auf diesem Gebiet durch den Einsatz einer Aktiv-Federung für den Fahrersitz von Rad-Schleppern untersucht. Dabei wurden die Erfahrungen vorangegangener Arbeiten /4, 11, 15/ aufgegriffen und durch die Beschränkung auf die Abstützung des Fahrersitzes wurden die bekannten Probleme aktiver Isolationssysteme bei hochfrequentem Anregungsinhalt und großen Nutzlasten bewußt ausgeklammert.

Bei den durchgeführten theoretischen Untersuchungen wurde die analoge Simulationstechnik angewendet. Ausgehend von den mathematischen Modellformulierungen für die Teilsysteme "Fahrzeug" und "Aktiv-Federung", die jeweils auf den Daten realer Bauteile basieren, wurde mit einem analogen Gesamtmodell eine Synthese der beiden Teilsysteme geschaffen, und schließlich die dynamischen Eigenschaften im Hinblick auf minimale Schwingungsbelastungen für den Fahrzeugführer optimiert.

RADSCHLEPPER MIT KONVENTIONELLER SITZFEDERUNG

Im ersten Untersuchungsschritt wurden die Schwingungseigenschaften eines serienmäßigen Rad-Schleppers mit konventioneller Sitzfederung analysiert, um Ausgangsdaten für die anschließende Integration der Aktiv-Federung zu schaffen.

Als Basisfahrzeug für die Untersuchungen diente ein Schlepper der 37 kW-Klasse, dessen relevante technischen Daten in Bild 1 aufgelistet sind. Die Angaben für Federsteifigkeit und Dämpfung der Schlepperreifen wurden /16/ entnommen.

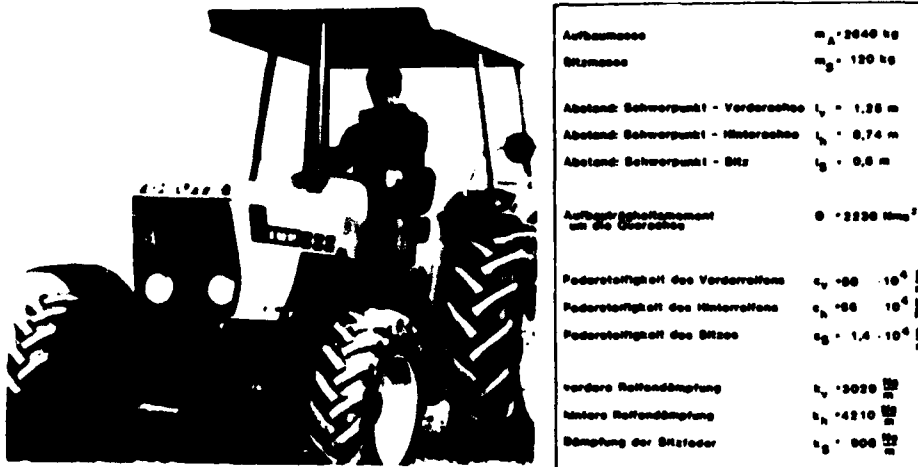


Bild 1: Techn. Daten eines 37 kW-Rad-Schleppers

Fahrzeugmodell

Aufgrund der Anordnung des Schleppersitzes in der Fahrzeugsymmetrieebene konnte auf die Nachbildung eines räumlichen Modells verzichtet und das in Bild 2 gezeigte Einspur-Modell zur Simulation des dynamischen Schwingungsverhaltens des Rad-Schleppers verwendet werden.

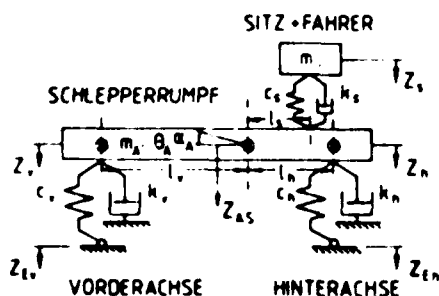


Bild 2: Einspur-Schwingungsmodell des Radschleppers

Die Abfederung des Aufbaus erfolgt ausschließlich über die vordere und hintere Reifenfederung. Der Schlepperrumpf wird zusammen mit allen Nebenaggregaten als starrer, massenbehafteter Balken betrachtet, auf dem der Sitz im Bereich über der Hinterachse angelenkt ist.

Die zur Beschreibung des Bewegungsverhaltens des Rad-Schleppers erforderlichen Differentialgleichungen wurden mit den im Modell angegebenen Parametern formuliert.

Schwingungseigenschaften

Zur Ermittlung der vertikalen Schwingungseigenschaften wurde das Fahrzeugsimulationsmodell neben der Anregung mit harmonischen Signalen zur Bestimmung der Frequenzgänge mit den Längsunebenheitsverläufen verschiedener Fahrbahntypen angeregt. Als repräsentativ für den Schleppereinsatz wurden die Unebenheitsverläufe einer befestigten Landstraße sowie eines unbefestigten Feldweges verwendet. Während die Landstraßenunebenheiten mit einem eigens entwickelten Meßgerät zur dynamischen Unebenheitsbestimmung ermittelt wurden, wurde der Feldwegverlauf synthetisch erzeugt. Nach /16/ beträgt die Differenz im Leistungsdichtespektrum der Unebenheiten typischer Landstraßen und Feldwege etwa eine Dekade. Da die spektrale Leistungsdichte

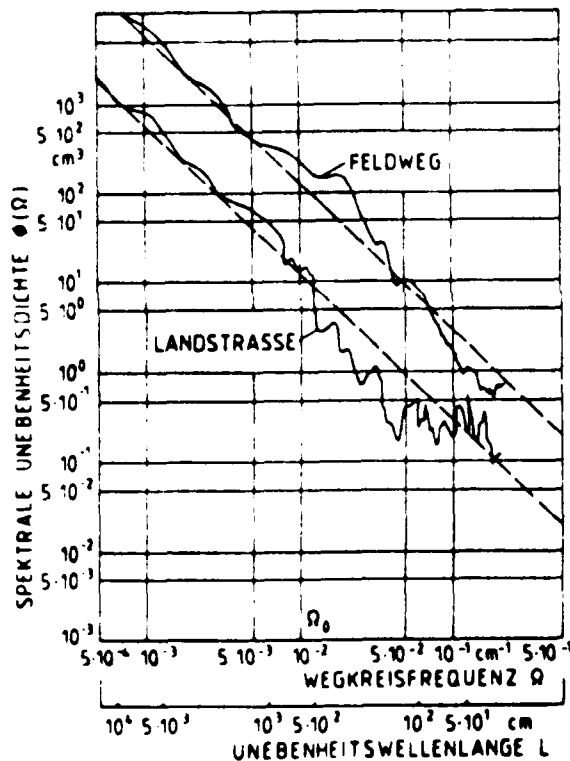


Bild 3: Leistungsdichtespektren der Unebenheiten einer befestigten Landstraße und eines unbefestigten Feldweges

aus dem Quadrat der Anregungsamplitude gewonnen wird, ergibt sich ein Amplitudenverhältnis Landstraße:Feldweg = $1:\sqrt{10}$. Diesen Zusammenhang spiegeln auch die im Bild 3 dargestellten und mit Hilfe eines FFT-Analysators ermittelten Leistungsdichtespektren der verwendeten Landstraßen- und Feldwegunebenheiten. Die bei harmonischer Anregung an den Reifenaufstandsflächen des Schleppermodells ermittelten Frequenzgänge für verschiedene Meßpunkte zeigt Bild 4.

Im Amplitudenfrequenzgang sind die Vergrößerungsfunktionen des Aufbauschwerpunktes, des Sitzanlenkpunktes sowie der Sitzoberfläche dargestellt. Der Funktionsverlauf für den Aufbauschwerpunkt ist gekennzeichnet durch zwei Maxima, die durch die Hubeigenfrequenz (3 Hz) und die Nick-

eigenfrequenz (3,75 Hz) bestimmt sind. Dagegen zeigt der Sitzanlenkpunkt im Bereich über der Hinterachse lediglich ein Maximum mit einem Vergrößerungsfaktor 5 im Bereich der Hubeigenfrequenz. Dieses Phänomen wird verursacht durch die

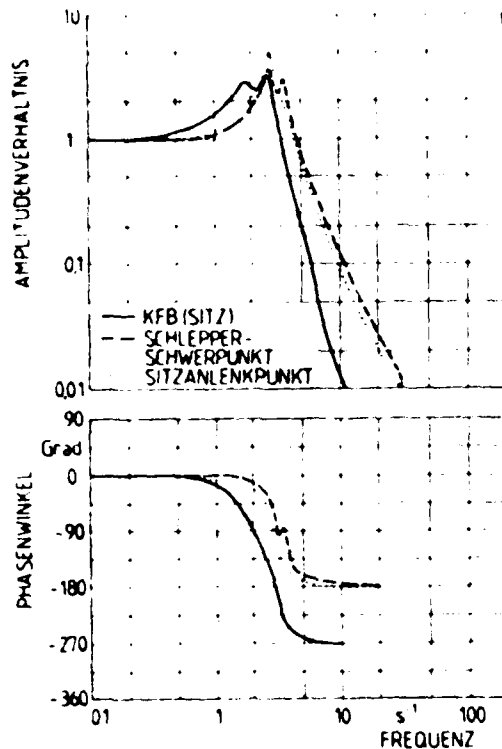


Bild 4: Frequenzgang des Einspur-schwingungsmodell des Rad-schleppers mit konventionell gefedertem Sitz

gen als auch die Wahrnehmungsstärken weisen für den Meßpunkt am Sitz die geringsten Schwingungsbelastungen auf, wodurch eine gewisse Isolationswirkung des konventionell gefederten Sitzes nachgewiesen wird.

Dennoch werden bei Feldwegfahrt Wahrnehmungsstärken $K > 110$ erreicht, korrespondierend mit Beschleunigungswerten $> 0,7 \text{ g}$, Belastungen, die bei längerer Einwirkung zu einer Beeinträchtigung der Gesundheit führen.

Im folgenden werden daher Möglichkeiten untersucht, diese hohen Schwingungsbelastungen für den Fahrzeugführer durch den Einsatz einer Aktiv-Federung wirksam zu reduzieren.

AKTIV-FEDERUNG

Die Funktion bekannter Aktiv-Feder-Systeme /2, 3, 4, 11, 15/ basiert auf dem Einsatz geregelter, längenveränderlicher Bauteile zur Abfederung der zu isolierenden Massen. Gelingt der Regelung die Einhaltung eines exakten Phasenversatzes von 180° zwischen Aktiv-Feder-Bewegung und Anregung, erfährt eine derart abgefederte Masse im Idealfall keine dynamischen Kräfte und ihre Absolutbeschleunigungen werden zu Null. In Voruntersuchungen /8/ wurde die Eignung verschiedener Aktiv-Feder-

Lage des Momentanzentrums der Nickschwingungen des Schlepperrumpfes nahe der Hinterachse. Der Funktionsverlauf des Sitzes erreicht bei der Eigenfrequenz der Sitzfederung von $1,8 \text{ Hz}$ ein Amplitudenverhältnis von $2,7$, das bis zur Aufbaueigenfrequenz auf $3,5$ ansteigt und dann mit wachsender Frequenz steil abfällt.

Bei stochastischer Anregung des Simulationsmodells durch die Unebenheitsprofile von Landstrasse und Feldweg wurden als Bewertungskriterien der Schwingungseigenschaften die in der VDI-Richtlinie 2057 definierte Wahrnehmungsstärke K , sowie die Effektivwerte der vertikalen Beschleunigung verwendet.

Bild 5 gibt die bei Fahrgeschwindigkeiten von $12,5 \text{ km/h}$ und 25 km/h ermittelten Werte am Rumpfschwerpunkt, am Sitzanlenkpunkt und am Sitz wieder. Sowohl die Effektivbeschleunigungen

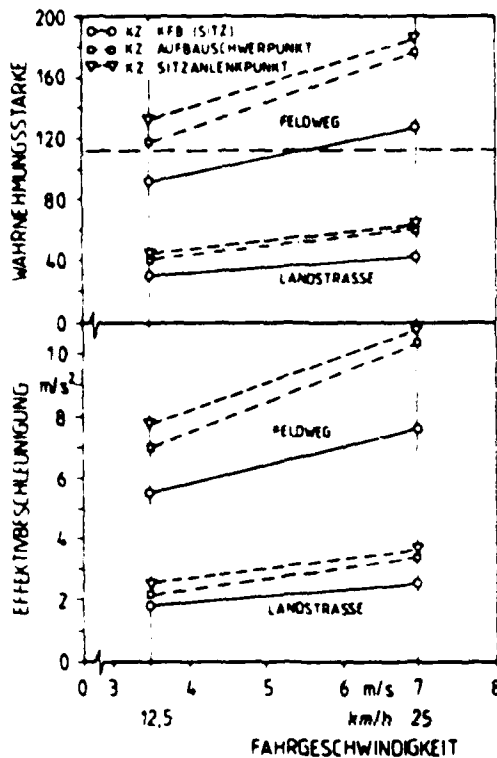


Bild 5: Wahrnehmungsstärke K und Effektivbeschleunigung am Rad-Schlepper mit konventioneller Sitzfederung (KFB)

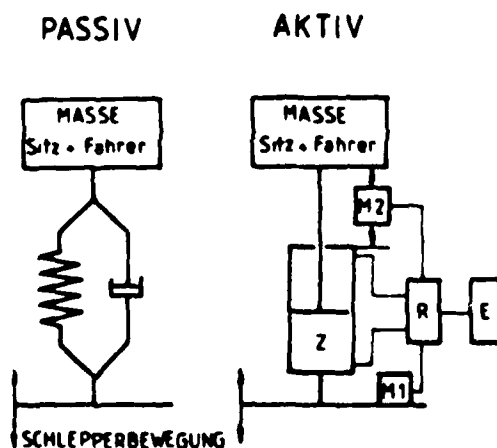


Bild 6: Passive und aktive Federungssysteme

Konzepte zur Sitzfederung bei Rad-Schleppern geklärt. Dabei zeigten elektrohydraulische Systeme die größten Vorzüge. Im Vergleich zu pneumatischen und mechanischen Ausführungen liefert die Hochdruck-Hydraulik in Verbindung mit elektronischen Steuerelementen hohe und präzise Antwortgeschwindigkeiten bei gleichzeitig hoher Leistung und Zuverlässigkeit. Es wurde daher ein Aktiv-Feder-System bestehend aus einem Hydraulikzylinder, Servoventil, Regeleinheit und Energiequelle ausgewählt, als analoges Simulationsmodell abgebildet und dessen dynamische Eigenschaften untersucht und optimiert.

Bild 6 zeigt den prinzipiellen Aufbau des Aktiv-Feder-Systems im Vergleich zur konventionellen, passiven Anordnung. Die Meßstellen M1 und M2 dienen zur Ermittlung der Schwingungsanregung und zur Erfassung von Soll/Ist-Wert-Differenzen.

Die zur technischen Darstellung der untersuchten Aktiv-Feder-Anordnung erforderlichen Bauteile zeigt der in Bild 7 dargestellte Hydraulikkreislauf.

Servo-Ventil

Als Bindeglied zwischen Elektronik und Hydraulik und zur Steuerung des Hydraulikzylinders kommt dem Servoventil eine wesentliche Bedeutung zu. Nach einer Untersuchung verschiedener Ventilbau-

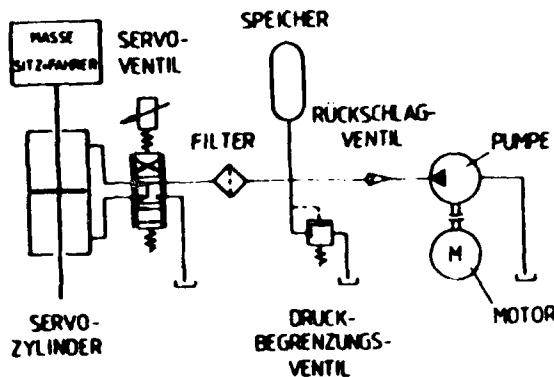


Bild 7: Hydraulikkreislauf der Aktiv-Federung

arten und Ventiltypen und nach Abschätzung des erforderlichen Volumenstroms wurde ein zwei-stufiges Serienventil mit einem Nenndurchfluß von 19 l/min bei einem Betriebsdruck von 210 bar und gutem Frequenzverhalten ausgewählt. Da die mathematische Erfassung des dynamischen Ventilverhaltens unter bestimmten Randbedingungen durch ein lineares Verzögerungsglied 2. Ordnung möglich ist, ist eine Ventilbeschreibung durch die folgende Differentialgleichung 2. Ordnung statthaft.

$$T_{v2}^2 \cdot \ddot{q} + T_{v1}^2 \cdot \dot{q} + q = V_v \cdot i$$

mit $T_{v1,2}$ - Zeitkonstanten

q - gesteuerter Volumenstrom

i - Steuerstrom

V_v - Verstärkungsfaktor

Die für das ausgewählte Ventil gültigen technischen Daten betragen:

Hersteller Typ	f_e [Hz]	D	T_{v1} [ms]	T_{v2} [ms]
MOOG (76-232)	210	1,1	1,67	0,76

Durch eine Analogrechenschaltung zur Simulation der o.g. Differentialgleichung konnten die Ventileigenschaften hinreichend genau nachgebildet werden. Die in Bild 8 gezeigten Amplituden- und Phasenfrequenzgänge zeigen lediglich im höherfrequenten Bereich vernachlässigbar geringe Abweichungen zwischen dem realen Servoventil und dem Simulationsmodell.

Servo-Zylinder und Servoantrieb

Der Servozylinder, als hydraulischer Linearmotor wirkend, transformiert die vom Servoventil gesteuerte Leistung in mechanische Leistung. Für den Aktiv-Feder-Einsatz wurde ein doppelt wirkender Gleichgangzylinder gewählt, der durch folgende technische Daten charakterisiert wird:

Hersteller	s [mm]	V_{ges} [cm ³]	A_k [cm ²]	m_k [kg]
MEBO	100	64	4,9	1

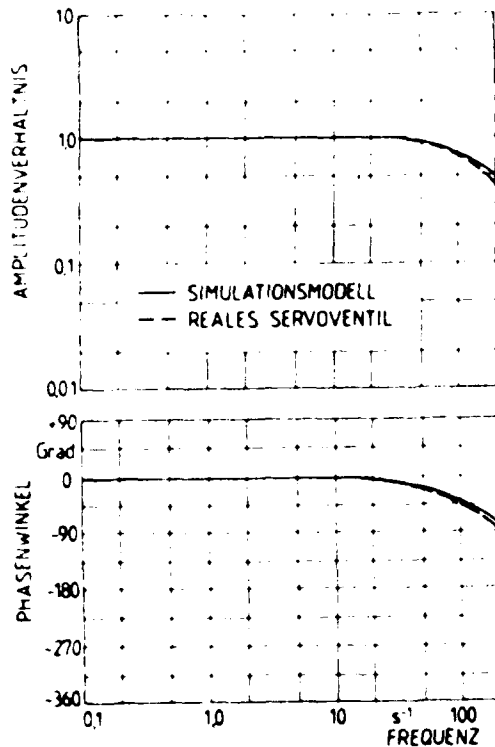


Bild 8: Frequenzgang des Servoventils
(Realteil und Simulationsmodell)

Die Zylinderbauart zeichnet sich durch einen hohen mechanischen Wirkungsgrad aus. Durch eine besondere Lagergestaltung unter Verwendung spezieller Dichtelemente wird stick-slip-freies Verhalten erzielt.

Für das dynamische Verhalten eines Servozylinders kann ebenfalls eine mathematische Formulierung in Form einer Differentialgleichung 2. Ordnung gewählt werden.

$$T_{z2}^2 \ddot{z}_z + T_{z1} \dot{z}_z + z_z =$$

$$\frac{1}{A_k} \int q \, dt$$

mit T_{z1}, T_{z2} - Zeitkonstanten

z_z - Weg der Kolbenstange

A_k - wirksame Kolbenfläche

q - gesteuerter Volumenstrom

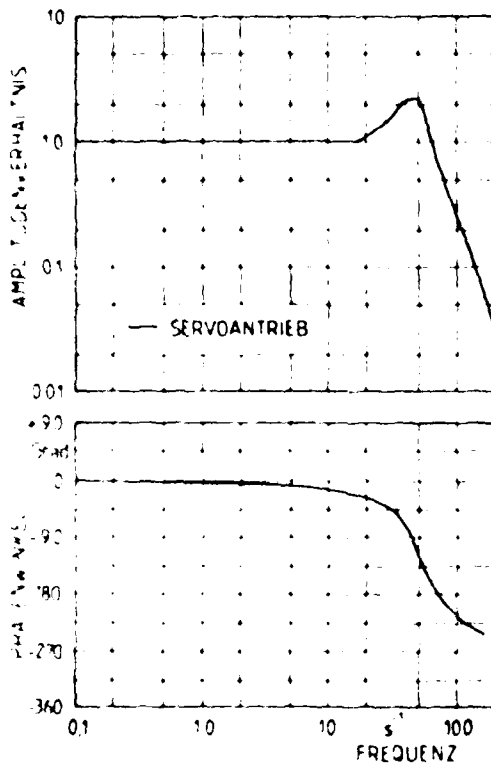
Die Abbildung der Differentialgleichung am Analogrechner führt zu einem Simulationsmodell zur Ermittlung der dynamischen Eigenschaften des Servozylinders.

Die Reihenschaltung von Servoventil und Servozylinder bildet den Servoantrieb, der im geschlossenen Regelkreis der Aktivfederung die Regelstrecke darstellt. Bild 9 zeigt den Frequenzgang des Servoantriebs. Da das Amplitudenverhältnis des Servoventils in einem weiten Frequenzbereich nahezu Eins ist und der Phasenabfall des Servozylinders deutlich früher einsetzt, wird das Gesamtübertragungsverhalten des Servoantriebs wesentlich durch den Servozylinder bestimmt.

Regelkreis

Zur Verbesserung der Übertragungseigenschaften der Aktivfederung wurde im nächsten Untersuchungsschritt durch Hinzufügen eines Reglers ein geschlossener Regelkreis hergestellt. Die Reglereigenschaften sollten so gewählt werden, daß sie die Abweichungen des dynamischen Verhaltens des Servoantriebs vom

Sollzustand, charakterisierbar durch ein Amplitudenverhältnis = 1 und einen Phasenwinkel = 0°, weitgehend kompensieren. Da kein bekanntes Regelelement die gestellten Forderungen nach Absenken der Amplitudenverhältnisse im Bereich der Servoantriebeigenfrequenz bei gleichzeitiger positiver Anhebung des Phasenwinkels erfüllt, wurde aufgrund der zu realisierenden Folgeregelung einer Kompensation der negativen Phasenwinkel Priorität eingeräumt. Die dazu erforderlichen differenzierenden Eigenschaften wurden durch die Auswahl eines PD-Reglers berücksichtigt, der durch die folgende Differentialgleichung darstellbar ist:



$y = K (x + T_v \cdot \dot{x})$
mit T_v - Zeitkonstante
 x, y - Eingangs-, Ausgangsgröße
 K - Reglerkonstante

Bild 9: Frequenzgang des Servoantriebs (Regelstrecke)

Den prinzipiellen Aufbau des Regelkreises zeigt Bild 10. Der

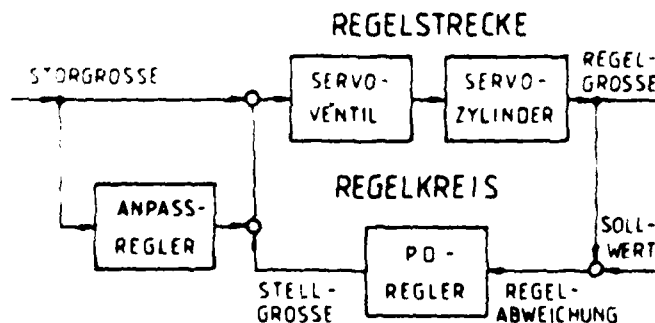


Bild 10: Regelkreis mit Störgrößenaufschaltung

PD-Regler formuliert aufgrund der Abweichung von Regelgröße und Sollwert eine auf die Regelstrecke wirkende Stellgröße, die das Übertragungsverhalten des Servoantriebs positiv beeinflusst. Zur Ermittlung optimaler Regelkenndaten wurde nach der Differentialgleichung des PD-Reglers ein analoges Simulationsmodell gebildet und mit den Modellen

von Servoventil und Servozylinder kombiniert. Die Abstimmung des PD-Reglers und die resultierende Wirkung auf das Übertragungsverhalten geht aus der Gegenüberstellung der Frequenz-

gänge des gesteuerten Servoantriebs und des geschlossenen Regelkreises in Bild 11 hervor. Die Eigenfrequenz des Aktiv-Feder-Systems wird durch

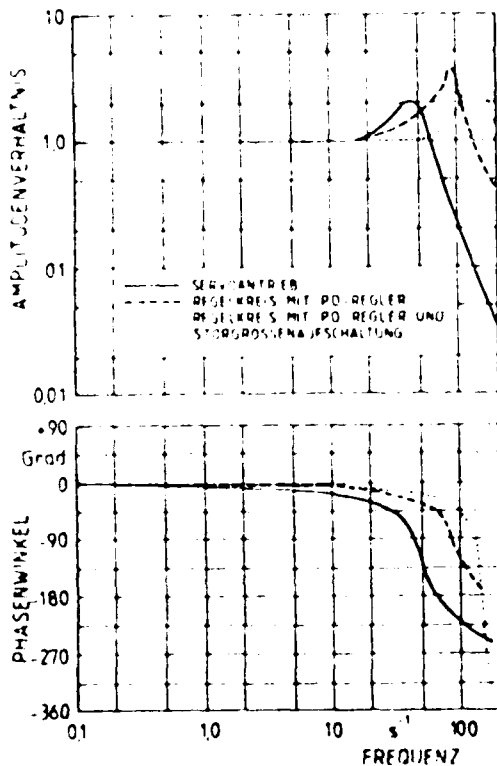


Bild 11: Frequenzgang des Servoantriebs und des geschlossenen Regelkreises mit und ohne Störgrößenaufschaltung

das Schließen des Regelkreises mit Hilfe des PD-Reglers von 45 Hz auf 90 Hz angehoben. Gleichzeitig steigt aufgrund der entdämpfenden Eigenschaften des differenzierenden Regelanteils das Amplitudenverhältnis und der Phasennachlauf wird kleiner. Eine im Anschluß durchgeführte Untersuchung zur weiteren Verbesserung der Regelgüte führte zu der in Bild 10 dargestellten Störgrößenaufschaltung, die bei optimal abgestimmtem Anpaßregler das Übertragungsverhalten günstig beeinflusst. Der mit Störgrößenaufschaltung ermittelte Frequenzgang zeigt in Bild 11 im Vergleich zum gesteuerten Servoantrieb bzw. zum einfachen Regelkreis mit PD-Regler eine Eigenfrequenz des Aktiv-Feder-Systems von 150 Hz. Im Frequenzbereich bis ca. 50 Hz wird ein nahezu konstantes Amplitudenverhältnis bei gleichzeitig verringertem Phasennachlauf erreicht. Die Resonanzstellenverschiebung zu höheren Frequenzen ist jedoch

mit dem Nachteil eines steigenden Amplitudenverhältnisses im Eigenfrequenzbereich verbunden. Unter Berücksichtigung des relativ niederfrequenten Anregungsspektrums ist jedoch dem Amplitudenanstieg bei höheren Frequenzen nur eine geringere Bedeutung zuzumessen. Vor der Anpassung des geschlossenen Aktiv-Feder-Regelkreises an das Schwingungsmodell des Rad-Schleppers wurde die Stabilität des Regelkreises mit Hilfe des NYQUIST-Kriteriums überprüft. Bei diesem Kriterium bildet der Frequenzgang des aufgeschnittenen Regelkreises die Bewertungsgrundlage.

Die Anwendung des NYQUIST-Kriteriums beim optimierten Regelkreis mit PD-Regler zeigt Bild 12. Der aus der geometrischen Addition der Frequenzgänge von Servoantrieb und PD-Regler resultierende Frequenzgang des aufgeschnittenen Regelkreises

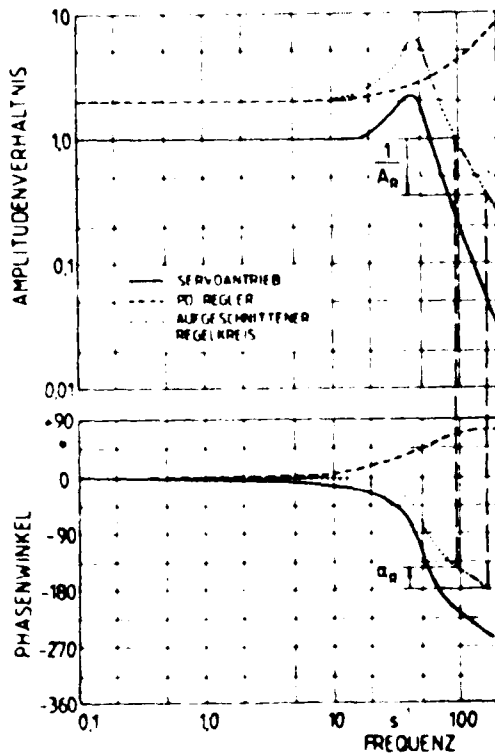


Bild 12: Stabilitätsuntersuchung
nach dem NYQUIST-Kriterium

bezogenen Beschleunigungen am Sitz sind in Bild 13 den entsprechenden Kurven der konventionellen Sitzfederung gegenübergestellt. Die mit Störgrößenaufschaltung arbeitende Aktiv-Feder-Version zeigt im Vergleich zur Version mit einfachem Regelkreis günstigere Amplituden- und Beschleunigungswerte. Gegenüber der konventionellen Sitzfederung bieten beide Aktiv-Feder-Versionen im Frequenzbereich bis ca. 15 Hz ein deutlich abgesenktes Beschleunigungsniveau. Im höherfrequenten Bereich resultiert aus der Tieffpasscharakteristik der konventionellen Federung ein steiler Amplitudenabfall, dem die Aktiv-Feder-Systeme aufgrund der auftretenden negativen Phasenwinkel nicht in der Lage sind zu folgen. Darauf sind auch die höheren Werte der bezogenen Beschleunigungen der Aktiv-Federung im Frequenzbereich > 15 Hz zurückzuführen. Die im Eigenfrequenzbereich der Aktiv-Feder-Systeme auftretenden hohen Beschleunigungswerte sind aufgrund des subjektiven Bewertungsempfindens des Menschen für die Gesamtschwingungsbelastung von geringerer Bedeutung. Die bei stochastischer Anregung des Schlepper-Simulationsmodells mit Fahrbahnunebenheiten ermittelten Werte der Wahrnehmungsstärke KZ und der Effektivbeschleunigung des konventionell und des aktiv gefederten Sitzes gehen aus Bild 14 hervor.

liefert eine Amplitudenreserve von $A_R = 3,0$ und eine Phasenreserve von $\alpha_R = 30^\circ$, und erfüllt damit die Stabilitätskriterien $A_R = 1$ und $\alpha_R > 0^\circ$.

SYNTHESE VON AKTIV-FEDERUNG UND RAD-SCHLEPPER

Zur Anpassung der Aktiv-Federung an das Schwingungsmodell des Rad-Schleppers wurde der Schwingkreis der konventionellen Sitzfederung durch den geschlossenen Regelkreis des aktiven Systems ersetzt. Als Störgrößensignal wurde die vertikale Bewegung des Schlepperrumpfes am Anlenkpunkt der Sitzfederung verwendet.

Schwingungseigenschaften

Die bei integrierter Aktiv-Federung ermittelten Amplitudenfrequenzgänge des Fahrersitzes sowie die auf die Erregungsamplitude

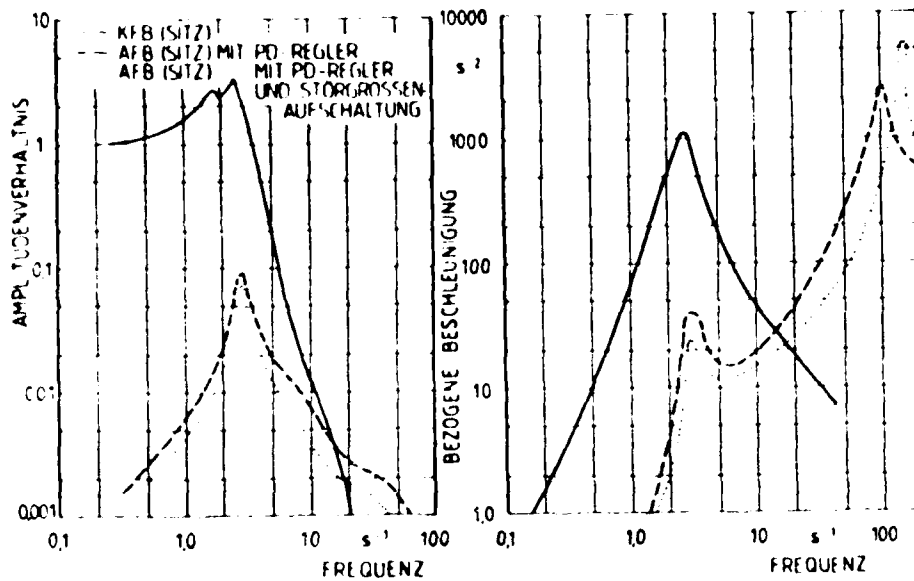


Bild 13: Amplitudenfrequenzgang und bezogene Beschleunigung bei konventionell (KFB) und aktiv (AFB) gefedertem Schleppersitz

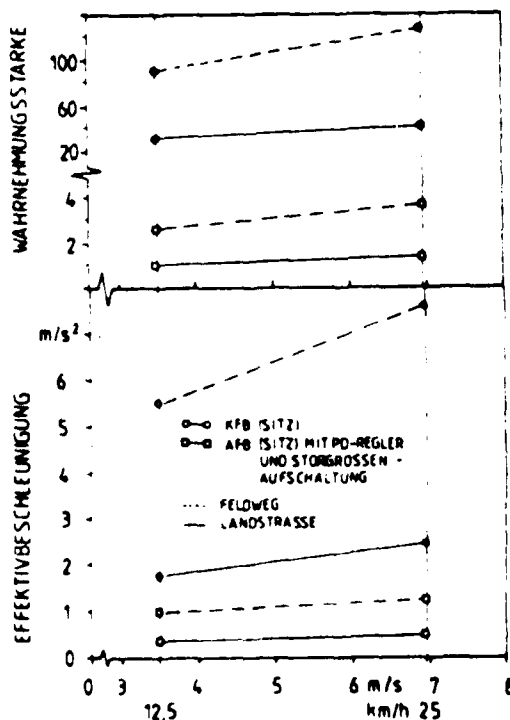


Bild 14: Wahrnehmungsstärke und Effektivbeschleunigung des konventionell (KFB) und des aktiv (AFB) gefederten Schleppersitzes

Die Darstellung zeigt ein durch den Einsatz der Aktiv-Federung im gesamten Fahrgeschwindigkeitsbereich deutlich abgesenktes Niveau der Beschleunigungen und der objektiven Schwingungsbelastungen. Liegen beim konventionell gefederten Sitz die Wahrnehmungsstärken bei Landstraßenfahrt zwischen KZ=30-35 und bei Feldwegbetrieb zwischen KZ=90-120, wird durch den optimal abgestimmten Aktiv-Feder-Regelkreis mit Störgrößen-aufschaltung ein Pkw-Komfortniveau erreicht. Diese lediglich im Hinblick auf Minimierung der Schwingungsbelastung ausgelegte Aktiv-Feder-Abstimmung führt jedoch auch zu relativ großen Relativbewegungen zwischen Sitz und Schlepperrumpf. Beim Feldwegbetrieb wurden mehr-

mals die Grenzen des Zylinderhubs überschritten, was durch eine zusätzliche Regelkreisschaltung und eine Zylinderendlagerdämpfung vermieden werden sollte. Da große Relativwege jedoch generell eine sichere Fahrzeugführung erschweren, sollte in zukünftigen Untersuchungsschritten der Einsatz einer Aktiv-Federung auf die gesamte Fahrerkabine mit integrierten Bedienelementen ausgedehnt werden.

Leistungsbedarf der Aktiv-Federung

Einen Zugang zur rechnerischen Abschätzung des erforderlichen hydraulischen Leistungsbedarf der Aktiv-Federung gestattet die Gleichung

$$P_p = \frac{1}{\eta_p} \cdot p \cdot A_K \cdot v_{K_{eff}}$$

mit Pumpenwirkungsgrad $\eta_p = 0,85$

Betriebsöldruck $p = 210 \text{ bar}$

Kolbenfläche $A_K = 4,9 \text{ cm}^2$

Mit den bei Fahrgeschwindigkeiten von 25 km/h ermittelten Kolbengeschwindigkeiten am Aktiv-Feder-Zylinder von 0,22 m/s bei Landstraßenfahrt bzw. 0,67 m/s bei Feldwegbetrieb errechnet sich ein Leistungsbedarf von 2,7 - 8,1 kW je nach Einsatzart. Aufgrund dieses hohen Leistungsbedarfs, insbesondere bei Feldwegbetrieb, erscheint der Einsatz einer Aktiv-Federung nur in den Schlepperkategorien mit hohem Leistungsangebot sinnvoll.

ZUSAMMENFASSUNG

Mit Hilfe eines analogen Rechenmodells zur Simulation der Schwingungseigenschaften eines Rad-Schleppers und eines einfachen Aktiv-Feder-Systems wurden die theoretischen Möglichkeiten einer aktiven Sitzfederung untersucht.

Das Aktiv-Feder-System, bestehend aus einem Servo-Hydraulikzylinder, Servoventil und Energiequelle wurde in einem geschlossenen Regelkreis mit PD-Regler und Störgrößenaufschaltung betrieben. Nach Ermittlung der Frequenzgänge der einzelnen Bauteile wurde das Aktiv-Feder-System in das Fahrzeugmodell integriert und eine optimale Abstimmung der Reglerkennwerte unter Beachtung der Stabilitätskriterien vorgenommen. Bei Schwingungsanregung des Gesamtmodells mit harmonischen Signalen, sowie mit den Fahrbahnunebenheiten von Landstraßen und Feldwegen bewirkt die aktive Sitzfederung eine deutliche Verringerung der Schwingungsbelastung für den Fahrzeugführer. Eine Abschätzung der erforderlichen Bedarfsleistung des Aktiv-Feder-Systems läßt einen Einsatz nur für Schlepper der gehobenen Leistungsklassen sinnvoll erscheinen.

LITERATUR

- /1/ Bender E.K. Some Fundamental Limitations of
Active and Passive Suspension
Systems
SAE 680750

- /2/ Calcaterra, P.C. Performance Characteristics of
Active Systems for Low Frequency
Vibration Isolation
SM Thesis, MIT, June 1967

- /3/ Calcaterra, P.C. and Research on Active Isolation
Schubert, D.W. Techniques for Aircraft Pilot
Protection
MRL-TR-138, Aerospace Medical
Research Laboratories 1967,
Wright-Patterson-Air Force
Base, Ohio/USA

- /4/ Coermann, R.R Untersuchung der Möglichkeit
Lange, W. einer aktiven Dämpfung für
Fahrersitze
Grundlagen Landtechnik, Bd. 21
(1971) Nr. 1

- /5/ Guillon, M. Hydraulische Regelkreise und
Servosteuerungen
Carl Hanser Verlag, München,
1968

- /6/ Hart, J. Abgefederte Kabine für ungefe-
derte Geländefahrzeuge
Automobiltechnische Zeitschrift
79 (1977) Heft 7/8

- /7/ Helms, H. Schwingungseigenschaften eines
gefederten Schleppersitzes
Grundl. Landtechnik, Bd. 26
(1976)

- /8/ Junker, H. Untersuchung eines aktiven Fe-
Seewald, A. der-Dämpfer-Systems zur Ver-
ringerung der Schwingungsbe-
lastung des Menschen im Kfz
DFG-Forschungsbericht He 525/14

- /9/ Kauß, W. Aktive Schwingungsisolierung
Göhlich, H. des Fahrerplatzes ungefederter
Fahrzeuge
Automobiltechnische Zeitschrift
84 (1982) Heft 9

- /10/ Köpper, R. Zur Bestimmung des erforderli-
chen Schwingungskomforts gelän-
degängiger Fahrzeuge und seine
Verwirklichung durch aktive Fe-

- derung
Dissertation TU Berlin, 1973
- /11/ Laetherwood, J.D.
Dixon, G.V. Active Vibration Isolation for Flexible Payloads
IES Proceedings, April 1968, pp. 407-413
- /12/ Owzar, A. Untersuchung des Schwingungsverhaltens von ungefederten luftbereiften Fahrzeugen
Automobiltechnische Zeitschrift 78 (1976), Heft 9
- /13/ Röhl, E.
Helling, J.
Junker, H. Entwicklung einer neuartigen Patientenlagerung für Rettungswagen
Proceedings of FISITA-Congress 1978, Budapest
- /14/ Röhl, E.
Junker, H. Entwicklung und Bau eines neuartigen Rettungswagens
Automobiltechnische Zeitschrift 81 (1979), Heft 12
- /15/ Stikeleather, L.W. The Development of an Active Seat Suspension for Off-Road Vehicles
Ph.D. Thesis, North Carolina State University 1968
- /16/ Wendeborn, J.D. Ein Beitrag zur Verbesserung des Fahrkomforts auf Acker-schleppern
Fortschr.-Bericht, VDI-Z. Reihe 14, Nr. 8 (1968)

A THEORETICAL INVESTIGATION OF AN ACTIVE SUSPENSION SYSTEM FOR WHEELED TRACTORS

H. JUNKER; A. SEEWALD

Inst. f. Kraftfahrwesen, TH Aachen, BR Deutschland

(Translated by K.G. Hammond, NIAE, Silsbee, England)

INTRODUCTION

Wheeled tractors, because of their operating conditions on uneven field tracks and in unconsolidated terrain, are, as a rule, subjected to strong vertical vibrations. Since, in addition, a separate suspension system for the tractor is deliberately rejected because of a conflict of aims with the correct fulfilment of important work tasks, the driver is liable to high vibration loads which, in extreme cases, can lead to reduced performance and even damage to health.

In the past, clear improvements to the vibration comfort of wheeled tractors could be obtained by means of improved adjustment and design of the seat suspension and seat damping. However, in many instances involving high loads excessive demands are placed on the conventional passive seat suspensions currently employed as the sole system of vibration isolation(10,12). The well-known physical limits of simple passive suspension systems stand in contrast to their many advantages(7,13).

For this reason the possibility of improvements in this area through the use of an active suspension system for the seat of a wheeled tractor was investigated within the framework of a project(8) promoted by the Deutsche Forschungsgemeinschaft. Experience gained in previous work(4,11,15) was assimilated and, by focusing on the seat mounting, the familiar problems of active isolation systems when dealing with a high-frequency excitation content and large working loads were deliberately set aside.

Analogue simulation technique was applied to the theoretical investigations carried out. Mathematical models of the subsystems "vehicle" and "active suspension" based on pertinent data from existing components formed a starting point for a synthesis of the two subsystems by means of an analogue gross model. Finally, the dynamic characteristics were optimised with regard to minimal vibration loads for the driver.

WHEELED TRACTORS WITH CONVENTIONAL SEAT SUSPENSION

In the initial research stage the vibration characteristics of a standard wheeled tractor with conventional seat suspension were analysed to provide original data for the subsequent integration of the active suspension.

As a base-line research vehicle a 37 kW tractor was used, the relevant technical data for which are listed in Fig. 1. The data concerning suspension stiffness and damping of the tractor were taken from(16).

Structural mass	$m_A = 2640 \text{ kg}$
Seat mass	$m_S = 120 \text{ kg}$
Spacing : centre of gravity - front axle	$l_v = 1.25 \text{ m}$
Spacing : centre of gravity - rear axle	$l_h = 0.74 \text{ m}$
Spacing : centre of gravity - seat	$l_S = 0.6 \text{ m}$
Structural moment of inertia about the lateral axis	$\theta = 2203 \text{ Nms}^2$
Spring stiffness of front tyre	$c_v = 50 \cdot 10^4 \frac{\text{N}}{\text{m}}$
Spring stiffness of rear tyre	$c_h = 56 \cdot 10^4 \frac{\text{N}}{\text{m}}$
Spring stiffness of seat	$c_S = 1.4 \cdot 10^4 \frac{\text{N}}{\text{m}}$
Front tyre damping	$k_v = 3029 \frac{\text{Ns}}{\text{m}}$
Rear tyre damping	$k_h = 4210 \frac{\text{Ns}}{\text{m}}$
Seat spring damping	$k_S = 908 \frac{\text{Ns}}{\text{m}}$

Fig. 1 Technical data for a 37-kW wheeled tractor

Vehicle model

Because of the disposition of the tractor seat in the vehicle plane of symmetry a three-dimensional model could be dispensed with and the two-dimensional model shown in Fig. 2 used to simulate the dynamic vibration behaviour of a wheeled tractor.

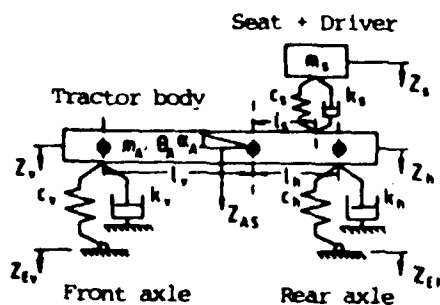


Fig. 2 Two-dimensional vibration model of a wheeled tractor

The springing of the structure is implemented exclusively through the front and rear tyre suspension. The tractor body is regarded, together with all its ancillary assemblies, as a rigid mass, to which the seat is linked in the area above the rear axle.

The differential equations necessary for describing the motion characteristics of a wheeled tractor were formulated in terms of the parameters given in the model.

Vibration characteristics

In order to measure the vertical vibration characteristics the vehicle simulation model was excited with the longitudinal roughness properties of different road types as well as with harmonic signals to define the frequency responses. The roughness properties of a paved highway and of an unpaved field track were used as representative of tractor operation. While highway roughness was measured with a purpose-built measuring apparatus for dynamic roughness determination, the field track properties were generated synthetically. According to (16) the ratio of the power density spectra of the roughness of typical highways to that of field tracks is approximately of the order of ten. If the spectral power density is obtained from the square of the excitation amplitude, a highway : field track ratio of amplitude of 1 : 10 is obtained. This relationship is also reflected in the power density spectra of highway and field track roughness used, which are presented in Fig. 3 and were measured with the aid of a FFT analyser. The measured frequency responses for harmonic excitation at the tyre contact surfaces are shown in Fig. 4 for different measuring points.

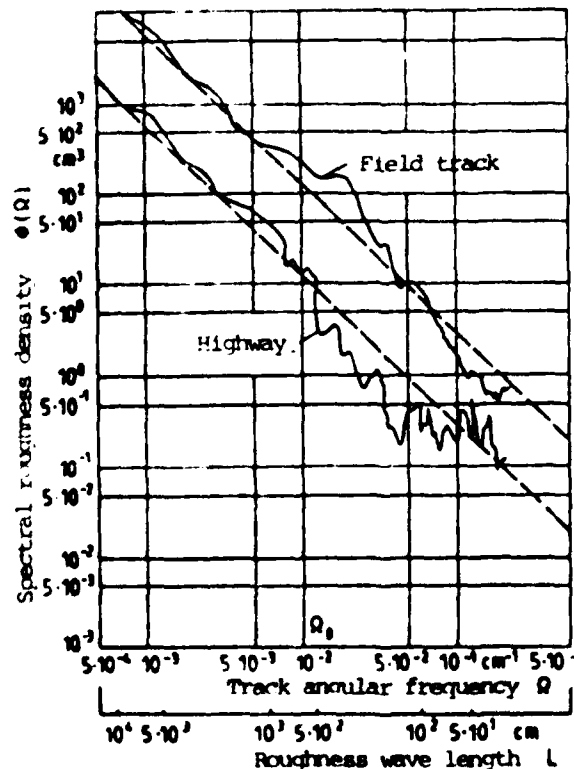
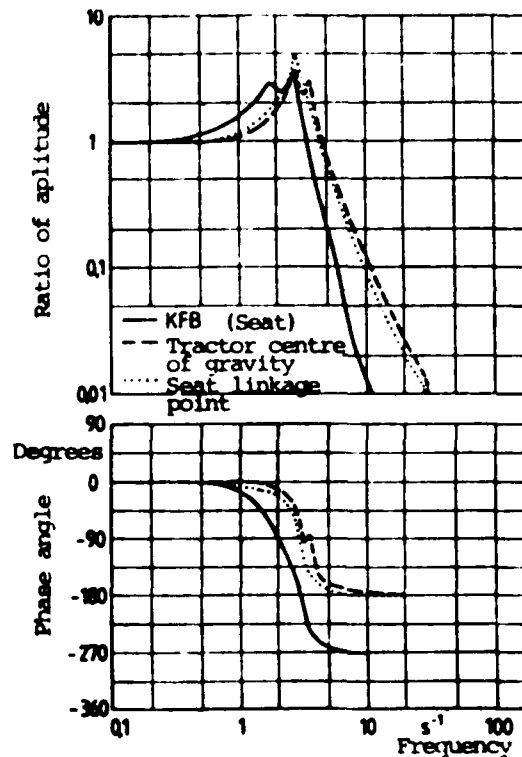


Fig. 3 Power density spectra of the roughness of a paved highway and an unpaved field track

The amplification functions of the body's centre of gravity, the seat linkage point and the seat surface are represented in the amplitude frequency response. The function curve for the centre of gravity of the body is characterised by two maxima, which are defined by the natural frequency of vertical vibration (3 Hz) and the pitch natural frequency (3.75 Hz). Conversely, the seat linkage point in the area over the rear axle only shows a maximum with an amplification factor of 5 in the range of the vertical natural frequency. This phenomenon is caused by the position of the instantaneous centre of the tractor body pitch vibrations near the rear axle. The function curve of the seat reaches a ratio of amplitude of 2.7 at a natural frequency for the seat suspension of 1.8 Hz, continuing to rise towards a body natural frequency of 3.5 and then falling steeply as frequency increases.

Fig. 4 Frequency response of the two-dimensional vibration model of a wheeled tractor with conventionally sprung seat



Perception strength K , defined in VDI Standard 2057, and the effective values for vertical acceleration were applied as criteria for evaluating vibration characteristics during stochastic excitation of the simulation model by means of the roughness profile of highway and field track.

Fig. 5 reproduces the measured values at the body's centre of gravity, at the seat linkage and at the seat for forward speeds of 12.5 km/h and 25 km/h. Both the effective acceleration and the perception strength values show the smallest vibration loads for the measuring point at the

seat, thus demonstrating that the conventionally sprung seat produces a certain degree of isolation.

However, perception strengths of $K > 100$ are reached over field tracks, corresponding to acceleration values of > 0.7 g. Loads of this magnitude lead to impaired health following prolonged exposure.

Therefore, the possibility is investigated of effectively reducing these high vibration loads on the driver by the introduction of an active suspension system.

ACTIVE SUSPENSION

The operation of existing active suspension systems^(2,3,4,11,15) is based on the use of controlled, longitudinally variable components for the suspension of the masses to be isolated. If the control system is successful in maintaining an exact phase shift of 180° between the movement of the active suspension system and the excitation, a mass suspended in this way will ideally experience no dynamic forces and its absolute acceleration will be zero. In previous research⁽⁸⁾ the suitability of various active suspension concepts for wheeled tractor seat suspension was examined, electro-hydraulic systems showing the greatest advantages. By comparison with pneumatic and mechanical solutions, high-pressure hydraulic systems combined with electronic control elements offered high, precise response speeds simultaneously with high performance and dependability. An active suspension system consisting of a hydraulic cylinder, a servo-valve, a control unit and a power source was therefore selected, reproduced as an analogue simulation model and its dynamic properties investigated and optimised.

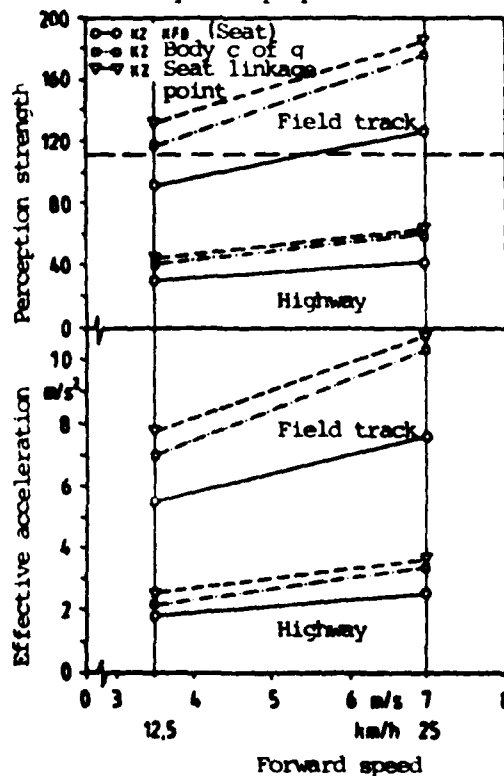
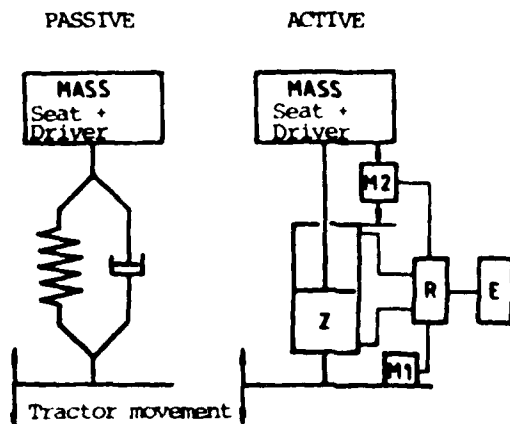


Fig. 5 Perception strength K and effective acceleration for a wheeled tractor with conventional seat suspension (KFB)

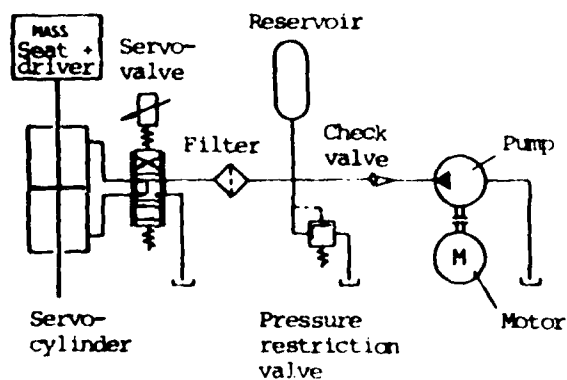
Fig. 6 shows the basic design of the active suspension system compared with the conventional, passive arrangement. The measuring points M1 and M2 are used to measure vibration excitation and register the theoretical and actual value difference.

Fig. 6 Passive and active suspension systems



The necessary components for a technical description of the active suspension layout under investigation are shown in the hydraulic circuit presented in Fig. 7.

Fig. 7 Active suspension hydraulic circuit



Servo-valve

The servo-valve forms an essential connecting link between electronics and hydraulics and a vital means of controlling the hydraulic cylinder. After investigation of different valve designs and types and assessment of the required flow volume, a two-stage production valve with a nominal flowrate of 19 l/m at an operating pressure of 210 bar and good frequency response was chosen. Since dynamic valve response under defined boundary conditions may be described by means of a second-order linear deceleration

term, it is legitimate to describe the valve by means of the following second-order differential equation

$$T_{V2} \cdot \ddot{q} + T_{V1} \cdot \dot{q} + q = V_V \cdot i$$

where $T_{V1,2}$ - time constants

q - controlled flow volume

i - control current

V_V - amplification factor

The technical data relating to the valve selected are:

Manufacturer Type	f_e [Hz]	D	T_{V1} [ms]	T_{V2} [ms]
MOCG (76-232)	210	1.1	1.67	0.76

Valve characteristics were reproduced accurately by means of an analogue computing circuit for simulating the above differential equation. The amplitude- and phase-frequency responses shown in Fig. 8 display divergences between the physical servo-valve and the simulation model in the higher-frequency range only; these are small enough to be disregarded.

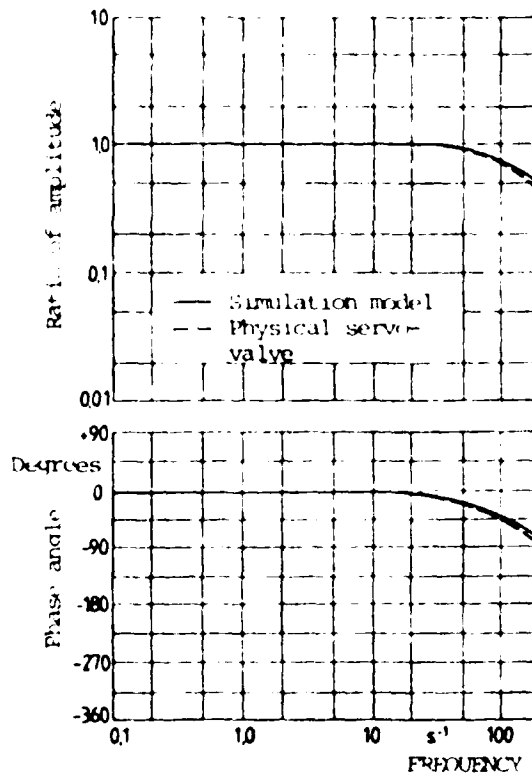
Servo-cylinder and Servo-drive

The servo-cylinder, which functions as an hydraulic linear motor, transforms the power controlled by the servo-valve into mechanical power. For use in an active suspension system a double-acting constant flow cylinder was chosen, which had the following technical characteristics:

Manufacturer	s [mm]	V_{ges} [cm ³]	A_k [cm ²]	m_k [kg]
MEBO	100	64	4.9	1

The cylinder design is distinguished by a high degree of mechanical efficiency. Stick-slip-free operation is achieved by means of a particular bearing configuration with the application of special seals.

Fig. 8 Frequency response of the servo-valve (physical component and simulation model)



A mathematical formula in the form of a second-order differential equation may similarly be chosen to describe the dynamic response of a servo-cylinder.

$$T_{z2}^2 \ddot{z}_z + T_{z1} \dot{z}_z + z_z = \frac{1}{A_k} q \, dt$$

where T_{z1} , T_{z2} - time constants

z_z - piston rod stroke

A_k - effective piston area

q - controlled flow volume

Reproducing the differential equation on an analogue computer creates a simulation model for measuring the dynamic characteristics of the servo-cylinder.

The serial connection of servo-valve and servo-cylinder forms the servo-drive, which represents the controlled range in the closed-loop control of the active suspension system. Fig. 9 shows the frequency response of the servo-drive. Since the ratio of amplitude of the servo-valve in a wide frequency spectrum is almost one and the phase drop clearly begins earlier,

the total transmission characteristics of the servo-drive are essentially determined through the servo-cylinder.

The Control Loop

In the next research stage a closed-loop control was created by the addition of a control unit in order to improve the transmission characteristics of the active suspension system. The characteristics of the control unit should be selected in order substantially to compensate for the divergences of the servo-drive's dynamic response from the theoretical state, characterised as a ratio of amplitude = 1 and a phase angle = 0°. Since no known control element fulfils the requirement set of lowering the ratios of amplitude in the range of the servo-drive's natural frequency while simultaneously raising the phase angle, priority was given to compensating for the negative phase angle on the basis of the servo-mechanism to be implemented. The differentiating characteristics required for this were provided for by the choice of a PD-control unit which may be described by the following differential equation:

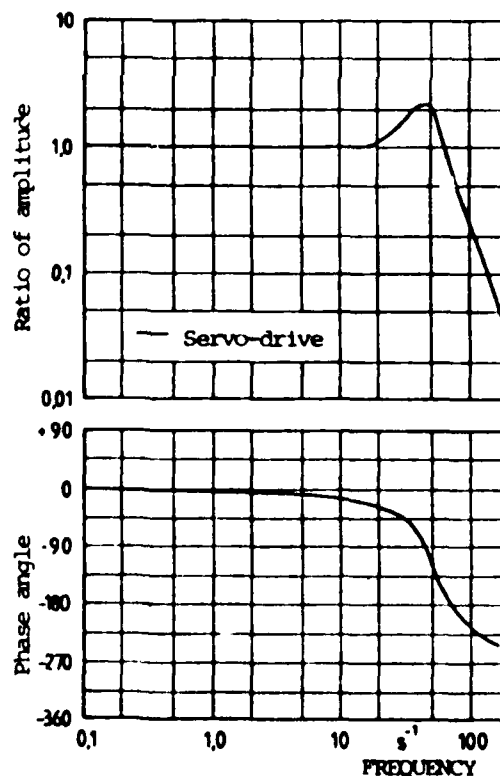
$$\dot{y} = K (x + T_v \cdot \dot{x})$$

where T_v - time constant

x, y - input and output quantities

K - control constant

Fig. 9 Frequency response of the servo-drive (controlled range)



The basic design of the control loop is shown in Fig. 10. The PD-control unit formulates a regulating variable acting upon the controlled range in terms of the divergence of controlled variable and theoretical value; this regulating variable positively affects the transmission characteristics of the servo-drive. An analogue simulation model was generated to measure optimal control characteristics in accordance with the differential equation of the PD-control unit and was combined with models of the servo-valve and the servo-cylinder. Synchronisation of the PD-control unit and the resultant effect on the transmission characteristics arises from the contrast between the frequency responses of the controlled servo-drive and of the closed-loop control in Fig. 11. The natural frequency of the active suspension system is raised from 45 Hz to 90 Hz by closing the control loop with the aid of a PD-control unit.

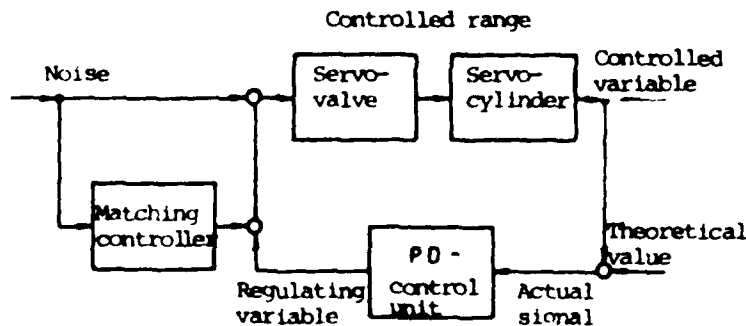
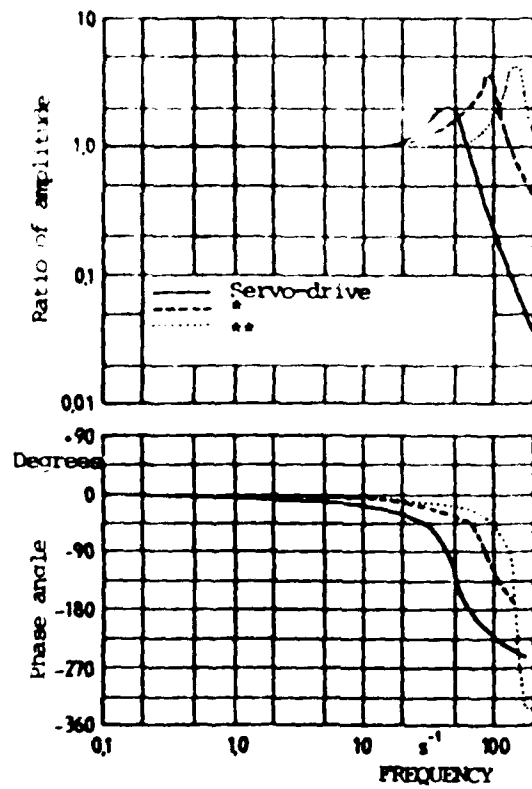


Fig. 10 Control loop with noise elimination

Simultaneously, the ratio of amplitude rises on the basis of the damped characteristics of the differentiating control fraction and the phase lag becomes smaller. Associated research to further improve quality of control led to the development of the noise elimination shown in Fig. 10 which favourably affects the transmission characteristics in conjunction with an optimally synchronised matching controller. Frequency response measured with noise elimination shows a natural frequency for the active suspension system of 150 Hz in Fig. 11 by comparison with the controlled servo-drive or with a simple control loop with a PD-control unit. In a frequency range up to ca. 50 Hz a nearly constant ratio of amplitude with a simultaneously reduced phase lag is achieved. The response shift towards higher frequencies is, however, associated with the disadvantage of a rising ratio of amplitude in the natural frequency range. In view of the relatively low-frequency excitation spectrum, however, only small importance should be attached to the amplitude rise at higher frequencies. Before matching the active suspension closed-loop control to the wheeled tractor vibration model, the stability of the control loop was verified with the aid of the Nyquist criterion. The frequency response of the open control loop forms the basis of this criterion.

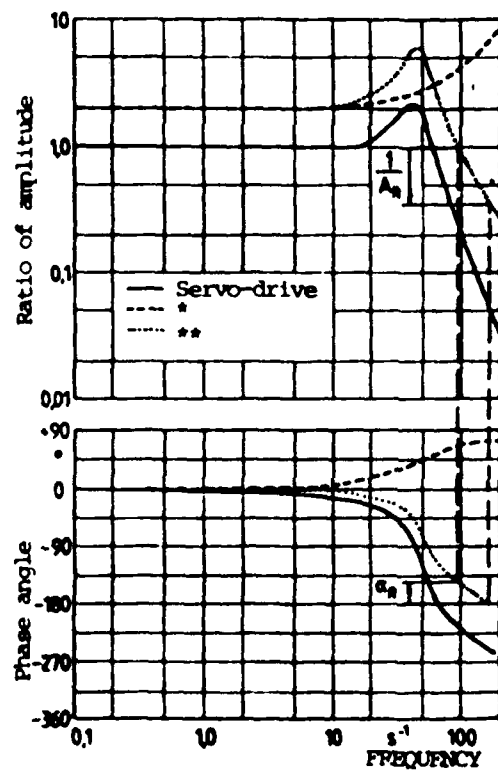
The application of the Nyquist criterion to an optimised control loop with a PD-control unit is shown in Fig. 12. The frequency response of the open control loop resulting from the geometrical addition of the frequency responses of the servo-drive and the PD-control unit provides an amplitude reserve of $A_R = 3.0$ and a phase reserve of $\alpha_R = 30^\circ$ thereby fulfilling the stability criteria $A_R = 1$ and $\alpha_R > 0^\circ$.



*Control loop with PD-control unit

**Control loop with PD-control unit
and noise elimination

Fig. 11 Frequency response of the servo-drive and of the closed-loop control with and without noise elimination



*PD-control unit
 **Open control loop

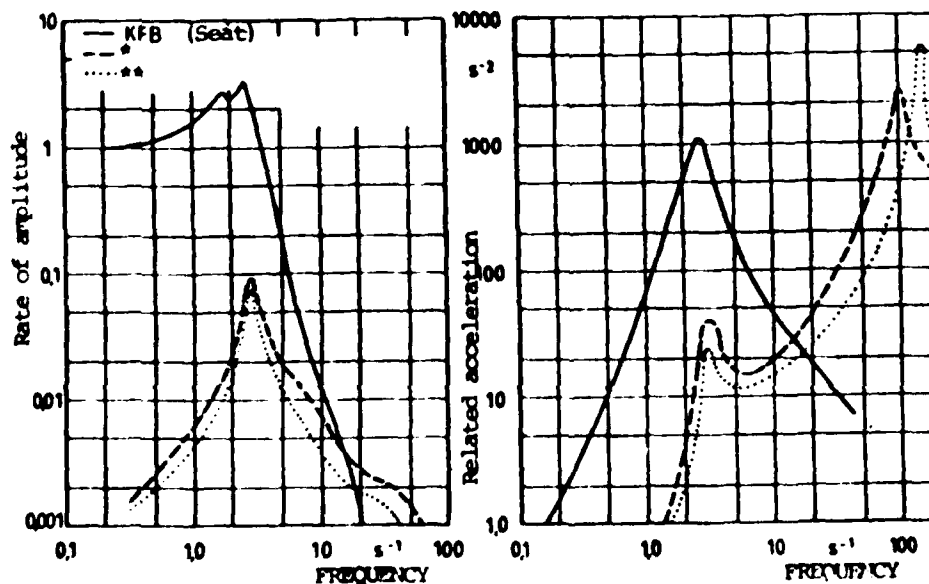
Fig. 12 Stability investigation according to the Nyquist criterion

SYNTHESIS OF ACTIVE SUSPENSION AND THE WHEELED TRACTOR

In order to match the active suspension system to the wheeled tractor vibration model, the oscillator of the conventional seat suspension was replaced by the closed-loop control of the active system. The vertical movement of the tractor body at the linkage point of the seat suspension was used as a disturbance signal.

Vibration properties

The amplitude frequency responses of the seat measured for integrated active suspension and the acceleration at the seat related to the excitation amplitude are compared in Fig. 13 with the corresponding curves for conventional seat suspension. The active suspension version, functioning with noise elimination, shows more favourable amplitude and acceleration values as compared to the version with a simple control loop. In contrast to the conventional seat suspension, both active suspension versions offer a clearly depressed acceleration level in the frequency range up to ca. 15 Hz. In the higher frequency range a steep decrease in amplitude results from the low pass characteristic of the conventional suspension which, because of the negative phase angle that occurs, the active suspension systems are incapable of following. This is also the reason for the higher related acceleration values of the active suspension in the frequency range >15 Hz. The high acceleration values occurring in the natural frequency range of the active suspension system are of lesser importance to the total vibration load because of subjective evaluative perception by the driver. The measured values for the perception strength KZ and the effective acceleration of the conventionally and actively suspended seats during stochastic excitation of the tractor simulation model with road surface roughness are shown in Fig. 14



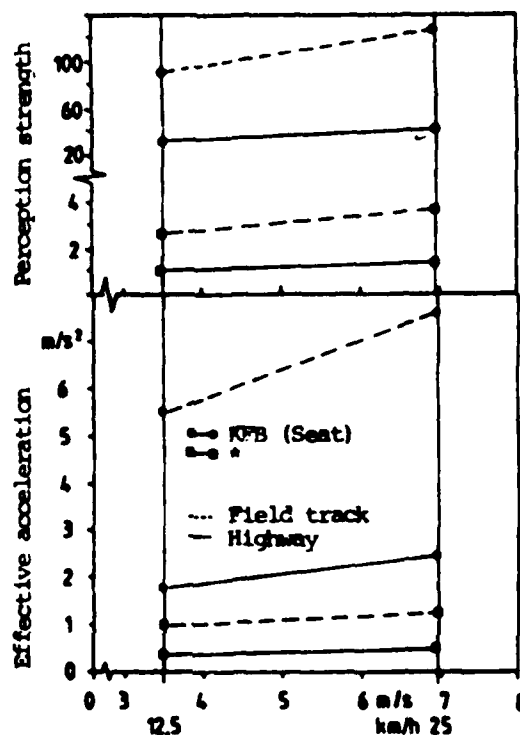
*AFB (Seat) with PD-control unit

**AFB (Seat) with PD-control unit and noise elimination

Fig. 13 Amplitude frequency response and related acceleration for conventionally (KFB) and actively (AFB) suspended tractor seats

*AFB (Seat) with PD-control unit and noise elimination

Fig. 14 Perception strength and effective acceleration of conventionally (KFB) and actively (AFB) sprung tractor seats



A clearly depressed level of acceleration and of objective vibration loads through the use of active suspension is shown in the total forward speed range. While the perception strength for a conventionally sprung seat during highway driving and field track operation lies between $KZ = 30-35$ and $KZ = 90-120$, respectively, a passenger-car comfort level is achieved through the use of an optimally synchronised active-suspension control loop with noise elimination. However, such synchronisation of the active suspension system, where the only aim is to minimise vibration loading, also leads to comparatively large relative movements between seat and tractor body. During field track operation the limits of the cylinder stroke were often exceeded, which should be avoided by means of a supplementary control loop circuit and a cylinder end-bearing damping. Since, however, a large relative degree of travel generally renders the stable conduct of the vehicle more difficult, the use of active suspension should be extended in future research to an entire cab with integrated controls.

Power requirements for active suspension

An approach to calculating the necessary hydraulic power requirement of an active suspension system is permitted by the equation:

$$P_p = \frac{1}{\eta_p} \cdot p \cdot A_K \cdot v_{K_{eff}}$$

where pump efficiency $\eta_p = 0.85$
 operating oil pressure $p = 210 \text{ bar}$
 piston area $A_K = 4.9 \text{ cm}^2$

For the measured piston speeds at the active suspension cylinder of 0.22 m/s during highway travel and 0.67 m/s during field track operation at forward speeds of 25 km/h, the calculated power requirement is equivalent to 2.7-8.1 kW, according to operational mode. Because of this high power requirement, especially during field track operation, the use of an active suspension system seems useful only for tractor categories with a high power availability.

SUMMARY

The theoretical possibilities of an active seat suspension were investigated with the aid of an analogue computer model designed to simulate the vibration characteristics of a wheeled tractor and of a simple active suspension system.

The active suspension system, consisting of a servo-hydraulic cylinder, a servo-valve and an energy source, was operated in a closed-loop control with a PD-control unit and noise elimination. After measurement of the frequency responses of the individual components, the active suspension system was integrated with the vehicle model and synchronisation of the control unit characteristics was optimised in terms of stability. During vibration excitation of the total model with harmonic signals and with the road surface roughness of highways and field tracks the active seat suspension achieved a clear reduction in the vibration load on the driver. It was concluded on the basis of evaluation of the necessary power requirement for an active suspension system that the application of such a system was useful only for tractors belonging to higher power classes.

REFERENCES

1. BENDER, E.K. Some fundamental limitations of active and passive suspension systems. SAE 680750
2. CALCATERA, P.C. Performance characteristics of active suspension systems for low frequency vibration isolation. SM Thesis, MIT, June 1967
3. CALCATERA, P.C. and SCHUBERT, D.W. Research on active isolation techniques for aircraft pilot protection. MRL-TR-138, Aerospace Medical Research Laboratories 1967, Wright-Patterson Air Force Base, Ohio, USA
4. COERMANN, R.R. and LANGE, W. An investigation of the possibility of active damping for drivers' seats (in German). Grundlagen der Landtechnik, 1971, 21 (1)
5. Guillon, M. Hydraulic Control Loops and Servo-Controls. Carl Hanser Verlag, Munich, 1968 (in German)
6. HART, J. A sprung cab for unsprung terrain vehicles (in German). Automobiltechnische Zeitschrift, 1977, 79 (7/8)
7. HELMS, H. Vibration characteristics of a sprung tractor seat (in German). Automobiltechnische Zeitschrift, 1976, 26

8. JUNKER, H. and SEENALD, A. An investigation of an active suspension-damper system to reduce the vibration load on a person in a vehicle (in German). DFG-Forschungsbericht, He 525/14
9. KAUS, W. and GOHLICH, H. Active vibration isolation of the driver's seat of an unsprung vehicle (in German). Automobiltechnische Zeitschrift, 1982, 84 (9)
10. KOPPER, R. Determining the necessary vibration comfort of terrain vehicles and its implementation through active suspension (in German). Dissertation, TU Berlin, 1973
11. LAETHERWOOD, J.D. and DIXON, G.V. Active vibration isolation for flexible payloads. IES Proceedings, April 1968, pp. 407-413
12. OWZAR, A. An investigation of the vibration characteristics of unsprung vehicles with pneumatic tyres (in German). Automobiltechnische Zeitschrift, 1976, 78 (9)
13. ROHL, E., HELLING, J. and JUNKER, H. Development of a new-type patient housing for ambulances (in German). Proceedings of FISITA Congress, Budapest, 1978
14. ROHL, E. and JUNKER, H. Development and construction of a new-type ambulance (in German). Automobiltechnische Zeitschrift, 1979, 81 (12)
15. STICKLEATHER, L.W. The development of an active seat suspension for off-road vehicles. Ph.D. thesis, North Carolina State University, 1968
16. WENDEBORN, J.D. A contribution to improving the drive comfort of agricultural tractors (in German). Fortschritt-Bericht, VDI-Z, Reihe 14, 8, 1968

LEISTUNGSSTEIGERUNG UND VERBESSERUNG DES FAHRKOMFORTS BEI SELBSTFAHRENDEN BAUMASCHINEN DURCH REDUZIERUNG EINSATZBEDINGTER NICK- UND HUBSCHWINGUNGEN

PROF. DR.-ING. WOLFGANG POPPY / DR.-ING. ALFRED ULRICH

KONSTRUKTION VON BAUMASCHINEN - TECHNISCHE UNIVERSITÄT BERLIN

Selbstfahrende ungefederte Baumaschinen - wie Radlader und Autokrane - neigen auf unebener Fahrbahn schon bei niedrigen Fahrgeschwindigkeiten zu erheblichen Nickbewegungen. Durch die dabei auftretenden dynamischen Beanspruchungen werden der Fahrer, die Maschine und die Fahrbahn hoch belastet und in ungünstigen Fällen erheblich gefährdet.

Eine wirkungsvolle und kostengünstige Schwingungsreduzierung läßt sich durch die Verwendung der Arbeitsausrüstung der Maschine als Absorbermasse erreichen, indem in ihre starre Abstützung ein Feder-Dämpfer-Element eingefügt wird. Die Auswirkungen dieses Schwingungsabsorbers auf die Fahr-sicherheit, die Bauteilbeanspruchung und den Fahrkomfort wurden am Fach-gebiet "Konstruktion von Baumaschinen" der Technischen Universität Berlin analytisch und experimentell untersucht. Fahrversuche mit Geräten unter-schiedlicher Größe haben gute Übereinstimmung mit den Ergebnissen der Rechnersimulation erbracht. Die Verbesserung der Fahr-sicherheit und des Fahrkomforts liegen bei 50 % gegenüber den konventionellen Maschinen.

1. EINLEITUNG

Selbstfahrende Erdbaumaschinen legen beim Einsatz auf der Baustelle nicht selten auch längere Fahrstrecken zurück und nehmen beim Transport zu den verschiedenen Einsatzorten "auf eigener Achse" am öffentlichen Straßen-verkehr teil. Aus wirtschaftlichen Gründen wird angestrebt, die Fahrzeiten zu minimieren. Der Fahrzeugführer wählt deshalb nach subjektiven Kriterien die jeweils höchstmögliche Fahrgeschwindigkeit. Diese wird jedoch wesent-lich durch das Schwingungsverhalten des Fahrzeugs und die sich daraus er-gebenden Beeinträchtigungen der Fahr-sicherheit und des Fahrkomforts be-grenzt.

Besonders ungefederte Baumaschinen neigen schon bei niedrigen Fahrgeschwin-digkeiten zu erheblichen Nickbewegungen, die zu einer hohen dynamischen Beanspruchung des Fahrers, der Maschine und der Fahrbahn und in ungünsti-gen Fällen zu einer erheblichen Gefährdung führen. Eine Erhöhung des Fahr-komforts, der Fahr-sicherheit und der Wirtschaftlichkeit läßt sich durch Reduzierung der Fahrzeugschwingungen, insbesondere der Nickschwingungen, erreichen.

2. MÖGLICHKEITEN FÜR DIE SCHWINGUNGSREDUZIERUNG AN ERDBAUMASCHINEN

2.1 Feder- und Dämpferwirkung der Fahrzeugreifen

Bei der Mehrzahl der Erdbaumaschinen ist der Reifen das alleinige Feder-Dämpfer-Element, das in der Lage ist, Fahrzeugschwingungen zu reduzieren (Bild 1). Durch Senken der Federsteifigkeit (Bild 2) und Erhöhen der Rei-fendämpfung (Optimum $D \approx 0,25$; Bild 3) ist es möglich, das Schwingungsverhalten einer Maschine positiv zu beeinflussen. Der heutige Stand der Tech-nik bei der Reifenentwicklung zeigt jedoch, daß ein weicher Reifen mit

optimalen Dämpfungseigenschaften zu Problemen hinsichtlich der Lebensdauer des Reifens, zu erhöhtem Rollwiderstand und zur Minderung der Lenkfähigkeit des Fahrzeugs führt.

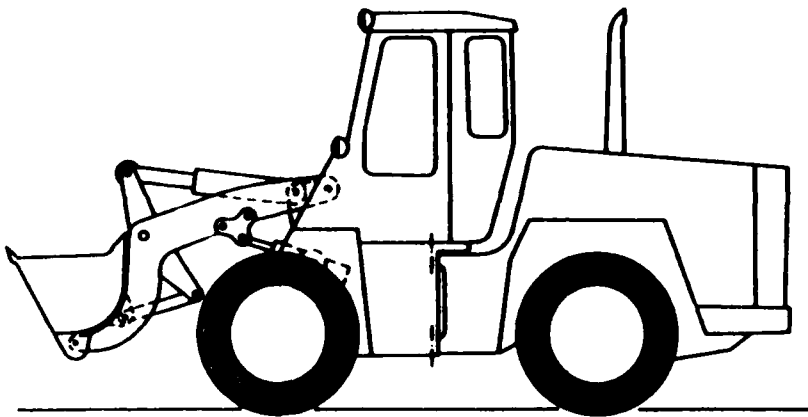


Bild 1. Reifen als Feder- und Dämpfer-Element beim Radlader

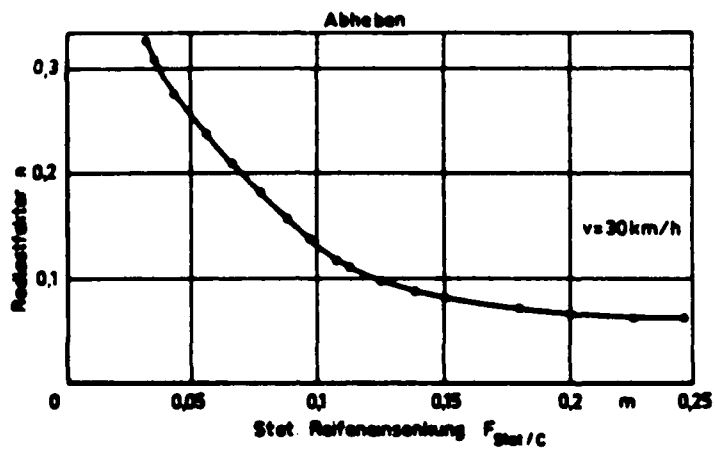


Bild 2. Achsbeschleunigung in Abhängigkeit von der Federsteifigkeit der Reifen

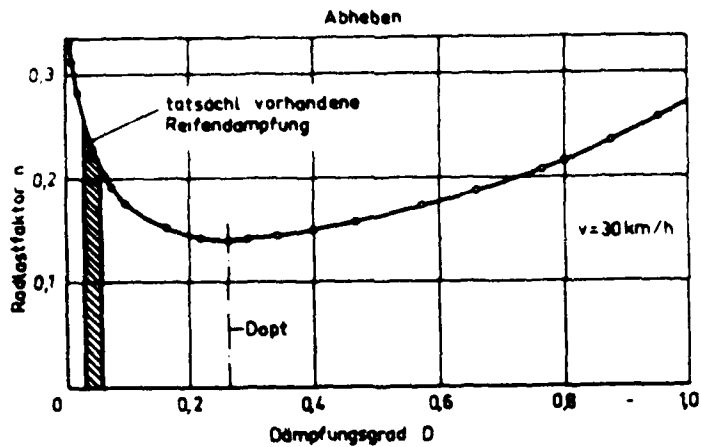


Bild 3. Achsbeschleunigung in Abhängigkeit von der Reifendämpfung

2.2 Achsfederungen

Der Einbau von Feder- und Dämpfer-Elementen zwischen Fahrzeugachsen und Aufbau ist die am häufigsten verwendete und wirkungsvollste Methode, Fahrzeugschwingungen zu reduzieren. Bei mobilen Baumaschinen ist eine Achsfederung beim Arbeitseinsatz jedoch häufig unerwünscht.

Durch einstellbare und sperrbare hydropneumatische Feder- und Dämpfer-Elemente kann die Federung im Fahrbetrieb ein- und beim Arbeitseinsatz ausgeschaltet werden. In Bild 4 und 5 ist die Anordnung und Steuerung einer hydropneumatischen Achsfederung dargestellt.

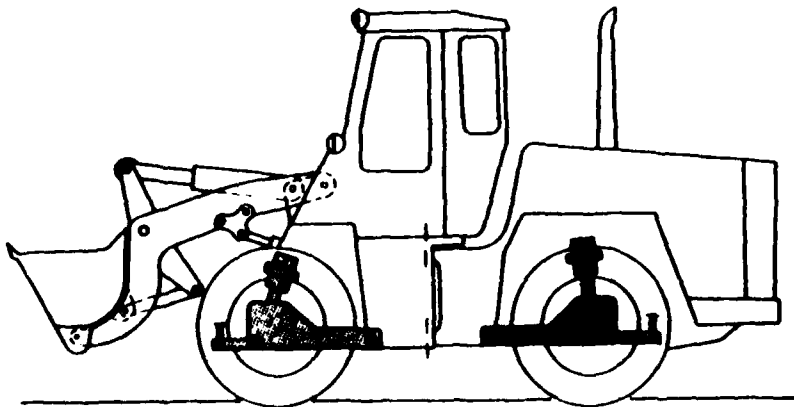


Bild 4. Radlader mit Feder- und Dämpfer-Elementen zwischen Achsen und Aufbau

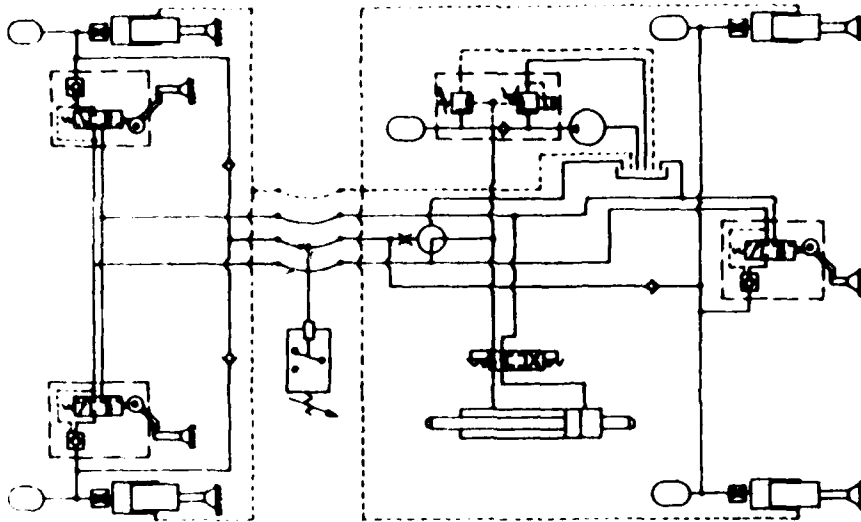


Bild 5. Schaltplan einer hydropneumatischen Achsfederung
(Zettelmeyer)

2.3 Schwingungsabsorber

Eine wirkungsvolle und kostengünstige Schwingungsreduzierung läßt sich durch die Verwendung der Arbeitsausrüstung der Maschine als Absorbermasse erreichen (Bild 6). Als Feder-Dämpfer-Element wird ein Membran-Druckspeicher in Verbindung mit einem Drosselventil geschaltet (Bild 7). Die Federkonstante und das Dämpfungsmaß des Feder-Dämpfer-Elementes werden so ausgelegt, daß es in Bezug auf die Schwingungen der Erdbaumaschine als Breitbandfilter wirkt.

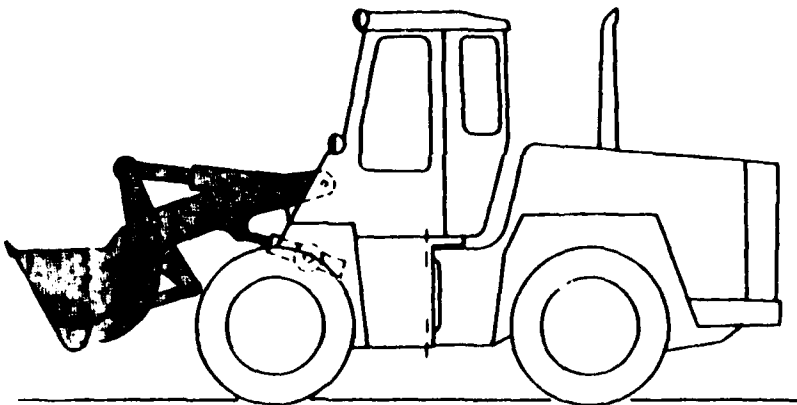
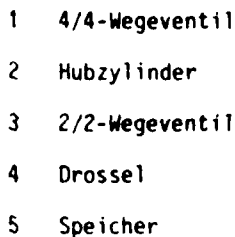


Bild 6. Verwendung der Ladeeinrichtung als Absorbermasse
zur Schwingungsreduzierung



3. SCHWINGUNGSVERHALTEN EINES RADLADERS

Für die analytischen Untersuchungen wurde ein Radlader gewählt. Das ungefederte Zweiachsfahrzeug hat über vier Räder Kontakt zur Fahrbahn, deren Unebenheiten als Schwingungen über die Reifen und Achsen auf den Fahrzeugrahmen übertragen werden.

Das vertikale Schwingungsverhalten des Radladers läßt sich wegen der Fahrzeuglängssymmetrie an Hand eines ebenen Schwingungsersatzmodells betrachten, wie es in Bild 8 für einen Radlader mit elastisch abgestützter Ar-

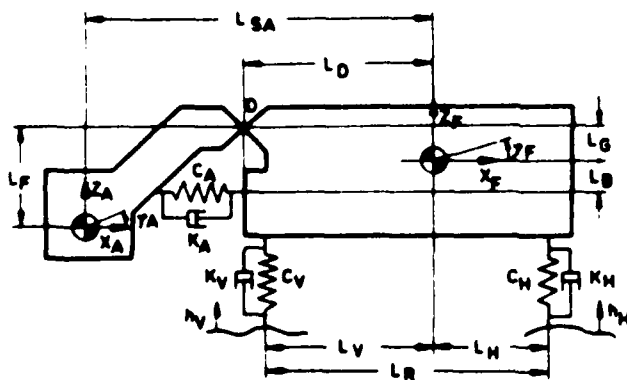


Bild 8. Schwingungsersatzsystem eines Radladers mit elastisch abgestützter Arbeitsausrüstung

beitsausrüstung dargestellt ist. Für die Berechnungen muß dabei die Hälfte der Fahrzeugmasse bzw. des Fahrzeugträgheitsmomentes herangezogen werden.

Ausgehend von diesem Ersatzmodell werden die Bewegungsgleichungen für die Zuck-, Hub- und Nickschwingungen des Radladers und seiner Arbeitsausrüstung aufgestellt und mit einem Analogrechner gelöst.

Zur Nachbildung der Fahrbahnunebenheiten bei der analogen Simulation dient ein Rauschgenerator, der eine regellose Ausgangsspannung $U(t)$ liefert. Mit diesem Fahrbahnsignal wird die Vorderachse des Radladers direkt angeregt, während die Erregung an der Hinterachse über ein Laufzeitglied eingeleitet wird, das aus Radstand und Fahrgeschwindigkeit berechnet wird.

Als Beurteilungsgröße für die Fahrsicherheit dient die dynamische Radlast an Vorder- und Hinterachse, zur Beurteilung des Fahrkomforts die vertikale und horizontale Sitzanregungsbeschleunigung.

Bei der analogen Simulation ist die Verwendbarkeit der Rechenergebnisse eng mit der Eingabe realistischer Fahrzeugdaten verknüpft. Für geländegängige Fahrzeuge, speziell für mobile Erdbaumaschinen, stehen die grundlegenden schwingungstechnischen Kenngrößen (Gewichte, Abmessungen, Schwerpunktlagen, Massenträgheitsmomente) nur in Einzelfällen oder unvollständig zur Verfügung. Die notwendigen Werte wurden deshalb aus Firmenangaben oder durch eigene experimentelle Untersuchungen ermittelt.

Entscheidend für eine genaue Berechnung des Schwingungsverhaltens ungefederter mobiler Baumaschinen ist auch die genaue Kenntnis der Feder- und Dämpferkennwerte der Reifen. Vorhandene statisch ermittelte Reifenkennwerte nichtrollender Reifen weichen vom tatsächlich auftretenden dynamischen Verhalten so weit ab, daß sie für die Simulation nicht geeignet sind. Die damit erzielten Rechenergebnisse können nur Tendenzen angeben. Die dynamische Reifeneinfederung wurde deshalb am rollenden Rad bei wirklichen Fahrvorgängen ermittelt. Sie liegt gegenüber der statischen Federkonstanten für die untersuchten Fahrzeugreifen (12.5-20, 10 PR und 17.5-25, 12 PR) im Mittel um 20 % niedriger.

Zur Ermittlung der für die Simulation benutzten Reifendämpfung wurden Ergebnisse von Mitschke (1) verwendet. Damit ließen sich in Abhängigkeit von der jeweiligen Achsresonanzfrequenz, dem Reifeninnendruck und dem Fahrzeuggewicht die Dämpfungskonstanten der benutzten Fahrzeugreifen bestimmen. Wegen des schmalen Frequenzspektrums, das eine ungefederte mobile Baumaschine aufweist, ist dies eine brauchbare Annäherung an die wirkliche Reifendämpfung, wenn die Unterschiede zwischen statischer und dynamischer Reifendämpfung nur gering sind.

3.2 Ergebnisse der Rechnersimulation

Die Beziehung zwischen Fahrzeugmasse, Massenträgheitsmoment (Y-Achse) und Schwerpunktlage bewirkt bei mobilen Baumaschinen eine starke Kopplung zwischen der Vorder- und der Hinterachse. Dies wird durch die Koppelmasse ausgedrückt. Sind Teile der Fahrzeugmasse - wie beim Radlader - außerhalb des Radstandes angeordnet, so ist die Koppelmasse negativ. Derartige Fahrzeuge neigen schon bei niedrigen Fahrgeschwindigkeiten zu starken Nickbewegungen, was die Fahrsicherheit durch hohe dynamische Radlasten und den Fahrkomfort durch starke Sitzanregungsbeschleunigungen in vertikaler und horizontaler Richtung erheblich verschlechtert.

Ein weiteres charakteristisches Merkmal ist das Auftreten von zwei Resonanzstellen bei der Übertragungsfunktion der dynamischen Radlasten (Bild 9 und 10). Die erste Resonanzstelle wird durch Nick-, die zweite höherfrequente Resonanzstelle durch Hubbewegungen erzeugt, d.h., die größten dynamischen Radlasten werden durch Nickbeschleunigungen verursacht.

Für die Koppelmasse $m_k = 0$ ist das Übertragungsverhalten an den Fahrzeugachsen unabhängig von der Fahrgeschwindigkeit. Bei negativer Koppelmasse zeigt sich hingegen eine systematische Abhängigkeit (Bild 9 und 10). Dieses Verhalten ist kennzeichnend für massengekoppelte Zweimassenschwinger und macht es erforderlich, die gewählten Beurteilungsgrößen stet. im Zusammenhang mit der Fahrgeschwindigkeit zu betrachten.

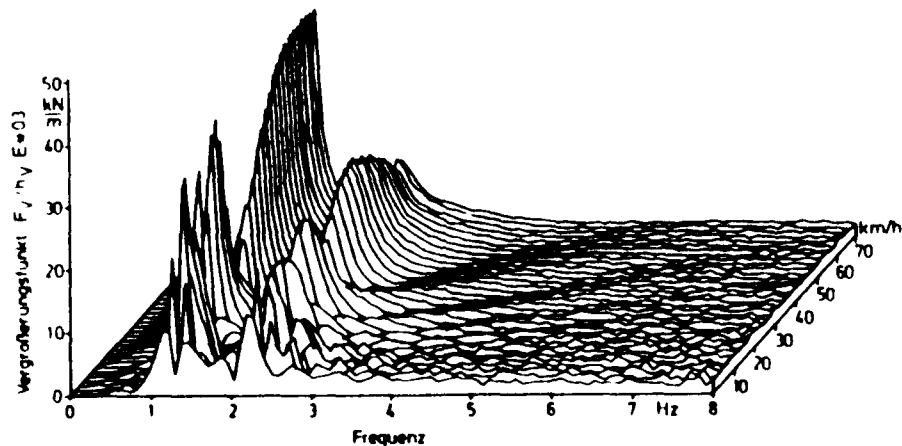


Bild 9. Vergrößerungsfunktion der dynamischen Vorderachslasten für einen Radlader mit starr abgestützter Arbeitsausrüstung

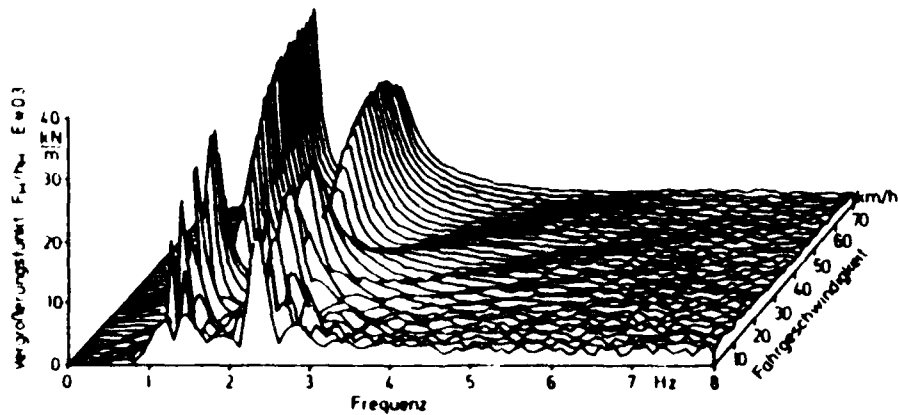


Bild 10. Vergrößerungsfunktion der dynamischen Hinterachslasten für einen Radlader mit starr abgestützter Arbeitsausrüstung

Die Schwingungsbeanspruchung des Menschen ist bei der Bedienung selbstfahrender Baumaschinen durch die geringe Reifendämpfung allgemein recht hoch. Die Lage des Sitzbefestigungspunktes ist dabei eine konstruktive Größe, die die Fahrersitzbeschleunigung negativ beeinflussen kann. Im Schwerpunkt des Fahrzeugs ist die vertikale Beschleunigung am geringsten (Bild 11) und dies damit der günstigste Sitzbefestigungspunkt. Diese Anordnung läßt sich aus konstruktiven Gründen nicht bei allen Maschinen verwirklichen. Bei Autokranen kommen zum Beispiel Sitzanordnungen von der Vorderachse bis hin zum Schwerpunkt vor.

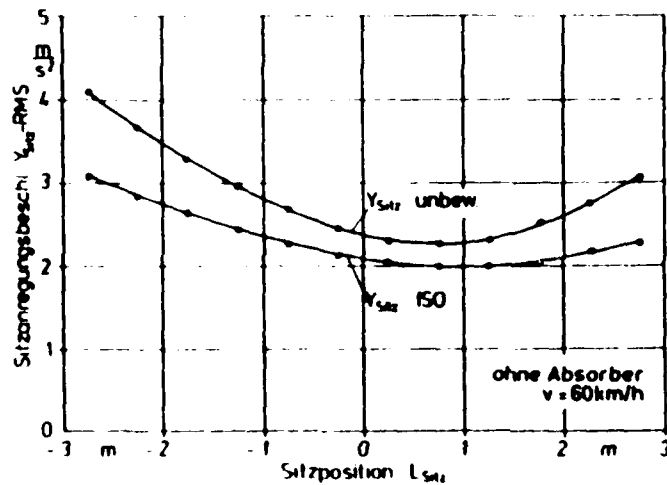


Bild 11. Vertikalbeschleunigung zwischen den Fahrzeugachsen bei einem Radlader

4. SCHWINGUNGSREDUZIERUNG DURCH ABSORPTION

4.1 Prinzip eines dynamischen Schwingungsabsorbers

Die Wirkungsweise eines dynamischen Schwingungsabsorbers läßt sich prinzipiell an einem Einmassenschwinger erklären, der mit einer zweiten elastisch angekoppelten Masse ausgerüstet ist (Bild 12).

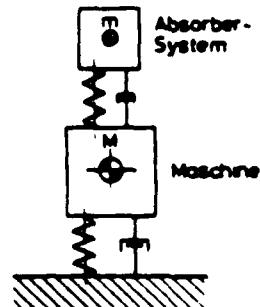


Bild 12. Dynamischer Schwingungsabsorber

Der Absorber ist im Prinzip ein Resonanzsystem, das auf der schwingenden Struktur angebracht wird und den zu reduzierenden Schwingungen entgegenwirkt.

Ist der Absorber so auf das Hauptsystem abgestimmt, daß das Verhältnis der Resonanzfrequenzen $\nu = 1$ ergibt und der Dämpfungsgrad $k = 0$ ist, wird die Resonanzstelle des Hauptsystems vollständig absorbiert (Bild 13). Diesem gewünschten Verhalten steht als Nachteil entgegen, daß zwei zusätzliche Resonanzstellen auftreten. Bei einer unendlichen Absorberdämpfung $k = \infty$ ist die Absorbermasse mit der Hauptmasse so verbunden, daß sie sich nicht gegeneinander bewegen. Das Absorbersystem ist dabei völlig funktionslos, so daß die eigentlich zu absorbierende Resonanzstelle wieder auftritt.

Zwischen den extremen Dämpfungswerten $k = 0$ und $k = \infty$ gibt es eine Dämpfung, bei der das Hauptsystem die kleinsten Schwingungen ausführt.

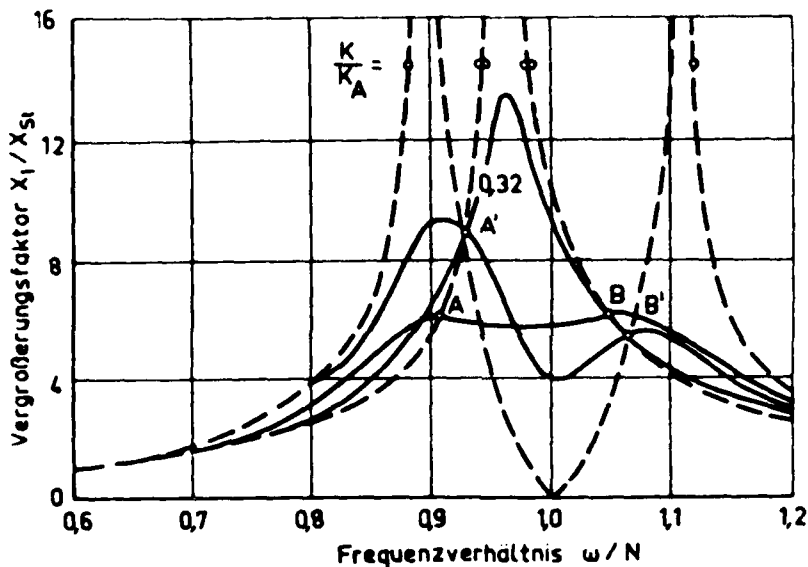


Bild 13. Übertragungsfunktion eines dynamischen Absorbers bei unterschiedlicher Dämpferabstimmung

4.2 Absorberabstimmung im Hinblick auf Fahrkomfort und Fahrsicherheit

Bei der Wahl der günstigsten Absorberabstimmung zeigen sich für die dynamischen Radlasten und die Fahrersitzanregungsbeschleunigung unterschiedliche Abstimmungsfrequenzen, jedoch annähernd gleiche Dämpfungsgrade von $D \approx 0,3$. Diese Dämpfung ist, wie Untersuchungen bei der Massenträgheitsmomentenbestimmung von Absorbermassen beim Radlader zeigen, praktisch nicht realisierbar. Vielmehr muß mit einer eigenen Dämpfung von $D \approx 1$ gerechnet werden.

Die in Bild 14 bis 25 dargestellten Rechenergebnisse zeigen das Verhalten bei dieser hohen Dämpfung und einer Absorberfrequenz von 1,4 Hz, die einen Kompromiß zwischen Fahrkomfort und Fahrsicherheit bilden.

Die Linearspektren der dynamischen Radlasten (Bild 16 bis 19) und der Sitzanregungsbeschleunigungen (Bild 22 bis 25) machen deutlich, daß die maßgebliche Reduzierung der Fahrzeugschwingungen bei der ersten Resonanzüberhöhung (Nicken) erreicht wird.

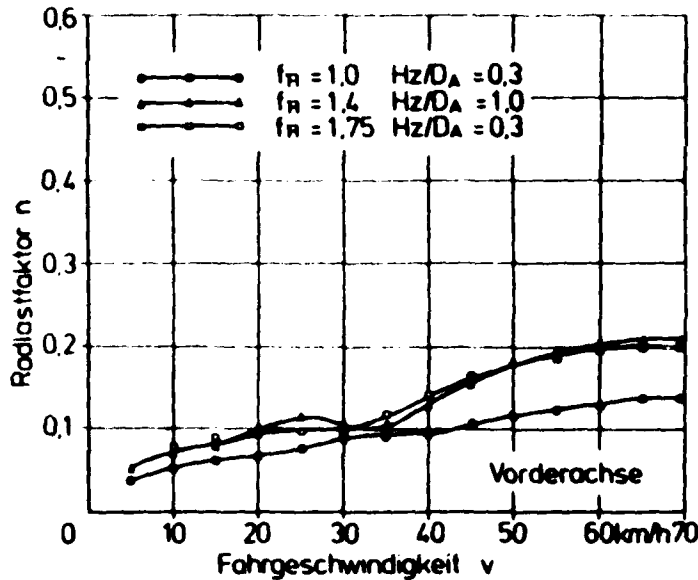


Bild 14. Radlastfaktor an der Vorderachse in Abhängigkeit von der Fahrgeschwindigkeit bei unterschiedlicher Absorberabstimmung

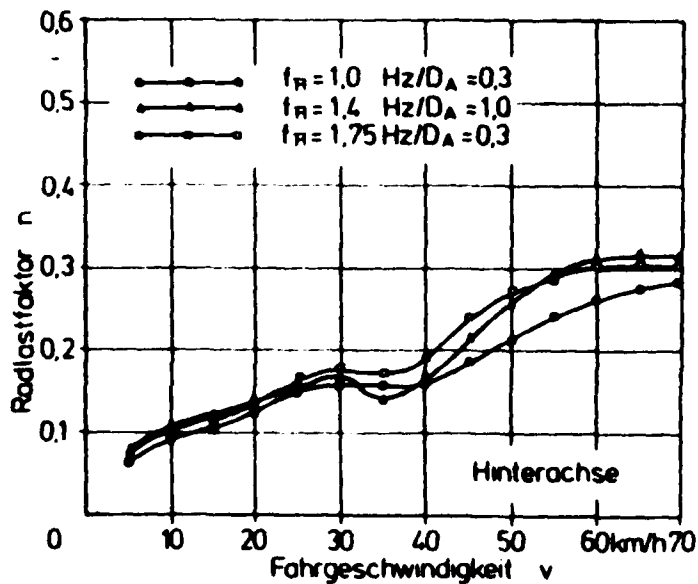


Bild 15. Radlastfaktor an der Hinterachse in Abhängigkeit von der Fahrgeschwindigkeit bei unterschiedlicher Absorberabstimmung

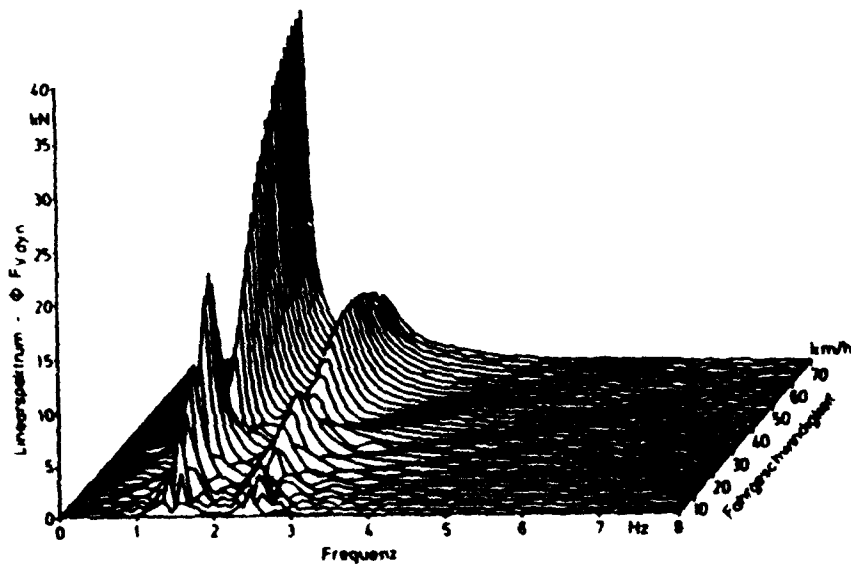


Bild 16. Linear-Spektrum der dynamischen Vorderachslasten eines Radladers mit starr abgestützter Arbeitsausrüstung in Abhängigkeit von der Fahrgeschwindigkeit

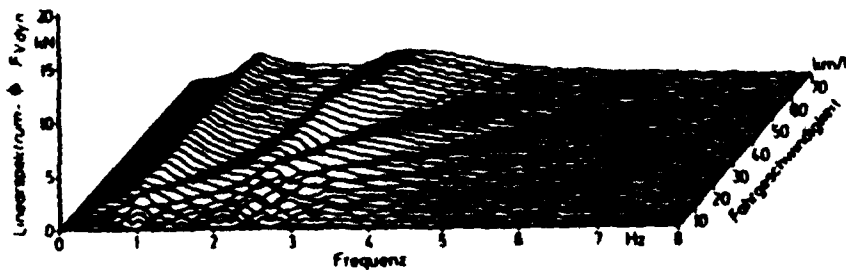


Bild 17. Linear-Spektrum der dynamischen Vorderachslasten eines Radladers mit elastisch abgestützter Arbeitsausrüstung in Abhängigkeit von der Fahrgeschwindigkeit

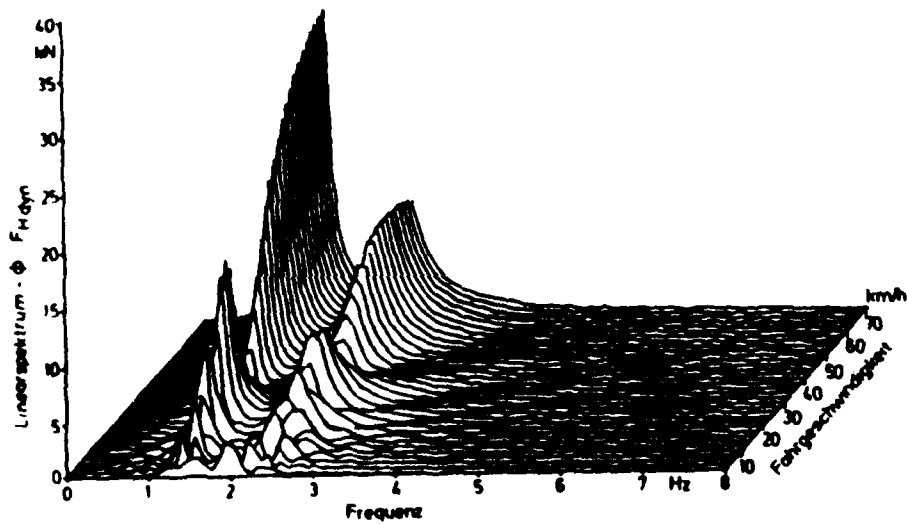


Bild 18. Linear-Spektrum der dynamischen Hinterachslasten eines Radladers mit starr abgestützter Arbeitsausrüstung in Abhängigkeit von der Fahrgeschwindigkeit

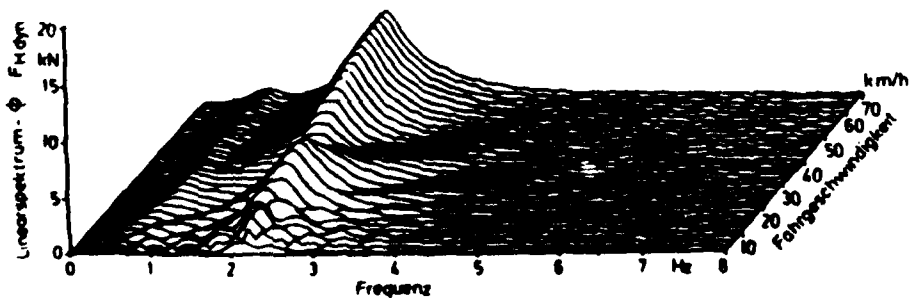


Bild 19. Linear-Spektrum der dynamischen Hinterachslasten eines Radladers mit elastisch abgestützter Arbeitsausrüstung in Abhängigkeit von der Fahrgeschwindigkeit

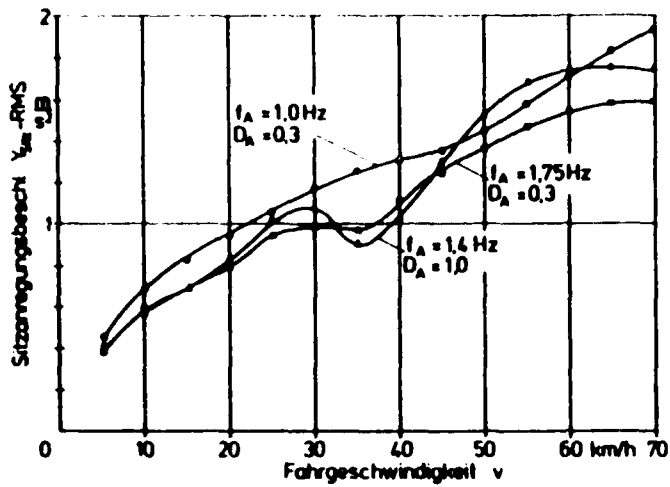


Bild 20. Vertikale Fahrersitzanregungsbeschleunigung in Abhängigkeit von der Fahrgeschwindigkeit bei unterschiedlicher Absorberabstimmung

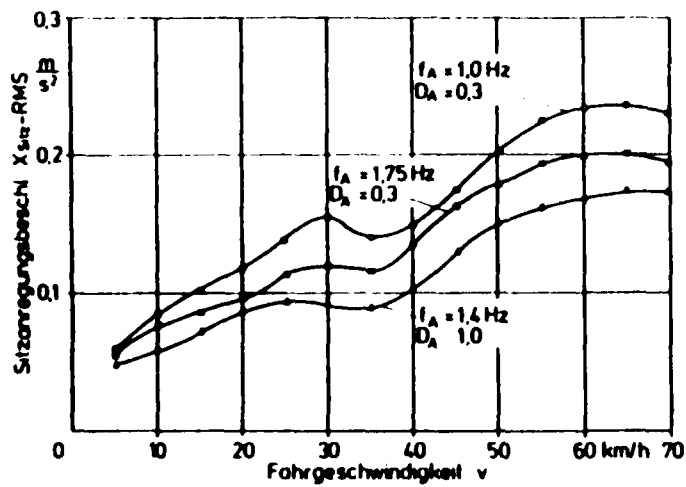


Bild 21. Horizontale Fahrersitzanregungsbeschleunigung in Abhängigkeit von der Fahrgeschwindigkeit bei unterschiedlicher Absorberabstimmung

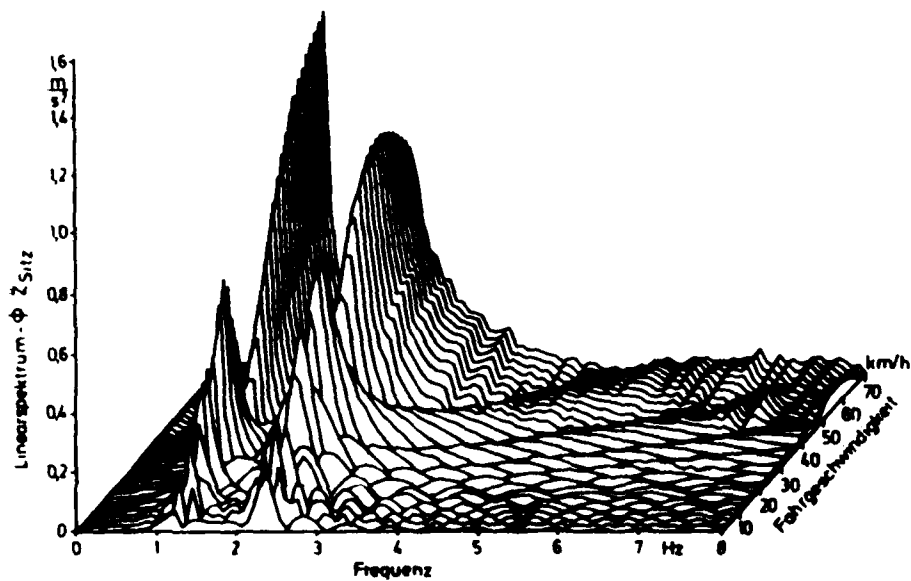


Bild 22. Linear-Spektrum der vertikalen Fahrersitzanregungsbeschleunigung eines Radladers mit starr abgestützter Arbeitsausrüstung in Abhängigkeit von der Fahrgeschwindigkeit

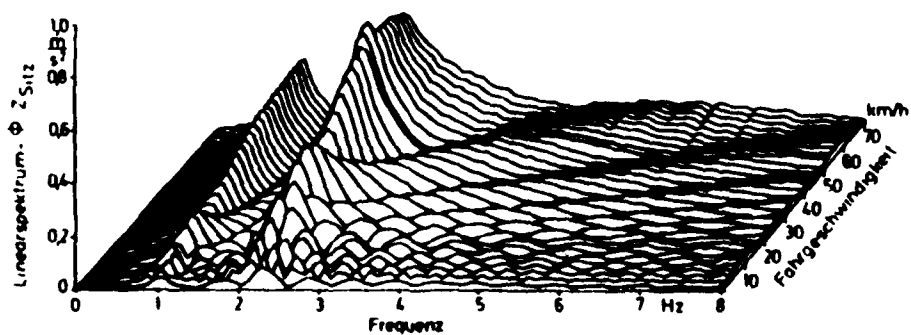


Bild 23. Linear-Spektrum der vertikalen Fahrersitzanregungsbeschleunigung eines Radladers mit elastisch abgestützter Arbeitsausrüstung in Abhängigkeit von der Fahrgeschwindigkeit

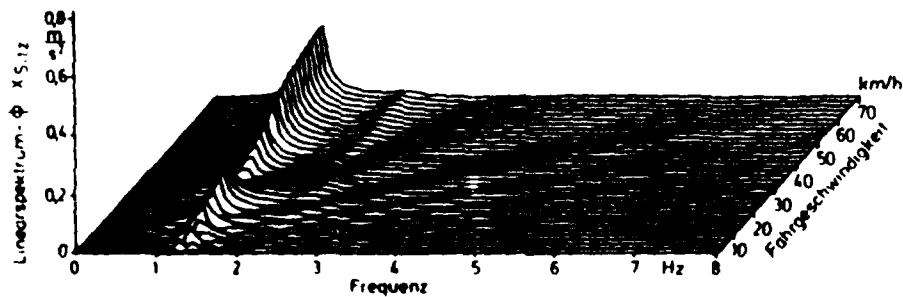


Bild 24. Linear-Spektrum der horizontalen Fahrersitzanregungsbeschleunigung eines Radladers mit starr abgestützter Arbeitsausrüstung in Abhängigkeit von der Fahrgeschwindigkeit

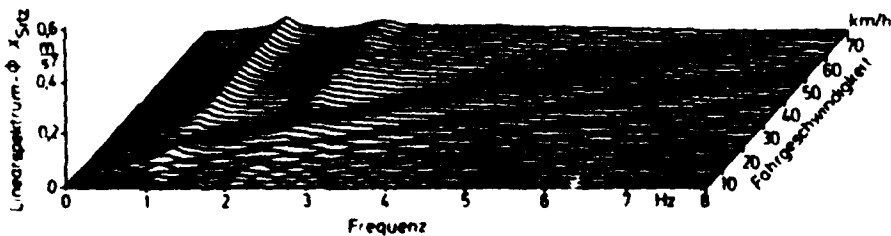


Bild 25. Linear-Spektrum der horizontalen Fahrersitzanregungsbeschleunigung eines Radladers mit elastisch abgestützter Arbeitsausrüstung in Abhängigkeit von der Fahrgeschwindigkeit

4.3 Absorberbewegung

Bei der praktischen Realisierung einer Absorption von Fahrzeugschwingungen durch Verwendung der Arbeitsausrüstung als Absorbermasse ist die dabei auftretende Absorberbewegung im Hinblick auf die beim Befahren öffentlicher Straßen geltenden Sicherheitsvorschriften von besonderer Bedeutung. Die Relativbewegung zwischen Fahrzeug und Arbeitsausrüstung soll möglichst gering sein.

Die in Bild 26 dargestellte relative Amplitudenverteilung zeigt, daß die benötigte Absorberbewegung selbst bei optimaler Absorberabstimmung nicht größer als ± 30 mm wird. Bei Verwendung einer realistischen Absorberdämpfung von $D_A \approx 1,0$ reduziert sich der maximal benötigte Absorberweg auf ± 15 mm. Derartig kleine Relativbewegungen der Arbeitsausrüstung lassen sich ohne Schwierigkeiten konstruktiv verwirklichen.

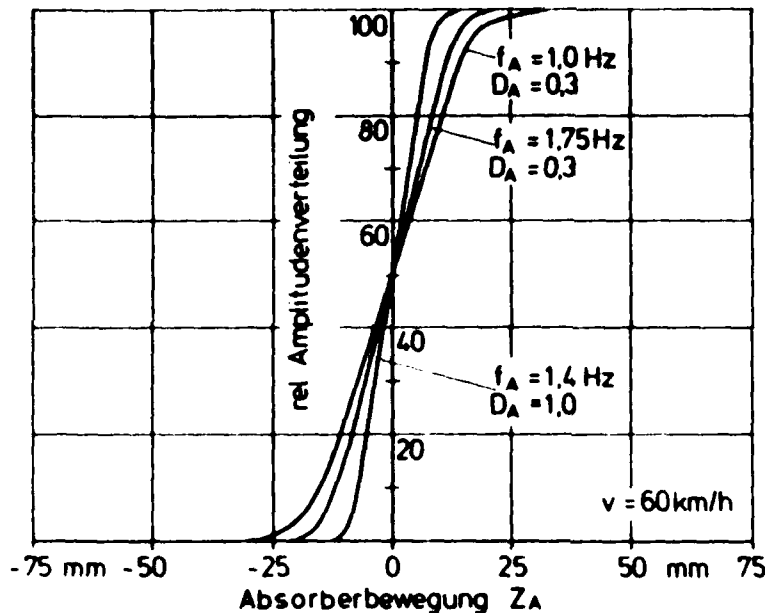


Bild 26. Relative Amplitudenverteilung der Bewegung der Arbeitsausrüstung bei unterschiedlicher Absorberabstimmung

5. FAHRVERSUCHE

Zur Überprüfung der durch die Rechnersimulation gewonnenen Ergebnisse wurden Fahrversuche mit einem der Simulation zugrunde gelegten Radlader durchgeführt. Diese ergaben eine gute Übereinstimmung mit der Rechnung, insbesondere hinsichtlich der erzielbaren Schwingungsreduzierung (Bild 27 bis 29).

Bemerkenswert sind Verhalten und Äußerungen des Fahrers, der den Versuchen zunächst mit größter Skepsis gegenüberstand, nach den Fahrten mit dem Schwingungsabsorber auf diesen aber nicht mehr verzichten wollte. Gerade die Vertrautheit mit dem üblichen Schwingungsverhalten der selbstfahrenden

Baumaschinen hat zu der allgemein anzutreffenden Vorstellung geführt, daß dies normal und nicht änderungsbedürftig ist. Dem stehen die überzeugenden Ergebnisse und Erfahrungen mit der Schwingungsabsorption durch elastisches Abstützen der Arbeitsausrüstung entgegen.

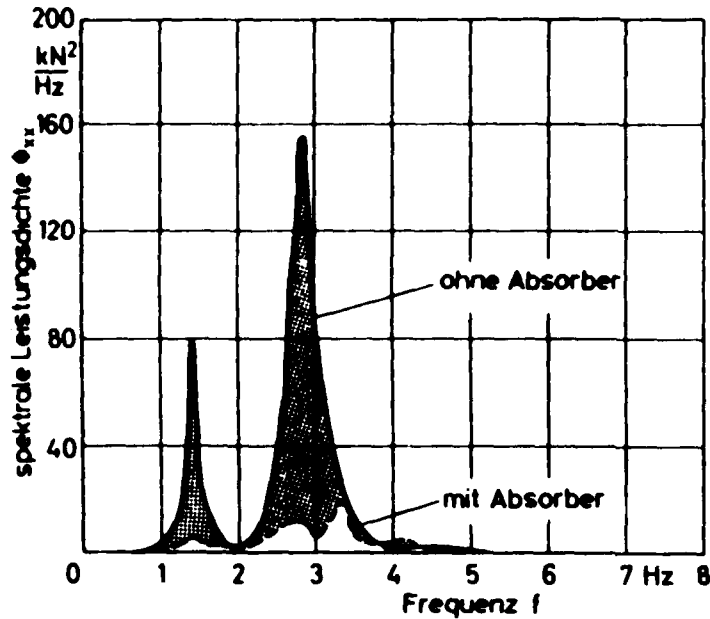


Bild 27. Schwingungsreduzierung an der Vorderachse eines Radladers

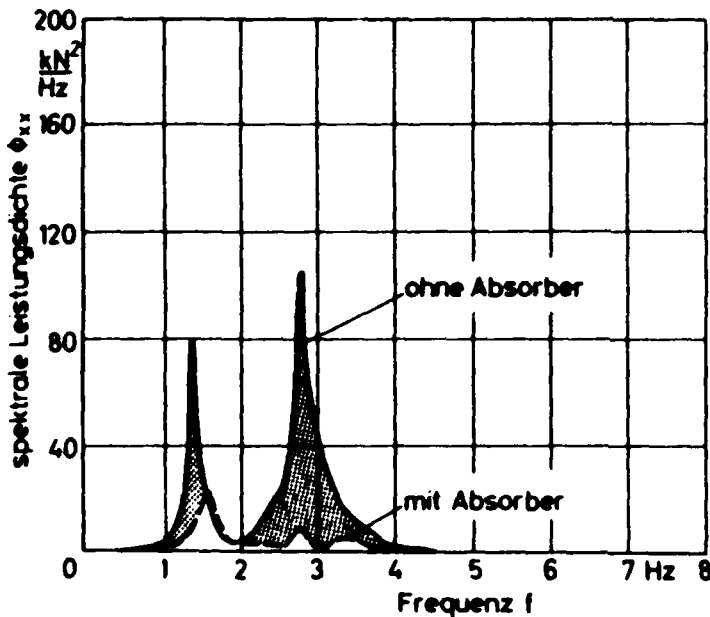


Bild 28. Schwingungsreduzierung an der Hinterachse eines Radladers

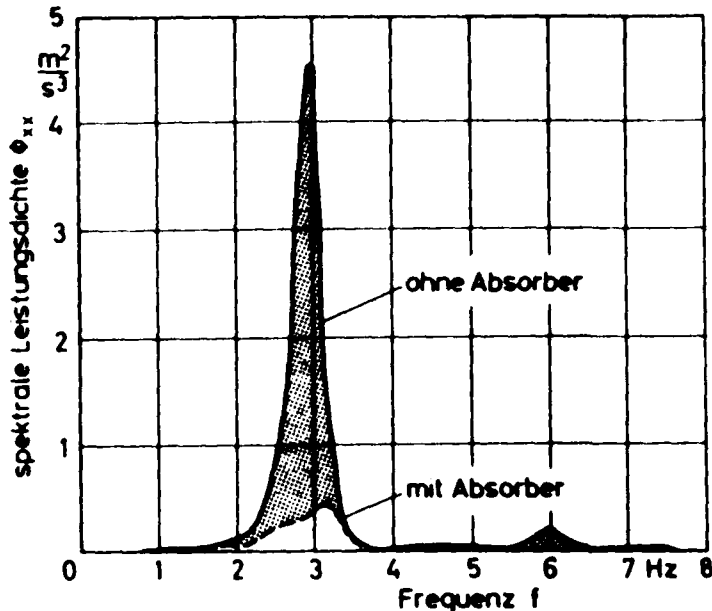


Bild 29. Schwingungsreduzierung am Fahrersitz eines Radladers

6. ZUSAMMENFASSUNG

In analytischen und experimentellen Untersuchungen werden der Fahrkomfort und die Fahrsicherheit ungefederter selbstfahrender Baumaschinen mit starrer und elastischer Abstützung der Arbeitsausrüstungen betrachtet. Fahrzeuge, bei denen ein wesentlicher Teil der Fahrzeugmasse außerhalb des Radstandes angeordnet ist - wie dies bei Radladern stets der Fall ist -, neigen schon bei niedrigen Fahrgeschwindigkeiten zu starken Nickbewegungen, die die Fahrsicherheit und den Fahrkomfort erheblich beeinträchtigen können.

Als Beurteilungsgrößen für die Fahrsicherheit dienen die dynamischen Radlasten und für den Fahrkomfort die vertikale und die horizontale Fahrersitzanregungsbeschleunigung. Die Abhängigkeit der dynamischen Radlasten und der Sitzanregungsbeschleunigung von der Fahrgeschwindigkeit ist bei diesen Fahrzeugen sehr unterschiedlich, so daß die Schwingungsgrößen stets für den gesamten Geschwindigkeitsbereich betrachtet werden müssen.

Die Lage des Sitzbefestigungspunktes zum Gesamtschwerpunkt des Fahrzeugs ist entscheidend für die Auswirkungen der Nickbeschleunigungen auf die Beanspruchung des Fahrers. Durch elastisches Abstützen der Arbeitsausrüstung und ihre Verwendung als Absorbermasse kann das Schwingungsverhalten der Maschinen wesentlich verbessert werden.

Bei der Abstimmung des Absorbers in Bezug auf die größtmögliche Reduzierung der dynamischen Radlasten und der Sitzanregungsbeschleunigung muß ein Kompromiß zwischen Fahrsicherheit und Fahrkomfort getroffen werden, wie er bei der Auslegung von Achsfederungen üblich ist.

Die beim elastischen Abstützen der Arbeitsausrüstung auftretenden Relativ-

Bewegungen zwischen Arbeitsausrüstung und Fahrzeugrahmen betragen bei einer in der Praxis realistischen Absorberdämpfung von $D \approx 1$ etwa ± 15 mm. Derartig kleine Relativbewegungen der Arbeitsausrüstung lassen sich ohne Schwierigkeiten konstruktiv verwirklichen.

Insgesamt zeigen die vorliegenden Ergebnisse, daß mit dem Prinzip der Schwingungsabsorption eine beträchtliche Erhöhung des Fahrkomforts und der Fahrsicherheit ungefederter selbstfahrender Baumaschinen erzielt werden kann. Fahrversuche mit einem Radlader bestätigen die Ergebnisse der Rechnersimulation.

7. SCHRIFTTUM

- Mitschke, M.: Dynamik der Kraftfahrzeuge. Springer-Verlag, Berlin, Heidelberg, New York, 1972
- Mitschke, M.: Fahrsicherheit und Straßenschonung von ungefederten Fahrzeugen. Deutsche Kraftfahrtforschung und Straßenverkehrstechnik, 1971
- Helms, H.: Grenzen der Verbesserungsfähigkeit von Schwingungskomfort und Fahrsicherheit an Kraftfahrzeugen. Dissertation, TU Braunschweig 1974
- Willumeit, H.-P.; Richter, B.: Über den Einfluß von frequenzabhängigen Dämpfern und Schwingungstilgern in der Radaufhängung eines Straßenfahrzeugs. Automobil-Industrie 16(1971) Heft 2, S. 67-72
- Sharon, I.: Untersuchungen über die Schwingungseigenschaften großvolumiger Niederdruckreifen, Dissertation, TU Berlin, 1975
- Ulrich, A.: Untersuchungen zur Fahrdynamik von Traktoren mit und ohne Anbaugeräte. Dissertation, TU Berlin, 1983

INCREASE IN PERFORMANCE AND IMPROVEMENT OF RIDE COMFORT OF SELF-PROPELLED CONSTRUCTION MACHINERY BY REDUCING PITCH AND VERTICAL VIBRATION

PROF. DR.-ING. W. POPPY and DR.-ING. A. ULRICH
KONSTRUKTION VON BAUMASCHINEN, TECHNISCHE UNIVERSITÄT, BERLIN
(Translated by Miss G. Bateman, NIAE, Silsoe, England)

Self-propelled unsprung construction machines - such as tractor-loaders and mobile cranes - are prone to pronounced pitching motion on uneven driving surfaces even at low forward speeds. Because of the dynamic loads which thus occur, the driver, machine and the driving surface are highly stressed and in unfavourable conditions are considerably endangered.

An effective and cheap method of reducing vibration is the use of the working attachment of the machine as an absorbing mass, with a spring and damping element set in its rigid support. The effect of this vibration absorber on safety, construction element stresses and ride comfort was analytically and experimentally investigated in the "Konstruktion von Baumaschinen" (Construction machinery design department) at the Technische Universität, Berlin. Driving tests carried out with equipment of various sizes correlated well with computer simulation results. Ride safety and comfort are improved by approximately 50% in comparison with conventional machines.

1. Introduction

When used on a construction site self-propelled earth moving machines frequently have to travel long distances; they are also used on the public roads for transport to various locations. For economic reasons it is desirable to reduce driving time to a minimum and, moreover, acting on subjective criteria, the driver of the vehicle selects the highest speed possible for the conditions. Speed is, however, essentially limited by the vibration behaviour of the vehicle and considerations of ride safety and comfort which result from this.

Unsprung construction machinery in particular is prone to considerable pitching motion even at low forward speeds; this gives rise to high dynamic stresses on the driver, the machine and the driving surface and in unfavourable conditions can be extremely dangerous. Ride comfort and

safety and economic efficiency can be increased by reducing the vehicle vibration, in particular the pitching motion.

2. Alternatives for vibration reduction on earth moving machinery

2.1 Spring and damping effect of vehicle tyres

Tyres are the only suspension elements on the majority of construction machines (Fig. 1). By reducing the spring stiffness of the tyres (Fig. 2) and increasing the damping ratio (Optimum $D = 0.25$; Fig. 3) it is possible to improve the vibration behaviour of a machine. The present state of technical development of tyres, however, shows that a soft tyre with optimum damping characteristics gives rise to problems with regard to the useful life of tyres, increased rolling resistance and a reduction in vehicle steerability.

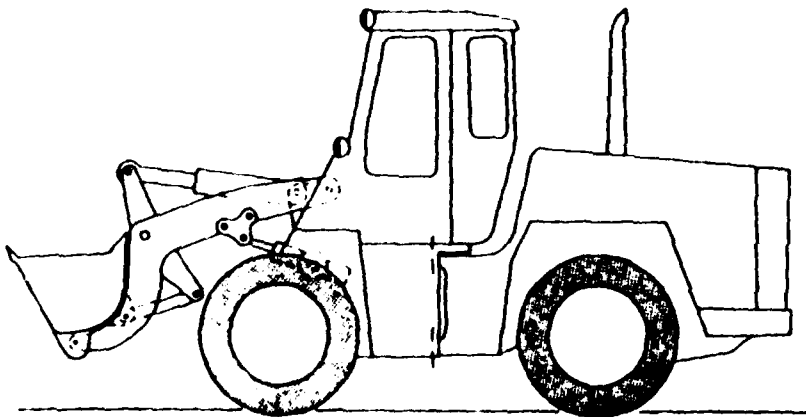


Fig. 1 Tyres as spring and damping elements on a tractor-loader

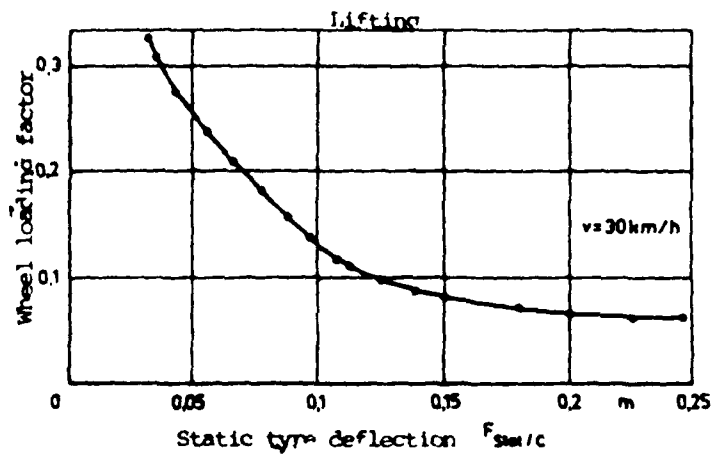


Fig. 2 Relationship between axle acceleration and spring stiffness of the tyres

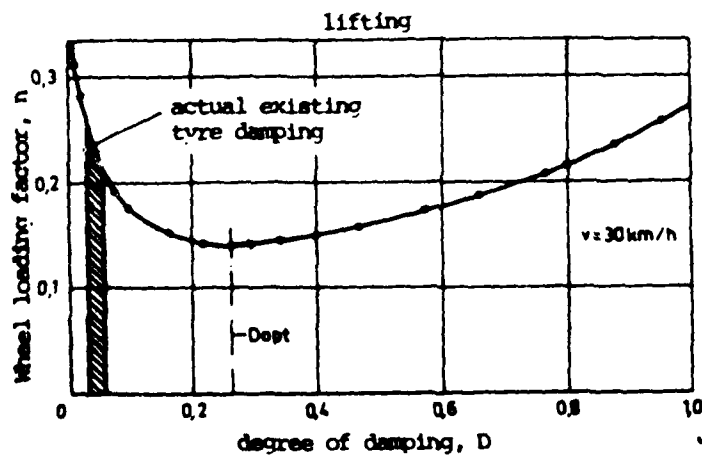


Fig. 3 Relationship between axle acceleration and tyre damping

2.2 Axle suspensions

The most frequently used and most effective method of reducing vehicle vibration is the insertion of suspension elements between the axles and the body of the vehicle. An axle suspension is, however, frequently

undesirable on mobile construction machines when they are in operation.

The suspension of some machines can be switched on during driving and switched off during working operations by means of adjustable and closable hydro-pneumatic spring and damping elements. The arrangement and control of a hydro-pneumatic axle suspension are shown in Figs. 4 and 5.

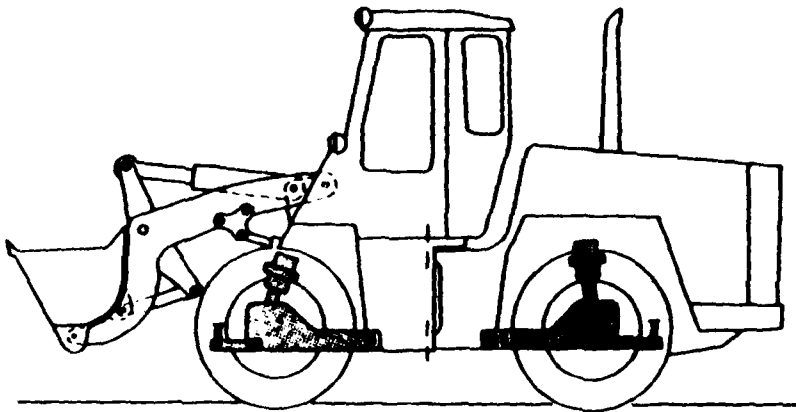


Fig. 4 Tractor-loader with suspension elements between axles and body

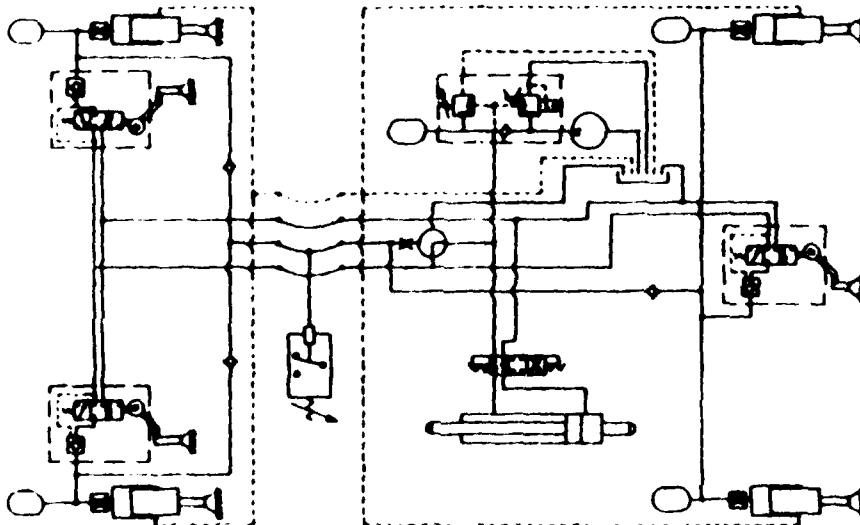


Fig. 5 Circuit diagram of a hydro-pneumatic axle suspension (Zettelmeyer)

2.3 Vibration absorber

An effective and cheap method of reducing vibration is the use of the working attachment of the machine as the absorbing mass (Fig. 6). A hydraulic accumulator connected to a pressure regulating valve is used as the spring and damping element (Fig. 7). The spring rate and the damping coefficient of the element are arranged so that they absorb machine vibration over a wide band width.

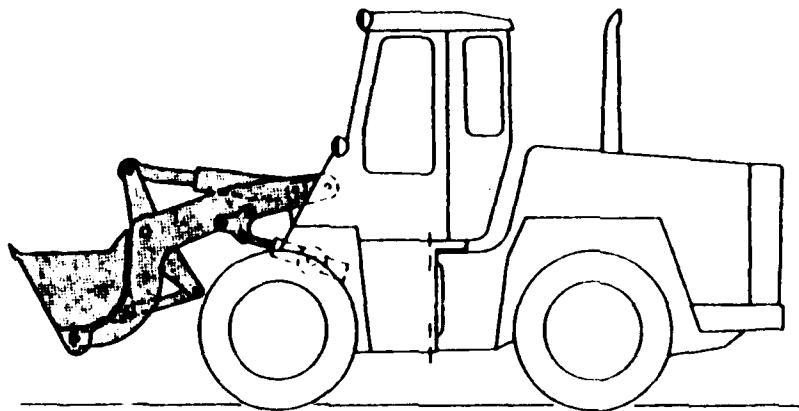


Fig. 6 Use of the loading device as an absorbing mass to reduce vibration

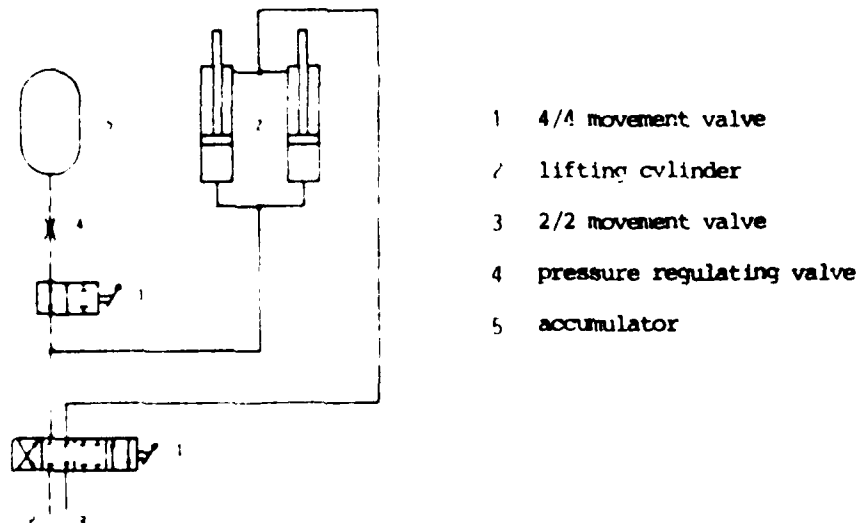


Fig. 7 Arrangement of an accumulator in the circuit of the lifting cylinder of a tractor-loader

3. Vibration behaviour of a tractor-loader

3.1 Computer simulation

A tractor-loader was selected for the analytical investigations. The unsprung two-axle vehicle has contact with the driving surface over four wheels; the unevenness of the surface is transmitted via the tyres and the axles to the vehicle frame in the form of vibrations.

Because of the lateral symmetry of the vehicle the vertical vibration behaviour of the tractor-loader can be observed using a "bicycle" vibration simulation model, as is shown in Fig. 8 for a tractor-loader with an elastically supported working attachment. Half of the vehicle mass and the moment of inertia must be used for the calculation.

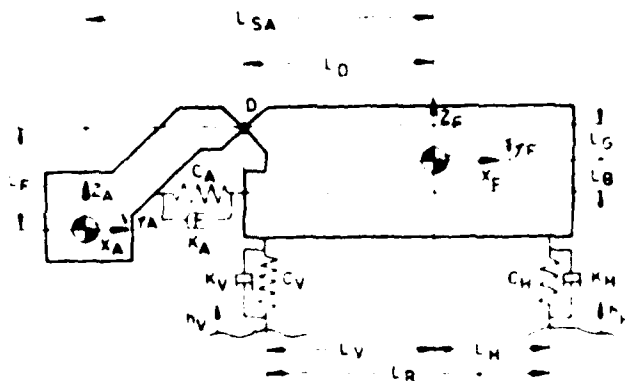


Fig. 8 Vibration simulation system of a tractor-loader with elastically supported working attachment

On the basis of this simulation model the equations of motion for the longitudinal, vertical and pitching motion of the tractor-loader and its work attachment have been established and solved using an analogue computer.

In order to simulate the surface unevenness in the analogue simulation a signal generator is used, which delivers a random voltage $U(t)$. The front axle of the tractor-loader is directly excited by this signal, while the excitation of the rear axle is passed in via a delay line, which is calculated from the wheel base and forward speed.

The dynamic wheel load on the front and rear axle is used to evaluate safety and the vertical and horizontal acceleration of the seat to evaluate ride comfort.

The usefulness of results obtained by computer simulation is highly dependent on the input of realistic vehicle data. Only in a few cases are the basic vibration characteristics (weight, dimensions, position of centre of gravity, mass moment of inertia) available for cross country vehicles, particularly for mobile construction machinery, or it may be that these characteristics are incomplete. The necessary values were therefore determined from data supplied by the manufacturer or by one's own experimental investigations.

Precise knowledge of the spring and damping characteristics of tyres is also important for exact calculation of the vibration behaviour of unsprung mobile construction machinery. Available statically determined tyre characteristics of non-rolling tyres deviate from the dynamic behaviour which actually occurs to such an extent that they are not suitable for simulation. The simulation results obtained using these characteristics can only indicate general trends. Dynamic tyre stiffness was therefore determined using a rolling driving wheel. It is on average approximately 20% lower when compared with the static stiffness for the vehicle tyres investigated (12.5-20, 10 PR and 17.5-25, 12 PR).

Results obtained by Mitschke⁽¹⁾ were used to determine the tyre damping used for the simulation. These results enable the damping coefficients of the vehicle tyres used to be determined in relation to the respective axle resonance frequency, tyre pressure and vehicle weight. Because of the narrow frequency spectrum of an unsprung mobile construction machine, this is a usable approximation of the actual tyre damping, if there is only a slight difference between static and dynamic tyre damping.

3.2 Results of the computer simulation

The relationship between vehicle mass, mass moment of inertia (Y-axis) and position of the centre of gravity gives a strong coupling between the front and rear axles on mobile machines. This is expressed by the coupling mass. If parts of the vehicle mass - as is the case with tractor-loaders

- are outside the wheel base, then the coupling mass is negative. Such vehicles are prone to pronounced pitching motion even at low forward speeds, which considerably affects safety because of high dynamic wheel loads and influences ride comfort by strong excitation accelerations of the seat in the vertical and horizontal direction.

A further characteristic is the occurrence of two resonances in the transfer function of the dynamic wheel loads (Figs. 9 and 10). The first resonance point is caused by pitching, the second higher frequency point by vertical movements, i.e. the greatest dynamic wheel loads are caused by pitching acceleration.

The transmission behaviour on the vehicle axles is independent of forward speed for the coupling mass $m_k = 0$. However, for negative coupling masses there is a systematic dependency (Figs. 9 and 10). This behaviour is characteristic for mass coupled two mass vibrating systems and means that the selected evaluation variables must be constantly observed in relation to forward speed.

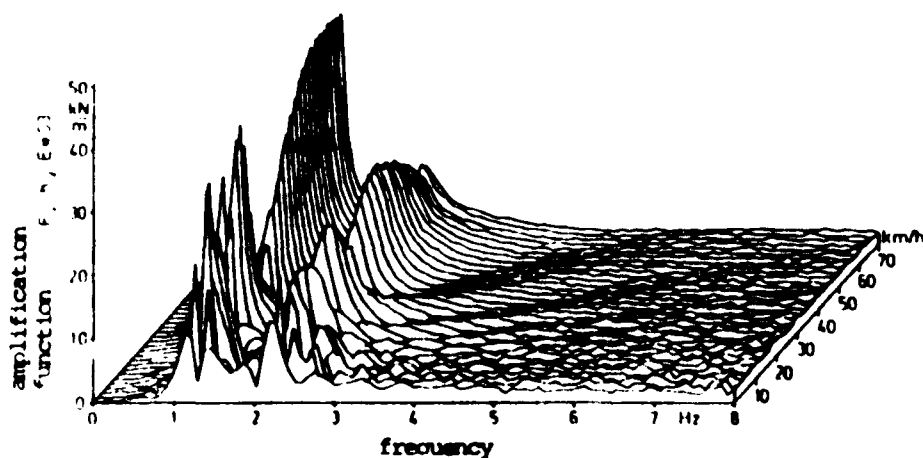


Fig. 9 Amplification function of the dynamic front-axle loads for a tractor-loader with rigidly supported working attachment

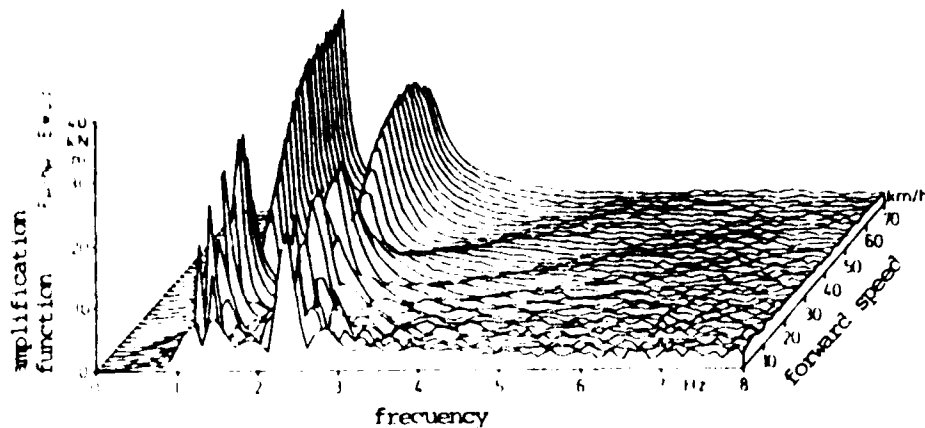


Fig. 10 Amplification function of the dynamic rear-axle loads for a tractor-loader with rigidly supported working attachment

The vibration stress experienced by operators is generally very high during the operation of self-propelled construction machines because of the limited tyre damping. The position of the seat attachment point is thus a design factor which can decrease acceleration of the driver's seat. Vertical acceleration is least at the centre of gravity of the vehicle (Fig. 11) and this is then the optimum seat attachment point. This arrangement is not possible on all machines because of design considerations. On mobile cranes, for example, the seat can be placed from the rear-axle up to the centre of gravity.

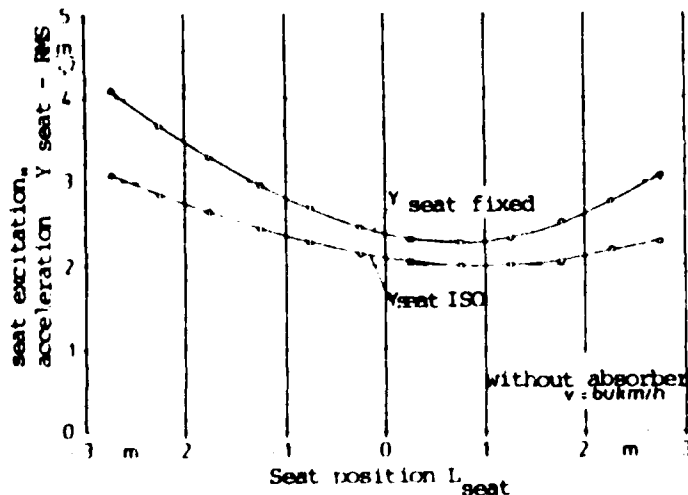


Fig. 11 Vertical acceleration between vehicle axes on a tractor-loader

4. Vibration reduction by absorption

4.1 Principle of a dynamic vibration absorber

The method of operation of a dynamic vibration absorber can be explained using a single oscillating mass, which is equipped with a second elastically coupled mass (Fig. 12).

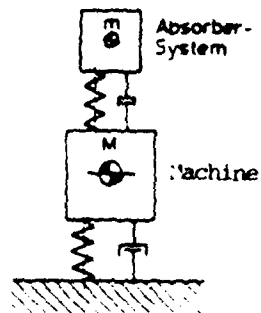


Fig. 12 Dynamic vibration absorber

The absorber is basically a resonance system, which is attached to the vibrating structure and counteracts the vibration which is to be reduced.

If the absorber is adjusted on the main system so that the relationship of the resonance frequency is $\nu = 1$ and the damping coefficient $k = 0$, the resonance point of the main system is completely absorbed (Fig. 13). A disadvantage of this desirable behaviour is the fact that two additional resonance points occur. With infinite absorber damping $k = \infty$ the absorbing mass is linked to the main body, so that they do not move against one another. The absorbing system is then completely redundant, so that the resonance point actually to be absorbed occurs again.

Between the extreme damping coefficient $k = 0$ and $k = \infty$ there is a damping level, at which the main system gives the smallest vibrations.

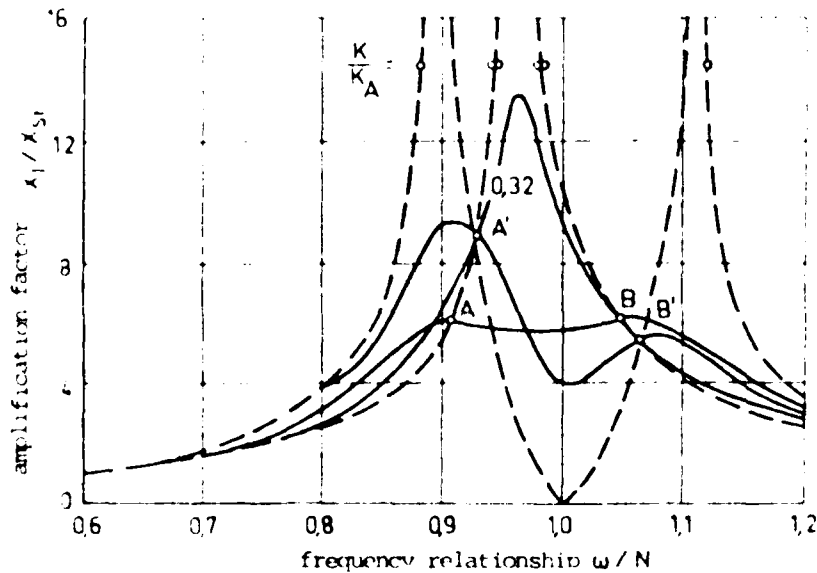


Fig. 13 Transfer function of a dynamic absorber at various damping adjustments

4.2 Absorber adjustment in relation to ride comfort and safety

There are various criteria for which the stiffness of the absorber suspension can be optimised. These include dynamic wheel loads and acceleration of the driver's seat. The optimum damping value is found to be constant with an approximate value of $D = 0.3$. As illustrated by tests to determine the moment of inertia of absorber masses on tractor-loaders, this damping is practically unobtainable. For practical purposes then a damping ratio of $D = 1$ is used.

The simulation results given in Figs. 14 to 25 show the behaviour with this high damping at an absorbing frequency of 1.4 Hz; this is a compromise between ride comfort and safety.

The linear spectra of dynamic wheel loads (Figs. 16 to 19) and the seat excitation acceleration (Figs. 22 to 25) show clearly that vehicle vibration is considerably reduced especially in the pitching mode.

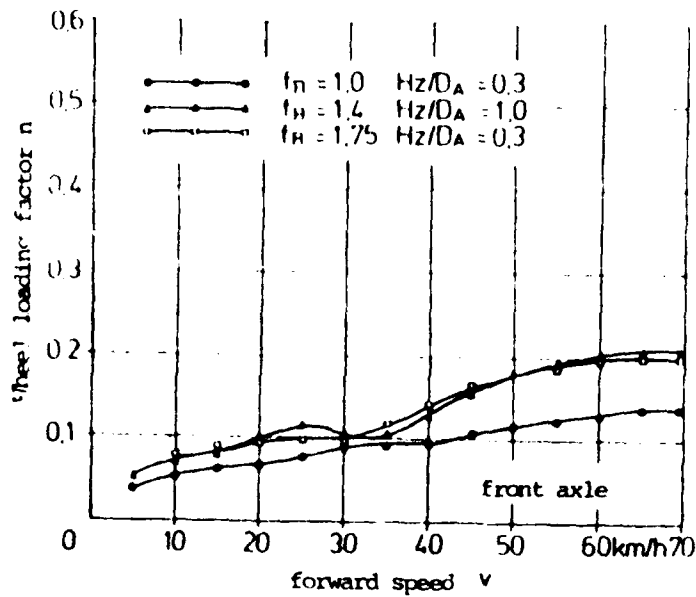


Fig. 14 Wheel loading factor on the front axle in relation to forward speed at various absorber adjustments

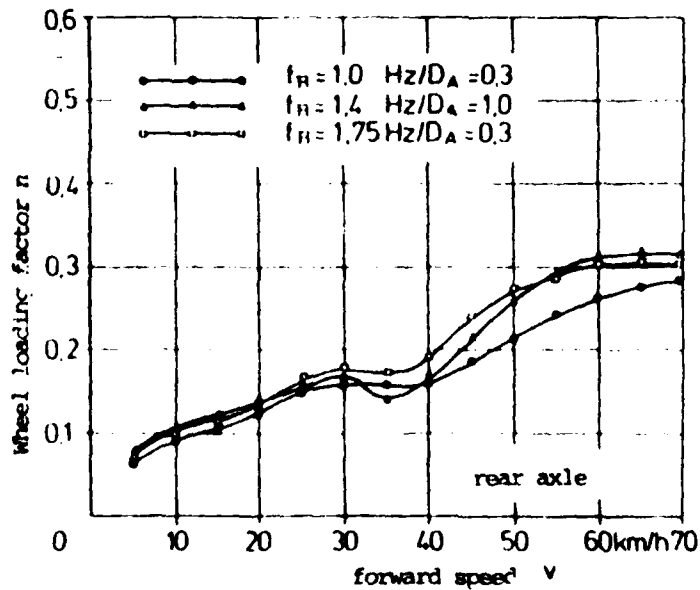


Fig. 15 Wheel loading factor on the rear axle in relation to forward speed at various absorber adjustments

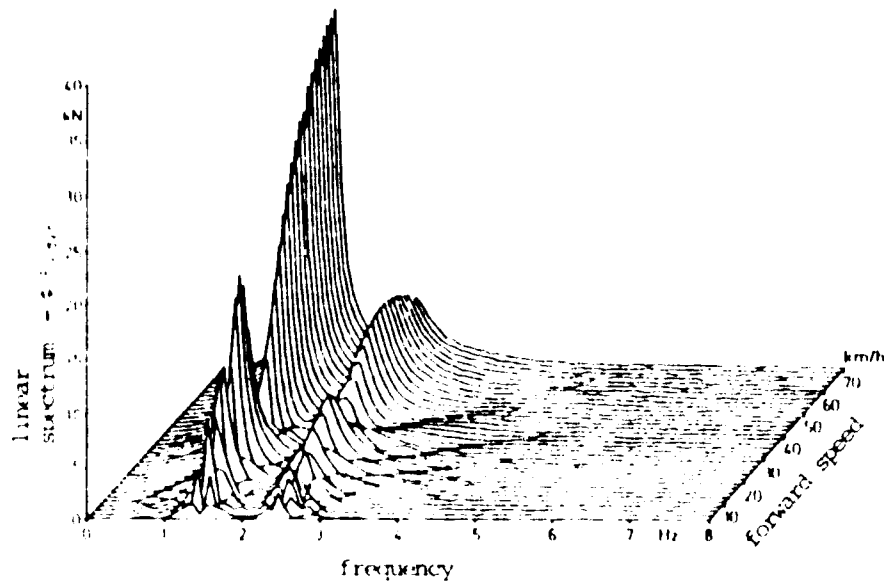


Fig. 16 Linear spectrum of dynamic front axle loads of a tractor-loader with rigidly supported working attachment in relation to forward speed

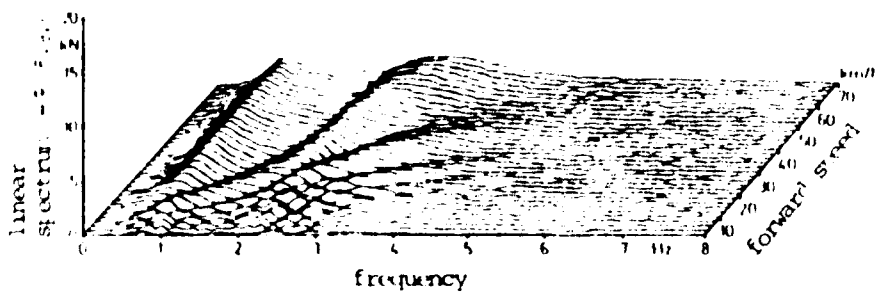


Fig. 17 Linear spectrum of dynamic front axle loads of a tractor-loader with elastically supported working attachment in relation to forward speed

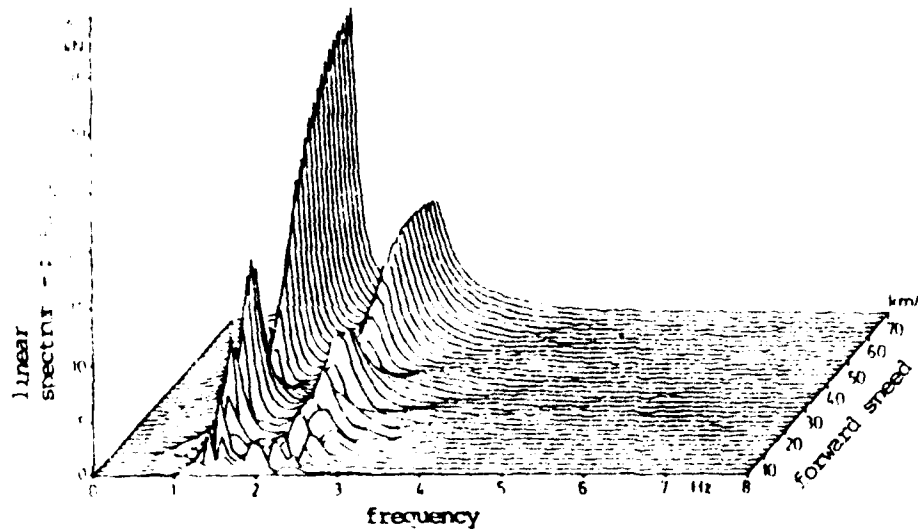


Fig. 18 Linear spectrum of dynamic rear axle loads of a tractor-loader with rigidly supported working attachment in relation to forward speed

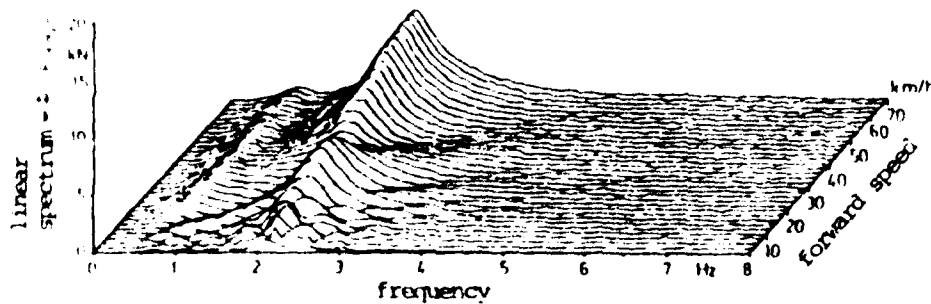


Fig. 19 Linear spectrum of dynamic rear axle loads of a tractor-loader with elastically supported working attachment in relation to forward speed

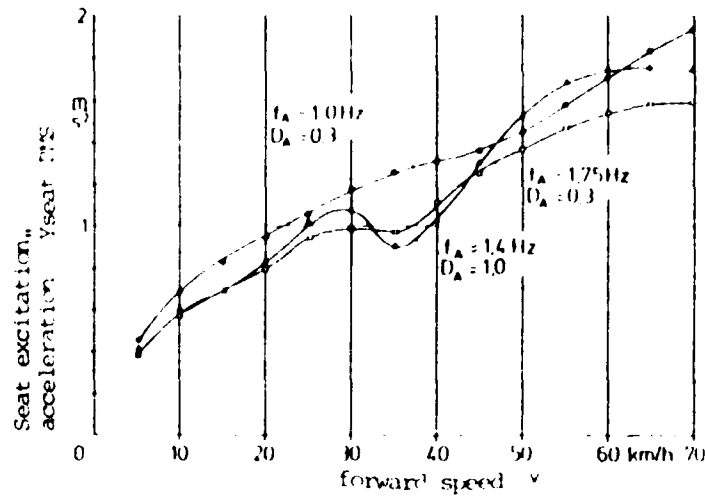


Fig. 20 Vertical excitation acceleration of the driver's seat in relation to forward speed for various absorber adjustments

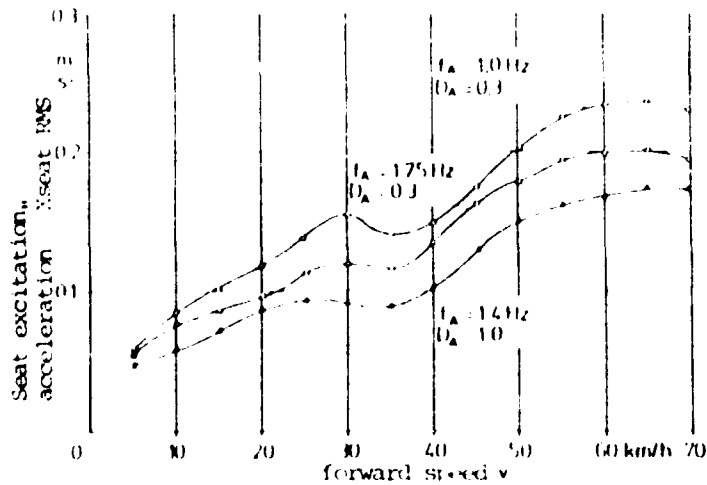


Fig. 21 Horizontal excitation acceleration of the driver's seat in relation to forward speed for various absorber adjustments

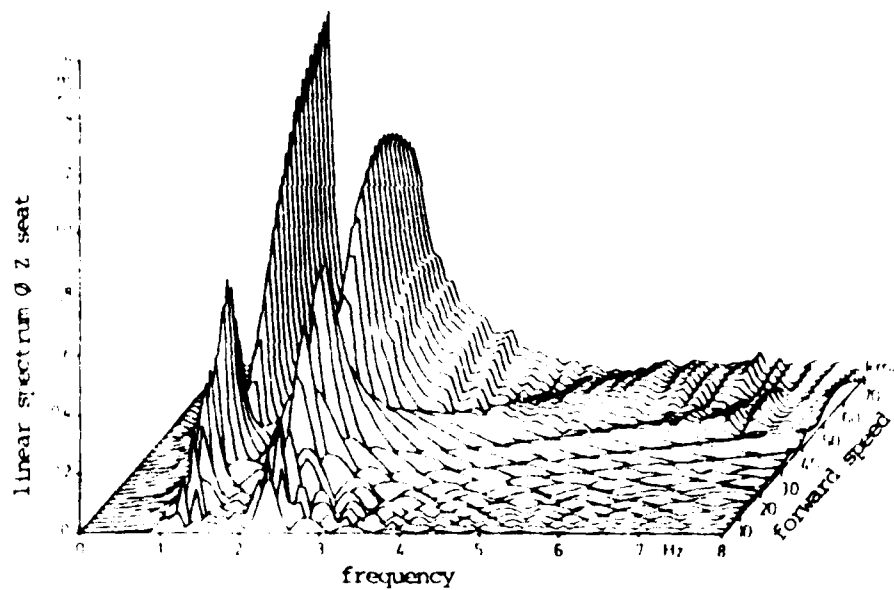


Fig. 22 Linear spectrum of vertical excitation acceleration of the driver's seat of a tractor-loader with rigidly supported working attachment in relation to forward speed

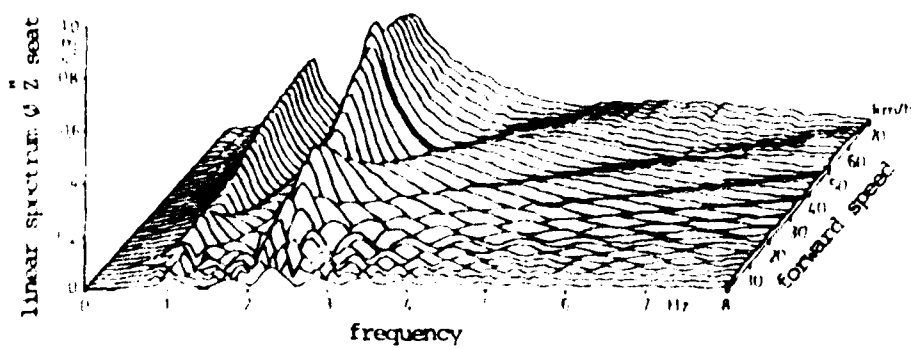


Fig. 23 Linear spectrum of vertical excitation acceleration of the driver's seat of a tractor-loader with elastically supported working attachment in relation to forward speed

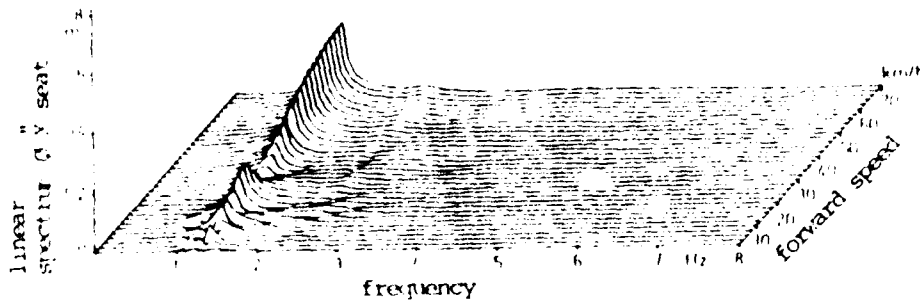


Fig. 24 Linear spectrum of horizontal excitation acceleration of the driver's seat of a tractor-loader with rigidly supported work attachment in relation to forward speed

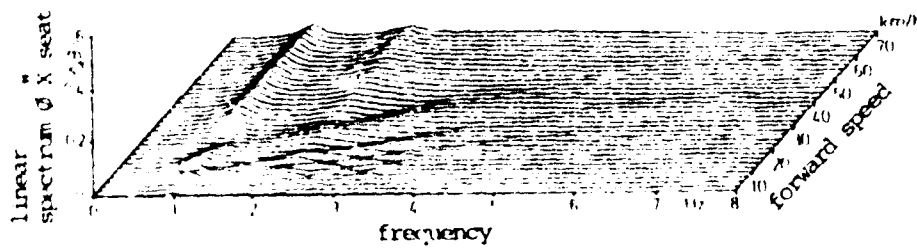


Fig. 25 Linear spectrum of horizontal excitation acceleration of the driver's seat of a tractor-loader with elastically supported work attachment in relation to forward speed

4.3 Absorber movement

In practice the absorber movement which occurs is of particular importance with regard to the safety regulations in force when travelling on public roads. The relative movement between vehicle and work attachment should be as small as possible.

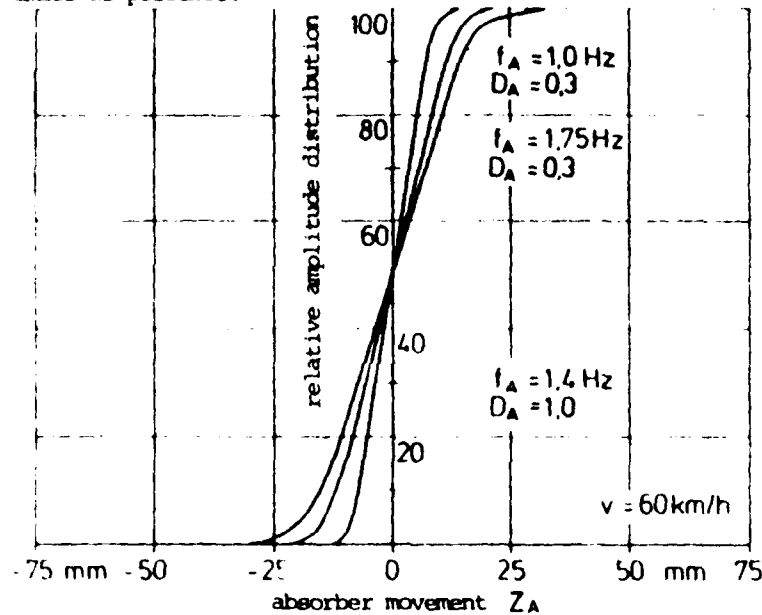


Fig. 26 Relative amplitude distribution of movement of working attachment with various absorber adjustments

The relative amplitude distribution given in Fig. 26 shows that the required absorber motion is not greater than $\pm 30 \text{ mm}$ even at optimum absorber adjustments. If a realistic absorber damping of $D = 1.0$ is used, the maximum required absorber movement is reduced to $\pm 15 \text{ mm}$. Such small relative movements of the working attachment can easily be accommodated.

5. Driving tests

To test the results obtained with the computer simulation driving tests were carried out with the tractor-loader which formed the basis of the simulation. These correlated well with the calculation, particularly with regard to the vibration reduction which can be obtained (Fig. 27 to 29).

The behaviour and opinions of the driver are significant as he regarded the tests very sceptically, however and he wanted to keep the vibration absorber after the tests. It is precisely the belief that the vibration behaviour of self-propelled machinery is normal that has led to the generally widespread view that it does not require remedying. Against this there are the convincing results and experiences with the vibration absorption by the elastic support of the working attachment.

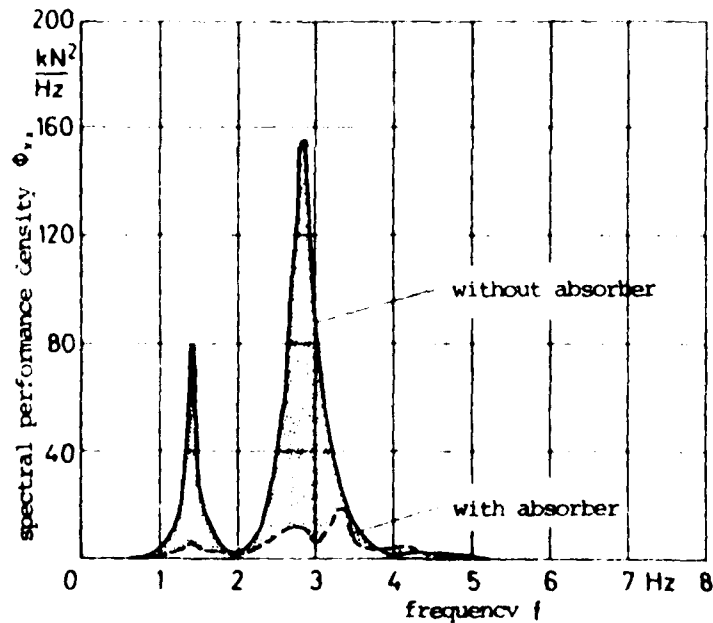


Fig. 27 Vibration reduction on the front axle of a tractor-loader

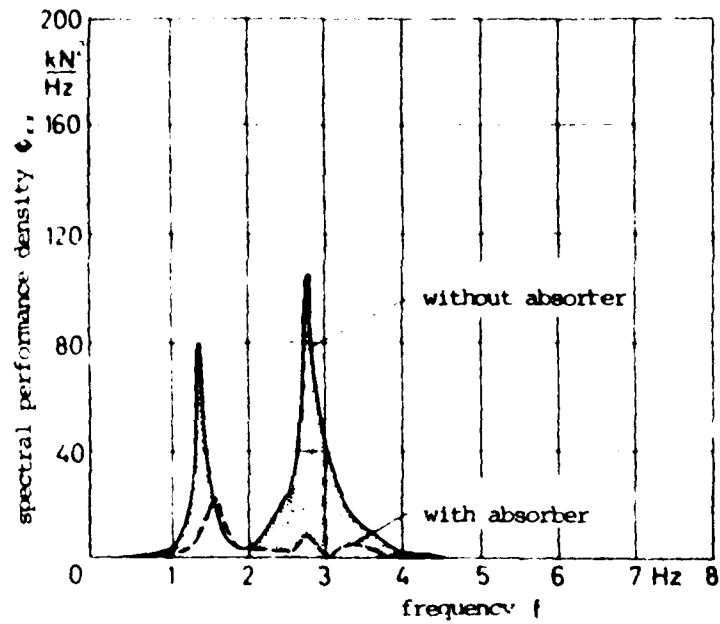


Fig. 28 Vibration reduction on the rear axle of a tractor-loader

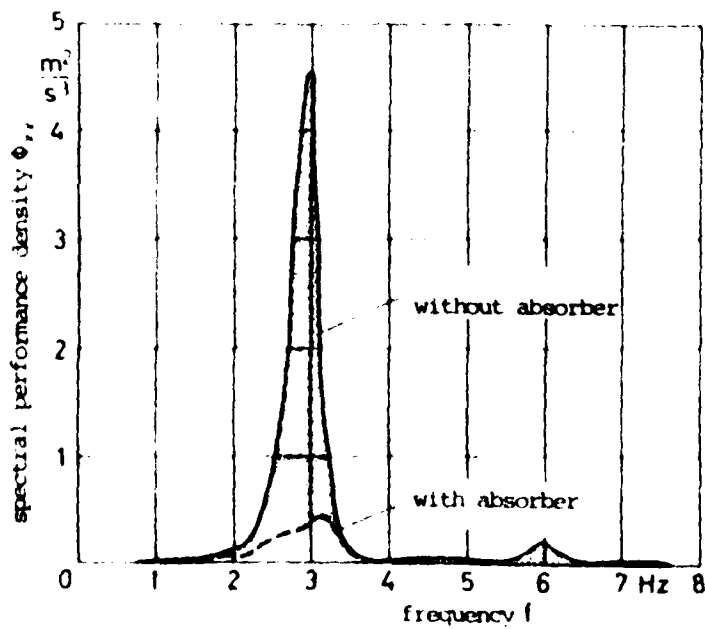


Fig. 29 Vibration reduction on the driver's seat of a tractor-loader

6. Summary

Ride comfort and safety of unsprung self-propelled construction machines with a rigid and elastic support of the working attachment are evaluated by means of analytical and experimental investigations. Vehicles which have a considerable part of the vehicle mass outside the wheel base - as is always the case with tractor-loaders - are prone to pronounced pitching motion, even at low forward speeds, which can considerably influence ride safety and comfort.

Dynamic wheel loads are used to evaluate safety and the vertical and horizontal excitation acceleration of the driver's seat to evaluate ride comfort. The dependency of the dynamic wheel loads and the excitation acceleration of the seat on forward speed is very variable for these vehicles, with the result that the vibration characteristics must be constantly observed for the total forward speed range.

The position of the seat attachment point in relation to the centre of gravity of the vehicle is decisive in the effect of the pitching acceleration on the stress to the driver. By elastic support of the working attachment and its use as an absorbing mass, the vibration of the machine can be considerably reduced.

By adjustment of the absorber to obtain the greatest possible reduction of the dynamic wheel loads and the excitation acceleration of the seat, a compromise must be achieved between ride safety and comfort; this is usual in the design of axle suspensions.

Relative movements between the working attachment and vehicle frame, which occur with elastic support of the attachment, are approximately ± 15 mm with an absorber damping of $D = 1$; it is possible to achieve this in practice. Such small relative movements of the working attachment can easily be incorporated in the design.

In conclusion the above results show that, using the principle of vibration absorption, ride comfort and safety on unsprung self-propelled construction machines can be considerably increased. Driving tests with a tractor-loader verify the results of the computer simulation.

7. Bibliography

MITSCHE, M. Dynamik der Kraftfahrzeuge (Dynamics of motor vehicles)
Springer-Verlag, Berlin, Heidelberg, New York, 1972


MITSCHE, M. Fahrsicherheit und Strassenschonung von ungefederten Fahrzeugen (Drive safety and minimum road damage with unsprung vehicles)
Deutsche Kraftfahrtforschung und Strassenverkehrstechnik, 1971

HELMS, H. Grenzen der Verbesserungsfähigkeit von Schwingungskomfort und Fahrsicherheit an Kraftfahrzeugen (Limits on the improvement of vibration comfort and safety on motor vehicles) Dissertation, TU Braunschweig 1974

WILLMEIT, H.-P.; RICHTER, B. Über den Einfluss von frequenzabhängigen Dämpfern und Schwingungstilgern in der Radaufhängung eines Strassenfahrzeugs (The influence of frequency dependent dampers and vibration absorbers in the wheel suspension of a road vehicle) Automobil-Industrie 1971 16 (2) 67-72

SHARON, I. Untersuchungen über die Schwingungseigenschaften grossvolumiger Niederdruckreifen (Investigation of the vibration characteristics of large volume low pressure tyres) Dissertation, TU Berlin, 1975

ULRICH, A. Untersuchungen zur Fahrdynamik von Traktoren mit und ohne Anbaugeräte (Investigation of the ride dynamics of tractors with and without mounted implements) Dissertation, TU Berlin, 1983



TOPIC 3
TRACK-SOIL INTERACTION

STRESSES IN SITU GENERATING BY BULLDOZERS

H. FUJII

T. SAWADA

T. WATANABE

OKAYAMA UNIVERSITY

KYOTO UNIVERSITY

OKAYAMA UNIVERSITY JAPAN

AD-P004 270

SYNOPSIS

The author carried out full-scale field tests and measured stresses in situ generating by bulldozers. These data were analyzed experimentally as well as theoretical by making numerical models. Five bulldozers are used on different types of soil such as cohesive soil, sandy soil and rockfill materials. Most measured stresses are much larger than the stresses calculated from nominal contact pressure. The stress variation by travelling a bulldozer on the ground, that is the time-stress ($t-\sigma$) relation or curve on the oscillograph shows particular shapes as if it were random vibration. These curves are classified into roughly four groups. As a bulldozer can drive without whole crawler tracks in contact with the ground, the contact pressure occurs three different type patterns according to the configuration of the ground surface. The particularity of $t-\sigma$ curve of a bulldozer is due to the disaccordance of the length of shoe and the distance of track rollers. And also, it is due to the indirect load transferred through track shoes. Since it comes from the structural characteristics of the bulldozers, "the Structural Stress Variation Model" is considered for "the three ground models".

INTRODUCTION

This paper reports about the stress in situ by bulldozers while travelling. The author has studied the field-compaction test of compaction equipment (3)(4)(5)(6)(7)(11). Bulldozer can be used as a compaction equipment such as small embankments or preliminary compaction in spite of its small nominal contact pressure. But their compaction effect is fairly useful. There has been research on crawler type vehicles such as bulldozers or tractors from the viewpoint of agricultural engineering (1)(9), but quite little from the viewpoint of compaction equipment (10). So the author executed the field compaction test using several bulldozers on different types of soil, measured the stresses in situ and considered that.

THE METHOD OF TEST

Full-scale field compaction tests were carried out on the site of two rockfill dams and one highway construction. Measurements were made of the stresses in situ, the acceleration, the velocity, the settlements of the surface, the deformation in the layer compacted, the penetration resistance and the density. The test sections were generally made 6 m wide and 10 m long, and sufficient soil was placed around the sections to prevent movements in the lateral directions. In the center of the sections were buried such instruments as earth pressure cells and accelerometers. Also the center of the section was chosen as the origin of the Cartesian coordinates, with the X axis being the short direction, the Y axis the long direction and Z axis the vertical direction.

Although measurements were made at only a single point the results obtained by shifting the equipment in the X-direction after each pass are assumed to be the same as if measurements were made at a number of locations. Soil used for the tests were three kinds of cohesive soils for impervious zones, rather small rockfill material for transition zones and soil originating from weathered granite. The soil characteristics obtained by laboratory and field tests are shown in Tab.1. Also the five bulldozers used are describe in Tab.2. The pressure cells used both the Carlson type and the strain gage type.

STRESS DISTRIBUTION UNDER CRAWLERS

Results of experiment

The schematic of BUL-1 and its crawler is shown in Fig.1. Before going into the main arguments, several assumptions need to be discussed. The first is that the ground is considered a semi-infinite, isotropic and homogeneous elastic body. When a load is placed on the boundary, normal and shearing stresses are generated in situ. Because the shearing stresses change their directions in accordance with the location of the rollers, they are assumed not to be related to compaction. The second

TABLE 1 INDEX PROPERTIES OF SOIL FOR TESTS

CLASSIFICATION	COHESIVE SOIL				ROCK M.
NOTATION	Ch-a	Ch-b	Ch-c	Ch-d	Rk
LABORATORY TESTS					
Unified Soil Classification	SC	SC-SM	CL	SM	GM
Specific Gravity	2.75	2.72	2.74	2.66	2.79
Maximum Dry Density tN/m^3	15.3	16.5	17.3	18.8	-
(g/cm^3)	(1.56)	(1.68)	(1.76)	(1.92)	-
Optimum Water Content %	25.3	21.6	18.6	11.5	-
Liquid Limit %	52-55	52-55	30	-	-
Plasticity Index	15-20	15-20	13	-	-
FIELD TESTS					
Dry Density Before Compaction tN/m^3 (g/cm^3)	11.8-13.7 (1.2-1.4)	12.8-15.7 (1.3-1.6)	14.7-15.7 (1.5-1.6)	16.3 (1.7)	19.6-21.6 (2.0-2.2)
After Compaction tN/m^3 (g/cm^3)	13.7-16.7 (1.4-1.9)	14.7-18.6 (1.5-1.9)	16.7-18.6 (1.7-1.9)	16.7-17.6 (1.7-1.8)	20.6-23.5 (2.1-2.4)
Water Content (%)	21-36	27-33	10-20	19-24	-
Gravel Content over #4 (%)	16-25	27-49	22-28	25	100

TABLE 2 CHARACTERISTICS OF BULLDOZER USING COMPACTION

NOTATION	GROSS WEIGHT kN(t)	CONTACT TO GROUND			CONTACT PRESSURE $\text{kPa(kg/cm}^2)$	USED SOIL				Rk
		LENGTH cm	WIDTH cm	AREA cm^2		Ch	a	b	c	d
BUL-1	108(11.0)	214	46	9800	55(0.56)	*	*	*	*	*
BUL-2	154(15.7)	243	51	12400	62(0.63)	*	*	*	*	*
BUL-3	380(38.7)	316	56	38400	107(1.09)	*	*	*	*	*
BUL-4	113(11.5)	220	40	17600	64(0.64)	*	*	*	*	*
BUL-5	94(9.6)	222	76	33744	27(0.28)	*	*	*	*	*

assumption is that $\sigma_z(P)$, which is the normal stress in the Z-direction caused by vertical load, is mainly related to the compaction. Although the stresses in three directions were measured, σ_z was used for the analysis because of this assumption. Two examples of the results in measurements are shown as Fig.2. Broken lines in Fig.2a are the results of a bulldozer BUL-1. They represent a compaction of the location of the roller on the X axis versus σ_z in situ at several depths. The measured values are rather scattered. In accordance with the first assumption, stress in situ due to the distributed load of the compaction equipment acting at the surface can be calculated by Boussinesq's equation (8). This equation should be used for the static load, but Brom and Forssblad (2) mentioned that the stress distribution for vibratory rollers also agreed with Boussinesq's equation. Therefore, the stresses are calculated from the static contact pressure of Tab.2. They are shown as the solid lines in Fig.2a. Comparing the solid lines and the broken lines (drawn by connecting the upper points of the measured values), both lines are similar in shape in spite of the differences of the magnitudes. Therefore, assuming the 'quasistatical loads' for the dynamic load due to compaction equipment, the stress distribution in situ can be calculated at least qualitatively. There is a tendency that the faster the speed, the larger the difference. The magnitudes change with the soil type. The stresses in the rockfill are larger than in the cohesive soil. The same tendencies exist with the other rollers. Fig. 2a shows the bulldozer BUL-1 running in second gear speed on cohesive soil. The measured value is about six times greater than the calculate value. The theoretical value is calculated by Boussinesq's equation as below.

$$\sigma_z = \frac{q}{2\pi} \left[\frac{mn}{\sqrt{1+m^2+n^2}} \frac{1+m^2+n^2}{(1+n^2)(m^2+n^2)} + \sin^{-1} \frac{m}{\sqrt{1+m^2}} \frac{1}{\sqrt{1+n^2}} \right] \quad \text{-----(1)}$$

where $m = a/b$, $n = z/b$ in Fig.6.

However, the calculated value is only 20 % greater than the measured value for the 26 ton tyre roller running in second gear speed on cohesive soil Ch-a shown in Fig.2b. Since the tyre roller has six rear tyres, the theoretical stresses in situ are the sum of the stress due to each tyre, under the assumption that superposition is valid. Where do the differences come from? One of the reasons for this could be the stress concentrations of Fröhlich's theory. Taking this into account, a 15-25 % increase of the stress calculated by Boussinesq's theory is produced even for rockfill materials.

Crawler Track - Ground System Model

1) Basic assumption

Although the nominal contact pressure of a bulldozer is rather small as shown in Tab.2, the measured value is much larger as shown in Fig.1a. If the whole load is transmitted to the track rollers, the front idler, and the sprocket of the bulldozer, and one of the rollers is on a track shoe, both the calculated and the measured stresses should almost coincide. However, the contact pressures of the bulldozer are changed by the ground characteristics such as bearing capacity and shape of ground surface. The big difference of the bulldozer compared with other rollers is that it has crawler tracks. Therefore, a bulldozer can be driven even when a portion of its crawler tracks is not in contact with the ground. The contact pressure of the bulldozer will change in accordance to the conformation of the ground surface it is moving over, and the load of bulldozer transfers indirectly from the track shoe to the ground. Thus the condition of load from the bulldozer is changed by ground conformation.

Actual ground surface is never horizontal and is composed of a number of horizontal parts, up grade parts and down grade parts. The items as follow are assumed.

- (i) The portion of same gradient surface is the same as the length of crawler tracks.
- (ii) The conformation of ground does not change while the track shoe is just in contact on the ground.
- (iii) The critical point of change slope is nominated as point C, and the grade of both sides are I_1 and I_2 , however, $|I| \leq \pi/2$
- (iv) The track shoe on the point C does not move while the track rollers are moving, a track shoe is plane and its contact pressure of any portion is uniform.
- (v) The load from track roller is transmitted statically to the track shoe just under it and never transmitted to other track shoes.
- (vi) The moving rollers mean the whole rollers on the track shoes such as front idler, track rollers and sprocket.

2) Crawler Track - Ground System Model and contact pressures

Due to I_1 and I_2 , $\Delta = I_1 - I_2 \geq 0$

Here we define the Crawler Track - Ground System Model. The relationship between the ground conformations and bulldozer are divided into three types, illustrated below using BUL-1 as an example.

- (i) Model I ($\Delta=0$), Horizontal type (Fig.3a)

If the ground surface is completely plane, the track shoes under the sprocket and front idler are slightly risen to the surface, so that the load is transmitted by the other track rollers (Case 4). Since the ground is usually not so rigid, the contact pressure occurs for all track

TABLE 3 LOCATION OF ROLLERS BEING CONTACT TO THE GROUND INDIRECTLY ON "CRAWLER-GROUND SYSTEM" MODEL (cf. FIG.3)

MODEL	LOCATION OF ROLLERS NO. CONTACT TO GROUND											NUMBERS OF ROLLER			
	BACK			POINT C				FRONT							
II	1	2	3	4	5	6	7						7		
		1	2	3	4	5	6	(7)					6		
			1	2	3	4	5	(6)	(7)				5		
				1	2	3	4	(5)	(6)	(7)			4		
					1	2	3	4	5	6	7		3		
				(1)	(2)	(3)	(4)	4	5	6	7		4		
					(1)	(2)	(3)	3	4	5	6	7	5		
						(1)	(2)	2	3	4	5	6	7	6	
							(1)	1	2	3	4	5	6	7	7
	III	1	2	3	4	5	6	7							7
		1	2	(3)	(4)	(5)	(6)	7						2-3	
			1	2	(3)	(4)	(5)	6	7					2-4	
						1	2	(3)	(4)	(5)	6	7		2-4	
							1	(2)	(3)	(4)	(5)	6	7	2-4	
								1	2	3	4	5	6	7	7

NOTICE 1 : 1st roller, that is sprocket
 2-6 : 2nd-6th roller, that is track roller
 7 : 7th roller, that is front idler
 () : roller No. rising, that is rollers not contact through track shoes

shoes under moving rollers as usual (Case 2). If the ground is very plane and very rigid, only the nails of the track shoes contact the ground and take the whole load (Case 8,9).

(ii) Model II Convex Case ; $\Delta > 0$ (Fig.3b; Tab.3)

The loading condition is changed with the relationship between the point C and the location of the centroid of the bulldozer while travelling. The centroid of BUL-1 is located between the second track roller and the third one. So, the loading condition is the same as Case 1 before reaching the front idler at point C. The shoes under the front idler and the first and the second track rollers do not touch the ground surface up to the time that the third track shoe reaches point C. That is, the number of shoes which transmit the load of the bulldozer changes sequentially through 7,6,5 and 4 until its centroid reaches point C. But then they change three to seven after its centroid passes through point C.

(iii) Model III Concave Case ; $\Delta > 0$ (Fig.3c; Tab3)

The loading condition is the same as Model I till the front idler reaches point C. According to the bearing capacity, sometimes no track shoes under track rollers touch the ground surface. In this case, the load is transmitted by 2-7 track rollers. The contact pressures of each case are shown in Tab.4. Fig.4 shows the theoretical stresses distribution of BUL-1 using the contact pressure in various cases in Tab.3. The theoretical stresses and the measured statical stresses almost coincide as is described later. But there are still the differences between the theoretical value and measured value while the bulldozer is travelling. For only the statical factor, this is too large to be readily explained. Therefore, the cause of the difference must not be the statical load but the dynamic load (3).

STRESS VARIATION AT A POINT IN SITU

Theoretical consideration - Structural Stress Variation Model

The stress variation at a point in situ resulting from a travelling bulldozer, that is the time-stress (t- σ) relation or curve, shows

TABLE 4 STATICAL CONTACT PRESSURES OF BUL-1 DUE TO GROUND CONDITION

	LOAD SITUATION	BEING CONTACT TO GROUND BY	CONTACT LENGTH (cm)	CONTACT PRESSURE kPa (kg/cm ²)	MIGHT OCCURED GROUND MODEL		
					I	II	III
CALCULATED							
CASE 1	DISTRIBUTED RECTANGULAR	ALL CRAWLER	214	58(0.59)	*	*	*
2		7 TRACK	19.5x7	86(0.89)	*	*	*
3		6 SHOES	x6	100(1.02)		*	*
4		5	x5	120(1.23)	*	*	*
5		4	x4	150(1.53)		*	*
6		3	x3	200(2.04)		*	*
7		2	x2	300(3.06)			*
8	LINE	7 GROCERS	2x7	836(8.54)	*		
9		5	2x5	1170(12.0)	*		
MEASURED				461-716 (4.7-7.3)	Rk		
				392-490 (4-5)	Ch		

particular shapes as shown in Fig.10, which are gotten on the oscillograph at full-scale field tests. They seem like random vibrations. If a bulldozer weren't using its crawlers, its theoretical $t-\sigma$ curve might be as shown in Fig.4, which is calculated by equation (1) under principle superposition, at the depth 10 cm under the surface travelled BUL-1. This is like a triangular load and is completely different from Fig.10 and also the other rollers such as tyre roller or steel roller. They are like three quarter sinusoidal curves and their shapes are almost the same respectively in spite of difference of their magnitude. To make sure whether these stress variations are random vibrations or native ones. Let's try to get the theoretical stress variations for the three types of CGS-Models. Fig.5 shows Cartesian coordinate on semi-finite soil mass. Y axis is the direction of bulldozer travelling and Z axis is vertical direction. Definitions of symbols are given below:
 $\sigma(x,y,z)$: the arbitrary point to calculate stress, $C(x,y,z)$: the point of ground just upon σ , $2ax2b$: the area of track shoe B_i , $\epsilon_i(x_i,y_i,0)$: the center of track shoe B_i , $(x_k,y_k,0)$: the location of moving roller R_k , P_k : the load transmitted by R_k , $q(i,t)$: contact pressure of B_i meanwhile R_k on it, v : the speed of bulldozer

$$Y_k = vt \quad \text{-----}(2)$$

$$q(i,t) = g(x_i, y_i, x_k, y_k, t, \Delta) \quad \text{-----}(3)$$

$$\begin{aligned} & P_k/(4ab) : t_L(i,k) \leq t \leq t_{NL}(i,k) \\ & = 0 : t_{NL}(i,k) \leq t \leq t_L(i+1,k) \end{aligned}$$

where $t_L(i,k)$: the time which roller R_k just moved to track shoe B_i , $t_{NL}(i,k)$: the time which roller R_k is just apart from B_i . So

$$t_{NL}(i,k) = t_L(i+1,k) \quad \text{-----}(4)$$

Coefficient of influence in Boussinesq's equation due to track shoe B_i is shown,

$$k(i) = f(x_i, y_i, a, b, z, \Delta) \quad \text{-----}(5)$$

The stress at σ caused by n track shoe is shown as

$$\sigma(z,t) = \sum_{i=1}^n g(i,t) \cdot K(i) \quad \text{-----}(6)$$

$$\sigma(z, Y_k) = \sum_{i=1}^n g(x_i, y_i, Y_k, \Delta) \cdot f(x_i, y_i, a, b, z, \Delta) \quad \text{-----}(7)$$

Results of calculation

Let's illustrate with a simple example where the ground is completely plane. As in the previous section, here we will consider the BUL-1 for an example: at first, the backward edge of B_1 and R_1 located just on the origin as shown in Fig.6a. As before, for this case, the load transfers from only five track rollers $R_1 \sim R_5$ to five of seven track shoes $B_1 \sim B_7$ of BUL-1 (fig.6). Since the distance for two track rollers and the length of track shoes is different, the load distribution at a moment changes as shown in Fig.6. As R_1 moves Y_1 cm on the crawler shoe B_1 , the other rollers R_i moves on B_j as shown in Fig.6a~Fig.6f. Fig.6a coincides with Fig.6e, although there is a difference of track shoes length (19.5 cm). The stress distributions in this load condition are shown in Fig.7a~Fig.7e respectively at $z=20$ cm. So the stress distribution changes suddenly at the time that any track roller R_i on any track shoe B_j moves to another

one B_j . The results of this calculation, that is, theoretical stress variation at a point is shown in Fig.8. Now, let's calculate more general cases for three CGS Models as mentioned before. The procedure of calculation is fairly complete but basically is the same as the former calculation. Another example is the case of track shoes under 7 moving rollers (front idler, sprocket and 5 track rollers) of BUL-1 contact when the ground is plane. Fig.9 shows the results of theoretical stress variation with time at a point in situ, which is due to the structure of bulldozer. So that, let's define this for Structural Stress Variation (Model). The depth of calculated stresses in Fig.9 is $z=22.2$ cm. They are the stress variations while the bulldozer is moving left to right. Axis of abscissa and ordinate show the travelling length of bulldozer L (cm) and normal stresses $\sigma(z, Y_k)$ (kg/cm²) respectively. Fig.9a is the calculated result of Model I. Let's compare with Fig.4 and Fig.9a. Fig. 4 is the stress distribution. It also can be read as the stress variation with time by changing the scale and by defining time for abscissa. Although the abscissa of Fig.9a is the length, it can be changed easily to time by dividing the speed for each case. Fig.9b is the case of Model II. The case of Model II convex-type ground, is calculated in the condition that the center of track shoe B_j keeps off its one half, ie. a cm, from the point C . Fig.9c is Model III in the case where 4 track shoes under moving rollers R_1, R_2, R_5, R_7 are in contact with the concave ground. Fig.9 shows the feature of each model or ground conformation. For stress variation on Model I ground, 4 larger peaks appear in the intermediate part and rather smaller 1 peak in front and 2 peaks in the rear. For Model II, 7 peaks seem triangular. For Model III Peaks appear in the front part and rear part.

COMPARISON OF MEASURED VALUE AND THEORETICAL VALUE

Classification of stress variation

Typical measured data are shown in Fig.10 by BUL-1. Abscissa is time and ordinate is stress. Stress variations in Fig.10 are roughly classified into four types as follows by connecting small peaks of stress variations.

Type(I) Trapezoid type (Fig.10a)

Type(II) One triangular type (Fig.10b)

This type can be classified as three types by the location of the largest value appearing;

TABLE 5 CLASSIFICATION OF THE MEASURED STRESS VARIATION AT A POINT (cf. FIG.12)

		NUMBERS OF DATA IN FIG.12							
		TOTAL	(i)		(ii)		(iii)		(iv)
			a	b	c	a	b		
COHESIVE SOIL	NO TRACTION	11	3	0	0	1	7	0	0
	TRACITON TA.	138	43	28	3	24	27	3	10
ROCKFILL MATERIAL	NO TRACTION	25	1	2	0	0	18	4	0
	TRACTION TA.	18	4	0	0	0	1	9	4
			30		3	25	53	16	
TOTAL		192	51	57		69		14	

- a: former part
- b: later part
- c: central part

Type(III) Two triangular type (Fig.10c,10d)

This is also classified into two types by the location of the largest value appearing;

- a: former triangular
- b: later triangular

Type(IV) Random type (Fig.10e,10f)

This includes all types other than the above.

Tab.5 shows the classifications of 192 measured stress variations by the types mentioned above. Since from the measured values are obtained from the field compaction test, there are quite a few cases where the bulldozer pulls a tamping roller.

Type (V) mostly occurs in any case, especially where there is no traction of tamping roller. If small differences are not taken into account, Fig. 9a and Fig.10a are similar as well as Fig.9b and Fig.10b, Fig.9c and Fig. 10c. So it can be said that the stress variation of bulldozer with time like the random vibration is due to its structural characteristics.

Quantitative comparison

The measured stress variations of BUL-4 and BUL-5 are shown in Fig.13a, 13b, and their calculated stress variation by Structural Stress Variation Model is shown in Fig.13c,13d. Different concave type stress variations occur for different bulldozers. On the other hand, most of the actual ground conformations are like Fig.12, which is just after 15 passes by BUL-4 on Ch-d soil. This figure shows microscopically small waves due to the track shoe of the bulldozer, but is microscopically concave at the point of the buried pressure cell. This phenomenon can explain why there are so many measured stress variations of type III. Fig.14a shows the stress in situ of BUL-3 which is measured when the bulldozer has travelled several centimeters and then the engine is stopped. In other words, it shows measured statical stress variation without any dynamic load such as vibration of engine or the shock of striking to the ground. On the other hand, Fig.14e shows the calculated stress variation of BUL-3, that is Stress Variation Structural Model Type III, measured on actual ground as shown in Fig.12. The geometrical shape maximum value and the location for both figures are fairly similar. Fig.14a and 14d is the measured stress variation where BUL-3 travels at 1st, 2nd and 3rd gear speed. Although the faster speeds show a larger magnitude of stress, the geometrical shape does not change fundamentally. So it can be said that the Structural Stress Variation Model is valid for estimating stress variation in situ due to a bulldozer.

REFERENCES

- 1) Bekkar, M.G. : Introduction to Terrain Vehicle System, Univ. of Michigan Press, pp.1-846, 1969
- 2) Broms, B.B., Forssblad, L. : Vibratory Compaction of Cohesionless Soils, Proc.7, ICSMFE, Vol.Sp, pp.1-19
- 3) Fujii, H. : Experimental Study on Compaction of Fill Dam, - Doctor Thesis for Kyoto University (in Japanese), pp.1-323, 1973
- 4) Fujii, H., Sawada, T., Watanabe, T. : Stress in situ by Bulldozer while

- Compacting — Experimental Studies on Compaction of Fill-Type Dams (IX)
 — (in Japanese) Tr. Japanese Society of Irrigation, Drainage and
 Reclamation Engineering (JSIDRE), Vol.81, pp.94-103, 1979
- 5) Fujii, H., Sawada, T., Watanabe, T. : Model of Stress Variation at Point
 in situ while Being Compacted by Bulldozer — Experimental Studies on
 Compaction of Fill-Type Dams (x) — (in Japanese), Tr. JSIDRE, Vol.83,
 pp.44-55, 1979
 - 6) Fujii, H., Watanabe, T., Sawada, T. : The Stresses in situ while
 Compacting by different Types of Compaction Equipments, Tr.
 International Conference on Compaction, Vol.1, pp.41-46, 1980
 - 7) Fujii, H., Watanabe, T. : Characteristics of Stress Variation in situ due
 to Bulldozer — Experimental Studies on Compaction of Fill-Type Dams
 (XI) — (in Japanese), Tr. JSIDRE, Vol.99, pp.40-52
 - 8) Harr, M.E. : Foundation of Theoretical Soil Mechanics, Mc Graw Hill,
 pp.1-380, 1966
 - 9) Masuda, S., Tanaka, T., Oida, A. : Soil Deformation under Model Shoe and
 its Reaction Evaluated from Shear Stress - Strain Characteristics,
 Proc. 3rd, ICTVS, pp.25-49, 1969
 - 10) Kuno, G., Awano, Y. : Full Scale Field Compaction Test by Compaction
 Equipments (in Japanese), Proc. Scientific and Technological Research
 Institute of Tokyo Univ. Vol.6, pp.376-393, 1952
 - 11) Sawada, T., Fujii, H., Watanabe, T. : Stress in situ generating by
 Bulldozer (III), Tr. JSIDRE, pp.422-423, 1978

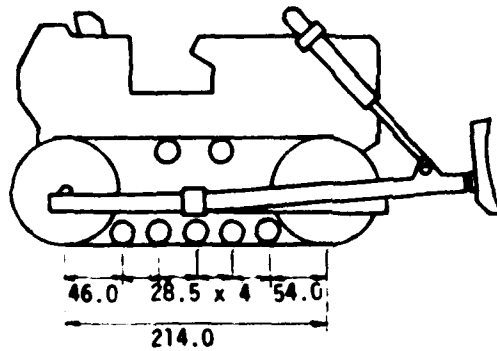


FIG. 1 DIMENSIONS OF A BULLDOZER(BUL-1)

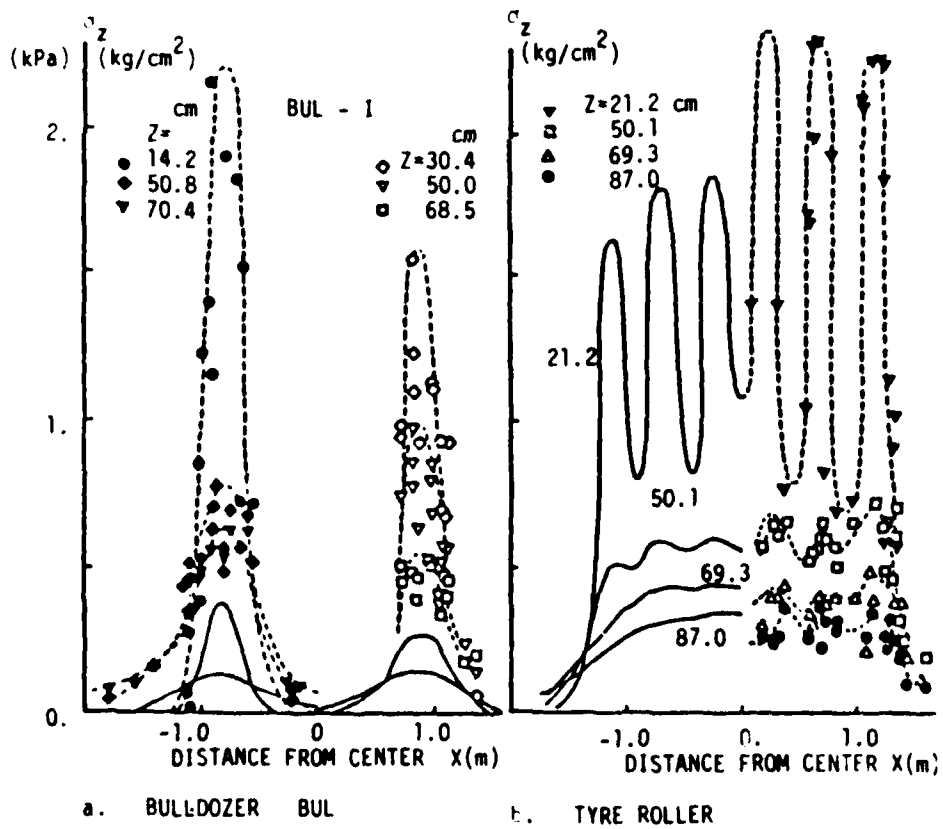


FIG. 2 EXAMPLE STRESS DISTRIBUTION IN SITU WHILE TRAVELLING A BULLDOZER(BUL-1) AND 26 TON TYRE ROLLER

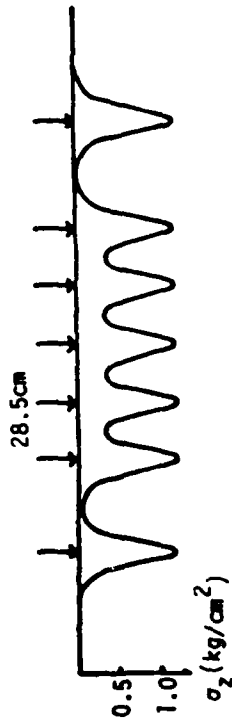


FIG. 4
STRESS DISTRIBUTION IN SITU, SUPPOSING
DIRECT LOADS ARE ACTED ON THE GROUND
SURFACE WITHOUT TRACK SHOE AT $Z=10$ cm

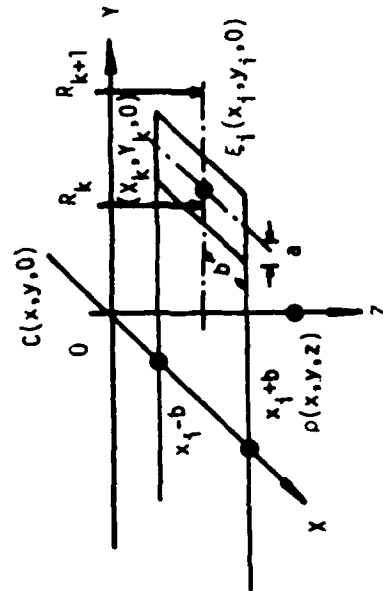


FIG. 5
COORDINATE AND THE LOCATION OF A TRACK SHOE
AND ROLLERS IN ORDER TO CONSIDERING
"STRUCTURAL STRESS VARIATION MODEL"

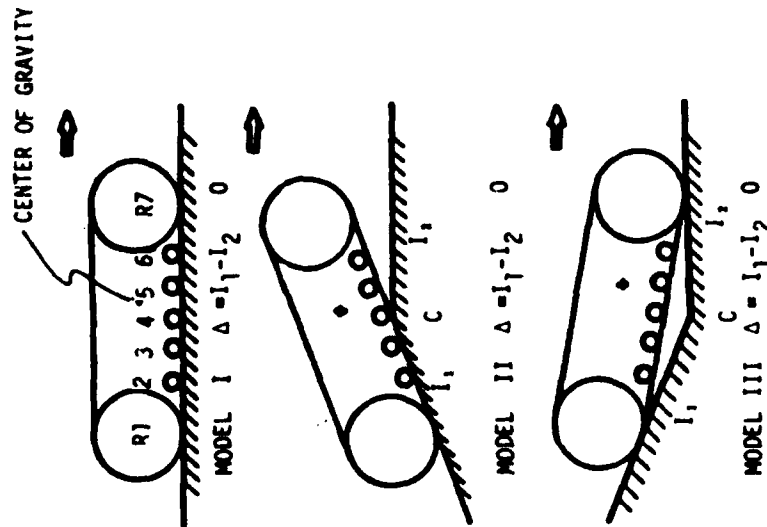


FIG. 3
THREE TYPE OF THE MODEL DUE TO BULLDOZER
AND GROUND SHAPE RELATIONS

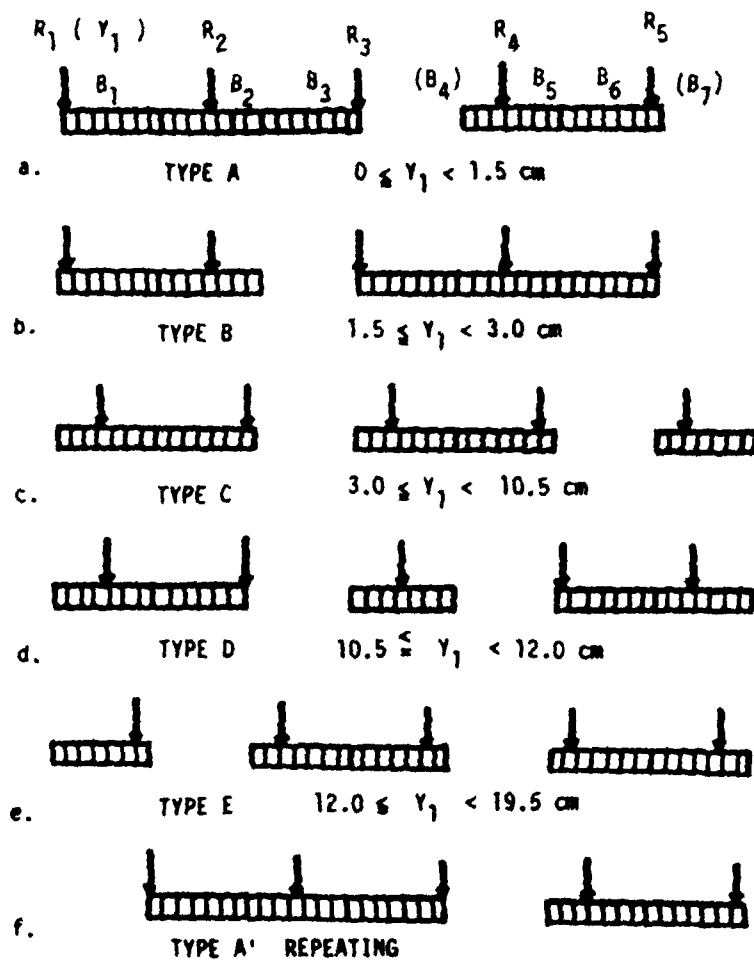


FIG. 6 RELATIONSHIP BETWEEN THE LOCATION OF FIVE ROLLERS AND TRACK SHOES LOADED OF BUL-1

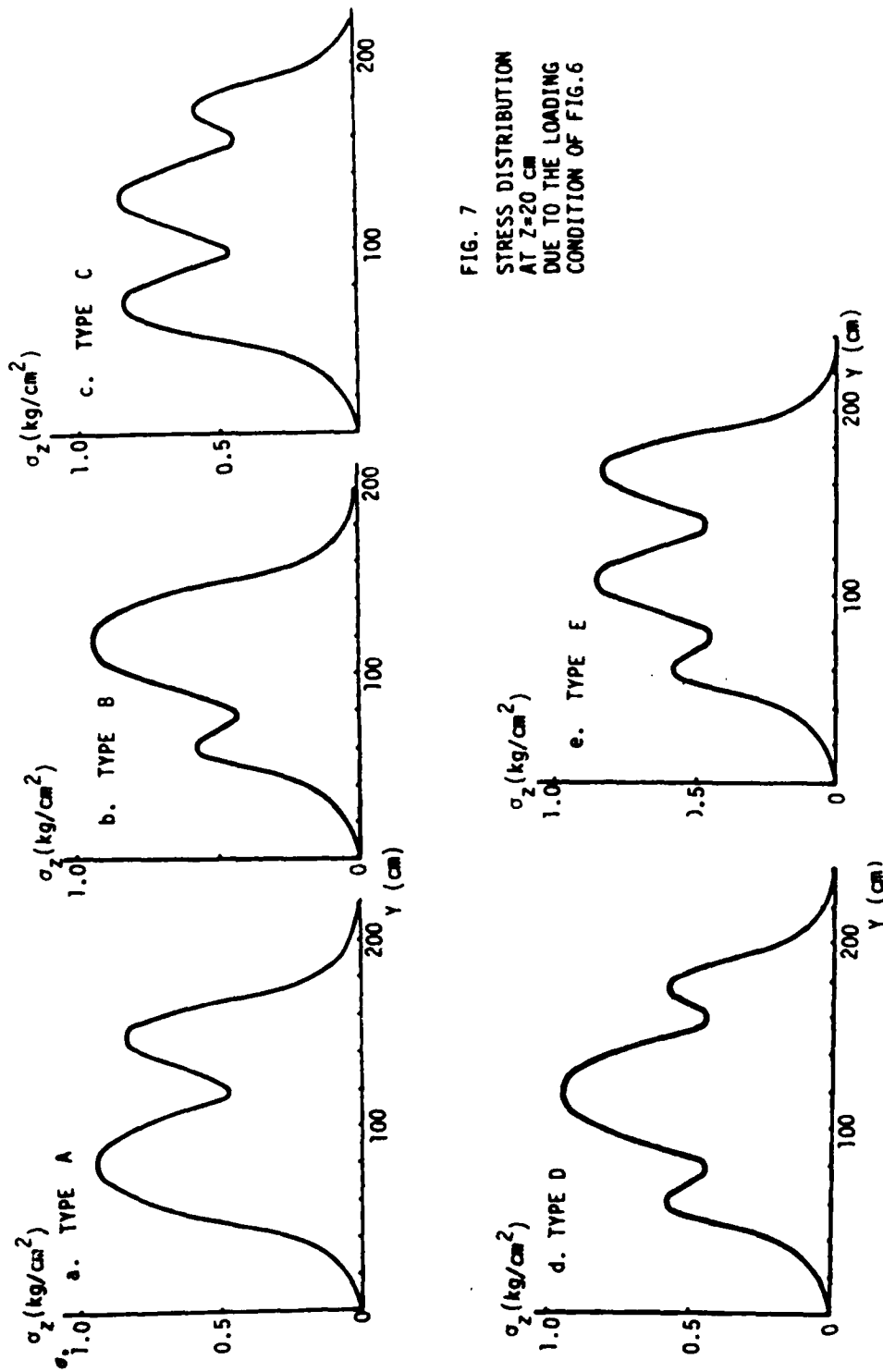


FIG. 7
STRESS DISTRIBUTION
AT $Z=20$ cm
DUE TO THE LOADING
CONDITION OF FIG. 6

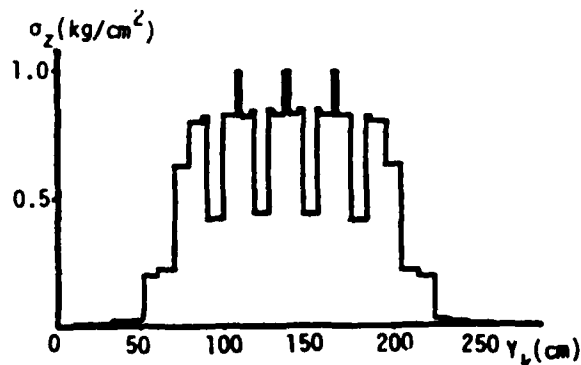


FIG. 8 THEORETICAL STRESS VARIATION CALCULATED BY "STRUCTURAL STRESS VARIATION MODEL" OF BUL-1 ON COMPLETELY PLANE GROUND

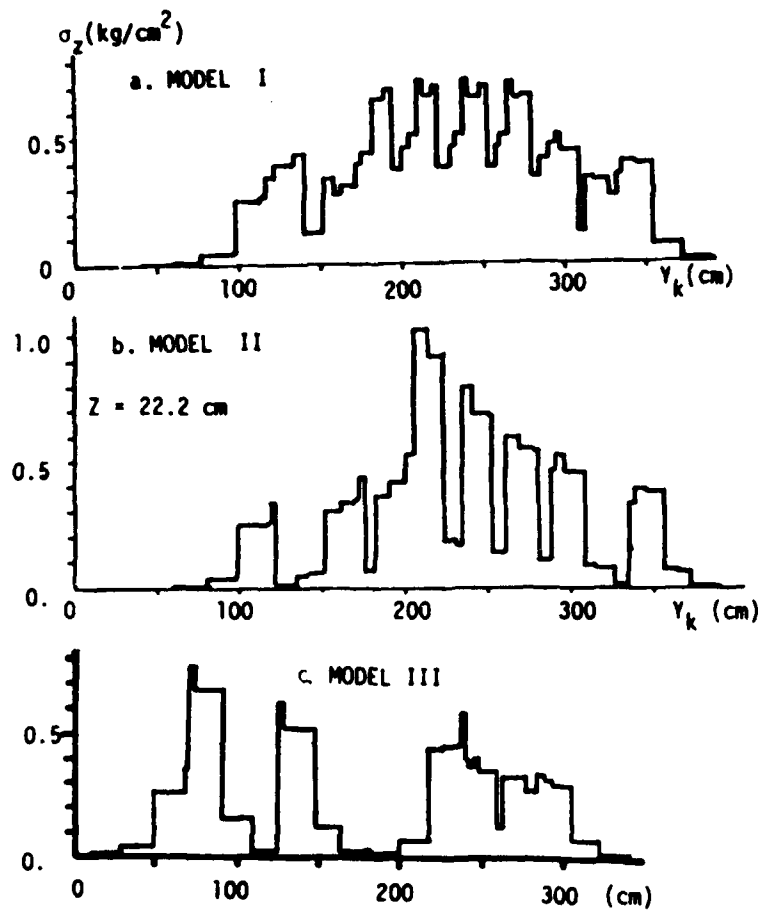


FIG. 9 THEORETICAL STRESS VARIATION CAUSED BY BUL-1 AT $Z=22.2$ cm DUE TO CGS MODEL

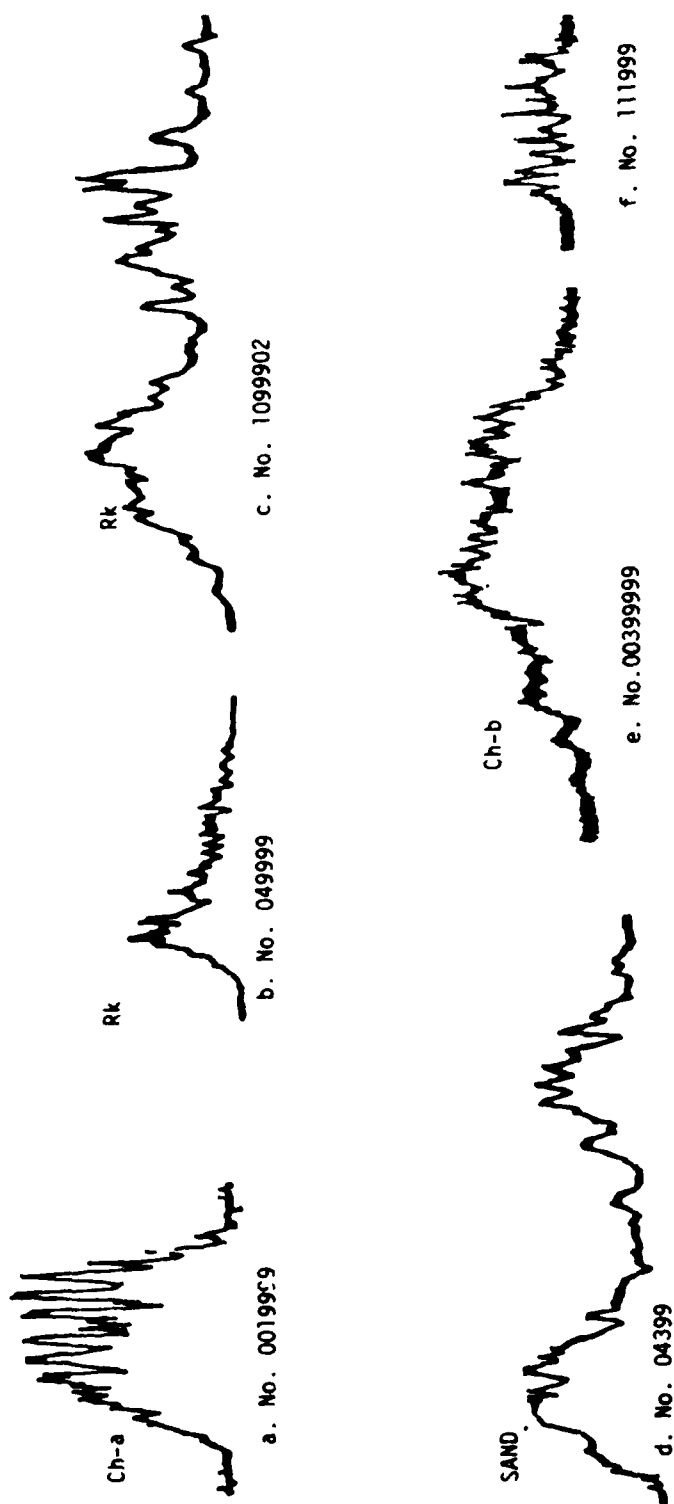


FIG. 10 EXAMPLES OF MEASURED STRESS VARIATION IN SITU BY BUL-1 ON VARIOUS SOIL

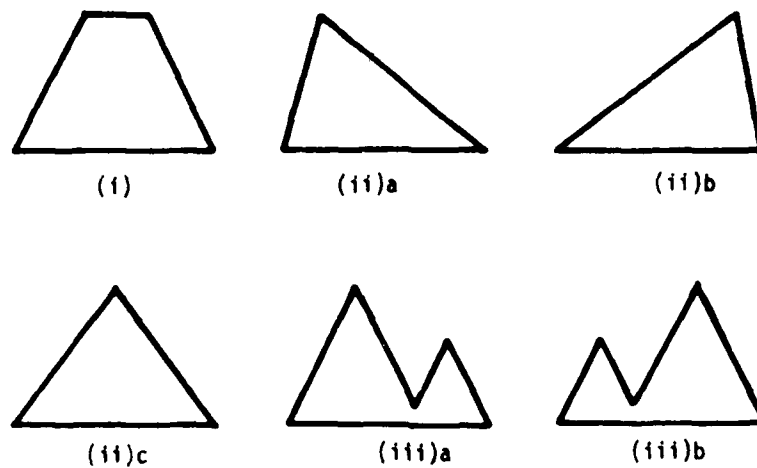


FIG. 11 SKETCHES OF SIX MEASURED STRESS VARIATION TYPE DUE TO BUL-1

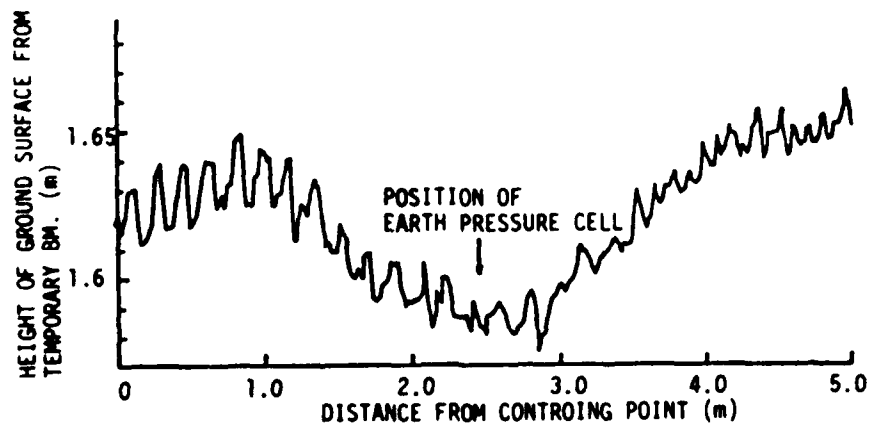


FIG. 12 A GROUND CONFORMATION OF Ch-d AFTER 15TH PASSES BY BUL-4

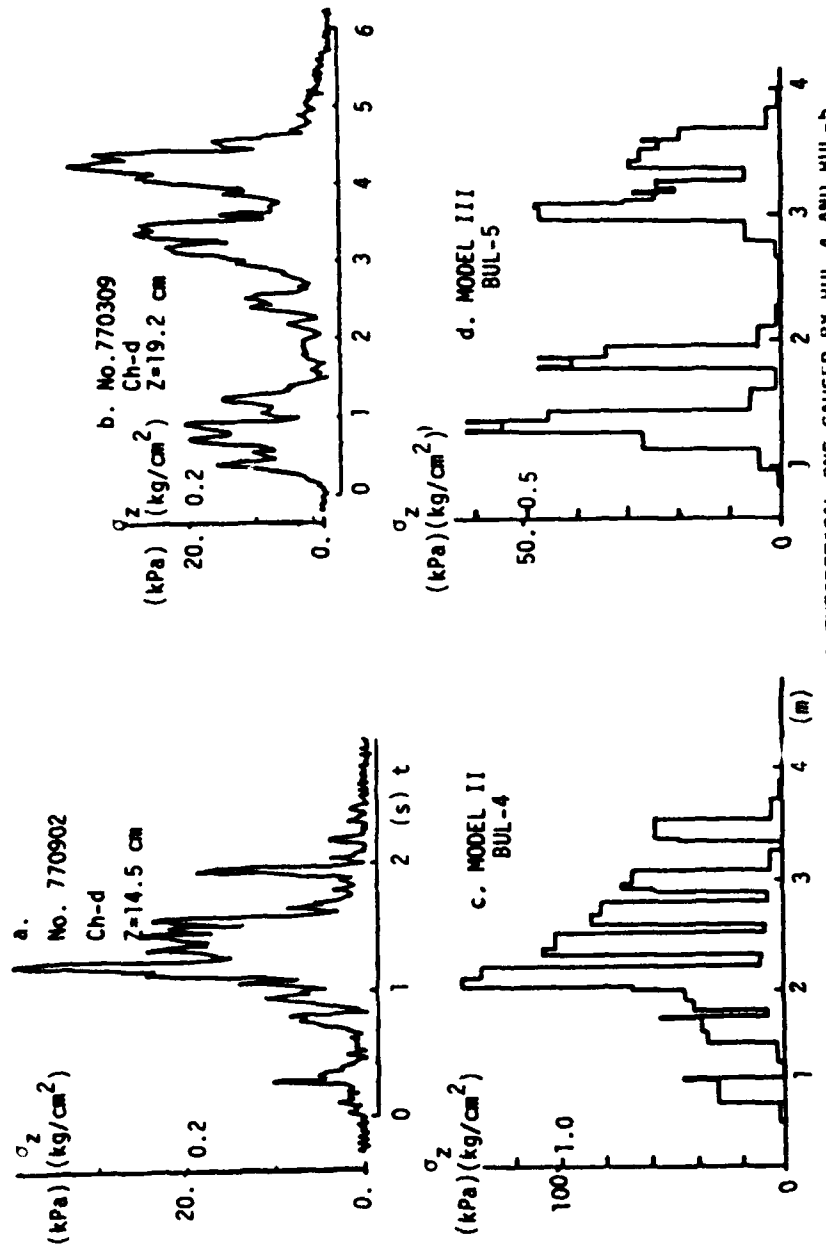
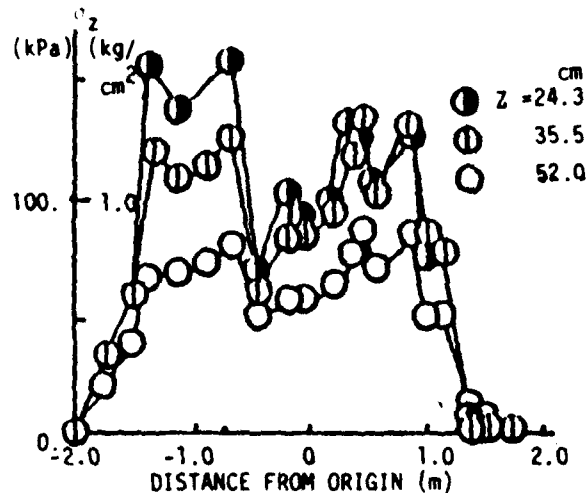
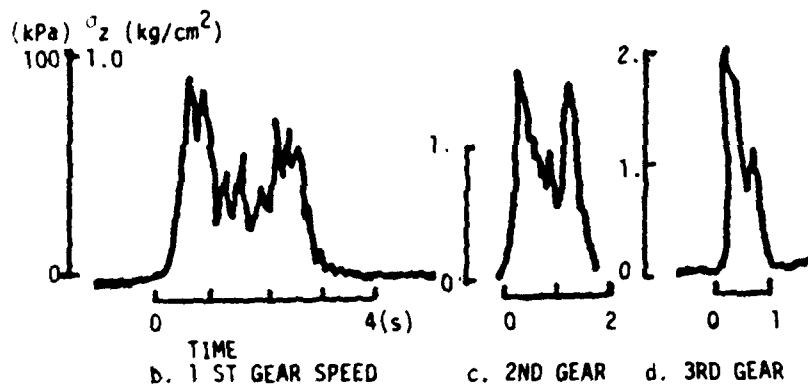


FIG. 13

EXAMPLES OF MEASURED STRESS VARIATION AND THEORETICAL ONE CAUSED BY BUL-4 AND BUL-5



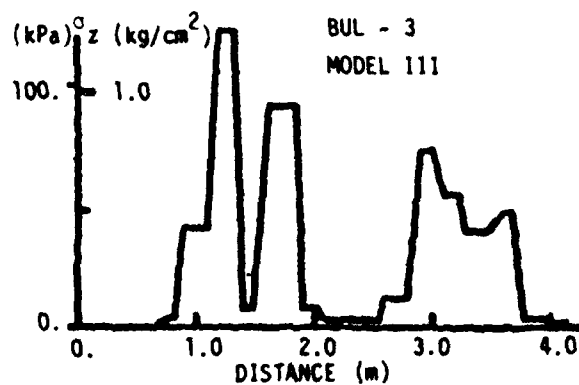
a. STATIC
STRESS VARIATION,
THAT IS NEITHER
TRAVELLING NOR
REVOLUTING ENGINE



b. 1 ST GEAR SPEED

c. 2ND GEAR

d. 3RD GEAR



e. THEORETICAL
STRESS VARIATION

FIG. 14 RELATIONSHIP TRAVELLING SPEED AND THE SHAPE
OF MEASURED AND THEORETICAL STRESS VARIATION
CAUSED BY BUL-3 IN CH-C SOIL

AD-P004 271

FINITE ELEMENT ANALYSIS OF GROUND DEFORMATION BENEATH MOVING TRACK LOADS

Leslie L. Karafiath

R&D Center, Grumman Aerospace Corporation, Bethpage, NY 11714, USA

INTRODUCTION

The major portion of the motion resistance forces encountered by vehicles traveling off-road is caused by the deformation of the ground under the vehicle load. Tracks were originally conceived as implements to distribute the vehicle load over a large area and thereby reduce the pressure to, and deformation of the ground. Tracked vehicles with rigid suspension systems distribute ground pressures nearly evenly and can, at low speed, traverse soft terrain not negotiable by other vehicles.

The requirement of the military for increased cross-country mobility of combat and support vehicles lead to the development of flexible tracks supported by sprung road wheels. While such suspension systems and tracks are necessary for good riding quality at high speed and for obstacle crossing capability, the role of the track in uniformly spreading the pressure over the ground contact area has been severely compromised. The pattern of pressure distribution beneath the tracks of military vehicles, as many measurements show, is characterized by peaks immediately beneath the road wheels rather than by uniformity over the contact area.

The soil response to nonuniform pressure distribution depends on the magnitude of the peak stresses and, if these induce plastic flow conditions in the soil, the duration of the peak stress impulses. The latter is inversely proportional to the velocity of travel. Researchers in the field of off-road mobility have long been intrigued by the idea of reducing motion resistances by increasing the speed of travel. This report presents a methodology which supplants intuition with an analytical tool suitable for the quantitative evaluation of the effect of both pressure distribution and travel velocity on motion resistance.

MODELING OF SOIL PROPERTIES IN VEHICLE-TERRAIN INTERACTION SIMULATION

The interaction between off-road vehicles and terrain is essentially a contact problem where the geometry of the running gear-soil interface as well as the stresses acting on it change with the operating conditions of the vehicle and the properties of the soil traversed. The solution of the problem requires that there be compliance between the interface geometry and stresses computed for the vehicle running gear and soil. Solution procedures to this exceedingly complex problem proposed by various researchers working in the field of off-road mobility, invariably resorted to simplifying idealizations. In regard to the vehicle, the most commonly adopted simplification is the assumption that the vehicle is moving at a steady, low speed. Even so, solutions based on empiricism or analogies have been preferred over analytical solutions by many who considered analytical formulations unsolvable. In these approaches a major consideration in modeling soil behavior has been the convenience of obtaining some description of soil properties in the field rather than

AD A14R 634

PROCEEDINGS OF THE INTERNATIONAL CONFERENCE ON THE
PERFORMANCE OF OFF ROAD (U) INTERNATIONAL SOCIETY FOR
TERRAIN-VEHICLE SYSTEMS M J DWYER AUG 84

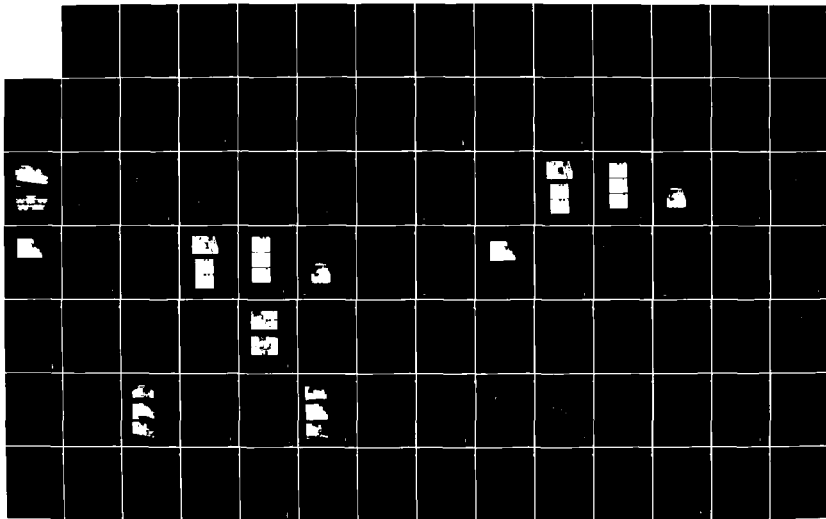
4/6

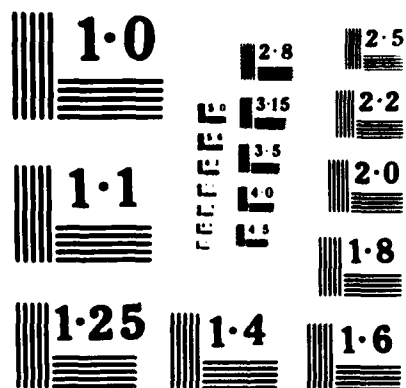
UNCLASSIFIED

DAJA45 R4 M 0251

F/G 13/6

NI





modeling soil behavior by material constants used in the applicable theory of soil behavior.

The most widely used soil property models in this category are:

- Cone Index. Theoretical justification for representing soil properties by cone penetration resistance in pneumatic tire-soil interaction was furnished by Freitag. He showed by dimensional analyses that in purely cohesive soils the cone index and in purely frictional soils the gradient of the cone index is the significant parameter which controls tire performance. Under any other conditions, the use of the cone index distorts the similarity and results in a low confidence level of the performance estimates based on its value
- Parameters of Pressure Sinkage Relationships. These parameters, obtained from plate-sinkage tests, are of variable dimensions and, therefore, conceptually incorrect. Their use for the determination of the vertical stresses at the running gear-soil interface is based on false analogy and is unsupportable by theory.

The advances in computer sciences and the general availability of computers for the numerical solution of nonlinear differential equations have changed the premises of the treating of vehicle-terrain interaction problems radically, and have made a rational approach to the formulation of these problems possible. In a rational approach, the properties of soil are modeled by the material constants which occur in the theory used for evaluating soil behavior in the interaction problem. Soil property models in this category are:

- Coulomb Strength (Cohesion & Friction Angle). Soil strength has long been recognized as the most important soil property governing mobility. Therefore, it is logical to use strength parameters for the characterization of soil behavior. The strength of soil defines the conditions for plastic state of stresses in the soil. Plasticity theory can be used for the determination of critical stress conditions occurring in various vehicle-terrain interaction problems. However, strength parameters by themselves are insufficient for the characterization of soil deformation behavior and, therefore, in vehicle-terrain interaction models based on plasticity theory various semi-empirical relations had to be used for the estimation of soil deformations
- Stress-Strain Properties. Early attempts to model the behavior of soil as a linear elastic material were of extremely limited validity in vehicle-terrain interaction simulation. Soil behavior being essentially nonlinear, various nonlinear relationships have been suggested by Kondner, Schofield-Wroth, Duncan-Chang and others to represent the nonlinear stress-strain behavior of soils. Recently, it has been shown (Ref. 1) that the parameters of nonlinear stress-strain relationships may be evaluated from field ring shear (Bevameter) tests, if properly conducted.

The scope of the present paper is restricted to the analysis of deformations in frictionless clay soils. The Ramberg-Osgood relationship, first proposed some 40 years ago to model the strain hardening behavior of metals, was found to represent the nonlinear stress strain relationships of clay soils, exhibiting strain hardening under rapid loading conditions, reasonably well. Since algorithms to treat material nonlinearities represented by the Ramberg-Osgood formula were already available in the finite

element code, this formula has been accepted to represent the nonlinear stress strain behavior of the frictionless clay material assumed in the analyses.

The Ramberg-Osgood representation of nonlinear stress-strain properties is:

$$\epsilon = \frac{\sigma}{E} + \frac{3\sigma_{0.7}}{7E} \left(\frac{\sigma}{\sigma_{0.7}} \right)^n \quad (1)$$

where the three parameters defining the nonlinear relationship are:

- E = initial tangent modulus
- $\sigma_{0.7}$ = stress at which the stress-strain curve has a secant modulus of $0.7E$
- n = exponent defining the rate of strain hardening in the plastic range.

Equation 1 is used in the finite element code to define the nonlinear stress-strain relationship in the plastic range, when the stress exceeds the yield point, σ_0 (Fig. 1). Up to that point, the stress-strain curve is linear. Strain upon unloading follows a linear path parallel to that in the elastic range, as shown in Fig. 1.

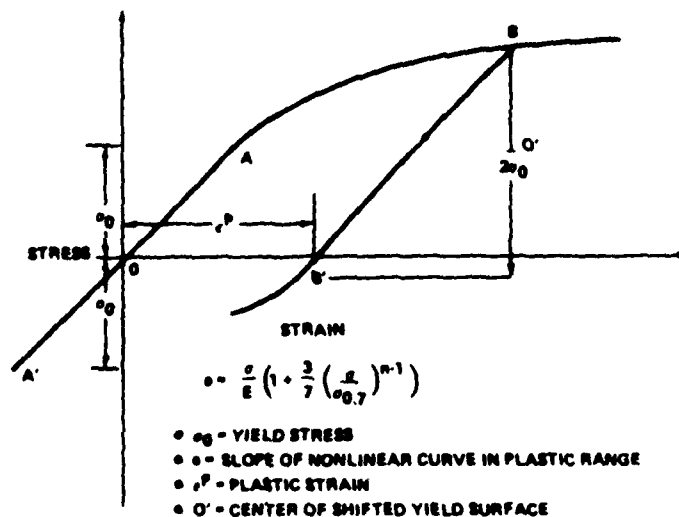


Fig. 1 Ramberg-Osgood Representation of Nonlinear Strain Hardening Stress-Strain Relationship

For the purposes of the analysis presented herein, the properties of the clay material were assumed to be represented by the following parameters:

- $$\begin{array}{ll} E & = 800 \text{ psi} \\ \sigma_0 & = 4.3 \text{ psi} \end{array} \quad \begin{array}{ll} n & = 6.0 \\ \sigma_0 & = 5.0 \text{ psi} \end{array}$$

A clay material of medium plasticity and high degree of saturation exhibiting the properties defined by the above parameters would have a cone n_{45} in the range of 35 to 45.

THE "DYCAST" FINITE ELEMENT CODE

The Dynamic Crash Analysis of Structures (DYCAST) code of the Grumman Research & Development Center was developed for the nonlinear, elastic-plastic, dynamic analysis of structures, primarily for the evaluation of the crashworthiness of various vehicle designs. For general information on the theoretical background of the code, the reader is referred to the DYCAST/GAC Theoretical Manual (Ref. 2). Program parameters and options, available elements, applicable nodal constraints and loading options are described in detail in the Users Manual (Ref. 3). The following discussion is limited to the adaptation of the code to the analysis of ground deformations beneath moving track loads, and problems associated with the use of the code for this purpose.

Of the elements available in the code, only the triangular membrane and the spring element were used in the analysis. Their usage is discussed in the next chapter. The triangular membrane element, defined by three nodes, used in the analysis assumes constant strain within the triangle. Transitional triangles are employed where different size triangles are joined in areas of mesh refinement. These triangles contain additional midside nodes, as necessary. To accommodate these additional nodes, a linear strain distribution is assumed within the transitional triangles.

Of the time integration method options available in the code the Explicit Modified Adams predictor-corrector method was used in the analysis presented herein. This integrator automatically chooses the time step to reflect current system stiffness and dynamic response.

Currently applied loading can be input in DYCAST in separable form,

$$P(x,t) = p(x) g(t)$$

where the $p(x)$ represents the spacial distribution of forces on node points and $g(t)$ is the time distribution of a load factor parameter. The function, $g(t)$ is input in DYCAST as a table of load factor versus time. Only one table is currently available in the code. Consequently, a new loading option has been added to the code to allow the simulation of the moving of the track load over the surface. This new option specifies a time delay between nodes accepting concentrated loads. Combination of this option with the specification of loading time history under the key word "PTME" allows the simulation of traveling track loads, as shown in Fig. 2.

DEVELOPMENT OF FINITE ELEMENT MESH

In vehicle-terrain interaction problems, the terrain is generally considered to be of large, often infinite extent. In the modeling of the behavior of such a continuum by a mesh of finite size, the conditions at the mesh boundaries require special attention. In dynamic analysis, rigid boundaries are the source of reflected stress waves which may or may not significantly affect the problem solution. In the present problem, the seat of soil deformations is in a shallow depth beneath the surface. The farther the mesh boundaries are from the seat of deformations the less the effect of the reflected stress waves on these deformations. Preliminary analyses were made to study the effect of stress waves on the deformations of the surface. The mesh used in the final analysis is shown in Fig. 3; nonlinear spring elements (not shown in Fig. 3) join the nodes at the

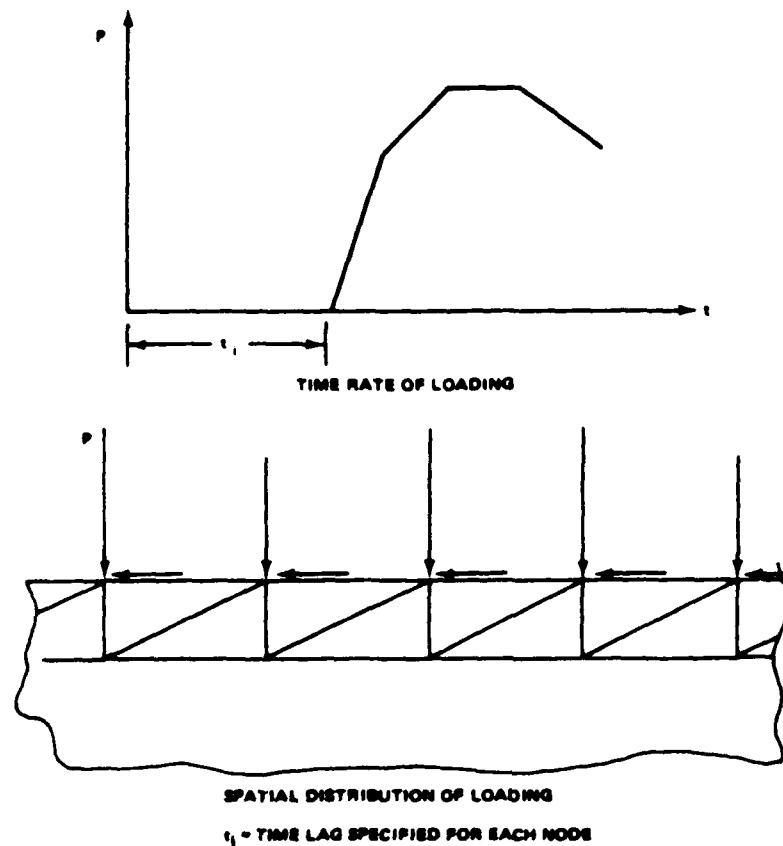


Fig. 2 Time Delayed Loading Option

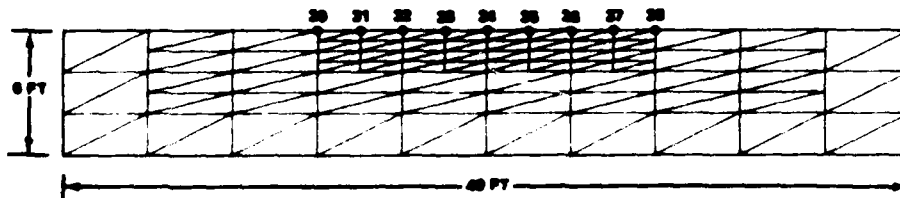


Fig. 3 Finite-Element Mesh Developed for Analysis of Ground Deformations

vertical boundaries of the mesh. The parameters of these nonlinear spring elements were estimated on the basis of the magnitude of passive earth pressure and associated displacements at the node locations. These springs lessen the reflection of horizontal stress waves from these boundaries and simulate the restraining effect of the continuum adjoining the vertical boundaries of the mesh.

All nodes at the horizontal mesh boundary at 6 ft depth were assumed to be fixed for the following reasons. While stresses and displacements of the terrain are often computed by formulas valid for a semi-infinite half-space, in reality the soft soil conditions of particular interest in mobility research occur only to some limited depth where bedrock or other

firm soil layer is encountered. Thus, in the vertical direction, it is more realistic to allow for a rigid boundary at some depth than to apply some artificial system there to simulate the effect of an adjoining infinite continuum of the same material.

PRESSURE DISTRIBUTION PATTERNS

Tracked vehicles transmit vertical forces through road wheels and their suspension systems to the tracks. Tractive (horizontal) forces in the track are generated by the driving sprocket. The track pad and shoes distribute these forces over the contact area. Various patterns of pressure distribution result, depending on the relative stiffness of the suspension system and the ground, and the flexibility and initial tension of the track.

To evaluate the effect of pressure distribution on ground deformation, three pressure distribution patterns have been selected for the analyses as shown in Fig. 4. All three are equivalent as far as total load is concerned and correspond to an average value of the vertical normal pressure of about 7.5 psi over the assumed 10 ft long x 1.25 ft wide contact area. For the convenience of reference, the pressure distribution at the top of Fig. 4 is called uniform, although allowance is made for a time rate of rise and decline of the uniform pressure over a 0.5 ft length at the ends of the contact area. The pressure distribution shown in the middle of Fig. 4 is referred to as a pattern with "low peaks," 1.58 times the uniform pressure. Between the peaks, there is a low pressure equaling 0.2 times the uniform pressure. The pressure distribution shown at the bottom of Fig. 4 is a pattern with "high peaks", 2.12 times the uniform pressure. The areas between the peaks carry no load.

The horizontal or tangential stresses as transmitted to the ground are assumed to be distributed in the same pattern as the vertical normal stresses. Their magnitude is assumed to be in a selected proportion to the vertical stresses. Several horizontal/vertical stress ratios have been selected in the analysis to evaluate the effect of this ratio on ground deformations.

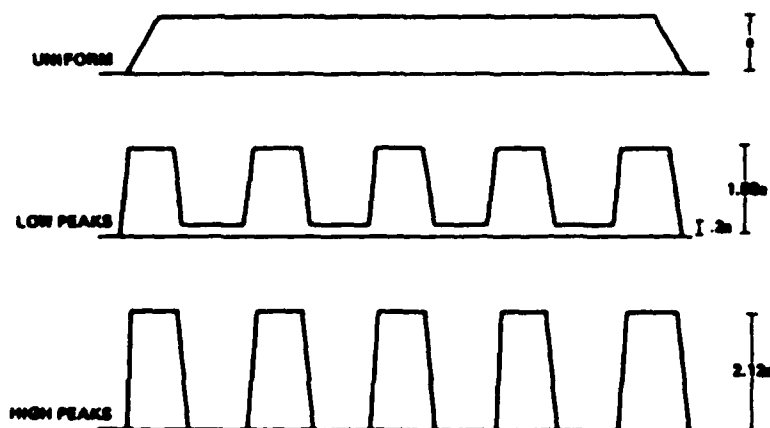


Fig. 4 Patterns of Pressure Distribution Assumed in the Analysis

The assumed pressure distributions are idealizations of distributions observed in various field experiments and represent a realistic approximation of pressure distribution variations expected to occur beneath tracks supported by five road wheels.

Since the triangular elements of the finite element code accept only loads concentrated at the nodes, the pressure distribution patterns were converted to concentrated loads acting on nodes 30 - 38 (Fig. 3).

SIMULATION OF VEHICLE TRAVEL

The representation of a continuum of large horizontal extent with a relatively small finite mesh poses problems for the simulation of traveling vehicle loads. The following two alternatives were considered for the simulation.

- The vehicle is assumed to travel at steady speed
- The vehicle accelerates from a standing position to a given speed and maintains that speed during passage of the vehicle over a point in the ground.

While this latter assumption is the desirable choice, its adoption would have required a much larger mesh than that shown in Fig. 3 and appreciable computer time for the analysis, since computations for the accelerating stage increase the total time significantly. The assumption of steady state speed, on the other hand, involves approximations in regard to the loads applied at the surface.

The assumption of steady state speed implies that the vehicle arrives at the mesh boundary with that steady speed. Thus, all nodes at the surface should receive loads for a duration appropriate for the travel velocity. However, the triangular elements adjoining the vertical boundary of the mesh are, except for the nonlinear springs, laterally unsupported and would, therefore, exhibit excessive and unrealistic strains if directly loaded. The compromise solution, adopted in the analysis, is that loading for a vehicle traveling from left to right starts at Node 30 and continues through Node 38 (Fig. 3). The track position of interest is when the loading reaches Node 38. At this time, the 10 ft contact length of the track covers five triangular blocks ending at Node 33. A typical deformed mesh corresponding to this position of the track is shown in Fig. 5.

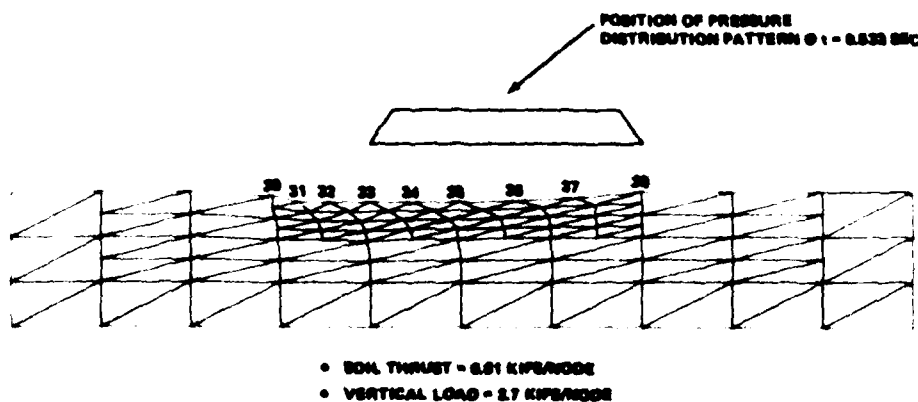


Fig. 5 Mesh at $t = 0.533$ sec Time, Deformed Under Uniform Pressure Moving at 30 ft/sec

Ground deformations in this position are thought to be representative of those occurring beneath a vehicle traveling at steady speed, hypothetically from an infinite distance. The deformations to the left of Node 33 are not necessarily representative of those occurring behind a tracked vehicle traveling at steady speed and definitely do not signify a rebound but rather the lack of loading in this part of the surface. The role of the part of the mesh to the left of the Node 33 is to simulate the action of the continuum behind the track, and not the determination of the deformations of that region.

CASES ANALYZED

In accordance with the scope of this project, the effect of the following input variations on ground deformation has been investigated:

- Soil thrust (tractive force)
- Pressure distribution
- Speed.

To keep the total number of analyses to a reasonable level, the effect of each of these input variables was analyzed for one combination of the other input variables only. The matrix of the analyzed cases is shown below.

SPEED FT/SEC	F_h/F_v							
	BRAKING				DRIVING			
	-.5	-.3	.1	0	.1	.3	.5	.67
10						U		
15						H,U,L		
20						L		
30	U	U	U	U	U	H,U,L	U	U
60						H,U,L		U

F_h = Horizontal force (soil thrust)

F_v = Vertical force

U = Uniform pressure distribution

L = Pressure distribution with "Low peaks"

H = Pressure distribution with "High peaks"

RESULTS OF THE ANALYSIS

The analysis of ground deformations beneath moving track loads brought forth an abundance of information on the time history of stresses in each element and displacements of each node of the mesh representing the soil mass. For brevity, only those results are reported herein which have direct bearing on track performance.

The full line in Fig. 6 shows the variation of soil thrust with slip due to ground deformation for the case of uniform pressure distribution. Soil

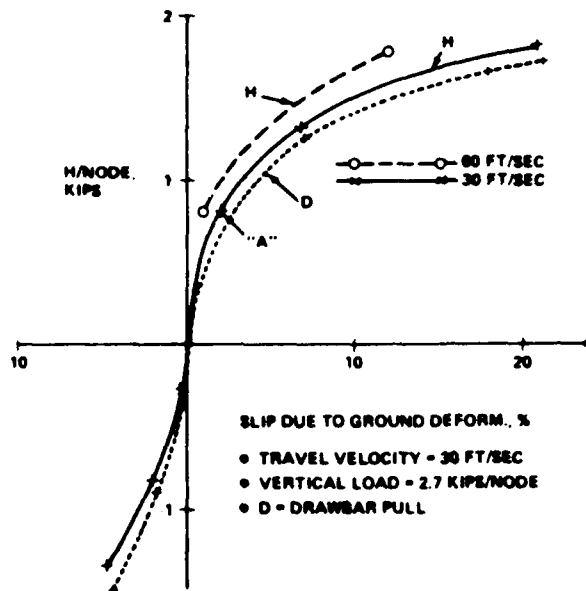


Fig. 6 Soil Thrust (H)-Slip Relationship for Uniform Pressure Distribution

thrust is the propelling force from which the motion resistance would have to be deducted to obtain the net drawbar pull. The major component of the motion resistance is due to the trim angle, obtained in the analyses. The dotted line in Fig. 6 shows the drawbar pull approximated as the soil thrust minus motion resistance due to trim angle. Point "A" in the figure indicates the case for which the deformed mesh is shown in Fig. 5.

The slip value shown in Fig. 6 is an average value of that portion of the slip which is caused by ground deformation. Note that ground deformation itself may be responsible for as high a slip as 20%.

Other components of the total slip include the slip due to tire deformations and separation of the solid-soil interfaces. The magnitude of the former is difficult to estimate but in all probability it is much smaller than that caused by ground deformation.

Separation of the solid-soil interfaces may occur whenever the shear stress exceeds the strength of the interface. This will be discussed in more detail later in connection with the displacement and velocity history of the individual nodes during passage of the track load.

Figure 7 shows the variation of sinkage with soil thrust for uniform pressure distribution for the whole range of soil thrust. The effect of pressure distribution with low and high peaks is shown for a limited range of soil thrust, encountered most commonly in driving conditions. At the right side of the figure, the coefficient of motion resistance due to the trimmed position of the track is shown. The solid line indicates that even pressure distribution is most helpful in keeping sinkage and motion resistance low; the increase of sinkage with the absolute value of soil thrust is the most important feature of track-soil interaction.

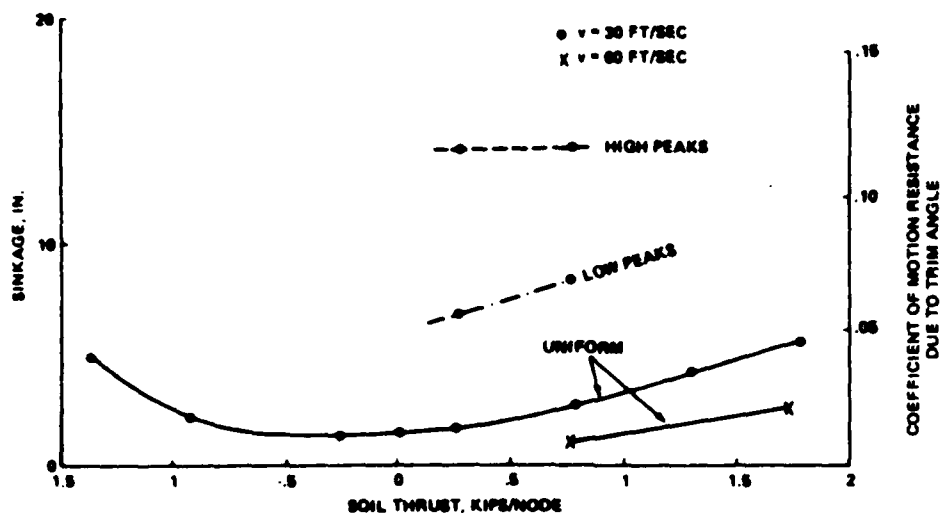


Fig. 7 Effect of Soil Thrust & Pressure Distribution Pattern on Sinkage & Coefficient of Motion Resistance

Figure 8 shows the effect of speed and pressure distribution on sinkage and the motion resistance generated by the trimmed position of the track.

It is apparent from the figure that, from the motion resistance point of view, evenly distributed pressures and high travel velocity are the most advantageous. An increase in the travel velocity from 10 to 60 ft/sec reduces the sinkage to about half of its maximum value exhibited at 10

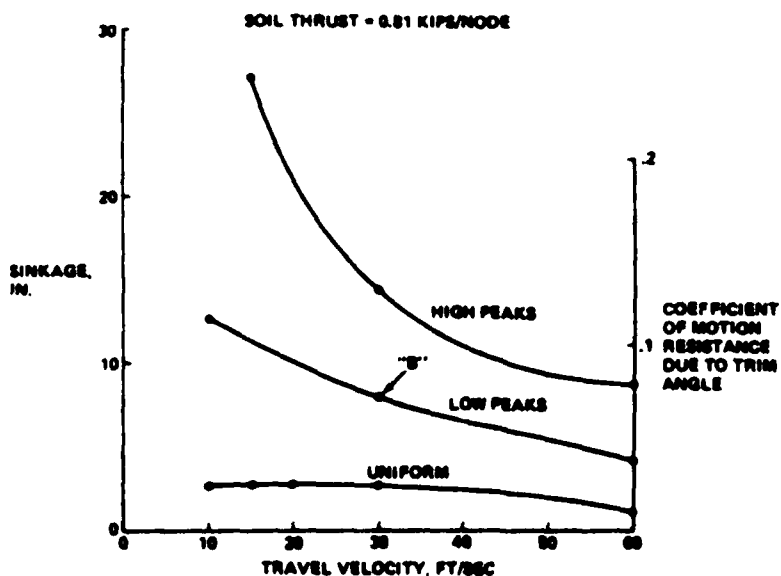


Fig. 8 Effect of Travel Velocity & Pressure Distribution Pattern on Sinkage & Coefficient of Motion Resistance

ft/sec in the case of uniform pressure distribution and even more in the case of pressure distributions with peaks. For the case indicated by "B" in the figure, the deformed mesh is shown in Fig. 9.

The magnitude of slip caused by the horizontal deformation of the ground is also affected by both the pressure distribution and travel velocity. Figure 10 shows the variation of slip with the pressure distribution pattern and travel velocity for a soil thrust of 0.81 kips/node, 30% of the vertical load/node. This useful and novel information on the interrelationship among slip, pressure distribution and track velocity refers to one type of clay soil. More important than the results shown in

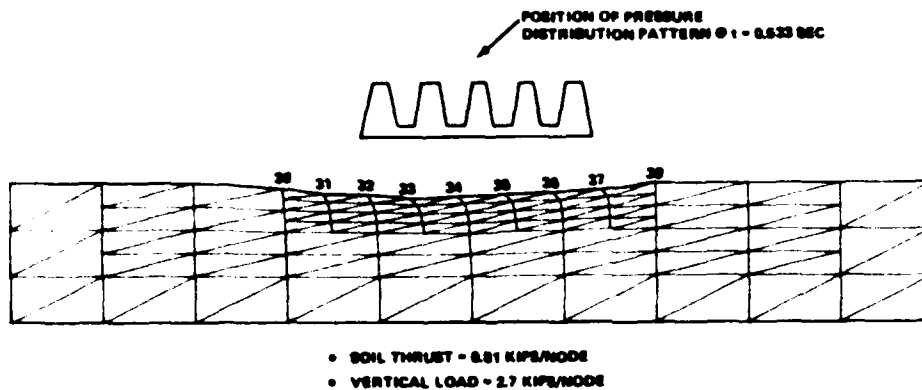


Fig. 9 Mesh at $t = 0.533$ sec Time, Deformed Under Pressure Distribution Pattern with Low Peaks, Moving at 30 ft/sec

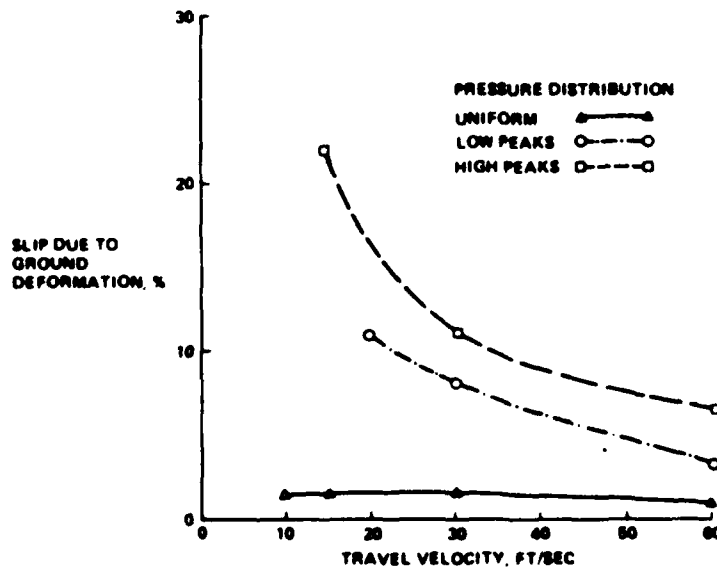


Fig. 10 Effect of Travel Velocity & Pressure Distribution Pattern on Slip Associated with the Development of Soil Thrust Amounting to 30% of Vertical Load

the figure for this soil is that the methodology to obtain such information has been developed and can be applied to other cases.

Displacements, velocities and accelerations of each node are computed for every time increment by the integration of the differential equations of motion. Of these, the displacements and velocities of the loaded nodes at the surface are of particular interest, since the vertical displacements of the surface nodes may be equated with sinkage and the horizontal displacements are the principal cause of slip. An example of the time history of x (horizontal) and y (vertical) displacements is shown in Fig. 11 for Node 33 for the case of a pressure distribution with low peaks and 30 ft/sec travel velocity. The effect of pressure variation is barely discernible in the plots. The total horizontal displacement of this node at the time it was just passed by the moving track load ($t = 0.5333$ sec) is opposite to the direction of travel and, in effect, reduces the distance traveled. This travel reduction is identified as slip in off-road mobility research terminology.

The time histories of x and y velocities of the same node, shown in Fig. 12, reveal that the slip is not uniform over the length of the contact area. The velocity variations reflect the changes in the pressure distribution. From the travel velocity and average slip, the track velocity computes as 32.8 ft/sec on the average. The first peak in the x velocity occurs shortly after the loading of Node 33 begins at $t = 0.2$ sec. The amplitude of the peak far exceeds the average track velocity indicating that the assumed rate of loading is too high. To eliminate this inconsistency, the development of an interface element, simulating

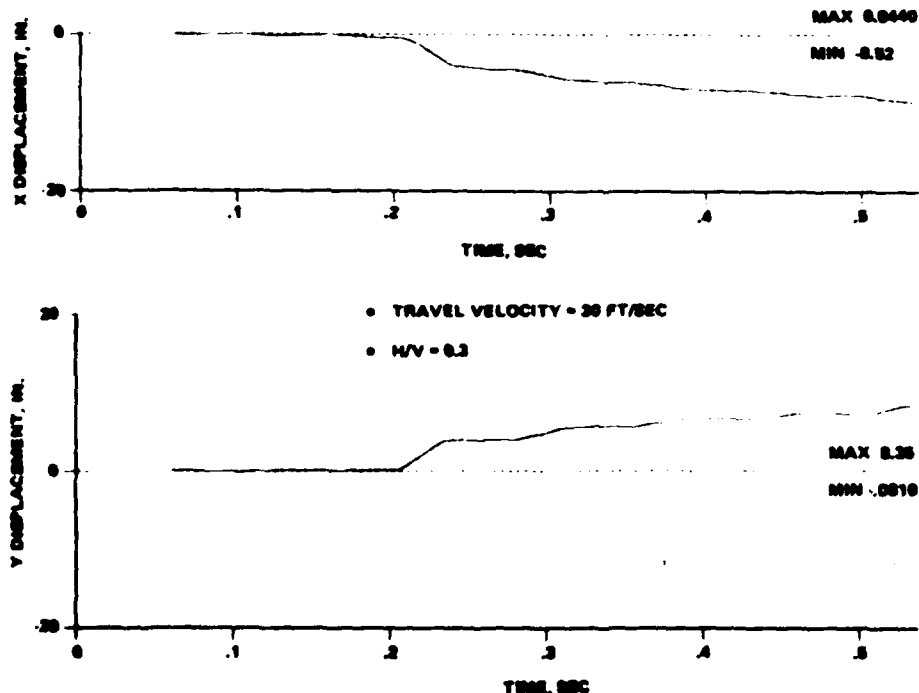


Fig. 11 Time Histories of X and Y Displacements of Node 33, Pressure Distribution with Low Peaks

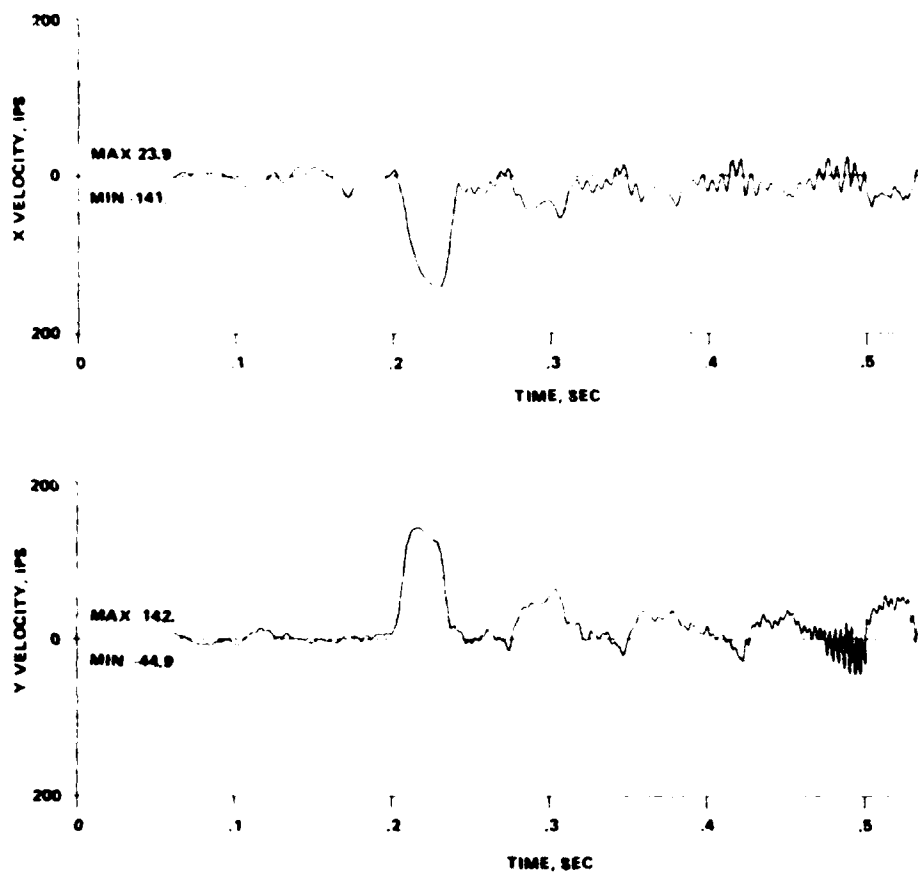


Fig. 12 Time Histories of X and Y Velocities of Node 33

the load transfer between track and soil, is contemplated. Such an element would allow for relative displacements between track and soil and the development of shear stresses consistent with an interface shear strength-displacement relationship.

The y velocities shown in Fig. 12 also show the response of the soil to the pressure impulses represented by the peaks in the pressure distributions. It is interesting to note that between the positive (downward) velocity peaks the velocities become negative (upward) corresponding to a soil response that tends to flex the tracks upward in between the road wheels.

CONCLUSIONS

A methodology, using finite element analysis techniques, has been developed for the determination of the deformation of clay soils under moving track loads. Nonlinear stress-strain properties as well as plastic behavior of soil have been modeled and together with the dynamic capabilities of the finite element code fully utilized in the analyses. This methodology, for the first time in off-road mobility research, makes the quantitative evaluation of the effect of pressure distribution and travel velocity on soil deformation induced slip, trim angle and motion resistance feasible. Results of the analysis of selected cases, shown graphically, indicate that these effects are significant. The method is also suitable for the performance of parametric analysis needed for design optimization.


REFERENCES

1. Janosi, Z.J. and Karafiath, L.L., "Improved Technique of Field Ring Shear Testing for Soil Strength Determination," Proc 7th Int Conf for Terrain Vehicle Systems, Calgary, Canada, Aug 1981
2. "DYCAST/GAC Nonlinear Structural Dynamic Finite Element Computer Code Theoretical Manual," Grumman Aerospace Corporation R&D Center Report RE-501, Aug 1974
3. "DYCAST/GAC Nonlinear Structural Dynamic Finite Element Computer Code Users Manual, Version 1.1," Grumman Aerospace Corporation R&D Center, June 1982

ACKNOWLEDGEMENTS

The work described in the paper was partially sponsored by the Tank-Automotive Concepts Laboratory of the U.S. Army Tank-Automotive Command (TACOM) Research and Development Center, Warren, Michigan.

Acknowledgement is due to Dr Allan Pifko, Senior Staff Scientist of the Grumman R&D Center and one of the principal developers of the DYCAST code, and Ms Patricia Ogilvie, Senior Program Analyst, for incorporating the time delayed loading option in the code, and for their cooperation in resolving problems encountered in running the program.



A RIG FOR TESTING THE SOFT SOIL PERFORMANCE OF TRACK SYSTEMS

E B MACLAURIN
MVEE CHERTSEY SURREY ENGLAND

INTRODUCTION

For a given level of performance the track and suspension system of a military tracked vehicle must be as light and compact as possible to maximise weight and volume available for crew and payload (armour protection, weapon and communication systems, ammunition, fuel, etc). Although track systems have been used on military vehicles for some seventy years methods for predicting their performance in soft soil - and actual performance measurements - are limited and, even with its shortcomings, the nominal ground pressure term* remains the performance comparator most commonly used by vehicle designers. This is partly because of the complexity of devising, proving and using improved methods and partly because military vehicle testing and training areas tend to be on sandy frictional soils where tracked vehicles rarely exhibit mobility problems. Operational areas are likely to include silty and clay soils where differences in track system design will affect performance to a much greater degree. If an improved track/soil model was available overall automotive system performance models could also be improved and designers would be able to make more rational choices between often conflicting requirements - for example:-

- increasing the number of wheels should improve soft soil performance and also reduce sponson height but increase cost and weight.
- increasing wheel diameter is likely to improve soft soil performance but increase sponson height, weight and cost.
- increasing track width should improve soft soil performance and reduce bush loading but will reduce space available inside the vehicle.
- increasing track pitch is likely to improve soft soil performance and reduce track weight but increase the level of vibration due to chordal action and reduce the life of track bushings.
- increasing track contact length is likely to improve straight line soft soil performance but may increase slewing moments required to steer the track.

The important soft soil performance parameters for a military tracked vehicle are generally:-

- Limiting go/no go soil strength - this defines the areas of terrain generally accessible to a vehicle under particular soil and weather conditions.

* NGP = vehicle weight/track width x track contact length x number of tracks.

AD-P004 272

- Tractive rolling resistance - the lower this is the greater the potential speed and range of a vehicle. Rolling resistance is usually considered divided between internal and external components - the internal being the proportion due to sprocket engagement, pin, bearing and seal friction, rubber hysteresis losses (road wheels, idlers, bushes, pads, return rollers), horn rubbing etc., and the external component due to work done in soil deformation.
- Net traction is required to enable a vehicle to climb gradients, accelerate and, for a skid steered vehicle, to steer although the straight line traction considered here will only give a comparative indication of traction required to steer a vehicle. The development of external traction (or drawbar pull) is important for towing dead vehicles, bulldozing, mine clearing, etc.
- The development of high tractive efficiency under traction conditions is important in that it affects vehicle acceleration and speed on gradients but is not as important for overall fuel efficiency as on, for example, an agricultural tractor used for ploughing.

SOIL/TRACK SYSTEM PERFORMANCE MODELS

A number of theoretical, semi-empirical or totally empirical models of soil/tracked vehicle performance exist although details of validation tests with most of these models are generally sparse. They include:-

1. The WES VCI method (Ref 1) which is a totally empirical method based on in-soil measurements of vehicle performance. Cone Index (CI), or Rating Cone Index (RCI), is used for describing soil strength. The method applies to cohesive fine grained soils and the first stage in using it is to compute a Mobility Index (MI) from vehicle parameters. In essence MI takes the form

$$MI = \frac{50 kW}{b^2 l} + \frac{W}{10 nbp}$$

where W = vehicle weight (lbf)
 b = track width (ins)
 l = length of track on ground (ins)
 n = total number of road wheels
 p = track pitch (ins)
 k depends on vehicle weight

Various other correcting factors for ground clearance, power/weight ratio, transmission type etc., are also included in MI but have a relatively small influence on its value. The second term looks promising in that it has units of pressure and appears to make allowance for the peaks of pressure which occur under road wheels. The first term however has the rather inappropriate units (for a cohesive soil/vehicle model) of specific weight and appears to give undue benefit to wide tracks. If figures for a typical heavy armoured vehicle are inserted into the relationship we get

$$MI = 100 + 7$$

i.e. the first term with its rather unsatisfactory form is by far the dominant one. The limiting go/no go soil strength VCI (Vehicle Cone Index) can then be estimated from an empirical relationship and is approximately proportional to MI. Drawbar pull and rolling resistance in soil of a particular strength can be estimated from simple relationships based on 'excess' RCI (actual RCI - VCI).

2. The Bekker method (2) uses the well known two part Bevameter instrument to measure soil values. A plate sinkage test is used to simulate vehicle sinkage and predict rolling resistance. A ring shear test is used to simulate and predict gross traction. Net traction is computed as the difference between gross traction and rolling resistance. The track is assumed to act as a rigid flat plate which may be reasonable for a crawler tractor with closely spaced wheels but is unlikely to be so for the usual type of military vehicle sprung track system. Although some impressive looking predictive equations have been published, details of validation studies of the method are limited.
3. The method is now being considerably extended by Wong (3) who still uses the basic bevameter instrument for measuring soil properties but in a vehicle mounted form with automatic data processing. The pressure sinkage relationship under repetitive loading and the slip sinkage characteristics of the terrain are also measured. In modelling the soil/vehicle interaction the track is assumed equivalent to a flexible and inextensible belt. Positions and diameters of roadwheels, sprocket, idler and support rollers are specified. Using the measured soil characteristics a system of equations are set up for the equilibrium of forces and moments acting on the track system and for conservation of track length. The deflected shape of the track and track/soil contact stresses are computed. Only a limited amount of data on validation studies have so far been published but the system shows promise especially if computer implementation is relatively simple and a range of 'standardised' soil values can be made available for use by designers. The lack of track link pitch as a vehicle parameter can be questioned since this has been shown to be a significant factor (4) as can the assumption that the road wheels are rigidly attached to the body although it would appear relatively easy to include suspension deflection effects.
4. Turnage has performed some laboratory tests with a modular track rig (5) in dry sands and near saturated clays. Cone Index was used to measure soil strength. The track was a belt type with bolted on shoes. Track contact length and width, and spacing and number of wheels could be altered. Most of the test work was with the sands but a preliminary dimensionless prediction term for clays was also suggested in the form

$$\frac{CI \text{ bl}}{W} \left(\frac{W}{W_{max}} \right)^{0.5}$$

W = Total load on track
W_{max} = Load to cause bogies to
 bottom out on suspension

$$ie \frac{CI}{MGP} \left(\frac{W}{W_{max}} \right)^{0.5}$$

$$\left(\frac{W}{W_{max}} \right)^{0.5}$$

$\left(\frac{W}{W_{max}} \right)$ is apparently a term to allow for the effects of load concentrations under the wheels but its derivation is not easy to follow.

5. In 1972 Rowland evolved the mean maximum pressure (MMP) term (4)

$$MMP = \frac{1.26W}{nbe (pd)^{0.5}}$$

d = diameter of road wheels
e = ratio, actual area of track link/nominal area, pb.

which correlated well with measured in soil pressure peaks under road wheels. Rowland postulated that MMP would be expected to give a guide to the soft soil behaviour of tracked vehicles and showed that it was linearly related to limiting go/no go soil strength (CI or RCI) in clay and organic soils. He also produced a relationship for external rolling resistance in clay soils (6)

$$C_{RE} = 0.28 \frac{(MMP)^{1.95}}{(CI)}$$

where C_{RE} = coefficient of external rolling resistance

and further hypothesised that $\frac{CI}{MMP}$ could be used as a describing mobility number for track systems and in the form

$$N = 2.8 \frac{(CI)^{0.72}}{(MMP)}$$

could be comparable to the WES pneumatic tyre mobility numbers and their predictive performance relationships (7).

THE MVEE MOBILE TESTER

A prime requirement of this investigation was some means of obtaining accurate in soil performance measurements for a variety of track system configurations. It was decided that a mobile tester of the type used by NIAE and others was the most adaptable and cost effective way of obtaining this information. Laboratory scale model testing can give useful information but would still need to be correlated with full scale testing. Full scale laboratory testing in soil pits presents formidable problems of soil processing especially with clay soils and has now been abandoned at MVEE. There are various experimental difficulties with using a vehicle to measure in soil performance - controlling slip for example - and extensive modifications would be required to fit different track system configurations to the vehicle.

The MVEE mobile tester (Fig 1) is based on a crawler chassis to enable it operate effectively in weaker soils and is capable of testing wheels (8) as well as the modular track rig described here. The track rig is carried in an arch frame and connected to the tester by parallelogram links which can also lift the rig clear of the ground when manoeuvring. Hydrostatic drive motors are accommodated within the

track rig and are connected to the track sprockets via roller chains. The track rig is normally freely pivoted in pitch to simulate straight running of a two track skid steered vehicle although pitch restraint can be applied to the rig to simulate certain types of articulated, wagon steer and half track vehicle. The position of the rig to frame pivot point can be adjusted to model different c.g. positions and 'traction centre' heights.

The track rig is 3.2 m from idler to sprocket centre with a nominal dimension of 2.0 m between front and rear wheels. The maximum road wheel size is 0.61 m dia and 2, 3 or 4 of these can be fitted. Up to eight 0.25 m dia wheels can be used. 0.36 m and 0.43 m dia wheels can also be fitted in various 2, 3, 4, 5 and 6 wheel configurations. A variety of link tracks up to a maximum width of 0.61 m can be used. A simple band track is also available.

The wheels are carried on pivoted balance beams to accommodate terrain roughness. When the rig was designed consideration was given to the use of an individual wheel sprung suspension but space was not available in the rig to accommodate the springs and the wide range of individual wheel loadings would have required a range of springs of various rates. The use of load equalising balance beams is a reasonable compromise - compared to a sprung suspension weight transfer is reacted between a forward set of equally loaded wheels and a rearward set of equally loaded wheels. With a sprung suspension weight transfer is generally proportional to the distance from the 'spring centre' (usually near the centre of the vehicle) and spring deflections will also alter the approach and departure angles of the track. The rig can be turned round to provide a forward or rear drive sprocket and approach and departure angles can be adjusted. Total ground load can be varied by means of ballast weights between approx 25 kN and 55 kN.

Tractive forces from the rig are measured by a pair of horizontal transducers. Sprocket torque is measured by a strain gauged shaft within the sprocket hub which carries torque between the chain sprockets and track sprockets. Signals are fed out via slip ring boxes. Sprocket speed is measured by a toothed ring and inductive pick up within the hub. Although other methods have been used forward speed is now measured by a toothed ring on the tester sprocket, tests having shown tester track slip to be very small under most conditions.

EXPERIMENTAL PROCEDURE

For the trials reported here the rig was used in its rear drive configuration with the external pivot point at mid-wheelbase and at a height above ground to give approximately the same ratio of traction centre height to wheelbase as c.g. height to wheelbase on a typical tracked armoured vehicle. Tests were generally performed at a vertical load of 55 kN although some tests were run at half this load. The following track system configurations were used:

No of wheels	Dia of wheels	Track (see Fig 2)			
		Type	width, b	pitch, p	Area ratio, e
8	0.254	A	0.343	0.117	0.831
4	0.610	A	0.343	0.117	0.831
		B*			
		C		0.230	0.831
		D		0.116	0.672
		E		0.116	0.814
	0.432	A B			
	0.254	A			
2	0.610	A			

* Track A less rubber pads.

All tracks rubber bushed except track C which is dry pinned.

Tests were performed by the progressive slip method. The track speed was held nominally constant and the parent vehicle speed varied to give a range of slips from approx -20% to +100% with slow transition through the important -5 to +30% slip region. Measurements of net thrust, sprocket input torque, sprocket speed and forward speed were recorded on magnetic tape.

Runs were made at two, (sometimes three) track tensions, with at least 12 runs per track configuration.

Soil strength measurements were made by cone penetrometer - at least 6 measurements per run - with a concentration of measurements in to 0 to 20% slip region. In rut measurements were also made.

Analysis

The magnetic tape recordings were played via filters and A/D converters into a computer for analysis and graph plotting. The tractive effort recordings were corrected for tester longitudinal acceleration. Gross traction P_G , net thrust or traction P_T , tractive rolling resistance R_T , tractive efficiency η , and slip s were computed as follows:

$$P_G = \frac{T}{r}$$

where T = sprocket torque
 r = effective sprocket radius

$$R_T = P_G - P_T$$

$$\eta = \frac{P_T v}{T \omega}$$

when v = forward speed
 ω = sprocket angular speed

$$s = \frac{\omega r - v}{\omega r}$$

P_G , P_T and R_T were divided by track weight to give the coefficients of gross traction C_G , net traction C_T and tractive rolling resistance C_R . C_G , C_T , C_R and η were plotted against slip.

RESULTS

Results from two test sites are reported here - both sugar beet fields after harvesting. Soil moisture content on both sites was unseasonably low giving comparatively high soil strengths.

Site A

The soil was a very silty medium/fine sand with over 30% silt or clay (USCS Classification SM/SC). Moisture content was around 20% giving average cone index values of around 450 - 500 kPa in the 0-150 mm layer. Laboratory triaxial tests on a sample of the surface soil shows it to be mainly cohesive with some frictional properties ($\phi = 9^\circ$).

Site B

The soil in this site was a clayey silt (USCS classification ML/ML-CL) with at least 50% silt or clay. Moisture content was around 29%. Average cone index values for the 0-150 mm layer were typically around 300 kPa.

Traction Curves

Typical traction curves from both sites are shown in Figs 3 and 4. High values of gross traction coefficient were obtained at Site A - in some cases exceeding 1.2. Traction coefficients were appreciable lower for Site B because of the weaker soil. A noticeable feature of the curves for Site A is the considerable increase in rolling resistance which occurs as traction develops. In some cases the coefficient of rolling resistance at 20% slip is over 3 times its value at the self propelled point. This considerable increase was somewhat unexpected and unlikely to be due increased internal resistance which would be comparatively small for rubber bushed tracks. For comparison, data for the rolling resistance/slip relationship of wheels was investigated. Rowland (9) reviewed available data and suggested empirical relationships:

For pneumatic tyres

$$C_R = (1 + s)$$

i.e. C_R proportional to slip and doubling between 0 and 100% slip and, for rigid cylindrical wheels

$$C_R = (1 - 0.75s)$$

i.e. rolling resistance actually reducing with slip. No such simple relationships are apparent for track systems, the rolling resistance being a function of traction and the track system configuration.

In a two track skid steered vehicle traction causes weight transfer from front to rear depending on the position of the 'traction centre', the wheel and track arrangement and wheelbase. A moving unsprung track system generally takes up a characteristic tail down pitch angle. At low traction this is due to progressive compression of the soil under the wheels. As traction increases the soil under the rear of the track will be subject to greater shear deformations due to slip. This will increase the likelihood of soil failure and extra sinkage under the rear of the track. The effect is sometimes referred to as slip sinkage.

With a sprung track system the frame or hull will take up an additional angle due to spring deflections. This will be increased by a raised sprocket (or idler if front driven) due to the vertical component of track (gross traction) force. Because the suspension will generally be considerably more compliant than the soil this component will also unload the soil under the rear wheel and thus increase loading still further on the adjacent wheels. The effect can be countered on front drive vehicles by means of so-called compensating idlers (Fig 5a). With a rear drive sprocket various arrangements are possible which interconnect a link between the final drive reduction gear and the rear wheel (Fig 5b). The extra cost and complication of these arrangements usually preclude their use although front mounted compensating idlers are quite widely used to counter vehicle nose dive when braking. Conversely soil offloading under end wheels may be beneficial when steering in reducing moments required to slew the track. An active suspension could be used to control soil normal forces under wheels.

In Fig 6 values of C_R are shown plotted against C_T as well as slip for 2, 4 and 8 wheel arrangements. It is noticeable that the increase in rolling resistance is much less marked with the two wheel arrangement where weight transfer is proportionately less than in the other arrangements and where track force does not off-load the rear wheel because it is rigidly attached to the track frame. The increase in rolling resistance thus appears to largely a function of weight transfer in the track system as traction increases. See Appendix for calculation of ground reaction loads.

Comparison of Different Configurations

All the arrangements were tested at a 'normal' tension (nominally 20% of weight on track system) and a 'tight' tension (nominally 30% of weight). High tension is sometimes thought to improve performance, especially in the go/no go region, presumably because of better 'bridging' effect between wheels although with sprung systems it also increases the tendency to offload the end wheels and hence increase loading on the remainder.

Averaging all the results from both sites gives the following values for C_{T20} and C_{RSP}

	Site A		Site B	
	Normal	Tight	Normal	Tight
C_{T20}	0.53	0.53	0.29	0.29
C_{RSP}	0.11	0.11	0.15	0.16

i.e. no significant difference between the pre-tensions.

Similarly one of the tracks was run without rubber track pads (track B in Fig 2) but again no clear trend was apparent - running without pads showing a slight increase in traction on one site and a slight decrease on the other. All the values of coefficient of traction at 20% slip C_{T20} , coefficient of rolling resistance at zero traction (the self propelled point) C_{RSP} , and the coefficient of rolling resistance at 20% slip C_{R20} were therefore averaged for each track system configuration neglecting track tension and the absence of track pads. These average values were then plotted against the dimensionless terms CI/NCP and CI/M to see if either can be used to adequately describe the measured data by means of empirical curves and form the basis of a simple tractive performance prediction system.

CI = average cone index in the 0-150 mm layer

$$M = \frac{W}{nbe (pd)^{0.5}}$$

The results are shown plotted in Figs 7 and 8.

The CI/NCP against C_{T20} plot (Fig 7a) shows an approximately linear relationship although with an appreciable amount of scatter in the low CI/NCP region and with no real indication of a limiting go/no-go value of CI/NCP . The 8 wheel configuration is seen to perform well as does the long pitch track (C) at low CI/NCP . The effect of wheel diameter is not readily apparent.

The plot of CI/NCP against C_{RSP} (Fig 7b) shows low resistance for the 8 wheel configuration at low CI/NCP and high resistance from the 2 wheel arrangement. The effects of wheel diameter and track pitch are not very apparent.

The CI/M against C_{T20} plot (Fig 8a) shows generally improved collapse of the data points and there is now an indication of a limiting go/no-go value of CI/M although no measurements are available for this region because of the comparatively firm soil conditions. Again the effects of wheel diameter and track pitch are not clear and in particular the long pitch track appears to 'underperform' with the weighting given to it in the M relationship. It was slightly unfortunate that on both test sites the long pitch track was tested on slightly firmer parts of the sites which makes it difficult to compare performance directly with the standard pitch track. The two wheel configuration is seen to perform comparatively well but this is probably because weight transfer effects

are comparatively small and there is little rise in rolling resistance with traction. A describing curve has been tentatively placed through the data points but no attempt has yet been made to ascribe any function to it.

The CI/M against C_{RSP} plot (Fig 8b) shows improved merging of the data points compared to CI/MGP . C_R includes both external and internal components even though CI/M is attempting to describe only the external resistance. It is difficult to see how the two components can be easily separated. The usual assumption is that measurements of internal rolling resistance from hard road trials also apply to the off-load condition although recent tests at MVEE have shown that terrain roughness can markedly increase internal rolling resistance apart from the effects of soil packing in the track system. All the tracks were rubber bushed except the double pitch which was dry pinned. The internal resistance of dry pinned tracks are generally appreciably higher than equivalent rubber bushed ones and are also more sensitive to pretension and gross traction forces. Measurements on a vehicle have shown the low speed hard road resistance of the double pitch dry pinned track to be approx 0.015 greater than the standard rubber bushed one (both at normal tensions). The measured C_{RSP} data points have therefore been reduced by this amount. It is planned to use the tester to measure the hard road resistance of all the configurations to see if there are any marked differences between them.

Fig 9 shows CI/M plotted against C_{R20} . No particular relationship is apparent and in nearly all configurations the rolling resistance coefficient actually increases at higher values of CI/M due to higher traction and the effects of weight transfer.

Fig 10 shows CI/M plotted against peak tractive efficiency η_p . Generally quite good merging of the data points is indicated with η_p not exceeding 75-80% even at high values of CI/M .

CONCLUSIONS

The mobile tester with modular track rig has proved a satisfactory way of gathering in field tractive performance data for track systems of different configurations.

The cohesive soil/track mobility number CI/M shows promise for forming the basis of a simple tracked vehicle performance prediction system but more data is required particularly in the important go/no go region where performance can be expected to be more sensitive to differences in track system configuration. At high traction consideration would also need to be given to weight transfer as affected by traction centre position, wheelbase and the departure angle of the track.

ACKNOWLEDGEMENTS

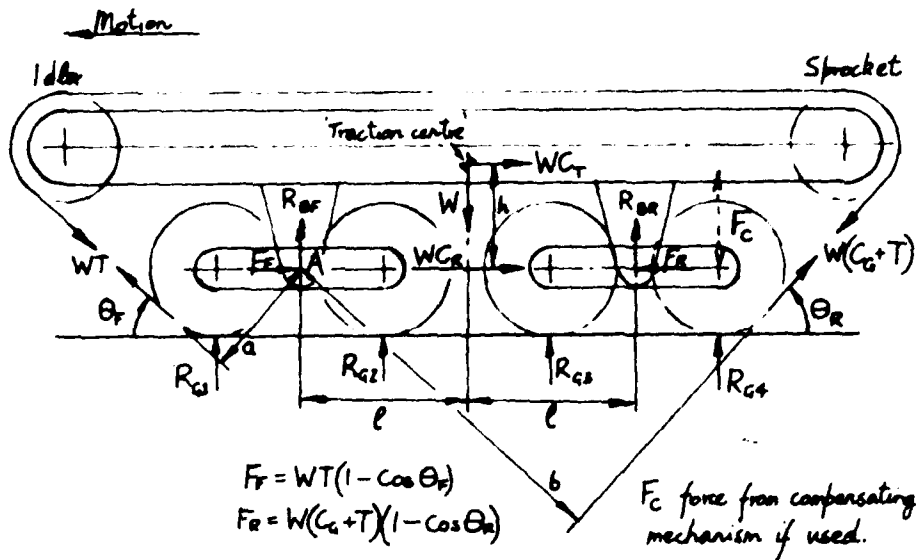
To Mr P Cox for organising and conducting trials.

REFERENCES

1. Rula, A A and Nuttall, C J. An Analysis of Ground Mobility Models (ANAMOB). WES Tech Report M-71-4 (1971).
2. Bekker, M G. Introduction to Terrain Vehicle Systems, 482-488, Ann Arbor Univ of Michigan Press (1969).
3. Wong, J Y. 'An Improved Method for Predicting Tracked Vehicle Performance' Proc 2nd European Conf ISTVS, 111-126, Ferrara (1983).
4. Rowland, D. 'Tracked Vehicle Ground Pressure and its Effect on Soft Ground Performance' Proc 4th Int Conf ISTVS, 353-384, Stockholm (1972).
5. Turnage, G W. Using Dimensionless Prediction Terms to Describe In-Soil Tracked Vehicle Performance, ASAE Paper No 73-1508 (1973).
6. Rowland, D. 'Soft Ground Performance Prediction and Assessment for Wheeled and Tracked Vehicles' Proc Conf on Off-Highway Vehicles Tractors and Equipment, I Mech E London (1975).
7. Turnage, G W. 'A Synopsis of Tire Design and Operational Considerations Aimed at Increasing In-Soil Tire Drawbar Performance' Proc 6th Int Conf ISTVS, 759-810, Vienna (1978).
8. MacLaurin, E B. 'The Effect of Tread Pattern on the Field Performance of Tyres' Proc 7th Int Conf ISTVS, 699-735, Calgary (1981).
9. Harding, C B L and Rowland, D. 'Drawbar Pull' Proc Conf on Drive Line Eng, I Mech E, Jersey (1970).

APPENDIX

The effect of traction forces on ground reaction loads.



Consider the 4 wheel equalising beam arrangement as used on the mobile tester track rig.

T = static track pretension, expressed as a ratio of vertical load on track system, and for a rear drive sprocket assumed to be maintained under traction conditions.

$R_{G1}, R_{G2}, R_{G3}, R_{G4}$ = vertical ground reaction forces under wheels.

Since the wheels are free-rolling, rolling resistance will effectively act through the wheel centres.

Taking moments about A for forces acting on 'body'

$$WC_T h + W(C_G + T)b + Wl = R_{BR} 2l + WTa$$

$$R_{BR} = \frac{W(C_T h + (C_G + T)b + l - Ta)}{2l}$$

Resolving vertically for forces acting on wheel 4

$$R_{G4} + W(C_G + T) \sin \theta_r = \frac{R_{BR}}{2}$$

$$R_{G4} = \frac{W(C_T h + (C_G + T)b + l - Ta)}{4l} - W(C_G + T) \sin \theta_R$$

Similarly for wheel 3

$$R_{G3} = \frac{W(C_T h + (C_G + T)b + l - Ta)}{4l}$$

Inserting the average values of Site A, 0.61m dia wheels, track A/B

C_{T20}	= 0.56	l	= 0.64 m
C_{G20}	= 0.81	θ_R	= 30°
h	= 0.30m	T	= 0.2
a	= 0.47m	b	= 1.10m

$$R_{G3} = 0.71W$$

$$R_{G4} = 0.21W$$

i.e. R_{G3} is almost 3 times its nominal value and R_{G4} is slightly less with very little load on wheels 1 and 2.

The inclusion of a compensating mechanism will introduce a vertical force between wheel 4 and the body which can be made some desired ratio of $W(C_G + T)$ and will increase R_{G4} and reduce R_{G3} .

The introduction of suspension springs makes the analysis more complicated in that applied forces will cause appreciable deflections and some form of computer based solution will be required.

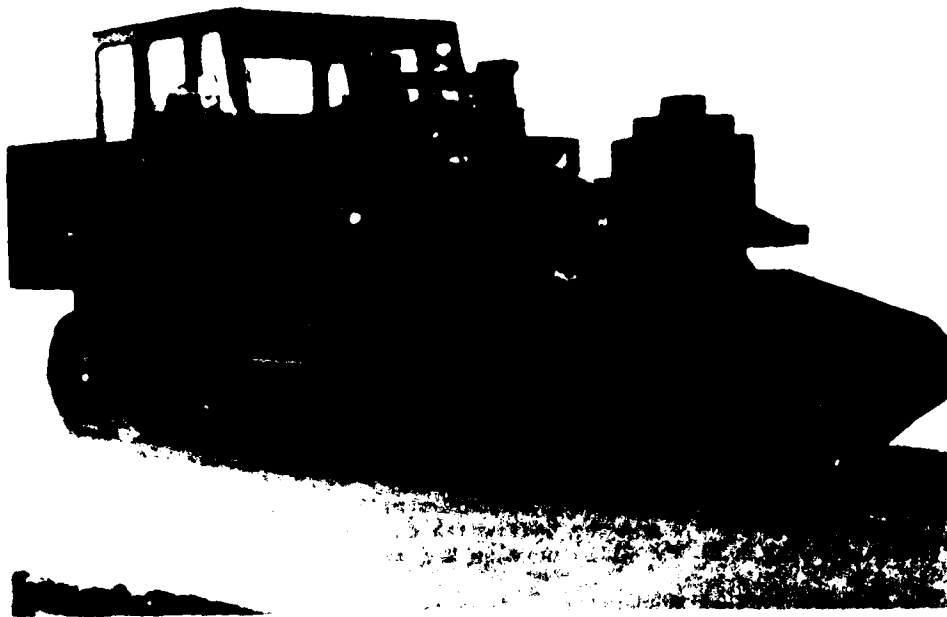


Fig 1 MVEE Mobile Tester with Track Rig

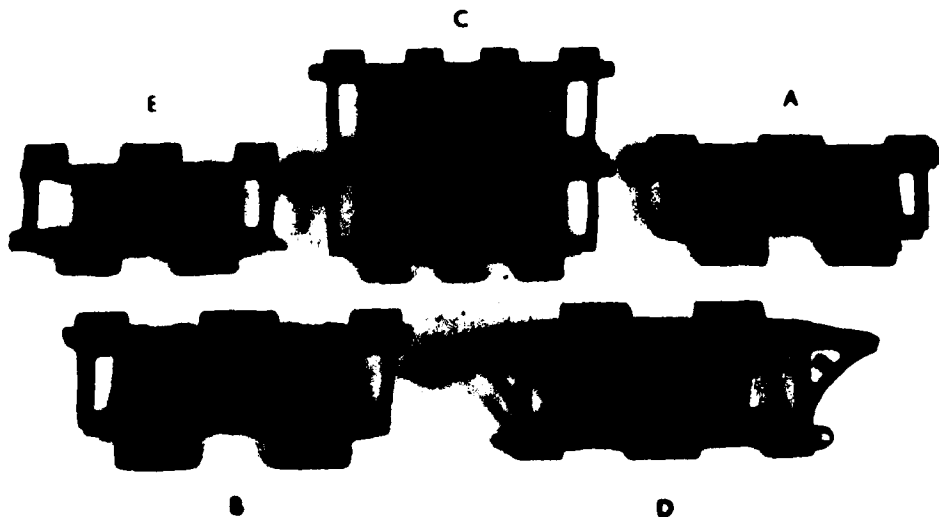
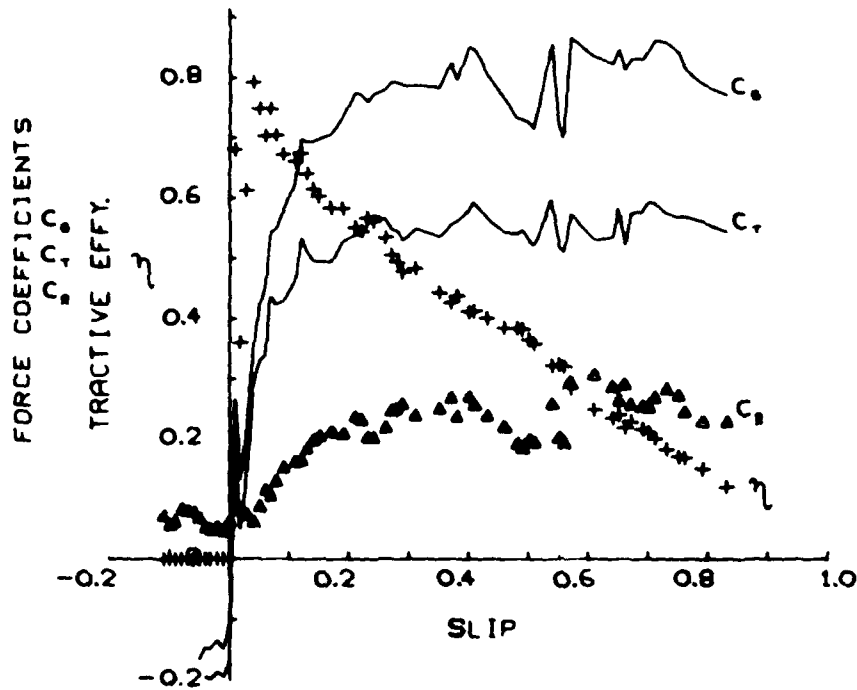
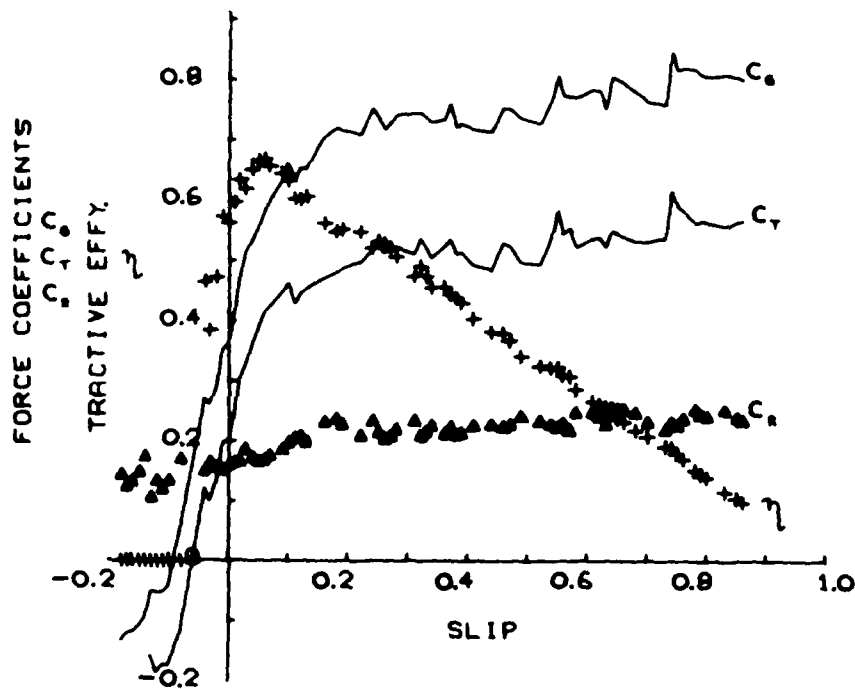


Fig 2 Track Links

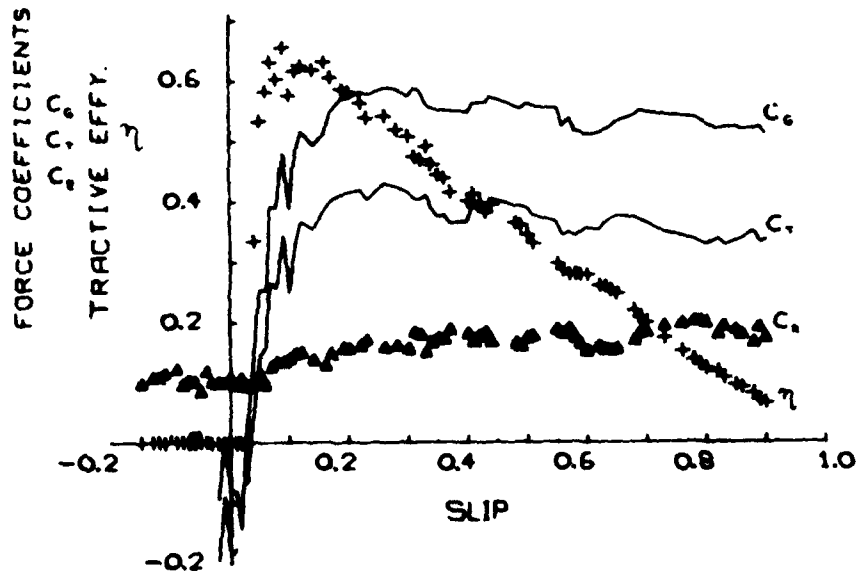


4 Wheels 0.61 m dia Track D

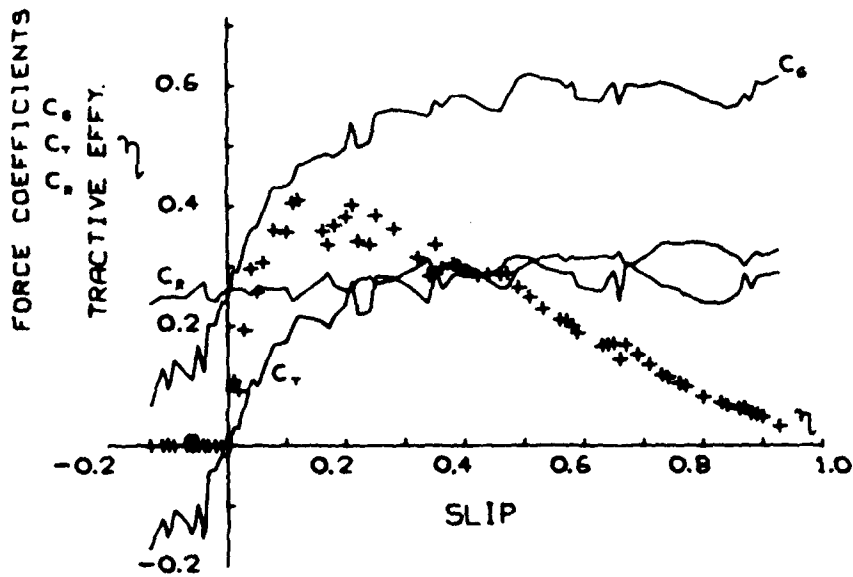


2 Wheels 0.61 m dia Track A

Fig 3 Typical Traction Curves Site A, 2 and 4 Wheel Configurations



8 Wheels 0.25 m dia Track A



2 Wheels 0.61 m dia Track A

Fig 4 Typical Traction Curves Site B, 2 and 8 Wheel Configurations

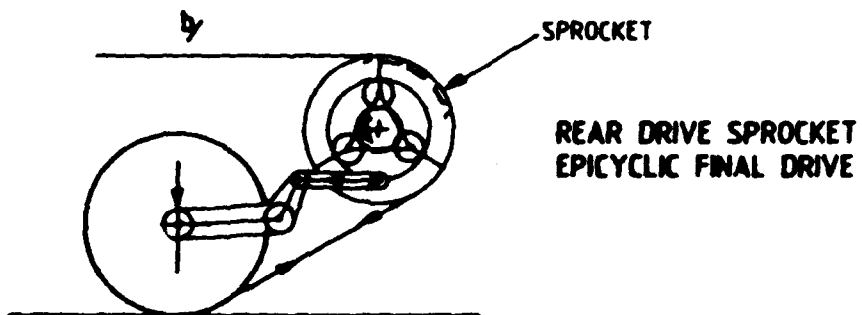
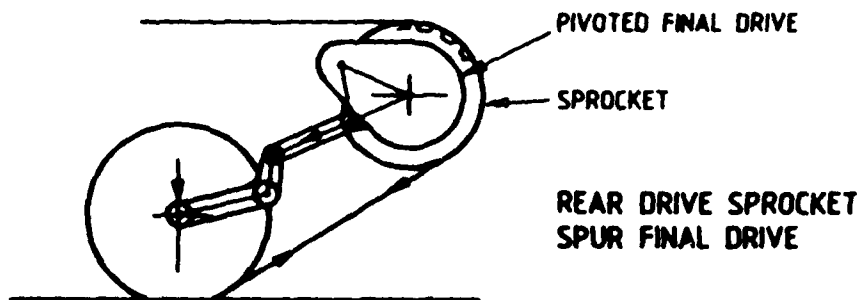
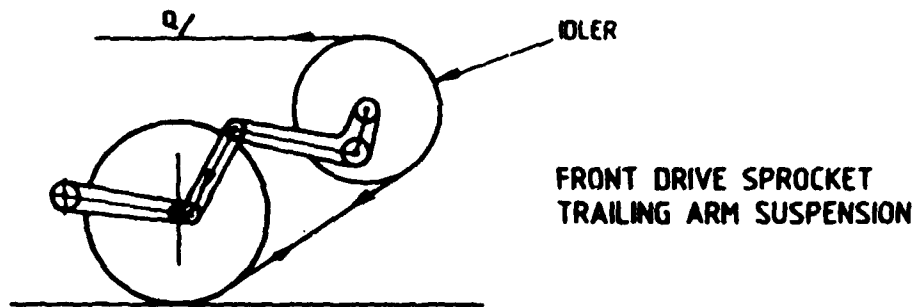
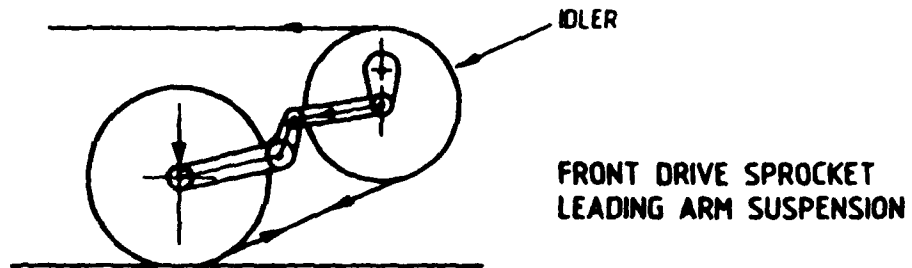


FIG 5 FORMS OF COMPENSATING MECHANISM FOR
APPLYING DOWNFORCE ON REAR WHEEL

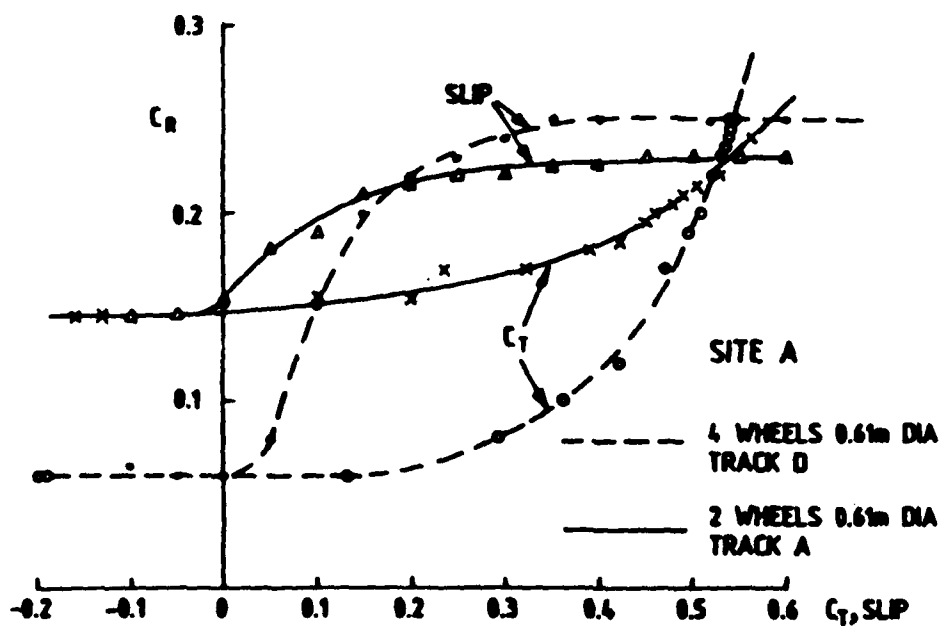
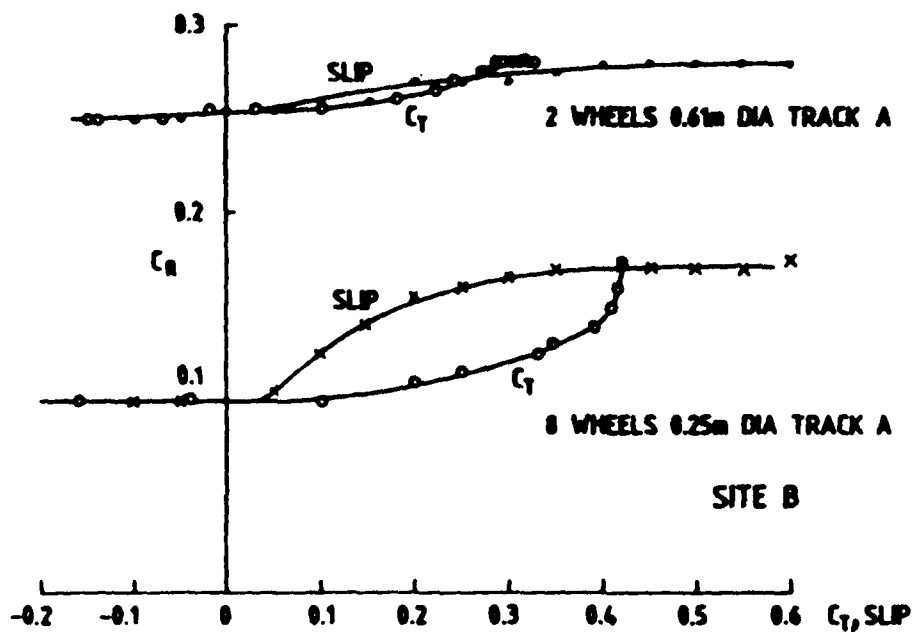


FIG 6
COEFFICIENT OF ROLLING RESISTANCE C_R PLOTTED AGAINST SLIP
& COEFFICIENT OF TRACTION C_T FOR 2 and 4 WHEEL CONFIGURATIONS
(SITE A) & 2 and 8 WHEEL CONFIGURATIONS (SITE B)

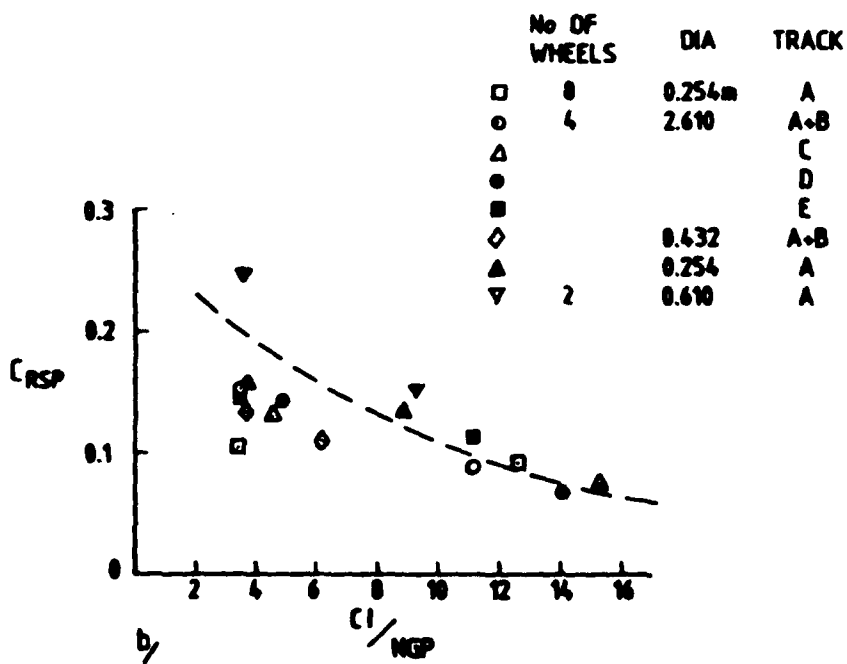
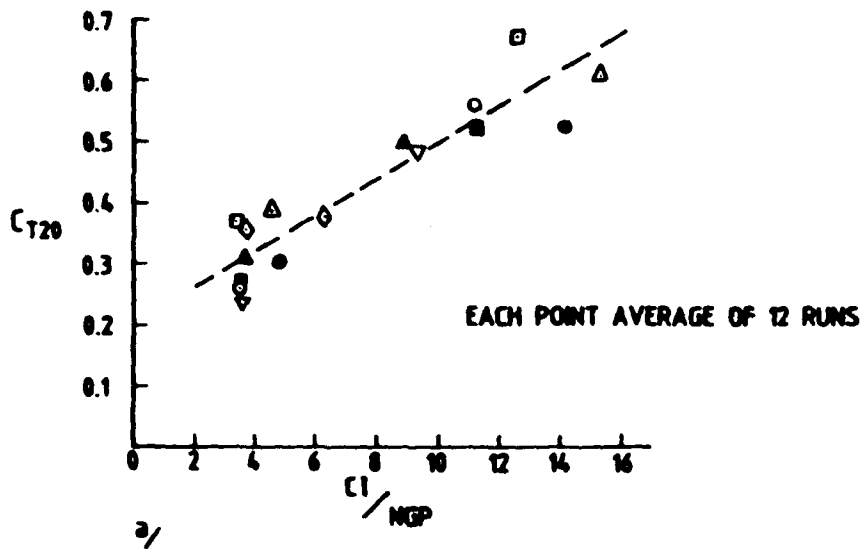


FIG 7
COEFFICIENT OF TRACTION AT 20% SLIP C_{T20} AND COEFFICIENT OF ROLLING RESISTANCE AT SELF PROPELLED POINT C_{RSP} PLOTTED AGAINST CONE INDEX OVER NOMINAL GROUND PRESSURE CI/NGP

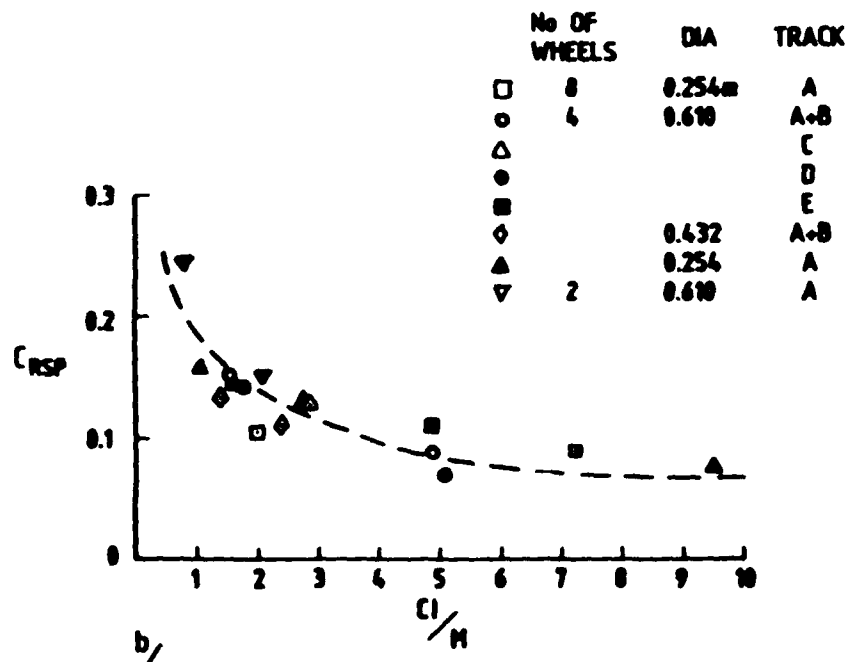
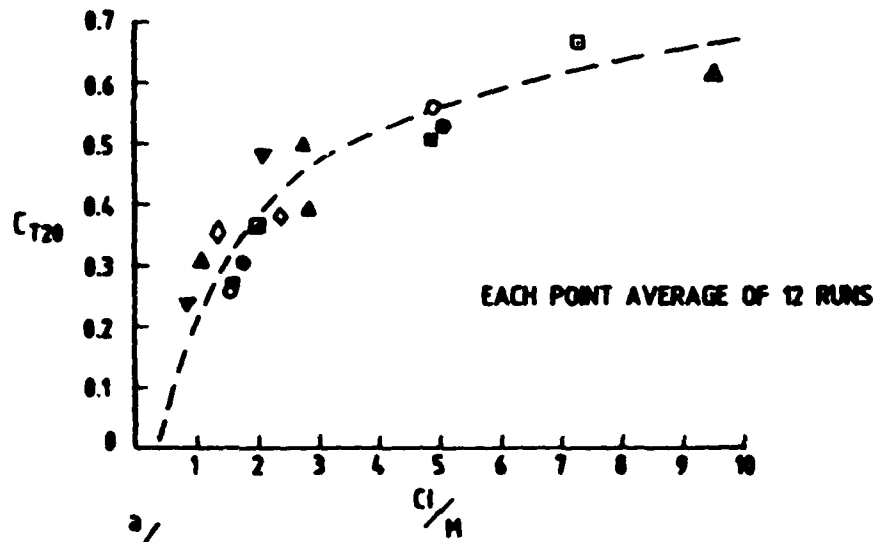


FIG 8
COEFFICIENT OF TRACTION AT 20% SLIP C_{T20} AND COEFFICIENT OF ROLLING RESISTANCE AT SELF PROPELLED POINT C_{RSP} PLOTTED AGAINST TRACK MOBILITY NUMBER C/M

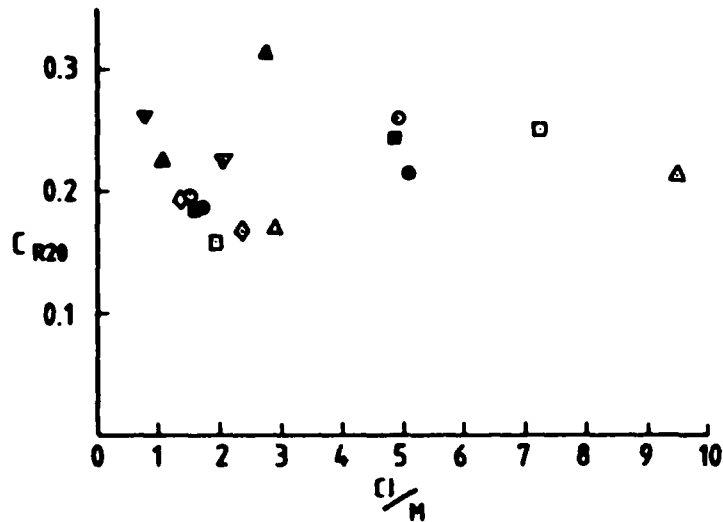


FIG 9 COEFFICIENT OF ROLLING RESISTANCE AT 20% SLIP C_{R20} PLOTTED AGAINST TRACK MOBILITY NUMBER C_l/H

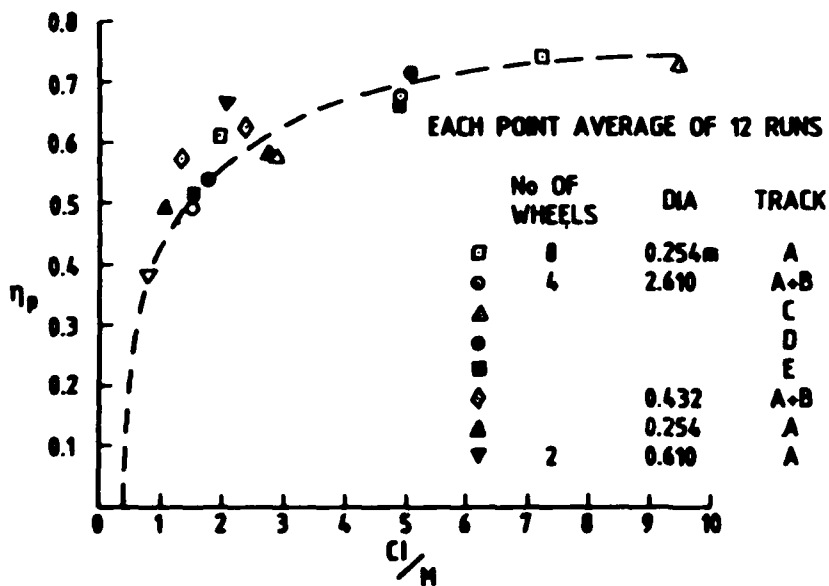


FIG 10 PEAK TRACTIVE EFFICIENCY η_p PLOTTED AGAINST TRACK MOBILITY NUMBER C_l/H

Die Abhängigkeit der Bodentragfähigkeit und der Zugkraft von der Abstandgrösse der Bodenplatten

A. Mierzwicki

Warsaw Technical University, Poland

1. Einführung

Bisher, in der theoretischen und experimentalen Arbeiten, die Abstandgrösse zwischen den Bodenplatten hat man nach dem Kriterium der maximalen Scherkräfte /der maximalen Haftkräfte/ bestimmt. Auf diese Weise wurde die Geometrie der Lückengliederkette bestimmt [1, 3]. Die Abstandgrösse, die 2 + 3 Breiten der einzelnen Bodenplatte beträgt, versichert grössere summarische Scherkraft P_H im Vergleich mit der traditionellen Raupenkette /ohne Abstände/. Der Zuwachs der Kraft P_H ist über den maximalen Bodenplattendruck beschränkt, der den Wert von 0,04 MPa nicht überschritten sollte [2]. Aus der eigenen Forschung des Autors [2] ergibt sich, dass der Senkungsanzeiger /Verhältnis der Vertikalsenkung zum horizontalen Schub in der selber Zeit/ für die Lückengliederkette im Vergleich mit der traditionellen Raupenkette 2 - 3 mal im Bereich der Drucke von 0,02 - 0,05 MPa grösser ist. Es verursacht den Zuwachs des Rollwiderstandes P_R , der über den entsprechenden Zuwachs des Haftkrafte nicht ausgeglichen ist. Als Ergebnis kriegt man die Minderung des Zugkrafte, die die Differenz zwischen der Haftkraft und dem Rollwiderstand ist.

Andere Weise der Bestimmung des Abstandes zwischen der Bodenplatten kann das Kriterium der maximalen Bodentragfähigkeit werden.

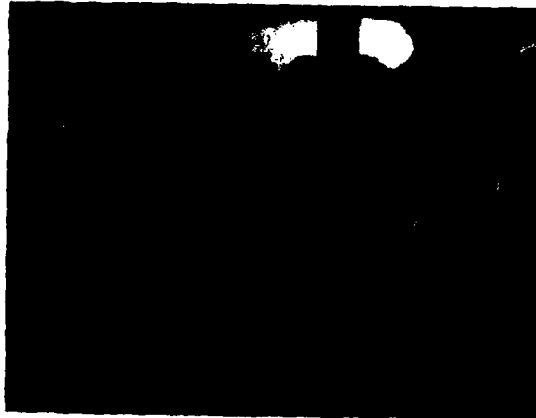
2. Die Abhängigkeit der Bodentragfähigkeit von der Abstandgrösse der Bodenplatten

Einfluss der Abstandgrösse zwischen den Bodenplatten der Raupenkette auf die Bodentragfähigkeit wurde experimental in den Modelluntersuchungen bestimmt. Früher wurde die Analyse des Senkungsprozesses des Bodenplattenpaares als das kleinste Fragment der Raupenkette durchgeführt. Die Analyse wurde auf der Basis der Aufnahmen, die das Senkungsprozess in den Grobsand gezeigt haben, getan. Der Fotoapparat, der für die Realisierung der Aufnahmen diente, war an dem Spannwerkzeug befestigt, an das selben Spannwerkzeug waren auch die Modelle der Bodenplatten eingespannt /Bild 1/. Es erlaubte auf den Erhalt des Bildes des Bodenkeiles /oder zwei Bodenkeile/ der sich unter dem senkenden Bodenpaar bildet /Bild 2/. Die Aufnahmen wurden für die Platten mit dem Sporn, denen Breite $l = 30$ mm und Höhe $h = 15$ mm waren, gemacht. Die Abstand S zwischen den Platten hat folgende werte angenommen: 0,6, 10, 15, 22 mm, was dem Verhältnis $s/l = 0, 0,2, 0,33, 0,5, 0,73$ entspricht.

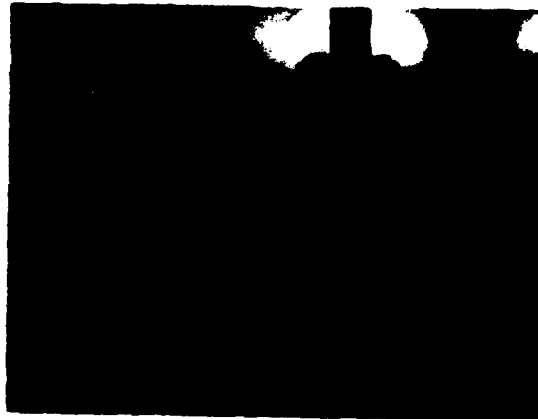


Bild 1. Der Prüfstand für die Fotoaufnahmen der Senkung des Bodenplattenpaares.

a



b



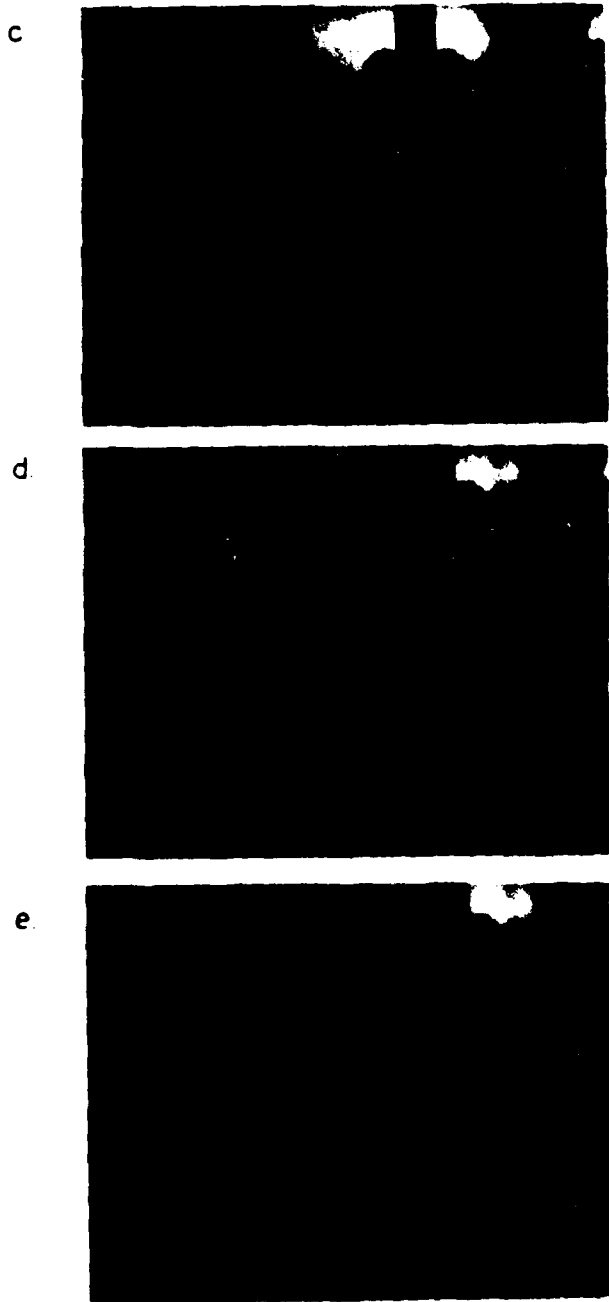


Bild 2. Die Bildung des Bodenkeiles unter dem senkendem Plattenpaar für: a/ $S = 0$, b/ $S = 0,2$ l, c/ $S = 0,33$ l, d/ $S = 0,5$ l, e/ $S = 0,73$ l.

Aus der Analyse treten folgende Folgerungen auf:

- 1/ Für die Abstandgrösse $S = 0 - 0,2$ l unter dem Plattenpaar entsteht ein gemeiner Bodenkeil. Änderung der Abstandgrösse in diesem Bereich soll auf die Bodentragfähigkeit unter der Raupenkette nicht beeinflussen.
 - 2/ Bei dem Abstand $S = 0,33$ l der Bodenkeil beginnt sich zu teilen. Man kann merken den Bodenausflusstrahl aus dem Bereich zwischen den Bodenplatten.
 - 3/ Bei dem Abstand $S = 0,5$ l der gemeine Bodenkeil besteht nur in vergehender Form. Es ergibt sich aus der Differenz zwischen der Ausflusstrahlgeschwindigkeit des Bodens aus dem Bereich zwischen den Bodenplatten und der Plattenumströmungsgeschwindigkeit des Bodens von der äusserlichen Seite.
 - 4/ Für den Abstand $S = 0,73$ l bilden sich zwei separate Bodenkeile unter jeder Bodenplatte was bedeutet, dass Einwirkung jeder Platte auf den Boden unabhängig ist.
- Die Messungen der Bodentragfähigkeit unter der Modellen der Raupenketten wurden auf dem Prüfstand, der auf dem Bild 3 gezeigt ist, getan.



Bild 3. Der Prüfstand für die Bodentragfähigkeitmessung unter der Raupenkette.

Die Bodentragfähigkeit war in der Funktion der Senkung aufgezeichnet.

Die Länge der getesteten Raupenkettensmodelle /Bild 4/ hat

man, beginnend vom Plattenpaar, über die Zugabe der Bodenplatten vergrössert.

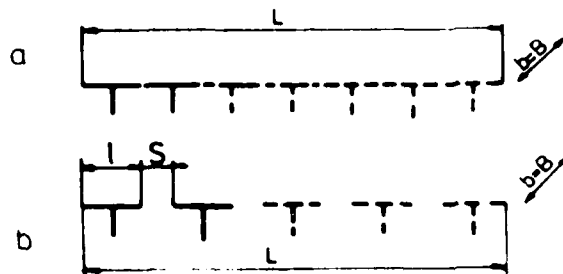


Bild 4. Das Schema der Raupenkettenmodelle: a/ die traditionelle Raupenkette /S = 0/, b/ die Raupenkette mit dem Abstand S.

Die Grösse der Bodenplatten /Breite l und Höhe h/ und die Abstände S wurden wie in der Analyse der Senkung angenommen. Die Forschungsergebnisse zeigt das Diagramm auf dem Bild 5. Auf der Basis der ergebnen Resultate kann man feststellen:

- 1/ Die maximale Tragfähigkeit tritt für die traditionelle Raupenkette /S = 0/ und die Raupenkette mit dem Abstand S = 0,2 l auf. Es folgt aus dem Fehlen des Bodenausflusststrahles zwischen dem Plattenpaar bei dem Abstand S ≤ 0,2 l. Die Einwirkung dieser Ketten kann man als gleichbedeutend der Platte BxL behandeln.
- 2/ Der Abstandzuwachs über S = 0,2 l verursacht die Minderung des Bodentragfähigkeit - wobei kann man zwei Bereiche unterscheiden:
 - für 0,2 l < S ≤ 0,5 l /wenn der Bodenkeil in vergehender Form besteht/ die Minderung der Tragfähigkeit beträgt ~ 3% für die Kette mit dem Abstand S = 0,33 l und ~ 4% für die Kette mit dem Abstand S = 0,5 l.
 - für S > 0,5 l die Bodentragfähigkeit nimmt ~ 30% ab. Es ist verursacht durch die unabhängige Einwirkung jeder Bodenplatte.

Der Rollwiderstand, der über die Gleichung [3] beschrieben ist, hängt von der Senkung ab.

$$P_R = \left[\frac{l \cdot k}{n+1} \right] z^{n+1}$$

- wo: l - Breite der Bodenplatte,
 k - Faktor der vertikalen Bodenverformbarkeit,
 n - Exponent, der die Eigenschaften und Struktur des Bodens bezeichnet,
 z - Senkung.

Ergebene Resultate der Bodentragfähigkeit zeigen, dass der Abstandzuwachs über S = 0,2 l /je mehr über S = 0,5 l/ bei der Konstanten vertikalen Belastung grössere Senkung ebenso

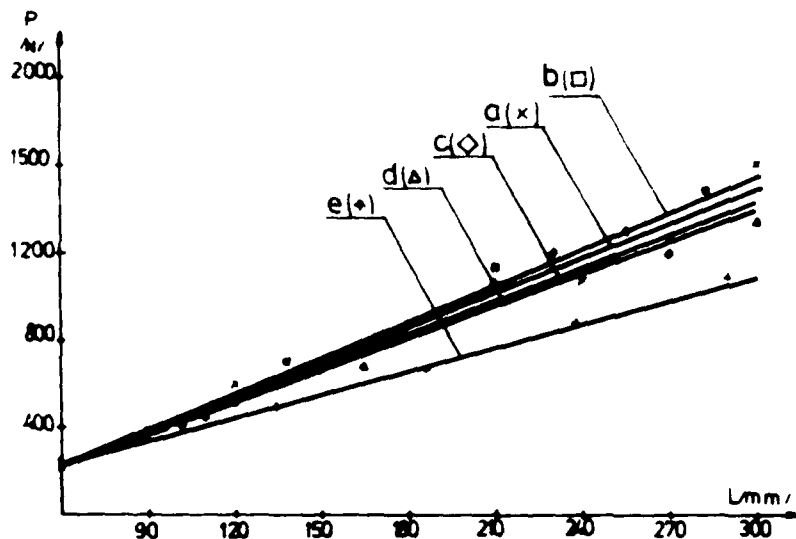


Bild 5. Die Bodentragfähigkeit unter der Raupenkettensmodelle bei der Senkung $z = 0,25$ l: a/ die traditionelle Raupenkette mit $S = 0$, b/ die Raupenkette mit dem Abstand $S = 0,2$ l, c/ $S = 0,33$ l, d/ $S = 0,5$ l, e/ $S = 0,73$ l.

grösser Rollwiderstand verursachen soll.

3. Die Abhängigkeit des Zugkraftes von der Abstandgrösse der Bodenplatten

Die Abhängigkeit des Zugkraftes von der Abstandgrösse der Bodenplatten wurde auch in den Modelluntersuchungen bestimmt. Die Untersuchungen hat man für 3 Raupenkettensmodelle mit dem Abstand $S = 0, 0,4$ l, $1,12$ l durchgeführt. Die Spalten wurden so angepasst, dass die den 3 unterschiedlichen Bereichen der Bodentragfähigkeit /siehe Kapitel 2/ entsprochen haben. Angenommene Abstände zwischen den Platten der Raupenkette haben keinen wesentlichen Einfluss auf die Haftkraft. Es ergibt sich daraus, dass bei diesen Spalten antstehen noch keine Bedingungen für die Entstehung der Bodenkeile vor jeder Bodenplatte. Die Scherfläche des Bodens ist tangential zu den Spitzen der Spornen - ähnlich wie bei der traditionellen Raupenkette [3]. Im Resultat, über die Zugkraftgrösse, entscheidet der Rollwiderstand.

Die Zugkraftmessungen wurden auf dem Prüfstand^{1/}, der auf dem

^{1/} Genaue Beschreibung des Prüfstandes befindet sich im Artikel "Traction Investigation of a Track Vehicle" veröffentlicht in Proceedings of the 7 th International Conference ISTVS in Calgary 1981.

Bild 6 gezeigt ist, durchgeführt.

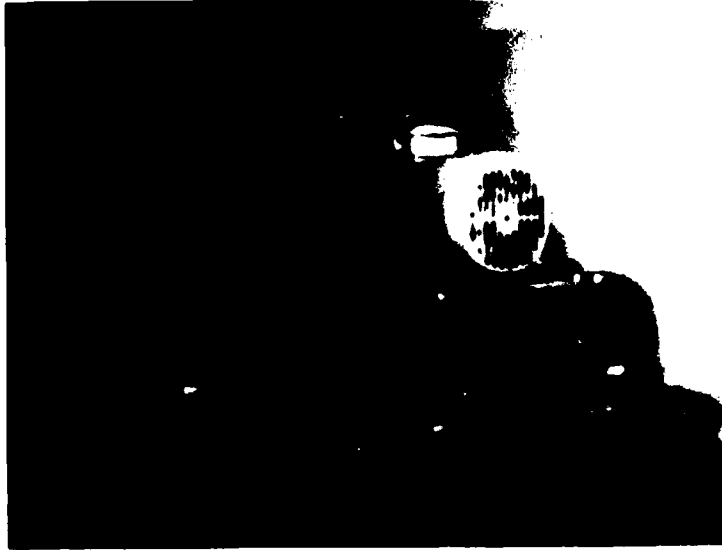


Bild 6. Der Prüfstand für die Zugkraft messung.

In den Forschungen hat man die konstante Last des Schleppermodells angenommen. Es verursachte, dass bei der selben Grösse der Bodenplatten und bei der konstanten aktiven Länge der Raupenkette die spezifische Drücke mit dem Abstandvergrößerung zu genommen haben. Für geprüfte Raupenketten der spezifische Druck p hatte folgende Werte:

- traditionelle Raupenkette / $S = 0$ / - $p = 0,033$ MPa,
- Raupenkette mit dem Abstand $S = 0,4$ l - $p = 0,042$ MPa,
- Raupenkette mit dem Abstand $S = 1,12$ l - $p = 0,07$ MPa.

Die Untersuchungsergebnisse wurden auf dem Diagramm /Bild 7/ vorgestellt.

Ergebene Resultate zeigen, dass der Zuwachs des Abstandes zwischen der Bodenplatten der Raupenkette verursacht die Minderung der Zugkraft. Es ergibt sich aus der Vergrößerung des Rollwiderstandes, der über die grössere Senkung verursacht ist. Der Zuwachs des Abstandes über $S = 0,5$ l, wenn die Einwirkung der Bodenplatten unabhängig ist, verursacht realativ grössere Zugkraftminderung als bei der Spalte $S \leq 0,5$ l.

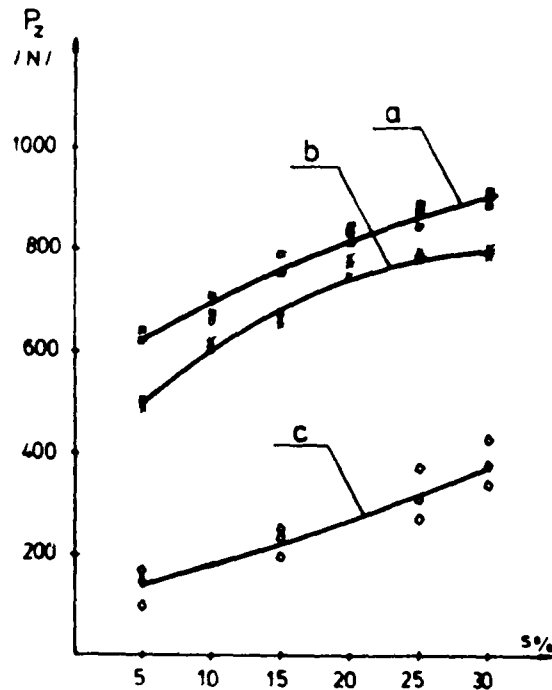


Bild 7. Die Abhängigkeit des Zugkraftes vom Abstand zwischen den Bodenplatten in der Raupenkette: a/ traditionelle Raupenkette /S = 0/, b/ Raupenkette mit dem Abstand S = 0,4 l, c/ Raupenkette mit dem Abstand S = 1,12 l.

4. Schlussfolgerungen

Ergebene Resultate betreffen die Modellbedingungen bezüglich der Versuchsmethode so wie des Bodens /Grobsand: Kohesion $k = 0$, Innenreibungswinkel $\varphi = 28^\circ$, Feuchtigkeit $w = 2\%$. Doch, die Analyse der Senkung der Raupenkette/der Bodenplatten/ in Abhängigkeit von dem Abstand zeigt deutlich, dass der Zuwachs der Spalte die Vergrößerung des Rollwiderstandes und nächst die Zugkraftminderung verursacht.

Schrifttum:

1. Bekker M.G. - Off the Road Locomotion; the University of Michigan Press, Ann Arbor 1956.
2. Mierzwicki A. - Shape and Spacing Optimization of the Track Elements in Crawler Undercarriage with Regard for Soil Bearing Capacity; Proceedings of the Conference Terrain Vehicle Systems, Wisła 1979.
3. Sołtyński - Mechanika układu Pojazd - Teren, Wydawnictwo MCN, Warszawa 1966.

THE DEPENDENCE OF SOIL BEARING CAPACITY AND DRAWBAR PULL ON THE SPACING BETWEEN TRACK PLATES

A. MIERZWICKI

WARSAW TECHNICAL UNIVERSITY, POLAND

(Translated by K.G. Hammond, NIAE, Silsoe, England)

Starting point for this investigation were the results of the drawbar pull tests which were published in Proceedings of the ISTVS Conference in Vienna - 1978 and in Calgary - 1981. Up to now in definition of the spacing between track elements the criterion of maximum shearing forces was applied.

In this work was applied the criterion of maximum soil bearing capacity under the track independence on the spacing between track elements.

In the paper the results of the model investigation were presented.

1. Introduction

The spacing between track plates has hitherto been defined in theoretical and experimental work in terms of the criterion of maximum shearing stresses (maximum thrust). The geometry of the spaced link track was defined in this way^(1,3). Spacing equivalent to 2-3 widths of a single track plate ensures a larger overall shearing stress P_H by comparison with the traditional track (without spacing). The increase in stress P_H is limited by the maximum track plate pressure, which should not exceed 0.04 MPa⁽²⁾. The author's own research⁽²⁾ has shown that the sinkage index (the relationship between vertical sinkage and horizontal thrust over the same period) for the spaced link track is 2-3 times greater than for the traditional track in the pressure range 0.02-0.05 MPa. Increased rolling resistance P_R is caused, which is not compensated for by the corresponding increase in thrust. As a result, a reduction in drawbar pull equivalent to the difference between thrust and rolling resistance occurs.

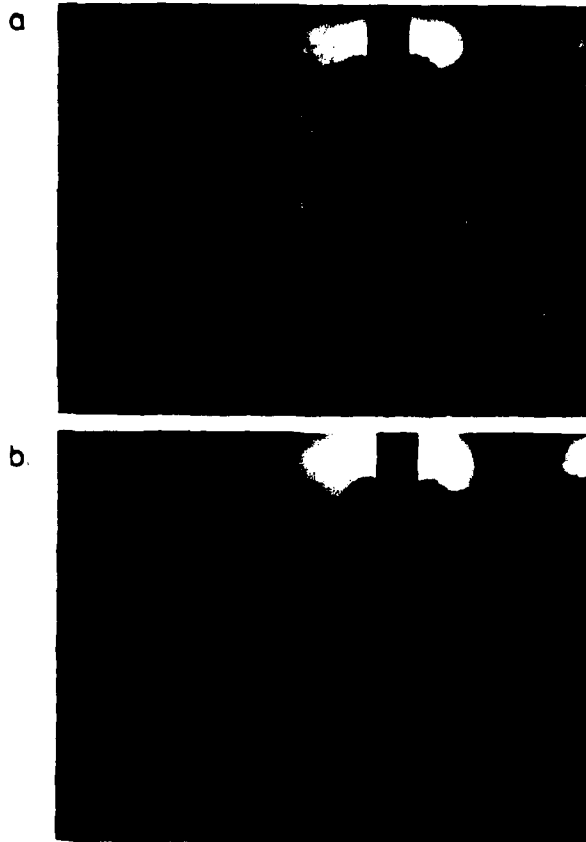
Another method of determining the spacing between the track plates is in terms of the criterion of maximum soil bearing capacity

2. The dependence of soil bearing capacity on the spacing of the track plates

The effect of the spacing between the plates of a track on soil bearing capacity was determined experimentally in model-based research. The process of sinkage of a pair of track plates as the smallest section of the track had already been analysed. This was carried out on the basis of photographs showing the sinkage process in coarse sand. The camera used was mounted on a clamp, to which models of the track plates were also fastened (Fig. 1). This enabled pictures to be obtained of the wedge-shaped groove (or two grooves) in the soil formed beneath the pair of track plates as they sank into the soil (Fig. 2). The photographs were taken for track plates, with a grouser, having a width $l = 30$ mm and a height $h = 15$ mm. The spacing S between the plates had the following values: 0, 6, 10, 15 and 22 mm, corresponding to S/l ratios of 0, 0.2, 0.33, 0.5 and 0.73.



Fig. 1 Test rig for photographs of sinkage of track plates



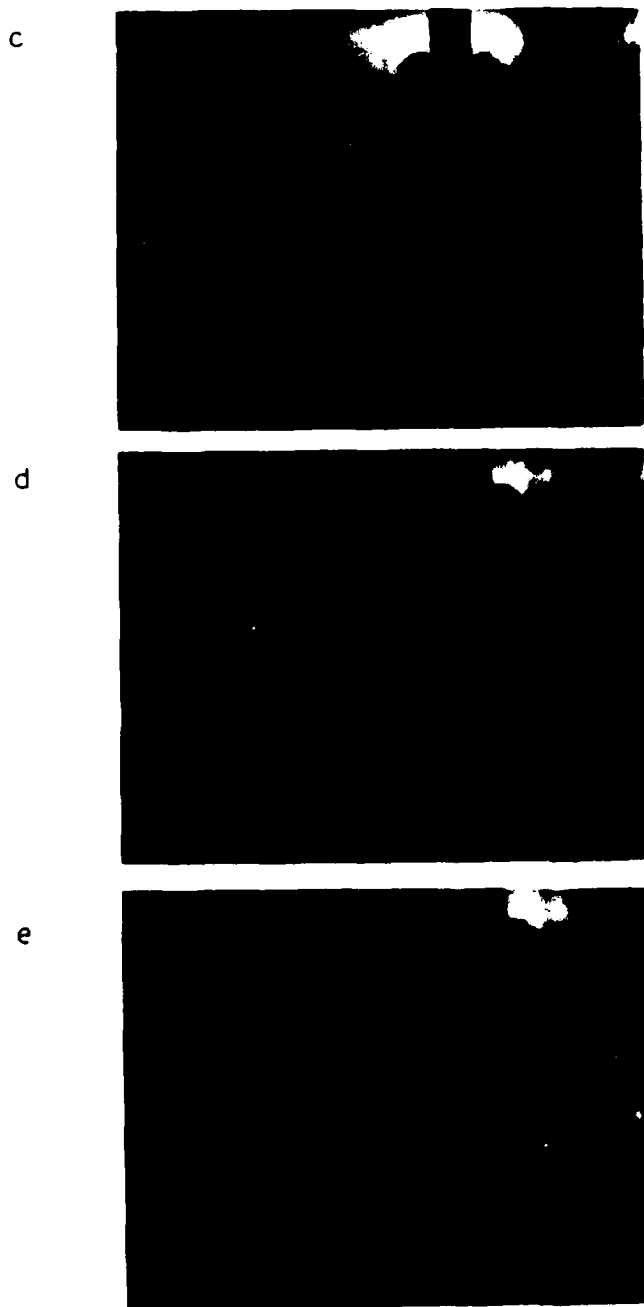


Fig. 2 Formation of wedge-shaped groove beneath the sinking pair of track plates for: (a) $S = 0$, (b) $S = 0.2$ l, (c) $S = 0.33$ l, (d) $S = 0.51$, (e) $S = 0.73$ l.

An analysis produced the following conclusions:

- (1) A common wedge-shaped groove is formed beneath the pair of track plates at a spacing $S = 0.02 l$. Alteration of the spacing within this range should not affect the soil bearing capacity beneath the track.
- (2) The wedge-shaped groove begins to divide at a spacing $S = 0.33 l$. The outward flow of the soil from the area between the track plates can be detected.
- (3) The common wedge-shaped groove exists only in vestigial form at a spacing $S = 0.5 l$. This arises from the difference between the outward flow speed of the soil between the track plates and the track plate by-pass speed of the soil from the external side.
- (4) Two separate wedge-shaped grooves beneath each track plate at a spacing $S = 0.73 l$, indicating that the action of each plate on the ground is independent.

Measurements of soil bearing capacity under models of tracks were carried out on the test rig shown in Fig. 3.

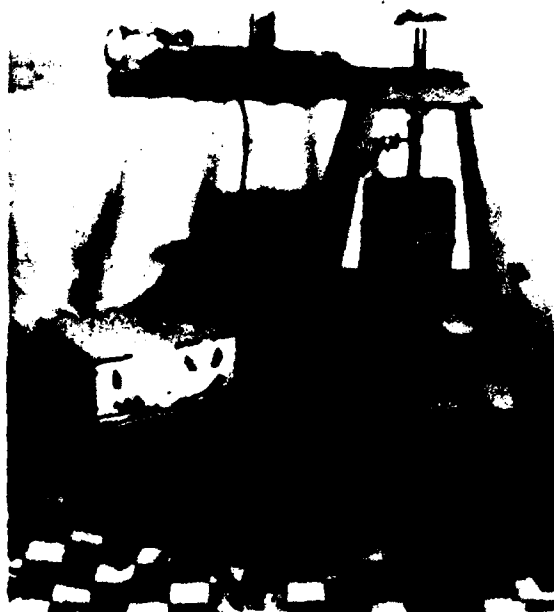


Fig. 3 Test rig for measuring soil bearing capacity under the track

Soil bearing capacity was plotted as a function of sinkage.

The length of the track model tested (Fig. 4) was increased by the addition of further track plates after the pair under consideration.

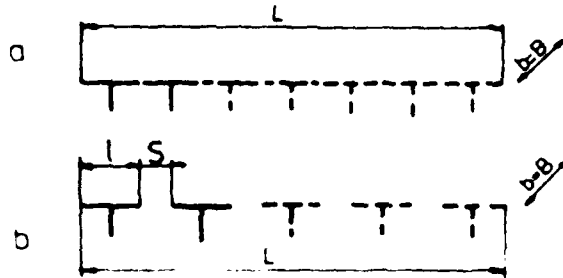


Fig. 4 Diagram of the track model: (a) traditional track ($S = 0$), (b) track with spacing S .

The size of the track plates (width l and height h) and the spacing S were assumed to be the same as for the analysis of sinkage. Research results are shown in the graph in Fig. 5. From these it can be established that:

- (1) Maximum bearing capacity is experienced with the traditional track ($S = 0$) and with a track at a spacing $S = 0.2 l$. This follows from the absence of soil outward flow between the track plates at a spacing $S \leq 0.2 l$. The action of these tracks can be treated as equivalent to the element $B \times L$.
- (2) A spacing increase over $S = 0.2 l$ reduces soil bearing capacity. Two ranges can be distinguished:
 - for $0.2 l < S \leq 0.5 l$ (when the wedge-shaped groove exists in vestigial form) the reduction in bearing capacity is equivalent to -3% for a track at a spacing $S = 0.5 l$.
 - for $S > 0.5 l$ the soil bearing capacity is reduced by -30%. This is caused by the independent action of each track element.

Rolling resistance, which is described by the equation (3), depends on sinkage.

$$P_R = \left[\frac{1}{n+1} k \right] z^{n+1}$$

where l - width of track element

k - factor of vertical soil plasticity

n - exponent denoting the characteristics and structure of the soil

z - sinkage

The results obtained for soil bearing capacity show that a spacing increase above $S = 0.2$ l (especially above $S = 0.5$ l) should cause greater sinkage as well as greater rolling resistance at a constant vertical loading.

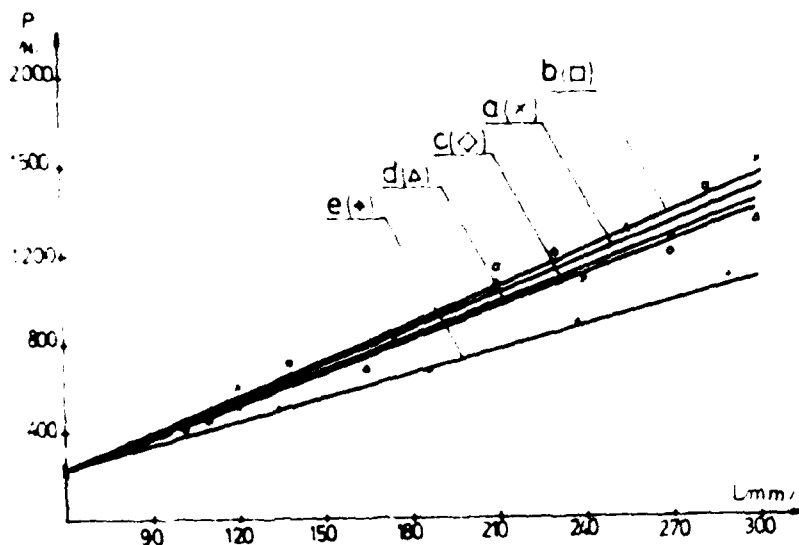


Fig. 5 Soil bearing capacity under track models for sinkage $z = 0.25$ l: a) traditional track, $s = 0$, b) track at spacing $S = 0.2$ l, c) $S = 0.33$ l, d) $S = 0.5$ l, e) $S = 0.73$ l

1. The dependence of drawbar pull on the spacing of the track plates

The dependence of drawbar pull on the spacing of the track plates was also determined in model-based research. Investigations were carried out for three tracks at spacings $S = 0, 0.4$ l and 1.12 l. Spacing was adjusted to correspond to the three different ranges of soil bearing capacity (see Section 2). The spacings adopted between the elements of the track have no essential effect on thrust. It follows that, given this spacing, conditions are not produced for the formation of wedge-shaped grooves before each track element. The plane of shear of the soil is tangential to the peaks of the grousers, much as is the case with the traditional track (3). As a result, drawbar pull is decided by rolling resistance. Measurements of drawbar pull were carried out on the test rig* shown in Fig. 6

*A precise description of the testing is given in "Traction Investigation of a Track Vehicle", Proceedings of the 7th ISTVS Conference, Calgary, 1981.

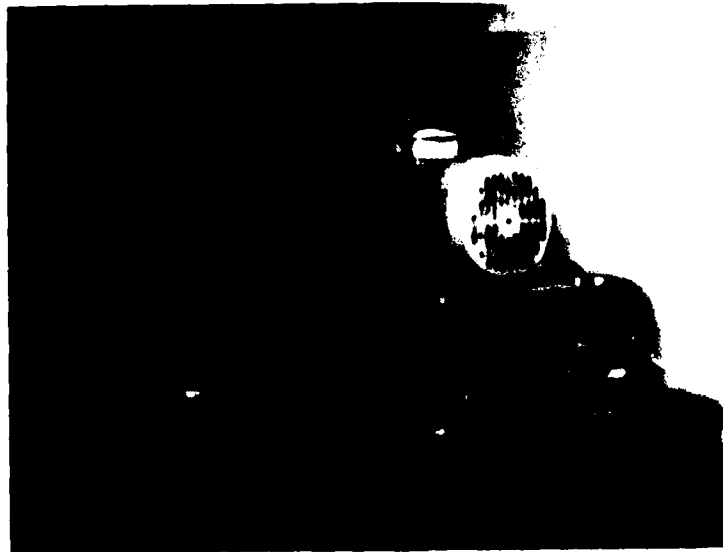


Fig. 6 Test rig for measuring drawbar pull

The weight of the model tractor was assumed constant in the research. Consequently, specific pressure rose with increased spacing for track plates of the same size and at constant effective length of track. The specific pressure p had the following values for the tracks tested:

- traditional track ($S = 0$) : $p = 0.033$ MPa
- track at spacing $S = 0.4$ l : $p = 0.042$ MPa
- track at spacing $S = 1.12$ l : $p = 0.07$ MPa

The results obtained show that the increased spacing between track plates causes a reduction in drawbar pull. This results from the increased rolling resistance caused by greater sinkage. Increased spacing over $S = 0.5$ l, when the action of the track plates is independent, causes relatively greater drawbar pull reduction than for the spacing $S \leq 0.5$ l.

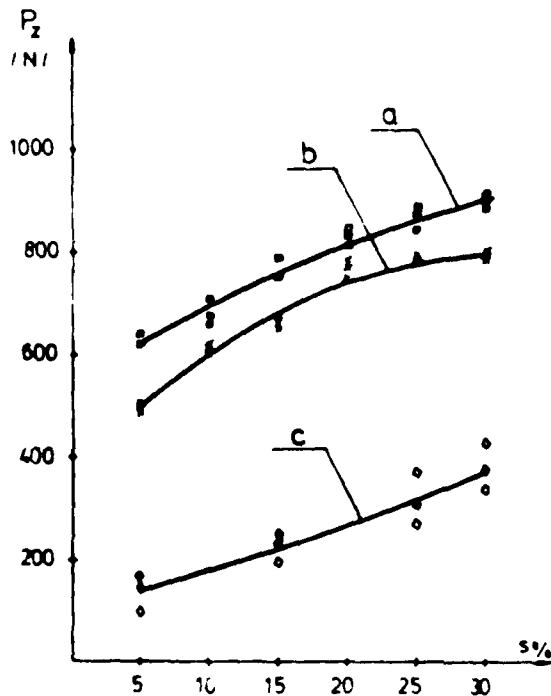


Fig. 7 The dependence of drawbar pull on spacing between track plates: a) traditional track ($S = 0$), b) track at a spacing $S = 0.4$ l, c) track at a spacing $S = 1.12$ l.

4. Conclusions

The results obtained agree well with the model conditions relating both to the research method and the soil (coarse sand: cohesion $k = 0$, internal angle of friction $\rho = 28^\circ$, moisture content $w = 2\%$). Analysis of the sinkage of the track (the track plates) dependent on spacing shows clearly that increased spacing causes an increase in rolling resistance and, consequently, a reduction in drawbar pull.

References

1. BECKER, M.G. Off the Road Locomotion; the University of Michigan Press, Ann Arbor 1956
2. MIERZWIŃSKI, A. Shape and Spacing Optimisation of the Track Elements in Crawler Undercarriage with Regard for Soil Bearing Capacity; Proceedings of the Conference Terrain Vehicle Systems, Wisla 1979
3. SOLTYSKI Mechanika układu Pojazd - Teren, Wydawnictwo MON, Warszawa 1966

The Dynamic Interaction Between Track And Soil

P. Parringer

Industrieanlagen-Betriebsgesellschaft m.b.H., 8012 Ottobrunn/Germany

Abstract

The knowledge of the dynamic interaction between track and soil is important to analyse high speed vehicles with flexible track.

This paper describes a possible method for the measurement of this interaction. Force- and displacement-sensors are fixed in and on the track to measure

- longitudinal-, transversal- and normal-load at one track-shoe,
- sinkeage of this track-shoe and the
- longitudinal- and transversal slip of this track shoe,

Furthermore soil parameters are defined and the dynamic behaviour of the soil is calculated and expressed in terms of these soil parameters. These parameters are one input to vehicle simulation models. Combined with well established parameters our newly defined parameters may serve as a basis to describe the mechanics of soil.

One of the main advantages of the proposed method is the indenpendency of measurement steps and analysis steps.

Several examples have been investigated and encouraging results have been obtained. Although the proposed method is purely a rheological approach, we feel that it may be a powerful tool to enhance our understanding of soil dynamics.

AD-P004 274

1. Introduction

There is one wellknown and improved method to describe the static interaction between track and soil defined by Bekker about 25 years ago [2,3,4]. Meanwhile, there were great efforts of innovation in the field of electronics especially in

- measuring and data transfer technics and
- computer technics.

This is one main reason for the existing wide gap between analytical background including the constitutive laws and the possibilities of todays computer technics. Efforts to close this gap have been made for example in [1,10,11].

At first view finite element methods would be a proper way to calculate the interaction between track and soil, but until now there are many restricting points. The most important two restrictions are first the unknown constitutive laws for soil with terrain cover and second the three dimensional elastic-plastic calculation of the dynamic interaction between track and soil is at present - practically speaking - nearly impossible.

For these reasons about five years ago the IABG decided to

- measure the dynamic interaction between track and soil in all practical important operating conditions, soils and soil conditions, and to try to
- find a relatively easy approach to describe this dynamic interaction (the system used today is shown in Figure 1).

The first step of this way is published in [5,6,7] and shown in this report.

2. Measuring equipment

The measuring equipment for the KPz-Leopard 1 and how it must be handled is shown in Figures 2 to 6. The most important restrictions for the choice of usable sensors were the absence of a power source on the track and the terrain cover.

For this reason optical sensors and sensors which need high power are impractical.

The chosen sensors for sinkeage and slip-measurements are simple mechanical systems with all disadvantages resulting from this fact. The moveable parts of these sensors are very light to prevent them from damage at high speed (test speed without damage was 30 km/h for the slip sensor and 60 km/h for the sinkeage sensor). It should be mentioned, that the accuracy for the slip measurement is very high because the slip can be measured directly. The load cell [6,8] shown in Figure 2, works quite well, has exactly the size of a track block with rubber pad and is able to withstand forces up to 100 kN in the three measuring directions (normal, longitudinal and transversal). Like the telemetry-transmitter and the displacement sensors the two load cells in one track block are waterprotected.

The smallest equipment to measure track soil interaction consists of one load cell, one sinkeage sensor und one telemetric unit with at least two channels (shown in Figure 6 for the right track). For the analysis of the interaction between a turning vehicle and soil, an equipment like the one shown in Figure 6 may be the easiest to work with. To get more information at the same time the newest measurements are made with two load-cells, sinkeage and slip sensors on one track within a distance of about two meters and a simpler equipment on the other track.

3. Test results

Typical filtered (lowpass RC-filter 24 dB, 10 Hz) test results are presented in Figures 7-10. The measured ground pressure and sinkeage distribution in Figure 7 shows that the pressure distribution is not uniformly and the first and last peak is relatively small (track pull forces at the outer road wheels). Because of the roughness of terrain the sinkeage needs to be calibrated as shown in Figure 7. Very important is the shown delay Δm of the sinkeage. This delay is one of the reasons for the larger delay of traction (Δw) in Figure 8 (pull is here negativ).

The second reason for this is the pull-slip relationship and the lack of normal load between the road wheels. The traction can only be built up, if there is a normal load and must be built newly for every road wheel.

This is important to show that in this case the traction-slip relationship is opposite to some theories, not much better than that of a wheeled vehicle with the same number of driven wheels.

The lateral forces in Figures 9 and 10, where the soil is very hard, show similar behaviour. The soil for the measurement substantiated in Figures 7 and 8 was not as hard as it might appear. A proof for this is that the trace in the grassland had a depth of about 50 mm.

Some further short comments to the turns in Figure 9 and 10 should be made:

Longitudinal load: The outer track was driven and the inner was broken. Because of motion resistance the sum of braking forces along the contact length of inner track is much smaller than the sum of towing forces at the outer track.

Normal load: The sum of normal load along contact length is, because of centrifugal forces, at the outer track higher than at the inner track. For the outer track (Figure 10) the maximum of normal load is at the rear of the vehicle, but it is obvious that at the last road wheel there can't be measured a normal load because of the pull in the track. The opposite effect is watched at the inner track (Figure 9). Here the first roadwheel shows no normal load.

Lateral load: A part of the sum of lateral load will be balanced by centrifugal forces (easy to see at Figure 10). The change of the direction of lateral load takes place approximately at the third road wheel (of seven road wheels).

Of course these test results, have a wide range of utilization. When checking the relationships between normal load, sinkeage, motion resistance, tractive effort and drawbar pull the user has to consider that the measured values are valid only at the position where the sensors are located and that in addition to the inhomogeneity of the soil the roughness of the terrain has a great influence to the measured forces (the load cell is fixed in one track block which is one of many track-blocks in a line coupled by very stiff rubber bearings).

4. Evaluation of dynamic soil-parameters

- The method for the calculation of so-called dynamic soil parameters (spring rate C_B and damping D_B of Figure 1) is shown in Figure 11. For the used test example the normal load F_z was calculated by an inverse function for $C_B = 0.5 \text{ kN/mm}$, $D_B = 0.03 \text{ kNs/mm}$ and the curve of sinkeage Z (Figure 11). Like the results of measurements the test values are in the kind of about 300 digital values along the contact length of track-soil interface. With a simple linear equation with three unknowns (equation 1 in Figure 11) the first results C_B , D_B and $C_B Z_p$ will be calculated as a function of longitudinal displacement.

As a function of these results the elastic and plastic soil deformation will be calculated with formulas 2 and 3 of Figure 11. If as usual the plastic soil deformation Z_p is not constant there is a need for one or more iteration -steps which cannot be shown, like the more complicated calculation with friction R_B , in this short overview. There are two reasons for the neglect of a constant coulombian friction R_B in the practical calculation: First it's impossible to measure a step-function in normal direction and second there are numerical instabilities in the results if there are two kinds of friction or damping in expanded equation 1.

The results of the test example are stable if all three points of detail A are within the steady state of the F_z and z -curve. The elastic-plastic soil deformation - normal load functions in Figure 12 are trivial but shows well the structure of this useful second illustration of soil behaviour.

For the real measured example of soft soil in Figure 13 the corresponding Figure 14 has the following meanings:

- The first picture (normal load above sinkeage) is only another picture of the measured results.
- In the next two picture the measured sinkeage is at every load point divided in plastic and elastic soil deformation.
- The area under the curve in the second picture is the energy which is needed to deform the soil under one pad. The motion resistance is a function of this energy.
- The energy-loss in the soil corresponding to the damping D_B is the area within the curves of the third picture and the slope of this curves shows the elastic soil stiffness (spring rate C_B). In theory these curves are elliptical (see Figure 12).

Without the first peak there are no great differences in soil stiffness (spring rate C_g is practical constant) of soft soil (Figures 13 and 14).

But in the harder soil presented in Figure 15 there is a great hardening effect from one peak to the next (test area exists of a very hard subsoil and a weaker top-layer). The comparison of the second pictures of Figures 14 and 15 shows very clearly that in the harder soil the soil dependent motion resistance is much smaller than in the weaker soil.

5. Closing Remarks

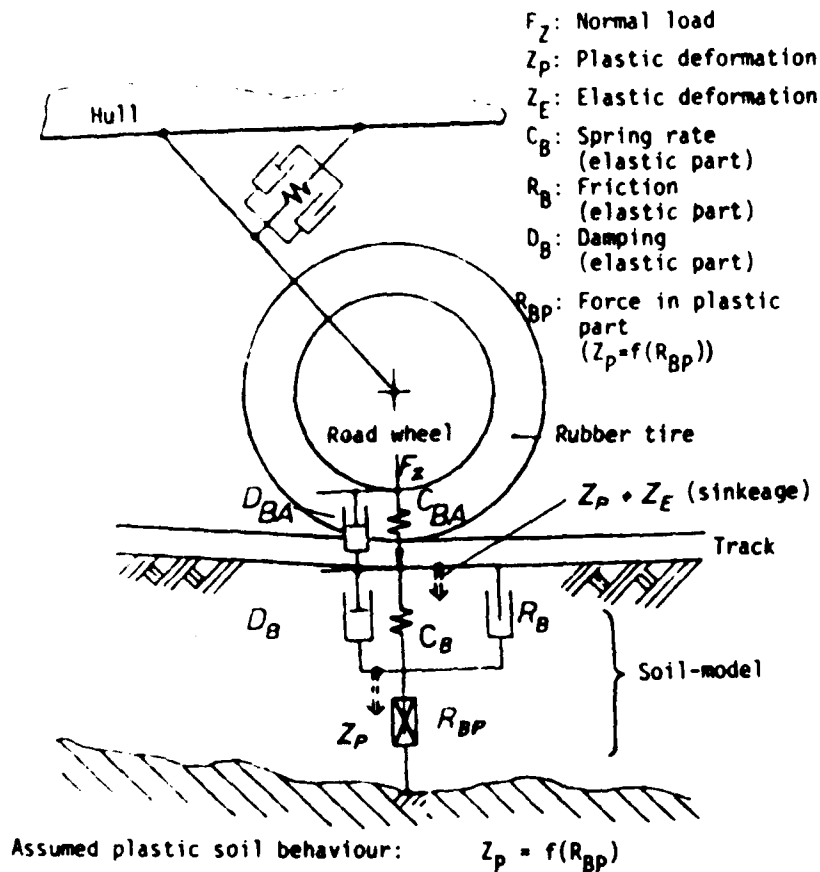
This paper is only a very brief discription of the hard- and software to measure and simulate the dynamic interaction between track and soil. Further studies have been made to improve the measuring-equipment and the soil-model for tangential direction of tracked and wheeled vehicles. For the measurements of the tire-soil-interaction in soft soils tire-deflection sensors [9] should be prepared and tested. They would be very useful to answer important questions about the use of central tire-inflation-pressure system (CTIPS) with stiff high-pressure-tires like the size 14.00 R20 18 PR in very soft soil.

Although this paper shows only the first step of a long way, the author believes in a wider use of this method in the future because of the following reasons:

- the measuring equipment will be cheaper
- the computation of soil parameters will be more sophisticated
- there is the possibility for automatisation in measuring and analysing steps.
Therefore it will be possible to measure and calculate a large number of parameters in one test area and discribe the real statistic distribution of soil parameters
- measurement steps and analysis steps are independent and can be improved separatly.

6. Acknowledgements

The author wishes to thank the German Federal Ministry of Defense for its help, guidance and financing the whole project. I thank also Mr.W. Raasch, Dr.H.Hahn and Prof. Dr.W.Söhne for their help and useful discussion and Dr.H.J.Römer for the field tests. Finally, the author wishes to express his sincere appreciation to Mr.W. Wallisch, Mr. G.Hammer, Mr. K.Pfister and Mr. O.Mohr of IABG for their support in preparing the force and slip-sensors and computer-models.



Assumed plastic soil behaviour: $Z_p = f(R_{BP})$

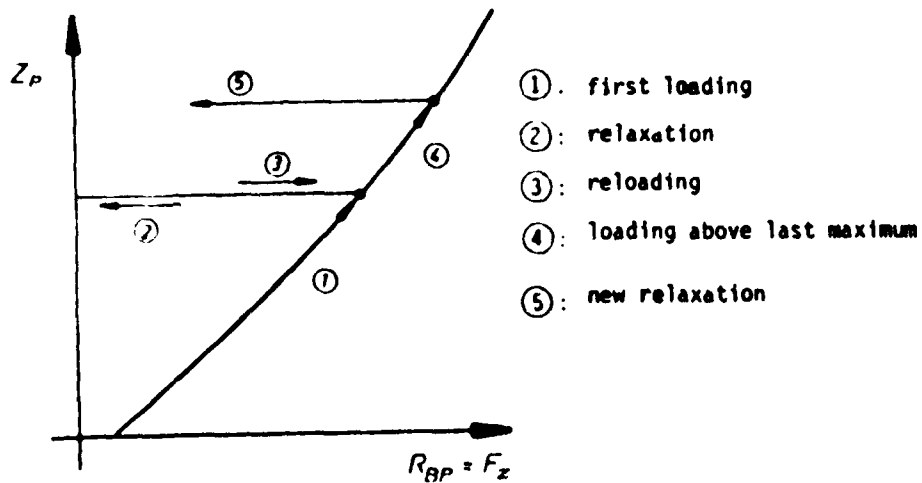


Figure 1: Track-soil-interaction

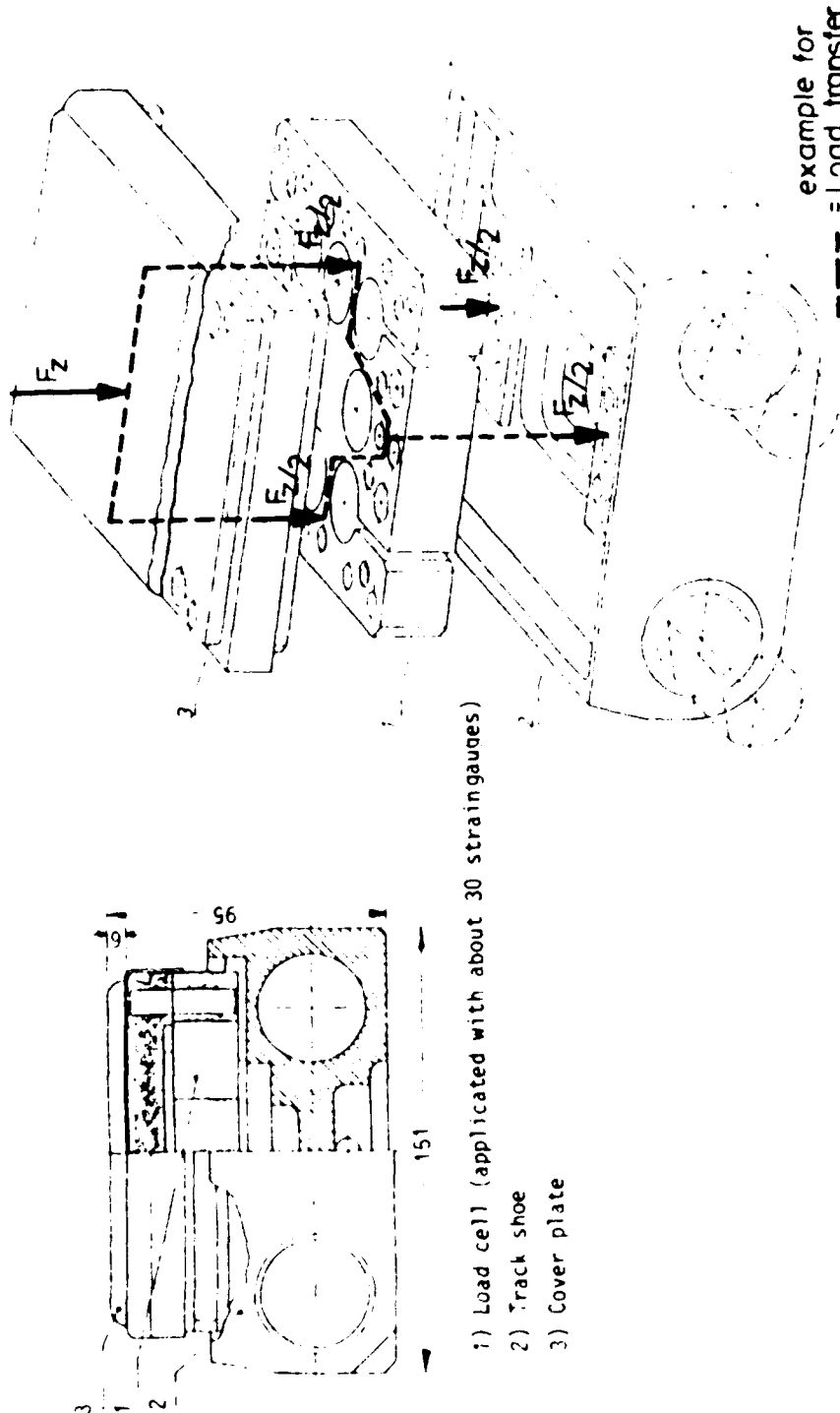
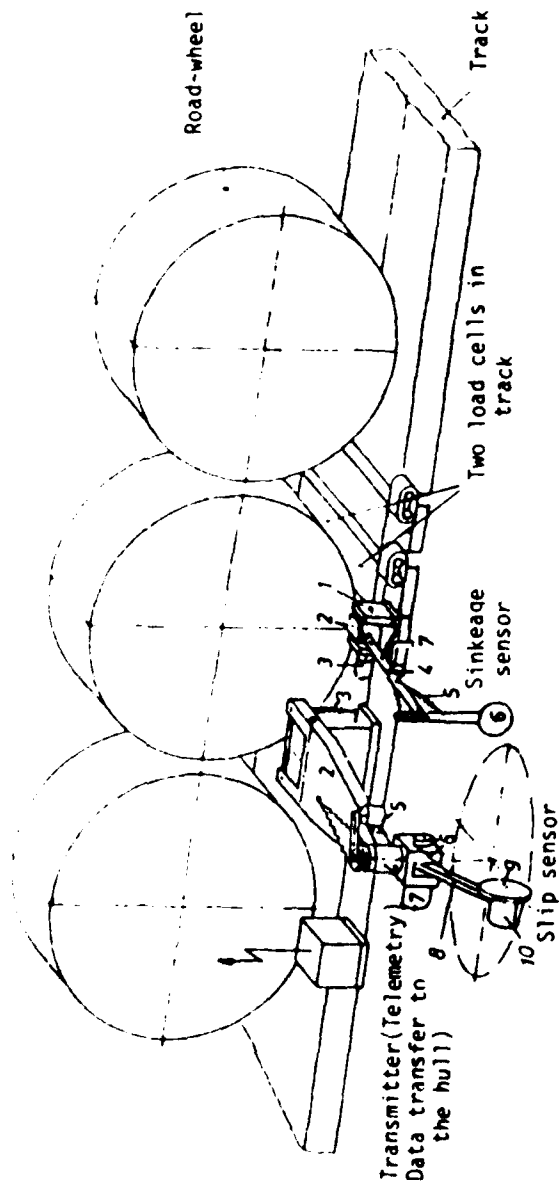


Figure 2: Load cell in track of KPz Leopard 1



Slip sensor:

- 1 = Cover (fixed on track)
- 2 = Boom
- 3 = Spring
- 4 = Bearing socket
- 5 = Transducer
- 6 = Bearing socket
- 7 = Transducer

- 8 = Cover (fixed on track)
- 9 = Measuring wheel
- 10 = Transducer

Sinkage sensor

- 1 = Cover (fixed on track)
- 2 = Cover for measuring arm
- 3 = Transducer (sinkage)
- 4 = Measuring arm
- 5 = Spring
- 6 = Sensor
- 7 = Spring

Figure 3 : Measuring Track

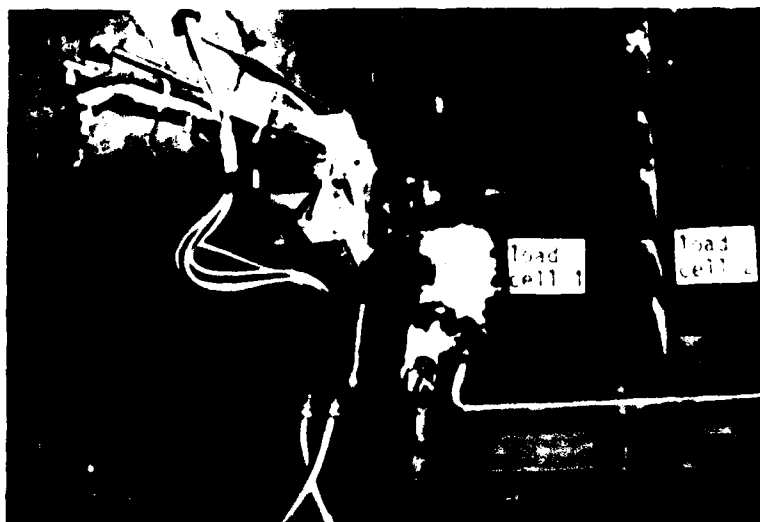


Figure 4: Sinkeage sensor and load cell in track

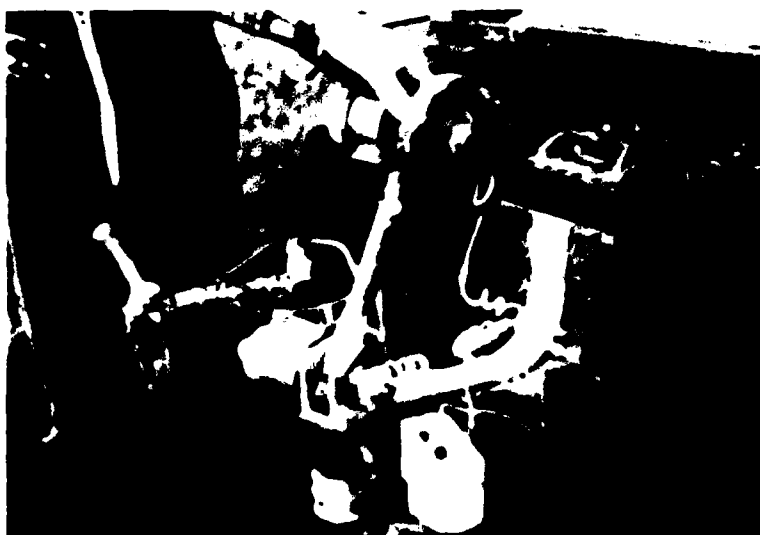


Figure 5: Calibration (field tests)

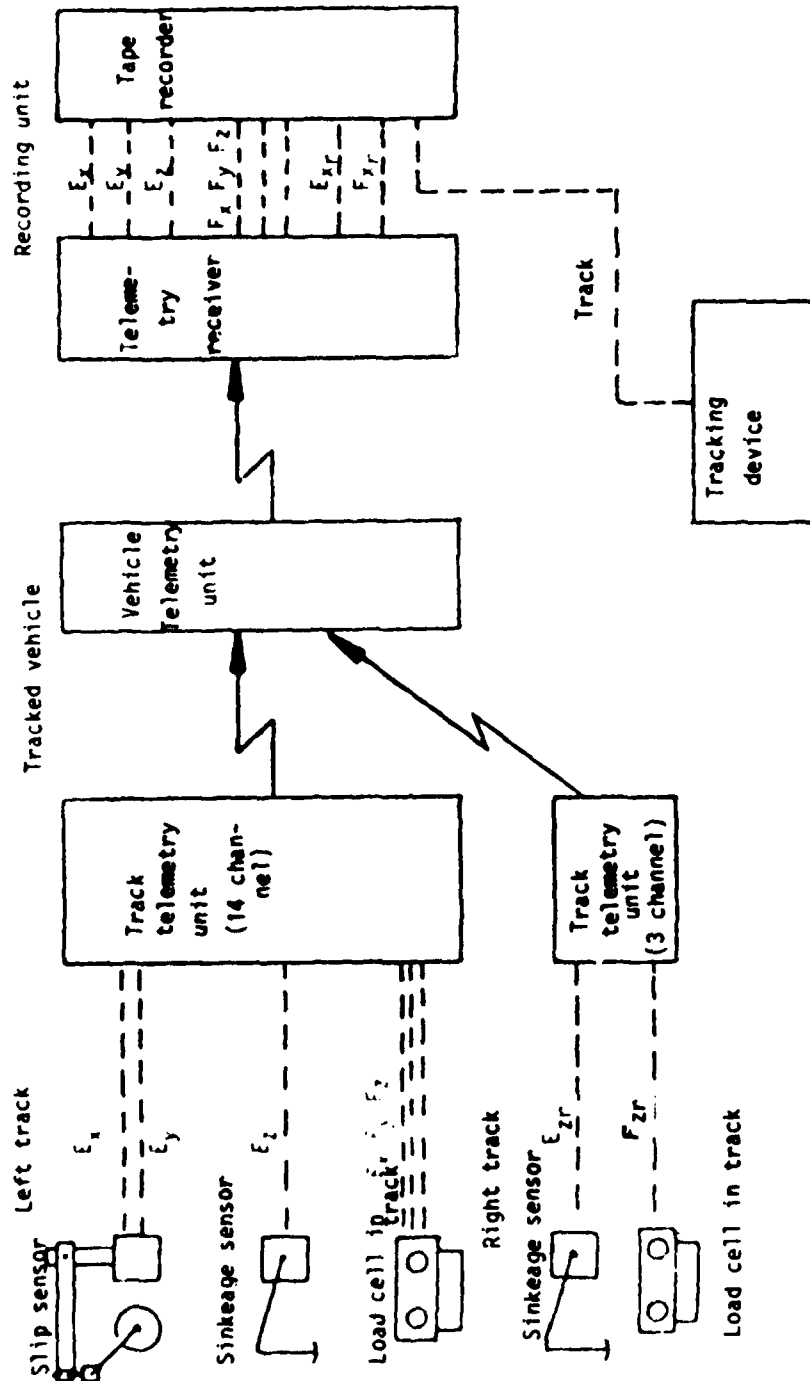


Figure 6: Flow chart of field tests with two measuring devices and a separate tracking device

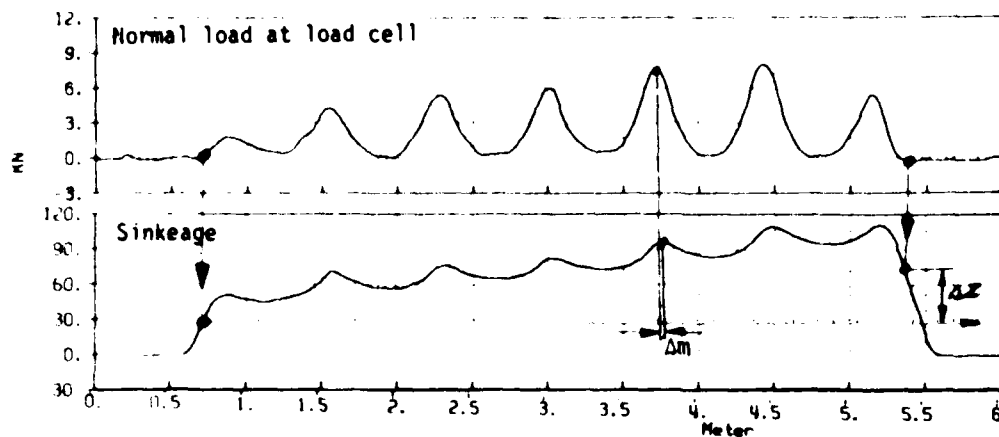
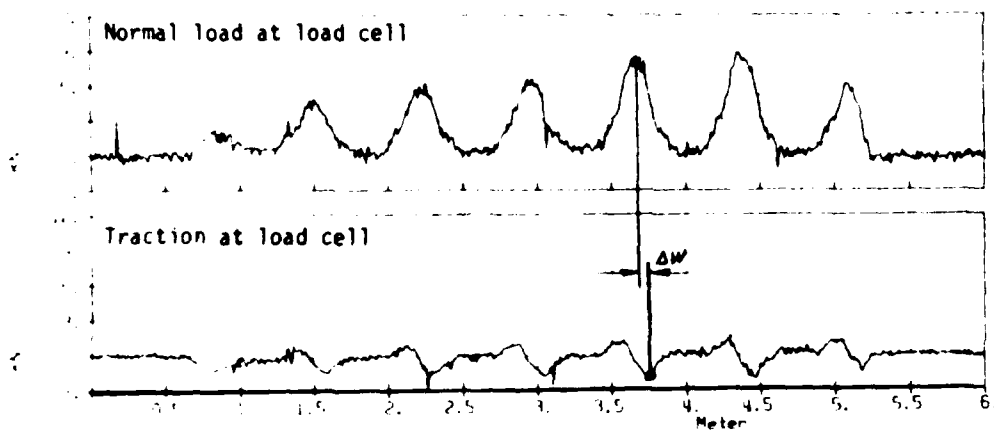


Figure 7: Measured normal load and sinkeage and calibration of sinkeage (there is a need of calibration because of the roughness of the terrain)



Traction is impossible without normal load; the built up of traction takes place separately at every road wheel.
The delay Δw is larger than Δm of picture 7 because of traction-slip relationship (soil: relativ weak grassland, trace depth: 50 mm)

Figure 8: Example for measured normal load and traction (unfiltered)

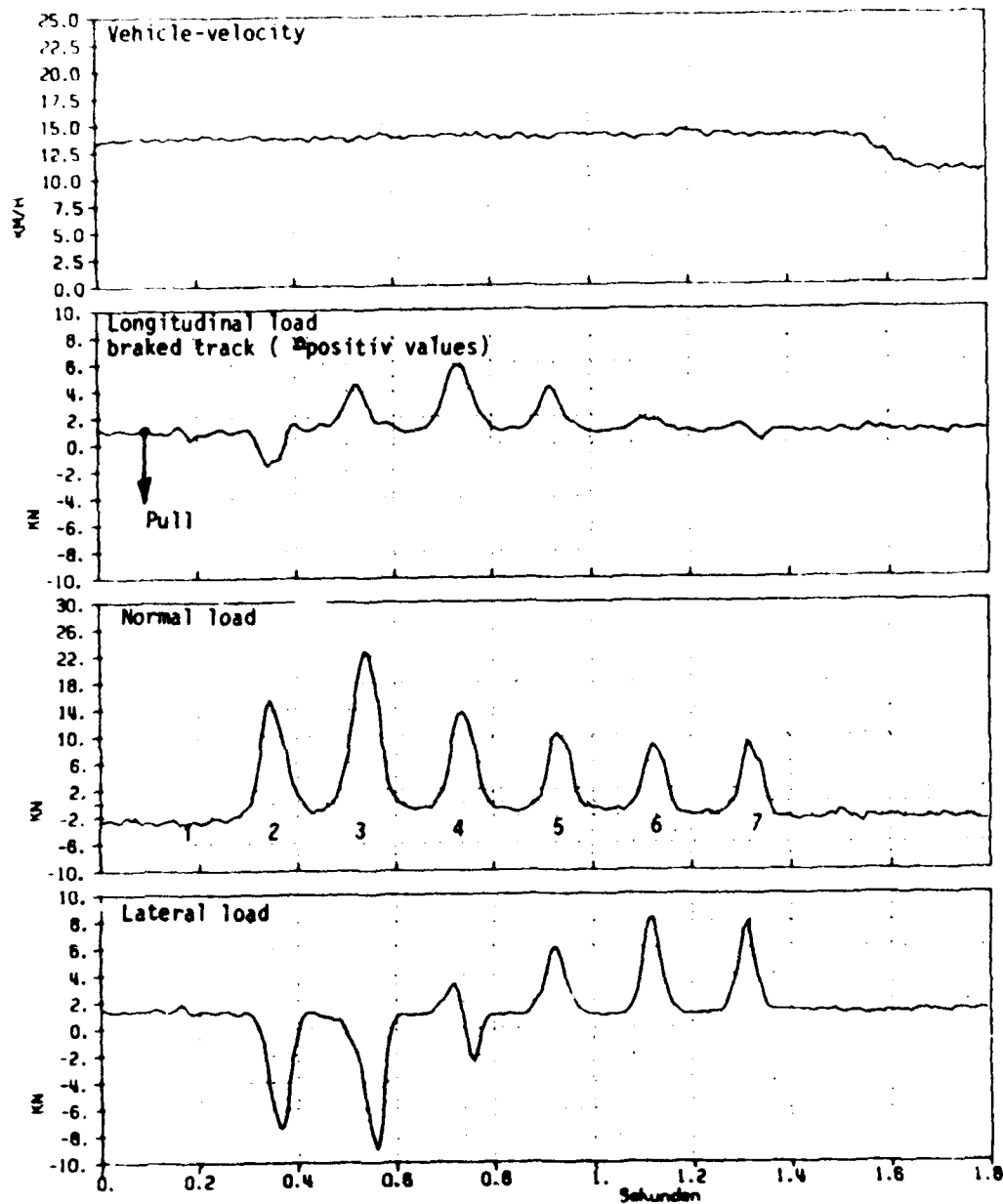


Figure 9: Left turn in first gear
(The load cell was fixed in left track = inner track)

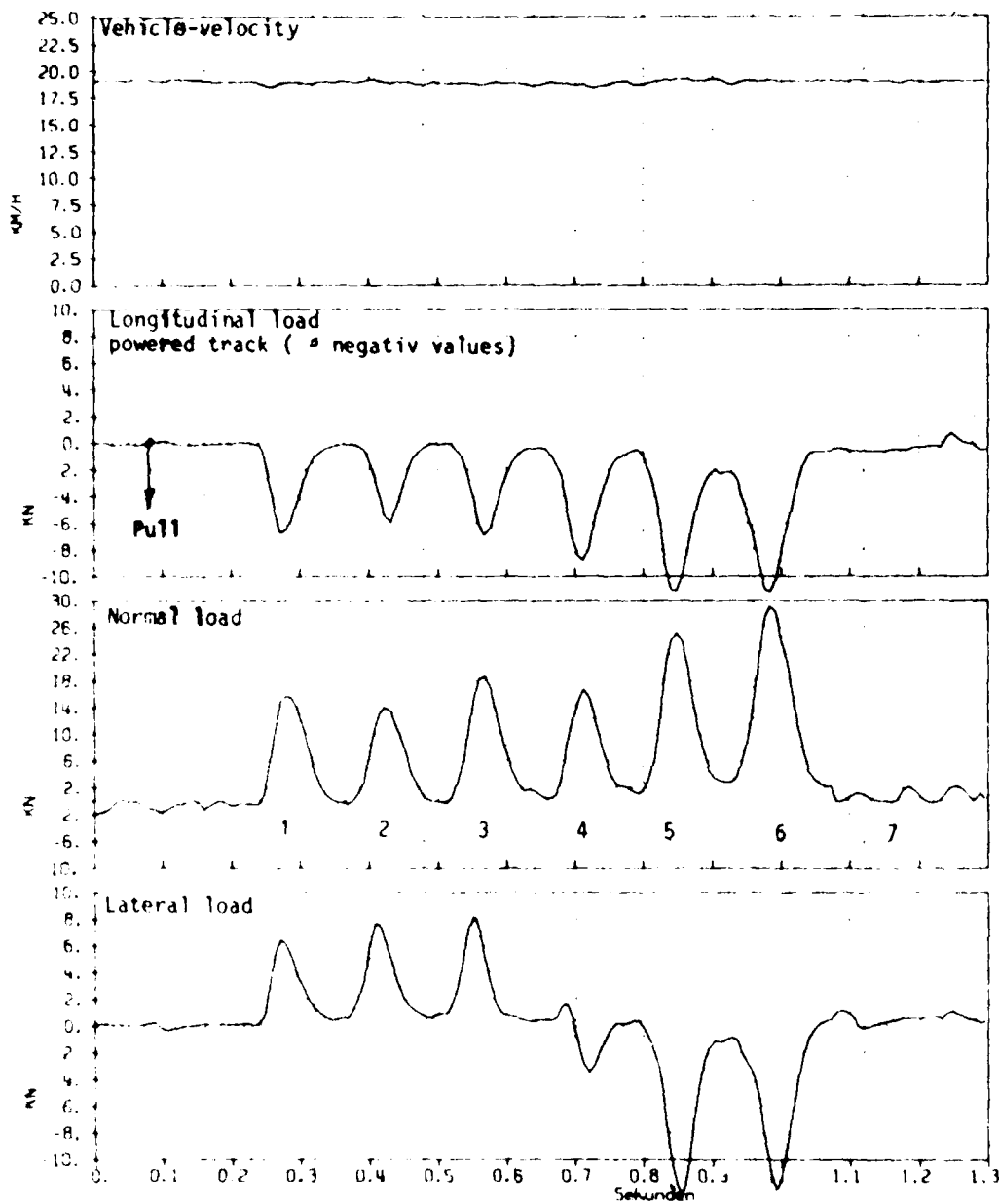
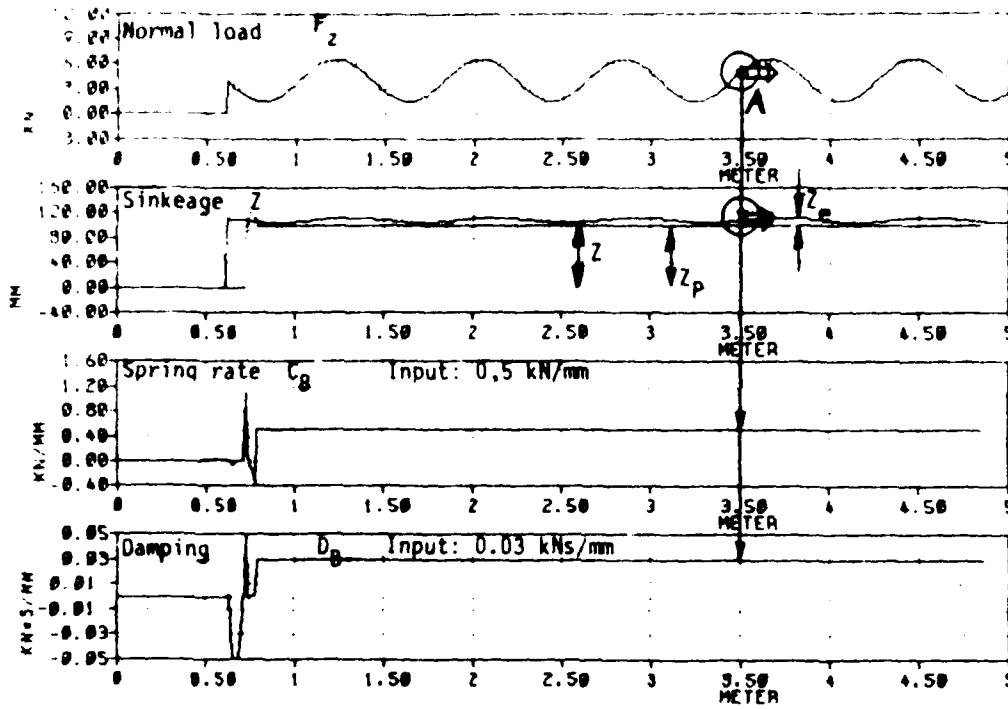
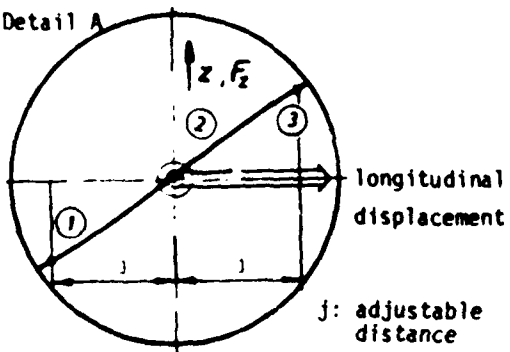


Figure 10: Right turn in first gear
(The load cell was fixed in the left track = outer track)



Evaluation without friction

Detail A



$$\begin{bmatrix} F_{z1} \\ F_{z2} \\ F_{z3} \end{bmatrix} = \begin{bmatrix} z_1 & \dot{z}_1 & -1 \\ z_2 & \dot{z}_2 & -1 \\ z_3 & \dot{z}_3 & -1 \end{bmatrix} \begin{bmatrix} C_B \\ D_B \\ C_B \dot{z}_p \end{bmatrix} \quad (1)$$

$$Z_p = C_B \dot{z}_p / C_B \quad (2)$$

$$Z_e = Z - Z_p \quad (3)$$

Figure 11: Test example and related calculation

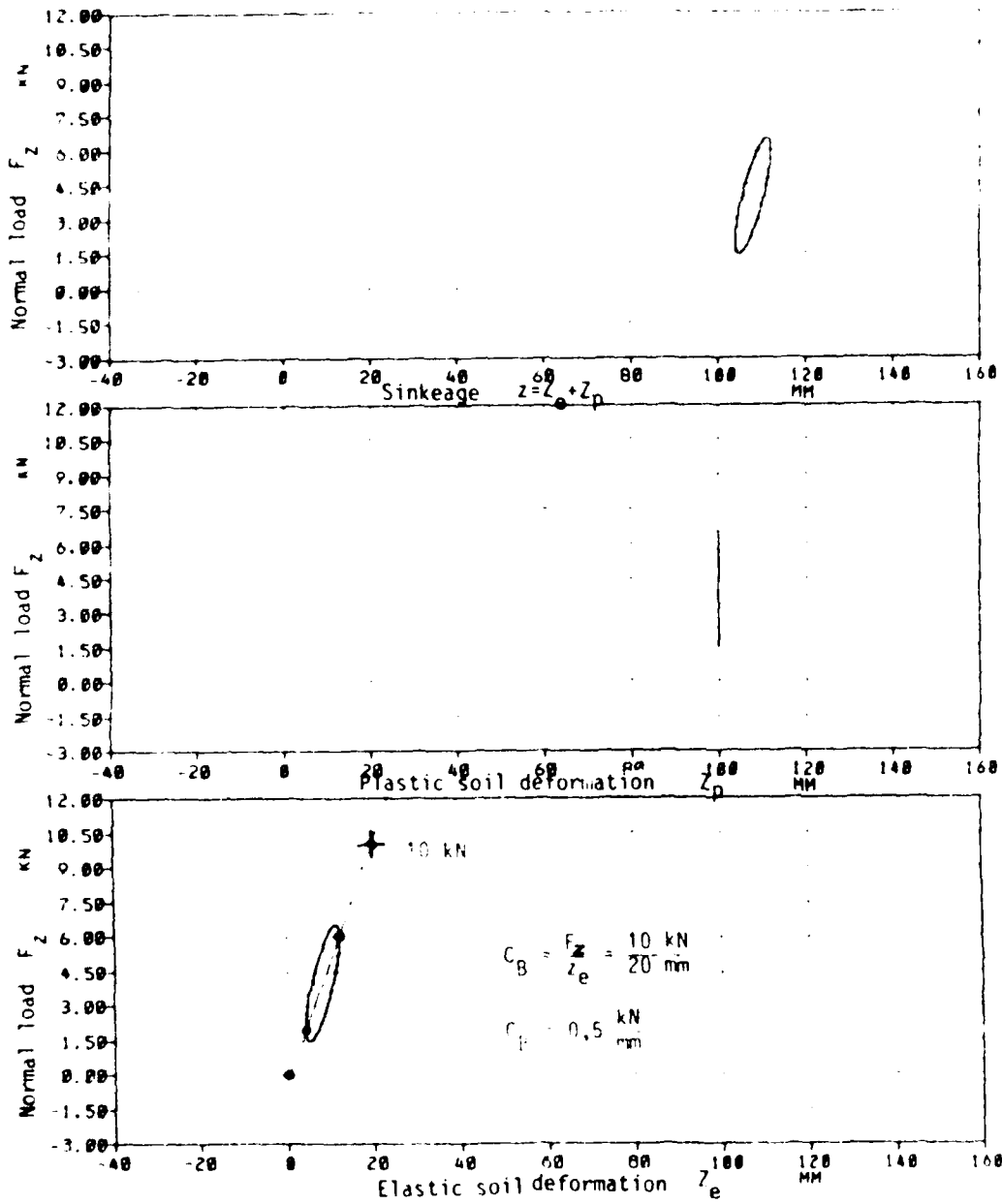
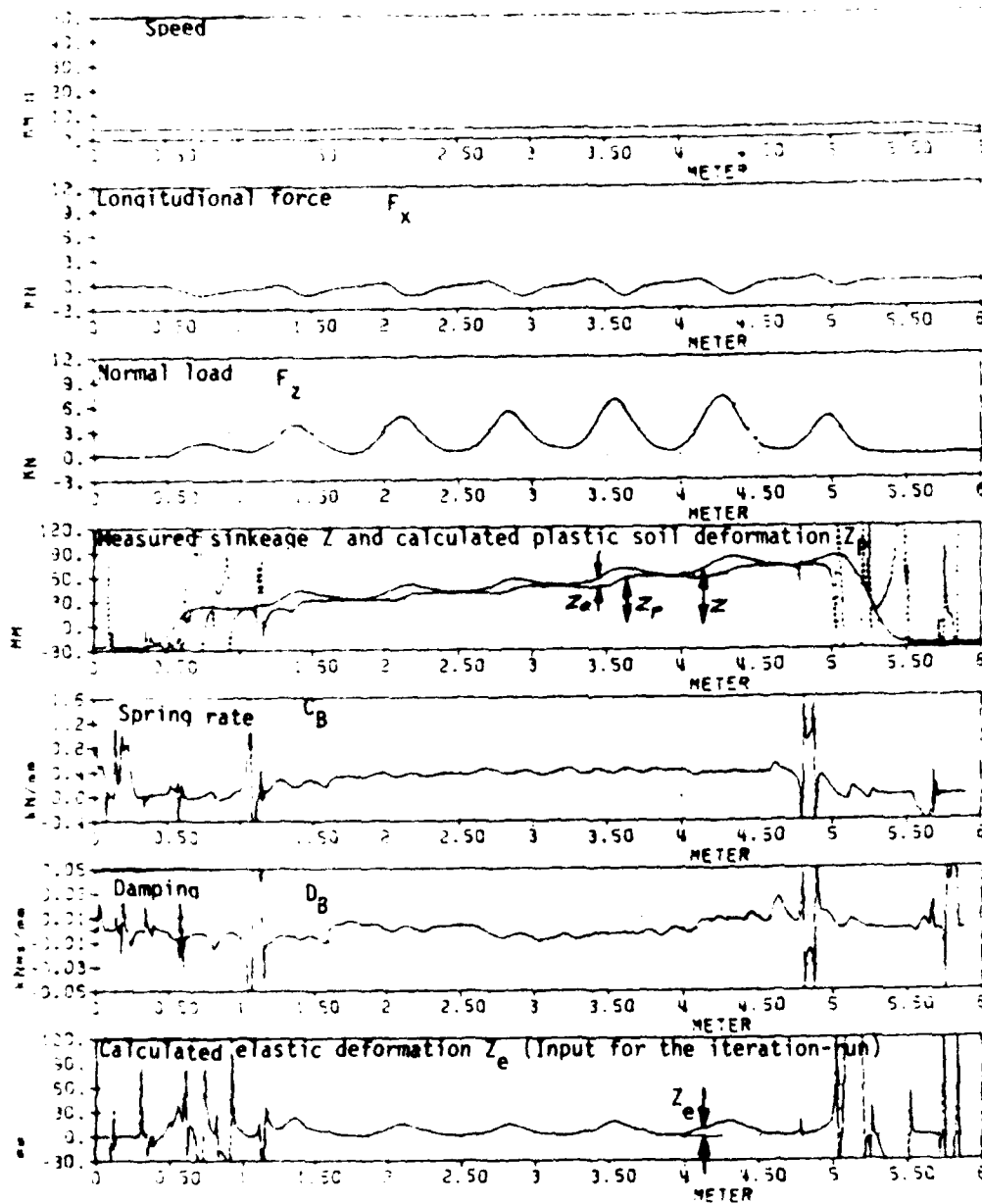
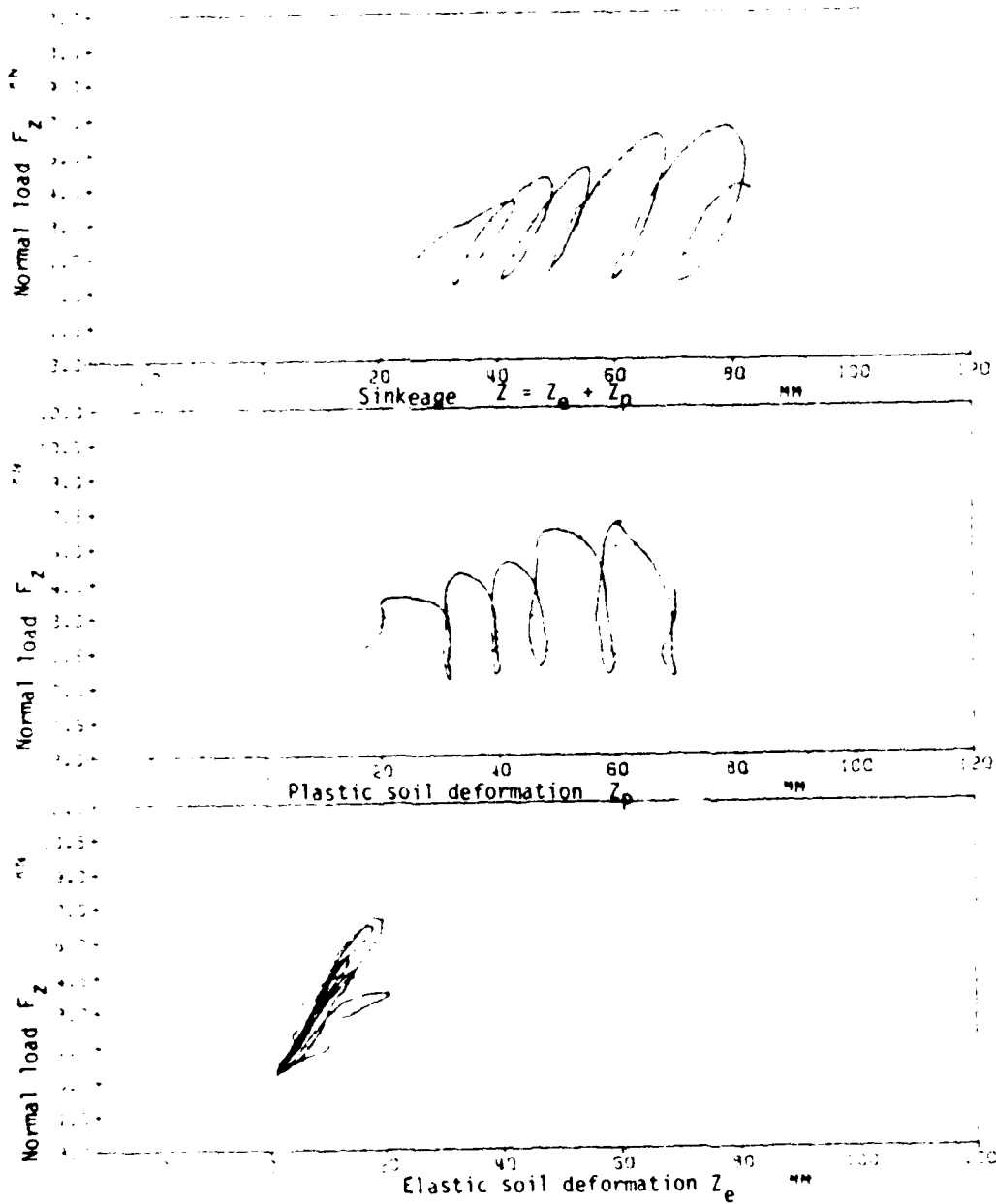


Figure 12: Elastic-plastic soil deformation and normal load (test example)



VERSUCH 23
Messwerte sind mit 5.00 Hz 24 dB gefiltert

Figure 13: Measured and calculated values as a function of position (time) for soft soil



5.00 Hz 24 dB def. tent

Figure 14: Elastic-plastic soil deformation and normal load for soft soil

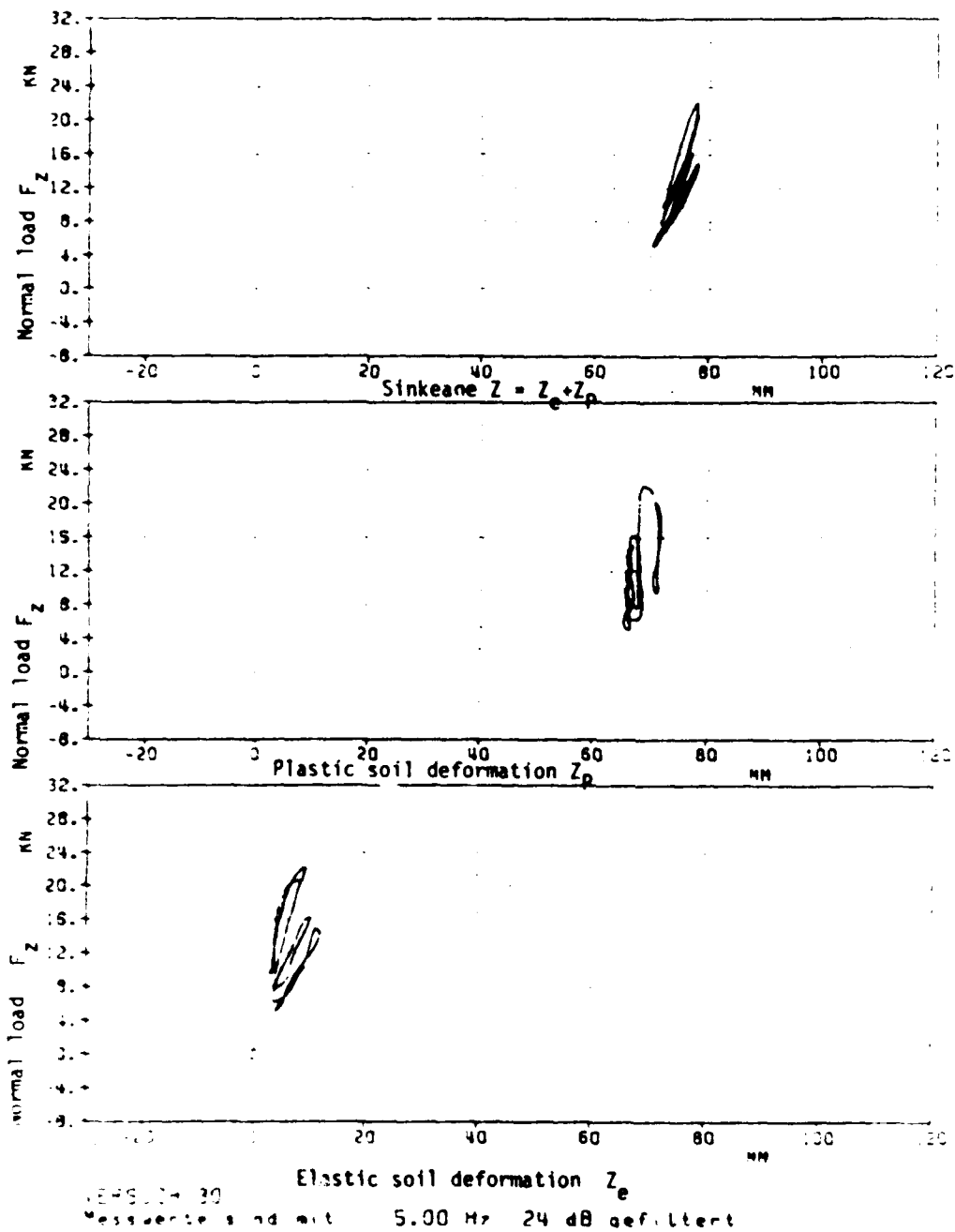


Figure 15: Elastic-plastic soil deformation and normal load for hard soil

Literature

- [1] Wong, J.Y.: "An improved method for predicting tracked vehicle performance".
2nd European ISTVS-Conference, Ferrara, Italy (1983)
- [2] Bekker, M.G.: "Theory of Land Locomotion".
Ann Arbor: The University of Michigan Press (1956)
- [3] Bekker, M.G.: "Off-the-road Locomotion".
Ann Arbor: The University of Michigan Press (1960)
- [4] Bekker, M.G.: "Introduction to terrain-vehicle systems".
Ann Arbor: The University of Michigan Press (1969)
- [5] Parringer, P.: "Die dynamische Wechselbeziehung zwischen Gleiskette und Boden".
Diss. Techn. Universität München (1982)
- [6] Pfister, K.: "Modifiziertes Kettenglied als Lastmeßzelle für die orthogonalen Bodenübertragungskräfte".
IABG Bericht B-TF 720 (1978)
- [7] Parringer, P.: "Fahrzeugbezogene Untersuchung dynamischer Bodenkennwerte".
IABG Berichte B-TF 976 (1979), B-TF 977 (1979) und B-TF 1305 (1982)
- [8] Autorenkollektiv des Forschungsstabes des japanischen Verteidigungsministeriums: "Die Untersuchung der besonderen Eigenschaften der Kettenkräfte am Boden gemessen mit einer dreiachsigen Kraftmeßdose".
Forschungsbericht Nr. 572
Übersetzung aus dem Japanischen, IABG Bericht B-TF 556 (1976)
- [9] Krick, G.: "Die Wechselbeziehungen zwischen starrem Rad, Luftreifen und nachgiebigem Boden".
Diss. Techn. Universität München (1971)
- [10] Karafiath, L.L. and Nowatzki, E.A.: "Soil Mechanics for Off-Road Vehicle Engineering".
Trans. S.A. Publications Clausthal, Germany (1978)
- [11] Baladi, G.Y.: "Analysis of Steerability of Tracked Vehicles; Theoretical Predictions versus Field Measurements".
7th International Conference of ISTVS, Calgary (1981)

ANALYSIS OF GROUND PRESSURE DISTRIBUTION BENEATH TRACKED
MODEL WITH RESPECT TO EXTERNAL LOADING

MAREK M. PONCYLIUSZ

I.M.R.C., TECHNICAL UNIVERSITY, WARSAW, POLAND

INTRODUCTION

This paper is a continuation of the investigation, results of which were presented at the last Conference ISTVS in Calgary in 1981 /Traction Investigation of a Tracked Vehicle Model/.

The results obtained then permitted to draw certain conclusions, however the necessity of rearrangement concerned with the test model and the frame of conducted investigation appeared simultaneously.

New research aimed at settling the effect of changes of the centre of gravity /C.G./ on tractive efforts and on distribution of ground pressure beneath the track /i.e. LEMP, NGP/. The location of C.G. varied according to the changes of external loadings.

The measurement of the drawbar pull and the distribution of pressure between track and soil layer were carried out in the model scale.

THE TEST-STAND

The model of the tracked self-propelled vehicle running in the mobil soil bin was the mechanical part of the test apparatus. The model and the soil bin were being described in the paper which was presented at the last Conference [1]. The system of registration of the drawbar pull underwent a changes. The vehicle model was connected with the immovable socle through an octagonal dynamometer designed according to [2]. The measuring system of drawbar pull had better sensitivity and linearity than previous one /Fig. 1/

The rigid steel plate enabling front loading of the model /with the aid of bob/ was mounted right over the front wheel /Fig. 2/.

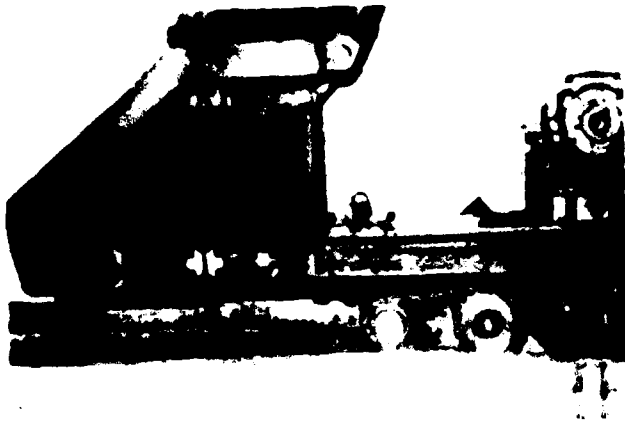


FIG. 1

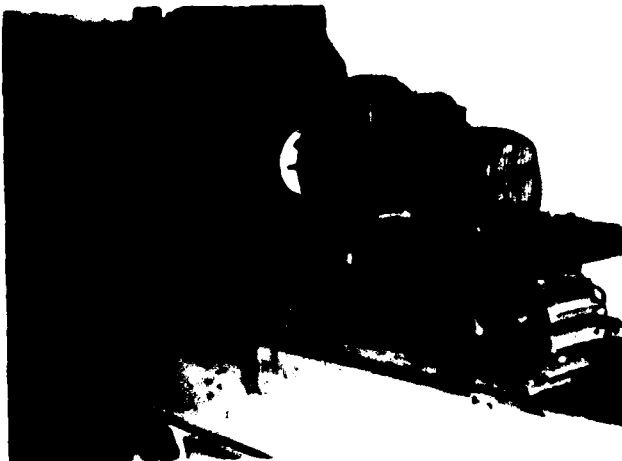


FIG. 2

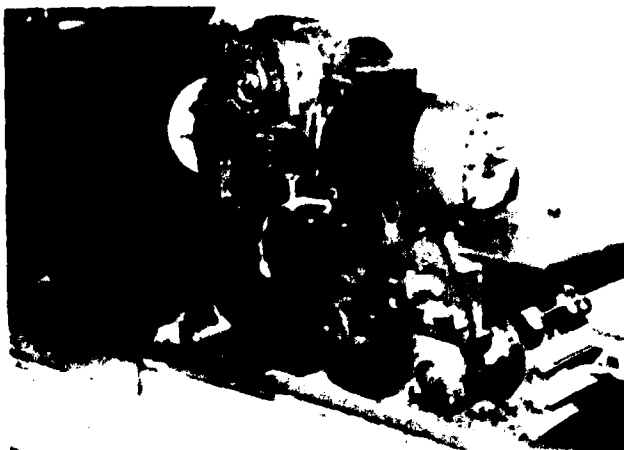


FIG. 4

PREPARATION OF THE SOIL

The soil prepared for measurements had specified mechanical constitution due to uniform mixing and humidification so that it possessed homogeneous structure, humidity and density in the whole bin.

Humidity of the soil was checked every day before beginning and after completion of the experiments.

Before each test the soil was mixed, levellized and compacted by means of mechanical compactor.

All the tests were carried out on the clayey sand.

The physical soil properties and the grain size distribution are shown in Table 1 and Fig. 3 respectively.

Table 1. Physical properties of the soil

wet density / kN/m^3 /	26,1
average water content /%/	9,0
cohesion /kPa/	10,0
angle of internal friction	29,0
bulk density / kN/m^3 /	16,0

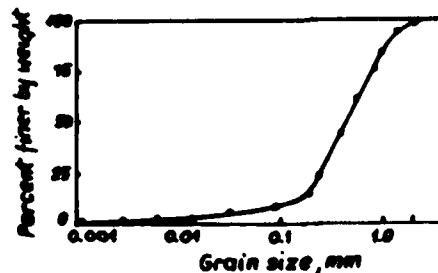


Fig. 3. Grain size distribution of tested soil.

TRACTIVE MEASUREMENTS

The disposable drawbar pull and the machine loading coming from the soil /when the track was rolling/ were registered during the tests. The tests were carried out for the value of slippage $s=20\%$ and $s=100\%$ /what means loosening the machine adherence with soil/.

In comparison with previous investigation there were increase of slippage value from $s=8,4\%$ to $s=20\%$. It was so, because the tendency to the lateral tilt occurred when the slippage value was $s=8,4\%$. It mainly took place after 2,0 or 2,5 m of riding. When slippage value was 20% model was not disposed to tilt itself.

The location of C.G. was varied in each serie of measurements.

The simulated external loading of the model was obtained by means of additional masses fastened down to the model at different places.

The following drafts of loading were separated:

- | | | | |
|----|--------------------|--------------------------------|-------------|
| a/ | an additional mass | 228 N /8,8% mass of the model/ | -Fig. 4 |
| b/ | " | 319 N /12,3% | " / -Fig. 5 |
| c/ | " | 547 N /21,0% | " / -Fig. 6 |
| d/ | " | 696 N /26,8% | " / -Fig. 7 |

Loadings, which simulated an action of a bulldozer blade were given up in discussed investigation /practically a horizontal component of force/. It was why, because this component of loading was simulated by means of a system of two horizontal parallel cords fastened to the model on the both sides and there was no possibility of determination of cord tension with a sufficient accuracy. The additional mass which created the tension in cords hung freely and was exposed to the action of uneven body forces.

Before each measurement the track was re-set in a determined which occurred every 35 revolutions of a track sprocket.

The number of revolutions resulted from transmission ratio of the chain drive.

This way a constant track tension /i.e. horizontal loading



Fig. 5



Fig. 6

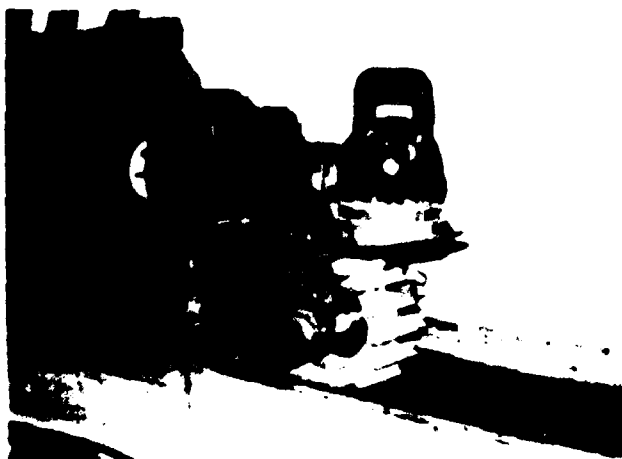


Fig. 7

the track sprocket and front wheel of the model/ was being obtained. Also each strain gauge was setting then to zero or to the constant fixed value by means of the digital voltmeter. It made sure about efficient accuracy of measurement.

DATA ANALYSIS

The conducted tests made possible to reveal some distinct regularities existing in correlations of the type of the used additional load /i.e. location of C.G./ and values of the drawbar pull as well as ground pressure distribution beneath a track of the model.

A value of the drawbar pull /D.P./ depends on a location of the centre of gravity /C.G./ The weight of the model varied, so some operations had to be introduced. When the model was loaded with an additional mass, the obtained values of D.P. were equated, so:

$$D.P._{an} = DP_m \frac{m_b}{m_m} \quad /1/$$

where:

$D.P._{an}$ - an analysed value of D.P.

DP_m - a measured value of D.P.

m_b - a basic mass of the model /265 kg/

m_m - a mass of the model when the $D.P._m$ was measured.

The loadings of the rollers were diminished too. An influence of the additional mass was eliminated, so variable values of D.P. could have been compared.

This way a phenomenon of a change of a C.G. was obtained without changing of a total mass of the model /in theory of course/.

The displacement of C.G. influences on a point's location /centre of the bearing reactions of the ground/.

The point's S location $/x_s/$ was computed by /2/ /fig.8/

$$x_s = \frac{F_E - F_C / 0,25 L + F_{FG} - F_{AB} / 0,5 L}{F_{AB} + F_C + F_D + F_E + F_{FG}} \quad /2/$$

where:

$F_{A3} \dots F_{FG}$ - reactions as shown in fig. 8

L - track ground contact length

The equation /2/ resulted from the equilibrium of moments of a bearing reactions F in relation to the point S .

Such a way of computing of x_S has been admitted as a correct one, because of intentionally high value of a ratio $\frac{L_T}{L_R}$,

$$\frac{L_T}{L_R} = 4,25$$

where:

L_T - track link pitch

L_R - pitch of supporting rollers.

It caused the decay of vertical loading of a track between two rollers [4]. It seemed that in this case the vertical loadings were concentrated around the rollers and equation /2/ was not saddled with a significant error.

A dependence between location of C.G. and x_S was shown in fig. 9 /point D = middle of the contact area of a track/. During the investigations C.G. was shifted on a limited scale of 0,146 m /24% of the track ground contact length L /. The centre of bearing reactions S changes on a scale of 0,120 m /20% L /. D.F. value depends on the location of C.G. / x_{CG} / as well as x_S - value.

All dependencies are non-linear; in accordance with the regression analysis /by means of the microcomputer with the plotter/ both are second-degree polynomial.

Figure 10 shows dependence $DP = f/\frac{x_{CG}}{L}/$, where x_{CG} is a displacement of C.G. measured from the location of C.G. for the model without additional mass.

In fig. 11 the course of function $DP = f/\frac{x_S}{L}/$ clearly shown that displacement of point S towards the front of the model causes an increase of D.F. to a certain degree; further displacement towards the centre of symmetry of the model /point D/ doesn't yield benefits, D.F. - value diminishes. This course of both functions $DP = f/\frac{x_S}{L}/$, $DP = f/\frac{x_{CG}}{L}/$ may be explained as follows:

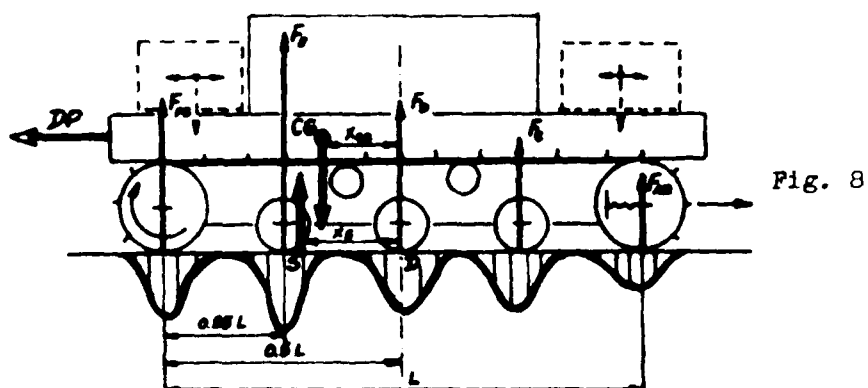


Fig. 8

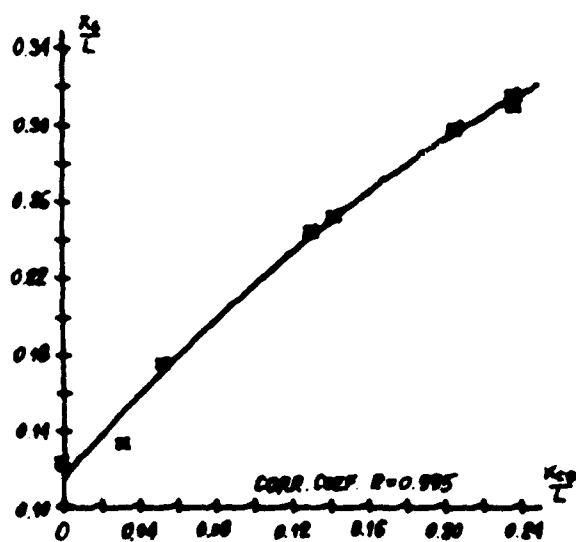


Fig. 9

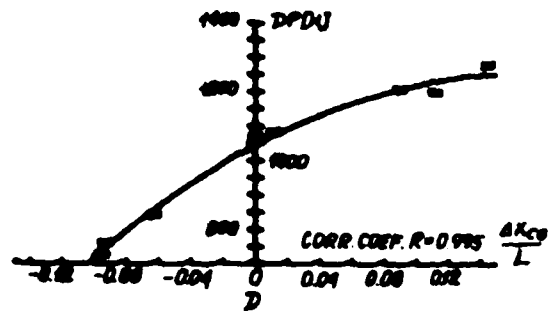


Fig. 10

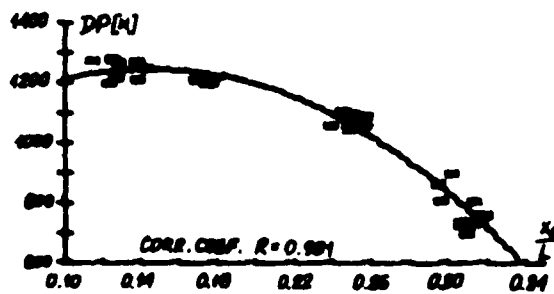


Fig. 11

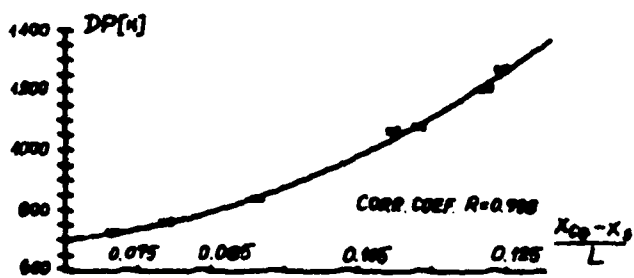


Fig. 12

1. When C.G. is shifted towards the rear of the model, the centre of the reactions is displaced in the same direction $/F_{AD} = 0, F_C = 0/$; a front of the model is unloaded, so the track ground contact area diminishes.

The tractive effort can be computed in accordance with:

$$T = b \int_0^L /c + p/x \cdot \operatorname{tg} \phi / \cdot /1 - \exp \frac{-j}{K} / dx \quad /3/$$

where:

- b - width of track
- c - cohesion
- p/x - normal pressure under track
- ϕ - angle of internal friction
- j - displacement of soil beneath a track
- K - coefficient of a compression of soil

When the track ground contact length $/L/$ is smaller, then a value of "j" diminishes as well as a value of force P.

The drawbar pull $/DP = P - R$, where R - rolling resistance/ decreases accordingly to the diminishing force P.

Then the displacement of C.G. towards front of the model causes the decrease of x_S and increase of D.P.

2. In accordance with [5] in the cyclically pressed ground beneath the track shearing parameters $/c, \phi/$ diminish after each cycle of the load.

In the ground loaded with pass of subsequent rollers the shear resistance becomes smaller. The loading of model's front can have an effect on increasing of D.P.

When $x_S/L > 0,12$ the value of D.P. begins to decrease. For $x_S = 0$ dependence $DP = f/\frac{x_S}{L}/$ reaches 71 per cent of $DP_{max}/1245 \text{ N/}$.

The function $DP = f/\frac{x_{CG} - x_S}{L}/$ is shown in fig. 12.

A parabolic dependence D.P. versus displacement $/x_{CG} - x_S/$ can be shown for the investigated model and given soil conditions. The above function has a high coefficient of correlation $/R = 0,998/$, therefore some conclusion can be drawn.

For uniform ground pressure distribution $/x_S = x_{CG} = 0/$ DP-value is not maximal $/1049 \text{ N/}$; minimum of the function

occurs for $\frac{x_{CG} - x_S}{L} = 0,055$ practically when both points are in line. The larger distance between points, the higher value of D.P.

CLOSING REMARKS

1. The results of investigations confirm an assumption that D.P. depends on the location of C.G. of the model. The D.P.-value varies between 720 N and 1300 N, i.e. almost 100 per cent more.

So great difference causes a necessity of the investigation of C.G. location's effect on the drawbar pull.

2. All the obtained dependencies like D.P. versus factors of the model's state of loading are non-linear.

3. The gauges fixed in the model permitted to the continuous recording of ground reactions loaded the model's frame. Computed centre of reactions depends on the location of C.G. of a tracked vehicle.

4. The ground pressure distributions obtained during investigations permit to establish a loading spectrum of models frame and to carry out its fatigue limit analysis.


5. The carried out analysis allows to make most favourable distribution mass of the model /for the used soil/.

6. The vertical loading of the frame is not uniform as well as the triangular.

Further research on propagation of stresses in ground beneath the track /related to the concentrated force F loading a roller/ is going on.

REFERENCES

- [1] A. MIERZWICKI, M. M. PONCYLIUSZ, Traction Investigation of a Track Vehicle Model, The Proceedings of the 7th Conference ISTVS, Calgary 1981

- [2] N. H. COOK, E. RABINOWICZ, Physical Measurement and Analysis, Addison + Wesley, Reading 1963
 - [3] D. ROWLAND, Tracked Vehicle Ground Pressure and It's Effect on Soft Ground Performance, The Proceedings of the 4th Conference ISTVS, Stockholm 1972
 - [4] V. SKOTNIKOV, A. PONOMAREV, A. KLIMANOV, The Mobility of the Machines /in Russian/, Minsk 1982
 - [5] K. KOGURE, T. KUDO, Shearing Properties of Sand Under a Repeated Loading Representing the Ground Pressure Distribution of a Tracked Vehicle, Journal of Terramechanics 1977, No 4.
- 

A COMPARISON BETWEEN A CONVENTIONAL METHOD AND AN IMPROVED
METHOD FOR PREDICTING TRACKED VEHICLE PERFORMANCE

J.Y. WONG and J. PRESTON THOMAS, TRANSPORT TECHNOLOGY
RESEARCH LABORATORY, CARLETON UNIVERSITY, OTTAWA, CANADA

INTRODUCTION

One of the most widely used conventional methods for predicting tracked vehicle performance is based on the assumption that the track in contact with the terrain is equivalent to a rigid footing. Furthermore, a uniform normal pressure distribution over the entire contact area is assumed if the centre of gravity of the vehicle is located at the midpoint of the contact length. On the other hand, if the centre of gravity is located in front or behind the midpoint of the contact length or if load transfer due to drawbar pull takes place, a sinkage distribution of trapezoidal shape will then be assumed. Based on these assumptions and the measured pressure sinkage and shear stress displacement relationships of the terrain, the tractive performance of tracked vehicles is predicted.

Experimental evidence has shown that while the conventional method may find applications in the prediction of the performance of crawlers with low ratios of roadwheel spacing to track pitch, commonly used in agriculture and the construction industry, it gives unrealistic prediction of the performance of tracked vehicles with high ratios of roadwheel spacing to track pitch designed for high speed operations. In the latter case, the normal pressure is usually concentrated under the roadwheels and is far from uniform. Consequently, the track in contact with the deformable terrain deflects and has the form of a curve. Furthermore, an element of the terrain under the track is subject to repetitive normal and shear loadings of the consecutive roadwheels. To take these factors into account, an improved method for predicting the performance of tracked vehicles with relatively short track pitch has been developed. The objective is to provide the designer, the procurement manager and the test engineer with a quantitative means whereby the effects of vehicle design parameters and terrain conditions on performance can be assessed more realistically than using the conventional method.

This paper describes a comparison of the normal pressure distribution, sinkage and drawbar pull slip relationship of a tracked vehicle as predicted using the conventional and the improved methods.

THE CONVENTIONAL METHOD

One of the widely used conventional methods assumes that the track behaves like a rigid footing. With the centre of gravity of the vehicle at the midpoint of the contact length, the normal pressure distribution is assumed to be uniformly distributed as shown in Fig. 1. On the other hand, if the centre of gravity is located in front or behind the midpoint of the contact length, a sinkage distribution of trapezoidal shape is assumed.

If the pressure-sinkage relationship of the terrain is known, such as that shown in Fig. 1, then the sinkage z of the track can be predicted by equating the reaction due to normal pressure p with the vehicle weight (1) (2). The functional relationship between sinkage z and pressure p for a given terrain can generally be expressed by

$$z = f(p) \quad (1)$$

It should be mentioned that the pressure-sinkage relationship may vary with terrain type and conditions. Various methods have been proposed for characterizing the pressure-sinkage relations of different kinds of terrain as described in references (1), (2), (3), (4) and (5).

Based on the predicted track sinkage z_0 , the motion resistance R_c due to terrain compaction can be predicted as follows:

$$R_c = b \int_0^{z_0} p dz \quad (2)$$

where b is the width of the track.

In addition to resistance due to compaction, the track may encounter resistance due to bulldozing effects (1). This should be taken into account in determining the total motion resistance.

If the shear stress - displacement relationship of the terrain under an appropriate normal pressure p is known, such as that shown in Fig. 1, the tractive effort of a track F can be predicted as follows:

$$F = b \int_0^l s dx \quad (3)$$

where l is the length of the track and s is the shear stress under the track which varies along the contact length (1), (2).

If the shear stress - displacement relationship can be described by a simple exponential function (1)(2), the tractive effort F at a given slip i can be expressed by (1)(2)

$$F = (Ac + W \tan \phi) \left[1 - \frac{K}{l} (1 - e^{-il/K}) \right] \quad (4)$$

where A and W are the contact area and normal load of the track, respectively; c and ϕ are cohesion and angle of internal shearing resistance of the terrain, respectively; K is the shear deformation modulus of the terrain.

It should be pointed out that the shear stress-displacement relationship may vary with terrain type and conditions. Various methods have been proposed for characterizing the shear stress - displacement relations of different kinds of terrain as discussed in references (1)(2) and (6).

Based on the predicted motion resistance and tractive effort, the drawbar pull-slip relationship of a tracked vehicle can then be estimated. The drawbar pull-slip relationship forms a basis for the comparison and evaluation of the tractive performance of off-road vehicles.

THE IMPROVED METHOD

When a tracked vehicle with relatively short track pitch travels over a deformable terrain, the normal load is usually concentrated under the roadwheels. However, the track segments between the roadwheels also take up load (7). As a result, they deflect and have the form of a curve. Furthermore, an element of the terrain under the track is subject to the repetitive loading of consecutive roadwheels (8). To predict the normal pressure distribution on the track-terrain interface, the pressure-sinkage relationship and the response to repetitive loading of the terrain have to be measured. Fig. 2 shows the response of a muskeg to repetitive loading (4). It shows that the stiffness of the muskeg during unloading and reloading is much higher than that in its virgin state and that it exhibits a certain amount of hysteresis.

When the terrain characteristics are known, the prediction of the normal pressure distribution is reduced to the determination of the shape of the deflected track in contact with the terrain. A detailed analysis of the mechanics of track-terrain interaction has been made. The track system with the major interacting forces are shown in Fig. 3. In the analysis, it is assumed that the track is equivalent to a flexible and inextensible belt and that the roadwheels are rigidly connected to the vehicle body. A set of equations for the equilibrium of the forces and moments acting on the track system and the conservation of overall track length have been derived. They establish the relationship between the shape of the deflected track in contact with the terrain and vehicle design parameters and terrain characteristics. The solution to this set of equations defines the sinkages of the roadwheels and the shape of the track segments between roadwheels. From these, the normal pressure distribution under a moving tracked vehicle can be predicted. The details of the analysis are described in reference (9).

To predict the shear stress distribution, the shear stress-displacement relationship of the terrain and the characteristics of the track-terrain shearing have to be determined. It should be mentioned that an element of the terrain under the track is also subject to shearing action of a repetitive nature. This is because the normal load applied to an element of the terrain under the track varies as the consecutive roadwheels roll over it. As a result, for a terrain exhibiting frictional behaviour, it undergoes the loading-unloading-reloading cycle in shear, similar to that for normal load. To predict the shear stress distribution on the track-terrain interface, the response to repetitive shear loading of the terrain must be known. Fig. 4 shows the response of a frictional medium (a dry sand) to repetitive shear loading. It indicates that for a frictional terrain, the shear stress-displacement relationship during reloading is similar to that with the terrain in its virgin state. This means that when re-shearing takes place after the previous loading-unloading cycle, the shear stress does not instantaneously reach its maximum value for a given normal stress. Rather a certain amount of shear displacement must take place before the maximum shear stress can be developed, similar to that when the frictional medium is being sheared in its virgin state. This phenomenon has been taken into account in the analysis. Together with the knowledge of the shear displacement developed under the track, which can be determined by a kinematic analysis of the track based on the concept of slip velocity (1)(2), the shear stress distribution under the track can then be predicted. Fig. 5 illustrates how the development of the shear stress under the track may be modified if the response of a frictional terrain to repetitive shear loading is taken into account for an idealized case. It should be pointed out that when the

repetitive shearing characteristics of the terrain are taken into consideration, the predicted total tractive effort of the vehicle at a given slip may be considerably lower than that when they are not taken into account, as can be seen from Fig. 5. The details of the analysis are given in reference (9).

When the normal pressure and shear stress distributions have been determined, the motion resistance, tractive effort and drawbar pull as functions of slip can be predicted. The prediction procedures have been programmed on a Hewlett-Packard 9845T microcomputer. The required inputs include both the vehicle and terrain parameters. The computer outputs include normal pressure and shear stress distributions, sinkage, motion resistance, tractive effort and drawbar pull at a given slip (8) (9).

A COMPARISON BETWEEN THE CONVENTIONAL METHOD AND THE IMPROVED METHOD

The normal pressure distribution, the sinkage of the track and the drawbar pull-slip relationship of a tracked vehicle, with basic parameters shown in Table 1, operating over a variety of terrains were predicted using the conventional and the improved methods. The parameters used to characterize the pressure-sinkage relationships and the response to repetitive normal load for a sandy terrain and two muskegs are given in Tables 2 and 3, respectively. The shear strength parameters of the terrains used in the predictions are given in Table 4. For further information concerning the methods used to characterize terrain behaviour, please refer to references (3), (4), (5), (6) and (9).

A comparison between the predicted normal pressure distributions using the conventional and the improved methods and field measurements over a sandy terrain and a muskeg are shown in Figs. 6 and 7, respectively. It can be seen from Fig. 6 that over the sandy terrain the maximum pressure predicted by the improved method is quite close to the measured one, whereas that estimated using the conventional method is 43.7 kPa, only about 10% of the maximum measured pressure. Over the muskeg, the normal pressure estimated using the conventional method is again 43.7 kPa, about 40% of the maximum measured. However, the maximum normal pressure predicted using the improved method is again quite close to the maximum measured as shown in Fig. 7. The reason is that in the improved method the response of the terrain to repetitive normal load has been taken into account. As mentioned previously, after the terrain has been compacted by the first roadwheel, it becomes much "stiffer" than in its virgin state. This promotes the concentration of normal pressure under the roadwheels. The behaviour of the terrain during the unloading-reloading cycle shown in Fig. 2 also explains why it is possible that the normal pressure at a point on the track segment between two adjacent roadwheels can be as low as zero, while the sinkage at that point as measured from the original terrain surface is not zero.

Figs. 8 and 9 show a comparison between the predicted sinkages of the vehicle using the conventional and the improved methods and the measured sinkages over the two types of terrain. It can be seen that in general the conventional method underestimates the sinkage. This is because the normal pressure estimated using the conventional method is considerably lower than the actual maximum pressure. On the other hand, it can be seen that fair to good agreement exists between the measured sinkages and those predicted using the improved method.

A comparison between the measured drawbar pull slip curves and those predicted using the conventional and the improved methods over the sandy terrain and the muskeg are shown in Figs. 10 and 11, respectively. It can be seen that the conventional method overestimates the drawbar pull of the vehicle over the full range of vehicle slip, particularly at low track slips. It is also shown that there is a close agreement between the measured drawbar pull and that predicted using the improved method. This is because the improved method gives a more realistic prediction of vehicle sinkage and hence motion resistance. Furthermore, the response of the terrain to repetitive shear loading, as described in the previous Section, has been taken into account in the improved method.

It is interesting to note that the significant difference in the drawbar performance between a crawler used in construction industry and a high speed tracked vehicle of similar size and weight reported in reference (10) is parallel to that between the two drawbar pull-slip curves shown in Figs. 10 and 11.

CLOSING REMARKS

It is shown that the improved method outlined in this paper gives a more realistic prediction of the performance of tracked vehicles with high ratios of roadwheel spacing to track pitch than the conventional method. The improvement achieved is due primarily to the inclusion of the response of terrain to repetitive normal and shear loadings and to the detailed analysis of the mechanics of track-terrain interaction.

It is believed that the improved method outlined in the paper provides a quantitative means for evaluating the effects of vehicle design parameters and terrain conditions on tracked vehicle performance and for comparing the performance of different tracked vehicle designs.

ACKNOWLEDGEMENTS

The improved method outlined in this paper was developed under contract arrangements with the Department of National Defence, Canada, through the Department of Supply and Services. The project was administered by the Vehicle Mobility Section, Defence Research Establishment Suffield, Alberta, Canada.

REFERENCES

1. M.G. Bekker, Introduction to Terrain-Vehicle Systems, The University of Michigan Press, 1969.
2. J.Y. Wong, Theory of Ground Vehicles, John Wiley, New York, 1978. Russian edition, Mashinostroenie Publishers of Moscow, U.S.S.R., 1982.
3. J.Y. Wong, "Data processing methodology in the characterization of the mechanical properties of terrain", Journal of Terramechanics, Vol. 17, No. 1, pp. 13-41, 1980.
4. J.Y. Wong, J.R. Radforth, and J. Preston-Thomas, "Some further studies on the mechanical properties of muskeg in relation to vehicle mobility", Journal of Terramechanics, Vol. 19, No. 2, 1982.
5. J.Y. Wong and J. Preston-Thomas, "On the characterization of the pressure-sinkage relationship of snow covers containing an ice layer", Journal of Terramechanics, Vol. 20, No. 1, 1983.
6. J.Y. Wong and J. Preston-Thomas, "On the characterization of the shear stress-displacement relationship of terrain", Journal of Terramechanics, Vol. 19, No. 4, 1982.
7. M.G. Bekker, Theory of Land Locomotion, The University of Michigan Press, 1956.
8. J.Y. Wong, "An improved method for predicting tracked vehicle performance", Proceedings of the Second European Conference of the International Society for Terrain-Vehicle Systems, Ferrara, Italy, October 3-5, 1983.
9. J.Y. Wong, M. Garber, and J. Preston-Thomas, "Theoretical prediction and experimental substantiation of the ground pressure distribution and tractive performance of tracked vehicles", to be published.
10. D.R. Freitag, Discussion on a paper entitled "Measurement of soil shear strength and deformation moduli and a comparison of the actual and theoretical performance of a family of rigid tracks", by B.M.D. Willis, Journal of Terramechanics, Vol. 2, No. 1, pp. 93-95, 1965.

Table 1
Vehicle Parameters

Vehicle Weight, kN	88.72
Number of roadwheels (for one track)	5
Radius of roadwheels, m	0.31
Distance between roadwheels, m	0.67
Distance between the centres of the sprocket and the tensioning wheel, m	4.03
Width of track, m	0.38
Track pitch, m	0.15
Initial track tension, kN	8.54
Weight of the track per unit length, kN/m	1.27
Height of track grousers, cm	4.7
Number of supporting rollers	0
Angle of approach of the track, degrees	23.8
Angle of departure of the track, degrees	16.4
Location of centre of gravity in the longitudinal direction (in front of the mid-point of the track contact length), m	0.13
Height of the centre of gravity, m	0.99
Location of drawbar in the longitudinal direction (distance from the mid-point of the track contact length), m	2.29
Height of drawbar, m	0.75

Table 2
Values of the Pressure-Sinkage and Repetitive Loading
Parameters for a Sandy Terrain (LETE Sand)

k_c	k_ϕ	n	k_o	A_u
kN/m^{n+1}	kN/m^{n+2}		kN/m^3	kN/m^4
102	5301	0.793	0	503,000

Note: k_o and A_u are parameters used to characterize the response to repetitive normal loading.

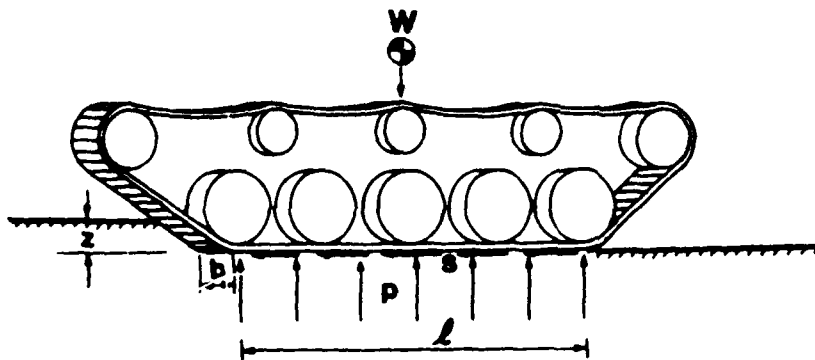
Table 3
Values of the Pressure-Sinkage and Repetitive Loading
Parameters for Two Types of Muskeg

Muskeg Type	Petawawa Muskeg A	Petawawa Muskeg B
$k_m, \text{kN/m}^3$	290	762
$M_m, \text{kN/m}^3$	51	97
$k_o, \text{kN/m}^3$	123	147
$A_u, \text{kN/m}^4$	23540	29700

Note: k_o and A_u are parameters used to characterize the response to normal loading.

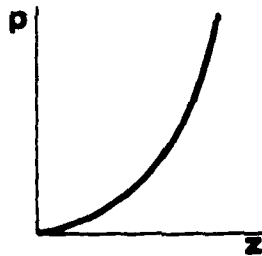
Table 4
Shear Strength Parameters of Various Types of Terrain

Terrain Type	Type of Shearing	Cohesion (Adhesion) kPa	Angle of Shearing Resistance degrees	K cm
LETE Sand	Internal	1.27	31.1	1.1
LETE Sand	Rubber-Sand	0.66	27.5	1
Petawawa Muskeg A	Peat (Internal)	2.83	39.4	3.1
Petawawa Muskeg B	Peat (internal)	2.55	39.2	3.1



$$p = \frac{W}{2bl}$$

$$z = f(p)$$



$$s = f(p, j)$$

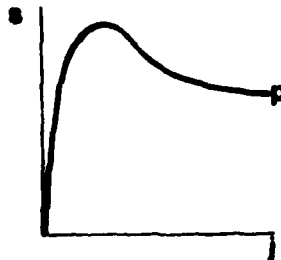


Fig. 1. The conventional method for predicting tracked vehicle performance.

MANIPULATOR DATA ACQUISITION SYSTEM
 Transport Technology Research Laboratory
 Carleton University, Ottawa, Canada

Pressure-Sinkage Experiment

Date: 22/07/81

Terrain: Petawawa Muskeg 84

Experiment number - 1

Data-Base Id.: P6-9-2

The footing radius (cm): 7.5

The X-increment (cm): 1.0

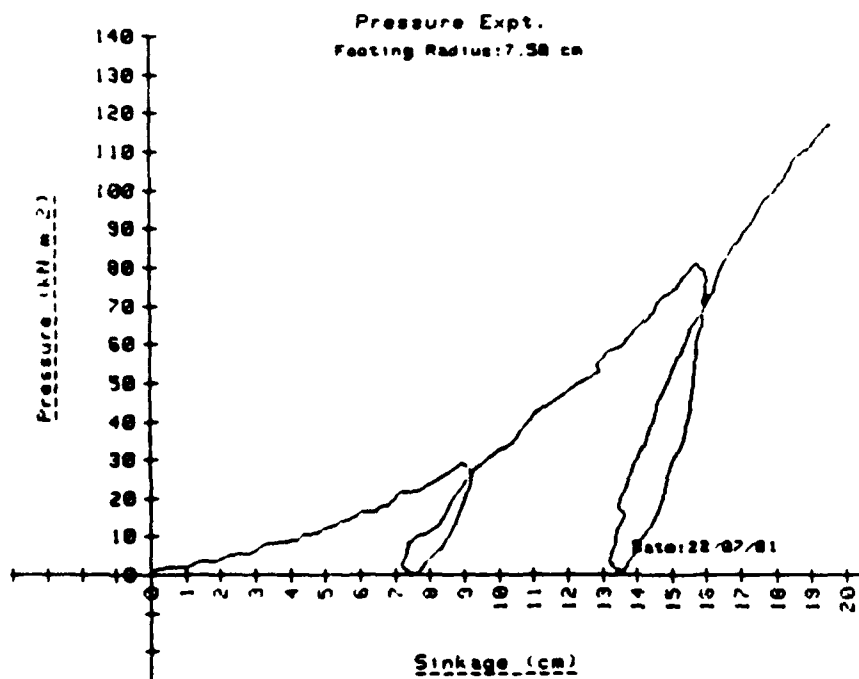


Fig. 2. Response of a muskeg to repetitive normal load.

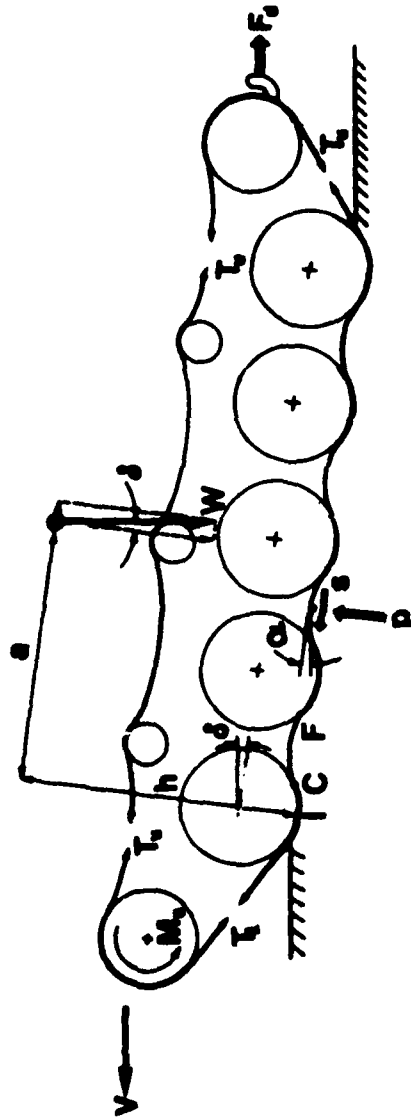


Fig. 3. Interaction between a flexible track and terrain.

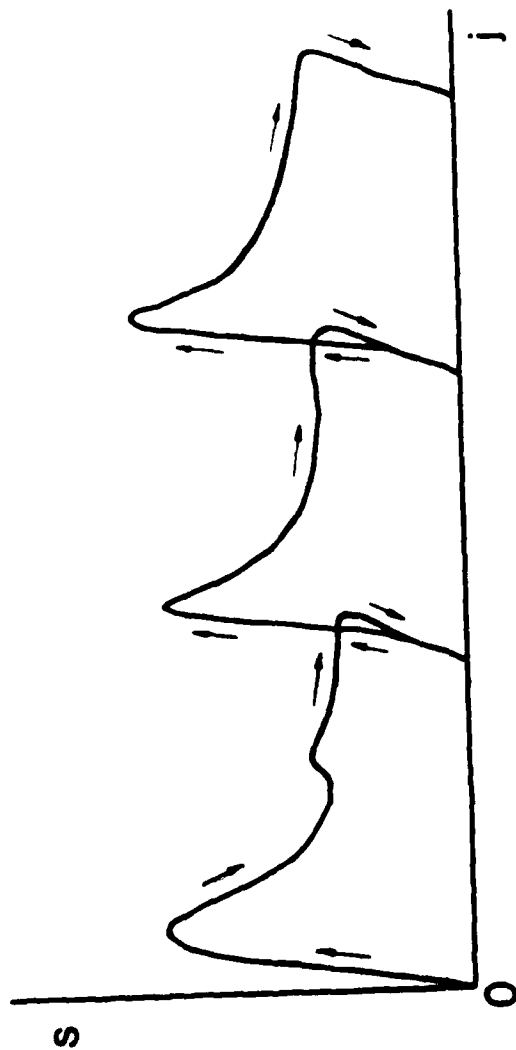


Fig. 4. Response of a frictional terrain to repetitive shear load.

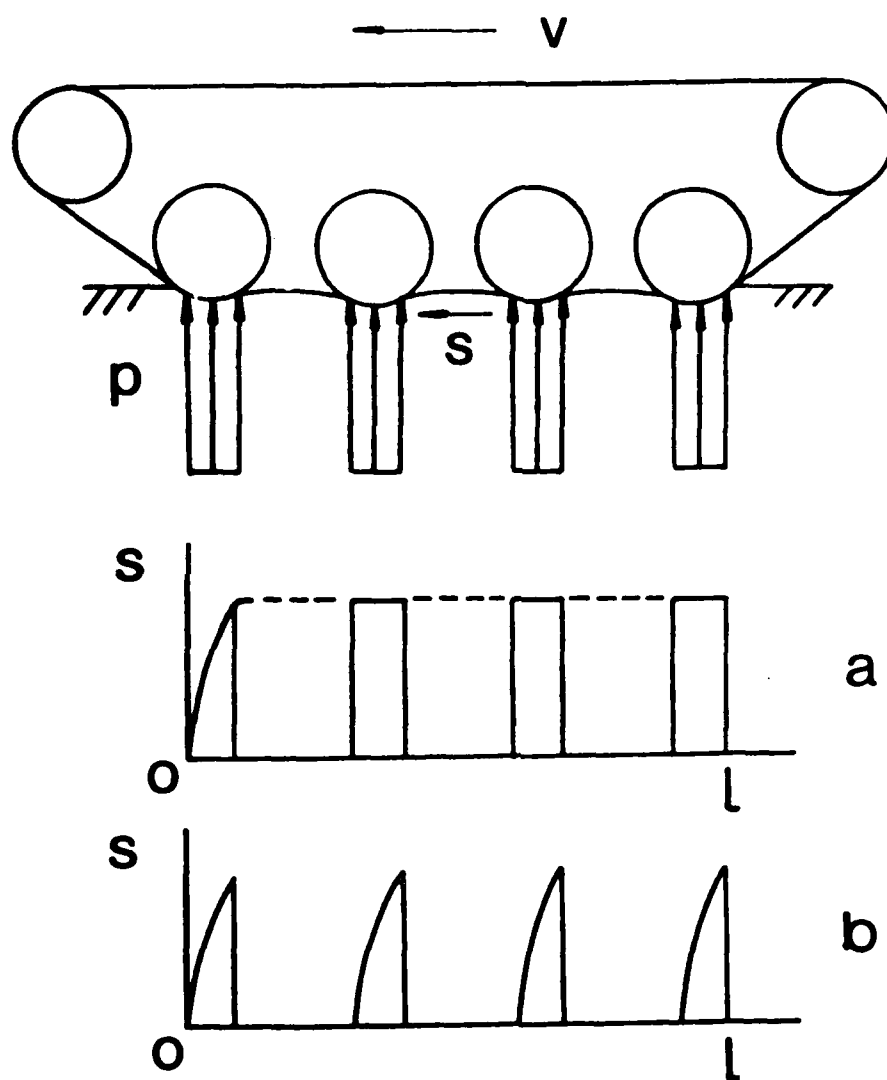


Fig. 5. Development of shear stress under a track over frictional terrain predicted by a) the conventional method and b) the improved method.

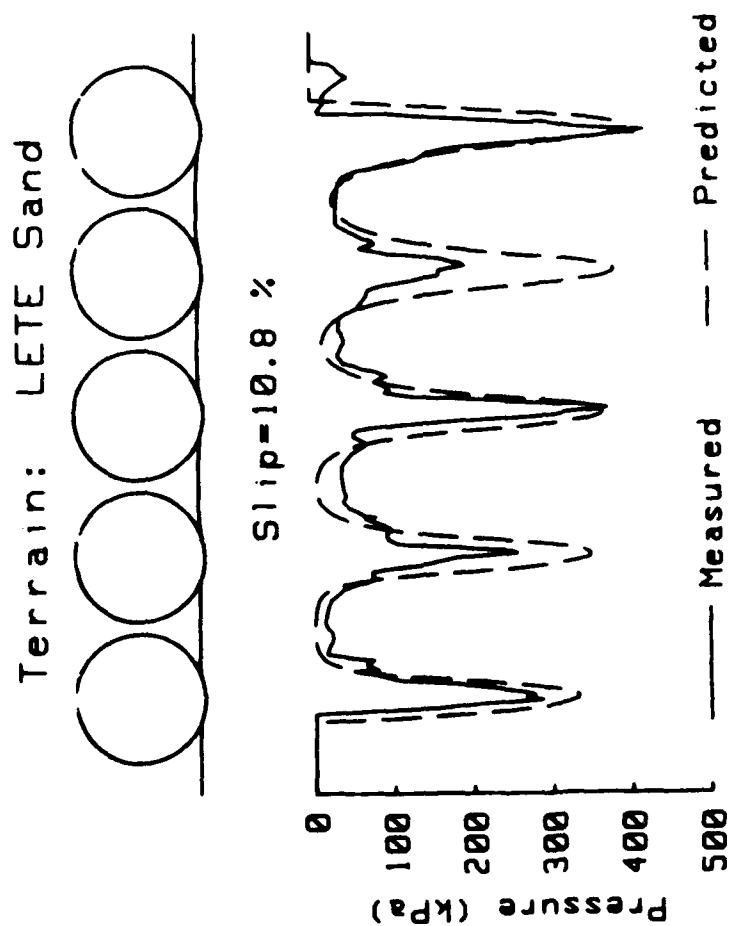


Fig. 6. Comparison of the pressure distribution predicted by the improved method with the measured one over a sandy terrain.

AD-A148 634

PROCEEDINGS OF THE INTERNATIONAL CONFERENCE ON THE
PERFORMANCE OF OFF-ROAD (U) INTERNATIONAL SOCIETY FOR
TERRAIN-VEHICLE SYSTEMS M J DWYER AUG 84

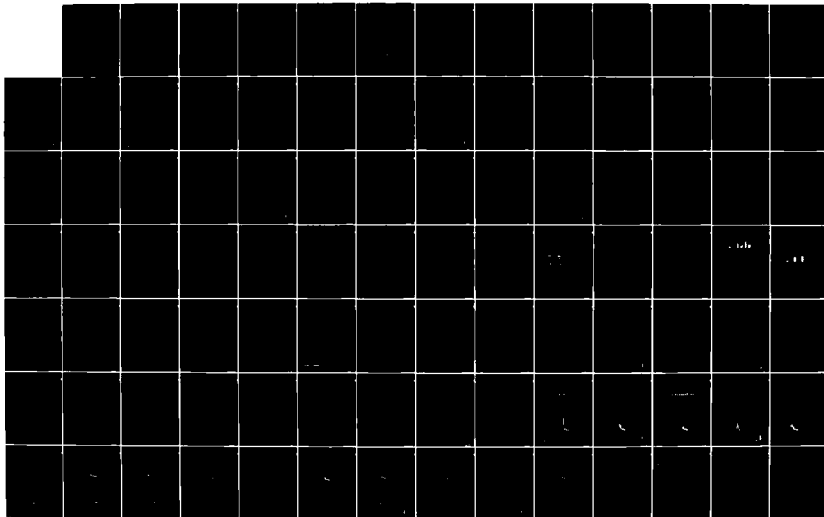
5/6

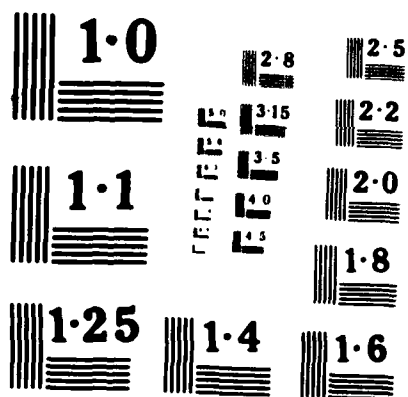
UNCLASSIFIED

DAJA45-84-M-0251

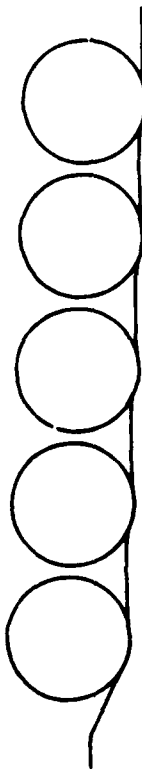
F/G 13/6

NL





Terrain: Petawawa Muskeg A



Slip = 2.7 %

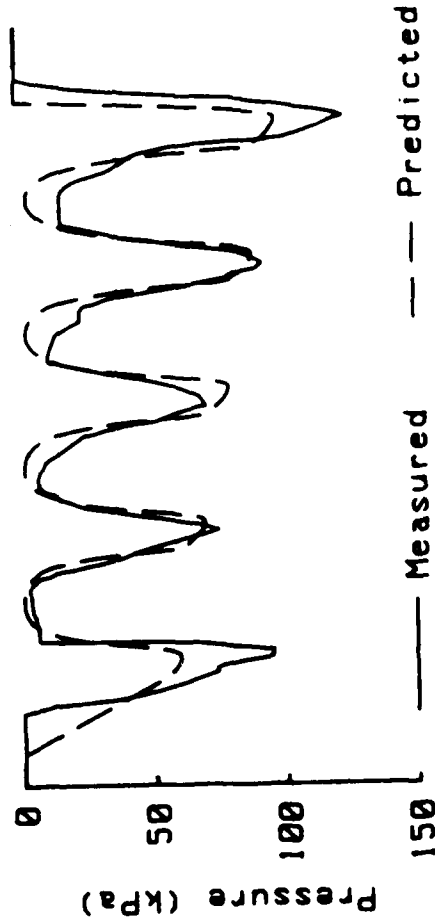


Fig. 7. Comparison of the pressure distribution predicted by the improved method with the measured one over a muskeg.

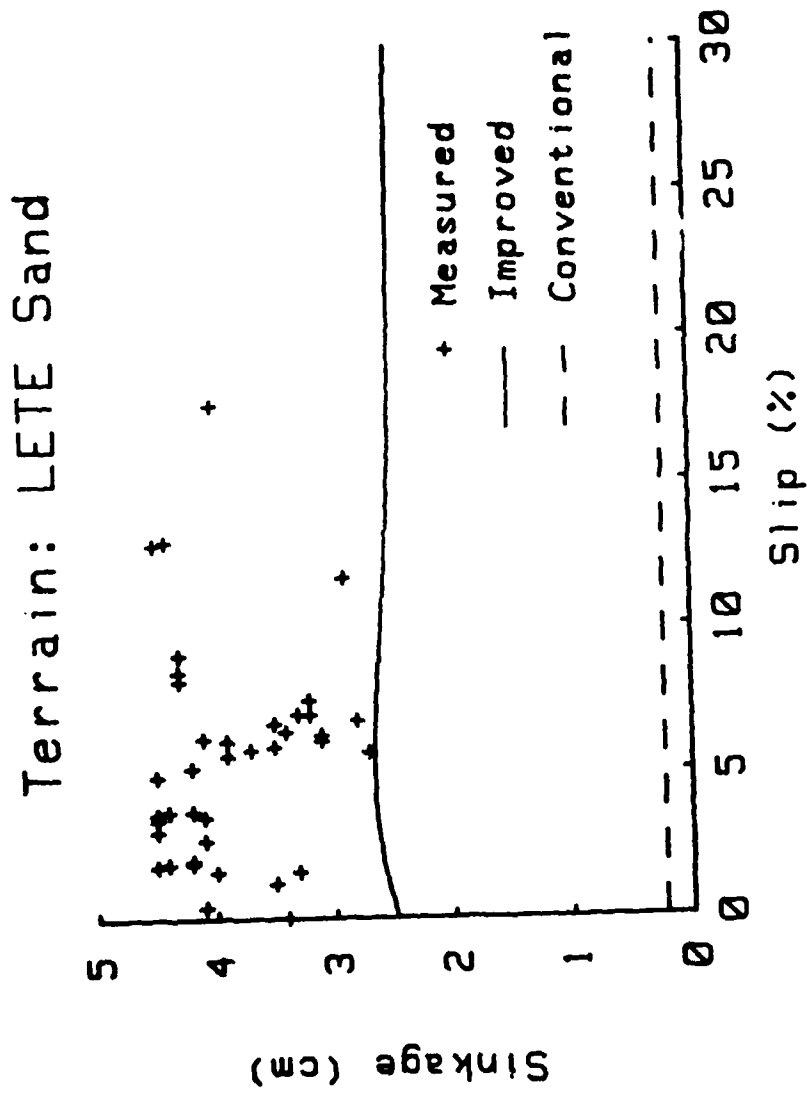


Fig. 8. Comparison of the sinkages predicted by the conventional and the improved methods with the measured ones over a sandy terrain.

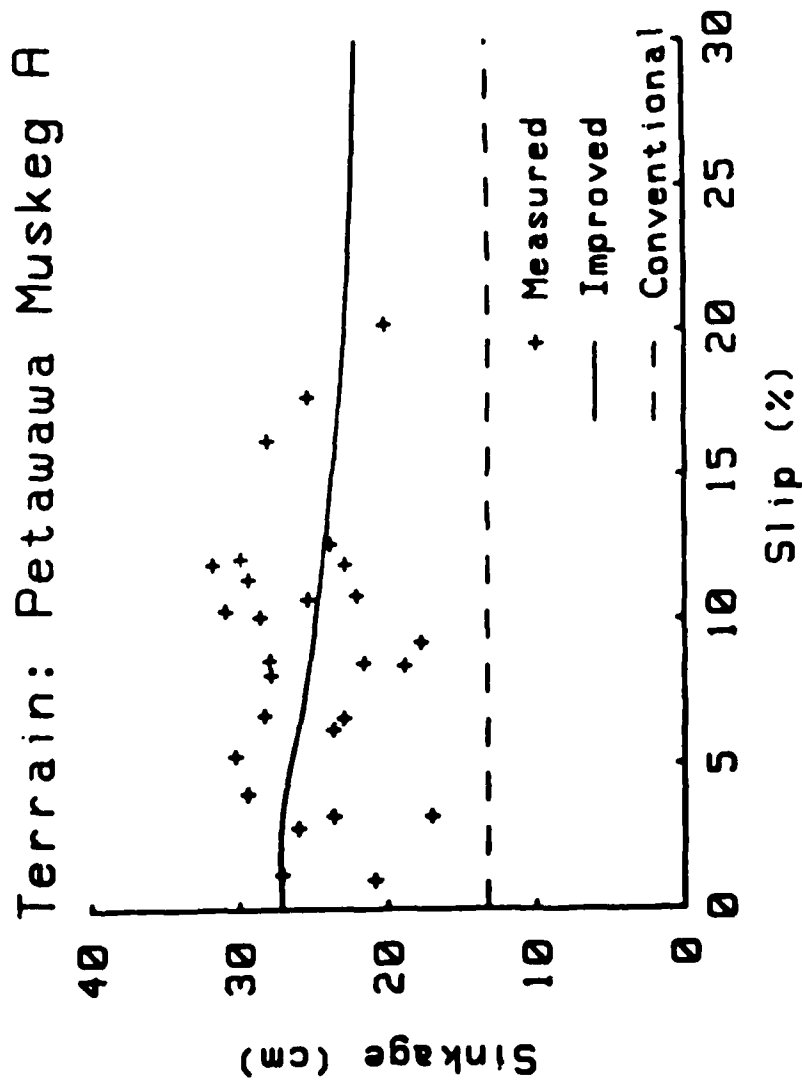


Fig. 9. Comparison of the sinkages predicted by the conventional and the improved methods with the measured ones over a muskeg.

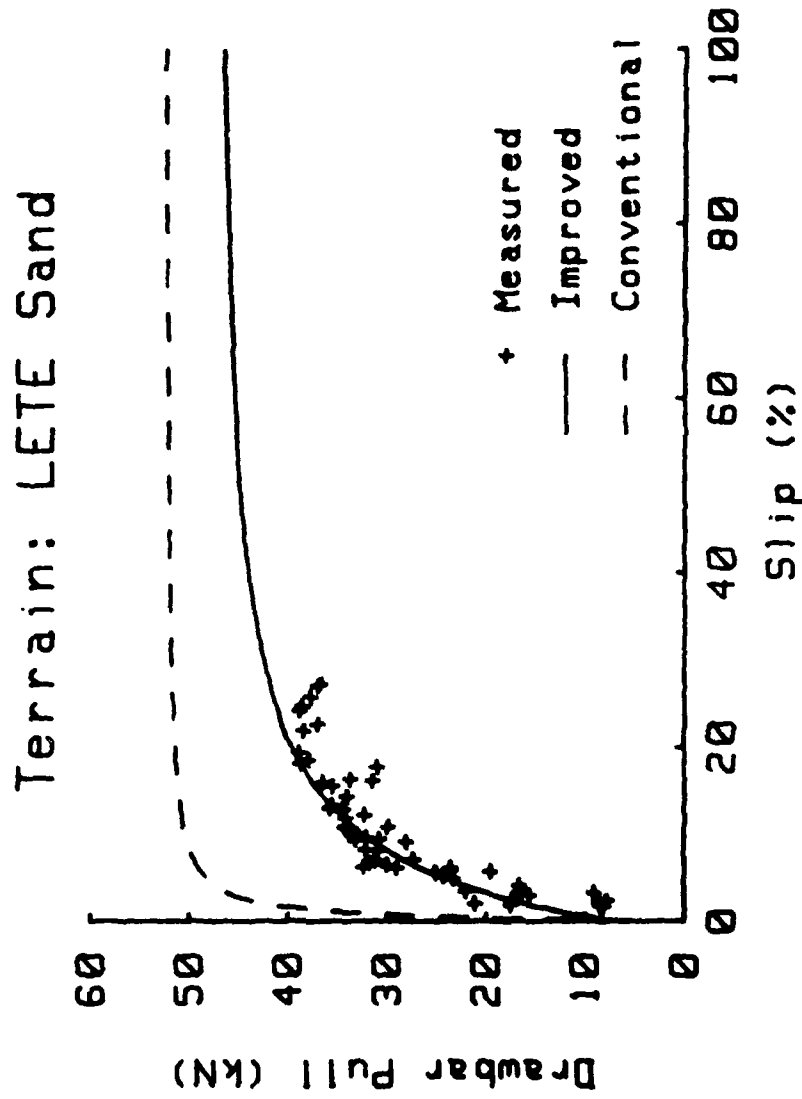


Fig. 10. Comparison of the drawbar performance predicted by the conventional and the improved methods with the measured one over a sandy terrain.

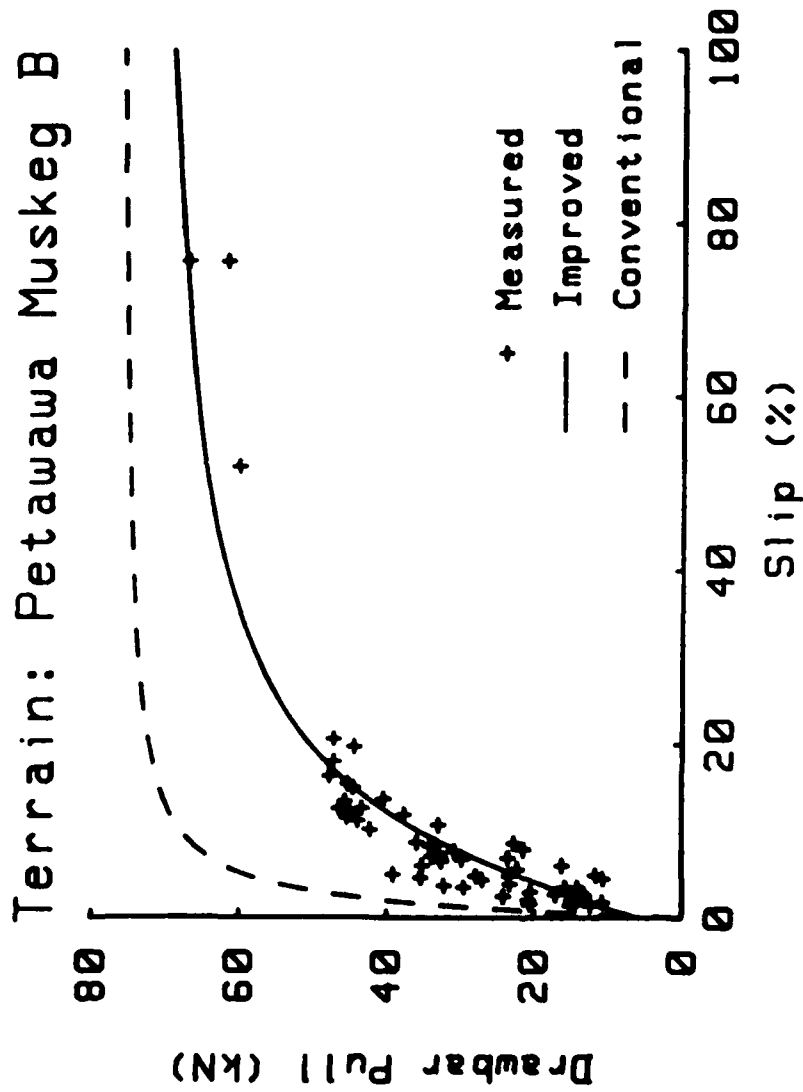


Fig. 11. Comparison of the drawbar performance predicted by the conventional and the improved methods with the measured one over a muskeg.

EFFECT OF HITCH POSITIONS ON THE PERFORMANCE OF TRACK-GROUSER SYSTEMS

K.N. YONG, H. ELMAMLOUK, and N. SKIADAKIS

GEOTECHNICAL RESEARCH CENTRE, MCGILL UNIVERSITY, MONTREAL, CANADA

INTRODUCTION

A number of previous research studies have been performed with the objective of developing a model to predict the performance and efficiency of tracks on ground terrain.

For proper modelling, several approaches documented in the literature have been based on:

1. Strip footing idealization of the track contact area with elastic stress distribution in the soil;
2. Energy dissipation within the failed soil mass; and
3. Energy conservation considerations for the track-grouser-soil system.

A change in the moment equilibrium of a track-grouser system will considerably affect its efficiency, since the pressure and sinkage distributions beneath the track will be altered. By and large most researchers report on the weight eccentricity effect, with little mention of the effect of the drawbar pull hitch position on track performance.

In this study, a predictive track model is developed based on energy principles to account for hitch position demonstrated in terms of the drawbar pull height. The experimental program conducted in the study is directed towards provision of results for comparison with the predictive model. It is reasoned that changes in the hitch position will induce differential sinkage causing variations in effective grouser penetration at the front and along the length of the track. Consequently, unless these are accounted for in motion resistance calculations, energy losses cannot be fully identified.

In the experimental program conducted to verify the theoretically predicted results, traction, drawbar pull and sinkage were measured on an experimental track under different test conditions, so that the efficiency of the track could be computed and compared to the predicted values.

EXPERIMENTATION

The experimental program consisted of a series of drawbar pull tests conducted in a test bed facility [Long and Kindisch, 1970] using a short-tired two-dimensional full track model, shown in Fig. 1. Since it was necessary to study the effect of the drawbar pull hitch position on the track performance, the drawbar pull height, e_y , above the level of the track was varied from 19.0 to 40.0 cm by assigning four different hitch positions: 19.0, 25.0, 33.0 and 40.0 cm. Table I is a summary of the experimental program.

AD-P004 277

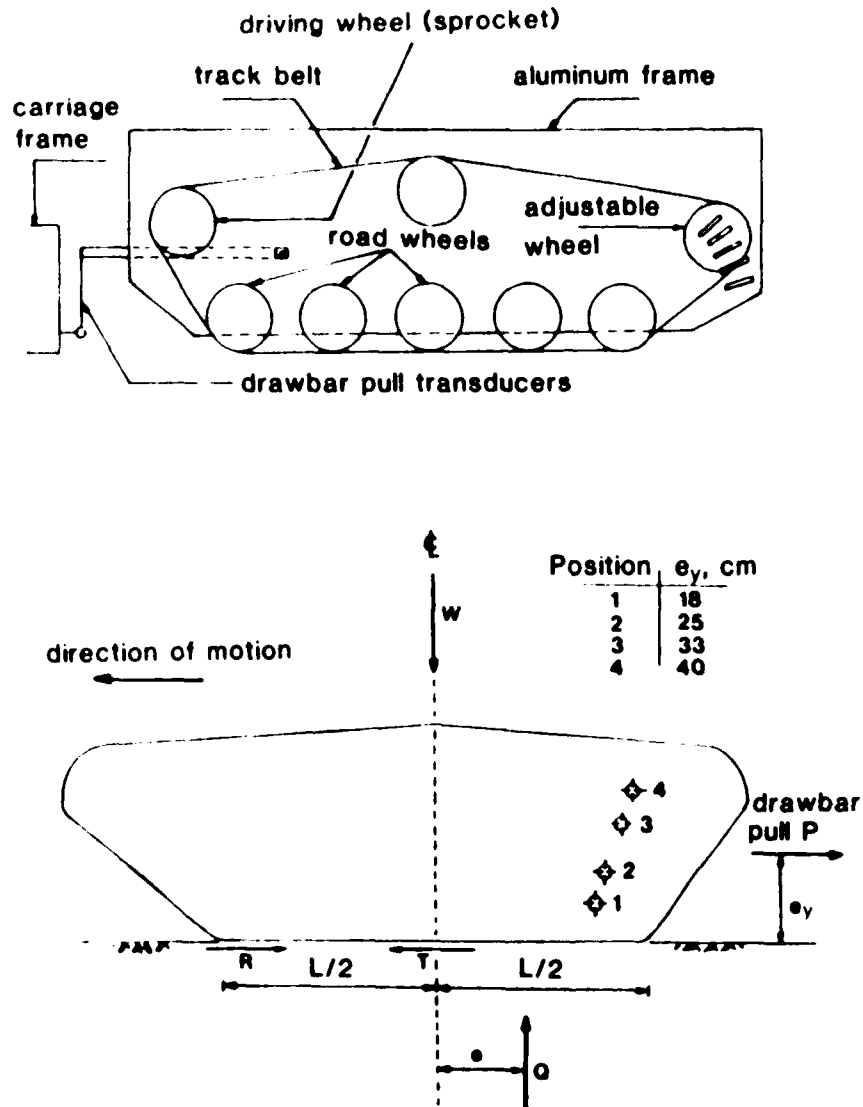


Fig. 1 Model Experimental Track Section and Drawbar Pull Hitch Position Locations

TABLE 1 EXPERIMENTAL PROGRAM

VARIABLES	
Soil	Kaolin clay, $S = 95-98\%$
Type of Grousers and Multiple Grouser	Standard, Passive and Aggressive (Yong et al., 1978)
Slip Rate	0 - 60%
Belt Tension	1.0 kN
Grouser Spacing	12.5 cm
Vertical weight	680 N
weight eccentricity	0.0 cm

OBJECTIVES AND MEASUREMENTS

1. Traction - slip relationships for different hitch positions.
2. Drawbar pull - slip relationships for different hitch positions.
3. Rear sinkage.
4. Track inclination.

ANALYSIS OF TEST RESULTS

The results of the drawbar pull tests conducted on each of the various grouser types can be expressed as force-slip rate relationships for each drawbar pull hitch position or force-'position'* relationships for different slips. The ratio between the drawbar pull and the traction force can be used as a measure of the track efficiency (Fig. 2). The higher the motion resistance is the higher the energy losses will be and the lesser will be the useful drawbar pull. Consequently, the efficiency of the track will be reduced. Figures 3, 4, and 5 show the relationship between drawbar pull, traction, sinkage, slip rate and position developed by the track section mounted by an aggressive grouser-track system. Similar results were obtained for two other grouser-track types. Traction, drawbar pull and rear sinkage were found to increase steadily with increasing slip rate.

During the whole series of testing, it was clearly observed that the drawbar pull was the highest for 'position' 1 at all slip rates, while the lowest values were recorded for 'position' 4. The measured traction forces were found to follow the same trends as indicated for the drawbar pull for all of the four 'positions'. While the rear sinkage showed an increase with increasing slip rate, it was found to be minimum for 'position' 1 and maximum for 'position' 4.

* 'Position' from thereafter will mean drawbar pull hitch position.

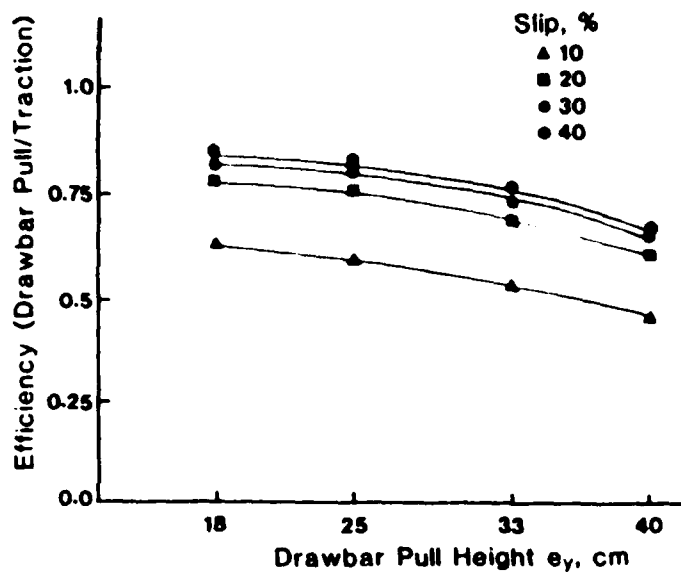


Fig. 2 Track Efficiency for Various Drawbar Pull Hitch Positions and Degrees of Slip

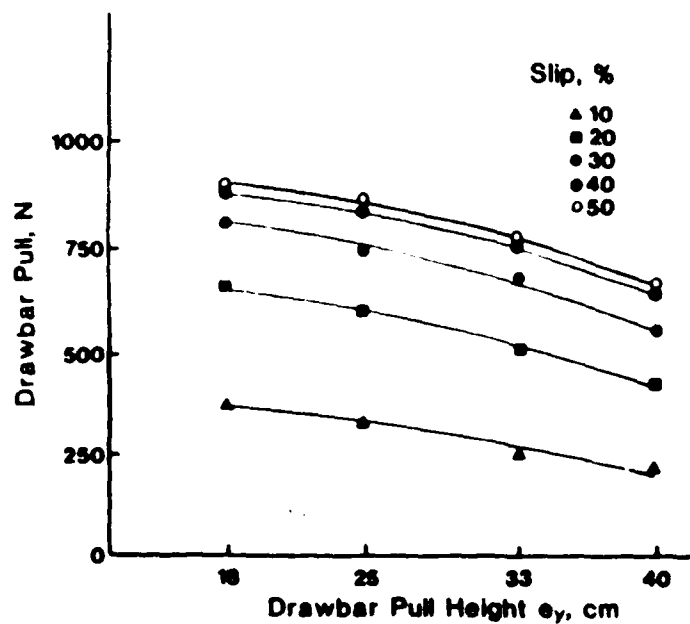


Fig. 3 Drawbar Pull Hitch Position Effect on the Drawbar Pull force for Various Slip Degrees

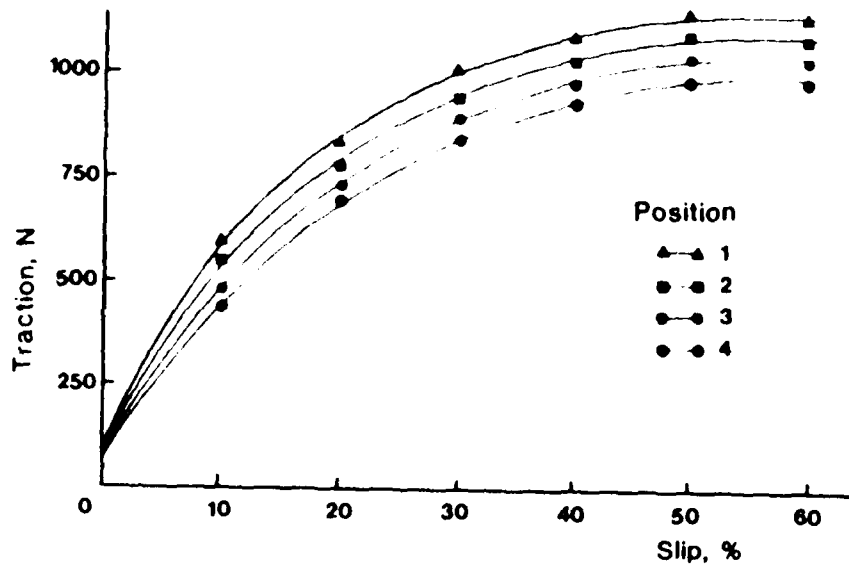


Fig. 4 Traction-Slip Relationship for Different Drawbar Pull Hitch Positions

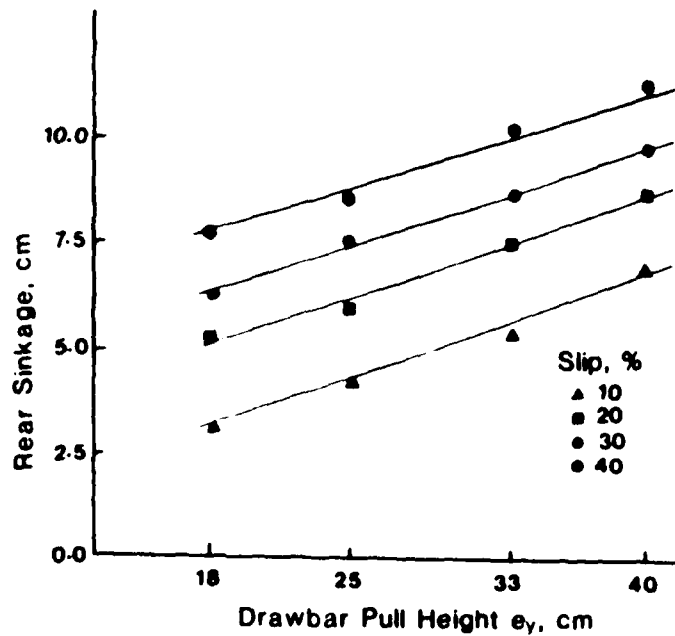


Fig. 5 Drawbar Pull Hitch Position Effect on the Rear Sinkage for Various Slip Degrees

PREDICTIVE MODEL

The energy balance equation for a track/grouser-soil system such as that shown in fig. 1 can be written as:

$$Mw = P v_c + D + C + S \quad (1)$$

where M = input torque applied at the sprocket

w = angular velocity of the sprocket

P = useful drawbar pull

v_c = carriage (vehicle) velocity

D = distortion energy ratio

C = compaction energy rate

S = shear slip energy rate

The analytical framework which is cast in terms of energetics is shown schematically in Fig. 6 where the prediction of the input (traction) and output (pull) energies of the full track under various loads, track/grouser characteristics and slip degrees are obtained using an iterative technique. The prediction procedure starts with a reasonable assumption of the pressure distribution beneath the track. As a first approximation an even pressure distribution can be assumed, i.e. eccentricity $e = 0$. From the measured pressure-sinkage relationships the corresponding grouser sinkage can be obtained. The excavated sinkage due to track slippage [1] can be added to obtain the total sinkage distribution beneath the track. Utilizing the sinkage-traction relationships, the mobilized traction force developed by each individual grouser can be obtained according to its displacement in the clay soil. Accordingly, the applied specific input energy (per unit travel) at the sprocket is calculated at any degree of slip using the following expression:

$$\text{Specific Input Energy} = I/(1-i) \quad (2)$$

where I = total mobilized traction beneath the track

i = slip degree = $1 - v_c/v$

v_c = carriage velocity

v = theoretical track velocity

The viscoplasticity analysis and computation of parasitic energy components as previously presented [2] can be used to predict the total energy losses (distortion, compaction, shear slip) beneath the track. This can be achieved by summing together the participation of each grouser beneath the track according to its sinkage and horizontal displacement $J = ix$ where x is the distance from the track contact point at the front to the position of the grouser under consideration.

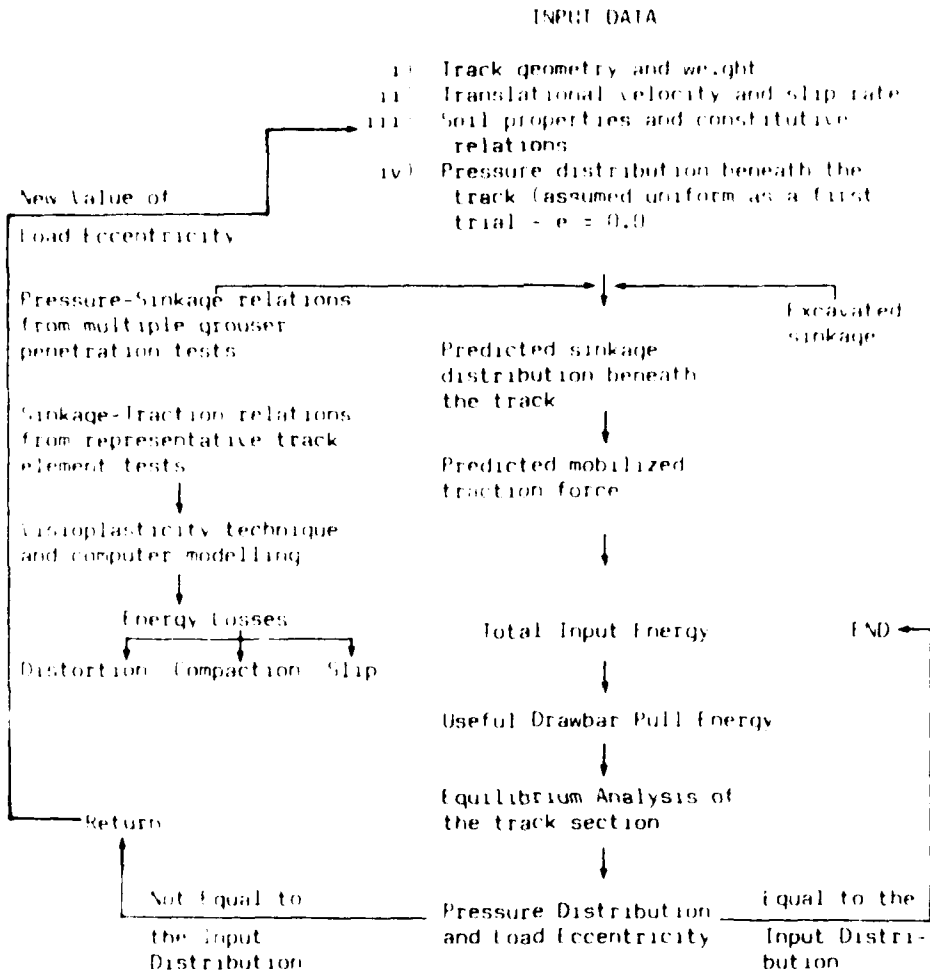


Fig. 6 Energy Analysis for the Track Performance Prediction

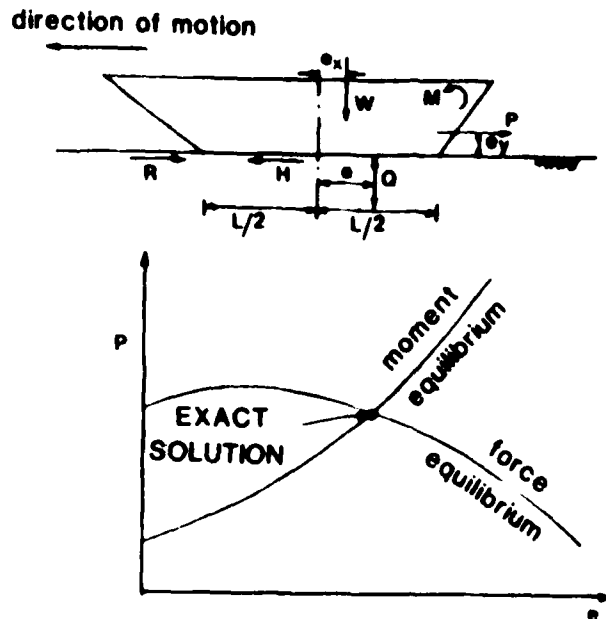


Fig. 7 Equilibrium Analysis of the Section Track

M - applied torque to the sprocket which is equal to the traction force multiplied by the radius r of the sprocket.

Taking the moment about point a , forces T , R , and Q are cancelled and the moment equilibrium equation can be written as

$$W(e - e_x) + M = P \cdot e_y \quad (4)$$

where e = eccentricity of the upward reaction Q from the centreline of the track loaded area

Equation (4) can be written as

$$e = e_x + \frac{P}{W} e_y - \frac{M}{W} \quad (5)$$

Three possible cases of pressure distribution can be obtained from the applied forces and moments, depending on the value of e as follows:

- 1) $e \leq L/6$: for this case both q_f and q_r are compression and the pressure distribution can be linearized to form a trapezoidal distribution as shown in the upper diagram of Fig. 8. The front and rear pressure q_f , q_r can be calculated using the following expressions:

$$\begin{aligned} q_f &= q_m (1 - 6e/L) \\ q_r &= q_m (1 + 6e/L) \end{aligned} \quad (6)$$

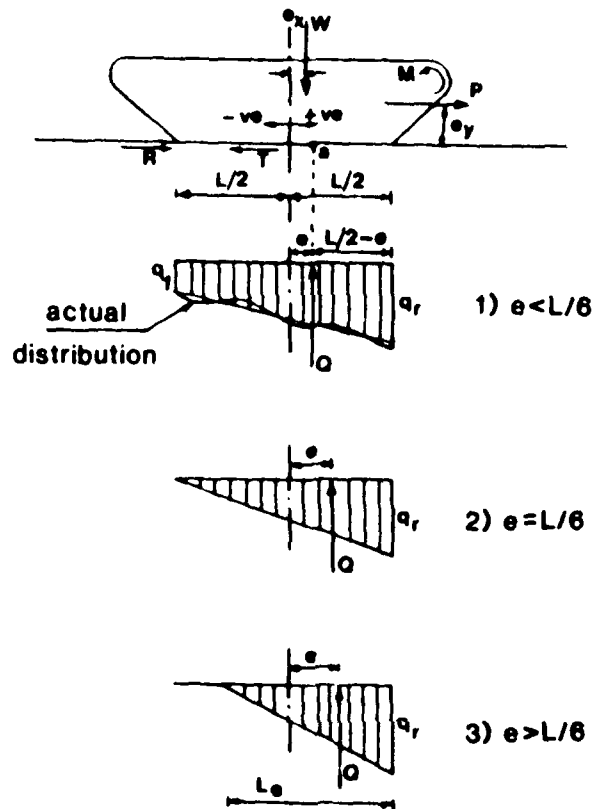


Fig. 8 Linearized Pressure Distributions Beneath the Track

where $q_m = W/bl$

- 2) $e = L/6$: Triangular pressure distribution which results from $q_f = 0$; the pressure at the rear point is given by

$$q_r = 2 q_m$$

- 3) $e > L/6$: In this case, part of the contact area beneath the track is unloaded and hence no pressure is transmitted to the supporting soil at the front portion of the track. The effective length of the bearing area is denoted as l_e . The lower diagram of Fig. 8 illustrates this case where the effective length l_e can be calculated as follows:

$$l_e = 3 (L/2 - e)$$

and the pressure at the rear is given by

$$\begin{aligned} q_r &= 2 q_m L/l_e \\ &= 2 q_m L/3 (L/2 - e) \end{aligned} \quad (7)$$

In addition to the energy consumed in deforming the soil due to slip (horizontal grouser displacement) some compaction energy loss is also incurred in track motion because of track sinkage. The procedure for computation of compaction energy due to track sinkage was developed previously [2] where this compaction energy can be calculated from the following equation:

$$\text{Specific compaction energy due to track sinkage} = \frac{(Z_r - Z_f)}{l(1 - i)} \frac{W}{b} \quad (3)$$

where Z_r, Z_f = track sinkage at rear and front, respectively

l = length of loaded area beneath the track

W = track weight

b = track width

Applying the equation of energy conservation, the total losses can be deducted from the input energy to yield the useful drawbar pull energy. This predicted drawbar pull satisfies only the force equilibrium condition of the track, but does not necessarily satisfy its moment equilibrium (since the assumed pressure distribution at the beginning is not necessarily the true one). Hence, equilibrium analysis of the track section as a free body is to be performed (Fig. 7) in order to obtain a new pressure distribution consistent with the predicted drawbar pull. A trial and error technique is then used where the new calculated pressure distribution is utilized in the next trial and the same procedure is repeated until the input and output pressure distributions are equal. At this stage, both the force and moment equilibriums of the track section are satisfied as shown in Fig. 7 and the drawbar pull is the exact value to be developed by the track under any given conditions as specified in the input data.

Equilibrium Analysis of the Section Track

To evaluate the pressure distribution beneath the track, its equilibrium under different straining actions should be considered as shown in Fig. 8 where a free body diagram of the section track is illustrated together with different possibilities of the generated pressure distribution. Straining actions of the section track can be identified in terms of the following forces and moments:

- w - the track weight which acts vertically at the centroid at distance e_x from the centreline of the track loaded area (positive towards the rear)
- T - mobilized traction force at the level of contact area beneath the track and the supporting soil
- R - motion resistance, assumed to act at the same contact level
- P - useful drawbar pull, assumed to act horizontally (the effect of track tilting is neglected) at height e_y above the contact level
- Q - total normal contact pressure beneath the track which is assumed to be linearly distributed

Effect of Drawbar Pull Position

The effect of the drawbar pull position on the predicted drawbar pull coefficient for the aggressive track system is shown in Fig. 9 for different slip rates. The results presented in this figure are the predicted values corresponding to the special case of zero weight eccentricity ($e_x = 0.0$). It is shown that there is an optimum pull eccentricity ratio (e_y/l) which produces the maximum pull coefficient for any specific slip. Plotted on the same figure is the line of maximums which connects the peaks of different curves. The optimum pull eccentricity ratio lies between 15 to 25 percent for this particular case of zero weight eccentricity. Increasing the pull eccentricity ratio beyond these specified limits considerably reduces the track performance due to the very significant taildown attitude of the track associated with the increase of the moment produced by the drawbar pull. The resulting tilting position of the track reduces the effective penetration height of the grousers at the track front while the track sinkage at the rear is increased. This situation causes motion resistance and energy losses to be of appreciable value and consequently reduces the efficiency of the track. A reduction of up to 100% in the drawbar pull coefficient will occur if the drawbar pull eccentricity ratio is increased from 20 to 60 percent.

Figures 10(a) to 10(d) examine the compound effect of both the pull eccentricity ratio (e_y/l) and the weight eccentricity ratio (e_x/l) on the predicted pull coefficient for different values of weight eccentricity ratio between -12 and +12%. From these figures it is concluded that the weight eccentricity can also play a great role in determining the track efficiency. Increasing the weight eccentricity towards the track front (-12%) will counteract the effect of the drawbar pull moment and lead to a more uniform pressure distribution beneath the track. In the other extreme (weight eccentricity ratio of 12%), the moment produced due to the weight eccentricity strengthens the effect of drawbar pull eccentricity in producing large pressure concentration towards the track rear, and consequently rapid reduction in the pull coefficient is obtained.

COMPARISON OF EXPERIMENTAL AND PREDICTED RESULTS

Figures 11, 12 and 13 show the predicted values of drawbar pull at different 'positions', for the standard, passive and aggressive track sections, respectively, used in the test series. The predicted results are expressed as a relationship between drawbar pull coefficient [drawbar pull/weight of track, P/W] and drawbar pull eccentricity ratio [height of drawbar pull above track level/length of track, e_y/l in %].

In addition, the experimentally measured values are plotted on the same figures with the predicted values, for reasons of comparison.

These figures clearly illustrate that the experimental and predicted results are in good agreement. Both the experimental and predicted values for the drawbar pull coefficients show an optimum pull eccentricity ratio which produces the maximum pull coefficient for any specific degree of slip. This eccentricity ratio is in the order of 20% for most cases.

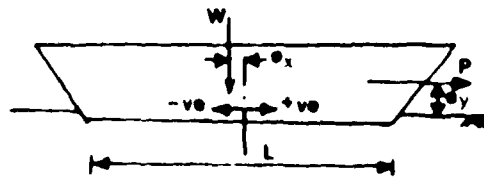
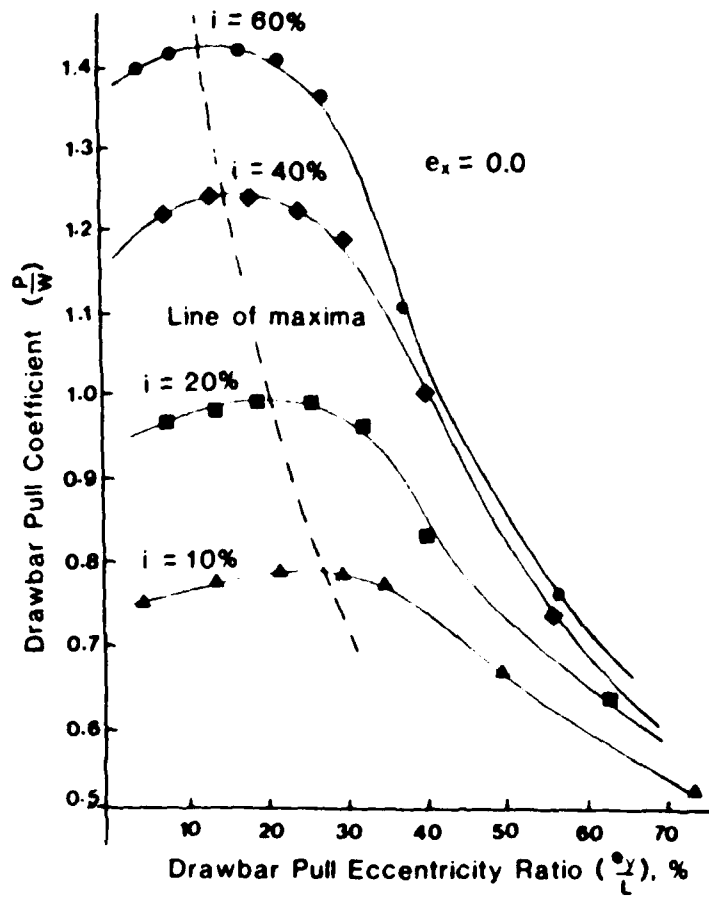


Fig. 7 Effect of Drawbar Pull Hitch Position on the Aggressive Track Performance

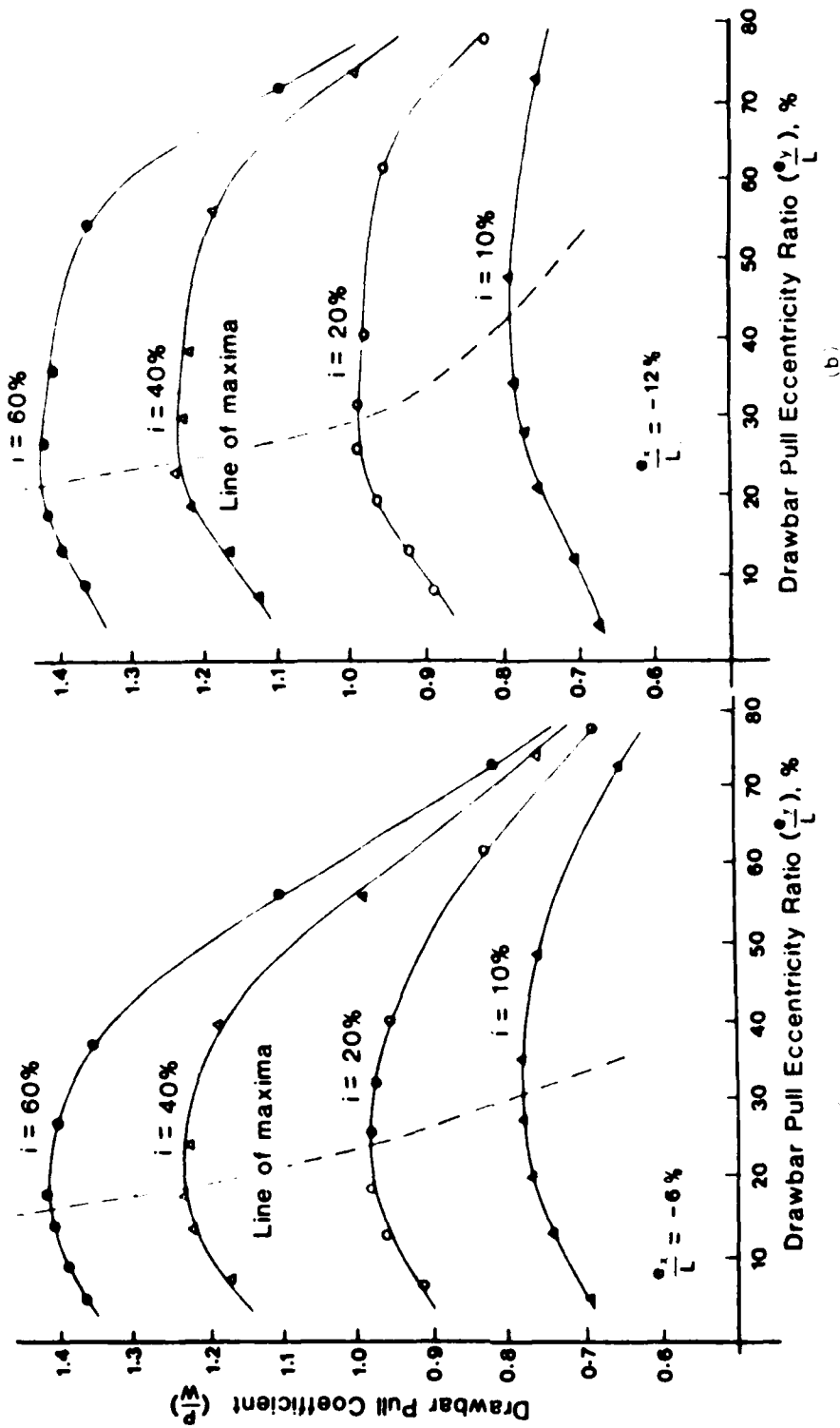


Fig. 10 Drawbar Pull Coefficient versus Pull Eccentricity Ratio (for various weight)

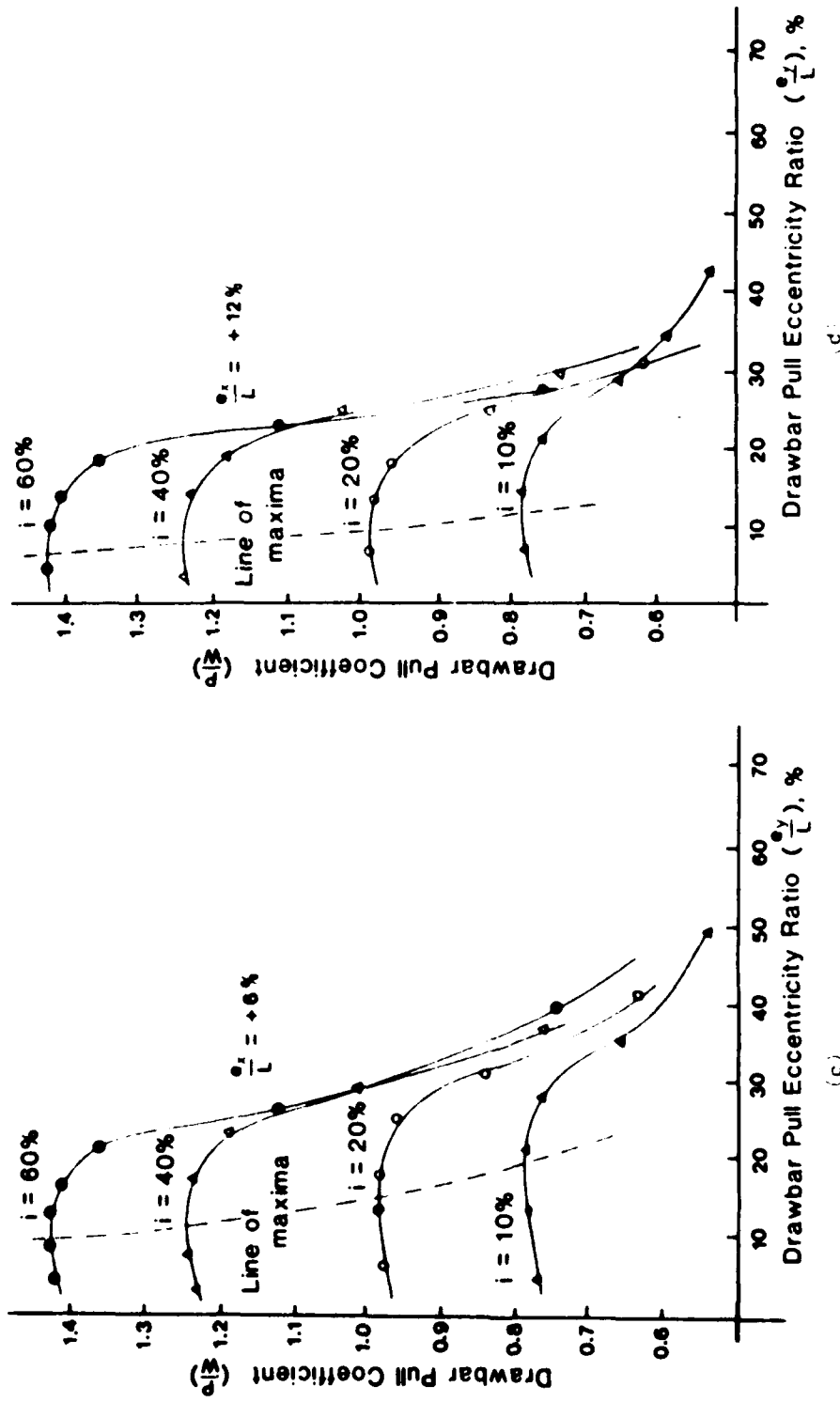


Fig. 10 Continued

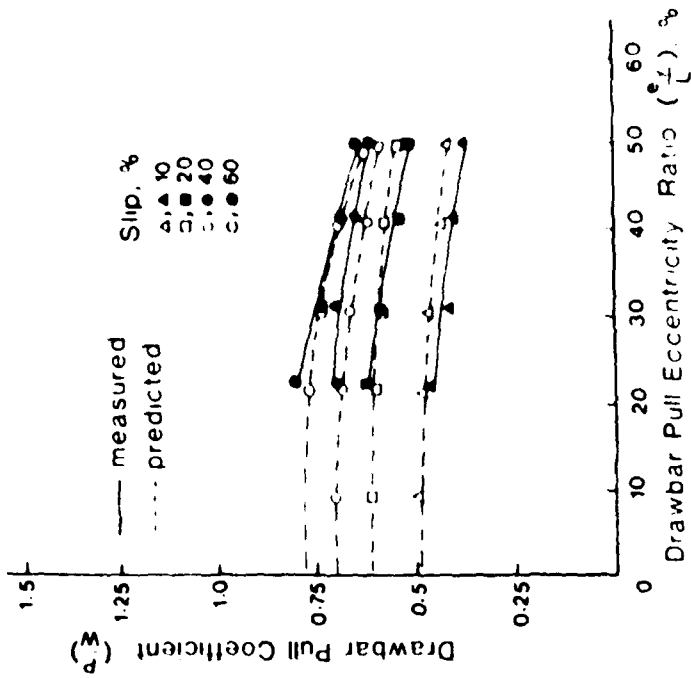


Fig. 11 Comparison of Measured and Predicted Drawbar Pull at Different Hitch Positions, Standard Track

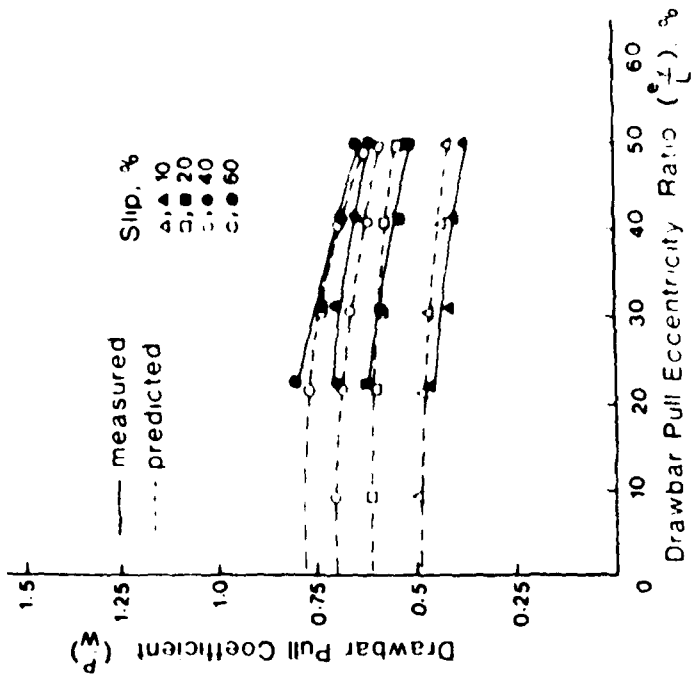


Fig. 12 Comparison of Measured and Predicted Drawbar Pull at Different Hitch Positions, Passive Track

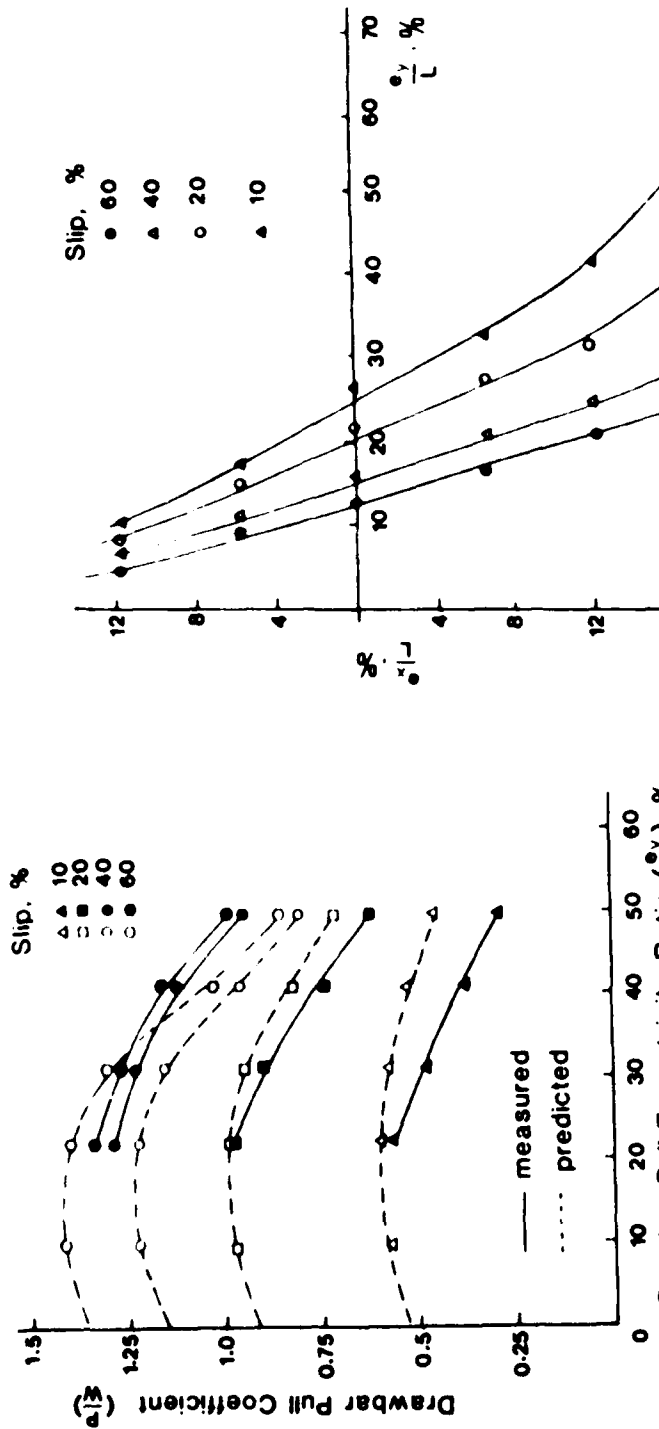


Fig. 14 Optimization Curves for Pull and Weight Eccentricities for the Aggressive Track

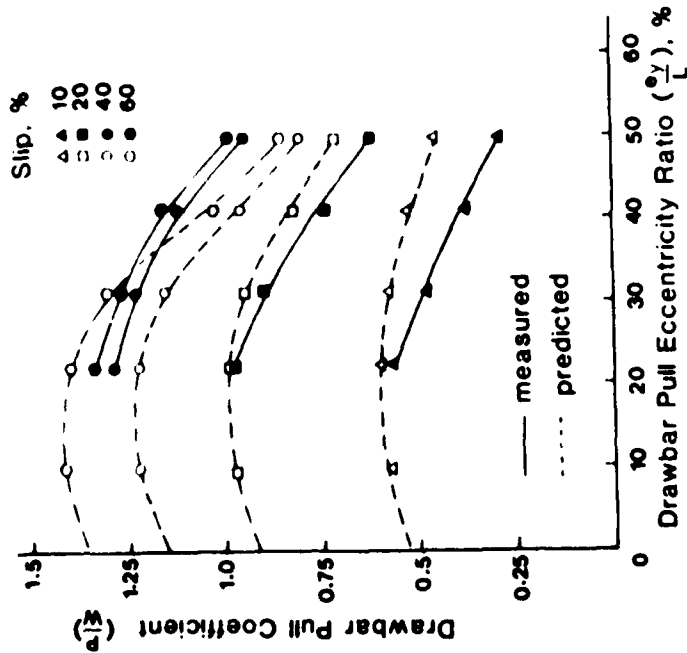


Fig. 15 Comparison of Measured and Predicted Drawbar Pull at Different Hitch Positions. Aggressive Track

CONCLUSIONS

The experimental program demonstrates the actual effects of the drawbar pull hitch position on the performance of tracks over soft soils.

For different track-grouser systems, it was found that both traction and drawbar pull deteriorate as the pull height is increased above the track contact level. In addition, track sinkage at the rear is considerably increased for higher hitch positions. Consequently, higher motion resistance and lower track efficiency can be experienced due to an increase of the drawbar pull height above a certain level.

Good correlation has been obtained between the experimentally measured track performance and the predicted values using the energetics predictive model. The importance of the hitch position can be further demonstrated from the predictive model in terms of the line of maximums shown in figs. 9 and 10. This line occupies a very narrow zone for the case of positive weight eccentricity (fig. 10(d)) where the moment produced by the weight and the drawbar pull are of the same sign, while this line extends to cover a wider range for the case of a negative weight eccentricity (fig. 10(a)) due to the opposite effect of weight and drawbar pull on the overall track moment equilibrium.

The results can be used to construct the optimization curve shown in fig. 14 for different degrees of slip. From this figure, it is possible to locate the best combination of the pull and weight eccentricity ratios in order to produce the maximum drawbar pulls and the highest track efficiencies. In other words, for any specified weight eccentricity it is possible to specify the associated drawbar pull eccentricity (or visa versa) which produces the maximum track performance at any desired degree of slip.

ACKNOWLEDGEMENT

This study was conducted under contractual arrangements with D.S.S. with project monitoring provided by Mr. J. Williams of D.R.F.S., Canada.

REFERENCES

1. Reece, A.R. (1964), "The Effect of Grousers on Off-the-Road Performance", J. Agricultural Eng. Res., Vol. 9, No. 4, p. 360
2. Yong, R.N., Youssef, A.F., and Elmagloul, H. (1978) "Soil Deformation and Slip Relative to Grouser Shape and Spacing", J. of Terramechanics, Vol. 15, No. 3, p. 129
3. Yong, R.N. and Windish, E. (1970) "Determination of Wheel Contact Stresses from Measured Instantaneous Soil Deformations", J. of Terramechanics, Vol. 7, Nos. 3 and 4, p. 57



GROUSER EFFECT STUDIES

Zhang Ke-jian

NORTH VEHICLE RESEARCH INSTITUTE, BEIJING, CHINA

ABSTRACT

After having finished the nonlinear finite element analysis of the sands under the tracked vehicle by a nonlinear finite element analysis program called NFAP, A modified Duncan model based on soil triaxial testing was suggested. The results of the experiment and the values predicted are well coincidence. The studies show that the grouser has important effect for the thrust on sands.

INTRODUCTION

Over a long period of time, the selection for structural parameters of a tractive device of vehicle is full of blindness. It led to the defeat of the tracked vehicle design due to lack of quantitative analysis on the basis of responses in off-road mobility analysis of tracked vehicle /1/. Thus the study of interactions of the soil-tractive devices to promote the off-road mobility will be of utmost importance. However, because of the complexity and nonlinear of surface soil property, up to now, the quantitative analysis of the interactions of the soil-tractive devices is still a problem that is not well solved.

The doctor's dissertation made by Perumpral at the Purdue university in 1969 is regarded as the earliest application of the finite element method in the field of terramechanics, on the basis of which he made calculations of the soil displacement field and the stress field under the rigid wheels /2/. As to the soil, he selected the segmented linear elastic strain-hardening model assuming that μ remains unchanged and E changes with the loading segments only. The computation results are close to that given by the WES research report based on the elasticity theory, but differ from the experimental results. The static and dynamic analysis were once carried out the soils under the rigid wheels by Chung and Lee /3/, who made use of the critical state concept put forward by Roscoe and Burland on saturated soils to study the soil nonlinearity and also made a comparison with the results computed by Perumpral. Besides, Yong, from 1972, began studying the possibility of applying the finite element method in the field of terramechanics and calculated the soil deformation energy loss under the loading conditions of both the rigid wheels /4/ and the flexible wheels

/5/ with the same consideration about the soil nonlinearity as Perumpral's.

In the early study of terramechanics, Bekker et al believed that the vehicle traction on sands depends on the vehicle weight while the grouser effect is very little according to the classical Coulomb theory. This authoritative understanding has been so deeply convinced by many people up to now that few people are willing to make deeper study about the track-soil system.

PRELIMINARY ATTEMPT ON QUANTITATIVE ANALYSIS

The track-soil interaction involves the track links in contact with the ground and the soil under its action. In the finite element analysis, the idealization of track-soil system and selection of the elastoplastic model and the analysis method will be of utmost importance. They involve computation accuracy and cost. The author /6,7/ made a finite element analysis of grouser effect by using the Drucker-Prager model in NFAP /8/.

1. Idealization of Track-Soil System

Theoretically speaking, it is better to analyze the grouser effect in a three-dimensional space. This is because the grouser shape changes in the direction of the track link width and the ratio of track link width to track link length is not large enough. Nevertheless, thousands of elements are required, even the three-dimensional displacement field and stress field of the soil under the track are to be roughly described. Even if the computer program could have the ability to carry out the computation, the computational work is too large to be accepted, and this requires simplification. At present, the midcross section of the track link in the width direction has been chosen for making a plane strain analysis because the grouser profile at this cross section can mostly represent the grouser profile of the whole link (account for 0.5 approximately) and is also the main part to offer the thrust. As a matter of fact, up to now, the wheel width has been assumed to be infinitely great in the finite element analysis of wheel (tyre) and soil interactions so as to carry out plane strain analysis.

In this study, the two links are 314 mm long and soil sample to be analyzed is 970 mm long and 405 mm high. The soil sample is subdivided, which includes 52 linear and 40 nonlinear elements with the total number of nodes being 128. To make the bandwidth of the stiffness matrix minimum, the nodes are basically numbered in a radiant manner. The constraints for the boundary displacement are close to the wheel-soil system analysis as made by Perumpral, Chung and Yong et al. In this study, as the soil considered is loose sand, it is reasonable to assume that the soil in contact with the track link is exerted a vertical uniformly distributed forces. The horizontal loading shall be converted from the vehicle field test data. In brief, the loading conditions are completely in conformity with the maximum traction conventional tests

of the tracked vehicles.

2. Selection of Elastoplastic Model and Analysis Method

The soil involved in this study is the dry loose sand, its volume density being 1.57 g/cm³, water content 0.6% and is categorized as rough sand according to the particle grade. Through the sample triaxial test, the four necessary soil constants are obtained as follows:

$$\begin{aligned} E &= 200 \text{ kg/cm}^2 & \mu &= 0.22 \\ C &= 0.04 \text{ kg/cm}^2 & \varphi &= 35.8^\circ \end{aligned}$$

In the NFAP program, the Drucker-Prager model is specially prepared for making plane strain analysis of soils and rocks. The model provided by Drucker and Prager is an extension of the Coulomb yield criterion [9]. In the principal stress space, the yield surface is a cone, its expression is

$$f = \sigma I_1 + J_2^{\frac{1}{2}} + k = 0 \quad (1)$$

where σ and k are positive constants. In the NFAP,

$$\sigma = \frac{\sin \varphi}{\sqrt{3} \sqrt{3 + \sin^2 \varphi}} \quad (2)$$

$$k = \frac{\sqrt{3} C \cos \varphi}{\sqrt{3 + \sin^2 \varphi}} \quad (3)$$

The yield surface defined by the von Mises yield criterion in the principal stress space is a column, its expression is

$$f = J_2^{\frac{1}{2}} - \tau_s = 0 \quad (4)$$

where τ_s is the test-determined yield stress in pure shear. Although the von Mises criterion was derived in accordance with nonfriction materials such as metals, the effective stress field and effective strain field obtained by using the criterion conditionally are still useful.

In this study, the increment iteration method is used in the nonlinear analysis technique. The load is to be increased step by step in 24 steps, when one load is charged it is allowed to regenerate the stiffness matrix and to do up to 15 equilibrium iterations. In view of the nonlinear property of the soil, when the Drucker-Prager model is applied, the relative error used to measure the convergence of the equilibrium iterations is taken as 0.02.

3. Computation Results and Discussion

The elastoplastic Drucker-Prager model (hereinafter referred to as Model 2) and the elastoplastic bilinear hardening von Mises model (hereinafter referred to as Model 3) were used in the computation.

Fig.1 shows the trace of node displacement obtained by using

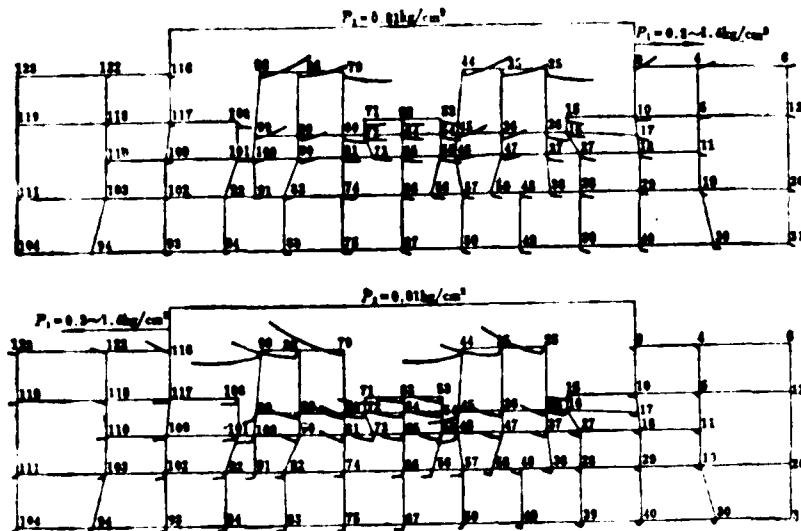


Fig.1 Node Displacement Traces

the Model 7, the top diagram indicating the reversal loading and the lower one indicating the forward loading. It can be seen from Fig.1 that the node displacement caused by forward loading is usually greater than by reversal loading. The displacement mean value of the 17 points in the neighborhood of the track links under forward and reversal loading conditions is taken. The displacement generated by $P_1 = 1.0 \text{ kg/cm}^2$ under the forward loading condition is equal to that generated by $P_1 = 1.16 \text{ kg/cm}^2$ under the reversal loading condition. Fig.2 illustrates the plastic area calculated by using the Model 7, the top diagram indicating the reversal loading and the lower one indicating the forward loading. It can be seen from this figure that the plastic area generated when $P_1 = 0.8 \text{ kg/cm}^2$ under the forward loading condition is analogous to that when $P_1 = 1.0 \text{ kg/cm}^2$ under the reversal loading condition; and the plastic area generated when $P_1 = 1.0 \text{ kg/cm}^2$ under the forward loading condition is analogous to that when $P_1 = 1.2 \text{ kg/cm}^2$ under the reversal loading condition. In other words, under the same applied loading condition, it is more easily for the forward loading to get yielding failure in soil; or the reversal loading may be 20% greater than the forward loading to make the same soil failure. The effective stress field and effective strain field as derived by using the Model 3 are illustrated in Figs.3 and 4. The top diagrams indicate the reversal loading and the lower one indicate the forward loading. Both figures are given in the form of contour. It is obvious from Figs.3 and 4 that when P_1 is equal to 1.0 kg/cm^2 , the effective stress and strain generated in the soil under the reversal loading condition are smaller than under the forward loading condition.

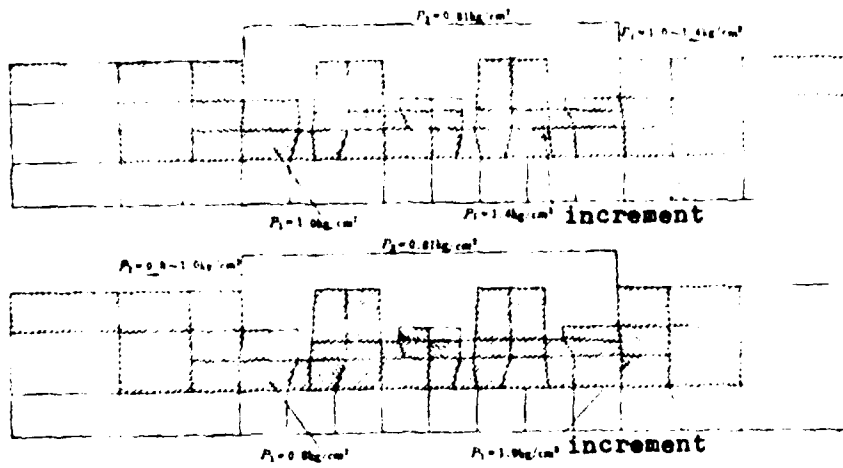


Fig.2 Plastic Yielding Areas

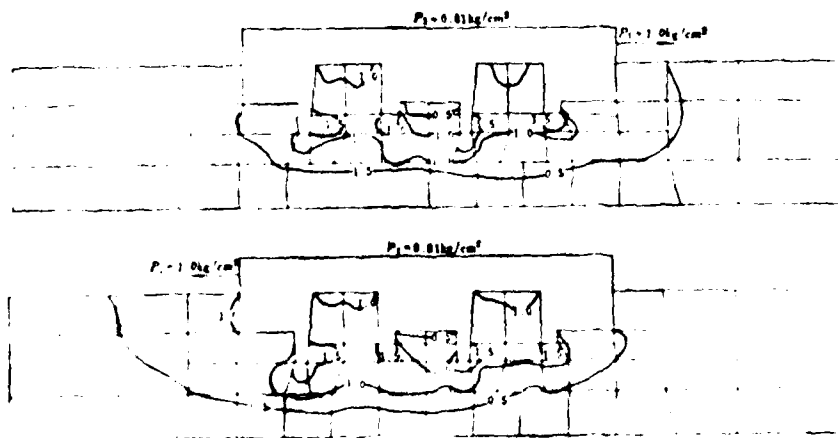


Fig.3 Stress Contours

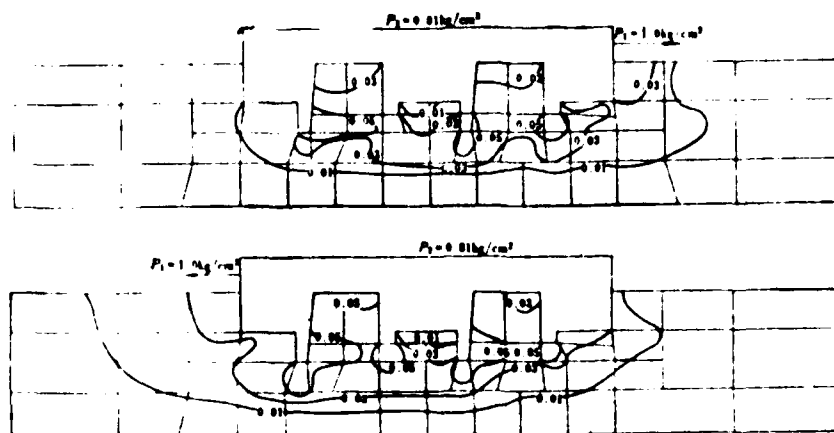


Fig.4 Strain Contours

For quantitatively describing the stress state of soil under the track, the $\sigma_{\max} - \sigma_{\min}$ figure is useful. Fig.5 is obtained from computation results by Model 7. It can be seen from Fig.5 that the pulling states appear on down-front of the low teeth and rear of the track link under the forward loading condition, but on down-front of the high teeth and rear of the track link under the reversal loading condition. The higher compressive stress states appear on down-front of the other grousers. It is obvious from Fig.5 that the responses under the forward loading and reversal loading are different. It shows once again that the grouser has important effect for the thrust on sands.

Fig.5 $\sigma_{\max} - \sigma_{\min}$ (o - pulling)

EXPANSION FOR NFAP

In the field of terramechanics, the constitutive models used in the finite element analysis are usually taken from geotechnical engineering. However, the properties of surface soils involved in terramechanics are obviously distinguished from the properties of soil in the foundations concerned in geotechnical engineering. Thus in using the constitutive models indiscriminately, the error would be introduced. In order to improve the confidence of computation, the author /10/ suggest a modified Duncan model based on soil triaxial testing.

1. Modification of Duncan Model

In terra-mechanical problems, while the vehicle travels on the ground, the lateral earth pressure σ_1 increases in some ratio with the axial pressure σ_3 . Under the proportionally loading conditions, soil mass has additional strength due to the increasing of σ_3 , thus the soil's stress-strain relations exhibit inclined asymptotes rather than level asymptotes. Fig.6 shows the triaxial testing results of the sand and sandy loam.

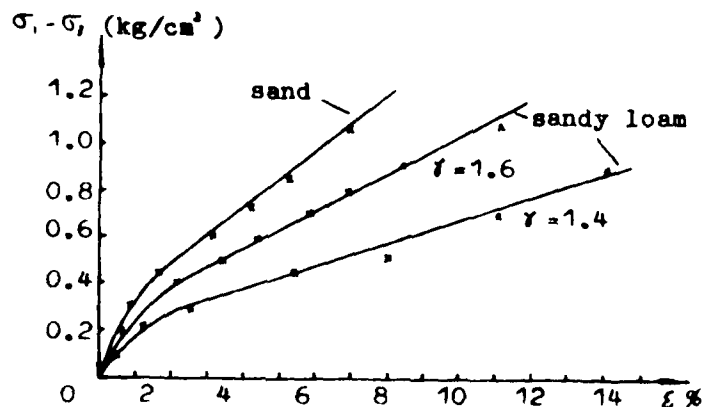
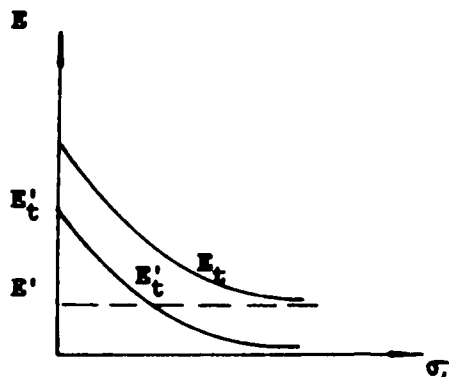


Fig.6 Triaxial Testing Results on Sand and Sandy Loam ($\Delta\sigma_1/\Delta\sigma_3 = 2$)

The tangent elastic modulus E_t is expressed in two different approaches according to the conditions of soils.

a) For the soils which have large density and higher consolidation pressure, when σ_3 is a constant, the hyperbolic regression equation of Duncan is acceptable for practical purposes. Its tangent elastic modulus E_t is shown in Fig.7. While $\Delta\sigma_1/\Delta\sigma_3$ is a constant, the value of E_t approaches

Fig.7 Relationship between E and σ_i

some fixed value E' and can be expressed as

$$E_t = E'_t + E' \quad (5)$$

For sandy loam

$$E' = 30 (\sigma_i + 0.25) \tan\left(\frac{9\pi}{K + 20}\right) \quad (6)$$

For sand ($C < 0.05$ kg/cm³)

$$E' = 30 (5 \sigma_i + 0.25) \tan\left(\frac{9\pi}{0.01K + 20}\right) \quad (7)$$

In Eqs.(6) and (7), K is bulk modulus (kg/cm³), and σ_i is an initial consolidation pressure (kg/cm³).

b) For the loose soil, relationship between stress and strain does not exhibit a hyperbolic relation. If a hyperbolic regression is used, a low confidence will be resulted. The elastic modulus of the soil is less than what is obtained by hyperbolic regression initially, but is greater after reaching a fixed stress level. In order to reflect this behavior of loose soil accurately, the expression of E'_t is modified as follows

$$E'_t = \frac{3}{4} \frac{K + 63}{83} \frac{(\sigma_i - \sigma_f) + \frac{1}{2}(\sigma_i - \sigma_f)_f}{(\sigma_i - \sigma_f)_f} E_1 \quad (8)$$

In view of the above analysis for E'_t , the author suggests that the tangent Poisson's ratio μ'_t could be obtained directly from the following equation:

$$\mu'_t = (1 - E_t/3K)/2 \quad (9)$$

Such a treatment will be simple and possibly more accurate, because μ'_t is modified accordingly.

2. Implementation of Modified Duncan Model in Finite Element Analysis

The formulation of the modified Duncan model discussed in the previous section has been implemented into the NFAP. The responses of soils loaded with track links are analyzed and the results are given below.

The three links are 450 mm long and the soil sample to be analyzed is 2350 mm long and 1630 mm high. The track links are subdivided into 19 linear elements and the soil sample are subdivided into 111 nonlinear elements. The total number of nodes is 173.

The displacement mean value of the 16 points in the neighborhood of track links under forward and reversal loading conditions are given. It is 0.164 mm under the forward loading condition and it is 0.153 mm under the reversal loading condition. The displacement under the forward loading condition is 7 % greater than that under the reversal loading condition.

It can be seen from Fig.8 that the stress generated under the forward loading condition is much more than that under the reversal loading condition. In order to compare the failure ratio of each layer of soils, their averages are listed below:

	Forward Loading	Reversal Loading
First Layer (0 - 5.8cm)	0.26	0.19
Second Layer (5.8-8.3cm)	0.37	0.29
Third Layer (8.3-13cm)	0.35	0.28

It can be seen that the failure ratio under the forward loading condition is more than 20% in each layer.

EXPERIMENT INVESTIGATION

A laboratory experiment was conducted to compare the predicted stress values with the measured values. The boundary conditions in both cases are similar. The uniform pressure on the soil surface is applied by a specially designed flexible track links. Four testings are repeatedly made for each scheme to eliminate the error of accidental factor in the testing. The adhesive traction of the track links is equal to the testing total traction minus the resistance caused by pushing soil. This resistance is computed by Bekker's equation /10/. Substituting for soil and track link parameters becomes:

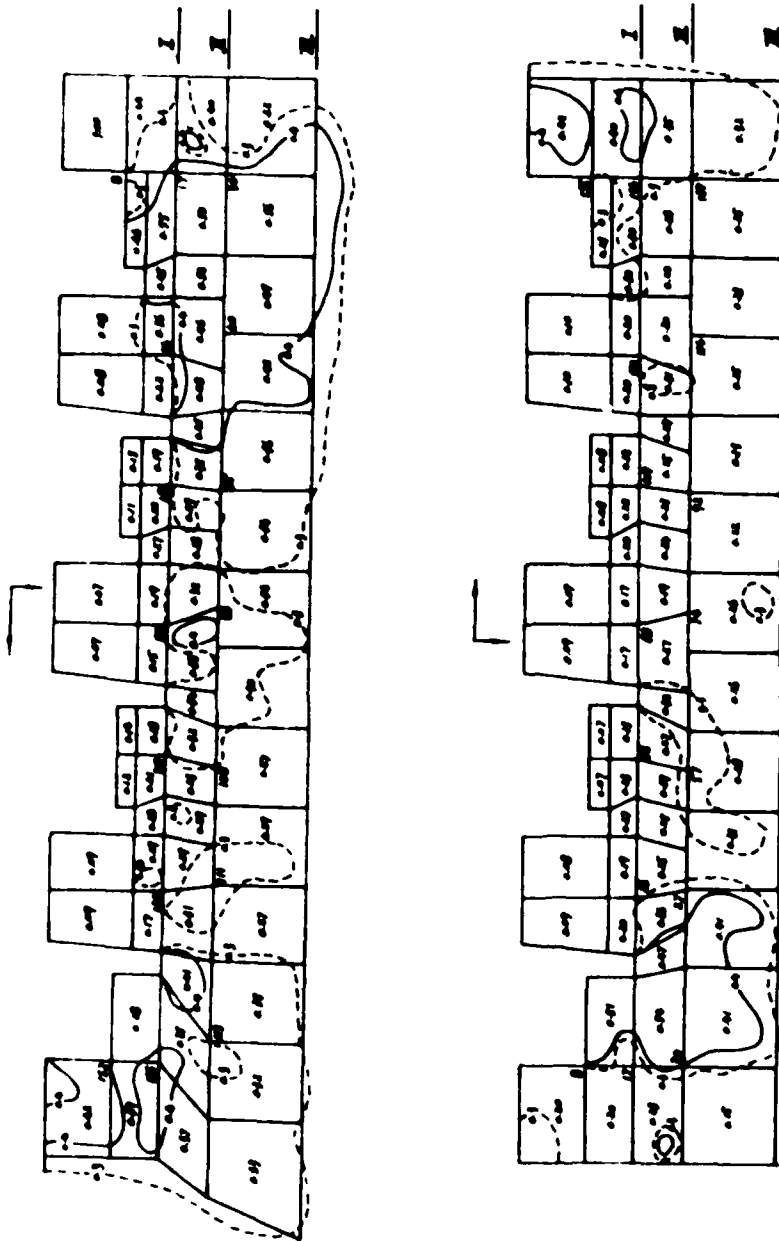


Fig. 8 Failure Ratio Contours of Soil Mass under Action of the Track Links

$$R_b = 8.775 Z + 0.555 Z' \quad (10)$$

where Z is the sinkage of track link.

The testing results show that the adhesive traction under the reversal loading condition is approximately 14% greater than that under the forward loading condition whether the number of the track link is one or two. Fig.9 shows the relationships between adhesive traction and horizontal displacement under one track link and two track links.

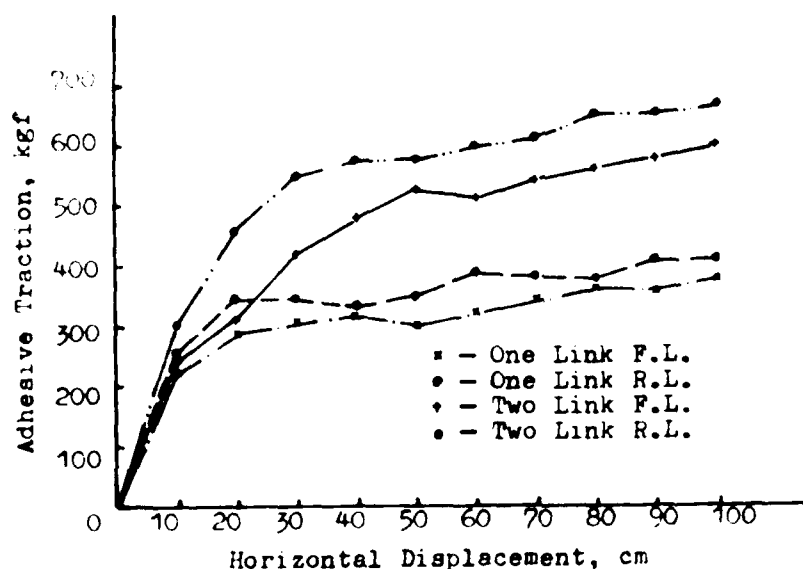


Fig.9 Relationship between Adhesive Traction and Horizontal Displacement

CONCLUSIONS

The results of computation and experiment show that the modified Duncan model and the expanded NFAP provide a means for quantitative analysis of terra-mechanical problems. The geometry of grouser has important effect for traction developed by track links on sands.

REFERENCES

- /1/ Andrews, J.N., Jr. and G.S. Sexton, " Relationship of obility Requirements and Testing." Off-Road Mobility Research Symposium, Cornell Aeronautical Laboratory, June. 1968.
- /2/ Perumpral, J.V., Liljedahl, J.B. and W.H. Perloff, " Numerical Method for Predicting the Stress Distribution and Soil Deformation Under a Tractor Wheel." Journal of Terramechanics. 8(1), 1971.
- /3/ Chung, T.J. and T.K. Lee, " Dynamics of Viscoelastoplastic Soil Under a Moving Wheel." Journal of Terramechanics. 12(1), 1975.
- /4/ Yong, R.N. and E.A. Fattah, " Prediction of Wheel-Soil Interaction and Performance Using the Finite Element Method." Journal of Terramechanics. 13(4), 1976.
- /5/ Yong, R.N., Fattah, E.A. and P. Boonsinsuk, " Analysis and Prediction of Tyre-Soil Interaction and Performance Using Finite Elements." Journal of Terramechanics. 15(1) 1978.
- /6/ Zhang Ke-jian and Zhang Xiang-lin, " Analysis of Grouser Effect Using the Finite Element Method." Acta Armamentarii, No.4, 1982.
- /7/ Zhang Ke-jian, " Discussion for Mechanical Model in Finite Element Analysis of Grouser Effect." Transactions of Chinese Society of Agricultural Machinery, No.2, 1983.
- /8/ Chang, T.Y. and S. Prachuktam, " NFAP — A Nonlinear Finite Element Analysis Program." Report No. SE76-3, The University of Akron, October 1976.
- /9/ Drucker, D.C. and W. Prager, " Soil Mechanics and Plastic Analysis or Limit Design." Quart. of Appl. Math. Vol. 10, No.2, 1952.
- /10/ Zhang Ke-jian and Zhang Xiang-lin, " Modified Duncan Model and Its Implementation." Proc. 1983 ASCE EMD Specialty Conference, Purdue University.
- /11/ Bekker, M.G., " Off-the-road Locomotion." Ann Arbor: University of Michigan Press, 1960.



TOPIC 4

PRACTICAL ASPECTS OF RIDE DYNAMICS

RIDE COMFORT OF OFF-ROAD VEHICLES

GUENTER H. HOHL

AUSTRIAN FEDERAL ARMY, VIENNA

1. INTRODUCTION

Because of the roughness of the terrain they encounter, cross country vehicles experience more shock and vibration than ordinary road vehicles. Hence off-road speed is usually limited by the ability of the operator to withstand these vibrations to negotiate and to retain adequate control of the vehicle. In addition to other factors, the comfort of the operator, which contributes to his general safety, also depends on the physical characteristics of the seat, which is the link between the driver and the vehicle.

In the last years great attempts have been made to improve the driver seat. Such developments however should not be at the expense of the driver's ability to "feel" the terrain. Still the operator is usually better situated than the other crew members as he is able to control speed (the main factor affecting vibration) and to observe obstacles in front of the vehicle. Soldiers sitting in the rear of a truck or in the crew compartment of a tracked vehicle are affected not only by vibrations but also by exhaust gas and, last, but not least, by psychological effects.

Hence a new definition of the term "Speed" should be made

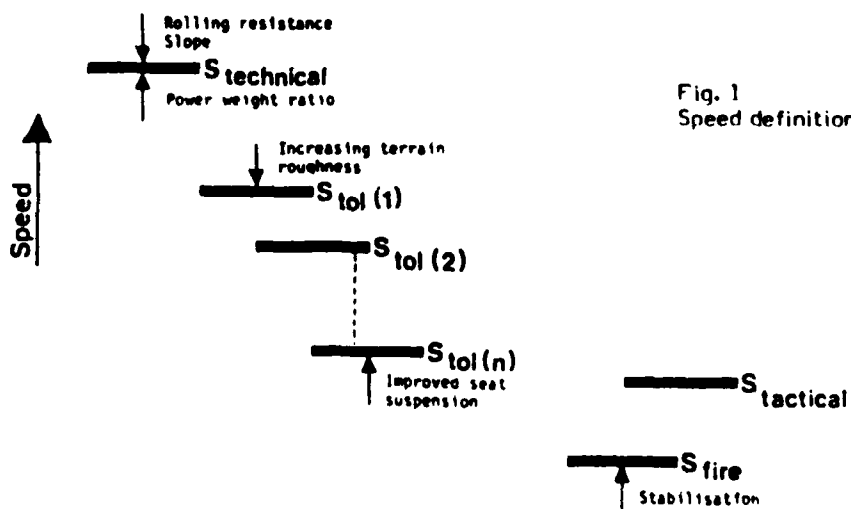


Fig. 1
Speed definition

S_{technical}

is defined as the highest speed which is possible from the technical point of view, excluding consideration of human factors. For certain terrain situations this speed is nearly proportional to the power/weight ratio and it decreases with the increase of rolling resistance and slope. As in recent years the power/weight ratio of cross country vehicles has been improved, the technical speed is relatively high, even under poor environmental conditions. In many cases however this high speed, although technically possible, can not be tolerated by the human body. The driver will reduce the speed to the

S_{tolerable}

This is defined as the speed which is tolerable for the crew members to carry out their duties efficiently. The tolerable speed will not be the same for all crew members, and therefore this speed is further subdefined by the several crew members (Crew member 1, 2 ... n) For military purpose the

S_{fire}

must also be considered. The "fire-speed" is defined as the speed in which the weapons are fired, achieving specific results in accuracy. S_{fire} will increase by using stabilisation devices. In military operations a cross country vehicle can not to be considered in isolation since it is employed in conjunction with other vehicles in a military formation for specific tactical tasks. Therefore the

S_{tactical}

the "tactical speed" must be considered. The tactical speed should not be higher than the lowest S_{tol}.

With these factors in view it is the intent of this paper:

- a) to present a general overview of national and international standards and recommendations and publications which deal with the field of measurement of whole body vibrations.
- b) to present a method to assess the ride comfort of cross country vehicles with "K-Wert" (K-value) according to VDI-recommendations.
- c) to report on tests, conducted by the author, with wheeled army vehicles of varying tire pressures, speed, tire-size, and terrain, and to present the results on a comparison test between wheeled and tracked armoured vehicles of the same size.

2. MEDICAL CONSIDERATIONS

The human body itself has no special sense organ to register mechanical vibrations, nor does it have any specific defense mechanism to counter those vibrations. The influence of mechanical vibrations on human subjects may be tested either by collecting statistical data or by experimental research. Both methods of investigation result in the conclusion that a human being exposed to mechanical vibrations can be affected by reduced comfort, fatigue decreased proficiency, and finally by impairment of his safety and health.

The reasons for human reactions to mechanical vibrations experienced by cross country travel can be categorized into three groups. These are

- Physical Effects
- Physiological Effects
- Psychological Effects

2.1 Mechanical models (Physical effects)

For the purpose of investigating the effects of mechanical vibrations, the human body should not be regarded as a rigid mass. Theoretical models of varying degree of complexity have been developed by several researchers to represent the human body as a mechanical system of masses, springs and dampers.

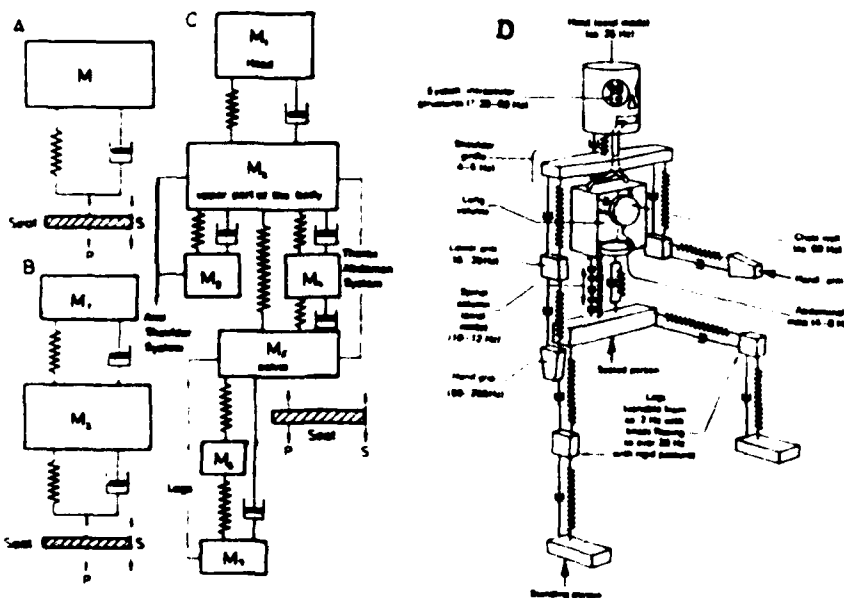


Fig. 2

Mechanical substitute system for the human body. (Dieckmann and Coermann modified by Dupuis)

- A 1mass-1spring1damper-system
- B 2masses-2springs-2dampers-system
- C 7masses-7springs-5dampers-system

D Multiple masses-springs-dampers system (Brüel & Kjær)

Dieckmann regards the accuracy of model A to be sufficient up to a frequency of 10 Hz, which includes the main resonance of the body. The second resonance between 10-13 Hz can be included with model B. A more complicated mechanical system representing the human body as a multiple masses-springs-dampers system has been published by Brüel & Kjær (6) a company which produces instrument for measuring and analysing mechanical vibrations.

When the human body is regarded as a simplified mechanical system the mechanical properties of the several linear and non linear elements should be known. Since these elements are influenced and interconnected in a very complex way and since the properties are very difficult to determine and therefore differ from person to person, mechanical and mathematic models can not be applied in every case. Moreover experiments with human beings are difficult, time consuming and in extreme cases unethical. Experiments with animals do not provide accurate comparison to human reactions in every case.

2.2 Physiological and Psychological Effects

Apart from the mechanical influence described in 2.1 physiological and psychological effects can also be observed. These effects are extremely complex and therefore very difficult to measure. In the range 1 - 3 Hz shortness of breath is detectable. The frequency of respiration is different from the vibration frequency of the lungs. Between 5 - 9 Hz the amplitude of the movement of viscera is at the maximum and the human body attempts to reduce this effect with bated breath. Vibrations in the sphere of low frequencies increase the pulse rate. The skin temperature of the legs drops during the impact of vibration. The expenditure of energy increases in ranges of all frequencies and is the effect of muscular exertion. A very striking effect of mechanical vibrations above 20 Hz is the partial suppression of muscular reflexes and is regarded as a disorder of the nerve centre.

Many studies on physiological effects, such as perception, discomfort, and pain, have been carried out on drivers of vehicles (tractors) or earth moving machines, and on aircraft pilots by varying the environmental conditions.

This research has determined that mechanical vibrations can result in physiological damage.

Table 1. Physiological symptoms dominate in the range of frequencies 1 to 20 Hz

<u>Symptoms</u>	<u>Frequency (Hz)</u>
General feeling of discomfort	4 - 9
Difficulty of breathing	2 - 4
Head symptoms	13 - 20
Abdominal pains	4,5 - 10
Speech disorder	13 - 20
Urge to urinate	10 - 18
"Lump in the throat"	12 - 16
Chest pains	5 - 7
Increased muscle contraction	4 - 9
Lower yaw symptoms	6 - 8

Vibrations with frequencies below 1 Hz can also result in general feelings of discomfort. These vibrations can cause kinetosis, or motion sickness, and the characteristics of these symptoms are quite different from those described above. Human reactions to vibrations below 1 Hz depend on a large number of external factors (e.g. age, sex, vision, activity and odours) which have nothing to do with the motion.

In addition the psychological effect of cross country travel should not be overlooked. In particular the crews of military vehicles, such as trucks and armoured tracked vehicles, are exposed to a high level of psychological stress. The crew members who cannot observe the obstacles and the rough terrain feel a general discomfort resulting from mechanical vibrations to an even greater extent than the driver. In an APC, for example, the crew is not only bothered by the vibrations but also by the exhaust, used air, the noise of the vehicle, and the battle.

3. FREQUENCY ANALYSIS

The set of equal comfort contours presented in the international standards are empirically determined so that a large sample of people were exposed to sinusoidal vibrations with a certain frequency and intensity. The problem is that the vibrations which occur in cross country rides are not periodical, therefore a frequency analysis must be conducted to demonstrate acceleration amplitude as a function of frequency.

3.1 Methods of frequency analysis

Digital Analysis

The rapid development of digital techniques can not be explained solely by the constant falling price of digital components. The advantages of digital techniques over analog techniques are mainly in the area of large dynamic range, very good stability and linearity and linear averaging. The digital technique is suitable for the storage of spectra for later comparison and for the transfer of data to external machines like computers.

Two groups of digital parallel analysers are in use:

- Digital Filters
- Fast Fourier Transform (FFT)

Digital Filters

Digital filtering is the best method for constant percentage band with analysis on a logarithmic frequency scale. Digital filters are used for octave, 1/3 octave or 1/12 octave analysis. The relevant recommendations and standards (ISO, VDI, DINORM) demand a frequency analysis not exceeding 1/3 octave band. Therefore a digital filter analyzer is practicable for analyzing random vibrations with regard to the effect on the human body. The fact that digital filters work up to the range of 20 kHz, one decade higher than FFT systems is for the analysis of vehicle vibrations of no importance.

3.2 Fast Fourier Transform (FFT)

The signal coming from the acceleration sensor via amplifier and recorder is a random curve and a function of time. There is a need to determine the frequency components, which usually can be performed by Fourier techniques. It will be useful to show the various forms of Fourier Transform.

1. Integral Transform

is the ideal form but only applicable with continuous signals. A continuous time signal $g(t)$ extending over all time, $-\infty < t < +\infty$ can be transferred into a continuous frequency spectrum extending also over all frequencies $-\infty < f < +\infty$ by the following formula

$$G(f) = \int_{-\infty}^{\infty} g(t) e^{-i2\pi ft} dt \quad (1)$$

Then it can be shown that the inverse function is

$$g(t) = \int_{-\infty}^{\infty} G(f) e^{i2\pi ft} df \quad (2)$$

This method is not usable for the irregular curves we have in vehicle vibrations.

2. Fourier series

This is a well known method described in many mathematics books and is useful and practicable for periodic time signals. One period can be compared between $-T$ and $+T$ of sine components in that form

$$G(t_k) = \frac{1}{T} \int_{-T}^{+T} g(t) e^{-i2\pi f_k t} dt ; g(t) = \sum_{k=-\infty}^{\infty} G(f_k) e^{i2\pi f_k t} \quad (3)$$

In this case a periodic and continuous signal is transformed into a sampled (discrete) frequency spectrum.

3. Sampled function

is the opposite of case 2. The sampled signals of time are transformed into a continuous form

$$G(f) = \sum_{n=-\infty}^{\infty} g(t_n) e^{-i2\pi f t_n} ; g(t_n) = \frac{1}{T_s} \int_{-T_s/2}^{T_s/2} G(f) e^{i2\pi f t_n} df \quad (5)$$

(6)

4. Discrete Fourier Transfer

The most FFT-analysers work on the principle of the so called "Discrete Fourier Transform" DFT. This means that both time and frequency domain are indiscrète -sampled. Strictly speaking the FFT is not really a classic Fourier transform is rather a calculating schema.

The Discrete Fourier Transform can be shown in the form of the FFT-algorithm

$$G(f_k) = \frac{1}{N} \sum_{n=0}^{N-1} g(t_n) e^{-\frac{j2\pi nk}{N}} ; g(t) = \sum_{k=0}^{N-1} G(f_k) e^{\frac{j2\pi nk}{N}} \quad (7)$$

The number (N) of the samples is the same in the frequency and time domain. DFT applies to discrete and periodic time signals, therefore the frequency spectrum is also periodic and discrete. Owing to this periodicity only a finite number are needed for the calculation.

In contrast to the traditional analysis where the signals are continuously processed the DFT stores the data of the time samples in a digital memory, and when this is full the whole memory is transformed into the frequency domain as one block.

The principle of this schema is described clearly in /5/.

4. STANDARDS AND RECOMMENDATIONS

4.1 Equal sensation curves

The first attempts to investigate the influence of mechanical vibrations were carried out by A. Mallock about 1900 when residents near Hyde Park complained about underground shocks. He discovered a relationship between frequency and acceleration and determined that vibrations of low frequencies of about 15 Hz are more unpleasant than those higher frequency ranges.

Since 1900 many investigators have attempted to measure the subjective reaction to objective measurable vibrations. Though the results vary in some cases they coincide in the fact that the subjective sensitivity is a function of frequency. One problem is that the human reaction to whole body vibrations differs from person to person and that human beings cannot remember the intensity of vibrations very well.

Although research done in the field of equal sensation curves is based on different methods, four principle experimental procedures can be seen.

Verbal description:

The test subject is asked to indicate when he feels that a constantly increasing sinusoidal vibration of a certain frequency has reached a level which is described for example as "perceptible" "comfortable" "tolerable" or "very uncomfortable" "uncomfortable" "mildly uncomfortable" "noticeable, but not uncomfortable" ... (for example Parks and Snyder 1961, Chaney 1964/65, Fothergill and Griffin 1977).

Comparison method

A "standard" sinusoidal vibration stimulus of a certain frequency and acceleration is presented to the subject. After a short pause the frequency is changed and the subject is required to indicate when the vibration appears equal in sensation to the standard (for example Ashley 1970, Shoenberg and Harris 1971, Dupuis 1960). Dieckmann's researches conducted in this manner was the basis for the first VDI-recommendations in 1963.

Rating method

The rating method merges the two methods described above. In this case the test subject has to present his subjective perception in a 10 cm long rating line. The scale is marked on both ends: one end with "0" representing "smooth" and the other with "10" representing "rough". The subjects were exposed to a number of sinusoidal stimuli of a certain frequency and acceleration. They were asked to evaluate each stimulus independently without comparing the stimuli with each other (Osborne and Clarke 1974).

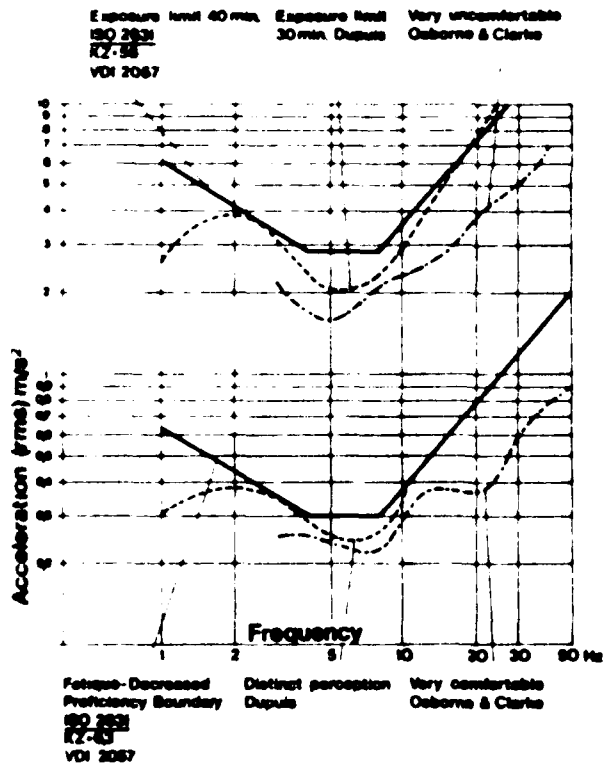


Fig. 7

Equal sensation
curve comparison
between the
standard and
different research

Relative intensity estimation method

The test persons are subjected to a pair of sinusoidal vibration stimuli of the same frequency. The second stimulus is the more intensive than the first. The subjects are required to evaluate the relative intensities of the two stimuli (Jones and Saunders 1974).

Although the results of different researchers do not coincide exactly, the principal shape of the curves of equal sensation is nevertheless similar. It was determined that in the range of low frequencies (lower than 8 or 10 Hz) the intensity of sensation is greater than in the range of high frequencies.

The equal comfort curves presented in the ISO and VDI- standards are useful for calculation but they do not accurately reflect human impressions of sinusoidal vibrations.

Studies by H. Dupuis, Osborne & Clarke (shown in Fig. 7) and Jones & Saunders for example reached conclusions which differ from the ISO/VDI-standards.

4.2 Standards and recommendations

Since the purpose of this paper is to assess the effects of mechanical vibrations on the crew members of cross country vehicles, only those elements of the respective standards and recommendations pertaining to sitting subjects in vertical direction (z-axes) are discussed. The vibration level indicated in the criteria curves are given in terms of RMS (root-mean-square).

The first international guide line in the field of vibration assessment was published by the German "Verein Deutscher Ingenieure" VDI (Society of German Engineers) in 1963. This VDI 2057 recommendation is based on Dieckmann's research carried out at the Max-Planck-Institute in Dortmund. Investigations of the late sixties and seventies came to the conclusion that biochemical and physiological reactions as well as the effects of vibration on proficiency boundary and health must also be considered.

ISO-Standards

Results of this research enabled the ISO (International Organisation for Standardisation), the World Wide Federation of National Standards Institutes, to develop the ISO-2631 standards.

The definitions and numerical values given in the ISO 2631 are only valid in the frequency range 1 to 80 Hz. For the assessment of mechanical vibration transmitted from solid surface to the human body four physical factors should be considered

- Intensity (acceleration rms)
- Frequency (1 - 80 Hz)
- Direction
- Duration (exposure time)

The fact that the human body has an increased sensitivity to vertical vibrations in the range 4 - 8 Hz is reflected in the tolerance curves which are represented as three straight lines in the logarithmic scales.

For the evaluation of human exposure to whole-body vibration three criteria can be distinguished:

- preservation of comfort "reduced comfort boundary"
- preservation of working efficiency "fatigue-decreased proficiency boundary"
- preservation of health or safety "exposure limit".

Exceeding the exposure specified by the curves pictured in Fig. 8 will in most situations cause noticeable fatigue and decreased job proficiency in most tasks. The degree of task interference depends on the subject and the complexity of the task. In the case of driving a vehicle in an off-road-situation there is every reason to believe that the degree of complexity is very high.

These criteria are intended only for average people considered fit for normal living routines and the stress of an average working day. For "reduced comfort boundary", the acceleration values are divided by 3,15 (10 dB lower) and for "exposure limits" the values are to be multiplied by 2 (6 dB higher).

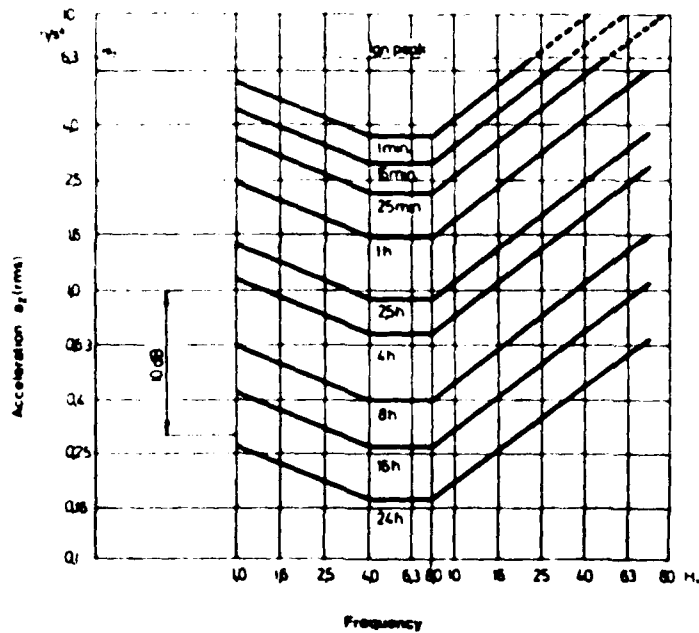


Fig. 4

ISO-2631
Equal sensation
curves. Vertical
vibration exposure
criteria curves
defining equal
"fatigue-decreased
proficiency
boundaries for a
sitting person

VDI-Recommendation

The tolerance curves presented in ISO 2631 provided the impetus to revise VDI 2057. The latest version (1979) adopted the principle shape (three straight lines) from ISO 2631 but kept up the K-value for the assessment of the degree of sensation perceived by human beings.

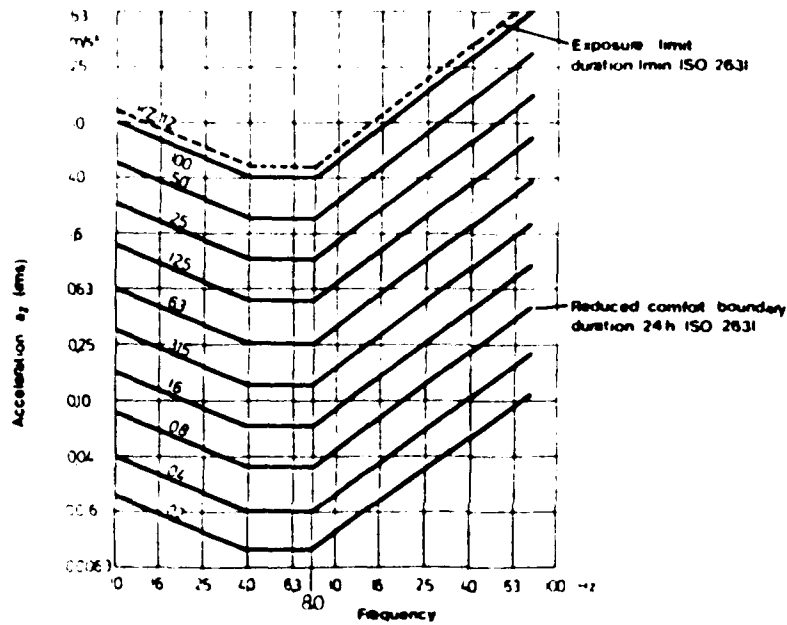


Fig. 5 VDI-2057 Equal sensation curves in vertical direction for a sitting person

In accordance with ISO 2631 a time dependent assessment and a classification into three main criteria "comfort", "fatigue" and "health", were introduced.

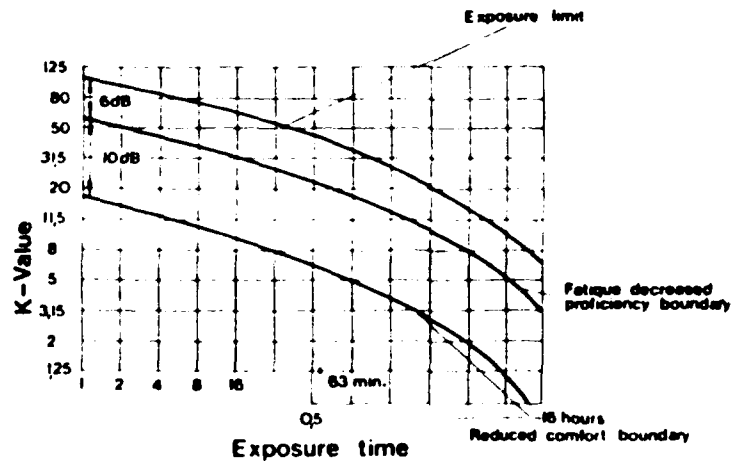


Fig. 6 VDI-2057 Permissible "K-value" in dependence from exposure time

As the K-curves are three straight lines in the logarithmic scale, three formula in the corresponding frequency ranges must be given.

K_Z (K-value in Z-direction):

$$\begin{array}{ll} 1 \leq f \leq 4 \text{ Hz} & K_Z = 10 \cdot a \sqrt{f} \\ 4 \leq f \leq 8 \text{ Hz} & K_Z = 20 \cdot a \\ 8 \leq f \leq 80 \text{ Hz} & K_Z = 160 \cdot a / f \end{array} \quad (9)$$

In the following tabulation the correlation between measured K-value (object degree of sensation) and subjective perception is given.

Table 3 Correlation between "K-value" and subjective perception

K-value	Subjective perception
< 0,1	not perceptible
0,1	perceptive boundary
0,4	little perception
1,6	normal perception
6,3	greater perception
	maximum perception

For random or distributed vibrations a method to calculate the K-value is given. The K-values of every range of a narrowband or a third-octave analysis can be calculated.

The total K-value (K_{tot}) is the root of the sum of the squared partial K-values (K_i)

$$K = \sqrt{K_1^2 + K_2^2 + \dots + K_n^2} = \sqrt{\sum K_i^2} \quad (10)$$

The two standards VDI 2057 and ISO 2631 are based on different philosophies but reach the same conclusion. For studies which compare vehicles in differing environmental conditions the VDI 2057 is more practicable. For investigation in the protection of the human body against occupational disease the ISO 2631 should be used.

5. EXPERIMENTAL METHODOLOGY

5.1 The test vehicles

Field test were carried out at an army training area, about 20 km southeast of Vienna. Two 5 ton 4x4 military trucks and two armoured vehicles, one wheeled and the other tracked, were available. For the determination of the influence of speed, terrain and the sitting position, all 4 vehicles were used. The comparison tests between diagonal and radial tires were conducted on vehicle A and B. The influence of tire size could be demonstrated on the armoured vehicle C. For the comparison of the suspension systems of tracked and wheeled vehicles model C and D were used.

Table 3 Specification of the vehicles

Model		A	B	C	D
Engine power	kW	88	130	236	208
Top speed	km/h	80	110	105	63
Overall height (Null)	mm	2970	2813	2730 (1950)	2170 (1600)
Overall length (Null)	mm	6570	6610	8335 (6900)	6240 (5870)
Overall width	mm	2400	2436	2500	2500
Net weight	ton	7,6	6,8	16	13
Wheel base/ Track contact length	mm	3700	3800	2800/ 1400	3192
Tread width	mm	1810/ 1670	1980	2070	2120
Number of tire		6	4	6	-
Tire size		9.00R20 9.00-20	14,5R20	14 R 20 13 R 20	-
Suspension System		Rigid axles Leaf spring	Rigid axles Leaf spring	Rigid axles Coil spring	Torsion bar

Vehicle B is a prototype and was designed and built between 1981 - 1983. Vehicle B is nearly 20 years old and of conventional construction. The principle variables influencing ride comfort are tire size, wheel number (the rear axle of Vehicle A has twin wheels) and spring characteristics. Though both vehicles are supplied with leave springs, the spring characteristic lines and the construction features are quite different.

Vehicles A has the classic leave spring construction with closely packed spring leaves, 11 on the front axle and 14 on the rear axle. Hence a considerable internal friction with damping function occurs. The static spring constant for the front axle spring is $C_{St} = 133 \text{ N/mm}$ and for the rear axle spring it is $C_{St} = 228 \text{ N/mm}$.

Vehicle B has the so-called "Parabola Leave Spring" with parabolic premolded leaves, 3 on the front axle and 4 on the rear axle. In order to reduce internal friction 4 mm spacers are fastened between the single spring leaves. The static spring constant for front axle spring is $C_{St} = 129 \text{ N/mm}$ and $C_{St} = 180 \text{ N/mm}$ for the rear axle spring.

The smooth character of the "Parabola Leave Spring" increases under dynamic conditions. While the ratio between C_{St} and C_{dyn} (dynamic spring constant) is about 4 the parabola leave spring, it increases to 20 on the conventional spring typ.

5.2 Equipment and experimental procedure

The accelerations were measured at 4 points by Piezoquarth accelerometers Brüel & Kjaer 8302. For the tests with the trucks one acceleration sensor was placed at the driver's seat inserted in a seat transducer. The other sensors were screwed to the wooden bench on the loading space to simulate the vibration impact to persons sitting in the front, in the middle and in the rear position.

The experiments on the armoured vehicles were carried out in a similar manner. For the calculation of the transmissibility, which is defined as the ratio of the amplitude of sinusoidal vibration to the seat sensor, a second accelerator was fixed at the bottom of the driver compartment.

The third accelerator was mounted at the commander-seat in the turret and the fourth sensor, in order to measure the ride comfort of one of the other crew members, was attached on a seat in the crew compartment.

The signals coming from the accelerators are amplified in a Brüel & Kjaer amplifier Typ 2635 and stored in the Tape Recorder 7005. The amplifier and tape recorder were placed in the cabin and were controlled by the assistant-driver.

The vibration signals stored at the Tape Recorder 7005 were analysed by the narrow band FFT analyser Brüel & Kjaer 2033. This FFT analyser sampled the input signals and converted each signal into digital form. The samples were collected in data blocks, and each data block was converted into the frequency domain by Fourier transformations.

The analyser was used in the range 1 - 10 Hz. The result of the FFT-analysis was a transfer function shown on a monitor screen. The frequency scale was displayed linearly, while the acceleration was shown alternatively on a linear or logarithmic scale. The 2033 FFT-analyser operated by sampling the input-signal and converting each sample into digital form.

The samples were then collected into data blocks. These data blocks were transformed by FFT into the frequency domain. A 400 line spectrum covers the chosen frequency 0 - 100 Hz, hence, the line spacing

$$f = 100 \text{ Hz}/400 = 0,25 \text{ Hz}.$$

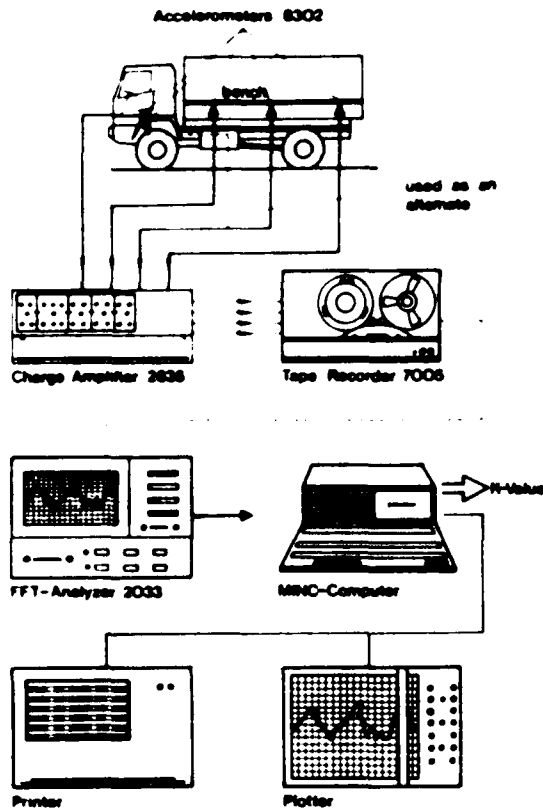


Fig. 10
Blockdiagramm

At the outset computer program (BASIC) of the Micro computer system MINC-11 recorded the RMS acceleration values of the 0,25 Hz steps coming directly from FFT-analyser. The FFT-analysis was also seen on the monitor screen of the computer terminal. For each acceleration value in the three frequency ranges 0 to 4 Hz, 4,25 Hz - 8 Hz, 8,25 Hz - 80 Hz according to formula (9) the K_i values were computed. In a second step these K_i -values were then squared, and added. The root of the sum is the K-value.

Immediately after the calculation was completed the K-value appeared on the screen. The output was:

- Acceleration/Frequency-plot shown in Fig. 10
- one page summary of acceleration values of the 0,25 Hz intervals plus K-Value
- summary of K-values of a test serie

PhysLab EDV



All tests were carried out in the following three surface situations

- ### Influence of sitting position

Position 1: rear seat
Position 2: front seat of the loading space/commander seat
Position 3: seat mount of the driver seat
Position 4: driver seat

Table 4 Ride comfort depending on sitting position

Vehicle	→ increasing K-value			
A	3	2	4	1
B	4	2	1	3
C	4	3	2	1
D	4	2	1	3

Except for vehicle A the driver is in the best situation. The reason is that vehicle A has an old seat construction. An example of a modern vibration damping seat suspension can be seen in vehicle B, where the inadequate seat mounting is compensated by the seat.

In all four vehicles it is clear that individuals sitting in the rear are always subject to greater shock and stress and the S_{tact} should be lower than S_{tol} for that seat.

Influence of speed

For all vehicles and in all varying situations the K-value increased with speed. This typical tendency, both typical and expected, can be seen in the figure below where the "K-value"/speed dependence for the several sitting positions in the three surface situations for vehicle A is plotted

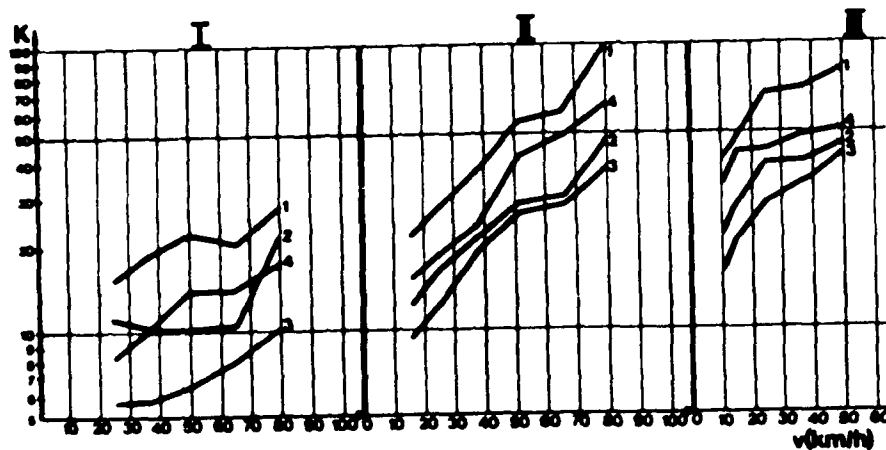


Fig 9 K-value - speed - dependence

Influence of terrain

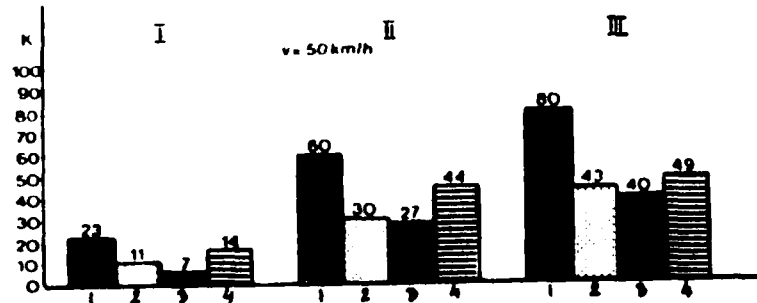


Fig 10 Vehicle A varying speed and terrain

The principle result that the K-values increase with increasing terrain roughness is in accordance with theoretical considerations. It is of interest to note that results pertaining to difference between roadway and paved street is higher than that between paved road and off road terrain. Hence with regard to ride comfort, bad road conditions are similar to terrain condition.

Influence of spring system

The differences in the spring system of vehicle A and B are described in 5.1. In the following table it is clear that the spring system has an important influence on the ride comfort of wheeled vehicles. For each member of the crew, in all terrain situations and in all speed ranges, the K-values are considerably higher for vehicle A compared with vehicle B.

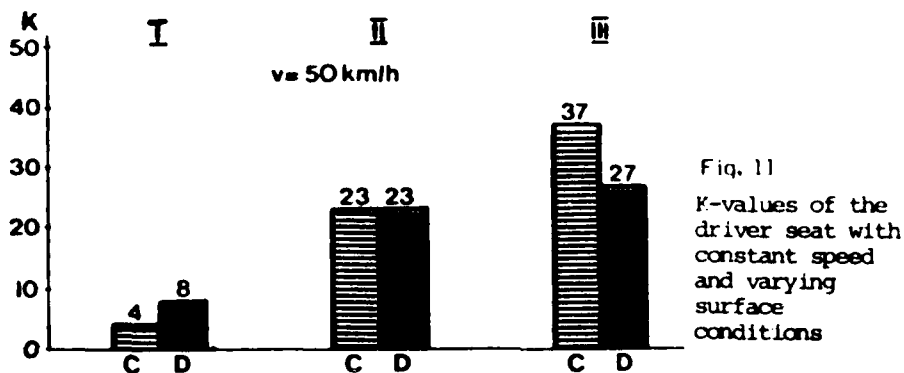
Table 5 K-values of the driver's seat of vehicle A and B

Speed	Terrain I		Terrain II		Terrain III	
km/h	A	B	A	B	A	B
10	-	-	-	-	37	29
15	-	-	22	30	43	27
25	15	9	29	30	65	51
37	19	10	39	37	69	65
50	23	17	59	43	80	69
65	21	15	64	59	-	-
80	30	16	104	71	-	-

Influence of tire pressure, tire type and tire size

The vehicle itself can also be seen as a system of masses, springs, and dampers. The tire is one of the springs of the system and a variation in inflation pressure or the use of diagonal tires instead of radial tires should have an influence on the ride comfort. But the test results showed that these factors are of minor influence. The same result was found when vehicle C was provided with tires of a smaller size. The differences in the K-values had no distinguishable tendencies and were in the range of inaccuracy of measurement.

Comparison between a wheeled and a tracked vehicle



The figure above shows clearly that the wheeled vehicle has better ride comfort on a natural road (i) and under poor road conditions (II). On the grass covered lawn (III) the tracked vehicle had the lower K-values. The reason may be that the suspension system of a wheeled version has the better damping characteristics when the wave length of the surface roughness is short. In cases of longer waves the tracked system has better accommodation facilities.

Concluding remarks

The main factor which can be influenced by the user of a vehicle system is the speed. Other factors are spring system and seat construction which can be altered by the designer. These components should also be considered in vehicle tests. For the transportation of casualties in vehicles the best location for the patients can be found by determining with the method described in this paper. That the tire characteristics have such a minor influence was one of the unexpected results of these tests.

The author will continue the test series with other cross country vehicles in order to measure and assess the vibrations in the three axes of the coordinate system. It is hoped that a relationship between defined terrain roughness and K-value will be found.

REFERENCES

- /1/ VDI 2057 Beurteilung der Einwirkung mechanischer Schwingungen auf den Menschen. Oktober 1963
- /2/ VDI 2057 Beurteilung der Einwirkung mechanischer Schwingungen auf den Menschen. Februar 1975/Mai 1981
- /3/ ISO 2631 Guide for the evaluation of human exposure to whole-body vibration. Second edition-1978-01-15
- /4/ DINORM S9010 Bewertung der Einwirkung mechanischer Schwingungen und Erschütterungen auf den Menschen
- /5/ Digital Signal Analysis Selected Reprints from Technical Review Brüel & Kjaer
- /6/ Notes taken at a seminar conducted by Brüel & Kjaer on shock and vibrations 1982.
- /7/ LUTZOW J.: Human Factors Wehrtechnische Monatshefte 1967 S 382-387
- /8/ LAMMERTZ R. und SCHNAUBER H.: Untersuchungen zur Schwingungsbelastung des Menschen und Auswertung der Meßdaten mit Prozeßrechner. Stahl und Eisen 96 (1976) Nr. 25/26 S 1345-1346
- /9/ COERMANN R.: Die Wirkung mechanischer Schwingungen auf den Menschen und seine Arbeitsleistung. Werkstatttechnik 52. Jahrgang 1962, Heft 1, S 18-25
- /10/ MATTHEWS J.: The Measurement of Tractor Ride Comfort SAE-paper 730 795
- /11/ DUPUIS H.: Arbeitsmedizinische Untersuchungen der Schwingungseinwirkung auf Wirbelsäule und Magen bei Kraftfahrern. 11. Internationaler automobiltechnischer Kongreß 1966.
- /12/ DUPUIS H.: Stand der arbeitsmedizinischen Bewertung mechanischer Schwingungen am Arbeitsplatz. Arbeitsmedizin Heft 10 S 236-243
- /13/ DUPUIS H. und andere: Vergleich regelloser Schwingungen eines begrenzten Frequenzbereiches mit sinusförmigen Schwingungen hinsichtlich der Einwirkung auf den Menschen. Ergonomics, 1972, Vol. 15, No. 3, S 237-265
- /14/ JONES A.J. & SAUNDERS D.J.: A Scale of Human Reaction to Whole Body, vertical, Sinusoidal Vibration. Journal of Sound and Vibration (1974) 35 (4) 503-520
- /15/ OBORNE D.J. and CLARKE M.J.: The Determination of Equal Comfort Zones for Whole-body. Vibration Ergonomics, 1974, Vol. 17, No. 6, 769-782
- /16/ DUPUIS H.: Zur physiologischen Beanspruchung des Menschen durch mechanisch Schwingungen VDI-Forschungsberichte



FURTHER DEVELOPMENT IN RIDE QUALITY ASSESSMENT

NEWELL R. MURPHY, JR.

U. S. ARMY ENGINEER WATERWAYS EXPERIMENT STATION, VICKSBURG, MISSISSIPPI

INTRODUCTION

Internationally, a growing concern has developed and widespread disagreement has occurred over the present methods for quantitatively describing and assessing the effects of vehicle vibrations on humans, and over the short- and the long-term effects of vibrations on drivers and occupants of heavy trucks, agricultural and earthmoving equipment, and military vehicles. None of the present methods is completely satisfactory; in fact, most criteria were developed for low-level "boulevard" rides and are highly suspect when applied to the severe vibrational levels encountered in earthmoving and military-type operations.

Today two predominant methods are used by the military to describe the effects of vehicle vibrations and human response: the absorbed power method (used largely in the United States) and the International Standards Organization (ISO) method (used extensively throughout European countries as well as in the United States). The two methods are similar in that both use frequency-weighted accelerations corresponding to human sensitivity to arrive at a single number which describes the vibration intensity. Portable ride meters have been developed to provide expedient field measurements of both absorbed power and the ISO accelerations.

In 1978, a NATO working group on mobility (NATO AC/225 (Panel II Working Group I)) composed of representatives from the United States, Canada, France, the Federal Republic of Germany, the Netherlands, and the United Kingdom adopted the Army Mobility Model (AMM) and its supporting absorbed power procedures for determining ride-limiting speeds for use in the model as comparison tools to provide a standardized reference for determining vehicle mobility performance. The AMM is also called the NATO Reference Mobility Model (NRMM). The use of absorbed power over the ISO method to describe effects of vehicle vibrations has caused resistance and concern, particularly among the European participants. The United States military and its NATO partners need agreed-upon, accepted standards to describe the various aspects of ride quality in meaningful terms for defining the vibrational effects on human health, safety, and performance of military tasks.

WHY ABSORBED POWER?

In 1968, personnel in the Mobility Systems Division at the Waterways Experiment Station (WES), in conjunction with the formulation and development of the components of the AMM, embarked on a comprehensive ride dynamics research and development program. The principal objective of the ride dynamics program was to develop a means for predicting ride-limiting speeds of vehicles as a function of terrain roughness. This objective required a quantitative measure of vehicle vibration that related to human acceptance of the vibration and response to vibration. WES decided to adopt a promising measure called absorbed power. This absorbed power quantity, purported to be a measure of the rate at which vibrational

energy is absorbed by a typical human, had been developed only recently at the U. S. Army Tank-Automotive Command as a result of a comprehensive, closely controlled laboratory program (Pradko, Lee, and Kaluza 1966). An attractive feature of absorbed power is that it is conceptually a scalar quantity and the resultant response of vertical and horizontal vibrations can be determined by directly summing the absorbed power in each component.

Since 1968, the WES has conducted numerous field tests with virtually every type of wheeled and tracked vehicle in terrains throughout the world. The absorbed power quantity has worked well in fulfilling the principal objective of describing ride-limiting speeds. A criterion of 6 watts of absorbed power was chosen as an upper bound of vibration that will permit crew members to effectively perform their tasks. Test results revealed that beyond the 6-watt level, a vehicle occupant can do little else except hold tight. Results have also shown that highly competitive drivers and crew members will accept absorbed power levels regularly ranging up to 10, 20, or more watts for periods up to 10 or 12 minutes (Berry 1975). The same tests showed that these high absorbed power conditions frequently caused minor injuries and bruises and often produced severe vehicle damage and a high risk of accidents and cargo damage. Thus, it is recognized that the 6-watt absorbed power level is not an absolute human tolerance limit to vehicle vibration and that crew members will, if necessary, accept considerably higher absorbed power levels at the risk of injury and vehicle and cargo damage. A broader range of test results has shown, however, that quite often only a small increase in speed can be attained at 15 or 20 watts over that at 6 watts, because the 6-watt absorbed power levels usually occur when the vehicle's suspension begins "bottoming out" and producing discrete shock loads. Slight increases in speed beyond this point significantly increase the intensity and frequency of these shock loads, which in turn rapidly increase the absorbed power levels. These high absorbed power conditions are not considered to be an effective or meaningful measure of basic ride characteristics. While the use of ride speed limits based on higher absorbed power levels will increase projected vehicle speeds in isolated terrain situations, the overall vehicle performance throughout an area generally will not be materially increased, and relative performances of two or more vehicles in the same area will rarely be changed.

THE ISO METHOD

In 1974, after a decade of serious committee deliberations, the ISO published a standard for describing human response to whole-body vibrations that was approved by 19 countries including the United States (ISO 1978). The ISO standard defines numerical limits for exposure to vibrations in terms of weighted root-mean-square (rms) accelerations in the frequency range of 1 to 80 Hz according to three criteria of increasing intensity--preserving comfort, working efficiency, and safety or health. These three limits are referred to, respectively, as the "reduced comfort boundary," "fatigue-decreased proficiency boundary," and the "exposure limit boundary." The preferred method of evaluation is to compare separately each rms acceleration level for 1/3-octave bands of specified center frequencies against the recommended level at each frequency. This procedure assumes that in regard to human tolerance there are no significant interactions between frequencies. An alternate method, which appears to be a more accurate representation for complex vibrations, sums the weighted accelerations to give an overall rms level expressed by a single quantity (Allen 1975). This single quantity method led to the development of portable ride meters. One such meter was built in the United States in 1978 by Endevco for the Society of Automotive Engineers (SAE) Ad Hoc Ride

Meter Task Force in accordance with specifications cited in ISO 2631 and SAE J1013. For vibrations occurring in more than one axis simultaneously, each axis is evaluated separately and vectorially summed. There has been much disagreement over the use of this method and a number of deficiencies have been highlighted by its critics. The most notable deficiencies cited are the lack of empirical support in a number of important areas, in particular the time-dependency relations on human response (Osborne 1983).

Because of these disagreements and concerns and other unanswered questions, a joint United States-Federal Republic of Germany effort was recently initiated to resolve these major issues. As a part of the Future Armored Vehicle Research (FAVR) program, a joint United States-Federal Republic of Germany ride test and evaluation program is scheduled to begin at Trier Proving Ground in May 1984, with similar follow-on tests in the United States. The main emphasis will be to jointly study and compare the results of the two methods.

Over the past 15 years of testing, WES has developed a large, unique data base containing detailed vertical, horizontal, and rotational acceleration measurements, along with the corresponding human subjective comments and ratings, terrain measurements, and vehicle characteristics. These data are stored on analog FM magnetic tape. As a starting point for this study, selected vibration data representing a wide variety of vehicles and terrain conditions are currently being reprocessed to analyze and compare relations produced by other proposed quantities, particularly the ISO standard.

This paper describes briefly some of the initial results of using only vertical vibration data from recent tests with a pair of wheeled vehicles to compare and evaluate the relative merits of the absorbed power and ISO criteria. Discussions include similarities between the two methods, the relations (or lack of relations) between subjective ratings and the absorbed power and ISO quantities, some notable deficiencies common to both, and the effects of psychological influence. Evidence indicating the validity of the 6-watt absorbed power level as a reasonable driver-imposed criterion of acceptability is presented along with plans for future work.

COMPARISON OF ABSORBED POWER AND ISO FILTERS

Human response to vibrations depends upon the frequency of the vibration. Curves of constant comfort or equal perceptions of vibrations as a function of frequency have been measured by many investigators. The precision and definition of these curves have improved with the progressive improvements in equipment and measuring instruments. Regardless of the improvements in precision, they all present basically the same characteristic trough shapes. For example, the keenest sensitivity of a seated subject exposed to vertical (buttocks-to-head) vibrations is in the range from 4 to 8 Hz. This range of maximum sensitivity is attributed to physical resonances of body parts and internal organs. Precise experiments and measurements indicate the most sensitive frequency of a seated subject to vertical vibration occurs at about 4.5 Hz, which is the resonance of the viscera. This critical resonance will vary somewhat among humans due to differences in body structure. Most likely, the less precise curves are better overall general representations of human sensitivity.

Any method that purports to evaluate vibrations in terms of human sensitivity must account for this frequency dependency. The frequency-weighting can be accomplished numerically by appropriately weighting the Fourier spectra of the vibrations. The frequency-weighting is more readily

accomplished in the analog domain through the use of band-pass filters. As mentioned previously, portable ride meters have been developed that filter input accelerations and produce on-the-spot measures of absorbed power and ISO ride values. Figure 1 shows a comparison of the absorbed power and the SAE/ISO ride meter filters for vertical vibrations. The standard ISO frequency-weighting factors specified in ISO 2631 are shown as discrete points. It is seen that the absorbed power and the ISO filters have the same basic shape. The absorbed power filter peaks (zero attenuation) at 4.5 Hz, while the SAE/ISO filter peaks at 5.8 Hz. The absorbed power filter is more restrictive because it attenuates (reduces) accelerations more heavily at frequencies beyond the 4.5-Hz peak. It is also seen that the curve representing the SAE/ISO filter of the Endevco ride meter corresponds very closely to the discrete points representing the standard ISO frequency-weighting factors. Obviously, because of these similarities, the respective quantities calculated from accelerations processed by these filters and frequency-weighting factors will produce similar performance patterns.

COMPARISON OF ABSORBED POWER AND ISO RESULTS

WES began its first comparison of the absorbed power and the ISO methods this past summer (1983) as part of a comprehensive analysis to resolve apparent discrepancies in results obtained from ride tests with a light dune buggy vehicle. This dune buggy had exceptionally stiff suspensions that produced extremely high acceleration and absorbed power levels, even on relatively smooth test courses. The absorbed power levels measured for the dune buggy were consistently two to three times higher than those measured on conventional vehicles for similar test conditions. The high absorbed power levels were not the issue. The issue that caused the concern was that the subjective ratings of three experienced WES test drivers consistently rated these unreasonably high absorbed power levels as acceptable rides. Numerous supplemental ride tests were conducted on the same test courses with two additional vehicles and three drivers to obtain "head to head" data for direct comparisons. One of the two vehicles was an M151 jeep which had a gross weight and size similar to that of the dune buggy. The principal performance results presented in this paper are limited mainly to data from representative tests with the dune buggy, one reference vehicle (an 8x8, 14-ton* armored vehicle), and one driver. These relations are representative of the relations obtained when comparing the combined results of the three vehicles and three drivers.

Figures 2 and 3 graphically depict the respective absorbed power and ISO ride meter results from tests with the two vehicles on two test courses. More detailed data are presented in Table 1. Figure 2 shows how vertical absorbed power and ISO weighted acceleration vary with speed for the two vehicles on a test course (course 4) of moderate surface roughness. The

* U. S. customary units of measurement used in this report may be converted to metric (SI) units as follows:

<u>Multiply</u>	<u>By</u>	<u>To Obtain</u>
inches	2.54	centimetres
miles	1.609347	kilometres
pounds (force)	4.448222	newtons
tons (force)	8896.444	newtons

exposure-limit time dependency boundaries representing the ISO acceleration limits for the most sensitive frequency region (4 to 8 Hz) of five selected exposure times are shown on the plots. The drivers' subjective ratings, based on a scale of increasing severity from 1 to 10, are also shown adjacent to the respective data points. The subjective rating scale used at WES to express the drivers' perception of ride quality is given below:

Subjective Index	Perception
1-2	Barely noticeable
3-4	Strongly noticeable
5-6	Uncomfortable
7-8	Extremely uncomfortable
9-10	Recommended limits (not willing to take for any sustained period of time)

Past experience indicates that when WES drivers are allowed to drive at their discretion, under guidelines of achieving the maximum safe speed, the subjective ratings fall within a range of about 6 to 7. This indicates that ride conditions with subjective ratings greater than 6 or 7 are really conditions of stress levels beyond the criteria of acceptability.

For both vehicles increases in speed produce corresponding increases in absorbed power and ISO acceleration. However, absorbed power and ISO do not increase at the same rate. Also, for any selected speed the absorbed power and ISO acceleration for the dune buggy are about twice the magnitudes of those recorded for the 8x8 vehicle. Yet, the driver's subjective ratings are consistently lower for the dune buggy at corresponding levels of absorbed power and ISO acceleration. According to the recommended ISO exposure limits, the results in Figure 2 indicate the 8x8 vehicle can be driven over test course 4 or a course of similar roughness at a speed of 20 mph for up to an hour and can be driven at speeds in excess of 50 mph for about a half hour. These same ISO limits indicate the dune buggy can be driven at a speed of 20 mph over such a course for only about 16 or 18 minutes, and at speeds beyond 40 mph the permissible ISO exposure time is less than one minute.

Figure 3 shows results similar to those of Figure 2 except the surface roughness of the test course is much more severe. The severity of the test course is reflected by the rapid increase in both absorbed power and ISO acceleration with increases in vehicle speed. Again, at any selected speed both the absorbed power and the ISO accelerations for the dune buggy are about twice the corresponding magnitudes recorded for the 8x8 vehicle. Also, the drivers' subjective ride severity ratings are lower for the dune buggy at corresponding levels of absorbed power and ISO acceleration. Noteworthy are the overall high subjective ratings. This particular driver, like the other two WES test drivers, is considered to be fit, tough, and competitive. As mentioned before, based upon their discretionary driving habits, subjective ratings greater than about 6 or 7 reflect levels beyond their self-imposed acceptability criteria. Figure 3 shows that the driver's subjective ratings for both vehicles are largely in the range from 7 to 10, indicating that the ride quality of the majority of the tests on this course exceeded the driver's criteria of acceptability. Subjective ratings of 8 to 10 mean the rides were exceptionally tough. The data in Table 1 reveal that these tests ranged from a maximum duration of about one minute to a minimum of 6 seconds. Based on combined consideration of the ISO recommended exposure limits and the high subjective ratings, it appears that neither of the two test vehicles could be driven

at speeds beyond about 10 mph on terrains with such levels of surface roughness for periods longer than about half an hour.

SIMILARITIES BETWEEN ABSORBED POWER AND ISO RESULTS

Figures 2 and 3 clearly show certain similarities in the manner that absorbed power and ISO acceleration increase with increases in speed as well as similar correlations with driver subjective ratings. Figure 4 illustrates further correspondence between the two ride quality measures. The two plots in Figure 4 reflect relations between ride-limiting speeds and terrain surface roughness for the dune buggy at three arbitrarily selected levels of absorbed power and ISO acceleration, respectively. This limiting speed versus surface roughness relation is exactly the type of format required as input to the *APM/NRPM* to depict vehicle ride performance relations. The ride performance relationships are very similar for both the absorbed power and the ISO acceleration measures. In fact, the relation for the 20-watt absorbed power level is almost identical to that for the 25-minute ISO level (the 25-minute exposure limit corresponds to an ISO acceleration level of 3.6 m/sec^2). Consequently, if so desired, the ride-limiting speeds based on the 6-watt absorbed power level customarily used in the *APM/NRPM* to describe ride performance could be replaced with ride-limiting speeds based on either a more suitable absorbed power level or a preferred level of ISO acceleration or permissible exposure time. The *APM/NRPM* requires a limiting speed-surface roughness relation to describe ride performance regardless of the criteria used to determine the limiting speeds.

PSYCHOLOGICAL IMPLICATIONS

Human reaction to vibration is a complicated dependency upon both physiological (physical) and psychological (mental) disturbances. Neither absorbed power nor ISO acceleration nor any other measure of purely physical motions can account for the psychological effects. Recalling the subjective index rating mentioned previously, the perception definitions deal only with thresholds caused by interactions of vehicle motions. However, without fail, during driver interviews regarding rides that were rated in the range of 8 to 10, the principal objection was attributed to lack of control of the vehicle. Although this reason does not fit into the perception definition, the psychological implications cannot be isolated or removed from the subjective ratings. This psychological influence of vehicle controllability depends strongly on the nature of the vibrations. That is, a ride composed of high-intensity, uniform accelerations will be perceived quite differently from one composed of low- to medium-intensity accelerations made up of recurring impulses and shock loads. This is a condition of high crest factors; i.e., ratio of maximum peak to rms accelerations where the ISO limits are admittedly questionable. It is the occurrence of harsh shock loads that often catapult driver and vehicle into the air and along with inducing momentary pain and possible injury seriously hinders the driver's capability to control the vehicle. This psychological distinction between uniform motions and motions composed of recurring impulses is the principal cause of the discrepancies in the subjective ratings recorded for the dune buggy.

Table 2 lists the respective speeds and driver subjective responses recorded from arbitrarily selected levels of absorbed power and ISO acceleration for the two test vehicles and three test courses with three levels of surface roughness.

Subtle yet important effects of psychological influence on the measures of performance can be seen in the table. Both absorbed power and ISO acceleration reflect the same effects. For example, for any given level of either absorbed power or ISO acceleration, the speeds of the 8x8 vehicle are about twice as high as the corresponding speeds for the dune buggy. According to current procedures for evaluating ride performance, the 8x8 vehicle would be considered far superior to the dune buggy. However, for any given level of either absorbed power or ISO acceleration, the subjective ratings are consistently higher for the 8x8. This difference in ratings says that a 6-watt ride in the 8x8 feels rougher or more severe than a 6-watt ride in the dune buggy.

Comparison of representative acceleration-time histories of the two vehicles reveals that, in fact, the dune buggy accelerations generally were rather uniform throughout and did not exhibit significant impulses or shock loads. This uniformity is attributed to the extremely stiff rear suspensions combined with the vehicle's "tail-heavy" weight distribution that prevented suspension "bottoming" and thus the associated shock loads. This condition is in contrast to the soft suspensions and high wheel travel on the 8x8 which produced gentle, low-frequency, high-displacement motions. These soft suspensions on the 8x8 resulted in low-intensity acceleration-time histories with dispersed harsh shock loads occurring when the suspensions "bottomed out." The intensity and frequency of these shock loads were moderate on relatively smooth courses but rapidly increased with increases in both speed and surface roughness.

The relations illustrated in Figure 5 provide an even broader understanding of this phenomenon between the dune buggy and the 8x8. Figure 5 is a standard ISO graph depicting the rms acceleration magnitudes for each of the standard 1/3-octave band center frequencies recorded from ride tests with the two vehicles. The results of the dune buggy ride reflect considerably higher absorbed power and ISO (summed) accelerations, yet lower subjective ratings than the 8x8. These two rides, which were both less than 15 seconds' duration, were very near the limits that the driver could tolerate.

The predominant acceleration for the dune buggy occurs in the 3- to 5-Hz range where both absorbed power and ISO acceleration are most sensitive. The dune buggy acceleration at the most sensitive absorbed power frequency (4.5 Hz) is nearly three times that of the 8x8. This explains the higher absorbed power level for the dune buggy. On the other hand, the predominant acceleration for the 8x8 is concentrated between 1 and 2 Hz where vertical absorbed power and ISO accelerations are much less sensitive. This low-frequency (1- to 2-Hz) acceleration predominance is characteristic of most conventional vehicles. Suspensions are customarily tuned to produce a sprung-mass resonance in the frequency range of 1 to 2 Hz and thereby isolate occupants from irritable vibrations in the 4- to 8-Hz region. It appears, at least for short duration travel, that drivers are more willing to accept the rather high uniform vibrations in the 4- to 8-Hz range caused by ultra-stiff suspensions rather than endure the recurring harsh jolts that occur from the softer conventional suspensions which tune the major resonances to the 1- to 2-Hz range.

This subjective willingness (as well as health implications) may well be reversed for long duration travels, such as occur during operations of agricultural and earthmoving equipment. This possible contrast between the effects of short- and long- duration vibrations provides a high potential for application of adaptive (adjustable) suspensions. It is interesting that the single-valued ISO accelerations obtained for the

dune buggy by summing over the frequency spectrum is more restrictive than the worst single frequency.

One other psychological factor worth noting is that observation of the subjective ratings in Table 2 reveal that, for any given level of absorbed power or ISO acceleration, the ratings increase with increases in surface roughness. That is, a 6-watt ride feels rougher on a rough course than it does on a smooth course.

HOW GOOD IS THE 6-WATT LIMIT?

There has been quite a bit of controversy and dissent over the use of the 6-watt absorbed power level as a ride-limiting criterion. The reason for its initial selection was a direct outcome of the results of Pradko, Lee, and Kaluza's laboratory study which established the absorbed power concept and subsequent 6-watt limit. The limits of its validity were explained earlier in this paper. The criterion has served well for many years as a sound, consistent measure of practical operational limits. It is not a human tolerance limit; experience has shown that competitive drivers and crews will accept considerably higher absorbed power levels for short durations, even at the risk of injury. However, test results have indicated the 6-watt level may be a good measure of a driver's self-imposed criteria of acceptability.

Figure 6 shows the relative and cumulative frequency distributions of the vertical absorbed power recorded at the driver's seat of a light wheeled vehicle while negotiating two cross-country mobility traverses. These data reflect the same WES driver in the same vehicle. The driver was instructed to drive the well-marked traverses at the fastest safe speed. There were a number of occurrences of factors other than ride, such as slopes, curves, and vegetation, that restricted the speed. However, it is seen that the percent of time the driver spent at ride levels above 6 watts was relatively small (3 minutes or 6 percent on one course and 10 minutes or 21 percent on the other course). Similar results have been obtained with other drivers when instructed to drive at their discretion for extended durations. However, experience has shown that the same driving instructions for short courses and short durations (1 minute or less) generally result in speeds limited by vehicle control and usually considerably higher absorbed power levels. In any instance, for rather long durations the 6-watt level appears to be a driver-preferred limit.

PLANS FOR FUTURE WORK

As mentioned previously, plans are being formulated under the FAVR program for a joint United States-Federal Republic of Germany program to begin in May 1984 to study the relative merits of the absorbed power and ISO procedures. Work will continue at WES using the existing data base to study and evaluate the merits of the two methods and other proposed criteria. Emphasis will be placed on the following areas:

Effects of impulses and shock loads on ride criteria.

Detailed analysis of crest factor levels and their effects on ride criteria.

Influence of rotational motion.

Effects of multi-axis vibrations on ride criteria.

Effects of duration of exposure.

Effects of vibrations on recumbent subjects.

CONCLUSIONS

Based on the results of this preliminary analysis, it is concluded that for short distance travel and limits based on safety and health:

Absorbed power and ISO weighted accelerations produce similar ride performance relations.

Human response to vibration is heavily influenced by psychological effects.

- At equal levels of intensity, rides with high crest factors feel more severe than rides with uniform acceleration.
- At equal levels of intensity, rides feel rougher on rough courses than on smooth courses.

Neither absorbed power nor ISO weighted accelerations account for psychological influences.

Vehicle control and not high vibration levels are the principal limits for short-duration travel.

Rides composed of recurring jolts tend to hinder vehicle controllability and are more objectionable than rides composed of more uniform motions.

For short-duration travel, drivers are more willing to accept rather high uniform accelerations in the sensitive frequency range (4 to 8 Hz) rather than endure recurring harsh jolts that occur from the softer conventional suspensions which tune major resonances to the 1- to 2-Hz range.

REFERENCES

Pradko, F., Lee, R., and Kaluzs, V. 1966. "Theory of Human Vibration Response," presented at the Winter Annual Meeting and Energy Systems Exposition of the American Society of Mechanical Engineers, New York.

Berry, L. G. 1975. "Advanced Concept Vehicle - Cargo," Master Test Report GM 265A, Headquarters, Modern Army Selected Systems Test, Evaluation, and Review, Fort Hood, Tex.

International Standards Organization (ISO). 1978. "Guide for the Evaluation of Human Exposure to Whole-Body Vibration," 2d ed., Publication ISO 2631.

Allen, G. R. 1975. "Ride Quality and International Standard ISO 2631 (Guide for the Evaluation of Human Exposure to Whole-Body Vibration)," 1975 Ride Quality Symposium, NASA TM X-3295/DOT-TSC-OST-75-40.

Osborne, D. L. 1983. "Whole-Body Vibration and International Standard ISO 2631: A Critique," The Human Factors Society, Inc.

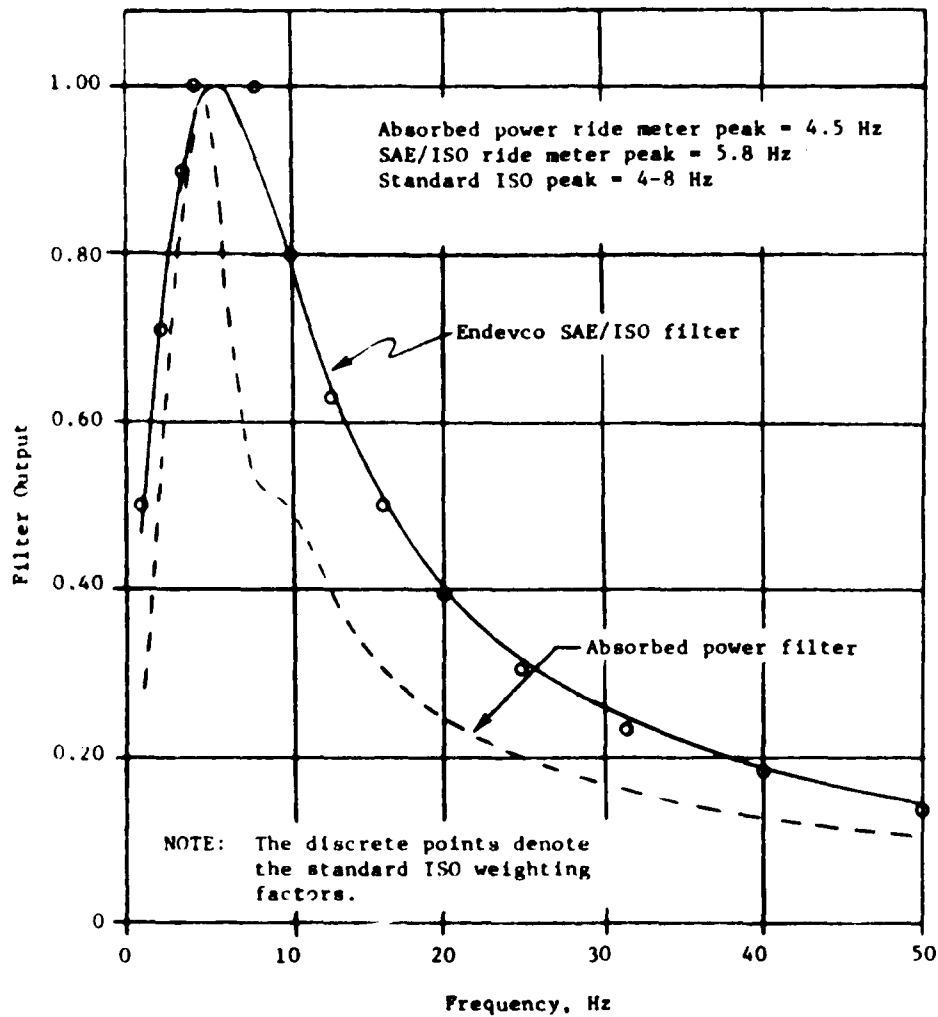


Figure 1. Comparison of normalized filters for vertical vibration, Endevco SAE/ISO filter, absorbed power filter, and standard ISO filter

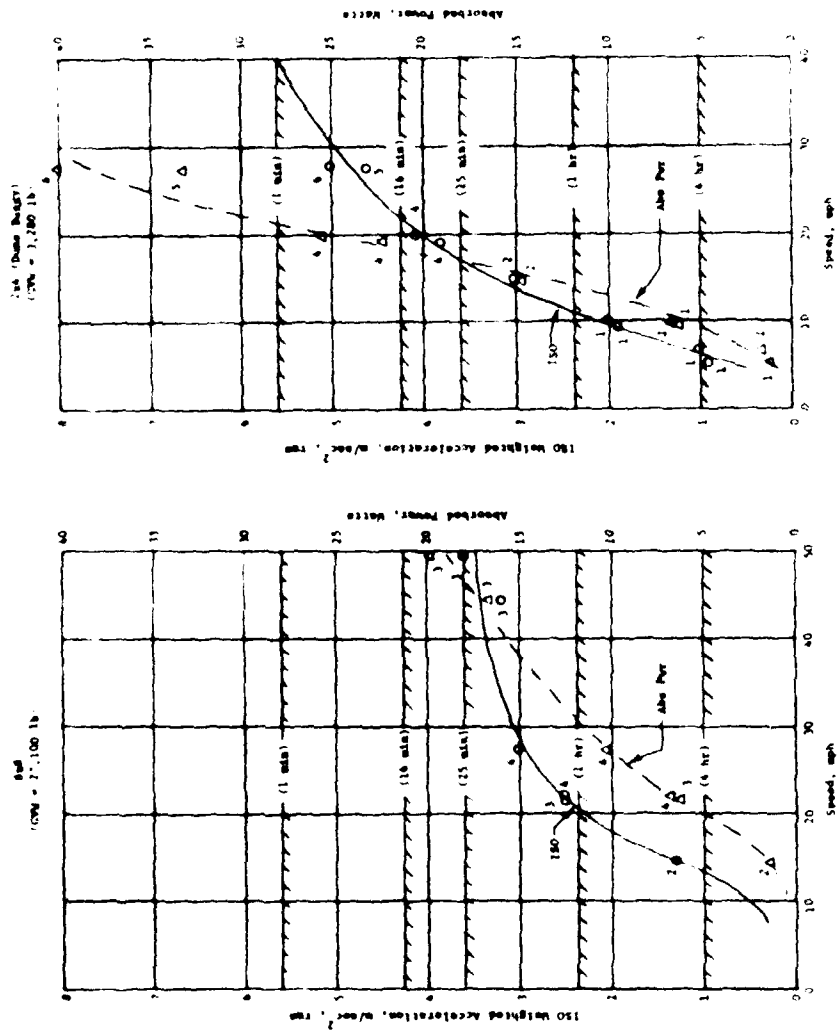


Figure 2. Comparison of vertical ISO weighted acceleration and absorbed power versus speed for the Red and the Sea Dune Buggy during ride tests on a 1.1 in. rms surface roughness. (NOTE: Numbers adjacent to data represent driver's subjective rating where 1 = ease, 2 = moderate, 3 = discomfort, 4 = unacceptable, 5 = intolerable.)

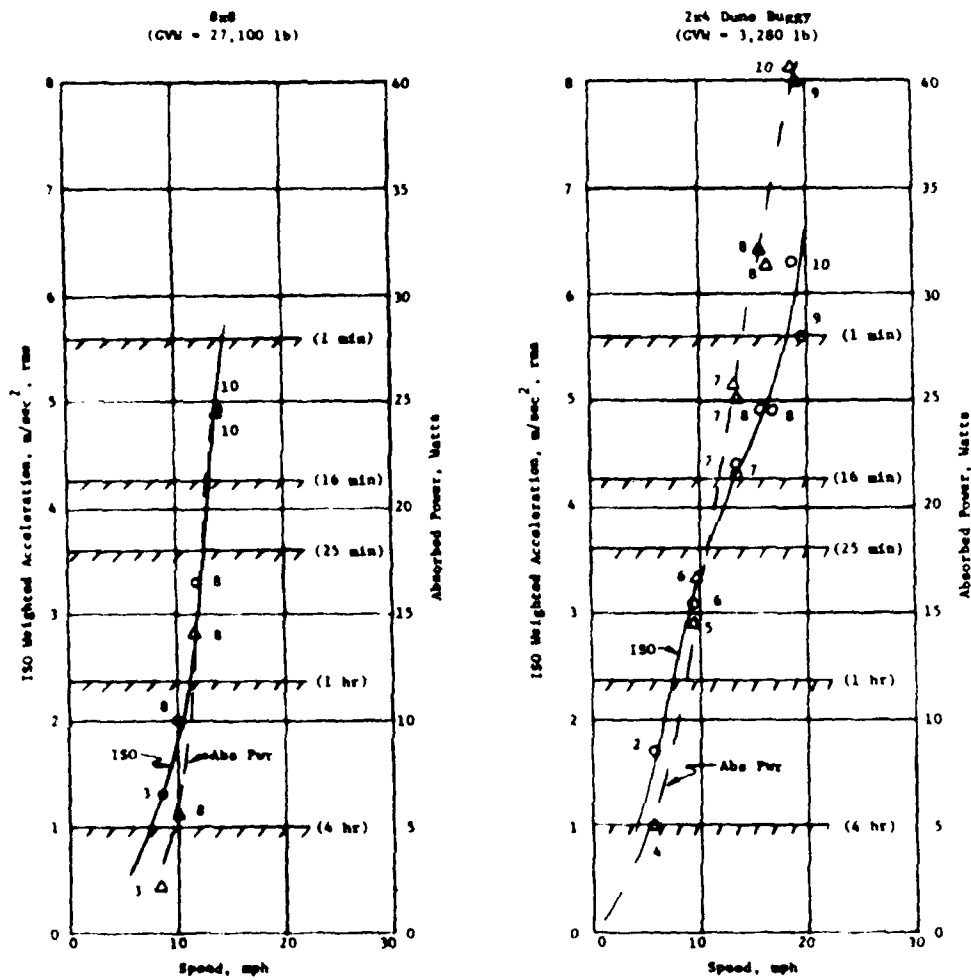


Figure 3. Comparison of vertical ISO weighted acceleration and absorbed power versus speed for the 8x8 and the 2x4 Dune Buggy during ride tests on Letourneau test course No. 7 (surface roughness = 2.8 in. (rms)). (NOTE: Numbers adjacent to data represent driver's subjective rating index.) Time lines represent ISO exposure limit boundaries.

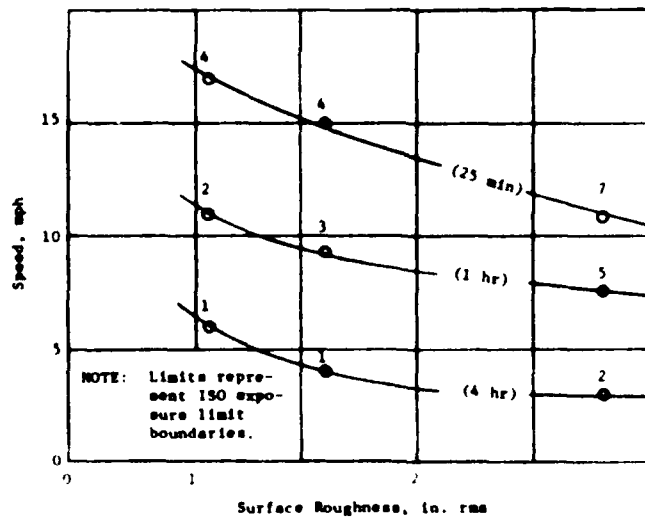
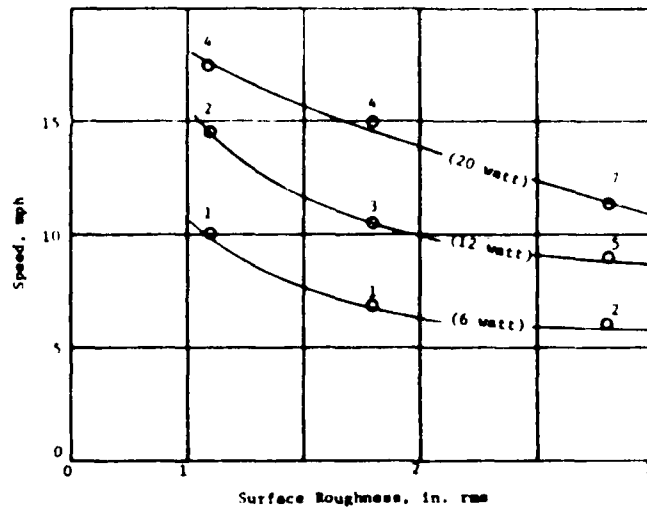


Figure 4. Comparison of absorbed power and ISO limiting-speed versus surface roughness relations for three selected levels of vertical vibrations (ride tests with the 2x4 Dune Buggy). (NOTE: Numbers above data denote driver's subjective rating index.)

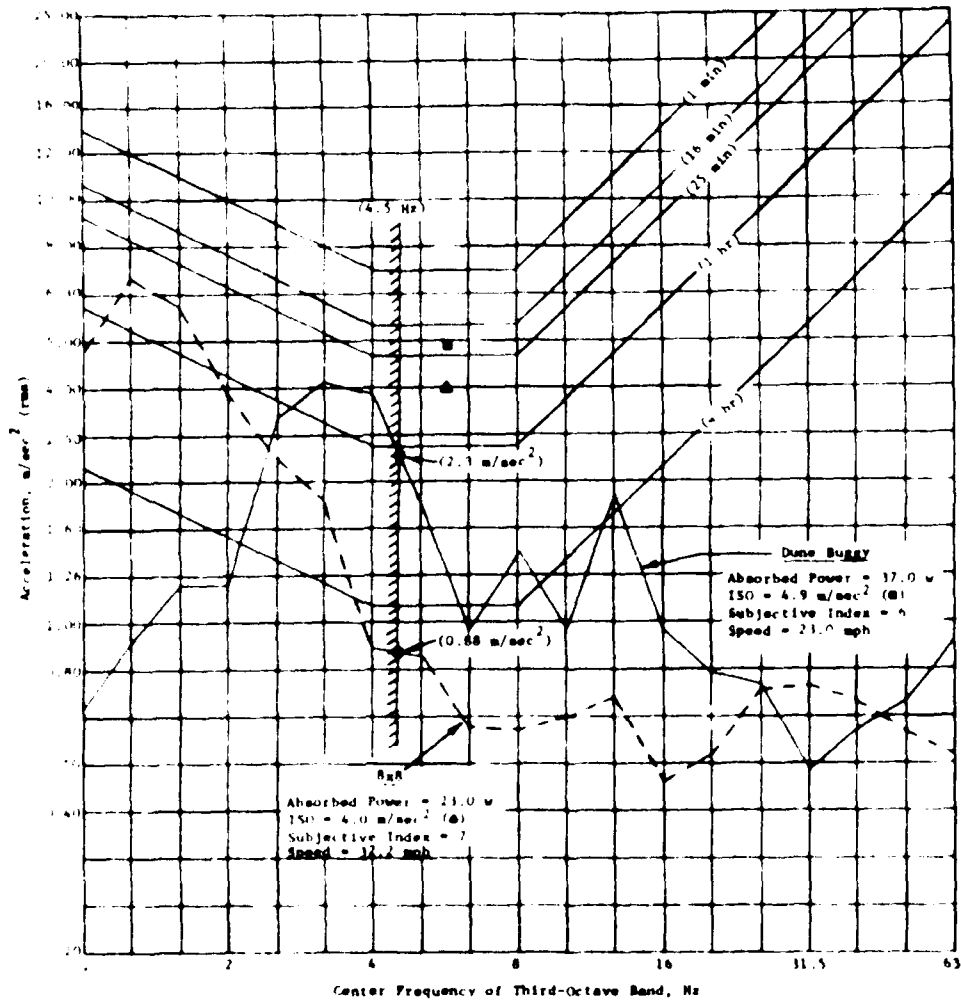
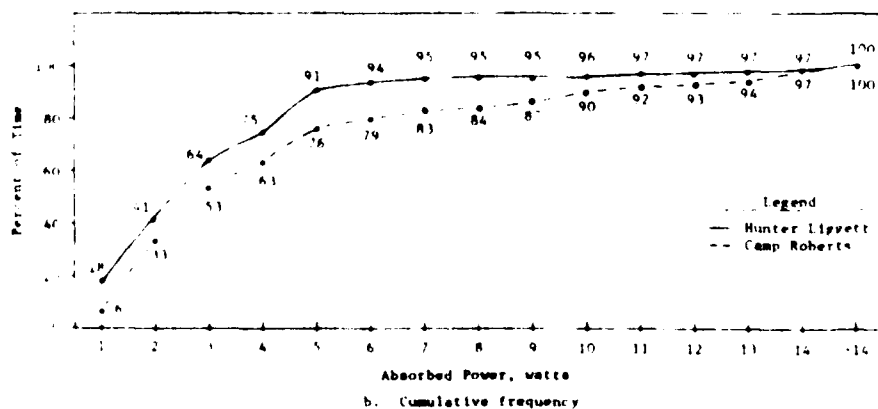
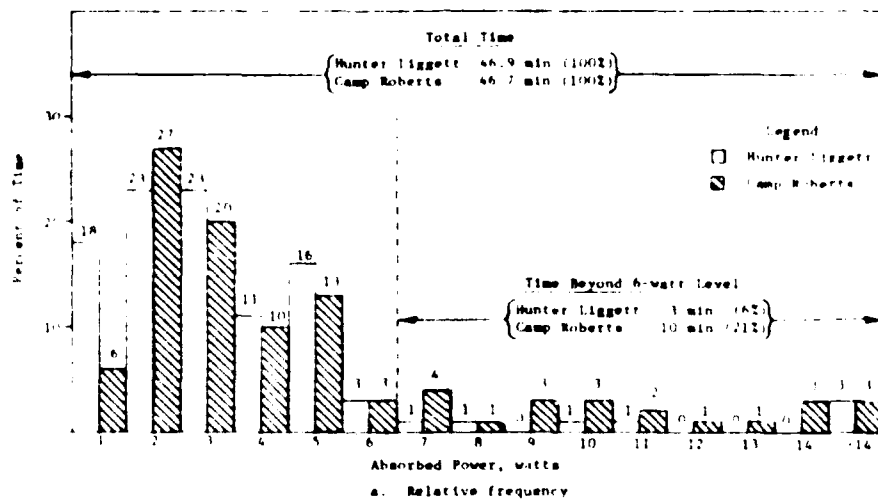


Figure 5. Comparison of ISO vertical acceleration exposure limits for 8x8 vehicle and Dune Buggy during ride tests on Letourneau test course No. 5 (surface roughness = 1.6 in., rms)



Statistic	Statistics	
	Hunter Liggett	Camp Roberts
Traverse length	22.4 mi	22.3 mi
Average speed	28.7 mph	28.6 mph
Total time	46.9 min	46.7 min

Figure 6 Relative and cumulative frequency distributions of vertical absorbed power measured at the driver's seat of a light wheeled vehicle on two mobility traverses

Table 1
Ride Data for 8x8 and 2x4 (Dune Buggy)

Vehicle	Test Course	Surface Roughness in., rms	Test No.	Time (sec)	Speed (mph)	Ride Meters		Subjective Index
						Absorbed Power watts	ISO Acceleration $\frac{g}{sec^2}$ (rms)	
8x8	Lot 4	1.1	30	23.5	14.5	1.4	1.3	2
			31	12.5	27.3	10.2	3.0	4
			32	15.9	21.4	6.4	2.5	3
			33	15.5	22.0	6.8	2.5	4
			34	7.7	44.3	16.6	3.2	3
			35	6.9	49.4	20.0	3.6	3
	Lot 5	1.6	36	23.6	14.4	5.4	1.9	5
			37	22.5	15.1	5.0	1.9	5
			38	30.5	11.2	2.7	1.2	3
			39	17.1	20.0	12.1	3.3	6
			40	13.4	25.4	12.4	3.5	4
			41	10.6	32.2	23.0	4.0	7
	Lot 7	2.8	42	39.0	8.7	2.2	1.3	3
			43	29.4	11.6	14.0	3.3	8
			44	34.1	10.0	5.7	2.0	8
			45	24.1	14.1	24.5	4.9	10
2x4 (Dune Buggy)	Lot 4	1.1	76	66.0	5.2	1.3	0.9	1
			77	62.5	6.5	1.5	1.0	1
			78	36.8	9.3	6.1	1.9	1
			79	34.3	9.9	6.6	2.0	1
			80	23.4	14.6	14.8	3.0	2
			81	23.3	14.6	14.8	3.1	3
			82	17.8	19.2	22.1	3.8	4
			83	17.3	19.7	25.5	4.1	4
			84	12.5	27.3	33.4	4.8	5
			85	12.2	27.9	40.5	5.0	6
	Lot 5	1.6	150	60.3	5.7	3.5	1.4	1
			151	59.5	5.7	3.2	1.3	1
			152	33.8	10.0	11.5	2.6	3
			153	34.8	9.8	9.9	2.4	2
			154	23.7	14.4	18.7	3.5	4
			155	24.6	13.9	16.8	3.3	3
			156	18.5	18.4	25.5	4.2	4
			157	18.5	18.4	23.0	4.0	3
			158	14.8	23.0	37.0	4.9	6
			159	Void	Void	Void	Void	Void
			160	14.6	23.4	32.3	4.7	5
			161	12.5	27.3	42.2	5.3	6
			162	12.0	28.4	35.1	5.1	6
			163	8.8	38.8	41.4	5.9	6
			164	8.7	39.2	36.6	5.3	6
			165	7.6	44.9	38.7	5.9	6
			166	7.8	43.7	34.7	5.3	7
	Lot 7	2.8	179	58.5	5.8	5.0	1.7	2
			180	55.9	6.1	5.0	1.7	2
			181	35.1	9.7	16.8	3.3	6
			182	34.0	9.5	14.5	3.1	5
			183	25.6	13.2	25.8	4.4	7
			184	25.1	13.6	25.1	4.3	7
			185	22.0	15.5	32.1	4.9	8
			186	20.5	16.6	31.4	4.9	8
			187	17.3	19.7	41.2	5.6	9
			188	18.2	18.7	42.8	6.3	10

Table 2
Comparison of Limiting Speeds versus Surface Roughness
for Selected Absorbed Power and ISO
Vertical Vibration Levels

Absorbed Power Levels					
Test Course	Surface Roughness in. (rms)	Limiting Speeds, mph			
		6-watt	12-watt	20-watt	40-watt
2x4 Dune Buggy					
4	1.1	10.0 (1)	14.5 (2)	17.5 (4)	27.5 (6)
5	1.6	7.0 (1)	10.5 (3)	16.0 (4)	25.0 (6)
7	2.8	6.0 (2)	9.0 (5)	11.5 (7)	19.0 (10)
Mx8					
4	1.1	22.0 (3)	31.0 (4)	52.0 (3)	--
5	1.6	15.0 (5)	22.5 (5)	30.5 (7)	--
7	2.8	10.0 (8)	10.5 (8)	13.0 (10)	--
ISO Levels					
Test Course	Surface Roughness in. (rms)	Limiting Speeds, mph			
		(4-hr) 1.06 m/sec ²	(2-hr) 2.36 m/sec ²	(25-min) 3.60 m/sec ²	(1-min) 5.60 m/sec ²
2x4 Dune Buggy					
4	1.1	6.0 (1)	11.0 (1)	17.0 (4)	40.0 (6)
5	1.6	4.0 (1)	9.5 (3)	15.0 (4)	38.0 (6)
7	2.8	3.0 (2)	7.5 (4)	11.0 (6)	18.0 (9)
Mx8					
4	1.1	14.0 (2)	20.5 (4)	50.0+ (3)	--
5	1.6	11.0 (3)	17.0 (6)	26.0 (4)	--
7	2.8	8.0 (3)	10.5 (8)	12.5 (8)	--

NOTE: Numbers in parentheses denote driver's subjective rating index (1 to 10). Dashes in columns denote levels could not be achieved due to vehicle control problems.



AD-P004 281

COMPARISON OF MEASURED AND SIMULATED RIDE COMFORT FOR AN AGRICULTURAL TRACTOR AND INFLUENCE OF TRAVEL SPEED AND TYRE-INFLATION PRESSURE ON DYNAMIC RESPONSE

C. STRAUSS, W. CHRIST

BATTELLE-INSTITUT E.V., FRANKFURT AM MAIN, FRG

INTRODUCTION

Off-road vehicles, wheeled or tracked, such as commercial vehicles (e.g. agricultural wheeled tractors, scrapers, excavating machines, trucks, truck tractors) or military vehicles (e.g. trucks, armoured vehicles and special-purpose vehicles) have to operate under extreme terrain conditions. One aspect of these conditions is the terrain roughness, which has an important influence, on the one hand on the vehicle stress, on the cargo or attached implements, and on the other hand on the ride comfort for the driver. Therefore, the need for reducing the shock and vibration levels, taking into account increasing travel speed, becomes an important criterion for the design of most of the above vehicles. The International Standards Organization (ISO) has proposed fatigue-decreased proficiency limits as a function of exposure time and excitation frequency, which are applicable to off-road vehicles /1/. When designing a new vehicle, the manufacturer has to make sure that the ISO criteria are satisfied, depending on the purpose of the vehicle and the expected time of exposure to shock and vibration.

Purpose and Scope

The purpose of this paper is to demonstrate the possibilities of the manufacturer to use a generalised mechanical system simulation program to compute the dynamic behaviour and the ride comfort of a vehicle travelling over a specified terrain.

A computer program has been implemented at Battelle-Institut, Frankfurt am Main, FRG, which is capable of analysing motion-constrained, rigid-body and closed-loop kinematic chain mechanisms /2/. This program is also capable of formulating automatically the equations of motion, constraints and input functions and simulating the static, kinematic and dynamic response of any two- or three-dimensional mechanical system. To formulate the mechanical system, the program uses a problem-oriented language that consists of definition, data, request and control statements.

Based on acceleration data for the centre of the front axle of an agricultural wheeled tractor (FRONT) and for the point where the driver's seat is attached to the chassis (SMPT),

which were measured while the vehicle was running on the ISO 5007 standard "smooth-track" profile, first a comparison of measured and simulated data is presented, using two different ways (time integration and eigenvalue/-vector analysis) of analysing the dynamic behaviour of the vehicle by means of the simulation program, applying a specially created postprocessor, which permits the eigenvalues/-vectors of a mechanical system computed by the main program to be combined with the spline coefficients of an excitation input profile /3/.

Next, the influence of different travel speeds (12.5 km/h, 25 km/h and 40 km/h) on the dynamic response and the ride comfort of the tractor is presented. Finally, the effect of different tyre pressures measured at different travel speeds on the ISO-weighted dynamic response is described and briefly discussed.

Analysis of Measured and Simulated Dynamic Behaviour

The results presented in this paper are related to a 4.6-t, wheeled, two-axle agricultural tractor (4x2) which has an axle spacing of 2.6 m, a spacing of adjacent wheels on one axle (front/rear axle) of 1.8 m, with a 13.6 - 28 AS front tyre (dia. = 1300 mm) and an 18.4 - R 38 rear tyre (dia. = 1710 mm); the vehicle has a drivers seat suspension; for the simulations which are presented in this paper the driver's mass was defined by a value of 70 kg. As will be seen later, the effect of the estimation of the inertial properties of the vehicle will cause some differences in the results of the simulation.

The presented dynamic response for the above points of the vehicle was measured by the Institut für Landtechnik, Prof. Göhlich, Technical University of Berlin, FRG. As for this special vehicle only the vertical component of acceleration was measured, while the vehicle was running at a constant speed of nearly 12.5 km/h over the ISO standard "smooth-track" profile, only this component of the various simulations is presented in this paper.

Part I of the Results

In the first part of this paper, a comparison between different types of possible dynamic simulation procedure results are presented, using the time integration analysis as a very expensive procedure and the eigenvalue/-vector analysis as a relatively cheap way of performing dynamic simulations which, however, is subject to boundary conditions (e.g. linearised system). The measured data are presented to demonstrate the capacity and accuracy of the applied program system and type of analysis.

The ISO standard "smooth-track" profile was used as the motion input excitation where the cubic spline coefficients are separately computed taking into account the different sizes of front and rear tyres; for this part of simulation, the travel speed is set at a value of 12.5 km/h according to the ISO standards.

In Fig. 1 the measured vertical acceleration data for the seat mounted point (SMPT) are plotted in the time domain; before being stored on computer tape, these data were filtered through a 20-Hz low-pass filter to avoid any influence of higher frequencies on the results obtained. These data are stored with a time step of 0.01 s, and more than 2900 measured points are plotted; to switch this result from time to frequency domain, an FFT (Fast-Fourier Transformation) algorithm was used to obtain the relationship between the effective acceleration values and the frequency (see Fig. 2). This figure shows the typical behaviour of the SMPT of a wheeled vehicle of the above specified geometry and mass proportion /4/. Fig. 3 and Fig. 4, respectively, show the corresponding results of the vehicle system with the time integration analysis, and in Fig. 5 and Fig. 6 the corresponding results of an eigenvalue/-vector analysis are shown. It can be seen that in the frequency domain the measured and the time-integrated results agree very well (main resonance peak between 1.0 m/s² and 1.1 m/s² in a frequency range from 2.6 Hz to 2.7 Hz), while the eigenvalue/-vector analysis reaches only 0.84 m/s² at a frequency of 2.7 Hz; in the time domain, all three plots show an almost similar dynamic behaviour of the SMPT of the tractor; one reason for the differences between the two types of analysis (the input data for both types of analysis are exactly the same) is as follows: describing a non-linear system with the eigenvalues and eigenvectors (linearised system), for example at a static equilibrium position, and performing a dynamic analysis, the mechanical system is treated as a system with an assumed constant stiffness, while the stiffness of the real system changes according to the different displacements (e.g. spring stiffness) and velocities (e.g. damping rate). Comparison between the measured and simulated acceleration behaviour for the second point (FRONT) yields the following results (see also Figs. 7 to 12): in the time domain all curves are located nearly within the same range; in the frequency domain the two main resonance peaks of the effective acceleration values of the simulated system are located around 1.8 Hz and 2.6 Hz, while the measured data show these peaks at 2.6 Hz and 3.3 Hz respectively; one important reason for this offset is the fact that the values of the inertial data of the vehicle which were used in the input files are estimated.

Part II of the Results

The next part of this paper describes the influence of different travel speeds on the dynamic response of the simulated tractor; again, two different types of analysis, i.e. time integration and eigenvalue/-vector analysis, are used for the simulation. In addition to the presented results for a travel speed over the ISO standard "smooth-track" profile of $v = 12.5$ km/h, two speeds are chosen: $v = 25$ km/h and $v = 40$ km/h. According to the first part of the paper, simulation was effected for the same two points of interest at the vehicle (SMPT and FRONT).

The results are presented in Figs. 13 to 20. While both types of analysis show the same trend of increasing acceleration at increasing speed, it is remarkable that especially at the speed of $v = 40$ km/h the time integration analysis shows nearly twice the acceleration data computed by means of the eigenvalue/-vector analysis. Therefore, it is obvious that for this range of travel speed (with the corresponding displacements and accelerations) the eigenvalue/-vector analysis does not satisfy the expected accuracy; the reasons for this effect were briefly discussed in the first part of this paper (see also /5/).

Part III of the Results

Finally, the influence of travel speed on the ride analysis (ISO-weighted ride comfort) was simulated for the vehicle system; also the influence of two tyre-inflation pressures (TIP 1 = front tyre: 1.5 bar, rear tyre: 1.4 bar; TIP 2 = front tyre: 1.0 bar, rear tyre: 1.0 bar) at different travel speeds on the ISO-weighted ride comfort is shown and briefly discussed; to show the effect of a seat suspension, simulations are being made for the driver's seat and for the SMPT. Tyre spring and damping rates were changed according to the reduced tyre inflation pressure. In the following figures the boundary curves are plotted for the different exposure times (according to the ISO standard). Figs. 21 to 24 show the ride analysis results for the above points (driver's seat, SMPT) at the vehicle system travelling at a constant speed of $v = 12.5$ km/h with two different tyre inflation pressures (TIP 1, TIP 2) on the ISO standard "smooth-track" profile; it can be seen, that implementing a seat suspension has the same effect of improving the ride comfort for the driver as reducing the tyre inflation pressure. The positive effect on the ride comfort of reducing the TIP for a tractor with seat suspension can be seen in Fig. 22 and Fig. 24 respectively. As decreasing TIP results also in increasing traction effort for extreme soil conditions, it may be of an interest to implement a central tyre inflation pressure system for a tractor to improve both ride comfort and traction effort.

Figs. 25 to 28 show the same type of analysis for a constant travel speed of the vehicle system of $v = 25$ km/h. According to the results presented above ($v = 12.5$ km/h) the same effect results for the different points, except for the driver's seat: the expected improvement of the ride comfort for the driver by reducing the TIP turns into a decrease in comfort; the same effect at the driver's seat is shown in Figs. 29 to 32, which present the corresponding simulation results for the vehicle travelling at a speed of $v = 40$ km/h: in these figures the acceleration response is "smoothed" at frequencies above 2 Hz, but in the range of lower frequencies the resonance peaks increase. In practice, 25 and 40 km/h would correspond to on-the-road tractor speeds, where a low TIP anyhow is not necessary (to increase traction) or possible (increase of tyre wear).

Conclusions

The comparison of the measured and simulated acceleration data for the two fixed points at the tractor chassis show a pretty good agreement in particular for the time integration analysis; comparing the results of the two types of analysis applied, the eigenvalue/-vector analysis will cause some errors at higher input excitations (increasing travel speed).

The well known effect, of improving the ride comfort by a seat suspension and by reducing the tyre inflation pressure was demonstrated. In this context the question arises whether a central tyre inflation pressure system will simultaneously improve both the ride comfort and the tractive effort for a wheeled vehicle operating under extreme soil conditions. The question of whether such a system can be realised implemented in a wheeled tractor has been answered by the engineers at least for general off-road vehicles, but it remains to be investigated whether the market will accept the additional cost; a detailed cost/effectiveness analysis would help the user to make the decision.

References

- /1/ ISO "Guide for Evaluation of Human Exposure to Whole Body Vibration", ISO 2631, 1974 (E).
- /2/ Sheth, P.N., Uicker, Jr., J.J., "IMP (Integrated Mechanisms Program), A Computer Aided Design Analysis System for Mechanisms and Linkages," Journal of Engineering for Industry, ASME Trans., Vol. 94, Series B, No. 2, May 1972, pp. 454-464
- /3/ Claar, P.W., "Generalized rigid-body dynamics system simulation and the application to the behavior of suspended agricultural tractors", Ph. D. Dissertation, Iowa State University, 1983
- /4/ Owzar, A., "Ein Beitrag zur Untersuchung des Schwingungsverhaltens von ungefederten luftbereiften Fahrzeugen", Dissertation, Technical University of Berlin, 1975
- /5/ Cipra, R.J., Uicker, Jr., J.J., "On the Dynamic Simulation of Large Nonlinear Mechanical Systems: Part I", ASME-paper, June 1980

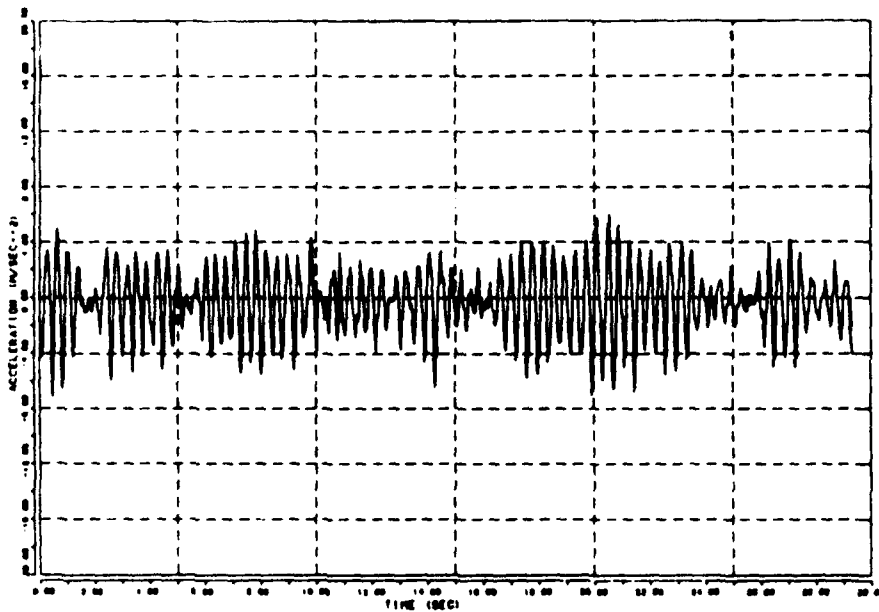


Fig. 1: Measured vertical acceleration data for the seat mounted point (SMPT) in the time domain

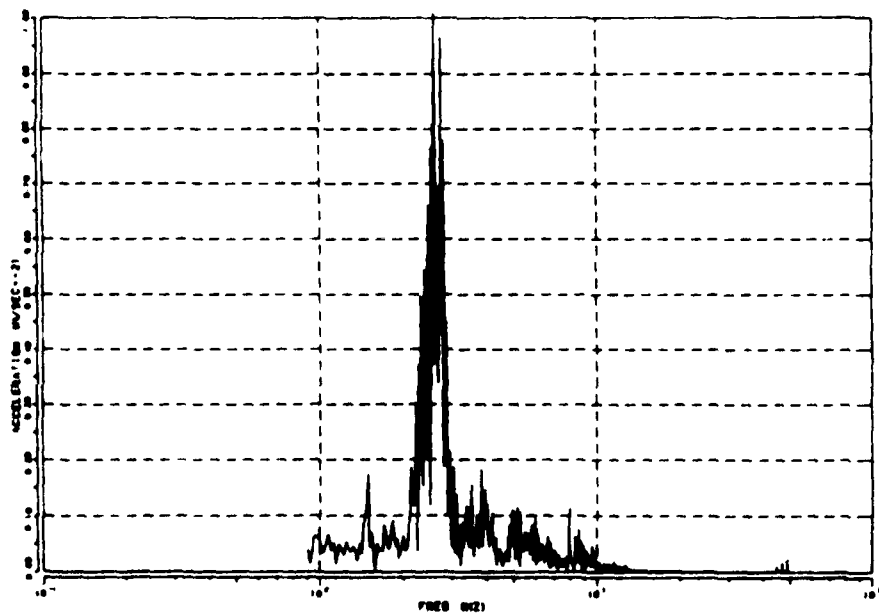


Fig. 2: Measured vertical acceleration data for the seat mounted point (SMPT) in the frequency domain

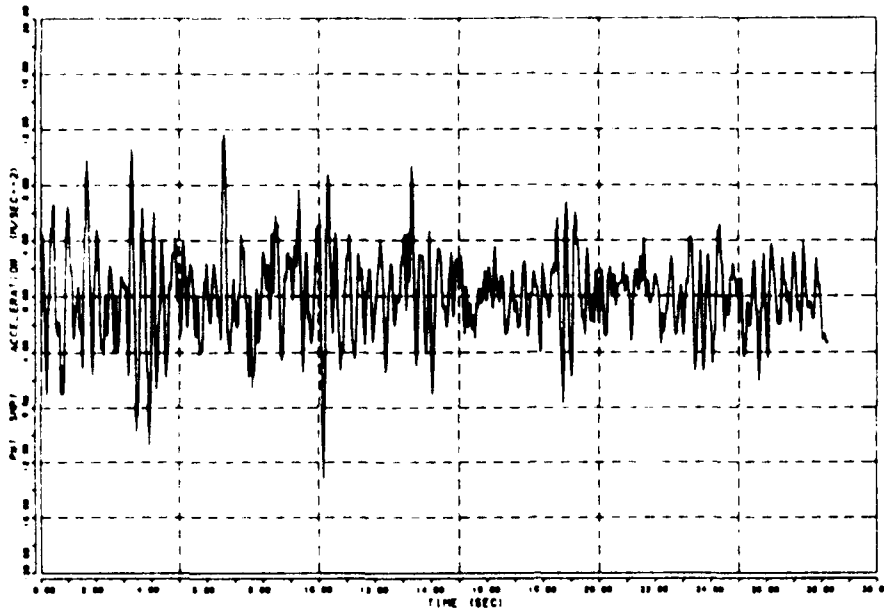


Fig. 3: Simulated (time-integration analysis) vertical acceleration data for the SMPT in the time domain

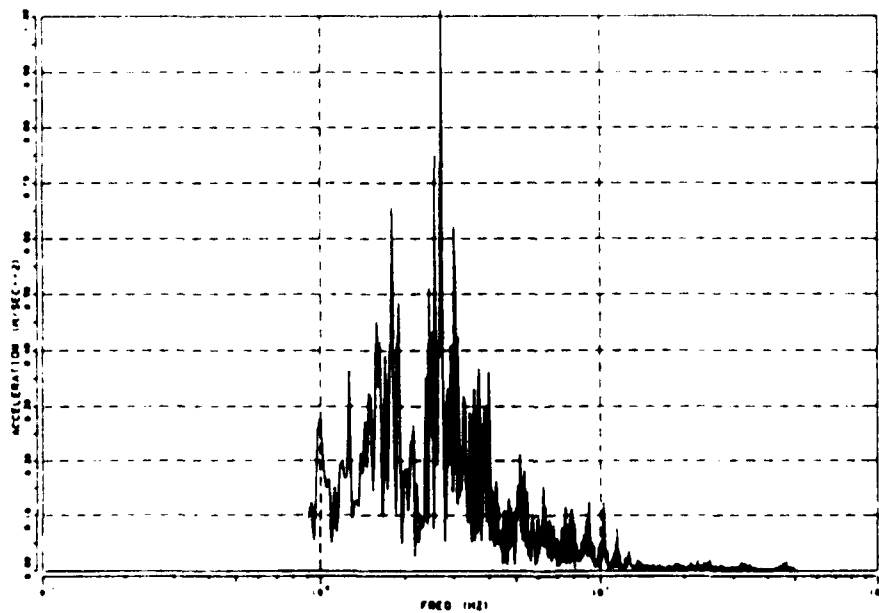


Fig. 4: Simulated (time-integration analysis) vertical acceleration data for the SMPT in the frequency domain

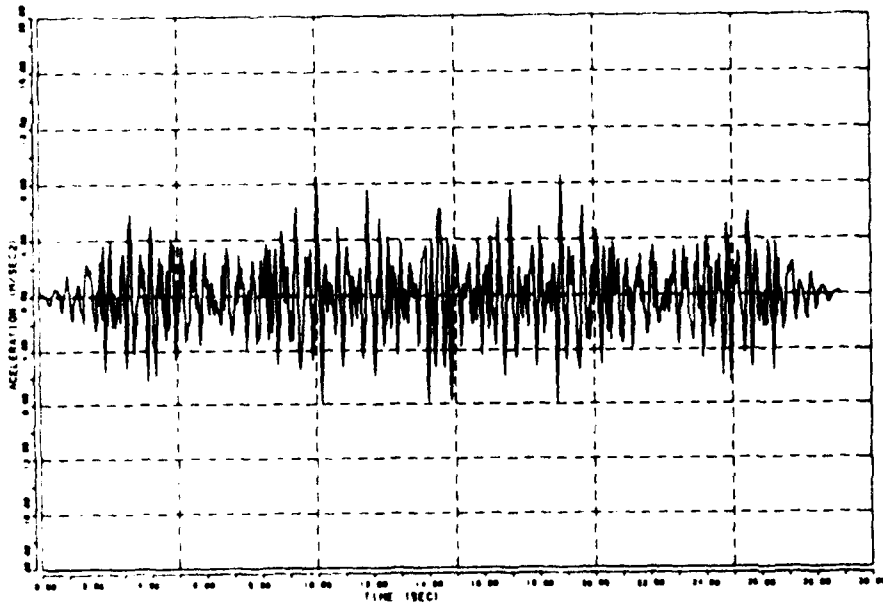


Fig. 5: Simulated (eigenvalue/-vector analysis) vertical acceleration data for the SMPT in the time domain

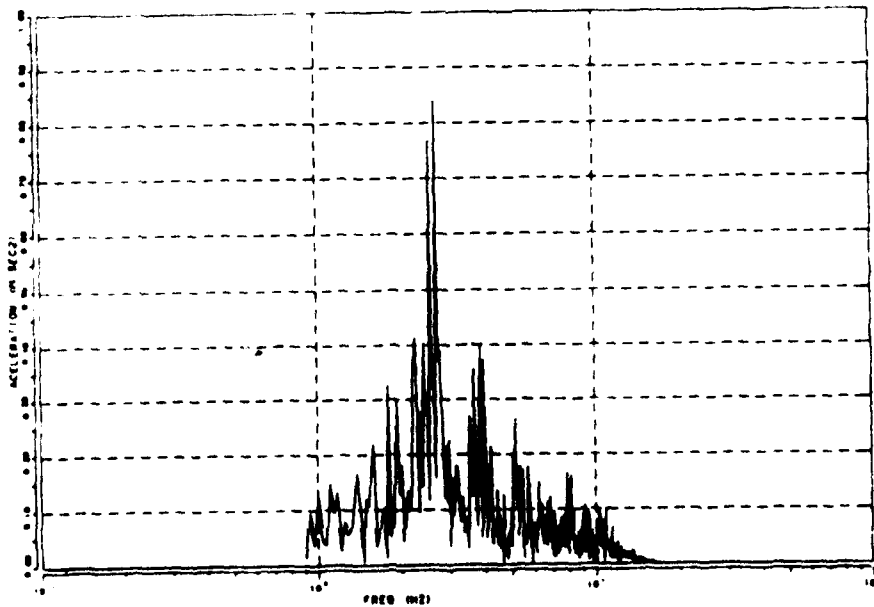


Fig. 6: Simulated (eigenvalue/-vector analysis) vertical acceleration data for the SMPT in the frequency domain

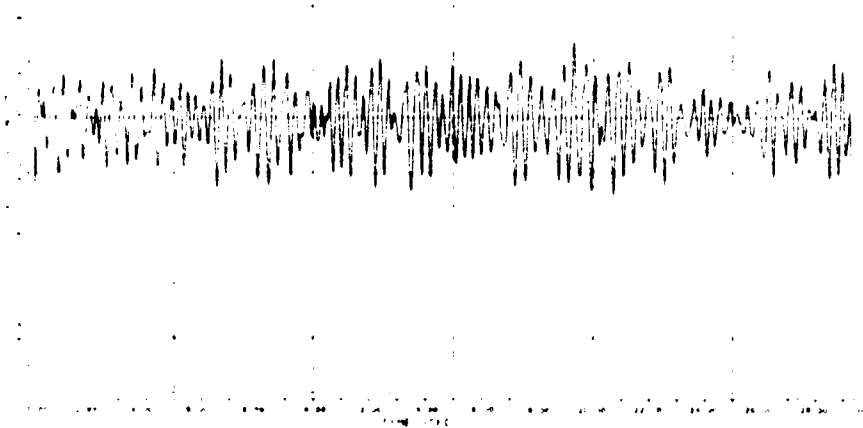


Fig. 7: Measured vertical acceleration data for the centre of the front axle in the time domain

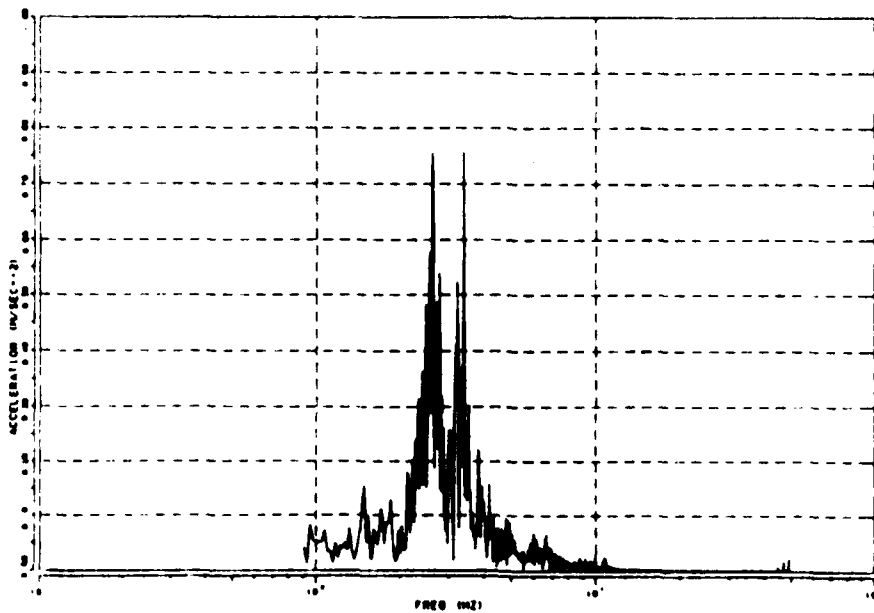


Fig. 8: Measured vertical acceleration data for the centre of the front axle in the frequency domain

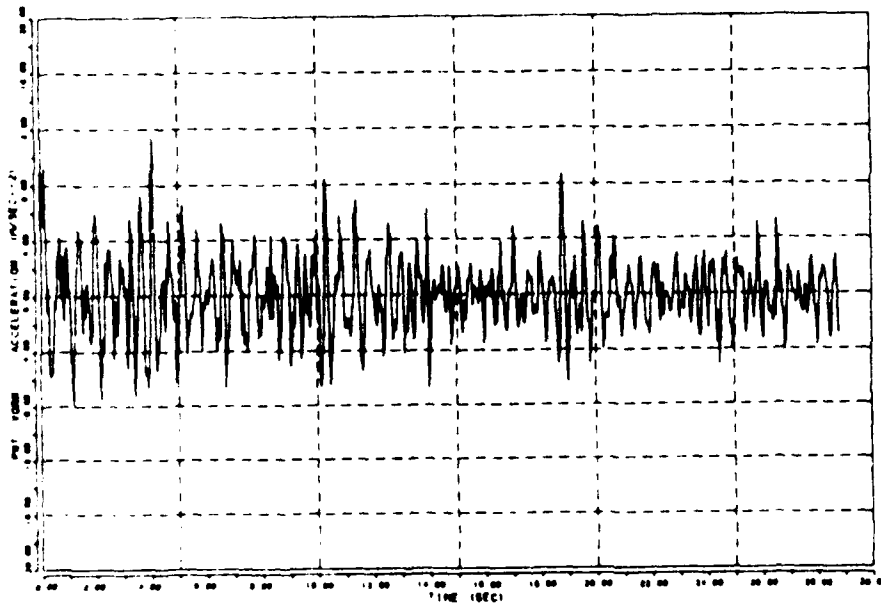


Fig. 9: Simulated (time-integration analysis) vertical acceleration data for the centre of the front axle in the time domain

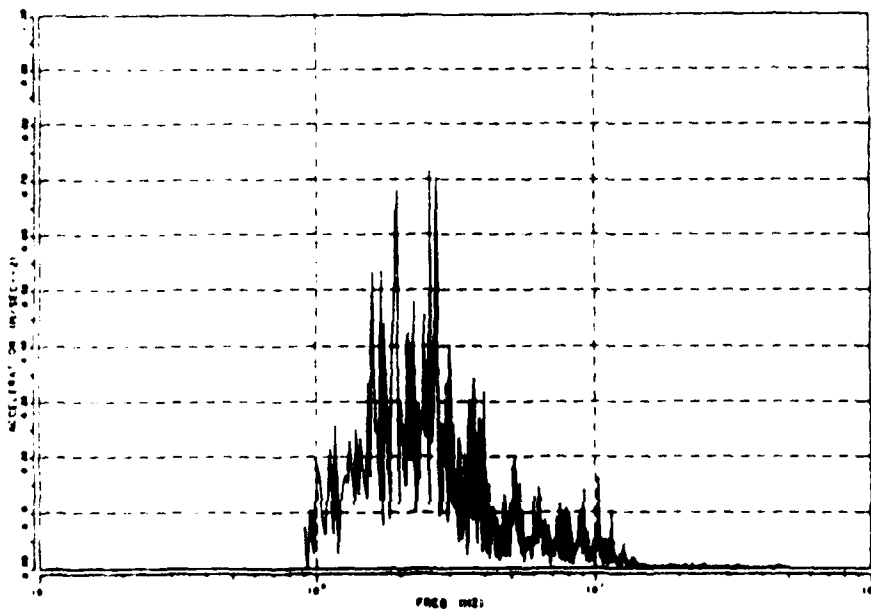


Fig. 10: Simulated (time-integration analysis) vertical acceleration data for the centre of the front axle in the frequency domain

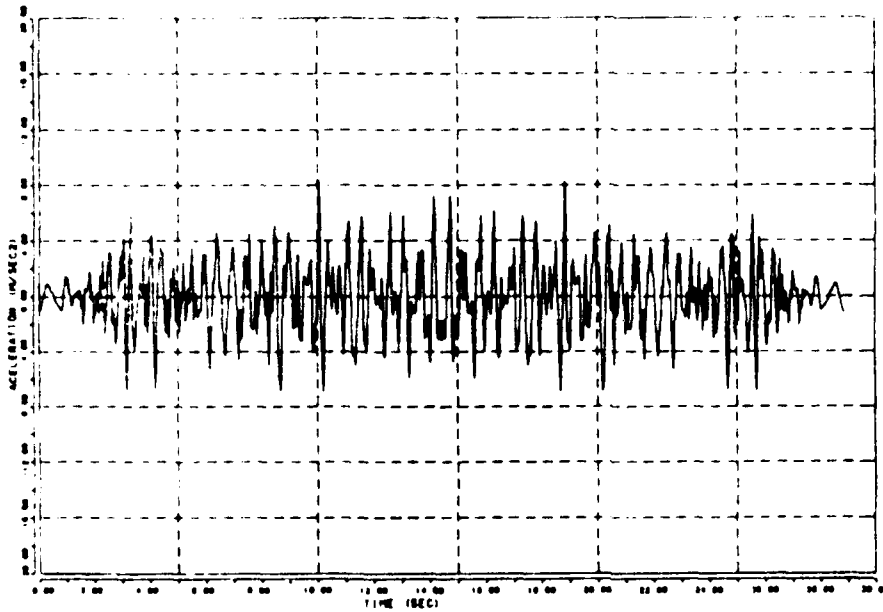


Fig. 11: Simulated (eigenvalue/-vector analysis) vertical acceleration data for the centre of the front axle in the time domain

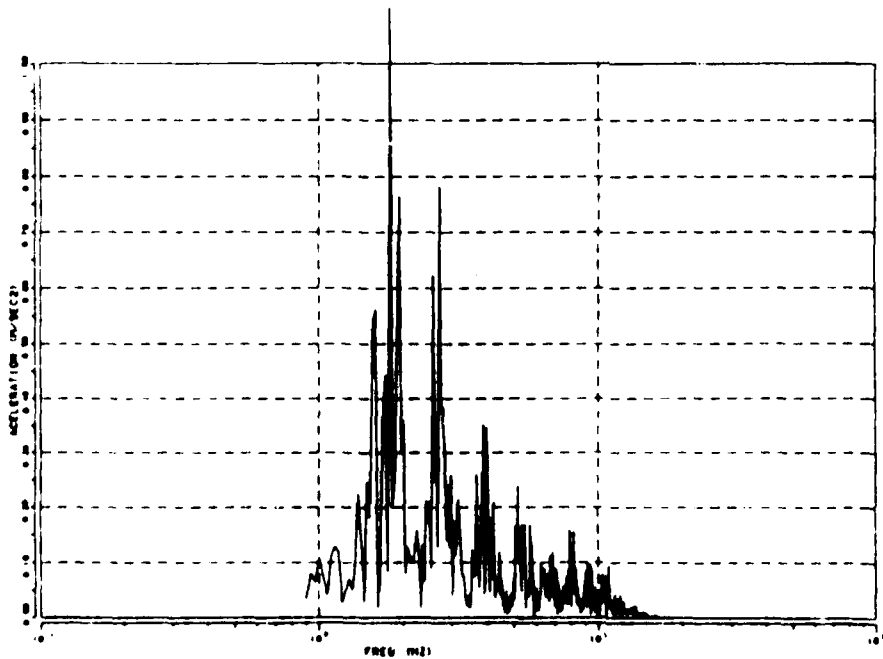


Fig. 12: Simulated (eigenvalue/-vector analysis) vertical acceleration data for the centre of the front axle in the frequency domain

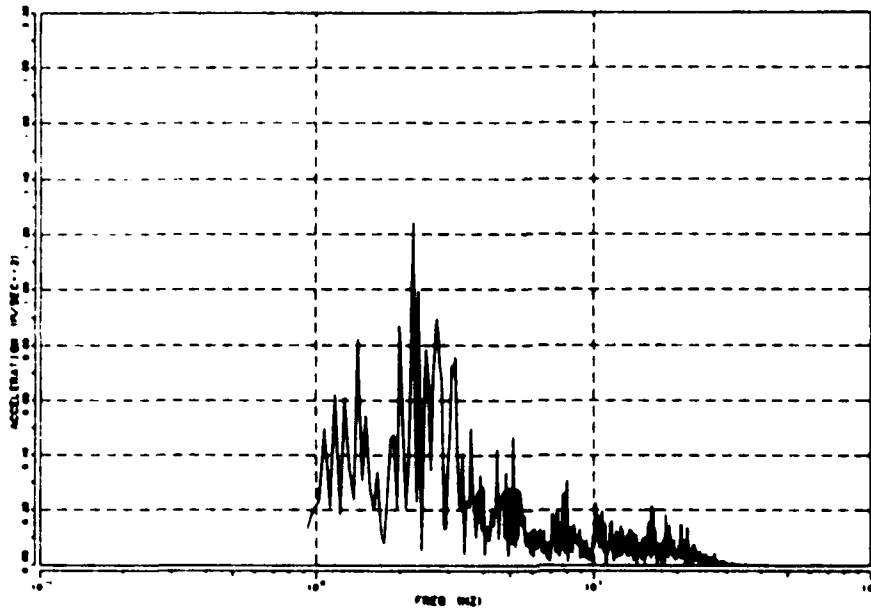


Fig. 13: Simulated (time-integration analysis) vertical acceleration data for the SMPT in the frequency domain at a travel speed of 25 km/h

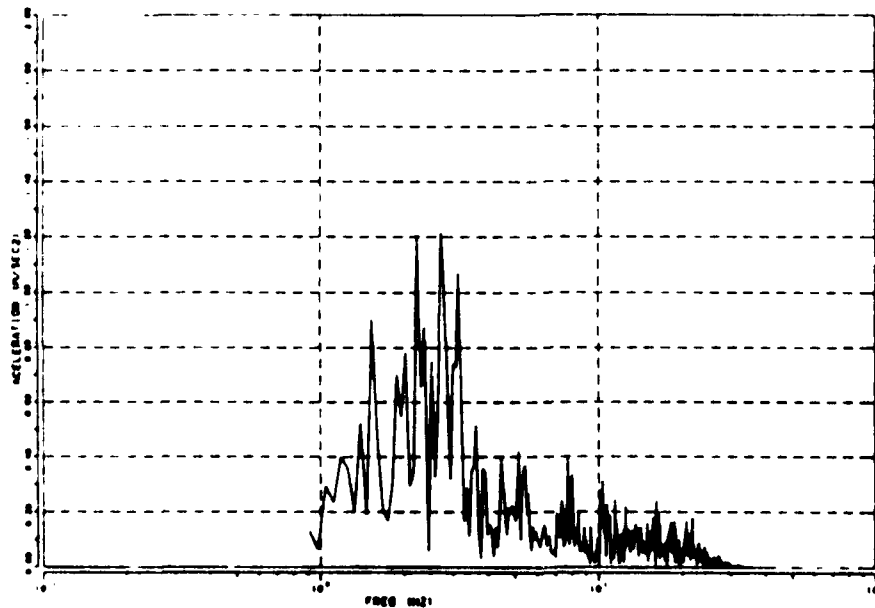


Fig. 14: Simulated (eigenvalue/-vector analysis) vertical acceleration data for the SMPT in the frequency domain at a travel speed of 25 km/h

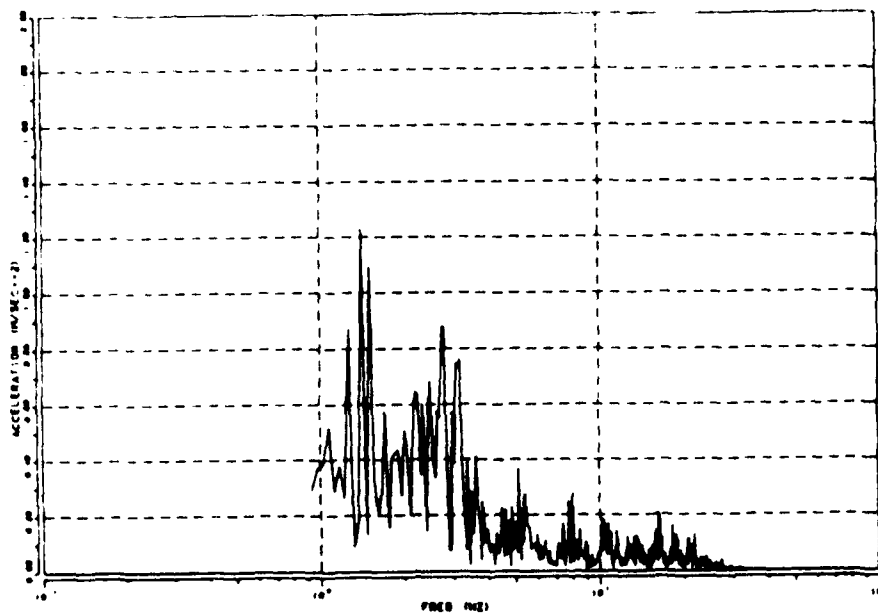


Fig. 15: Simulated (time-integration analysis) vertical acceleration data for the centre of the front axle in frequency domain at a travel speed of 25 km/h

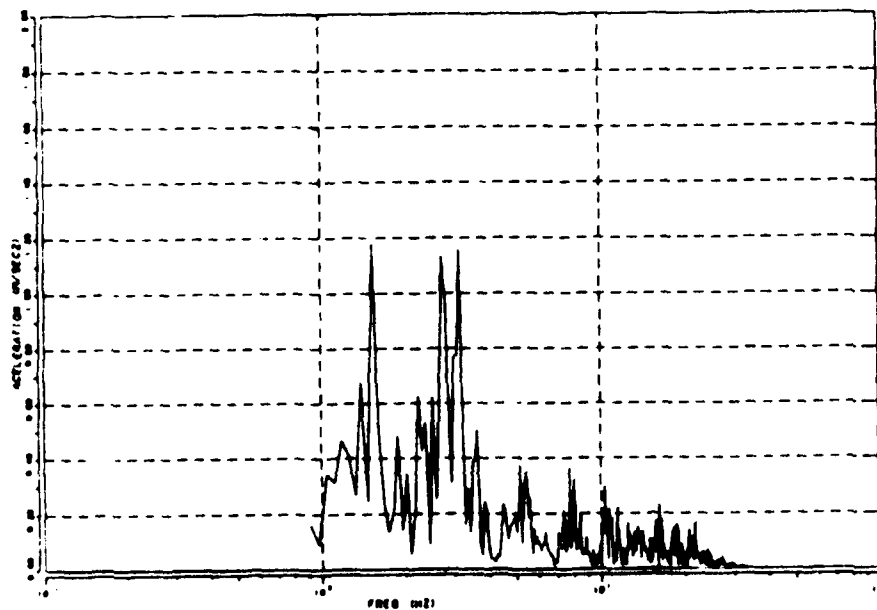


Fig. 16: Simulated (eigenvalue/-vector analysis) vertical acceleration data for the centre of the front axle in the frequency domain at a travel speed of 25 km/h

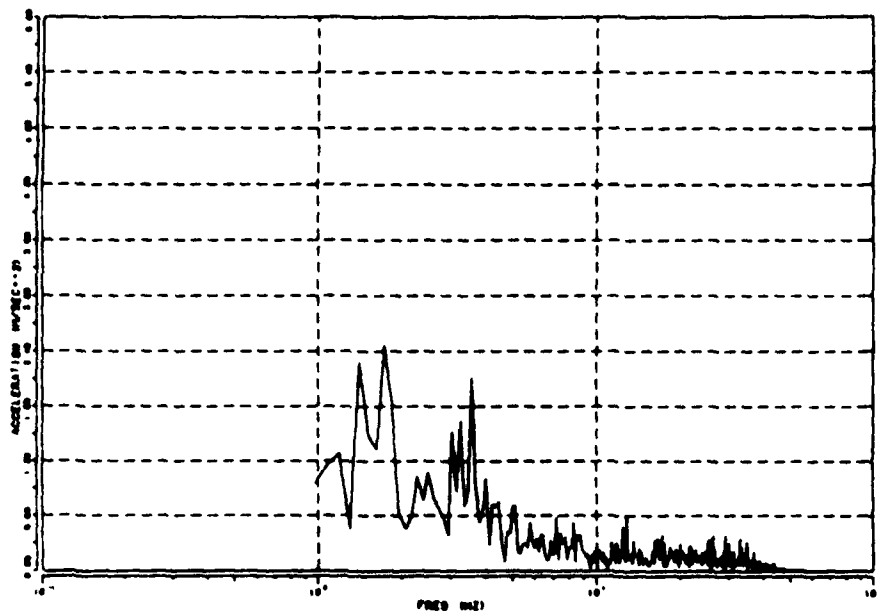


Fig. 17: Simulated (time-integration analysis) vertical acceleration data for the SMPT in the frequency domain at a travel speed of 40 km/h

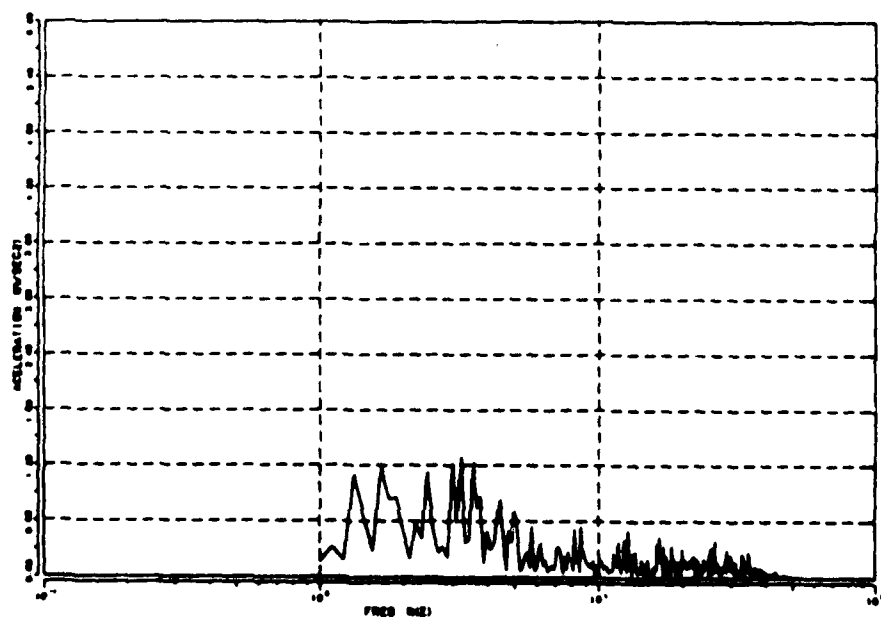


Fig. 18: Simulated (eigenvalue/-vector analysis) vertical acceleration data for the SMPT in the frequency domain at a travel speed of 40 km/h

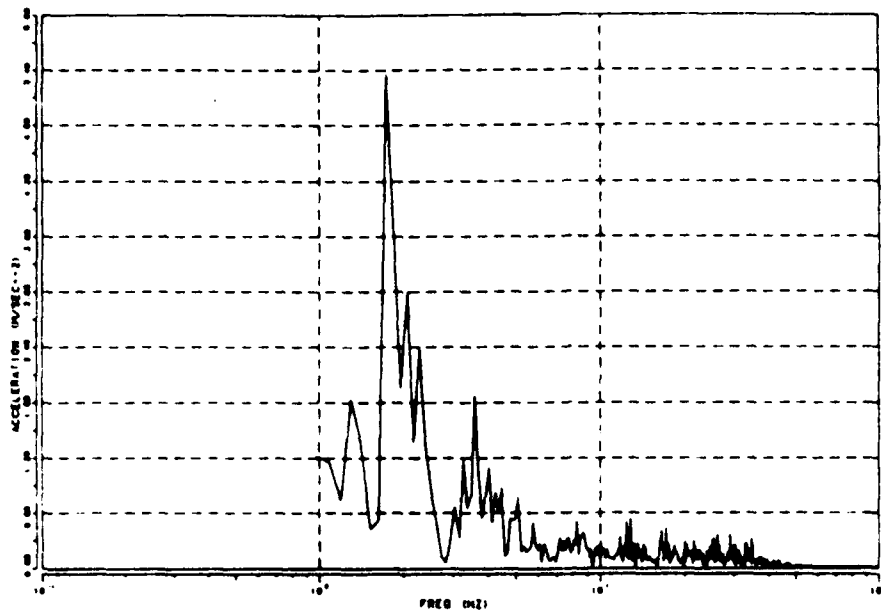


Fig. 19: Simulated (time-integration analysis) vertical acceleration data for the centre of the front axle in frequency domain at a travel speed of 40 km/h

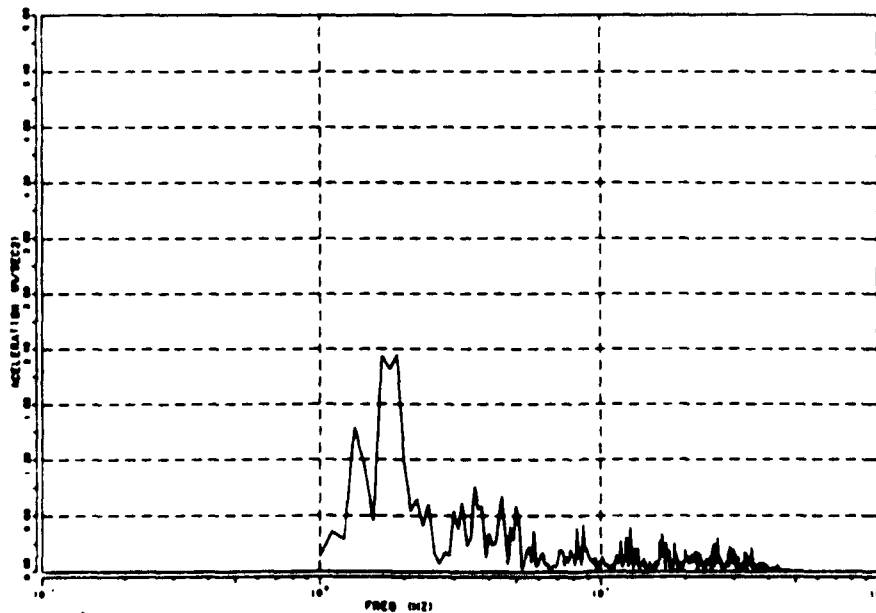


Fig. 20: Simulated (eigenvalue/-vector analysis) vertical acceleration data for the centre of the front axle in the frequency domain at a travel speed of 40 km/h

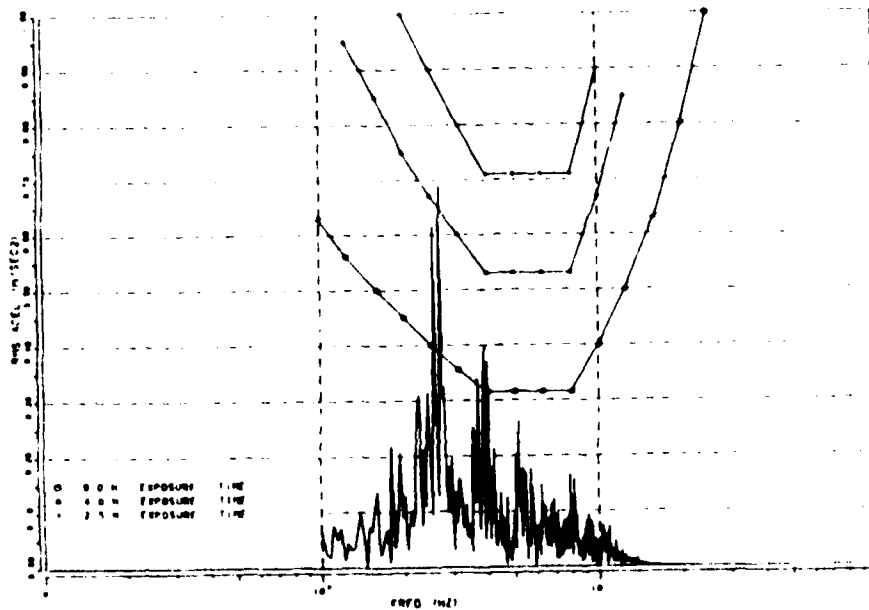


Fig. 21: ISO-weighted RMS acceleration for the SMPT
($v = 12.5$ km/h; P1)

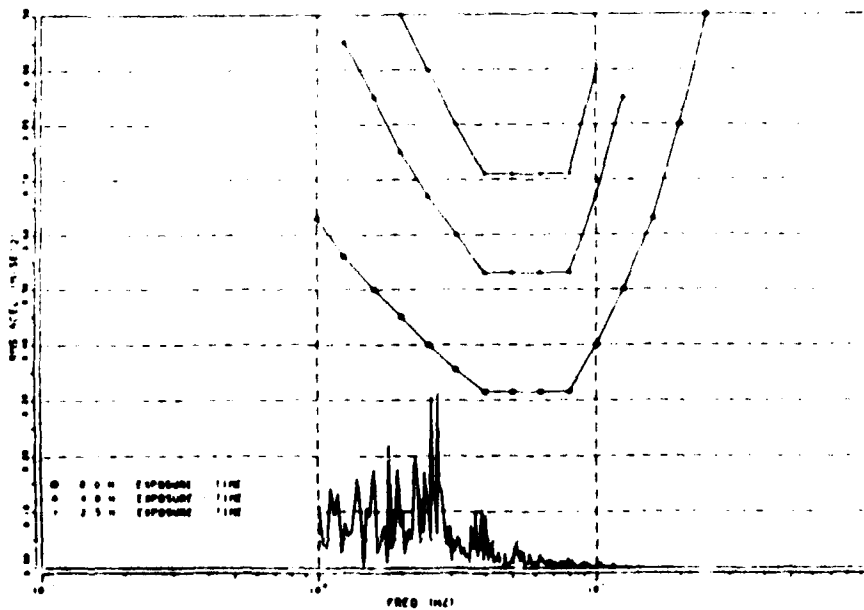


Fig. 22: ISO-weighted RMS acceleration for the driver's
seat ($v = 12.5$ km/h; P1)

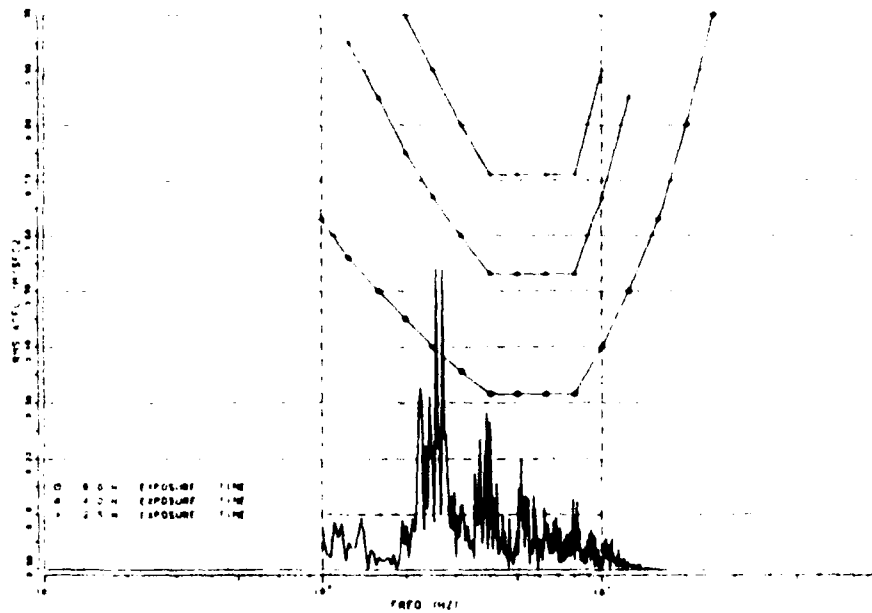


Fig. 23: ISO-weighted RMS acceleration for the SMPT
($v = 12.5$ km/h; P2)

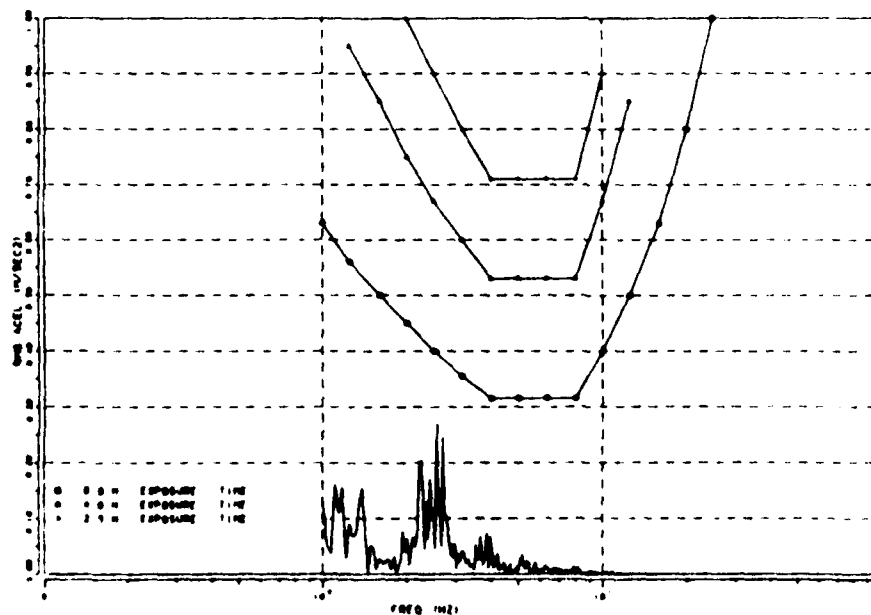


Fig. 24: ISO-weighted RMS acceleration for the driver's
seat ($v = 12.5$ km/h; P2)

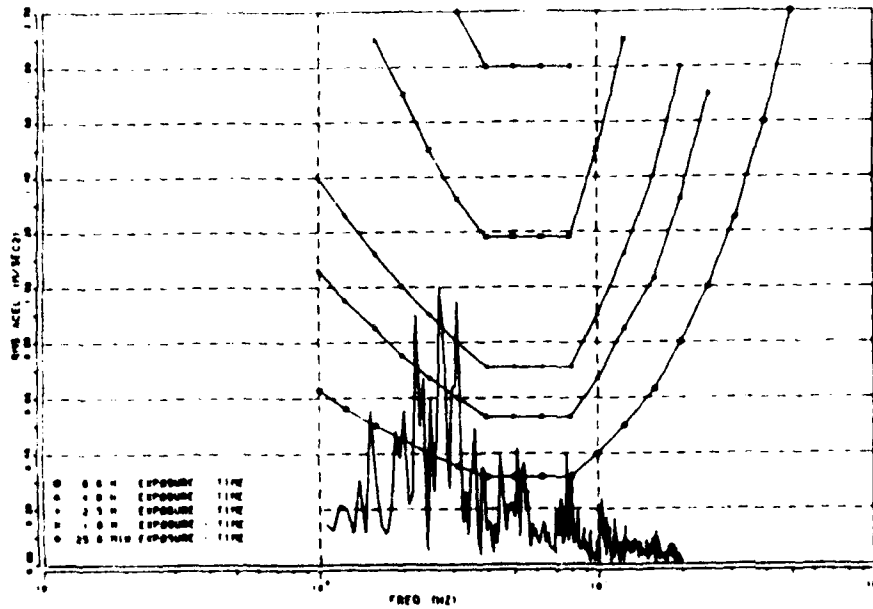


Fig. 25: ISO-weighted RMS acceleration for the SMPT
($v = 25$ km/h; P1)

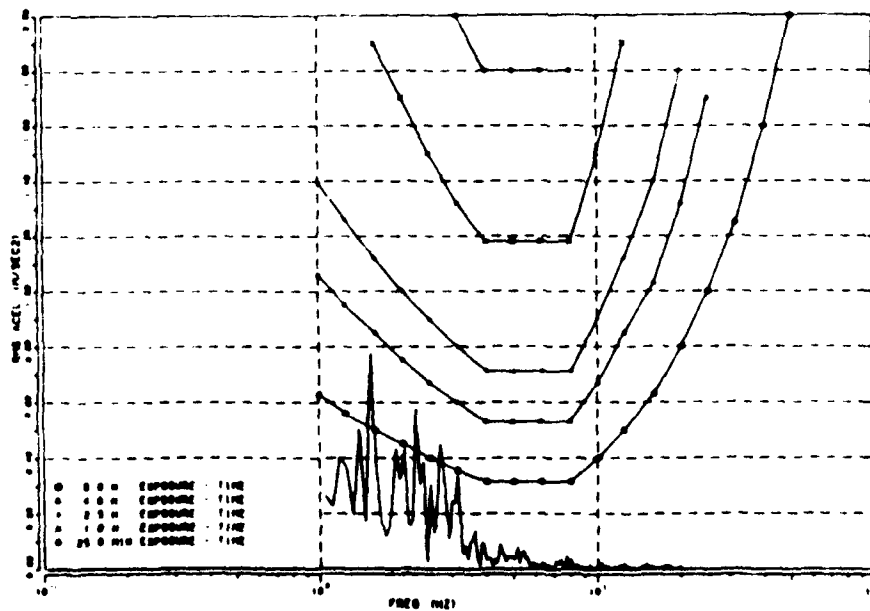


Fig. 26: ISO-weighted RMS acceleration for the driver's
seat ($v = 25$ km/h; P1)

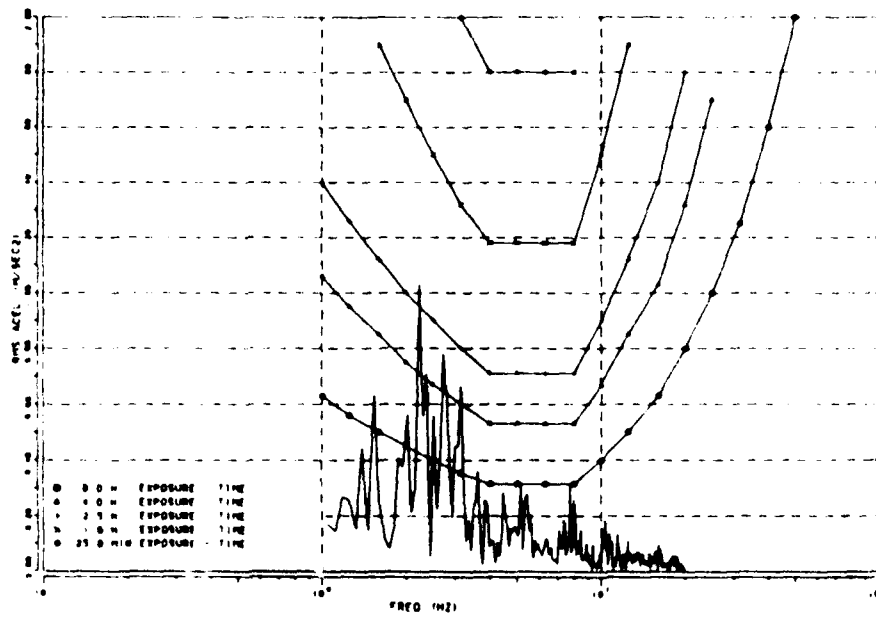


Fig. 27: ISO-weighted RMS acceleration for the SMPT
($v = 25$ km/h; P2)

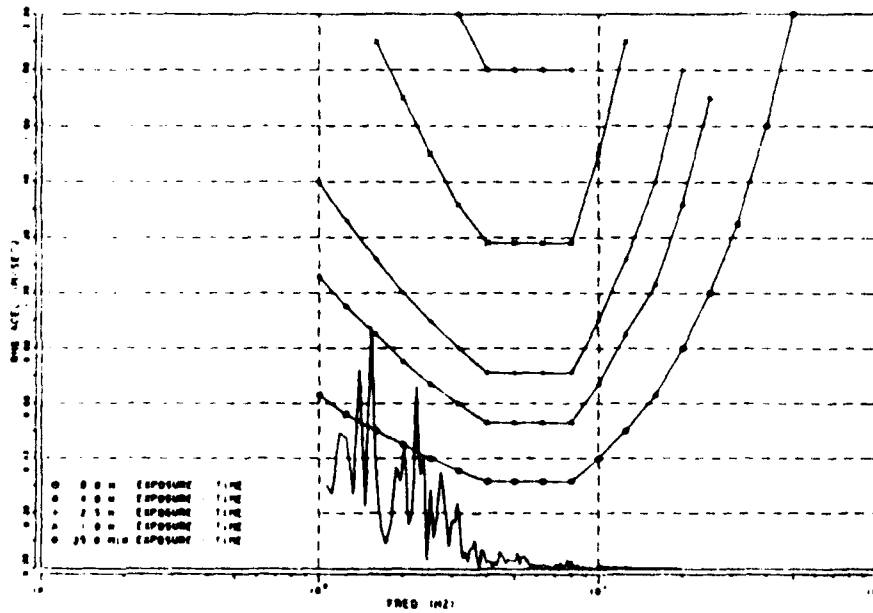


Fig. 28: ISO-weighted RMS acceleration for the driver's
seat ($v = 25$ km/h; P2)

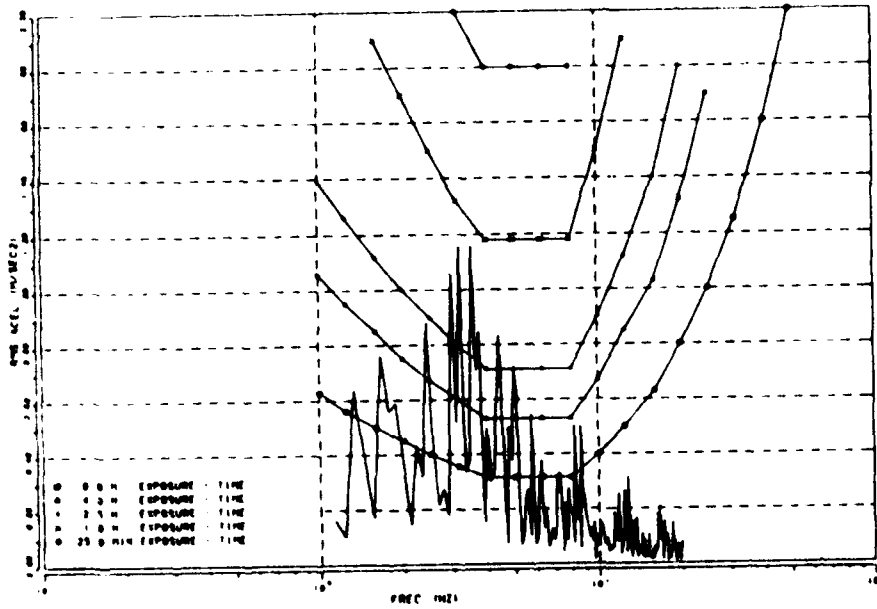


Fig. 29: ISO-weighted RMS acceleration for the SMPT
($v = 40$ km/h; P1)

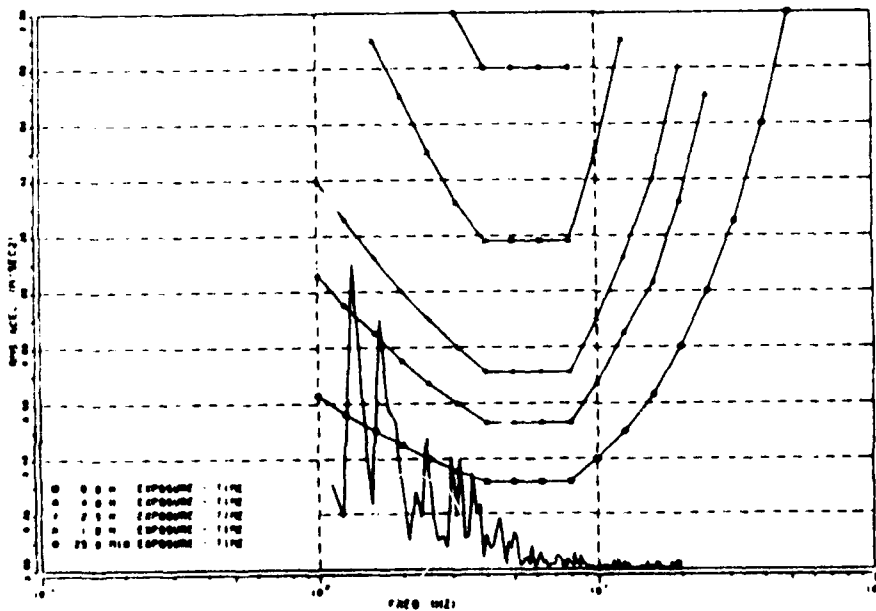


Fig. 30: ISO-weighted RMS acceleration for the driver's
seat ($v = 40$ km/h; P1)

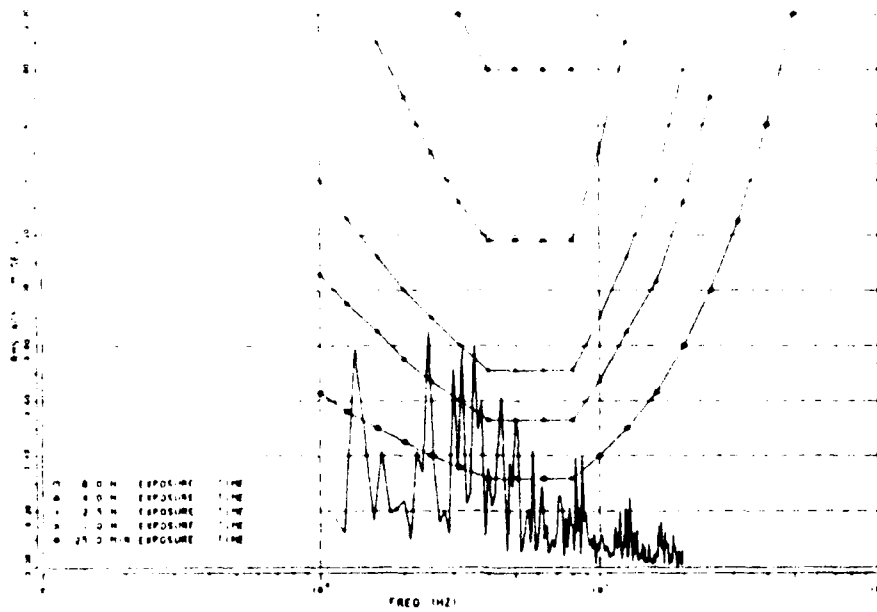


Fig. 31: ISO-weighted RMS acceleration for the SMPT
($v = 40$ km/h; P2)

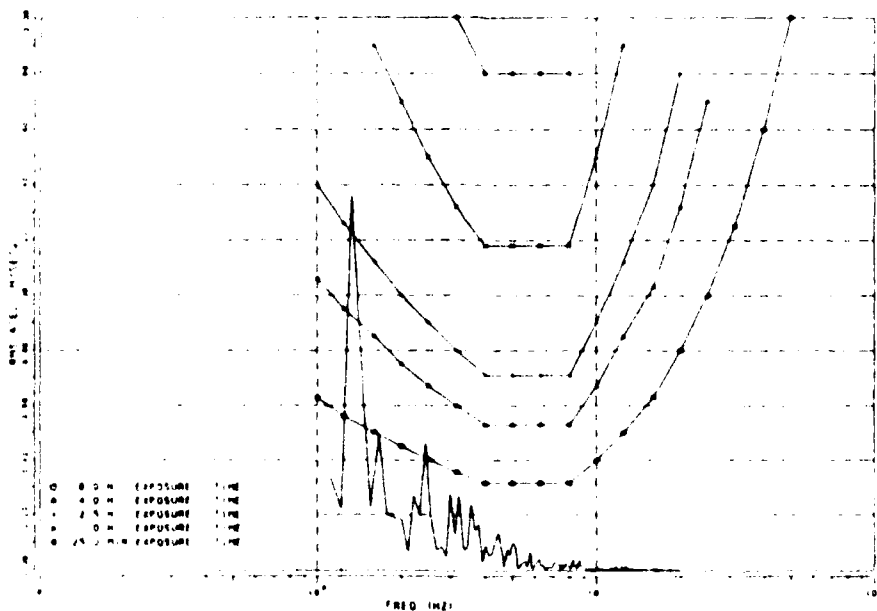


Fig. 32: ISO-weighted RMS acceleration for the driver's
seat ($v = 40$ km/h; P2)



CHARACTERISTICS OF FARM FIELD PROFILES AS SOURCES OF TRACTOR VIBRATION

K. OHMIYA, K. MATSUI

FACULTY OF AGRICULTURE, HOKKAIDO UNIVERSITY, SAPPORO, JAPAN

ABSTRACT

To evaluate farm field profiles as sources of tractor vibration, profiles of meadows and rough terrains were measured and analyzed. A slope angle measuring apparatus with a vertical gyroscope was made to measure profiles using the slope integration method. Periodic unevenness was not found in the measured profiles, therefore it may be assumed that profiles of farm fields, except plowed field and field with furrows, are random and non-periodic. Power spectral densities(0.1-3.5c/m) of measured profiles could be approximated by a straight line on a log-log paper. The mean value of spectral slope(2.3) was steeper than that of the recommended classification of road roughness by ISO(TC108), however, it is suggested that the classification by ISO may be useful to select the profile of test tracks for the vibration test of tractors or the durability test of tractors and implements. Then the coherency functions were calculated to investigate the correlation between two parallel tracks spaced for the tread width of tractor(1.5m), and the value of the coherency functions were small beyond 0.2c/m of road frequency. Therefore it is surmised that profiles of paths of tractor wheels are independent.

INTRODUCTION

Vibration of agricultural tractors and implements are mainly excited by the irregularities of terrain, and it is necessary to investigate the irregularities of the roughness of agricultural fields and roads. Therefore many investigators have measured and analyzed the roughness of them^{1),2)}. The irregularities of runways^{3),4)}, road surfaces⁵⁾ and rough terrains^{6,7)} have also been investigated. "Generalized Terrain-Dynamic Inputs to Vehicle" was discussed by ISO/TC108 and the profiles of artificial tracks for the measurement of seat vibration of tractors and implements were standardized by BS⁸⁾ and ISO⁹⁾.

Thus, many reports described the irregularities of various surfaces, however, the profile of a terrain was investigated as one track and the irregularity of a terrain was evaluated by a measurement of one or two tracks. As an agricultural tractor runs over a terrain, the tractor vibrates by the displacement of terrain which acts on each tractor wheel and it is considered that a tractor is a six degree freedom vibration system. Then, it should be noted that the profiles of terrain are recognized as two parallel tracks which a tractor runs over and it is necessary to investigate the correlation between two parallel tracks.

This paper describes the profile measuring system, the roughness of agricultural fields and the correlation between two parallel tracks which a tractor runs over.

Power spectral densities and coherency functions were calculated by the computer in Hokkaido University (FACOM 230-75, HITAC M200).

MEASURING METHOD

1. Measuring Method of Profiles of Terrain

The conventional method for the measurement of profiles is surveying by a level and a staff, but it is very tedious and it requires much skill.

It is also possible to measure profiles by a string and a scale, however, it is difficult to measure them for long period because of the slack of the string. Therefore many measuring apparatuses for terrain profile have been developed¹⁰⁾. Servo-seismic method¹¹⁾ and surface following wheel and linear potentiometer plus accelerometer method¹²⁾ are available for the measurement of road profiles, but it does not seem that they are suitable to measure profiles of a rough terrain such as seen in an agricultural field. Then it was found that the apparatus used for the slope integration method¹³⁾, which was developed by the University of Michigan and the Land Locomotion Research Laboratory, was suitable for measuring of agricultural fields. The principle of this measuring method may be described as follows: the two quantities to be considered, namely the elevation y and the horizontal component x of a distance along the ground travel, may be related by equations:

$$y - y_0 = \int_0^l \sin \theta \, ds \quad (1)$$

and

$$x = \int_0^l \cos \theta \, ds \quad (2)$$

where y_0 is the elevation of the ground at the beginning of the run and θ is the slope angle of the ground under the vehicle distance l from the origin. To solve the problem two quantities must be measured continuously: the distance traveled by the vehicle, and the slope angle of the ground¹⁴⁾.

The wheelbase of the apparatus affects the accuracy of the elevation severely, so the numerical calculations were done to determine the wheelbase of the apparatus¹⁵⁾. In order to measure and analyze the roughness of agricultural fields, the measured maximum spatial frequency may be equal or below 3-4 c/m, because the essential frequencies of tractor vibration are below approximately 8Hz¹⁶⁾ and the spatial frequency of 4c/m may be equivalent to the frequency of 8Hz of vibration as a tractor runs at a speed of 2m/sec. 150mm of the wheelbase was selected and a self erecting

AD-A148 634

PROCEEDINGS OF THE INTERNATIONAL CONFERENCE ON THE
PERFORMANCE OF OFF-ROAD (U) INTERNATIONAL SOCIETY FOR
TERRAIN-VEHICLE SYSTEMS W J DWYER AUG 84

6/6

UNCLASSIFIED

DAJA45-84-W-0251

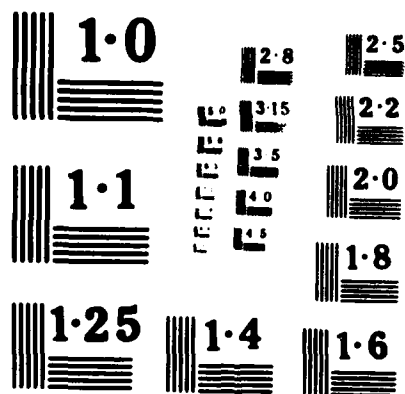
F/G 13/6

NL



DATE
FILMED
85

DT



gyroscope (Tab. 1) was used to measure the slope angle of the terrain.

Fig. 1 shows the general view of the slope angle measuring apparatus. This apparatus has three wheels, one is the front wheel and other two are rear wheels, and the radius of wheel is 150mm. An electric magnetic proximity sensor produces a voltage pulse at 39.5mm increments of travel.

Table 1. Vertical gyroscope

Model	VG23 (Tokyo Aircraft Instrument CO., LTD)
Sources of Electricity	DC 14 \pm 2V 0.6A
Range	Pitch Angle \pm 55°
	Roll Angle \pm 70°
Accuracy of Self Erection	under 0.4°

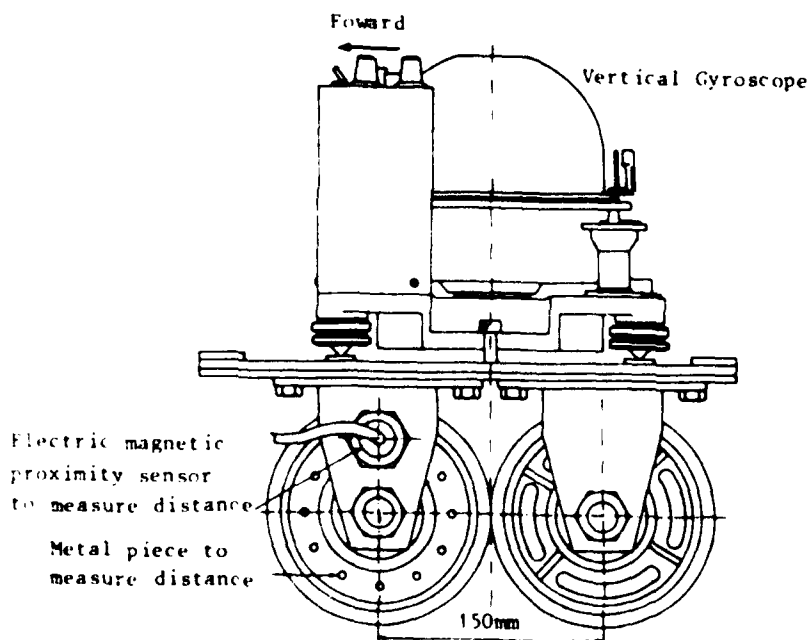


Figure 1. General view of the slope measuring apparatus

The slope angle at every 50mm increment of travel were calculated and profiles were calculated by Eq. (3) and (4).

$$Y(n) - Y(0) = \sum_{i=1}^n \tan \theta_{i-1} \times \Delta x$$

$$\Delta x = \cos \theta_{i-1} \times \Delta l$$

(4)

where

$$Y(n): \text{the elevation at } x = \sum_{i=1}^n \cos \theta_{i-1} \times \Delta l$$

$Y(0)$: the elevation at the beginning of the run

Δl : a unit travel (50mm)

2. The Accuracy of the Profile Measuring System

In order to inspect the accuracy of the profile measuring system using the slope integration method, artificial undulations were made in a soil bin and the slope angle measuring apparatus ran over the surfaces of the artificial terrain. Fig. 2 shows the elevation of the artificial terrain and the elevation measured by the apparatus.

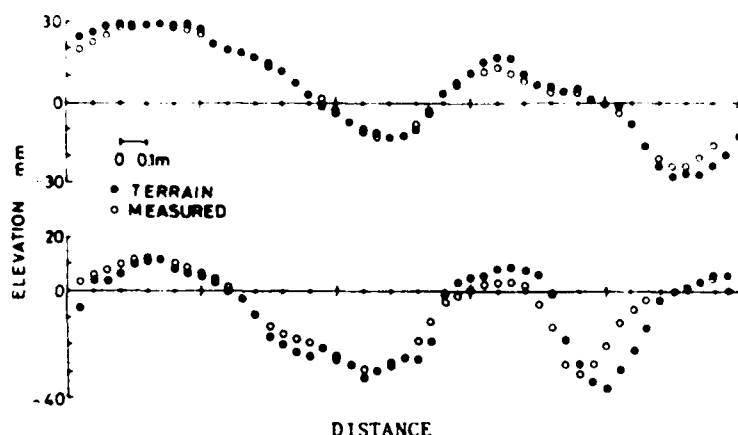


Figure 2. The elevation of the terrain and measured

It seems that the elevation measured by the apparatus is nearly equal to the elevation of the artificial terrain. The power spectral densities were calculated and shown in Fig. 3. Power spectral densities of measured profile are almost in agreement below 3-3.5 c/m.

From the results mentioned above, it is possible to measure the undulation of the terrain under approximately 0.3m of the wave length by the profile measuring system using the slope angle integration method. If the wheelbase of the apparatus is shorter, the spatial frequency of the terrain which the apparatus can measure would be also higher, however, the appa-

tus with shorter wheelbase may not run over the terrain. Therefore, it is recognized that the profile measuring system using the slope integration method and the slope angle measuring apparatus are suitable for measuring profiles of agricultural fields.

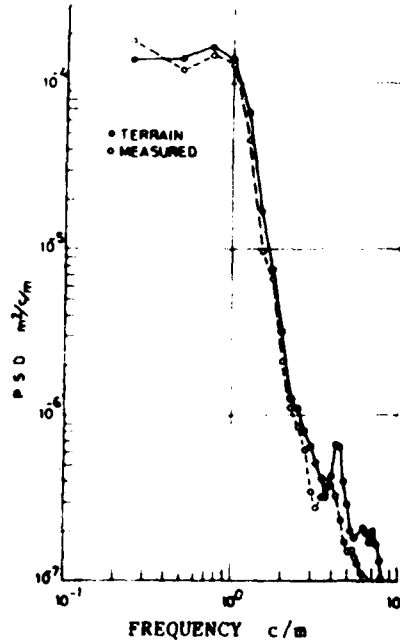


Figure 3. Power spectral densities of measured and original

RESULTS AND DISCUSSION

1. Measuring Sites

Five meadows and two roads were selected for the measurement and analyzation of the profiles of agricultural fields, since tractors run over meadows at high speed and surfaces of meadows are so hard and rough that the vibration of tractor caused by the irregularities of the meadow may be severe. Five meadows and two roads are in the Faculty of Agriculture, Hokkaido University. Tab.2 shows the outline of each meadow and road.

Meadow A-1 and A-2 are in the same place and profiles of A-1 were measured from east to west and A-2 were measured from south to north.

Road F is a rough farm road and G is a concrete track of the tractor pull test.

Table 2. The outline of meadow and road

Name	Length	Numbers of measured tracks	Space of each track
Meadow A-1	45m	19	2.5m
Meadow A-2	45m	19	2.5m
Meadow B	25m	11	0.5m
Meadow C	50m	21	1.5m
Meadow D	50m	11	1.5m
Meadow E	50m	5	1.5m
Road F	50m	4	1.5m
Road G	35m	2	1.5m

2. The Roughness of Agricultural Fields

Fig. 4 shows profiles of meadow A-1 and Fig. 5 shows profiles of meadow A-2. It does not seem that periodic undulations are not found in both profiles.

It does not seem that there are any correlations between the two profiles that are side by side in Fig. 4 and 5. The measured data of the profiles were transformed into the power spectral densities (P.S.D.) of terrain roughness and calculated P.S.D. curves of the profiles of meadows and roads are illustrated in Fig. 6-13.

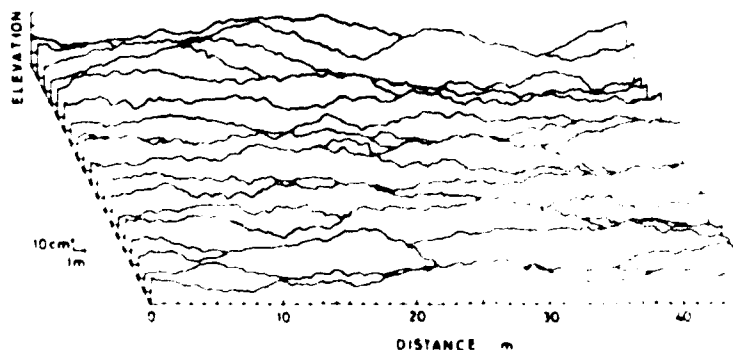


Figure 4. Profiles of meadow A-1

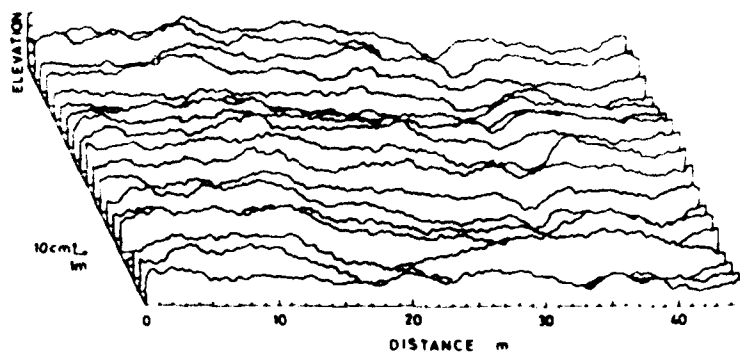


Figure 5. Profiles of meadow A-2

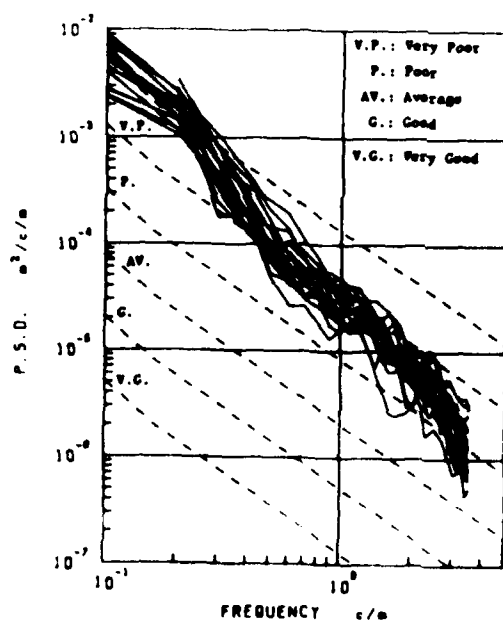


Figure 6. P.S.D. curves of roughness of meadow A-1

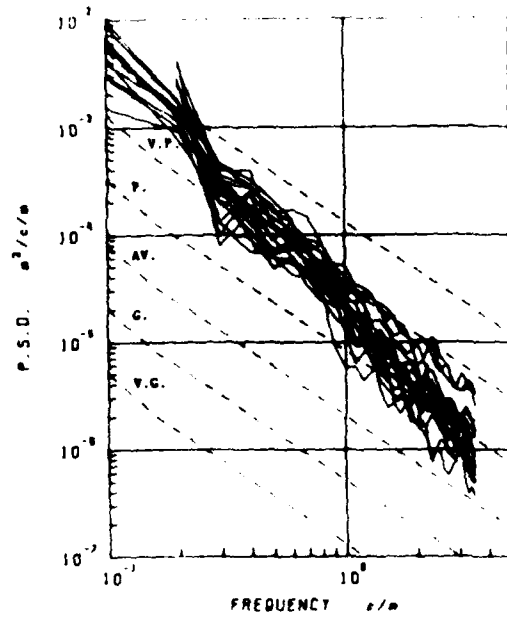


Figure 7. P.S.D. curves of roughness of meadow A-2

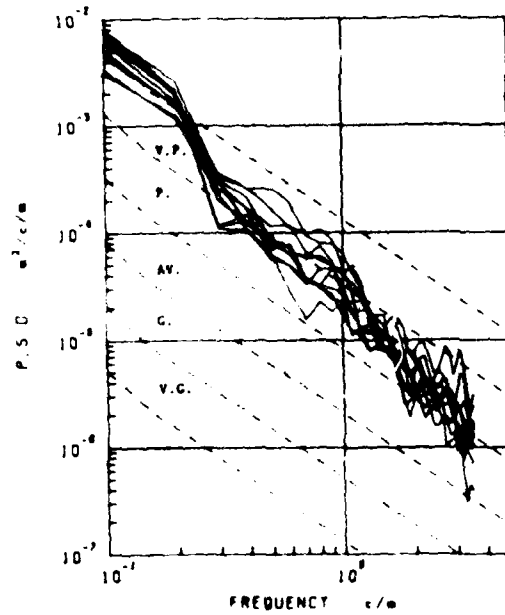


Figure 8. P.S.D. curves of roughness of meadow B

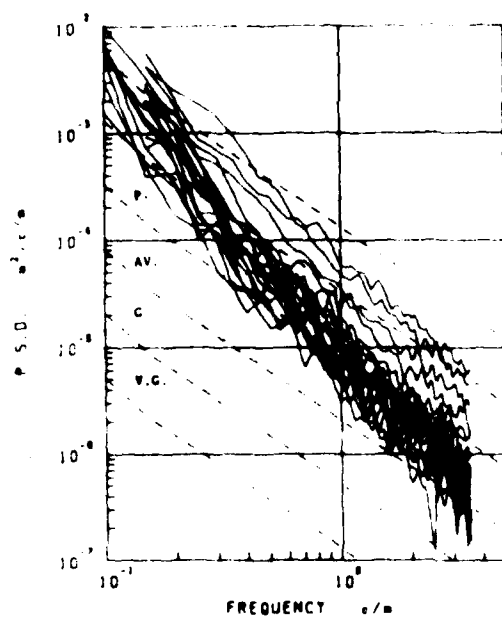


Figure 9. P.S.D. curves of roughness of meadow C

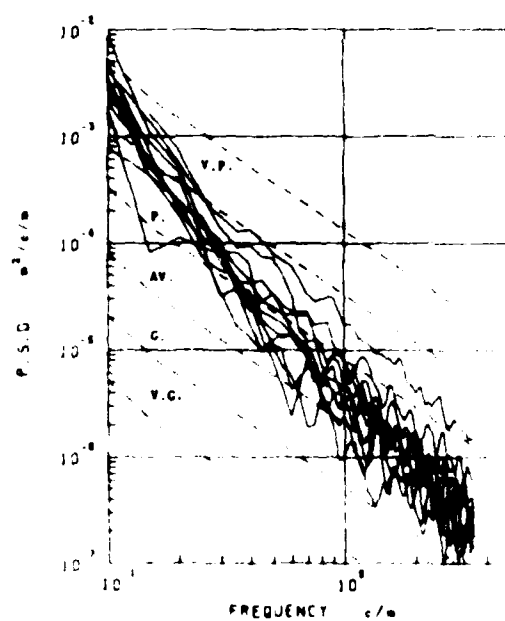


Figure 10. P.S.D. curves of roughness of meadow D

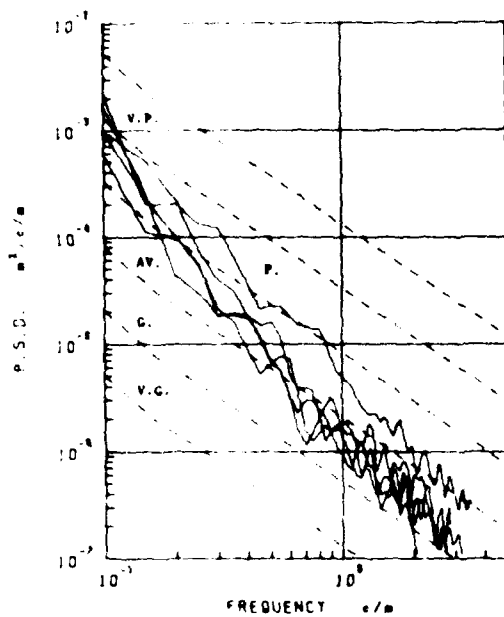


Figure 11. P.S.D. curves of roughness of meadow E

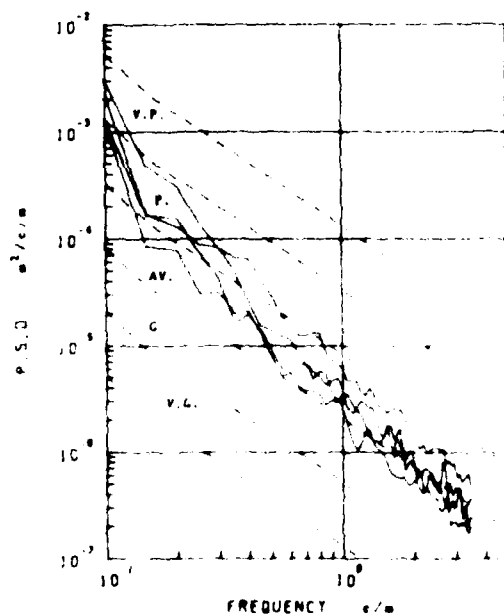


Figure 12. P.S.D. curves of roughness of road F

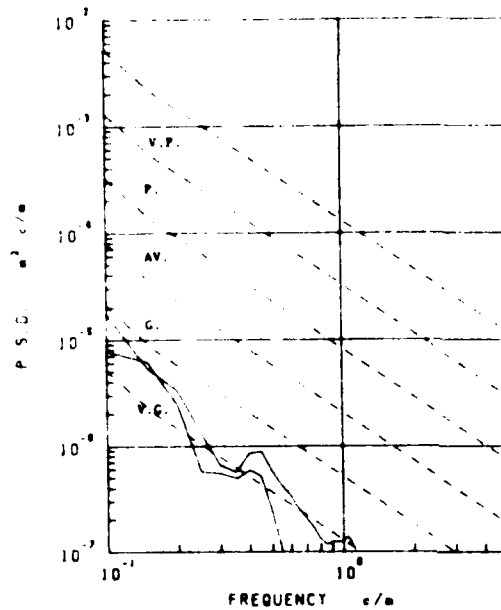


Figure 13. P.S.D. curves of roughness of road G

Fig. 6-11 show that no periodic undulations are found in the rough terrain like meadows, such as many researchers investigated. As P.S.D. curves are illustrated on a log-log paper, curves may be approximated by one straight line. ISO/TC108 investigated the recommended classification of road roughness for the mobile road, and the roughness is classified by the P.S.D. and P.S.D. curve is approximated by two straight lines on a log-log paper (Eq. 5,6).

$$P(f) = P(f_0) \left(\frac{f}{f_0}\right)^{-W_1} \quad (f \leq f_0) \quad (5)$$

$$P(f) = P(f_0) \left(\frac{f}{f_0}\right)^{-W_2} \quad (f \geq f_0) \quad (6)$$

where $P(f)$: P.S.D. of profile $m^2/c/m$

f : spatial frequency c/m

f_0 : $1/2\pi \approx 0.16c/m$

W_1, W_2 : constant $W_1=2$

$W_2=1.5$

The roughness is classified into five grades, very poor, poor, average, good and very good by ISO. The roughness of meadow A-1, A-2 and B were in the range from very poor to poor, meadow C and D were in the range from poor to average, meadow E was in the range from average to good, road F was in the range from poor to average and road G was in the range of very good.

It seems that P.S.D. calculated from data obtained may be approximated by one straight line on a log-log paper. The slope was calculated by Eq. (7) and the mean value of the slope of P.S.D. curve of each terrain is shown in Tab. 3.

$$P(f) = A (f)^{-W} \quad (7)$$

where A, W : constants

Table 3. The slope of P.S.D. curve

Terrain	W^*
Meadow A-1	2.3
Meadow A-2	2.4
Meadow B	2.3
Meadow C	2.2
Meadow D	2.2
Meadow E	2.1
Road F	2.0
Road G	2.0

* W is calculated in the spatial frequency from 0.1 to 3.5 c/m

The slope recommended by ISO is 2 (equal or below $1/2W$ c/m) and 1.5 (equal or over $1/2W$ c/m), and the total mean value of P.S.D. curves of meadows was 2.3. Thus the slope of P.S.D. curves measured is steeper than the slope recommended by ISO, as in the case that Fujimoto investigated the roughness of haul roads for earth moving machinery¹⁷⁾. Therefore the characteristics of the irregularities of agricultural fields such as meadows may be somewhat different from the automobile roads, in other

words, the amplitude of long wavelength undulation of the meadow is larger and the amplitude of short wavelength undulation of the meadow is less than that of the automobile road. However, the meadow A-1, which was evaluated as very rough terrain by our observation, is valued in the range from very poor to poor, meadow E, which was evaluated as smooth terrain by our observation, is valued in the range from poor to good and road C, which is a smooth concrete track, is valued in the range of very good. Thus there seems to be some correlation between the roughness which is evaluated by our observation and the classification of roughness which is recommended by ISO. Consequently it is suggested that the classification of roughness by ISO may be useful in the selecting of the roughness of test track for the vibration measurement of tractors or for the durability test for tractors and implements.

3. Correlation between Two Parallel Tracks

A farm tractor has mostly two axles and four wheels, thus it runs over two parallel tracks. Tractors can be vibrated not only in the vertical mode, the longitudinal mode and the transverse mode but also in the pitch mode, the roll mode and the yaw mode, if the characteristics of two parallel tracks are not the same and each tractor wheel is excited by the displacement of the terrain. Therefore the correlation between the two parallel tracks which a tractor runs over was investigated.

In this paper it is assumed that the tread width of tractor is 1.5m wide. Fig. 14 shows one of the example of P.S.D. curves of two parallel tracks which were 1.5m apart. The roughness of both tracks seems to be almost the same, since both P.S.D. curves are nearly equal.

The mode of tractor vibration depends on the irregularities so that the correlation between the two parallel tracks should be investigated. If there is a correlation between the two parallel tracks, the tractor does not vibrate in the transverse and the roll mode and does not vibrate in

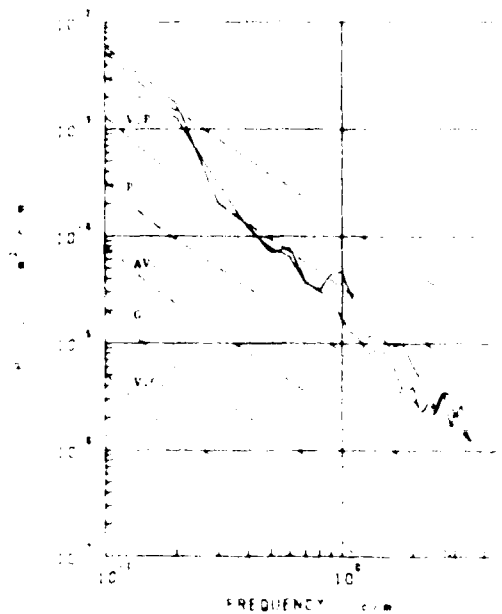


Figure 14. P.S.D. curves of two parallel tracks(measured C)

the longitudinal and the pitch mode so severely. Then the coherence function between the two parallel tracks was calculated to consider the correlation between them.

The coherence function ($r^2(f)$) was calculated by Eq. (8).

$$r^2(f) = \frac{|P_{ZX}(f)|^2}{P_{ZZ}(f) \cdot P_{XX}(f)} \quad (8)$$

where P_{ZZ}, P_{XX} : auto spectral densities of displacements
of each track

P_{ZX} : cross spectral densities of displacements
between the two parallel tracks

f : spatial frequency

Figs. 15-17 show the coherence function between two parallel tracks. From Fig. 15, the coherence function has a large value below 0.2 c/m and has a small value over 0.2 c/m. The coherence function is a function of the linearity between the power of input and the power of output. The value $r^2(f) > 1$ indicates the response is not attribute to

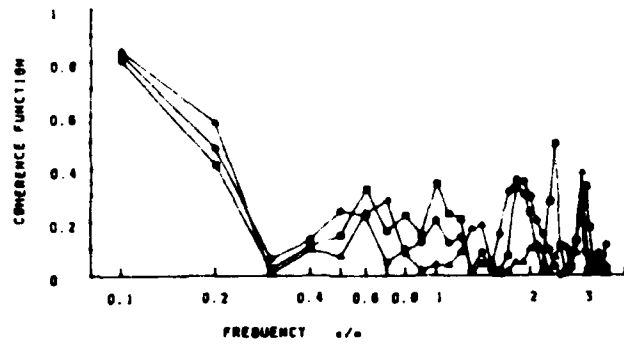


Figure 15. Coherence function of two parallel tracks (meadow B)

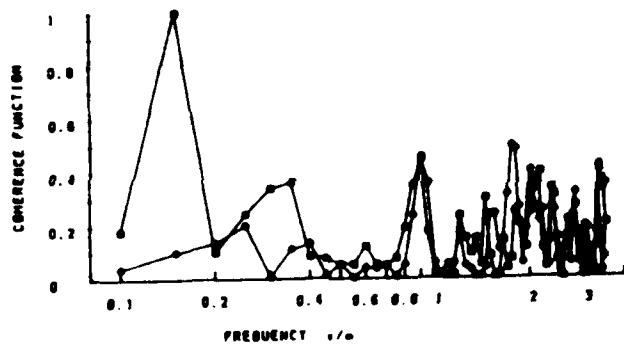


Figure 16. Coherence function of two parallel tracks (meadow D)

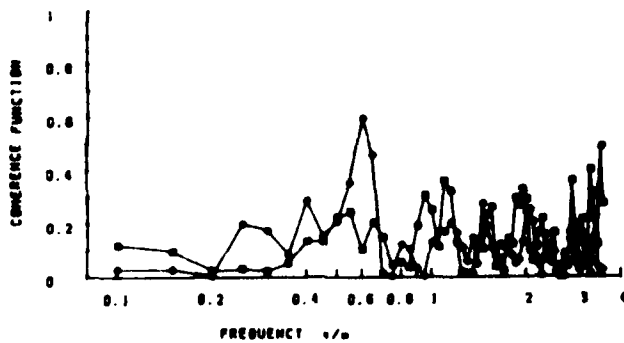


Figure 17. Coherence function of two parallel tracks (meadow E)

the input, due, for example, to extraneous noise or nonlinearity of the system¹⁸⁾. Therefore $r^2(f)$ nearly equal to zero in Fig. 15-17 indicate that the correlation between the two parallel tracks is very small and the two parallel tracks are independent of each other.

CONCLUSIONS

- (1) An apparatus, which has a self erecting vertical gyroscope, has been developed to measure the slope angle of terrain and the profiles of agricultural fields and roads have been measured by the slope integration method. It is found that the slope integration method is suitable to measure rough terrains such as agricultural fields and the data obtained contains under 4c/m of likely interest for tractor vibration.
- (2) Five meadows and two roads were selected to measure the profiles of terrains in order to investigate the roughness of farm fields. The roughness of meadows was not the same grade that would compare with each other, but no periodic undulations were found in all meadows and roads examined. Therefore it is recognized that profiles of farm fields, except plowed fields and fields with furrows, are random and non-periodic.
- (3) Power spectral densities (spatial frequency: 0.1-3.5 c/m) of profiles measured could be approximated by one straight line on a log-log paper, and the mean value of spectral slope (2.3) was steeper than that of the recommended classification of road roughness by ISO/TC108. Then the characteristics of agricultural fields such as meadows may be somewhat different from automobile roads. However, it is suggested that the classification by ISO is useful to select the profile of test track for vibration tests or durability tests of tractors and implements.
- (4) The roughness of two parallel tracks on which the tractor runs over is almost the same. In order to investigate the correlation between two

tracks, the coherence functions were calculated. Values of the coherence function were small, namely it is nearly equal to zero, so two parallel tracks are independent of each other.

Consequently, it should be recognized that the roughness of two parallel tracks are almost the same but there is little correlation between them, since the value of the coherence function is smaller than unity. Therefore a tractor may vibrate not only in the vertical, the longitudinal and the transverse mode but also in the pitch, the roll and the yaw mode.

REFERENCES

1. Wendenborn, J.G., The Irregularities of Farm Roads and Fields as Sources of Farm Vehicles Vibration, J. of Terramechanics, Vol.13, No.3, 1966, 9-40
2. Matthews, J., Ride Comfort for Tractor Operators IV, J. agric. Engng. Res., Vol.11, No.1, 1966, 44-57
3. Walls, J.H. et al, Some Measurement and Power Spectra of Runway Roughness, N.A.C.A TN3305, 1954
4. Thompson, W.E., Measurements and Power Spectra of Runway Roughness at Airports in Countries of the North Atlantic Treaty Organization, N.A.C.A TN4303, 1958
5. Pevzner, Ya.M., Statistical Description of the Micro Profiles of Automobile Roads, J. of Terramechanics, Vol.1, No.4, 1964, 5-14
6. Kozin, F. et al, Statistical Studies of Stubble Ground Roughness, Land Locomotion Laboratory Report, No.8931, LL 95, 1963
7. Bogdanoff, J.L. et al, Introduction to a Statistical Theory of Land Locomotion II, J. of Terramechanics, Vol.2, No.3, 1965, 17-27
8. BS4220, Methods of Test for Seats on Agricultural Wheeled Tractors Part 1, 1974
9. ISO5008, Agricultural Wheeled Tractors and Field Machinery - Measurement of Whole-body Vibration of the Operator, 1979
10. Hveem, F.N., Devices for Recording and Evaluating Pavement Roughness, Highway Research Board Bulletin 264, 1962, 1-23
11. Spangler, E.B., Servo-Seismic Method of Measuring Road Profile, Highway Research Board Bulletin 323, 1962, 33-41

12. La Barre, R.P. et al, The Measurement and Analysis of Road Surface Roughness, MIRA Report, No.1970/5, 1970
 13. Sattinger, I.J. et al, An Instrumentation System for the Measurement of Terrain Geometry, Research Report of the Land Locomotion Research Laboratory, No.4, 1956, 13-19
 14. the same as 13.
 15. Ohmiya, K. et al, Studies on Agricultural Terrain Profiles I, J. of the Soc. of Agric. Mach. JAPAN, Vol.44, No.1, 1982, 17-22(in Japanese)
 16. the same as 2.
 17. Fujimoto, Y., Spectrum Analysis of Road Roughness for Earthmoving Machinery, J. of Terramechanics, Vol.20, No.1, 1983, 43-60
 18. Edited by Harris, C.M. and Crede, C.E., Shock and Vibration Handbook, McGRAW-HILL BOOK CO., 1976, 27-7
- 